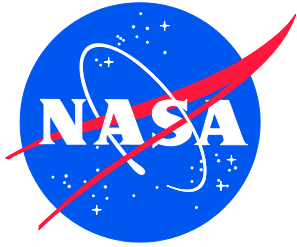


NASA/TM-20210017934
NESC-RP-20-01585



Arecibo Observatory Auxiliary M4N Socket Termination Failure Investigation

*Gregory Harrigan/NESC and Azita Valinia/NESC
Langley Research Center, Hampton, Virginia*

*Nathan Trepal
Kennedy Space Center, Florida*

*Pavel Babuska and Vinay Goyal
The Aerospace Corporation, El Segundo, California*

NASA STI Program Report Series

Since its founding, NASA has been dedicated to the advancement of aeronautics and space science. The NASA scientific and technical information (STI) program plays a key part in helping NASA maintain this important role.

The NASA STI program operates under the auspices of the Agency Chief Information Officer. It collects, organizes, provides for archiving, and disseminates NASA's STI. The NASA STI program provides access to the NTRS Registered and its public interface, the NASA Technical Reports Server, thus providing one of the largest collections of aeronautical and space science STI in the world. Results are published in both non-NASA channels and by NASA in the NASA STI Report Series, which includes the following report types:

- **TECHNICAL PUBLICATION.** Reports of completed research or a major significant phase of research that present the results of NASA Programs and include extensive data or theoretical analysis. Includes compilations of significant scientific and technical data and information deemed to be of continuing reference value. NASA counterpart of peer-reviewed formal professional papers but has less stringent limitations on manuscript length and extent of graphic presentations.
- **TECHNICAL MEMORANDUM.** Scientific and technical findings that are preliminary or of specialized interest, e.g., quick release reports, working papers, and bibliographies that contain minimal annotation. Does not contain extensive analysis.
- **CONTRACTOR REPORT.** Scientific and technical findings by NASA-sponsored contractors and grantees.

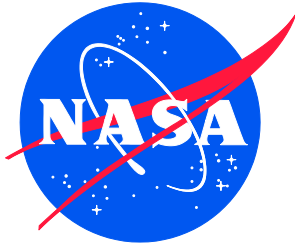
- **CONFERENCE PUBLICATION.** Collected papers from scientific and technical conferences, symposia, seminars, or other meetings sponsored or co-sponsored by NASA.
- **SPECIAL PUBLICATION.** Scientific, technical, or historical information from NASA programs, projects, and missions, often concerned with subjects having substantial public interest.
- **TECHNICAL TRANSLATION.** English-language translations of foreign scientific and technical material pertinent to NASA's mission.

Specialized services also include organizing and publishing research results, distributing specialized research announcements and feeds, providing information desk and personal search support, and enabling data exchange services.

For more information about the NASA STI program, see the following:

- Access the NASA STI program home page at <http://www.sti.nasa.gov>
- Help desk contact information: <https://www.sti.nasa.gov/sti-contact-form/> and select the "General" help request type.

NASA/TM-20210017934
NESC-RP-20-01585



Arecibo Observatory Auxiliary M4N Socket Termination Failure Investigation

*Gregory Harrigan/NESC and Azita Valinia/NESC
Langley Research Center, Hampton, Virginia*

*Nathan Trepal
Kennedy Space Center, Florida*

*Pavel Babuska and Vinay Goyal
The Aerospace Corporation, El Segundo, California*

National Aeronautics and
Space Administration

Langley Research Center
Hampton, Virginia 23681-2199

June 2021

Acknowledgments

The team would like to thank the many peer reviewers who provided valuable input to this report.

The use of trademarks or names of manufacturers in the report is for accurate reporting and does not constitute an official endorsement, either expressed or implied, of such products or manufacturers by the National Aeronautics and Space Administration.

Available from:

NASA STI Program / Mail Stop 148
NASA Langley Research Center
Hampton, VA 23681-2199
Fax: 757-864-6500



NASA Engineering and Safety Center Technical Assessment Report

Arecibo Observatory Auxiliary M4N Socket Termination Failure Investigation

June 15, 2021

Report Approval and Revision History

NOTE: This document was approved at the June 15, 2021, NRB. This document was submitted to the NESC Director on June 17, 2021, for configuration control.

Approved:	<i>Original Signature on File (MK)</i>	6/17/21
	NESC Director	Date

Version	Description of Revision	Office of Primary Responsibility	Effective Date
1.0	Initial release	Azita Valinia, NESC Chief Scientist, GSFC	6/15/21
1.1	Minor edits to executive summary for clarification	Azita Valinia, NESC Chief Scientist, GSFC	6/23/21

Table of Contents

Technical Assessment Report

1.0	Notification and Authorization	9
2.0	Signature Page	10
3.0	Team List	11
3.1	Acknowledgments	11
4.0	Executive Summary	12
5.0	Assessment Plan	14
6.0	Failure Event Introduction and Observatory Overview	15
6.1	Arecibo Observatory Timeline	16
6.2	Aux M4N Cable Structure Description.....	18
6.3	Investigation Process and Report Structure	22
6.4	Fabrication Process	23
7.0	Data Analysis	26
7.1	Arecibo Observatory Structural Loading Assessment	26
7.2	Failure Analysis of M4N Aux Socket/Cable	26
7.2.1	Socket and Cable	27
7.2.2	Zinc Casting	32
7.2.3	Wires	37
7.2.4	Metallography	58
7.2.5	Corrosion	70
7.2.6	Summary and Conclusions – Failure Analysis	78
7.2.7	Mechanical Testing.....	81
7.3	Structural Assessment of Auxiliary Main Socket Joint	86
7.3.1	Finite Element Model	86
7.3.2	Material Property Development Testing and Strength Properties	87
7.3.3	Boundary Conditions and Loads.....	88
7.3.4	Socket Joint Physics.....	89
7.3.5	Analysis-Test Correlation	91
7.3.6	Strength Assessment	93
7.3.7	Cumulative Damage	94
7.3.8	Discussion on Transient Loading (e.g., Hurricane Maria, earthquakes).....	100
7.3.9	Effects of As-built Wire “Brooming”	100
7.3.10	Effects of Defects within Zinc Spelter.....	102
7.3.11	Summary Based on Analysis Predictions	106
7.4	Design Factors and Standards.....	106
7.4.1	Insufficient Design Factor of Safety	106
7.4.2	Design Standards	107
7.4.3	Qualification Methodology Discussion	107
7.4.4	Redundancy	109
7.4.5	Live Load to Dead Load (LL/DL) Ratio.....	109
7.4.6	Cable Nonlinearity	111
7.4.7	Design Factors of Safety	112
7.5	Root Cause Analysis and Failure Progression	113
7.5.1	Design	113
7.5.2	Loads and Environments in Service	114
7.5.3	Build Variability	115
7.5.4	Inspections	116
7.5.5	Environmental Assisted Degradation	117
7.5.6	Failure Mechanisms	118

7.6	Failure Progression	119
7.7	Summary of Findings.....	120
8.0	Findings, Observations, and NESC Recommendations	121
8.1	Findings	121
8.2	Observations	123
8.3	NESC Recommendations	124
9.0	Alternative Viewpoint(s)	124
10.0	Other Deliverables	124
11.0	Lessons Learned.....	124
12.0	Recommendations for NASA Standards and Specifications.....	124
13.0	Definition of Terms.....	124
14.0	Acronyms and Nomenclature List.....	126
15.0	References.....	127
Appendix A. KSC Failure Analysis Report		129
Appendix B. MSFC Materials Characterization Testing.....		466
Appendix C. Structural Analysis of the Failed Arecibo Observatory Auxiliary Main Socket Joint.....		550
Appendix D. Arecibo Reference Drawings, 1992.....		585

List of Figures

Figure 6.0-1.	Tower 4, including Socket.....	15
Figure 6.0-2.	Wire Strands inside Failed Socket.....	16
Figure 6.0-3.	Pulled-Out Cable Wire, Strands and Zinc (side view).....	16
Figure 6.2-1.	Color-coded Diagram of Feed Platform Support Structure with Upgrade Indications .	18
Figure 6.2-2.	Elevation Drawing S-2, highlighting Failed Aux M4N Cable in Red.....	19
Figure 6.2-3.	Horizontal Cable Projections, Drawing S-1, highlighting Failed Aux M4N Cable in Red.....	19
Figure 6.2-4.	Feed Platform Plan, Drawing S-9, highlighting Failed Aux M4N Cable in Red	19
Figure 6.2-5.	Cross Section of 1x127 Structural Strand	20
Figure 6.2-6.	Cable Details, Drawing S-13, Specific to Failed M4N Auxiliary Cable	21
Figure 6.2-7.	WWW Shop Drawing for Open Strand Socket	21
Figure 6.2-8.	Nomenclature used to Describe Parts of Failed Socket.....	22
Figure 6.4-1.	Aux M4N Wire Reconstruction (left) and Interim Forensic Analysis of Zinc Spelter and Wires showing Wire Fracture Pattern of Wire Segments Left in Socket Termination (right)	25
Figure 6.4-2.	2003 Photo of Aux M4N (left) showing ~0.5-inch Zinc Seating Extrusion and 2019 Photo (right) showing ~1 3/8-inches Extrusion [ref. 1].....	25
Figure 7.2.1.1-1.	As-received Socket Cavity	27
Figure 7.2.1.1-2.	Overlays of Intact Wires that Pulled Free of Joint, with Full Broom Above	28
Figure 7.2.1.1-3.	Dimension Diagram and Specification Row from Structural Strand and Wire Rope Catalog [ref. 8].....	28
Figure 7.2.1.2-1.	As-received Cable End Section	29
Figure 7.2.1.2-2.	Cable Cross Section.....	29
Figure 7.2.1.3-1.	(Appendix A Figure 30). Photo of Socket Base with Top of Socket at Top of Image ..	30
Figure 7.2.1.3-2.	(Appendix A Figure 31). Zinc Socket Cavity Transverse Section Labeling	31
Figure 7.2.1.3-3.	(Appendix A Figure 32). Section of Zinc with Encased Wires before (left) and after (right) Removal of Zinc via Dissolution in Acid.....	32
Figure 7.2.2.1-1.	(Appendix A Figure 1). 3 o'clock Half of Socket Cavity.....	33
Figure 7.2.2.1-2.	(Appendix A Figure 53). Gap between Socket Wall Inner Diameter and Zinc Casting Outer Diameter nearest Socket Base	33

Figure 7.2.2.1-3.	(Appendix A Figure 54). Gap between Socket Wall Inner Diameter and Zinc Casting Outer Diameter at Casting Cap.....	34
Figure 7.2.2.2-1.	(Appendix A Figure 57). Close-up View of a Single Gas Bubble in Zinc Casting with Corrosion Product Buildup on Walls.....	35
Figure 7.2.2.2-2.	(Appendix A Figure 283). Etch of Longitudinal Cut Face and Zinc Grains below Casting Cap	36
Figure 7.2.2.2-3.	(Appendix A Figure 2). Oblique View of Casting Cap Immediately above Second Gas Bubble	37
Figure 7.2.3.1-1.	Representation of Cable Wire Map at Socket Base (varies with distance from end)	38
Figure 7.2.3.2-1.	Stereomicroscope Images of Similar Surface Defects found on Wires G, AN, and AO	39
Figure 7.2.3.2-2.	Stereomicroscope Images of Surface Defect found on Wire AR (nick visible in top row left image was likely from sectioning)	40
Figure 7.2.3.2-3.	Stereomicroscope Images of Surface Defect found on Wire BA	40
Figure 7.2.3.2-4.	SEM Images of Surface Defect found on Wire BA.....	41
Figure 7.2.3.2-5.	Reconstruction of Wire Locations following Zinc Removal with Identified Fracture Morphology	42
Figure 7.2.3.2-6.	Fatigue Cracking in Heavily Drawn Steel Wires [ref. 9]	44
Figure 7.2.3.2-7.	Closer Image of Surface-initiated Fatigue Crack in Heavily Drawn Steel Wire [ref. 9]	44
Figure 7.2.3.2-8.	Fatigue Fracture Surface with Secondary Cracks.....	45
Figure 7.2.3.2-9.	Closer Image of Internally Initiated Fatigue Crack, showing Facet Area [ref. 9]	45
Figure 7.2.3.2-10.	Images of Gradually More Progressively Cold-drawn Pearlitic Steel Wire Specimens Failed by Tensile Overload [ref. 10]	46
Figure 7.2.3.2-11.	Images of Aux M4N Socket Wire AS	47
Figure 7.2.3.2-12.	Images of Aux M4N Socket Wire U	48
Figure 7.2.3.2-13.	Images of Aux M4N Socket Wire Z.....	49
Figure 7.2.3.2-14.	Images of Aux M4N Socket Wire EH.....	50
Figure 7.2.3.2-15.	Images of Aux M4N Socket Wire S	51
Figure 7.2.3.2-16.	Reconstruction of Wire Locations following Zinc Removal with Identified Fracture Morphology (outline color of overlay) and Percent Necking (fill color of overlay)	52
Figure 7.2.3.3-1.	(Appendix A Figure 58). Measurement of Wire-end Displacement of Wire BC within Zinc Casting (image was taken from 3 o'clock half)	53
Figure 7.2.3.3-2.	(Appendix A Figure 71). Slice 3a was Sectioned Longitudinally, Revealing Second Gas Bubble below Casting Cap.....	53
Figure 7.2.3.3-3.	(Appendix A Figure 89). Wire Embedment in Zinc Casting.....	54
Figure 7.2.3.3-4.	(Appendix A Figure 102). Relatively Large Volumes of Corrosion Visible in Wire Channels above Wires	54
Figure 7.2.3.3-5.	(Appendix A Figure 69). Closer View of Back of Socket Cavity on Slice 9a (view 1).....	55
Figure 7.2.3.3-6.	(Appendix A Figure 70). Closer View of Back of Socket Cavity on Slice 9a (view 2).....	55
Figure 7.2.3.3-7.	(Appendix A Figure 65). View of Casting Cap Side of Brittle Fracture Region in Back of Socket Cavity on Slice 3a (view 1)	56
Figure 7.2.3.3-8.	(Appendix A Figure 66). View of Casting Cap Side of Brittle Fracture Region in Back of Socket Cavity on Slice 3a (view 2)	56
Figure 7.2.3.3-9.	(Appendix A Figure 104). Image of Faceted Surface within Socket Cavity	57
Figure 7.2.3.3-10.	(Appendix A Figure 68). View of Casting Cap Side of Brittle Fracture Region in Back of Socket Cavity on Slice 3a	57
Figure 7.2.3.3-11.	(Appendix A Figures 85, 86). Surface of Additional Longitudinal Cut made on Slice 3a	58

Figure 7.2.4-1.	(Appendix A Figure 79). Zinc Grain Structure Adjacent to Cable/Zinc Slug	59
Figure 7.2.4-2.	(Appendix A Figure 74). Directional Changes in Elongated Grain Direction from Grains analyzed in Slice 3c (from Appendix A Figure 288)	60
Figure 7.2.4-3.	(Appendix A Figure 75). Directional Changes in Elongated Grain Direction from Grains Analyzed in Slice 9g (from Appendix A Figure 293).....	60
Figure 7.2.4-4.	(Appendix A Figure 78). Measurements taken on Appendix A Figure 295 from Plane Adjacent to Cable/Zinc Slug.....	61
Figure 7.2.4-5.	(Appendix A Figure 80). Metallograph Image of Tint Etch of Large Grains Near Socket Base and Zinc Casting Outer Diameter	62
Figure 7.2.4-6.	(Appendix A Figure 81). Metallograph Image of Tint Etch of Large Grains Present Near Socket Base and Zinc Casting Outer Diameter.....	63
Figure 7.2.4-7.	(Appendix A Figure 82). Metallograph Image of Tint Etch of Small Grains Present Near Socket Base and Cable/Zinc Slug Boundary	64
Figure 7.2.4-8.	(Appendix A Figure 83). Cracks Present in Appendix A Figure 295 Adjacent to Cable/Zinc Slug Boundary	65
Figure 7.2.4.1-1.	(Appendix A Figure 55). Close-up View of Crack Present in Zinc Casting at 12 o'clock (9 o'clock half)	67
Figure 7.2.4.1-2.	(Appendix A Figure 56). Close-up View of Crack Present in Zinc Casting at 12 o'clock (3 o'clock half)	67
Figure 7.2.4.1-3.	(Appendix A Figure 84). Cracks and Voids Found during Metallography of Slice 3c	68
Figure 7.2.4.1-4.	(Appendix A Figure 287). Metallographic Specimens of 6 o'clock Side of Longitudinal Cut Face of Slice 3c	68
Figure 7.2.4.1-5.	(Appendix A Figure 288). Metallographic Specimens of 6 o'clock Side of Longitudinal Cut Face of Slice 3c	69
Figure 7.2.4.1-6.	(Appendix A Figure 289). Metallographic Specimen of 12 o'clock Side of Longitudinal Cut Face of Slice 3c	69
Figure 7.2.5-1.	(Appendix A Figure 96). 3 o'clock Side of Inner Diameter Socket Wall, showing Surface behind Outer Diameter of Zinc Casting	70
Figure 7.2.5-2.	(Appendix A Figure 97). 9 o'clock Side of Inner Diameter Socket Wall, showing Surface behind Outer Diameter of Zinc Casting	71
Figure 7.2.5-3.	(Appendix A Figure 98). Outer Diameter of 3 o'clock Side of Zinc Casting of Slices 3a, 3c, and 3e.....	71
Figure 7.2.5-4.	(Appendix A Figure 99). Wire Holes in Zinc Casting.....	72
Figure 7.2.5-5.	(Appendix A Figure 100). Corrosion around Wire Hole.....	73
Figure 7.2.5-6.	(Appendix A Figures 69 and 70). Closer View of Back of Socket Cavity on Slice 9a	74
Figure 7.2.5-7.	(Appendix A Figure 101). Extensive and Relatively Thick Corrosion on Zinc Casting Wire Channels	74
Figure 7.2.5-8.	(Appendix A Figure 102). Relatively Large Volumes of Corrosion Visible in Wire Channels above Wires (wire channel for Wire AN is pointed to here)	75
Figure 7.2.5-9.	(Appendix A Figure 103). Embedded Wire (wire AN) removed from Wire Channel ..	75
Figure 7.2.5-10.	(Appendix A Figure 105). Wire AE, Mechanically Removed, showed Similar Quantity of Corrosion along Length of Wire embedded in Slice 3g, as seen on Wire AN in Figure 7.2.5-9.....	77
Figure 7.2.5-11.	(Appendix A Figure 172). Hydrochloric Acid Wire Fracture Reveal on Slice 9g	77
Figure 7.2.5-12.	(Appendix A Figure 106). Wires AI and AJ had Visibly Good Adhesion of Zinc along Wire Surfaces that were Embedded in Slice 3g.....	78
Figure 7.2.7.1-1.	Location of Wires Approximately 15 ft from Socket.....	82
Figure 7.2.7.2-1.	Metallography of Socket Slug Material.....	83
Figure 7.2.7.2-2.	Metallography of Ingot Material Showing Equiaxed Grains.....	83

Figure 7.2.7.2-3.	Metallography of Ingot Material Showing Elongated Grains	84
Figure 7.2.7.2-4.	Comparison of Small-scale Tensile Results	85
Figure 7.2.7.2-5.	DIC of Standard Size Tension Specimen	85
Figure 7.2.7.2-6.	Comparison of Compression Strength at 8% Strain	86
Figure 7.3.1-1.	Socket is Modeled as a Simplified Version that does not consider Clevis Pin and Holes.....	87
Figure 7.3.2-1.	True Stress-Strain Curves for the Range of Zinc Material Properties (left) and Baseline Steel Material Property (right).....	88
Figure 7.3.4-1.	As Loading in Cables Increases (left to right), the Zinc Distributes Load amongst Wires within the Socket in a Mechanism Analogous to Metal Matrix Reinforced Composites	90
Figure 7.3.4-2.	Comparison of Representative Zinc Plastic Strain Fields for Three Different Wire Brooming Configurations highlighting Bands of Significant Shear for Less-broomed Cable Ends.....	91
Figure 7.3.5-1.	Highest Stresses were not Predicted to be Planar; Failure Surface followed a Spheroid Shape, matching Stepped Patterns seen in Forensic Investigation.....	92
Figure 7.3.6-1.	Wire Stresses are Highest in Outer Wires; Wire Stress was Relatively High Compared with the Material Capability, Regardless of Zinc Material Model	93
Figure 7.3.7-1.	Stress History and Hysteresis from Repeated Loading above Proof Load Level.....	96
Figure 7.3.7-2.	Yield State Shown in Red for Zinc and Wires for each Analysis Step.....	97
Figure 7.3.7-3.	Modified Goodman Diagram showing Separation of Finite and Infinite Life Regions with Annotations for Aux M4N Operational Space	98
Figure 7.3.7-4.	Cumulative Damage Can Occur due to Combination of Cyclic Loading and Sustained Loading	99
Figure 7.3.9-1.	As-built Wire Distribution compared with Ideal Brooming Configuration and Poorly Broomed Configuration	101
Figure 7.3.10-1.	Pictographic Representation of Wire Stress over Cross Section and Initially Failed Wires at 3 o'clock Side.....	103
Figure 7.3.10-2.	Finite Element Model Visualization of Three Initially Failed Wires	103
Figure 7.3.10-3.	Model Cross-sectional Stresses for Differing Numbers of Failed Wires showing Stress Redistribution Radially and Circumferentially	104
Figure 7.3.10-4.	Pictographic Representation of Failure Progression Overlaid on Forensics Failure Mode Coloring.....	105
Figure 7.3.10-5.	Plastic Strain Field Comparison between Three Failed Wires (left) and 38 Failed Wires (right)	105
Figure 7.4.6-1.	Stress Response in Wire is Nonlinear with Increasing Applied Tension Load	111
Figure C-1.	Socket is Modeled as Simplified Version that does not Consider Clevis Pin and Holes.....	552
Figure C-2.	True Stress-Strain Curves for the Range of Zinc Material Properties (left) and Baseline Steel Material Property (right).....	553
Figure C-3.	Clevis Joint was not Modeled in Baseline FEMs as its Effects were Found to be Insignificant.....	553
Figure C-4.	Operational Load is Roughly 600,000 lb (see Appendix D)	555
Figure C-5.	Temperature (F) and Wind (mph) Trends between October 30 and November 2, 2020 (timescale in seconds).....	555
Figure C-6.	Strain Measurements in Microstrain between October 30 and November 2, 2020 (timescale in seconds).....	556
Figure C-7.	As Loading in Cables Increases (left to right), the Zinc Distributes Load amongst Wires within Socket in Mechanism Analogous to Metal Matrix Reinforced Composites	557

Figure C-8.	Comparison of Representative Zinc Plastic Strain Fields for Three Different Wire Brooming Configurations, highlighting Bands of Significant Shear for Less-broomed Cable Ends.....	558
Figure C-9.	Highest Stresses were not Predicted to be Planar; Failure Surface followed a Spheroid Shape, matching Stepped Patterns seen in Forensic Investigation.....	560
Figure C-10.	Many Outer Wires Exhibited a Shear-type Failure (orange and yellow), while Inner wires exhibited Cup-cone Failure (gray and purple)	560
Figure C-11.	Wire Stresses are Highest in Outer Wires; Wire Stress was Relatively High Compared with Material Capability, Regardless of Zinc Material Model	563
Figure C-12.	Stress History and Hysteresis from Repeated Loading above Proof Load Level.....	566
Figure C-13.	Yield State (shown in red) for Zinc and Wires for each Analysis Step.....	567
Figure C-14.	Modified Goodman Diagram showing Separation of Finite and Infinite Life Regions with Annotations for Aux M4N Operational Space	568
Figure C-15.	Cumulative Damage Can Occur due to Combination of Cyclic Loading and Sustained Loading	569
Figure C-16.	Isometric Views of As-built Wire Brooming within Failed M4N Socket.....	571
Figure C-17.	As-built Wire Distribution compared with Ideal Brooming Configuration and Poorly Broomed Configuration	571
Figure C-18.	Outer Wire Stresses Increase with Decreasing Levels of Quality Brooming.....	572
Figure C-19.	Pictographic Representation of Wire Stress over Cross Section and Initially Failed Wires at 3 o'clock Side.....	574
Figure C-20.	FEM Visualization of Three Initially Failed Wires.....	574
Figure C-21.	Model Cross-sectional Stresses for Differing Numbers of Failed Wires showing Stress Redistribution Radially and Circumferentially	575
Figure C-22.	Pictographic Representation of Failure Progression Overlaid on Forensics Failure Mode Coloring.....	576
Figure C-23.	Plastic Strain Field Comparison between Three (left) and 38 Failed Wires (right)	576
Figure C-24.	Stress Response in Wire is Nonlinear with Increasing Applied Tension Load	582

List of Tables

Table 5.0-1.	NASA Investigation Roles and Responsibilities	14
Table 6.1-1.	Arecibo Observatory Timeline [reprinted from ref. 1]	16
Table 6.3-1.	Top-level Fishbone Structure (ratings not shown)	23
Table 7.2.3.1-1.	Identification of Fractured and Intact Wires.....	38
Table 7.2.7.1-1.	Wire Tensile Test Results.....	81
Table 7.4.2-1.	Design Factors of Safety from Various Industry Standards [ref. 22]	107
Table 7.4.5-1.	Load Factors required in Evaluation of Load Combinations.....	110
Table C-1.	Overall Confidence in Model, Assessed using Confidence Matrix along with Mitigation Options for Areas of Low Confidence.....	562
Table C-2.	Design Factors of Safety from Various Industry Standards [ref. 22]	578
Table C-3.	Load Factors required in Evaluation of Load Combinations.....	581

Technical Assessment Report

1.0 Notification and Authorization

The NASA Engineering and Safety Center (NESC) was requested to support the Arecibo Observatory failure investigation in determining the root cause of the Auxiliary M4N cable failure. The NESC and Kennedy Space Center (KSC) led an integrated NASA investigation with support from Marshall Space Flight Center (MSFC) and The Aerospace Corporation that included forensic investigation of failed hardware, finite element modeling, materials characterization, and root cause analysis. Investigation was conducted in collaboration with Wiss, Janney, Elstner Associates, Inc. (WJE).

The key stakeholders for this assessment are the University of Central Florida (UCF), the National Science Foundation (NSF), and the NASA Science Mission Directorate (SMD).

The following table lists the key personnel and major historical dates of the assessment:

NESC Lead	Azita Valinia, NESC Chief Scientist
NESC Technical Lead	Gregory Harrigan, NESC Associate Principal Engineer
Approval to Proceed	August 24, 2020
Assessment Plan	February 18, 2021
Final Report	June 15, 2021

2.0 Signature Page

Submitted by:

Team Signature Page on File – 6/24/21

Dr. Azita Valinia

Date

Prepared by:

Mr. Gregory Harrigan

Date

Significant Contributors:

Mr. Pavel Babuska

Date

Dr. Vinay Goyal

Date

Mr. Nathan Trepal

Date

Signatories declare the findings, observations, and NESC recommendations compiled in the report are factually based from data extracted from program/project documents, contractor reports, and open literature, and/or generated from independently conducted tests, analyses, and inspections.

3.0 Team List

Name	Discipline	Organization
Core Team		
Azita Valinia	NESC Lead	GSFC
Gregory Harrigan	NESC Technical Lead	KSC
Pavel Babuska	Structural Engineer	The Aerospace Corporation
Jerry Buhrow	Materials and Processes Engineer	KSC
Vinay Goyal	Systems Engineer	The Aerospace Corporation
Eric King	Materials and Processes Engineer	MSFC
Michael Lane	KSC Prototype Shop	KSC
Nathan Trepal	Materials and Processes Engineer	KSC
Consultants		
Kausar Imtiaz	NASA Technical Fellow for Structures	JSC
John Ivester	Metrology Engineer	MSFC
William Prosser	NASA Technical Fellow for NDE	LaRC
Rick Russell	NASA Technical Fellow for Materials	KSC
James Smith	NESC TDT Structures Deputy	JSC
Bryan Tucker	Materials and Processes Engineer	MSFC
Matthew Jarrett	Senior Engineer	WJE
Jonathan McGormley	Principal Engineer	WJE
Brian Santosuosso	Principal Engineer	WJE
Robert Warke	Materials and Processes Engineer	WJE
Business Management		
Kay Little	Program Analyst	LaRC/MTSO
Assessment Support		
Linda Burgess	Planning and Control Analyst	LaRC/AMA
Jonay Campbell	Technical Editor	LaRC/KBR
Kylene Kramer	Project Coordinator	LaRC/AMA

3.1 Acknowledgments

The team would like to thank the many peer reviewers who provided valuable input to this report.

4.0 Executive Summary

NASA was asked by the University of Central Florida (UCF), the organization managing Arecibo on behalf of the National Science Foundation (NSF), to support the investigation into the Arecibo Observatory auxiliary cable failure. The scope of work included technical support of NSF-led efforts, independent forensics and failure analysis of the Auxiliary Main (Aux M4N) socket, independent modeling of the socket, materials testing, and fishbone analysis to determine the most probable contributors and failure scenario. The overall effort was a collaboration between the NASA Engineering and Safety Center (NESC); Kennedy Space Center (KSC); Marshall Space Flight Center (MSFC); Wiss, Janney, Elstner Associates, Inc. (WJE); and The Aerospace Corporation. The primary objectives were to support the NSF's investigation and provide an independent assessment of any systemic concerns that could impact NASA or the broader engineering community.

KSC led the forensic investigation of the Aux M4N socket joint in collaboration with the NESC, WJE, and The Aerospace Corporation. Additionally, outside experts in the field of structural cabling were consulted on the team's findings. The integrated NASA investigation team evaluated all available investigation data through cause-and-effect analysis and developed a most probable failure scenario. Forensic data and observations were evaluated in combination with structural modeling, materials testing, and additional background data gained through literature review and from WJE.

The NASA/Aerospace team concludes that the most probable cause of the Aux M4N cable failure was a socket joint design with insufficient design criteria that did not explicitly consider socket constituent stress margins or time-dependent damage mechanisms. The socket attachment design was found to have an initially low structural margin, notably in the outer socket wires, which degraded primarily due to zinc creep effects that were activated by long-term sustained loading and exacerbated by cyclic loading. Additionally, a few wires showed evidence of hydrogen-assisted cracking (HAC) and wire surface defects that may have contributed to initial outer wire failures.

In-service inspections showed evidence of progressive zinc extrusion on several Arecibo sockets, which in hindsight indicated significant cumulative damage. However, the design did not contain set service-life inspection intervals with pass/fail inspection criteria, nor did it specify an end-of-life capability requirement associated with service life degradation. Design verification should account for a worst-case build condition that is traceable to in-service inspection of features (e.g., zinc creep/extrusion).

A combination of low socket design margin and a high percentage of sustained loading revealed an unexpected vulnerability to zinc creep and environments, resulting in long-term cumulative damage and progressive zinc/wire failure. The resulting core-pullout failure mode that preceded observatory collapse was found to be (1) unique compared with other industry applications, (2) insufficiently addressed within existing standards, and (3) a potential risk for similar designs that should be characterized.

The unexpected vulnerability was further compounded by an effective design factor of safety that was significantly less than the minimum to ensure structural redundancy in the event of a cable failure. After the Aux M4N failure and before the main cable failure, additional loads analyses incorrectly asserted acceptable positive margin for the remaining structure despite no

understanding of why a cable had failed at half the rated breaking strength. In hindsight, the structure was vulnerable to collapse after the Aux M4N failure.

The team recommends additional research on the mechanics of spelter sockets, development of inspectable pass/fail criteria for time-dependent failure modes, and risk assessment for sockets in service. Research should include examination of additional Arecibo sockets to further knowledge on progressive failure mechanisms and inform guidance on best practices for spelter socket design and usage.

The investigation team offers the body of work to the community as an incremental step in understanding the contributing factors and toward the goal of preventing similar occurrences.

5.0 Assessment Plan

Spelter sockets of this type are used throughout industry with no documented examples of this type of failure. The NESC engaged in the investigation to support root cause determination of the Aux M4N socket failure, provide technical expertise toward restoring Arecibo capability prior to the eventual collapse, and inform NASA/industry of systemic risk or recommendations to update industry standards.

The overall Arecibo failure investigation is managed by the NSF and their contractor, Thornton Tomasetti (TT). Root cause investigation into the Aux M4N socket/cable failure was led by an integrated team consisting of NASA, The Aerospace Corporation, and WJE, who conducted forensic investigation of the recovered Aux M4N socket, materials characterization, finite element modeling, and fishbone/fault tree analyses.

- The NESC’s role throughout the investigation was to provide independent technical support/assessment, management of the overall investigation efforts, and independent assessment of the Aux M4N root cause including any systemic risk.
- KSC Engineering led sectioning/forensics of the socket with support from WJE and the NESC. KSC was originally contacted by UCF in mid-August 2020 for failure analysis and nondestructive evaluation (NDE) expertise to evaluate both the Aux M4N and the compromised Arecibo structure; this effort was funded by the Science Mission Directorate (SMD) and the NESC.
- The Aerospace Corporation, as part of the NESC team, conducted finite element modeling and participated in NASA’s independent root cause analysis toward characterizing socket/cable mechanics and developing a likely progression of failure.
- MSFC conducted materials-level testing to characterize socket constituent material behavior and inform finite element modeling studies.
- The integrated NASA/Aerospace team developed a fishbone analysis of the Aux M4N socket that integrated all available information and led to findings and NESC recommendations regarding the root cause and corrective actions.
- Additional group(s), including TT, were tasked by the NSF with investigating the overall Arecibo failure; these investigations are not integrated into the NESC team’s work and may provide additional data/insight into the failure.
- NASA and WJE are publishing independent reports that summarize investigation findings and reference each other’s work where applicable (see Table 5.0-1). All NASA data products are included as appendices within this report.

Table 5.0-1. NASA Investigation Roles and Responsibilities

Category	Leading Roles		Comments
	NASA	WJE	
Fishbone/Fault-tree Investigation	✓		WJE provided significant data used in the disposition of NASA fishbones
Forensic Analysis/Reconstruction	✓		NASA KSC led the forensic analysis with WJE collaboration
Materials Testing	✓		NASA KSC/MSFC characterized material properties that informed structural assessment
Socket Structural Assessment	✓		NASA developed finite element models of as-built Aux M4N socket, performed sensitivity studies
Design Factors of Safety	✓	✓	NASA leveraged WJE expertise on the factors of safety used in civil engineering applications
Loads Model		✓	WJE developed a loads model after failure that informed structural assessment and revealed errors
Expert Interviews		✓	WJE/NASA jointly conducted expert interviews
Historical Knowledge		✓	NASA leveraged WJE knowledge-base on the key events, facility designs, operation, inspections, etc.

6.0 Failure Event Introduction and Observatory Overview

The Arecibo Observatory is a radio astronomy, solar system radar, and atmospheric physics facility of the NSF, operated under cooperative agreement by the UCF. The facility was home to a telescope that was uniquely capable of characterization and orbital refinement of planets, comets, and asteroids; detecting optically invisible gas and revealing areas of interstellar space obscured by cosmic dust through its detection capability in the radio spectrum; and studying Earth's upper atmosphere through the combination of incoherent scatter radar and optical Light Detection and Ranging (LIDAR).

At 2:35 a.m. local on August 10, 2020, the Aux M4N structural cable failed during normal observatory operations. The failed cable was a primary component of the system used to suspend the large, steel-framed platform (feed platform) above the telescope reflector dish. The naming convention for the Aux M4N cable refers to which cable construction (Main or Auxiliary), which tower (Tower 4), and which side of the tower (North or South). Thus, the Aux M4N is denoted as an auxiliary cable terminating on the North side of Tower 4. Tower 4 and the socket termination of Aux M4N are shown in Figure 6.0-1. In the left image, the socket can be seen disconnected from the cable and resting on the deck of Tower 4 platform. Figures 6.0-2 and 6.0-3 show the remnants of the socket cavity and the failed cable end with pulled out wires.

On November 6, 2020, one of the four original main cables of Tower 4 failed. This second cable failure differed from the Aux M4N failure in that it was one of the original main cables, which employed a different structural strand construction and a different cable termination. Finally, on December 1, 2020, a second original main cable at Tower 4 failed, causing a chain reaction of failures and load imbalances in the observatory suspension cable system that led to the total collapse of the observatory and supporting tower segments.



Figure 6.0-1. Tower 4, including Socket



Figure 6.0-2. Wire Strands inside Failed Socket



Figure 6.0-3. Pulled-Out Cable Wire, Strands and Zinc (side view)

6.1 Arecibo Observatory Timeline

Table 6.1-1 shows a timeline of relevant events associated with the Arecibo Observatory.

Table 6.1-1. Arecibo Observatory Timeline [reprinted from ref. 1]

Date	Event
1960	Design and construction begins for the Arecibo Ionospheric Observatory.
Nov 1, 1963	Opening of the Arecibo Ionospheric Observatory.
Oct 1, 1969	NSF assumes oversight of the observatory from the Department of Defense.

Date	Event
Sept 1971	NASA joins with NSF to form the National Astronomy and Ionospheric Center (NAIC).
1971	Cornell University named to operate/manage the observatory.
1972-1974	Primary reflector receives new aluminum panel surface and S-band radar equipment is installed.
Sept 1981	Replacement of center backstay A12-3 due to six wire breaks.
1992-1997	Design and construction of Gregorian Dome upgrade and ionospheric radar line feed completed.
Apr 4, 2003	Condition survey performed by Ammann & Whitney. Towers T-4 and T-12 aux main cable sockets noted as having ½-inch separation from base of socket.
2003	Cable sag measurements and cable tension analysis performed by Ammann & Whitney.
Sept 15, 2004	Tropical Storm Jeanne impacts observatory with maximum wind speeds of 70 miles per hour (mph).
Aug 29, 2006	Cable sag measurements and cable tension analysis performed by Ammann & Whitney.
Feb 3, 2010	Crack in feed platform vertical truss member identified.
Sept 2010 - Feb 2011	Strengthening repairs to feed platform trusses completed. Telescope to operate under new dome movement limits.
2011	SRI International named to operate/manage the observatory.
Jan 13, 2014	Magnitude 6.4 earthquake centered approximately 50 miles north of Arecibo in the Atlantic Ocean.
Mar 11, 2014	M8-4 Jumper system installed to bypass upper splice box cable with nine broken wires observed after earthquake.
Jun 13, 2016	LIDAR cable scan completed to measure tension.
Sept 7, 2017	Hurricane Irma passes near observatory, no damaged observed.
Sept 20, 2017	Hurricane Maria impacts observatory with peak winds of 105 mph. Line feed falls into reflector.
2018	UCF named to operate/manage the observatory.
Feb 18, 2019	Inspection of Aux M4N showing separation of zinc varying from ¾ inch to 1 3/8 inches.
Jan 7, 2020	Magnitude 6.4 earthquake centered approximately 50 miles southwest of Arecibo in Indios.
Mar 2020	Design for replacement of M8-4 cable completed.
Jul 20, 2020	Tropical Storm Isaias impacts observatory with peak winds of 45 mph.
Aug 10, 2020	Cable Aux M4N failed.
Aug 11, 2020	Gregorian Dome moved to stowed position.
Sept 20, 2020	Planned stabilization of structure.
Nov 6, 2020	Cable M4-4 failed.
Nov 19, 2020	NSF announces decision for a controlled demolition of Arecibo.
Dec 1, 2020	Cable M4-2 fails, resulting in collapse of the telescope.

6.2 Aux M4N Cable Structure Description

The Arecibo Observatory was originally constructed in 1963 and was progressively upgraded/updated over its lifespan. In the 1990s, the structure was upgraded to include auxiliary main cables that provided a counterbalancing axial force to the original main cables and increased the capability of the feed platform to support the Gregorian Dome below the platform (the upgrade history is shown in Figure 6.2-1).

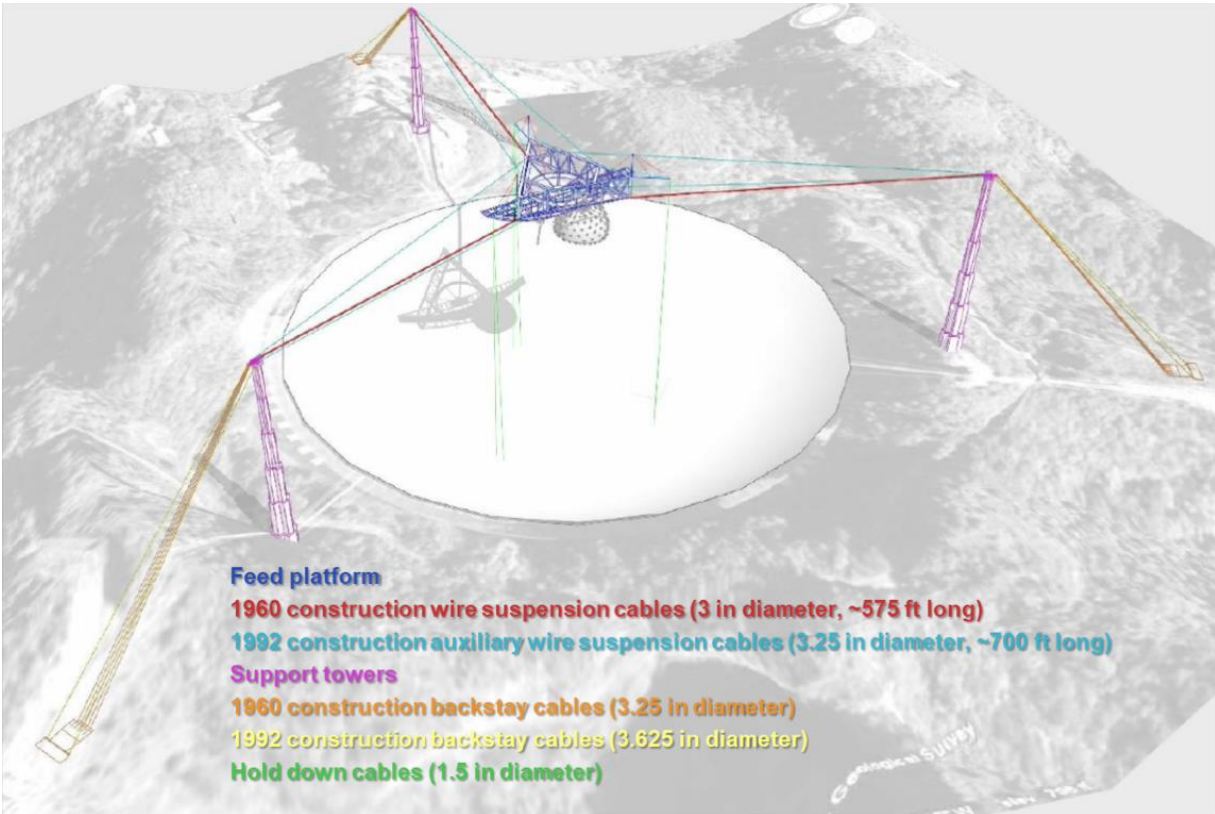


Figure 6.2-1. Color-coded Diagram of Feed Platform Support Structure with Upgrade Indications

The cable suspension structure consisted of three towers spaced 120 degrees apart that supported main, auxiliary, and backstay cables. The three towers are denoted as Tower 4, Tower 8, and Tower 12, representing their closest position to a cardinal clock face. Towers 4 and 8 had North/South designations, while Tower 12 had an East/West designation for adjacent hardware. For the original design, each tower supported four original 3.0-inch diameter main cables and five 3.25-inch diameter backstay cables. After the upgrades in the 1990s, each tower received another pair of 3.25-inch auxiliary main cables and two additional 3.625-inch backstay cables to support the upgraded mass of the Gregorian Dome. The Aux M4N cable is shown in red highlight for various views in Figures 6.2-2 through 6.2-4.

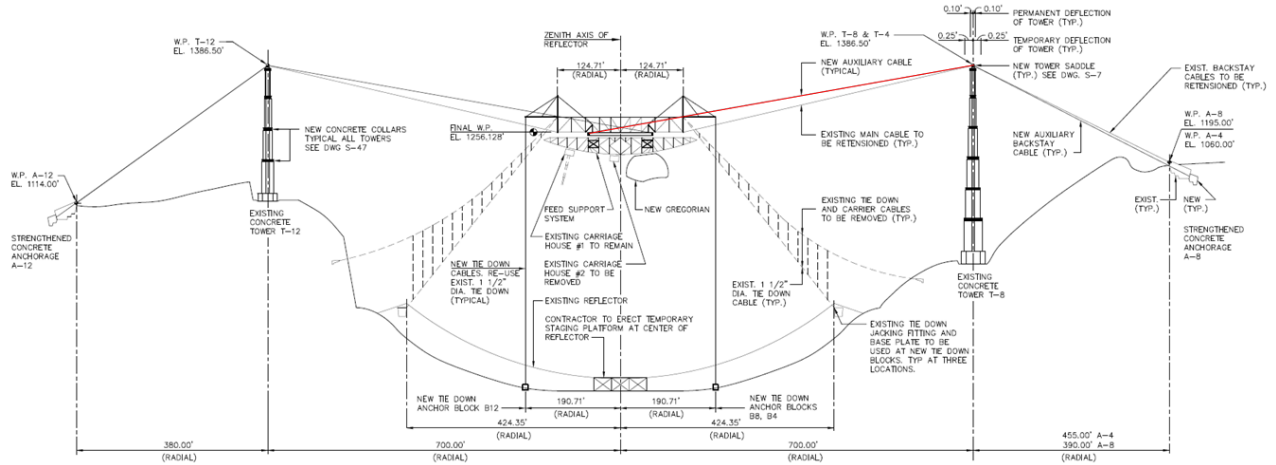


Figure 6.2-2. Elevation Drawing S-2, highlighting Failed Aux M4N Cable in Red

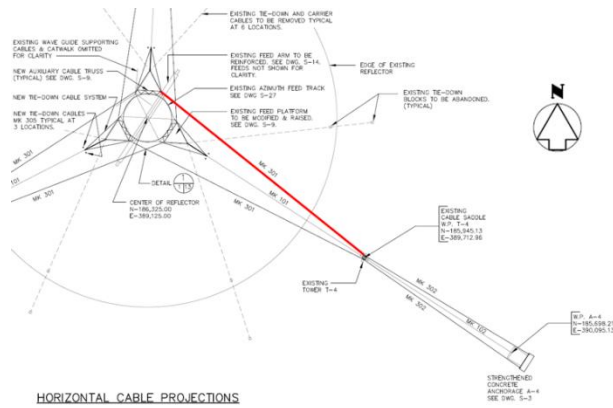


Figure 6.2-3. Horizontal Cable Projections, Drawing S-1, highlighting Failed Aux M4N Cable in Red

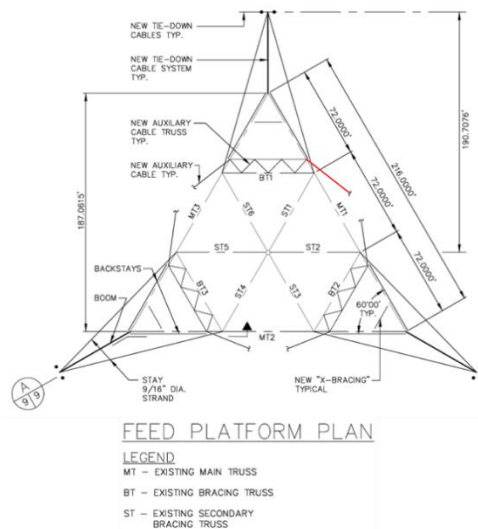


Figure 6.2-4. Feed Platform Plan, Drawing S-9, highlighting Failed Aux M4N Cable in Red

The failed Aux M4N cable was specified as structural strand per American Society for Testing and Materials (ASTM) Standard A586-91 [ref. 2], premium grade, Class A steel galvanized wire coating, with a minimum rated breaking strength of 1,313 kips. Cables were manufactured at the Williamsport Wirerope Works (now Wirerope Works, Inc. [ref. 3]) in 1993.

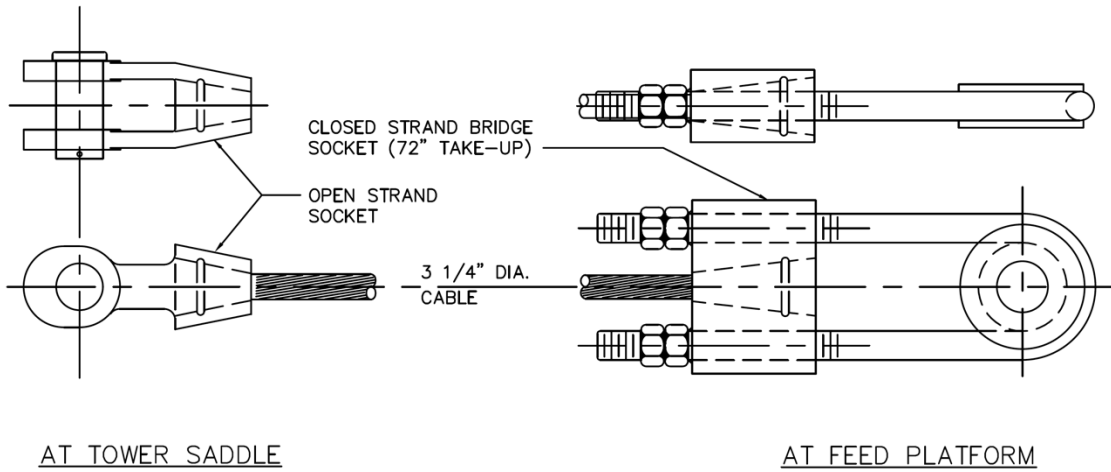
The Aux M4N structural strand follows a 1×127 construction and consists of 126 individual 0.25-inch diameter wires wrapped around a single, seven-wire strand in six concentric rings with a pattern of 6, 12, 18, 24, 30, 36 wires, as shown in Figure 6.2-5. Each individual wire has a specified minimum yield strength of 160 ksi, minimum ultimate tensile strength of 220 ksi, and elastic modulus of 23,000 ksi. Note that the main and backstay cables did not use this same 1×127 structural strand construction and are not detailed in this report.



Figure 6.2-5. Cross Section of 1×127 Structural Strand

An open spelter socket termination was used on the tower end of the cable, while a closed bridge spelter socket was used at the feed platform end, shown in Figure 6.2-6. All sockets and components were specified to be hot-dipped galvanized in accordance with ASTM A123 [ref. 4]. Casting material used in the spelter was to be “High Grade,” meeting ASTM B6 requirements for commercially pure zinc [refs. 1, 5]. There were no available tensile or compressive strength specifications for the zinc as a structural material. However, a substantial effort was undertaken to characterize the zinc material properties for use in the structural analysis and to anchor failure analysis observations. Discussion on the zinc occurs in later sections of this document.

The nomenclature applied to the failed Aux M4N open spelter socket in question is shown in Figures 6.2-7 and 6.2-8.



AUXILIARY CABLES: MK 301
N.T.S.

Figure 6.2-6. Cable Details, Drawing S-13, Specific to Failed M4N Auxiliary Cable

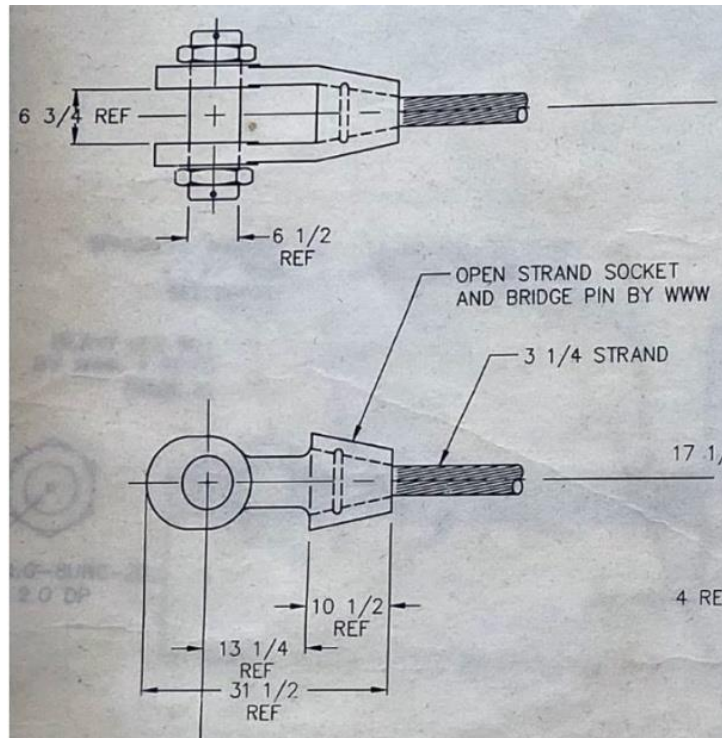


Figure 6.2-7. WWW Shop Drawing for Open Strand Socket

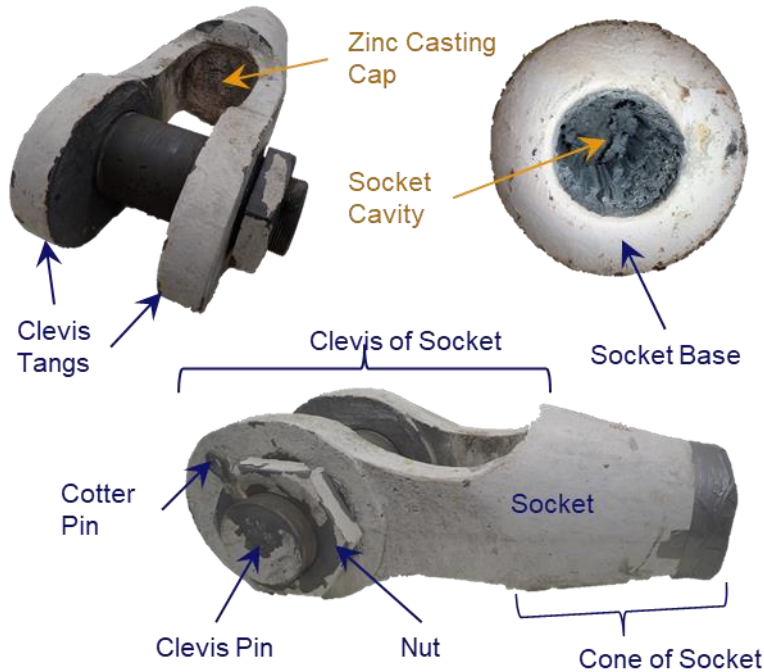


Figure 6.2-8. Nomenclature used to Describe Parts of Failed Socket

6.3 Investigation Process and Report Structure

The NASA/Aerospace team developed a best-effort systematic fishbone and evaluated supporting and refuting evidence for each potential causal factor of the M4N Auxiliary Main cable. Cause and effect hypotheses were developed for each factor and evaluated for credibility using supporting/refuting evidence. Data were sourced from NASA/Aerospace independent testing/analysis, WJE, and other external referenced material. Rating criteria used by the team assigned a credibility rating and a contribution level based on a weighing of evidence. The credibility rating and a severity of contribution were used to rank potential factors and develop credible failure scenarios. A scenario matrix was developed from the fishbone dispositions and prioritized based on the credibility rating (see Table 6.3-1). This matrix was used to develop a likely progression of failure and most probable contributing factors.

Table 6.3-1. Top-level Fishbone Structure (ratings not shown)

1. Design	2. Loads/Environments (In-service)	3. Build Variability
a. Insufficient Design Criteria	a. Improper Nominal Loads Characterization	a. Zinc Spelter
b. Material Incompatibility	b. Improper Survival Loads Characterization	b. Wires
c. Insufficient Qualification	c. Improper Moisture Environment Characterization	c. Wire Brooming
d. Insufficient Acceptance Criteria		d. Socket Outer Casing
		e. Poor Wire/Zinc Bond
4. Maintenance	5. Environmental Assisted Degradation	6. Failure Mechanisms
a. Insufficient Training – <u>not rated</u>	a. Corrosion	a. Fatigue
b. Insufficient Inspection	b. Hydrogen-assisted Cracking (HAC)	b. Creep
c. Inadequate Instrumentation – <u>not rated</u>	c. Stress Corrosion Cracking	c. Strength
d. Repairs – <u>not rated</u>		

Note: Schedule constraints and incomplete access to data resulted in consideration of some evidence that was not fully independently verified and in a few bones in the fishbone analysis not receiving a formal rating.

The main body documents a subset of the overall effort with a focus on analysis that supports the findings, failure progression, and NESC recommendations. The comprehensive data and analyses are contained in appendices or referenced to external sources. The investigation team offers the body of work to the community as an incremental step in understanding the contributing factors and toward the goal of preventing similar occurrences.

6.4 Fabrication Process

The team evaluated the fabrication process of zinc spelter sockets to gain an understanding of typical construction standards, the load transfer mechanism, and potential vulnerabilities. Information was sourced from discussions with industry experts and literature research and was used in the root cause analysis process to understand observations from forensic analysis and support modeling/simulation studies.

Open spelter socket terminations similar to those used at Arecibo have extensive usage within industry and historically are considered a highly efficient and reliable safety-critical cabling mechanism. The fabrication and build verification process is inherently manual and workmanship sensitive. The key steps in the preparation and manufacture of open spelter socket terminations are:

- Install seizing at the termination of the socket. This involves “tying off” a portion of the cable to provide a root location where the individual wires will not separate and can exit the socket.
- Broom the wires by unwinding and straightening the wire segments above the seizing. Wires form an expanded shape to occupy the volume of the conical socket.
- Ultrasonically clean the broomed wires by dipping in a citrus-based solvent and then drying.
- Apply zinc ammonium chloride flux by dipping for a prescribed time and allowing to dry.

- Install the socket hardware around the broomed wires, ensuring the cable is aligned concentrically with the socket at the location of seizing.
- Seal socket opening to ensure no molten zinc can flow from the bottom of the socket.
- Preheat the socket to a specified value to better match thermal shock of molten zinc pour.
- Fill the heated socket with molten zinc.
- The target temperature for pouring zinc is between 800 and 875 degrees Fahrenheit (°F). This is accomplished by increasing the zinc temperature during ladling by up to 100 °F to accommodate the cooling that occurs during the manual process of transferring molten zinc.

After construction, the socket terminations commonly receive a proof test load as a workmanship screen to ensure adequate bond strength developed between the zinc and broomed wires and to seat the constituents within the conical socket [ref. 6]. The proof load level can be specified by the customer as a percentage of rated breaking strength or some proportion of design load. A proof test to 50% of the rated breaking strength is a common target load value. Note that the authors were not provided any record of the individual cable termination proof test data, so the exact history of Aux M4N was not independently verified.

Interviews by WJE/NASA were conducted with two industry experts: Thomas Secules (retired), formerly of Wirerope Works, Inc., and Timothy Klein, WireCo WorldGroup. The goal of the separate interviews, conducted on April 29 and 30, 2021, was to discuss the fabrication process with industry experts, confidentially review failure analysis data and model reconstruction of the Aux M4N build, learn about acceptance criteria of such socket termination designs, and review inspection photos suggesting creep of the zinc at the termination. The interview commentary is summarized here:

- Neither expert had knowledge of failures in open spelter sockets similar to that of Aux M4N (partial section fracture leading to cable core pullout).

Author's note: The authors do not know if this is because the Arecibo Observatory application is fundamentally unique, if the build of Aux M4N is unique, or if other cables that failed in Arecibo contained a partial core pullout as well. The authors were not given the ability to review the final failed state of the Main cable failures that occurred during final observatory collapse.

- Both experts briefly independently reviewed failure analysis/modeling reconstruction (Figure 6.4-1 images and additional data) of the Aux M4N socket and stated that the wire brooming construction and zinc pour look typical of similar sockets within industry and are not indicative of any fabrication defects.
- Additional discussion of the Aux M4N socket with Thomas Secules indicated that the fabrication process is controlled through best-practice wire brooming, inspection of the socket prior to zinc pour, and, finally, workmanship screening by proof testing of the constructed termination.
- Brooming quality is largely controlled through training with a seniority system in place that would have relied on the most experienced fabricators for this socket size. The likelihood of process escapes for this socket was verbally stated as unlikely.
- Both experts reviewed photos taken through observatory service life showing 0.5 inch of zinc seating extrusion in 2003 and approximately 1 3/8 inches extrusion in 2019. Both stated that

this degree of zinc movement looked atypical versus other similar sockets and was indicative of socket damage (see Figure 6.4-2).

- The industry experts indicated that creep of the socket termination constituents is not typically a priority concern or even taken into account. American Society of Civil Engineers (ASCE) Standard 19 C3.3.1.5 [ref. 7] discusses creep in the context of overall structure shape/stability but not for the cable termination itself.

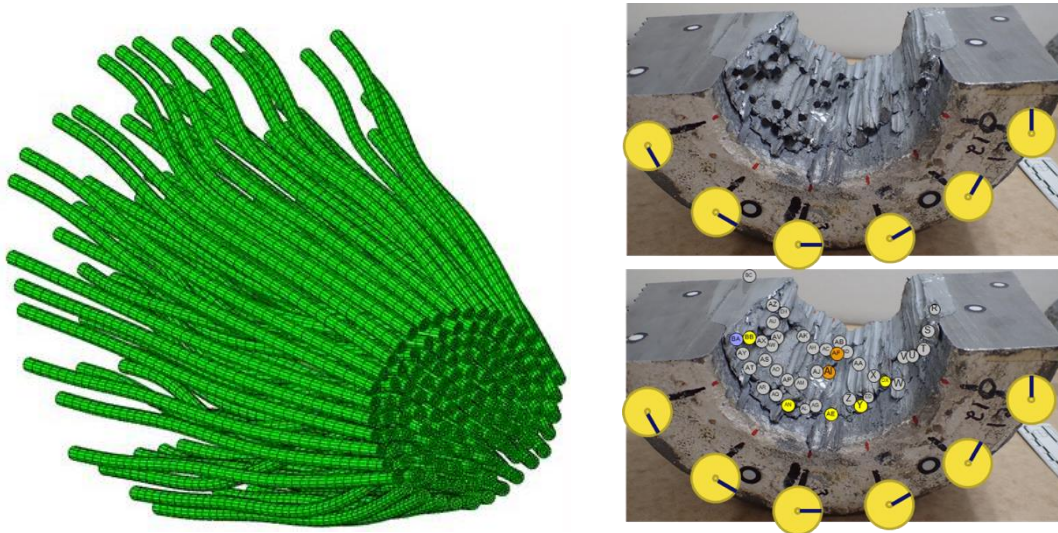


Figure 6.4-1. Aux M4N Wire Reconstruction (left) and Interim Forensic Analysis of Zinc Spelter and Wires showing Wire Fracture Pattern of Wire Segments Left in Socket Termination (right)



Figure 6.4-2. 2003 Photo of Aux M4N (left) showing ~0.5-inch Zinc Seating Extrusion and 2019 Photo (right) showing ~1 3/8-inches Extrusion [ref. 1]

F-1. The Aux M4N socket build process and original construction was typical of zinc spelter open-socket terminations.

F-2. Zinc extrusion of Aux M4N socket as documented in 2019 indicated an unquantified degree of damage and a nonconformance.

F-3. Creep behavior of the zinc spelter socket termination constituents (zinc or broomed wires) is not a failure mode typically evaluated for these sockets.

7.0 Data Analysis

The NESC assessment process used a combination of data from independent NASA assessment and referenced data from the WJE investigation. NASA, The Aerospace Corporation, and WJE worked collaboratively during the investigation but are providing separate independent assessments. The facility overview is summarized in the following section as background information but is discussed in detail in the WJE report [ref. 1].

7.1 Arcibo Observatory Structural Loading Assessment

The first load experienced by a newly manufactured socket is the socket proof test to 50% of the specified cable breaking strength. In the case of Aux M4N, this corresponds to a load of roughly 660 kips.

The auxiliary main cables were originally installed to support 602 kips of dead load that included all modifications to the feed platform, the new Gregorian Dome, cables, and tie-down loads at a temperature of 90 °F. Design loads also considered a 50-mph wind loading at 90 °F, which produced an auxiliary main cable tension of 615 kips, and a survival loading with a wind speed of 100 mph at 90 °F, which increased the auxiliary main cable tension to 622 kips. WJE obtained the TT model and performed sensitivity studies on the receiver position, total receiver load, and cable sag measurements to determine distribution of cable tension in the observatory. Although not independently verified by The Aerospace Corporation and NASA, WJE found that tension in the Aux M4N cable could have been up to 15% higher than reported on the original design drawing. The distribution of cable tensions varied based on analysis assumptions, and the reader is encouraged to review the WJE analysis [ref. 1] for additional details.

7.2 Failure Analysis of M4N Aux Socket/Cable

NASA and WJE collaborated on a material forensics plan for the Aux M4N socket, clevis pin, and cable end. During the forensic investigation, results and observations were continuously peer reviewed and analyzed by the combined NASA/WJE team, in addition to other investigation elements, including finite element modeling of the as-built configuration and materials testing to establish a likely progression of failure.

Evidence was protected from further degradation to the extent feasible while at Arcibo and through transportation to KSC for further laboratory analysis. Visual inspection and chemical analysis were the first tasks, followed by nondestructive analysis, which included radiography and magnetic particle inspections, metrology, and three-dimensional (3D) laser scanning. 3D laser scanning was performed prior to sectioning and after each sectioning step to improve the surface topography captured from within the socket cavity and to aid in the construction of an

as-built finite element model. 3D prints were made as forensic support aids from the 3D laser scans.

Next, the socket was dissected, first longitudinally into left and right halves, followed by transverse cuts in each half starting from the casting cap side of the socket halves and moving toward the wire fractures near the socket base. During the sectioning process, areas of interest were analyzed and/or sectioned off for further microscopy. The zinc casting was analyzed by metallography, and the wire fractures were extracted from the zinc for fractography. Lastly, material testing was performed on socket and virgin material to characterize mechanical properties and metallurgy. Additional details of the failure analysis are contained in Appendix A.

7.2.1 Socket and Cable

7.2.1.1 Socket

3D laser scanning performed prior to dissection identified a few notable features for additional study in the as-received socket (Figure 7.2.1.1-1). First, a slight angle to the clevis tangs was observed that did not appear to affect removal of the clevis pin from the tangs or result in impingement on the clevis pin due to the angle of the tangs. Second, a skew was noted in the socket cavity with respect to the socket end where the cable entered. The positioning is approximately 5° toward 9 o'clock and 5° toward 12 o'clock. The left image in Figure 7.2.1.1-2 is a top-down view of the socket cavity showing a 5.2° skew in the cavity with respect to the centerline. An overlay of the intact wires (pulled out) from a reconstruction of the as-built wire brooming demonstrates how the wires were approximately positioned within the socket. Above the overlay is a full wire model with the fractured wires shown semi-transparent to indicate the asymmetry in the fractured wires. The right image in Figure 7.2.1.1-2 is a 3 o'clock-to-9 o'clock view of the socket cavity showing a 5° skew in the cavity with respect to the centerline. The intact wires are overlaid on top of the laser scan, and a full wire model is shown above with the fractured wires semi-transparent, showing the asymmetry in the fractured wires.

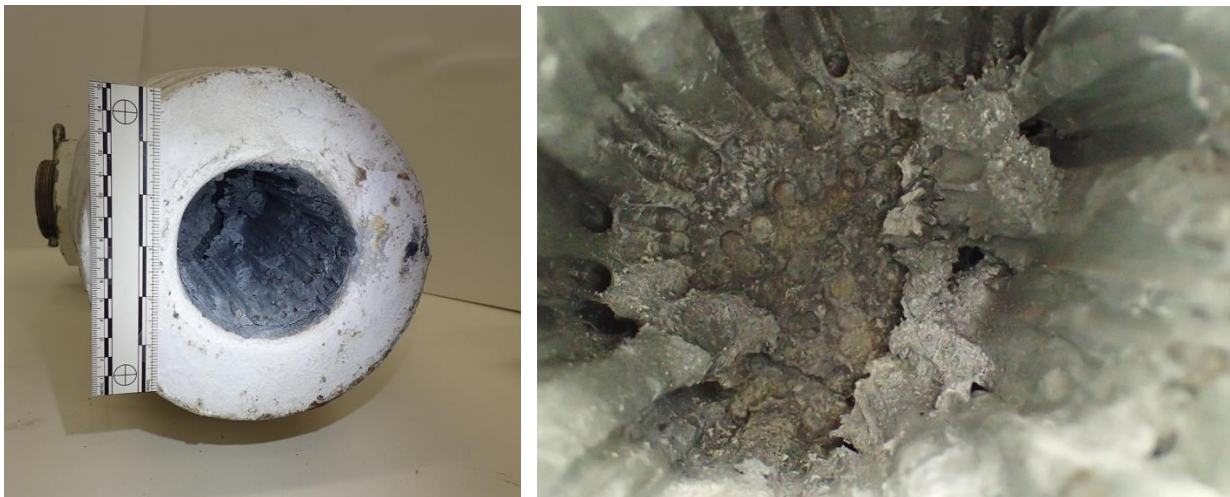


Figure 7.2.1.1-1. As-received Socket Cavity

The skew in the cavity is explained by the pattern of wire fractures; most fractured wires were located between approximately 2 and 7 o'clock. Between these two positions, progressively more inner ring wires were fractured. This pattern differed from the rest of the clock positions around the socket, where only outer ring wires had fractured, and six outer ring wires did not fail

(9 o'clock position, opposite the bulk of the fractured wires). Further analysis on the cause of the observed fracture pattern is discussed in later report sections.

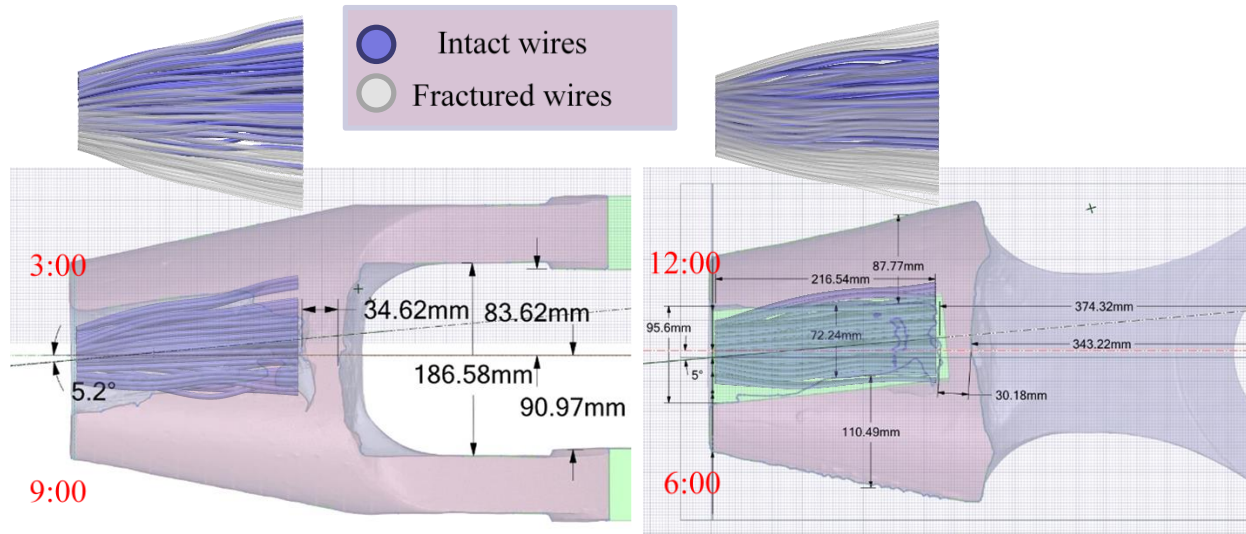
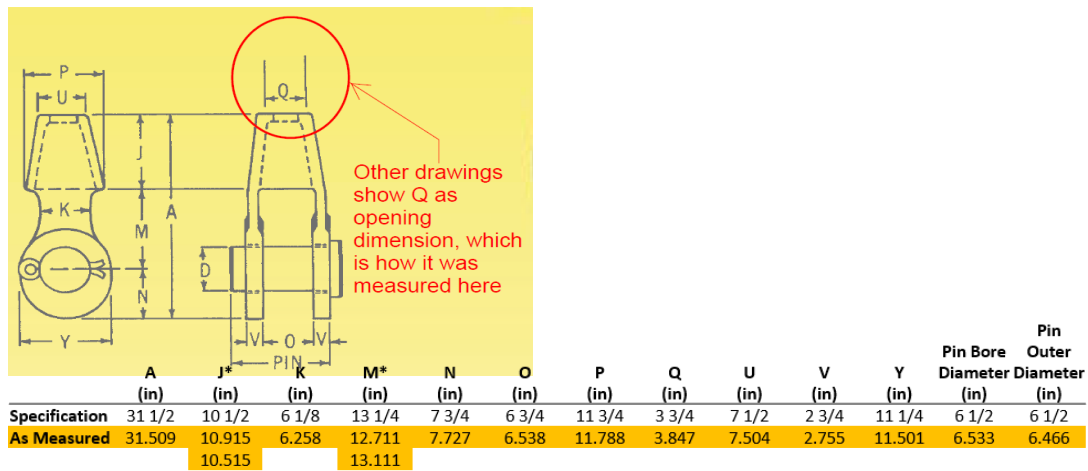


Figure 7.2.1.1-2. Overlays of Intact Wires that Pulled Free of Joint, with Full Broom Above
 Left images are top view of socket; right images are a 9 o'clock view.

Metrology measurements were taken of the socket and clevis pin and compared with specifications within the structural stand and wire rope catalog [ref. 8]. Comparison of measurements against the specification values shows variability (± 0.25 inch), as seen in Figure 7.2.1.1-3. The socket is a steel casting, and some amount of variability in the final dimensions is expected due to the nature and amount of precision in the casting process of this type and size. From discussion with industry experts, each foundry defined the socket casting dimensions to meet the drawing tolerances. Magnetic particle inspection was performed on the outer cone of the cast socket forging and revealed no cracks.



*Draft allowance for mold release produces a taper at J-M interface. Measurements were made at inner edge of cone which gives a larger number (~0.4 in greater than minimum material condition). Numbers come in if draft allowance is ignored which is shown in the lower column.

Figure 7.2.1.1-3. Dimension Diagram and Specification Row from Structural Strand and Wire Rope Catalog [ref. 8]

The as-measured metrology measurements for the socket and clevis pin are highlighted in gold.

7.2.1.2 Cable

The cable comprised 126 0.25-inch diameter wires and a center wire comprising seven smaller-diameter wire strands. Wires were arranged in concentric rings consisting of, from outside to inside, 36, 30, 24, 18, 12, and 6 wires (see Figures 7.2.1.2-1 and 7.2.1.2-2).



Figure 7.2.1.2-1. As-received Cable End Section



Figure 7.2.1.2-2. Cable Cross Section

F-4. Socket housing dimensions were within wire rope catalog specifications.

F-5. The Aux M4N cable met the drawing requirements for a 3.25-inch diameter cable (see Appendix D).

F-6. The Aux M4N cable end section and socket cavity are skewed compared with the socket's longitudinal centerline axis.

7.2.1.3 Sectioning

The socket was initially sectioned with a band saw to remove the clevis tangs. The socket cavity was protected and media blasted to remove the paint coating prior to magnetic particle inspection of the socket cone outer diameter. A longitudinal cut was made along the 5:30 to 11:30 clock positions, creating what were labeled the 3 o'clock and 9 o'clock halves of the socket cone. (Figure 7.2.1.3-1).

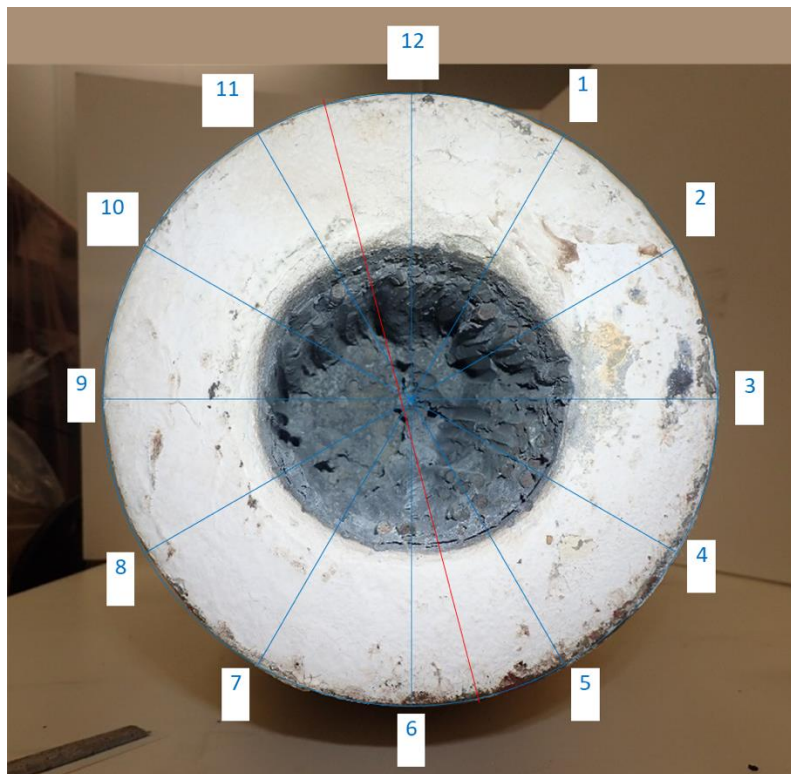


Figure 7.2.1.3-1 (Appendix A Figure 30). Photo of Socket Base with Top of Socket at Top of Image

The 12 o'clock position around the socket base is associated with the top of the socket, and the 3 o'clock position is associated with the right side of the socket, as if looking at the socket from the feed platform, facing the tower. The red line identifies the intended plane for the initial longitudinal cut of the socket cone. Note that the cut was intended to be slightly off-center to avoid any visually identifiable fracture surfaces. The fracture surface of one wire was partially cut.

Transverse slices of each half of the socket were made, starting near the casting cap and moving toward the socket base with each subsequent cut. Slices were named 3a, 3c, 3e, and 3g for the

3 o'clock half and 9a, 9c, 9e, and 9g for the 9 o'clock half (see Figure 7.2.1.3-2); 3a and 9a are the transverse slices that include the casting cap, and 3g and 9g are the transverse slices that include the socket base.

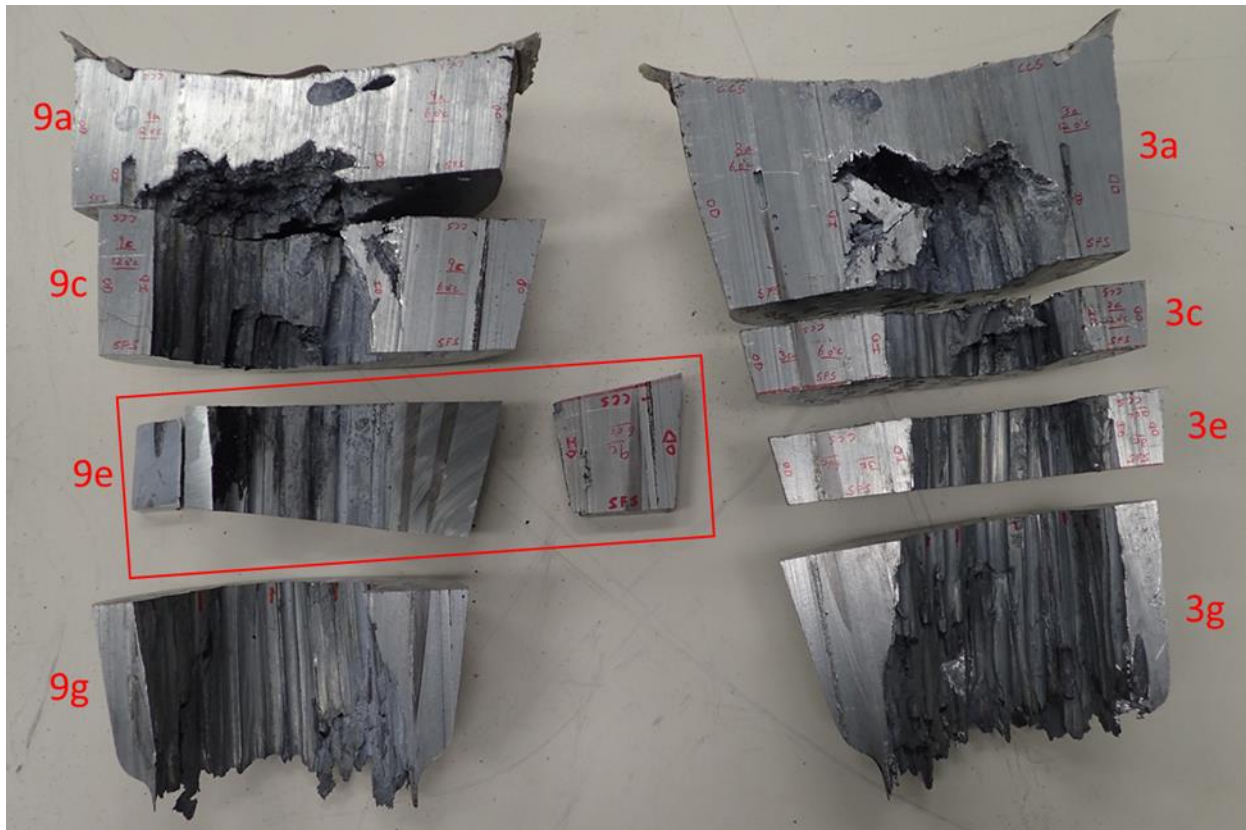


Figure 7.2.1.3-2 (Appendix A Figure 31). Zinc Socket Cavity Transverse Section Labeling

The wire fracture surfaces embedded in the socket zinc casting were in various states of accessibility, with some protruding from the casting, some observed along the concave surfaces of the casting inner diameter, and others completely buried in zinc and not visible (where the transverse band saw cut revealed the presence of these wires within the zinc casting volume). Initially, wire fracture surface removal was attempted by mechanical means. Abrasive cutoff wheels were used to cut the slices into smaller, more manageable pieces to access the individual fractured wire ends during dissection and hydrochloric-acid zinc removal, and to cut samples for scanning electron microscopy (SEM), mechanical testing, and metallography.

Fractography analysis of the wires required removal of the zinc surrounding the wires to expose any fracture surfaces encased by the zinc because of the overall socket failure. The left image in Figure 7.2.1.3-3 shows one of the removed sections of zinc with varying amounts of zinc encasement around the wires and the fracture surfaces. To expose the fracture surfaces of wires for analysis, the zinc was removed via dissolution in hydrochloric acid. The right image in Figure 7.2.1.3-3 shows the same section of zinc after exposure, revealing the encased wires and their associated fracture surface. Additional sectioning of casting was subsequently performed to examine features and create test coupons for mechanical properties testing.



Figure 7.2.1.3-3 (Appendix A Figure 32). Section of Zinc with Encased Wires before (left) and after (right) Removal of Zinc via Dissolution in Acid

7.2.2 Zinc Casting

7.2.2.1 Socket Housing to Zinc Casting Interface

After longitudinal sectioning of the socket, the internal cross section of the zinc casting was examined (see Figure 7.2.2.1-1). A gap was observed at both the casting cap and socket base sides of the zinc casting between the zinc casting outer diameter and the socket cone inner diameter. The gap was tight near the socket base but not as large as the gap at the casting cap (Figures 7.2.2.1-2 and 7.2.2.1-3).

The larger gap at the casting cap was due to open shrinkage of the zinc casting during solidification. The mastic coating on the surface of the casting cap was found to not fully seal this gap. The gap was a path for moisture intrusion and environmental degradation of the zinc casting and was adjacent to the steel socket wall, which likely accelerated degradation via galvanic corrosion. The tight gap near the socket base was mostly devoid of corrosion product (i.e., it likely only opened after the socket failure). The amount of corrosion observed due to the galvanic corrosion process was also useful in assessing the amount of corrosion expected to have evolved elsewhere in the socket following the ultimate failure.

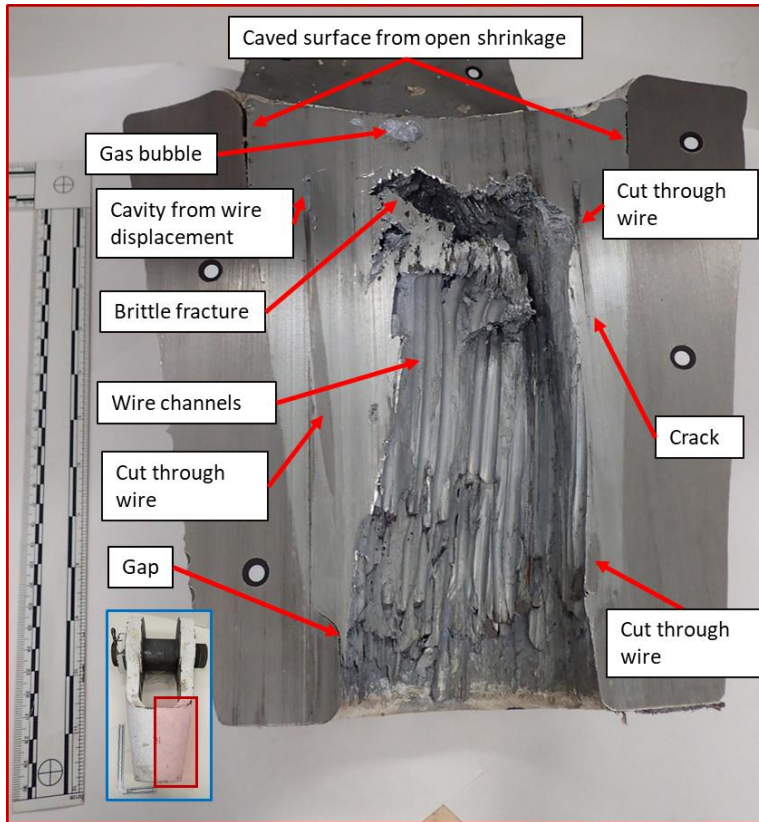


Figure 7.2.2.1-1 (Appendix A Figure 1). 3 o'clock Half of Socket Cavity
 Socket base is aligned with bottom of image.

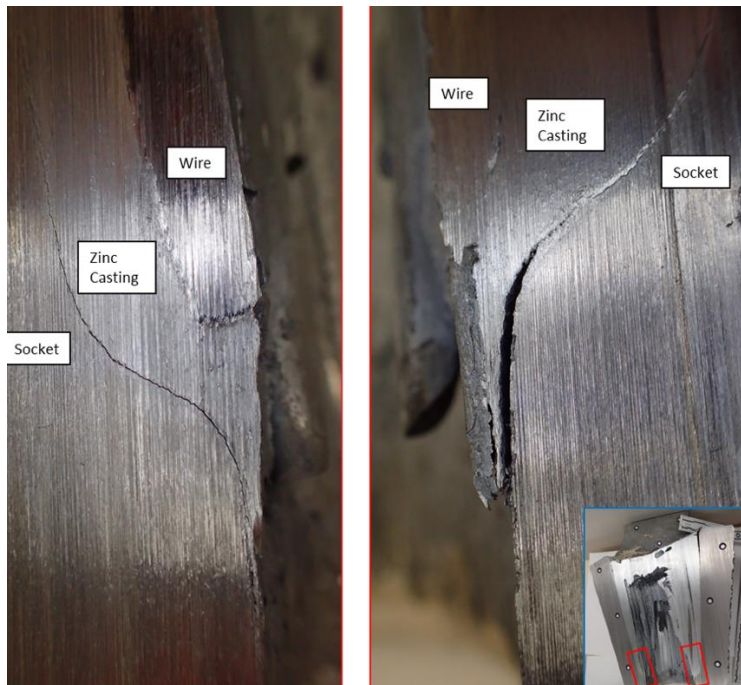


Figure 7.2.2.1-2 (Appendix A Figure 53). Gap between Socket Wall Inner Diameter and Zinc Casting Outer Diameter nearest Socket Base

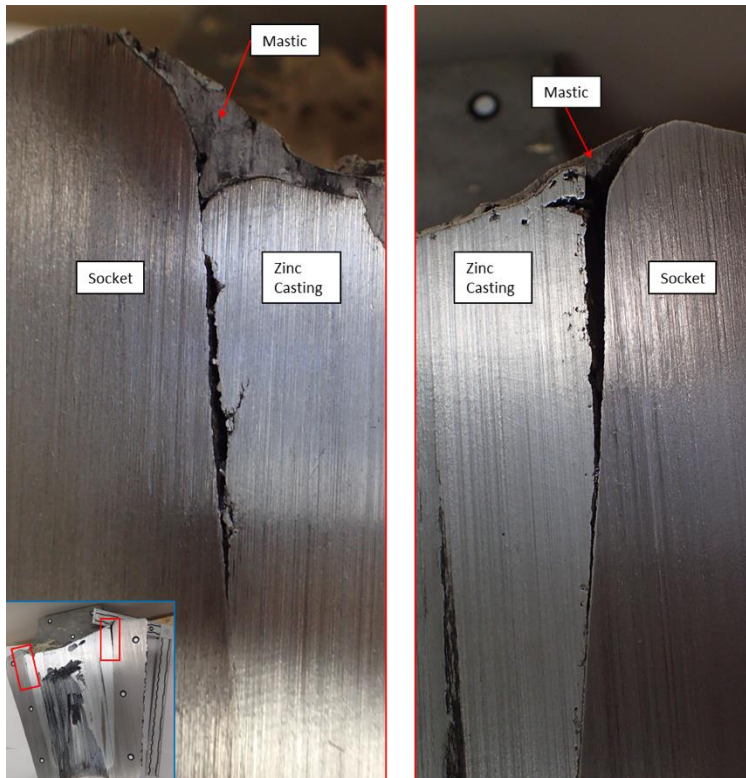


Figure 7.2.2.1-3 (Appendix A Figure 54). Gap between Socket Wall Inner Diameter and Zinc Casting Outer Diameter at Casting Cap

7.2.2.2 Voids

Gas bubbles were found adjacent to the casting cap, one of which is shown in Figure 7.2.2.2-1). These gas bubbles are positioned dimensionally within the socket where the zinc casting completed its solidification.

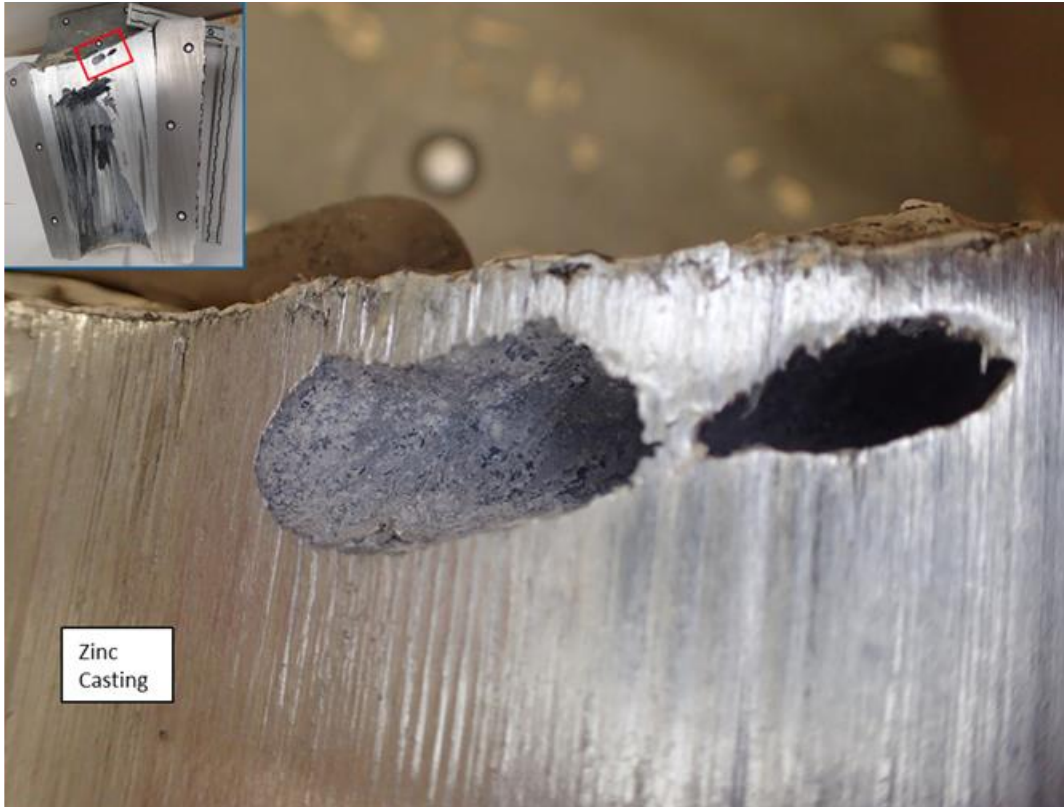


Figure 7.2.2.2-1 (Appendix A Figure 57). Close-up View of a Single Gas Bubble in Zinc Casting with Corrosion Product Buildup on Walls

Gases may exist in liquid zinc during casting due to dissolution, entrapped air during filling, or reactions with the mold wall, dross, and/or slag. Because liquid zinc has a greater solubility for gases than solid zinc, the gases concentrate in the remaining liquid zinc during solidification. When the casting exterior solidifies before the interior, the remaining gases become trapped, and their concentration eventually exceeds the solubility limit of the remaining liquid zinc as it solidifies further. At that point, the gases come out of the liquid solution but are unable to pass through the encompassing solid zinc. As a result, they become entombed at the boundary between the surrounding converging solidification fronts. This scenario is confirmed by examining the macro-etch of the surrounding zinc (see Figure 7.2.2.2-2), which shows grain orientation around the gas bubble and how it grows during solidification.

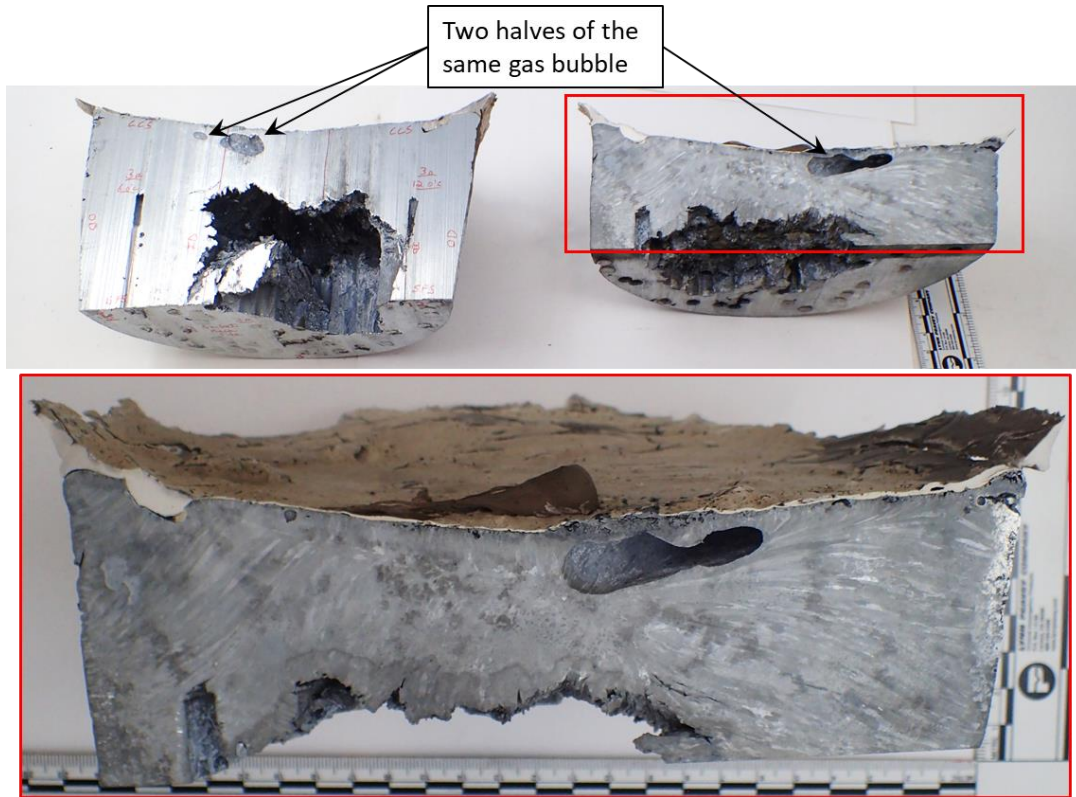


Figure 7.2.2.2-2 (Appendix A Figure 283). Etch of Longitudinal Cut Face and Zinc Grains below Casting Cap

Observed gas bubbles were surrounded by zinc and filled with corrosion product, most likely zinc oxide. The first gas bubble had a path to the brittle fracture region below it. The second gas bubble had cracks on the casting cap side of the gas bubble, where corrosion was more heavily present; these cracks were the likely pathway for moisture to ingress the bubble cavity and corrode the zinc walls. The casting cap was covered in a mastic coating, but this coating had cracks in it and may not have been present for the entire life of the socket (see Figure 7.2.2.2-3).

Smaller-sized pores were also seen in the zinc. These were probably air that was entrapped during filling, dislodged too late during solidification, and trapped locally, separate from the larger gas bubbles.



Figure 7.2.2.2-3 (Appendix A Figure 2). Oblique View of Casting Cap Immediately above Second Gas Bubble

F-7. Gas bubbles located above wire ends were trapped during the solidification process.

F-8. Smaller-sized porosity inherent to the casting process was found intermittently throughout the bulk zinc.

7.2.3 Wires

7.2.3.1 Wire Mapping

Wires were traced and labeled to indicate whether they had fractured, whether they had slipped from the socket, and their location of termination (see Table 7.2.3.1-1 and Figure 7.2.3.1-1).

Of the 126 cable wires, 56 fractured within the socket, and 70 did not fracture, instead pulling free of the socket joint (i.e., the zinc failed before the wire). The cable section that pulled free from the socket joint had 94 wires still encased together in zinc from the socket cavity, referred to as the cable/zinc slug.

Examination of the wires from the failed cable showed that of the 94 wires in the cable/zinc slug, 26 were fractured wires that mated to the fractured wires in the socket and 68 were intact wires that did not fracture. Of the 32 remaining cable wires not accounted for in the cable/zinc slug, 30 wires were fractured and mated to the fractured wires in the socket and 2 were intact wires that did not fracture; all 32 were outer ring wires. In other words, 0 to 2 intact wires pulled free of the socket individually, and the other 30 to 32 outer ring wires came free of the cable/zinc slug due to insufficient surrounding zinc and/or from the forces after core pullout and subsequent impact.

Table 7.2.3.1-1. Identification of Fractured and Intact Wires

A	AA	BA	CA	DA	EA	Fractured	56
B	AB	BB	CB	DB	EB		Intact
C	AC	BC	CC	DC	EC	Total Wires (not including center wire) 126	
D	AD		CD	DD	ED		
E	AE		CE	DE	EE		
F	AF		CF	DF	EF		
G	AG		CG	DG	EG		
H	AH		CH	DH	EH		
I	AI		CI	DI	EI		
J	AJ		CJ	DJ	EJ		
K	AK		CK	DK	EK		
L	AL		CL	DL	EL		
M	AM		CM	DM	EM		
N	AN		CN	DN	EN		
O	AO		CO	DO	EO		
P	AP		CP	DP	EP		
Q	AQ		CQ	DQ	EQ		
R	AR		CR	DR	ER		
S	AS		CS	DS	ES		
T	AT		CT	DT			
U	AU		CU	DU			
V	AV		CV	DV			
W	AW		CW	DW			
X	AX		CX	DX			
Y	AY		CY	DY			
Z	AZ		CZ	DZ			

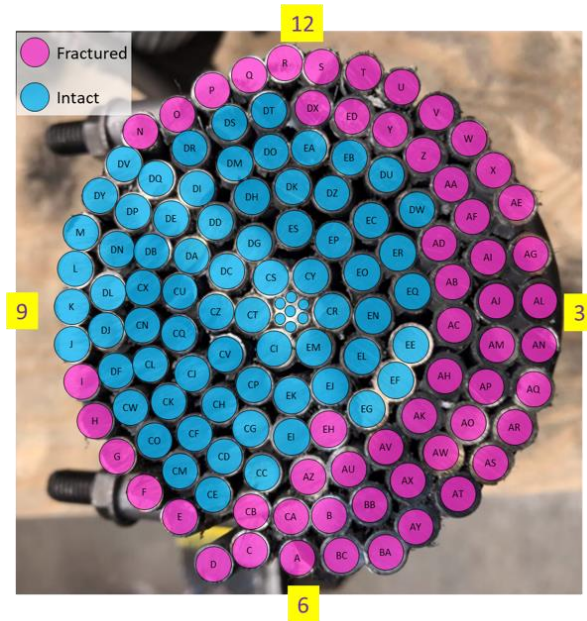


Figure 7.2.3.1-1. Representation of Cable Wire Map at Socket Base (varies with distance from end)

F-9. Fifty-six of 126 wires fractured in the socket.

F-10. Seventy of the 126 wires did not fracture; the zinc failed before the remaining wires failed.

7.2.3.2 Wire Surface Examination

Five of the fractured wires had surface defects. Four defects appeared to be from a machine or tool (wires G, AN, AO, AR), and one was a scribe-like defect (wire BA) (see Figures 7.2.3.2-1 through 7.2.3.2-4).

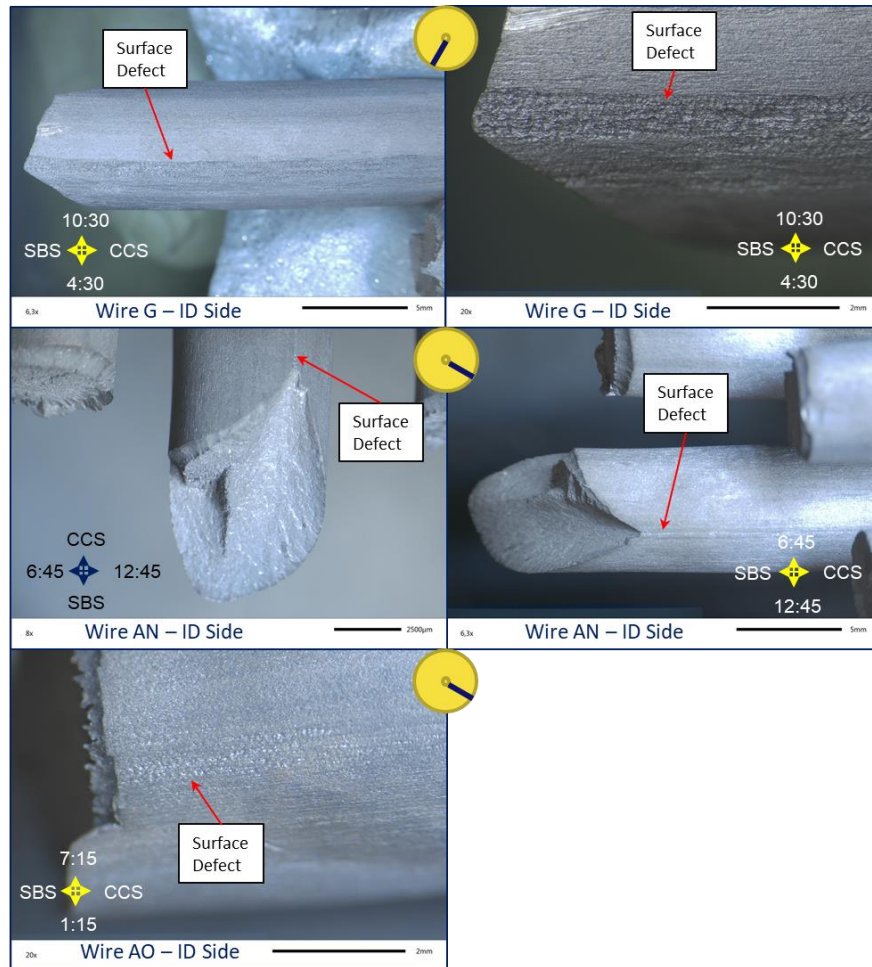


Figure 7.2.3.2-1. Stereomicroscope Images of Similar Surface Defects found on Wires G, AN, and AO

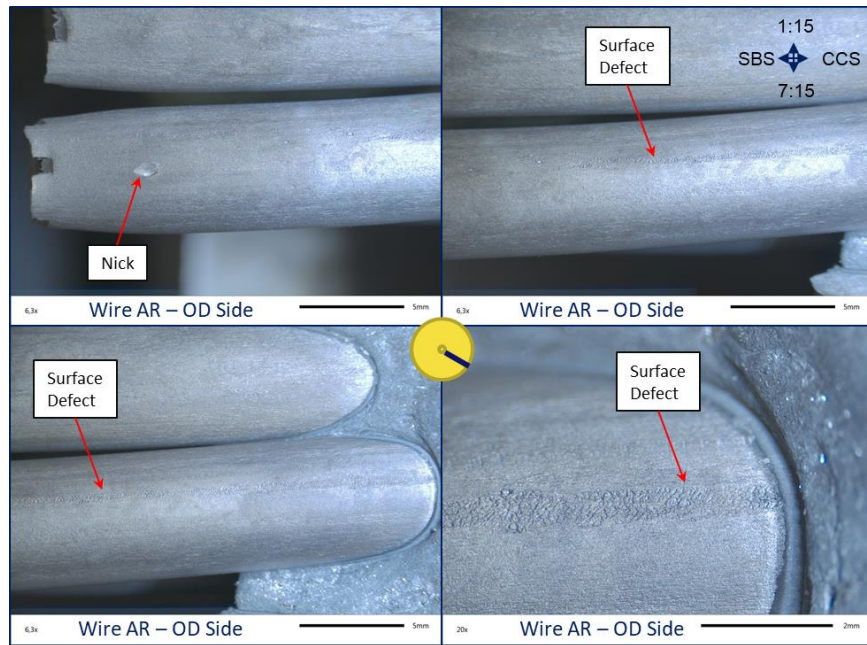


Figure 7.2.3.2-2. Stereomicroscope Images of Surface Defect found on Wire AR (nick visible in top row left image was likely from sectioning)

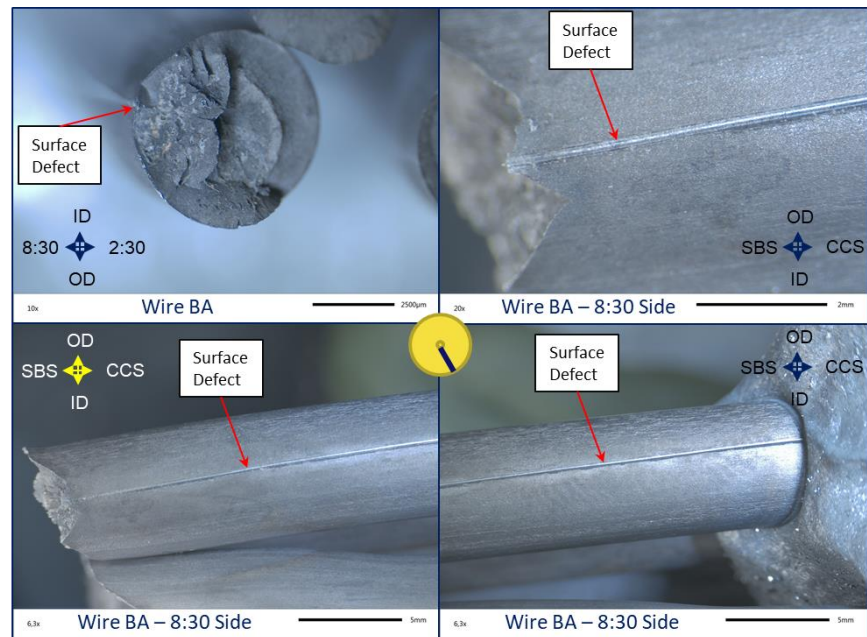


Figure 7.2.3.2-3. Stereomicroscope Images of Surface Defect found on Wire BA

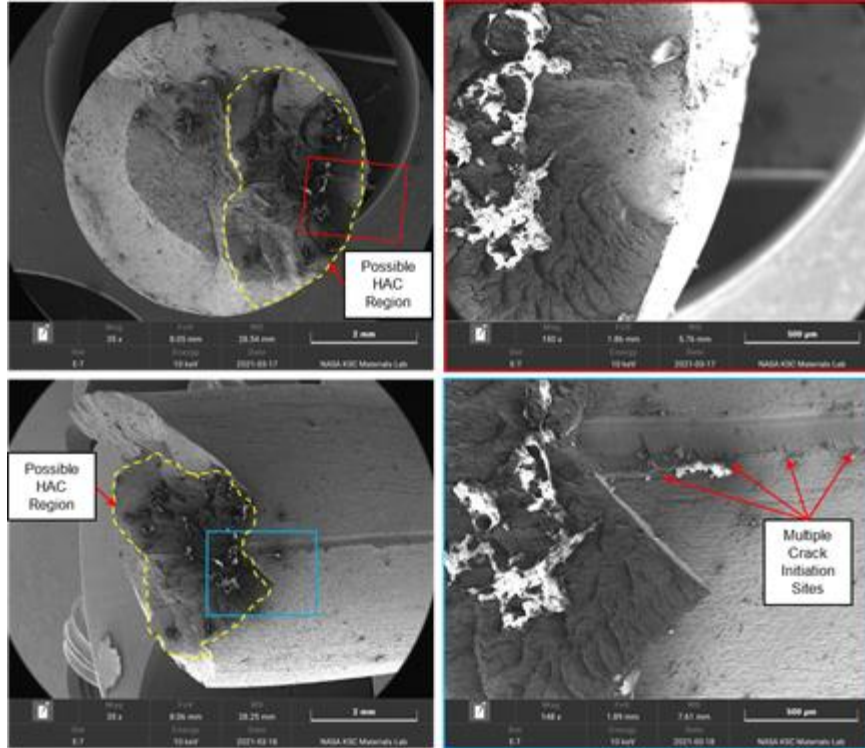


Figure 7.2.3.2-4. SEM Images of Surface Defect found on Wire BA

Two of these defects (wires BA and AN) appeared to be influential in the wire fracture, including the scribe-like groove, where multiple cracks developed along the length of the wire within the defect (Figure 7.2.3.2-3 and 7.2.3.2.4). One of the defects was not influential in the fracture surface (wire AR). The machining or tooling defect appears to have had little detrimental effect on the strength of the wires, whereas the scribe-like groove was significant based on the subsequent determination that it was an initiation point for probable HAC.

F-11. Wire surface defects were found on five fractured wires. Defects on two wires likely influenced the fracture, one of which was an initiation site for probable HAC.

Figure 7.2.3.2-5 shows a rearrangement of the pieces from slices 3g and 9g into their approximate as-built configuration following the acid-bath zinc removal process, with wire label overlays that correspond to the identified fracture morphology. Forty-four of the 56 wire fracture morphologies were cup-cone fractures, nine were shear, and the remaining three were mixed-mode fractures, which included a progressive failure mechanism believed to be HAC (one cup-cone/HAC and two shear/HAC).

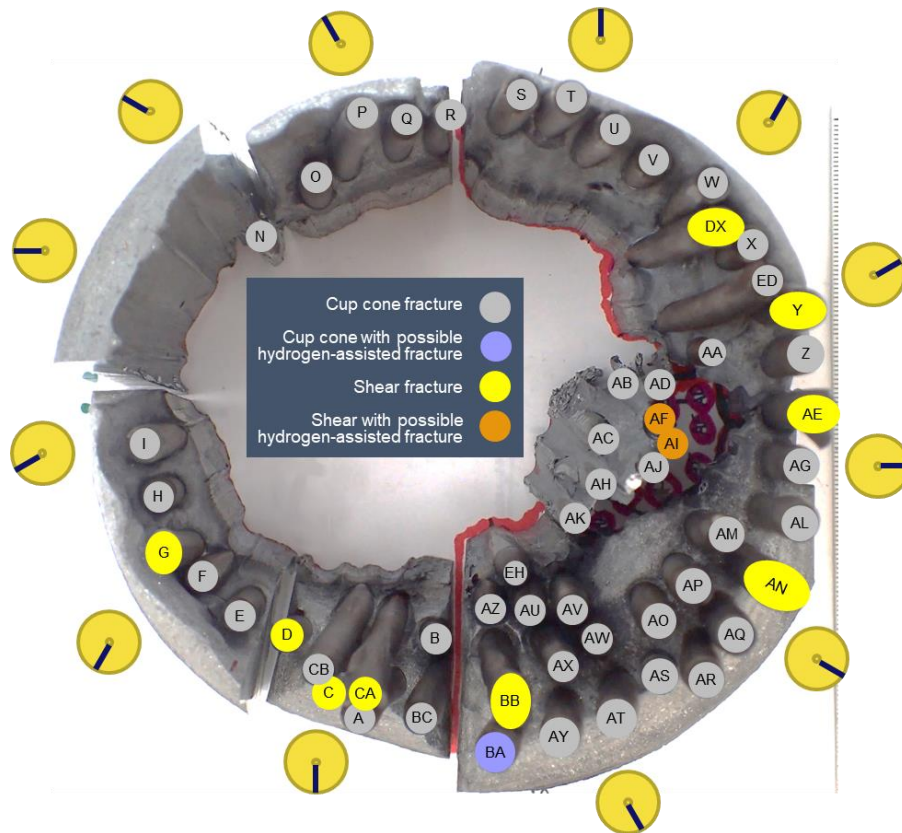


Figure 7.2.3.2-5. Reconstruction of Wire Locations following Zinc Removal with Identified Fracture Morphology

7.2.3.2.1 Cup-cone Fracture

The expected fracture mode for the wires is cup-cone fracture, where the wires fail in uniaxial tension due to ductile failure. The fracture mechanics of cup-cone fracture begin with yielding of the material, commonly referred to as necking. Eventually, microvoids begin to occur within the wire. Those microvoids coalesce within the central cross section of the wire, creating a fibrous fracture surface. Finally, once sufficient cross section has failed and the maximum shear stress is met, the remaining donut-shaped cross section fails in shear, creating a cup-like fracture surface on one side of the fracture and a cone-like fracture surface on the mating side of the fracture.

7.2.3.2.2 Shear Failure

Most of the shear failures appear to be from outer ring wires. Shear failure occurs when stress triaxialities are not in balance, which is more likely to occur around the socket perimeter where there is less zinc on the outer wire perimeter to provide equal compressive stress compared with the zinc on the inside wire perimeter.

7.2.3.2.3 Wire Fracture Categorizing

Wire fracture surfaces were extracted and examined by stereomicroscopy and categorized (i.e., cup-cone, shear, other). A range of fracture types were selected for further analysis using SEM, including cup-cone fracture (e.g., significant versus minimal necking, flat versus rough fibrous region), shear, and other fracture surface types.

7.2.3.2.4 *Fatigue*

Fatigue cracking may not always exhibit beach marks or striations. Fatigue may be present without either of these classic signs of fatigue. However, fatigue in pearlitic steel wires is well characterized, including when beach marks and striations are not identifiable.

The left side of Figure 7.2.3.2-6 shows a fatigue crack that initiated on a heavily drawn steel wire surface, and the right side shows a fatigue crack that initiated internal to the heavily drawn steel wire. For the surface-initiated crack, secondary cracks become deeper with an increasing fatigue crack length because stresses increase with crack length. This is seen in Figure 7.2.3.2-7, where the fatigue crack initiated at the arrow and grew to the dotted line, at which point the fracture mode shifted to microvoid coalescence (MVC). Figure 7.2.3.2-8 shows the wavy shape of these secondary cracks observed on the fracture plane. Figure 7.2.3.2-9 shows a close-up image of an internally initiated fatigue crack, which has a distinct facet region around an inclusion from which the crack initiates. This facet region of the fatigue crack is characterized as a rough area, which includes the primary fracture plane perpendicular to the wire axis, with additional planes having different angles with respect to the wire axis. Outside the facet area, the fatigue crack grows by the same means as shown in Figures 7.2.3.2-7 and 7.2.3.2-8 [ref. 9]. The example fatigue cracks shown in Figures 7.2.3.2-6 through 7.2.3.2-9 do not represent any of the wire fracture surfaces examined by stereomicroscopy and SEM in the Aux M4N socket.

Figure 7.2.3.2-10 represents tensile overloads over a range of progressively cold-drawn pearlitic steel wire specimens [ref. 10]. Figures 7.2.3.2-11 through 7.2.3.2-14 show a range of tensile overloads from the cold-drawn pearlitic steel wires from the Aux M4N socket. The fractures in these images fit well within the range of tensile overload fractures shown in Figure 7.2.3.2-10. Additionally, in Figure 7.2.3.2-15, an Aux M4N socket tensile overload wire failure can be seen with a defect in the center. Even around the defect in the center, the fracture surface does not exhibit the material characteristics of fatigue fracture. None of the fractures exhibit the material fatigue fracture characteristics for cold-drawn pearlitic steel wires shown in Figures 7.2.3.2-6 through 7.2.3.2-9, which show a flat fracture surface with progressively larger and farther-spaced secondary cracks opening perpendicular to the primary flat fracture surface. No material failure evidence was identified that would be attributed to fatigue fracture of the Aux M4N wires, other than the potential for the HAC fractures to have progressed from cyclic loading.

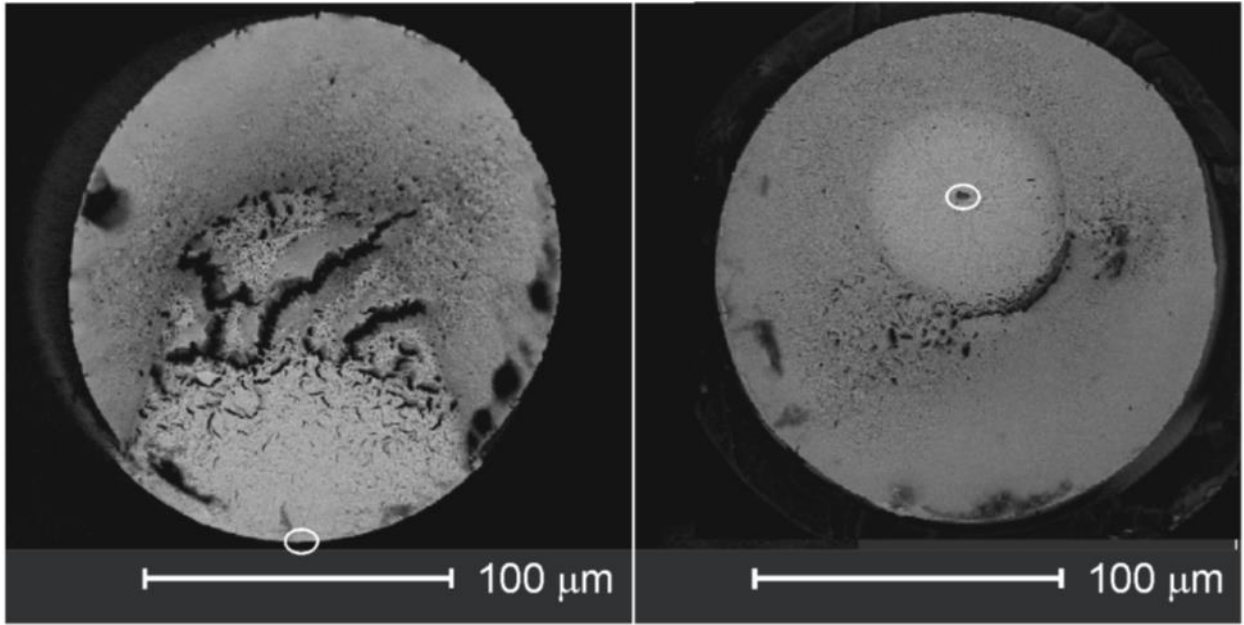


Figure 7.2.3.2-6. Fatigue Cracking in Heavily Drawn Steel Wires [ref. 9]

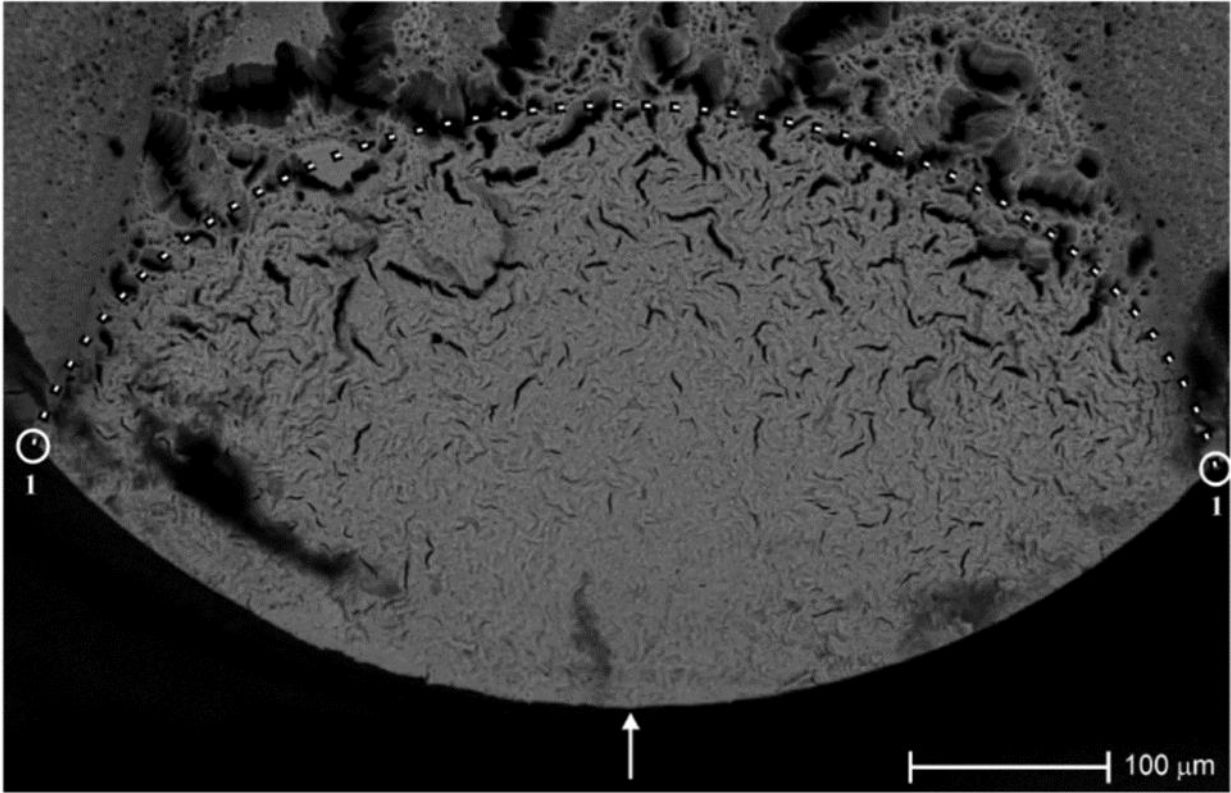


Figure 7.2.3.2-7. Closer Image of Surface-initiated Fatigue Crack in Heavily Drawn Steel Wire [ref. 9]

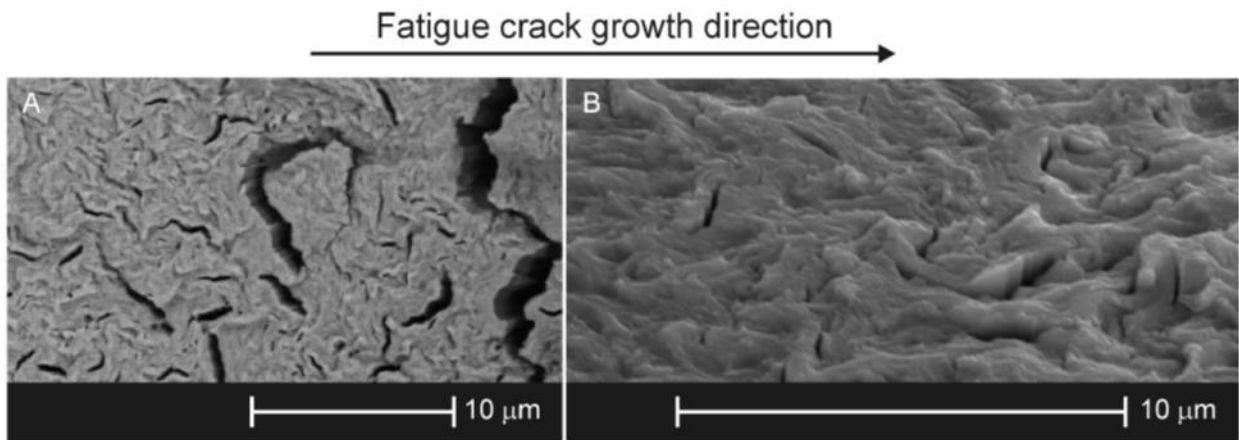


Figure 7.2.3.2-8. Fatigue Fracture Surface with Secondary Cracks
((A) looking down on fracture plane; (B) profile view of fracture plane) [ref. 9]

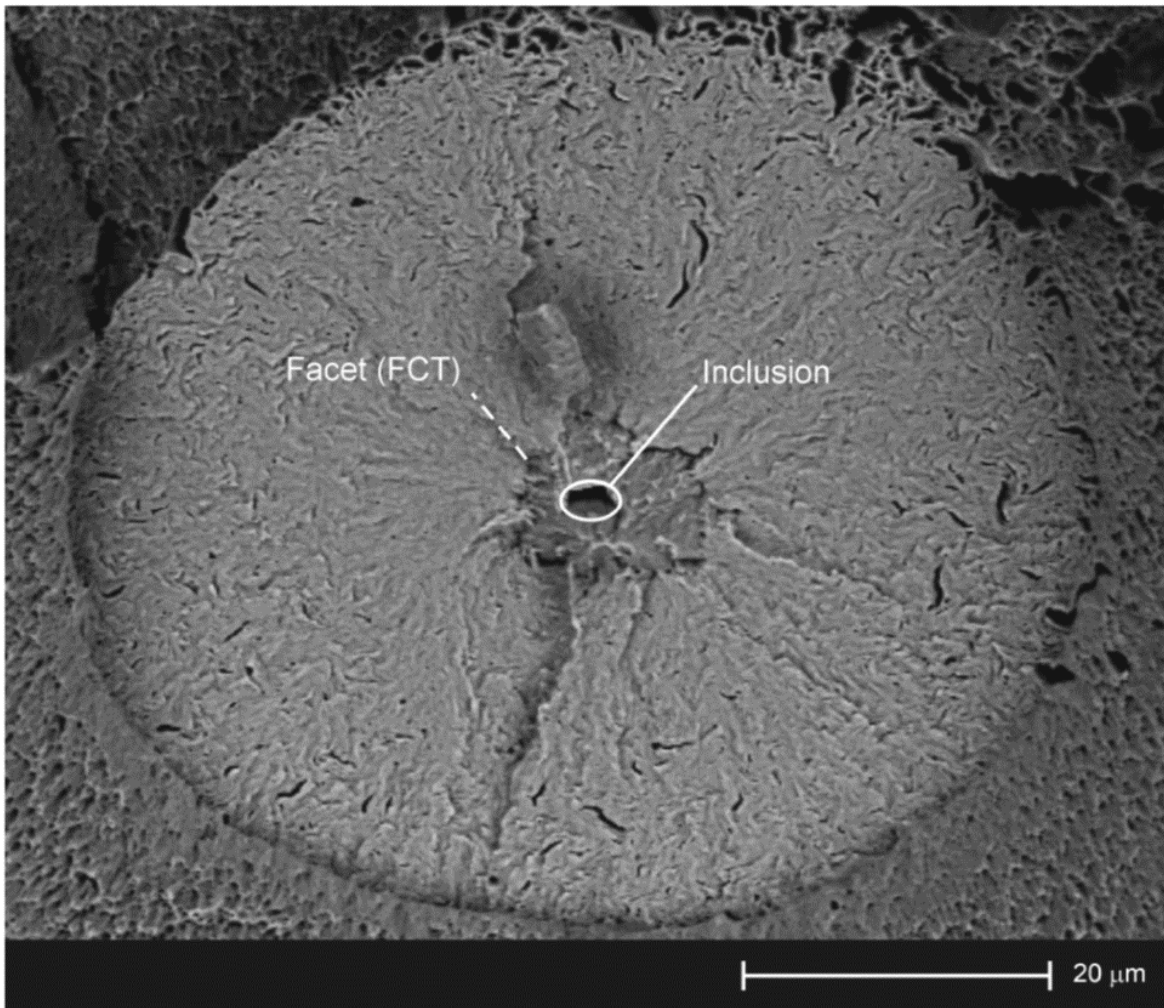


Figure 7.2.3.2-9. Closer Image of Internally Initiated Fatigue Crack, showing Facet Area [ref. 9]

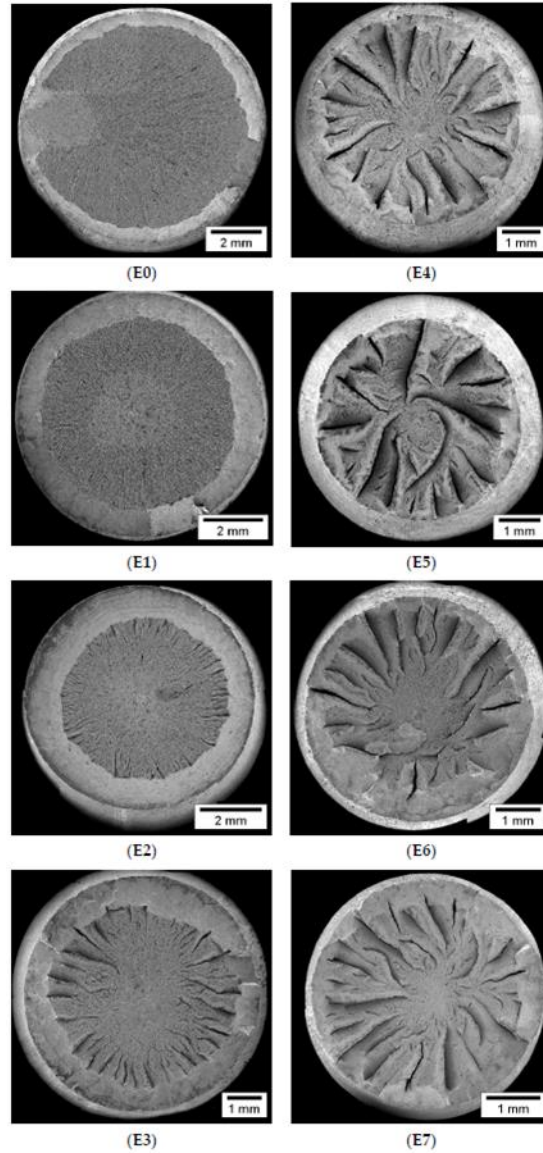


Figure 7.2.3.2-10. Images of Gradually More Progressively Cold-drawn Pearlitic Steel Wire Specimens Failed by Tensile Overload [ref. 10]

ID
 7:30  1:30
 OD

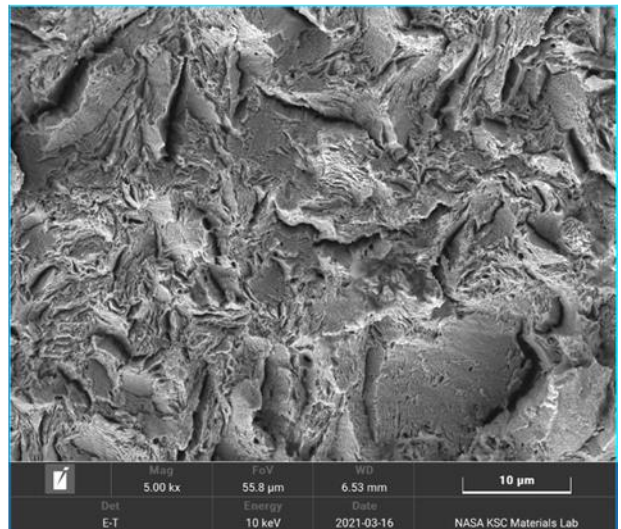
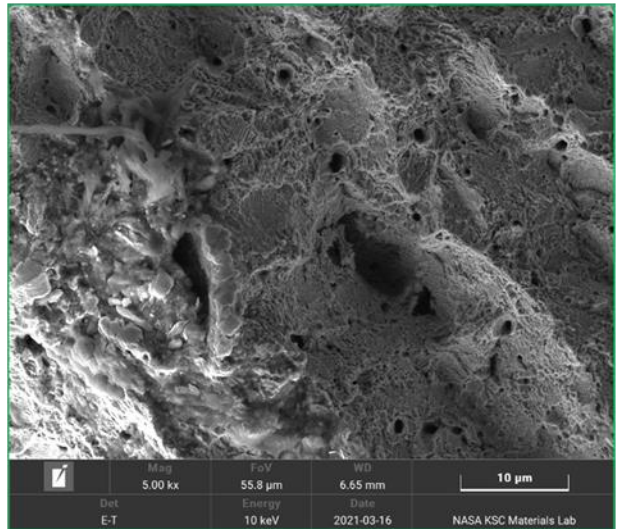
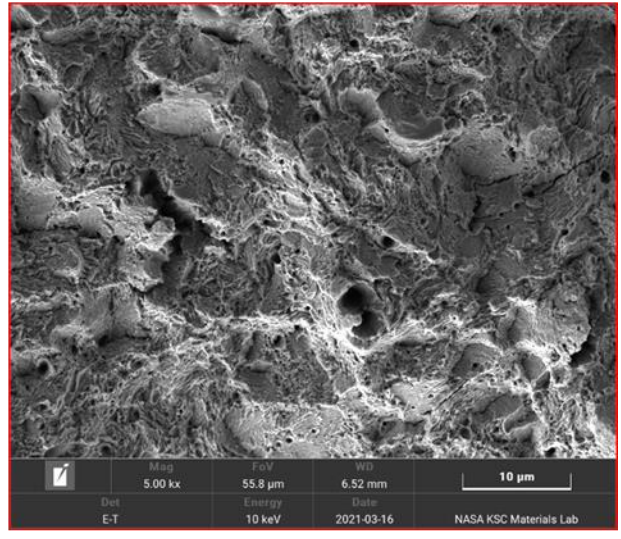
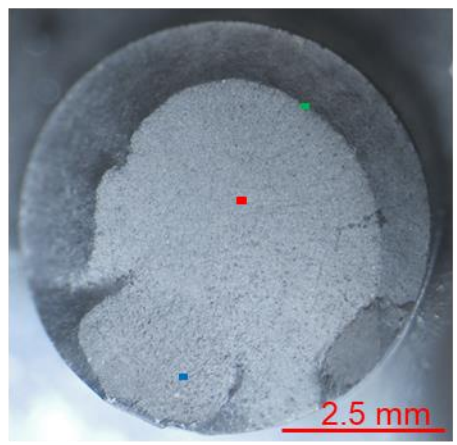


Figure 7.2.3.2-11. Images of Aux M4N Socket Wire AS

ID
 3:15  9:15
 OD

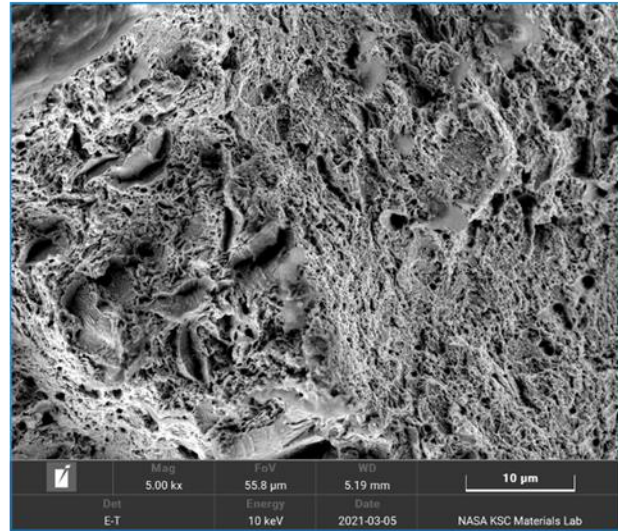
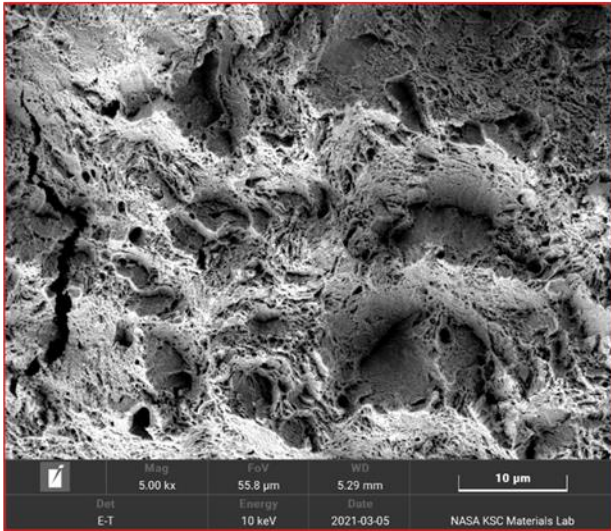
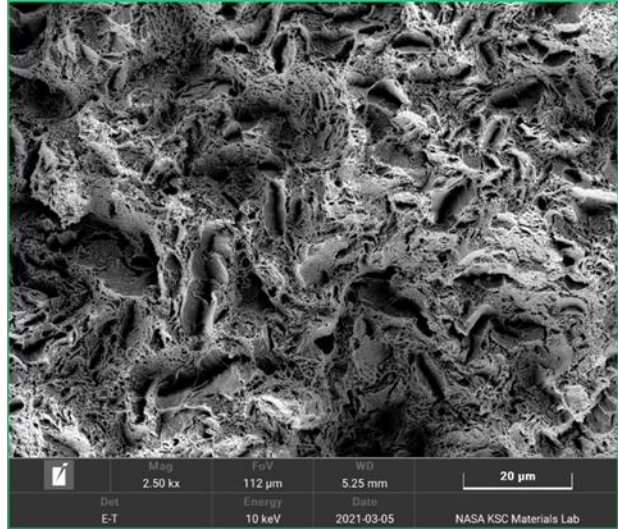
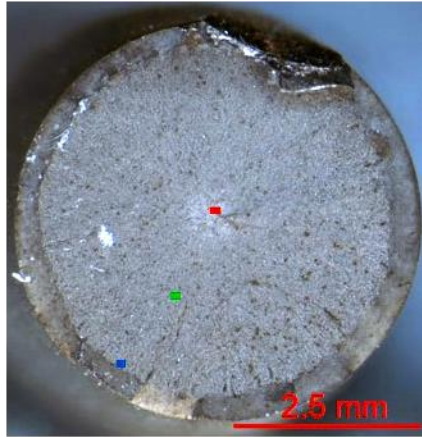


Figure 7.2.3.2-12. Images of Aux M4N Socket Wire U

ID
 5:15  11:15
 OD

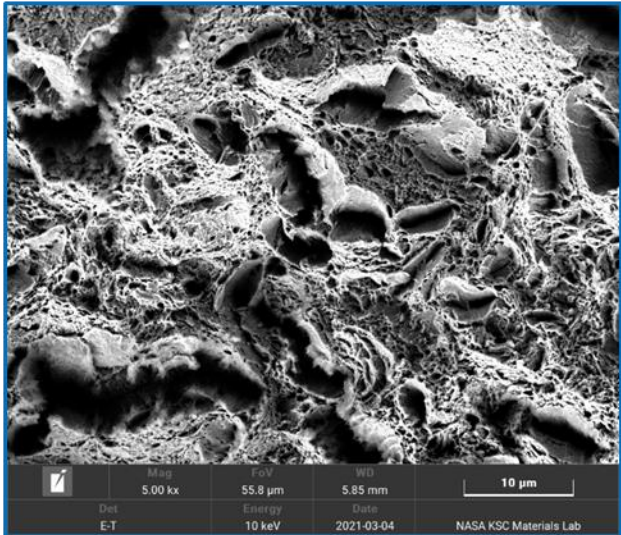
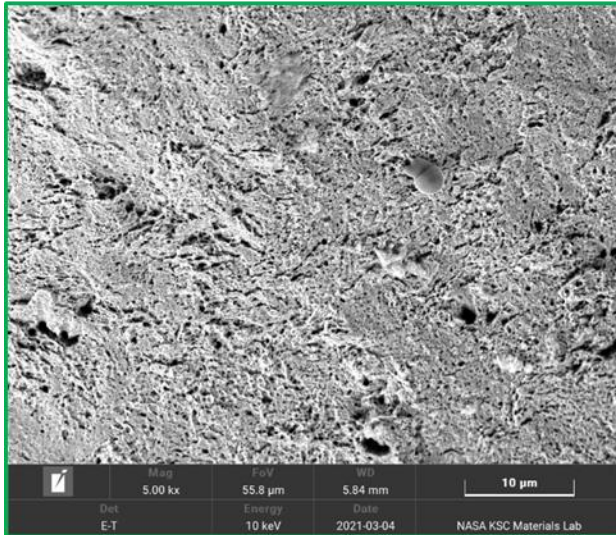
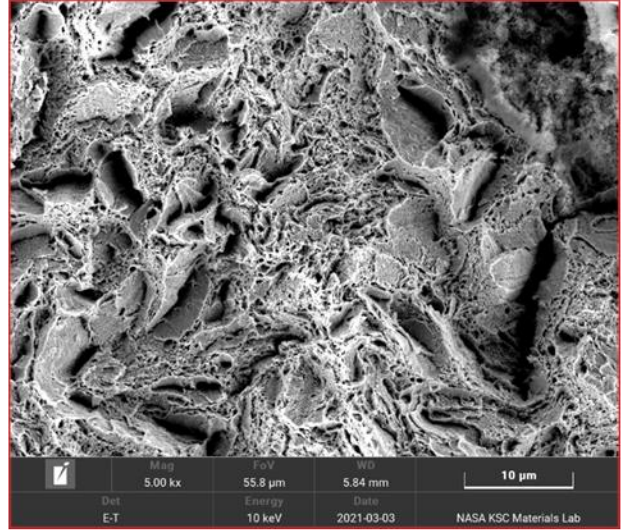
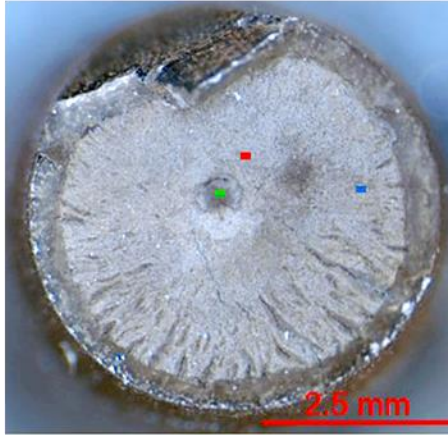


Figure 7.2.3.2-13. Images of Aux M4N Socket Wire Z

ID
 7:45  1:45
 OD

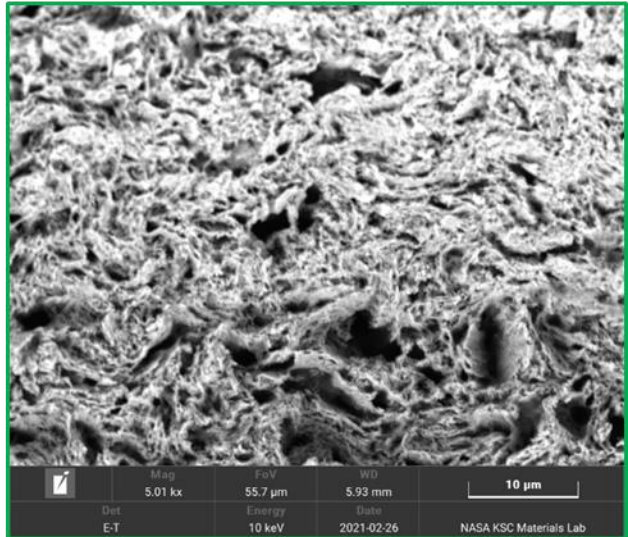
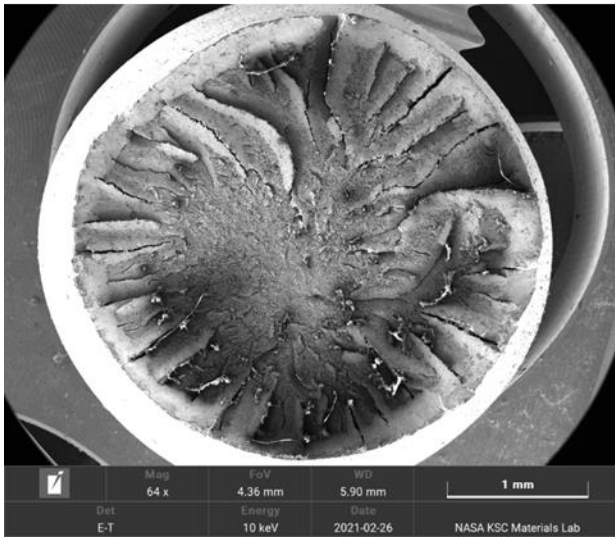
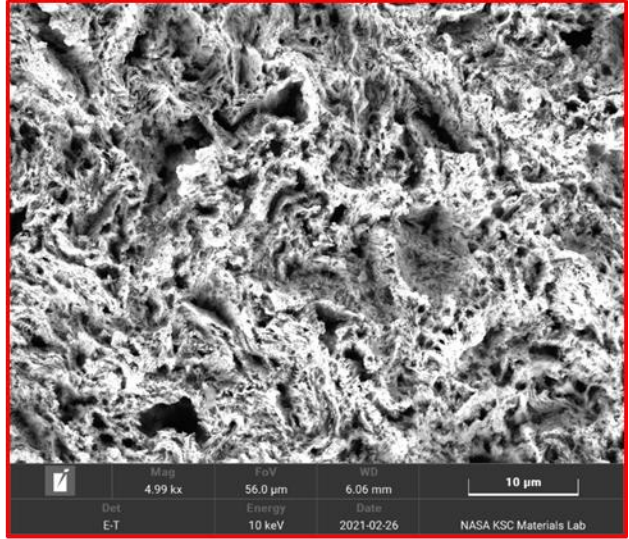
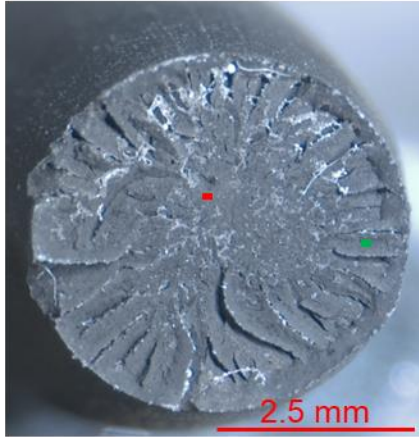


Figure 7.2.3.2-14. Images of Aux M4N Socket Wire EH

ID
2:45  8:45
OD

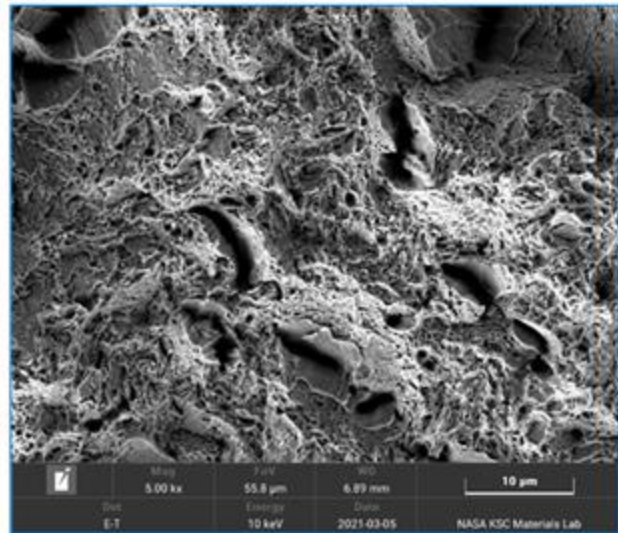
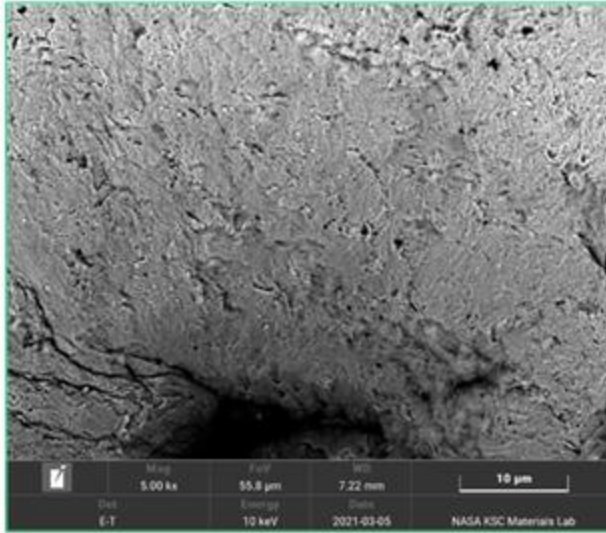
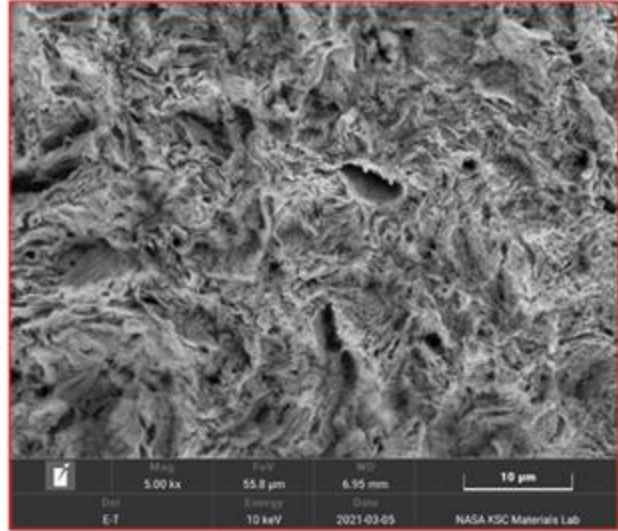
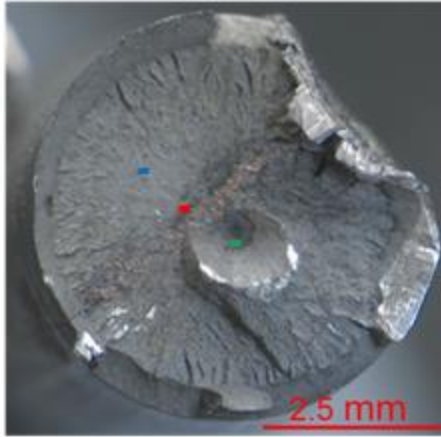


Figure 7.2.3.2-15. Images of Aux M4N Socket Wire S

Figure 7.2.3.2-16 shows a rearrangement of the pieces from slices 3g and 9g into their approximate as-built configuration following the acid-bath zinc removal process, with wire label overlays that correspond to the identified fracture morphology and the percent of necking evident. Examination of the necking evident in the fractured wires showed that the outer ring wires generally had the smallest amount of necking and the inner ring wires had the largest amount. This indicates that either the outer wires had less desirable mechanical properties than the inner wires or that there were anisotropy, temperature, or strain rate variations between the inner and outer wires. Mechanical testing of the wires did not uncover any anomalies in wire strength, and patterns of anisotropy and significant variations in temperature between the inner and outer wires were unlikely. Therefore, the inner wires most likely experienced a lower strain rate than the outer wires due to the outer wires being more highly stressed and failing first. Subsequently, stresses on the inner wires increased as the outer wires failed.

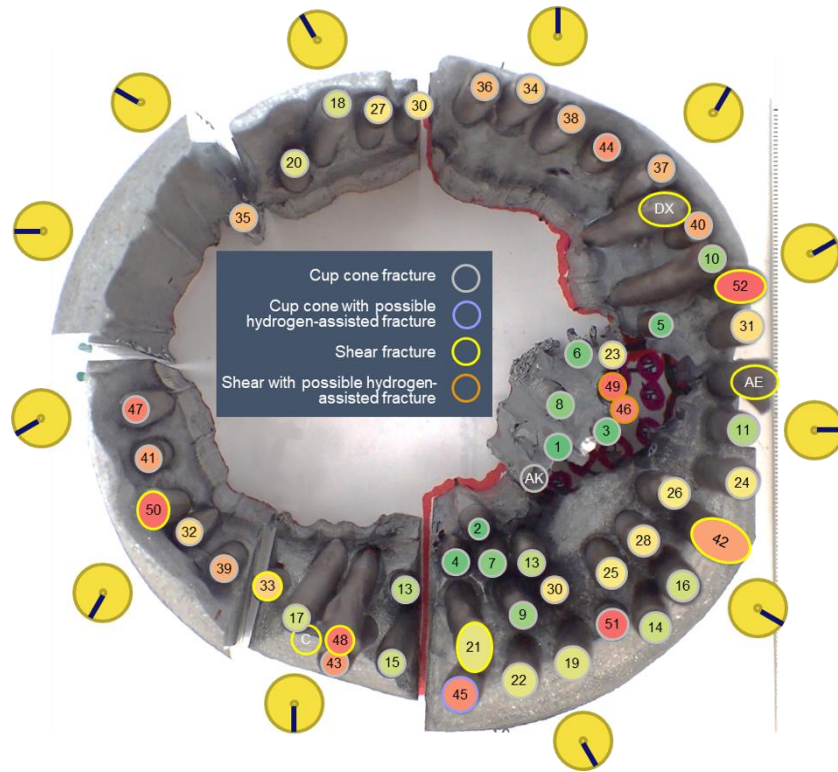


Figure 7.2.3.2-16. Reconstruction of Wire Locations following Zinc Removal with Identified Fracture Morphology (outline color of overlay) and Percent Necking (fill color of overlay)

F-12. Forty-four of the 56 wire fracture morphologies were cup-cone fractures, nine were shear fractures primarily from the outer ring, and the remaining three were mixed-mode fractures, which included a progressive failure mechanism believed to be HAC (one cup-cone/HAC and two shear/HAC).

F-13. Outer ring wires typically had less necking than inner ring wires and are expected to have failed first.

F-14. Excluding the HAC fractures, none of the wires examined by microscopy and SEM exhibited fatigue fracture.

7.2.3.3 Wire Movement within Zinc Casting

Wire ends near the casting cap, exposed on sectioning, have wire channels of varying lengths near the back of the casting. Wires exposed toward the exterior of the zinc casting exhibited less displacement than wires near the brittle fracture region, showing that some amount of displacement of the wires through the zinc occurred after the casting had solidified (see Figures 7.2.3.3-1 and 7.2.3.3-2 compared with Figures 7.2.3.3-3 and 7.2.3.3-4).

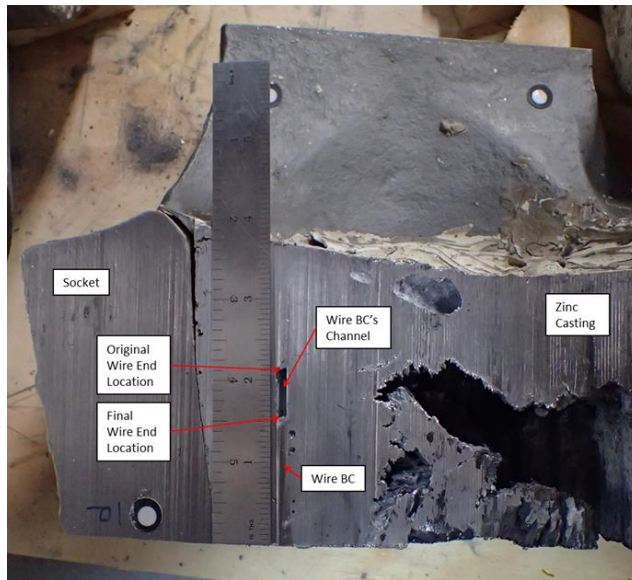


Figure 7.2.3.3-1 (Appendix A Figure 58). Measurement of Wire-end Displacement of Wire BC within Zinc Casting (image was taken from 3 o'clock half)

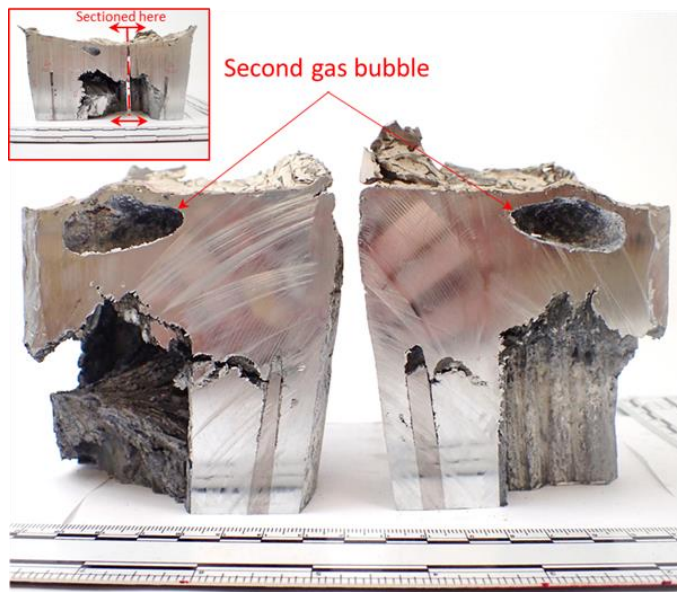


Figure 7.2.3.3-2 (Appendix A Figure 71). Slice 3a was Sectioned Longitudinally, Revealing Second Gas Bubble below Casting Cap

Additionally, the wires close to the brittle fracture region were displaced wholly or in part due to the formation of the brittle fracture feature. The variation in the amount of wire displacement suggests that wires with more displacement fractured later in the joint failure progression.

Figure 7.2.3.3-3 shows an example of embedded wires in a lower piece of the socket cavity with little or no gap between the top of the wire and the surrounding zinc. Wire AB is shown to have moved at least 1 inch down its original wire channel toward the socket base at some time after zinc solidification.



Figure 7.2.3.3-3 (Appendix A Figure 89). Wire Embedment in Zinc Casting

Figure 7.2.3.3-4 shows an example wire channel with more corrosion product on the surface in the back of the socket cavity.

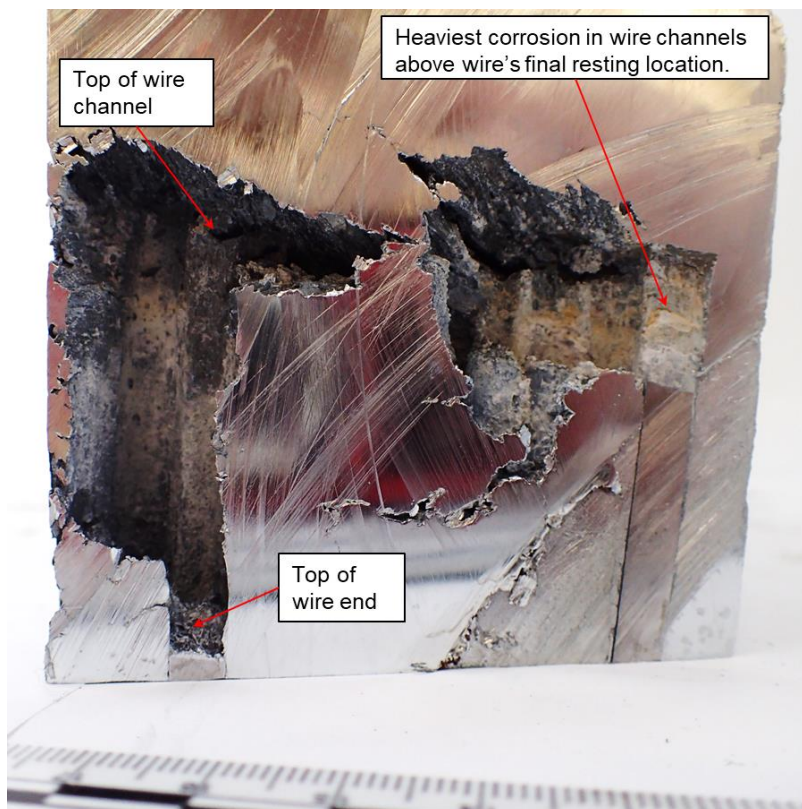


Figure 7.2.3.3-4 (Appendix A Figure 102). Relatively Large Volumes of Corrosion Visible in Wire Channels above Wires

Sectioning of the socket revealed differences in wire channel lengths associated with wire position in the socket, where inner wires showed longer channels than outer wires due to

differing rates of socket extrusion or the occurrence of brittle fracture tearing or wire-zinc bond failure. It is unclear exactly what contributed to the final form of the wire channel lengths and cleavage cavity size; however, this evidence supports the outer wires failing first and transferring load radially inward before subsequent wire failure and, finally, core pullout.

The back of the socket cavity opening has two distinct regions. One region is the wire imprint region. This region is flat and parallel with the socket base, with wire-end imprints containing both heavy amounts of zinc oxide and trace amounts of iron oxide (see Figures 7.2.3.3-5 and 7.2.3.3-6). The flat surface and heavy corrosion suggest a poor bond between the zinc and wire ends and indicate a casting defect. This region does not exhibit the same faceted appearance as the neighboring brittle fracture region from slice 3a.



Figure 7.2.3.3-5 (Appendix A Figure 69). Closer View of Back of Socket Cavity on Slice 9a (view 1)

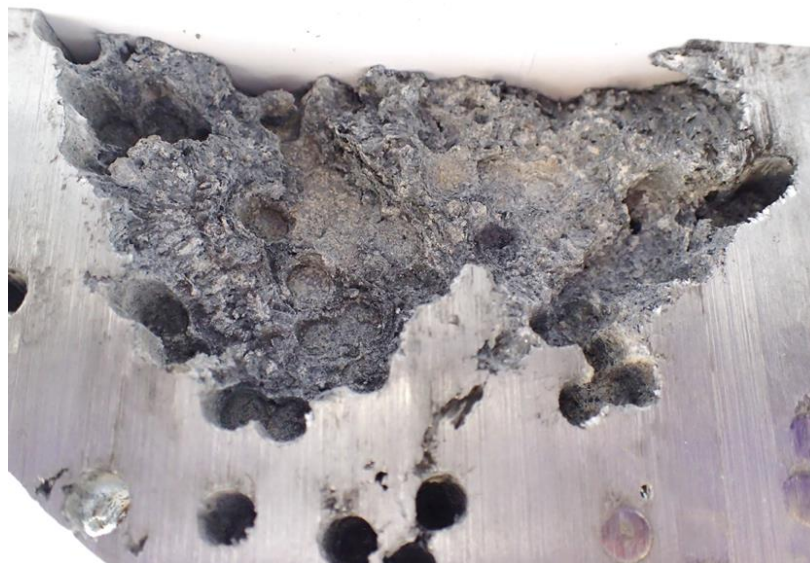


Figure 7.2.3.3-6 (Appendix A Figure 70). Closer View of Back of Socket Cavity on Slice 9a (view 2)

The other distinct region is a faceted surface exhibiting brittle fracture, characteristic of cleavage fracture. The brittle fracture region forms a cone shape that comes to a point just behind one of the large gas bubbles shown in Figures 7.2.3.3-7 and 7.2.3.3-8. The fracture surface extends from wire channels in the cable-end section outer diameter (that pulled free of the socket) to just below the gas bubble.

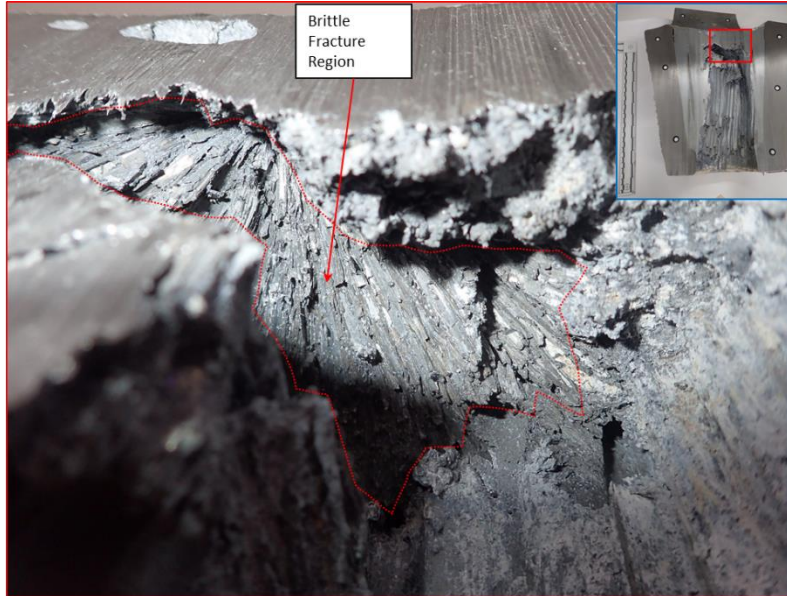


Figure 7.2.3.3-7 (Appendix A Figure 65). View of Casting Cap Side of Brittle Fracture Region in Back of Socket Cavity on Slice 3a (view 1)



Figure 7.2.3.3-8 (Appendix A Figure 66). View of Casting Cap Side of Brittle Fracture Region in Back of Socket Cavity on Slice 3a (view 2)

The largest amounts of corrosion were seen along the wire channels. The adjacent brittle fracture region's faceted surface exposes the elongated portion of the zinc grains. Along the faceted surface, most of the corrosion buildup was on ridges and protrusions; the flat surfaces exhibited a dull gray appearance, having only a relatively light amount of corrosion (see Figure 7.2.3.3-9).

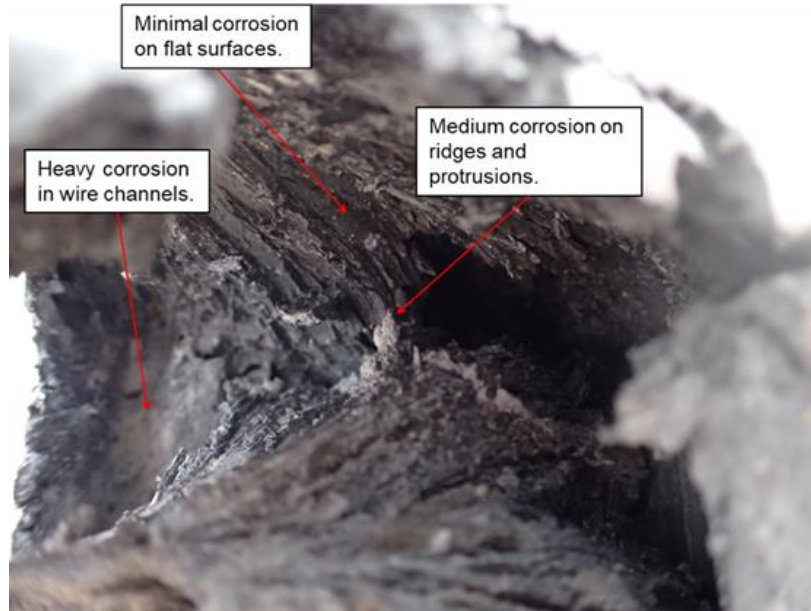


Figure 7.2.3.3-9 (Appendix A Figure 104). Image of Faceted Surface within Socket Cavity

Additionally, the ends of many elongated grains appear lifted from the surrounding surface (see Figure 7.2.3.3-10). Note that significant swarf from the fracture analysis (FA) cutting process is visible along edges and protrusions within the image.

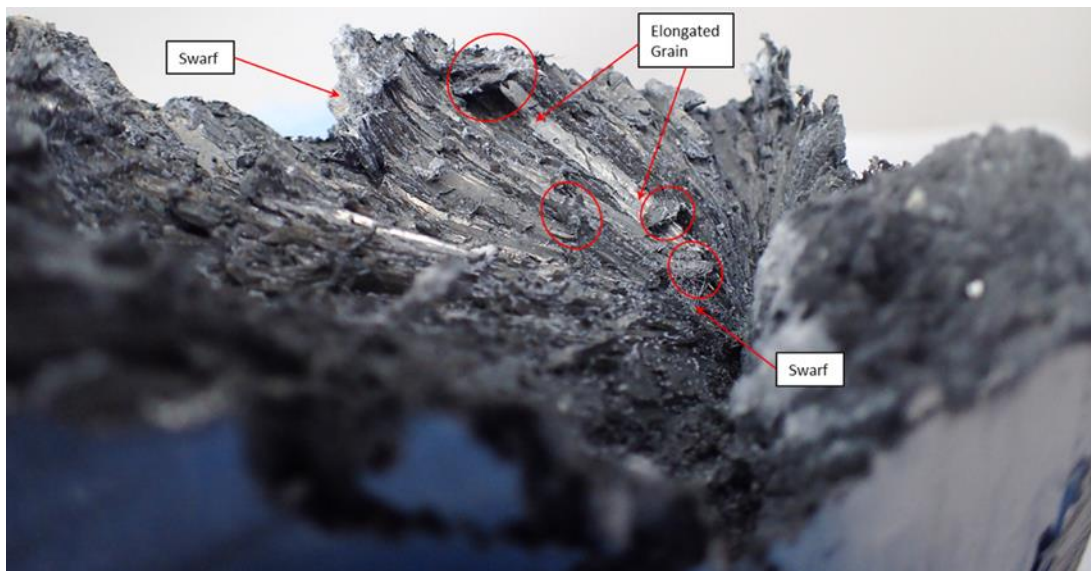


Figure 7.2.3.3-10 (Appendix A Figure 68). View of Casting Cap Side of Brittle Fracture Region in Back of Socket Cavity on Slice 3a

Cracks from the faceted structure are seen on the abrasive saw cut surface that extends from the tops of the wire channels (the zinc inner diameter) to an embedded wire end near the zinc outer

diameter (see Figure 7.2.3.3-11). The crack extends past the wire on a different transverse plane toward the outer diameter of the zinc casting. The crack seen in Figure 7.2.3.3-11 physically connects with the crack that extends around the cable-end section interface between the faceted surface and the tops of the wire channels.

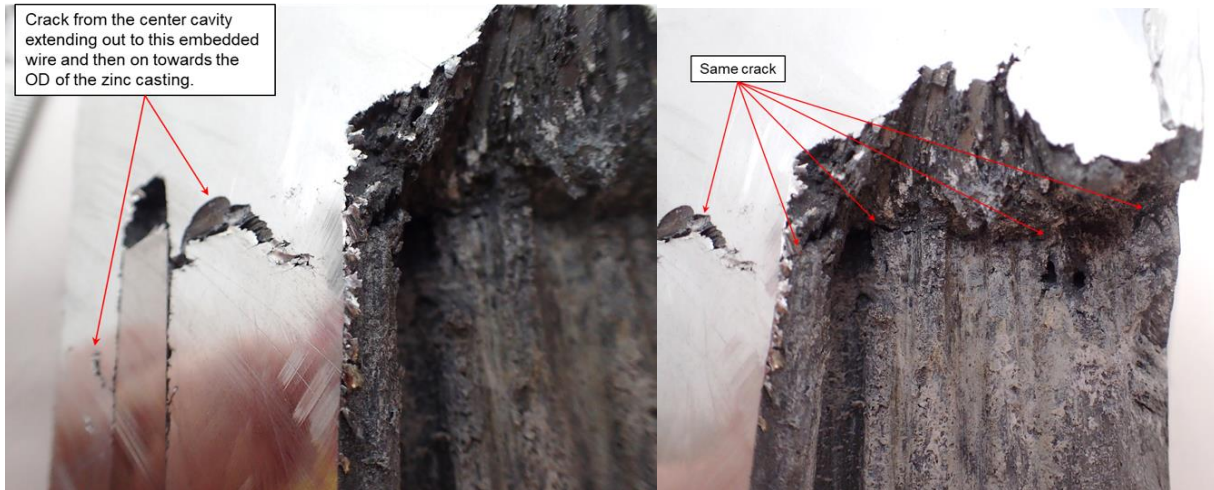


Figure 7.2.3.3-11 (Appendix A Figures 85, 86). Surface of Additional Longitudinal Cut made on Slice 3a

F-15. Wire imprint region of the zinc in the back of the socket cavity is heavily corroded and poorly bonded to the wire ends.

F-16. The brittle fracture region of the zinc in the back of the socket cavity is corroded, with faceted surfaces that expose the elongated portion of the grains (i.e., cleavage fracture), and the ends of the grains have lifted up (i.e., a peeling failure).

7.2.4 Metallography

Metallographic samples were taken from the several regions in the zinc casting. The macro-etchant revealed an elongated grain structure with significant variation in grain size and length (see Figure 7.2.2.2-2).

Smaller, fine elongated grains solidified outward from the individual wire diameters. Larger, long elongated grains solidified inward from the socket wall. The thickest and longest grains solidified inward from the socket cone wall and grew at an angle upward toward the casting cap. A thin layer of elongated grains solidified downward from the casting cap. Grain size and orientation indicate that the socket housing and cable bundle were significant heat sinks during solidification, resulting in a large dissipation through the socket base volume. Longer and larger grains emanating from the socket wall near the casting cap grew for the longest time.

Gas bubble locations signify the last molten volumes of zinc. The casting generally solidified from the bottom up and the outside in with some significant grain growth outward from the cable bundle, but less growth from outer individual wires toward the back of the socket. Next, a thin layer of zinc solidified across the top of the molten pour, solidifying from the top down to a boundary that meets the rest of the solidified zinc and intersects the large gas bubbles.

Figure 7.2.4-1 shows that the zinc grain structure adjacent to the cable/zinc slug, which pulled free of the socket near the socket base, is very fine. Intermittent cracks are visible, running parallel with the cable/zinc slug boundary plane (50 times magnification). Grain orientation in the socket, adjacent to the cable-end section that pulled free of the joint, approaches parallel to the cable-end section (Figures 7.2.4-2 and 7.2.4-3).

However, the orientation changes to approximately perpendicular to the cable-end moving away from the cable-end section interface to the inner cone wall of the socket. Measurements were taken from the plane adjacent to the cable-end section that pulled free of the socket to the approximate location where the grain orientation is elongated (Figure 7.2.4-4).

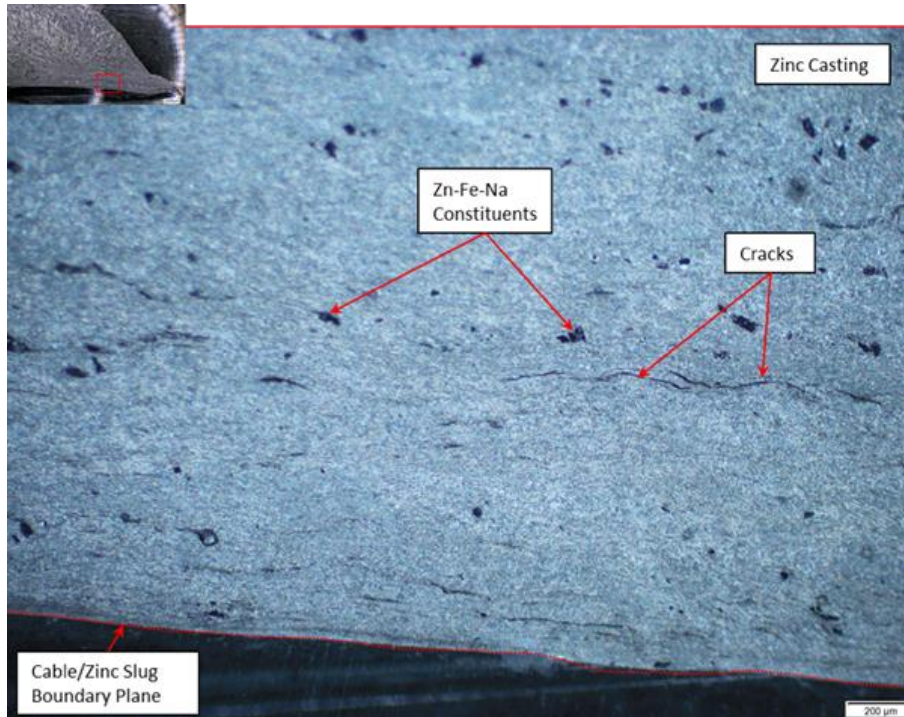


Figure 7.2.4-1 (Appendix A Figure 79). Zinc Grain Structure Adjacent to Cable/Zinc Slug

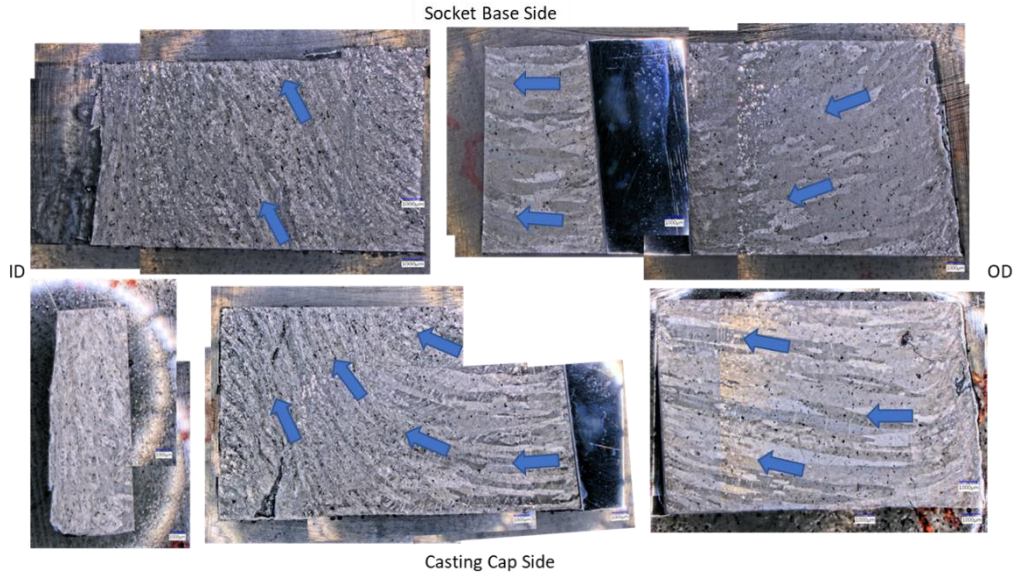


Figure 7.2.4-2 (Appendix A Figure 74). Directional Changes in Elongated Grain Direction from Grains analyzed in Slice 3c (from Appendix A Figure 288)



Figure 7.2.4-3 (Appendix A Figure 75). Directional Changes in Elongated Grain Direction from Grains Analyzed in Slice 9g (from Appendix A Figure 293)

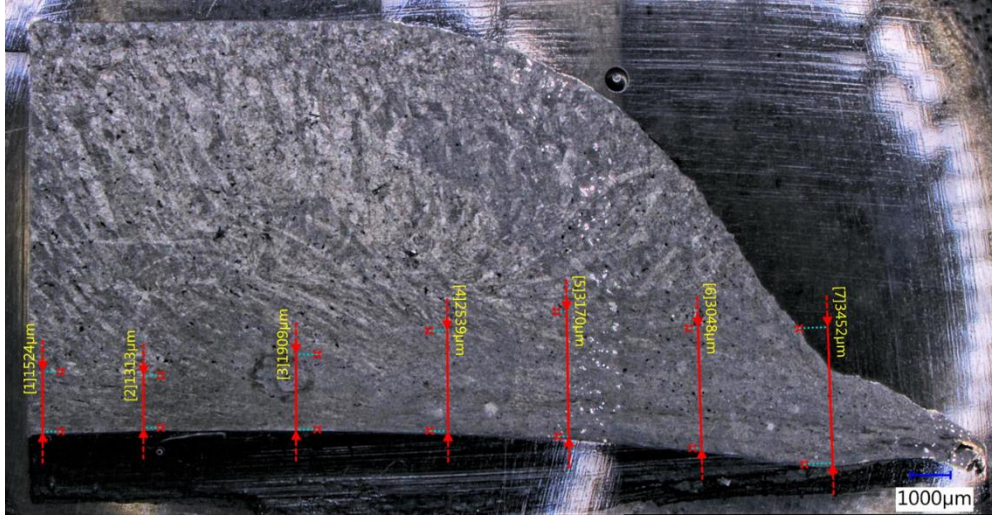


Figure 7.2.4-4 (Appendix A Figure 78). Measurements taken on Appendix A Figure 295 from Plane Adjacent to Cable/Zinc Slug

The metallographic specimen in Figure 7.2.4-4 was microetched with Klemm’s 1 Reagent tint etchant to reveal the metallurgical structure within the grains. Figures 7.2.4-5 and 7.2.4-6 show some of the grain structure features in the larger grains near the zinc casting outer diameter. This tint etch reveals internal grain features associated with deformation mechanisms (e.g., slip planes and twin boundaries) that would be expected in highly stressed zinc. Additionally, recrystallization is evident, where new grains are crystallizing within the original grains. While this makes identifying the original grain boundaries difficult, it appears that the individual deformation mechanisms are confined to their original grains and not traversing their original grain boundaries.

Very little research was identified regarding cyclically loading commercially pure polycrystalline zinc. One study noted that the main difference between unidirectional compression and cyclic compression-compression loadings in commercially pure polycrystalline zinc is that twin boundary cracks are not contained within their grain boundaries in compression-compression fatigue tests [ref. 11]. Without evidence of the deformation mechanisms traversing grain boundaries, it difficult to discern the contribution of any additional cyclic loading damage from the accumulated sustained loading damage within the zinc.

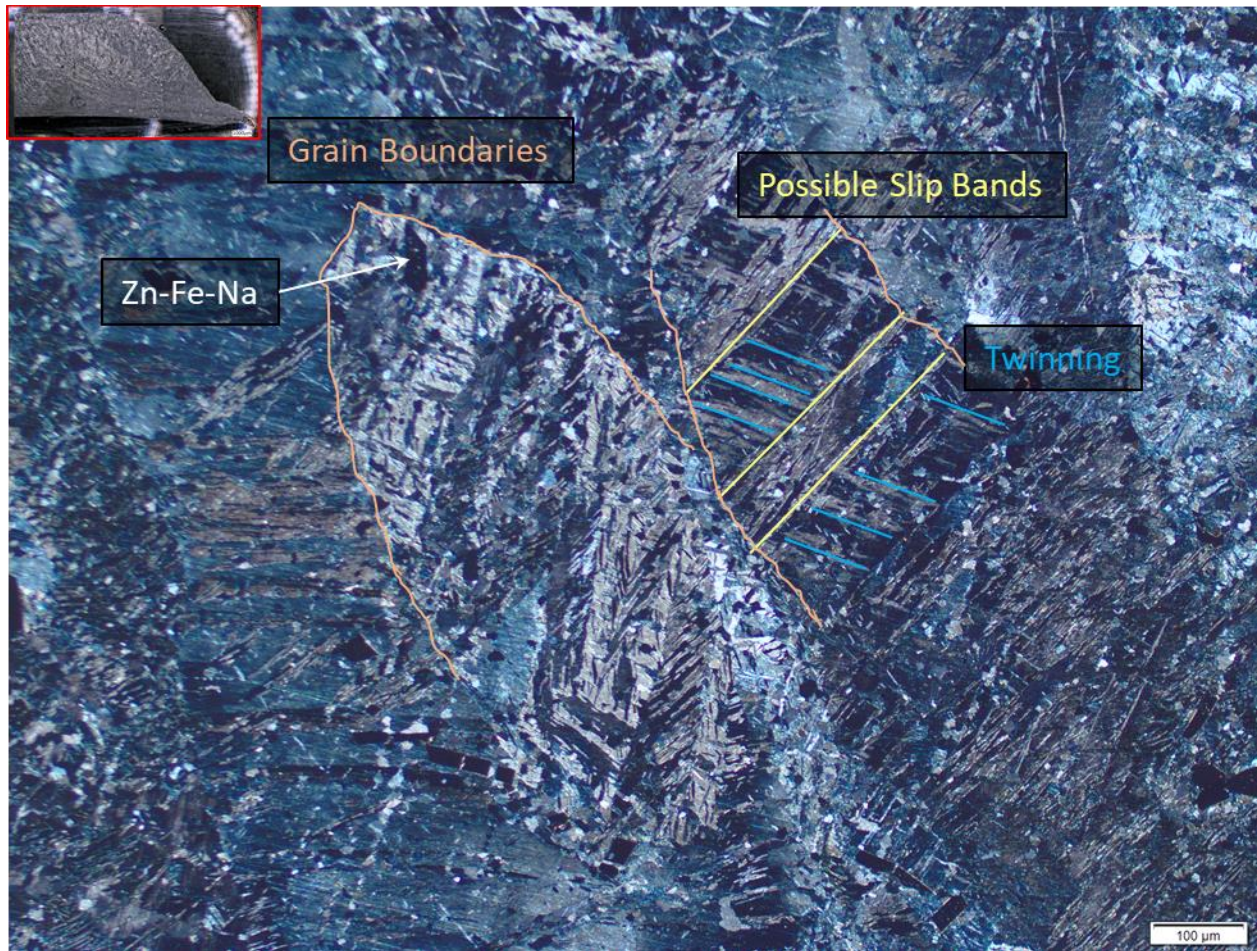


Figure 7.2.4-5 (Appendix A Figure 80). Metallograph Image of Tint Etch of Large Grains Near Socket Base and Zinc Casting Outer Diameter

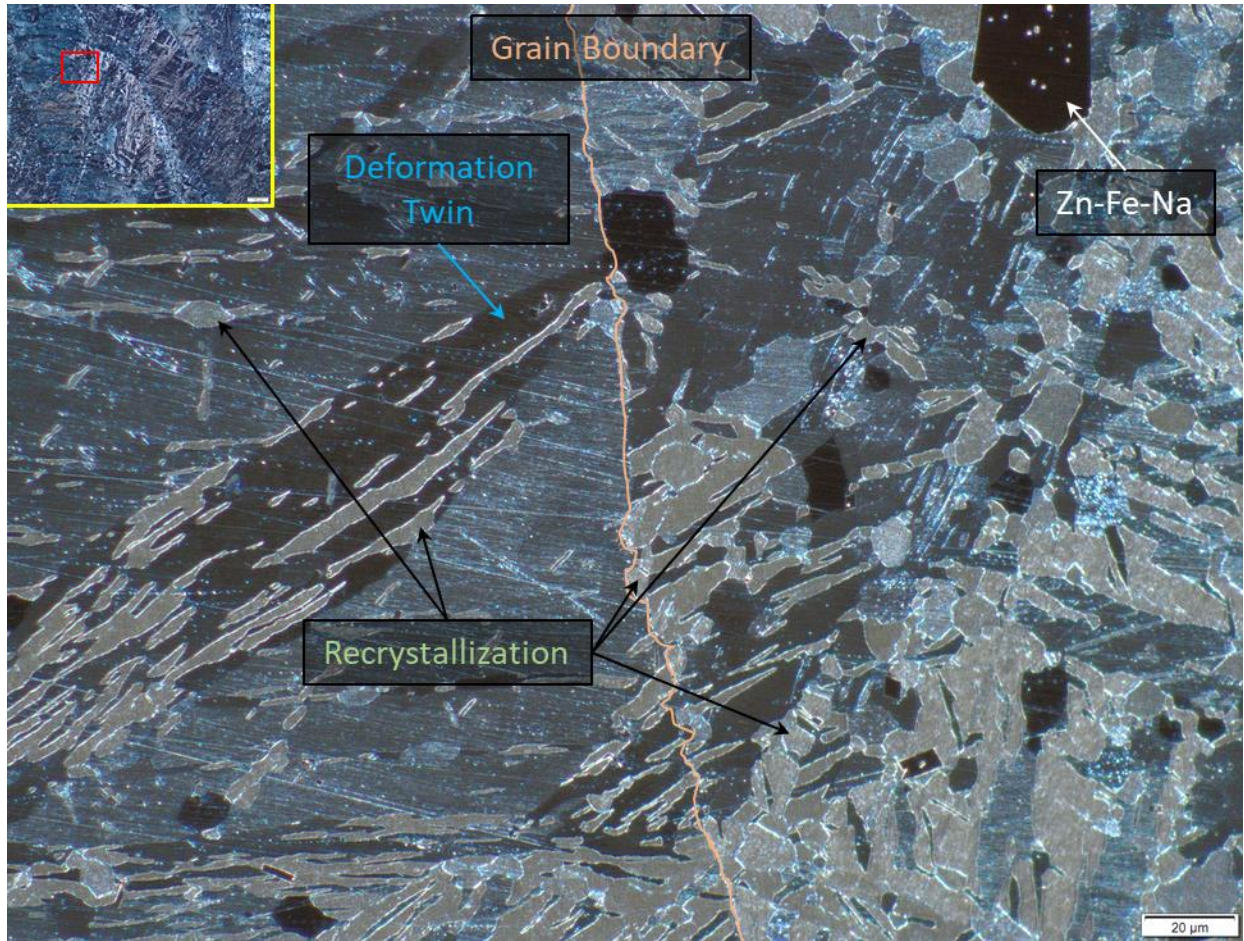


Figure 7.2.4-6 (Appendix A Figure 81). Metallograph Image of Tint Etch of Large Grains Present Near Socket Base and Zinc Casting Outer Diameter

Figure 7.2.4-7 is a tint etch revealing the microstructure near the cable/zinc slug boundary, which shows that the grains have fully recrystallized. The recrystallized grain boundaries are generally aligned 45° to the stress axis, which runs parallel to the cable/zinc slug boundary. This result appears consistent with histograms of uncavitated high-purity zinc grain boundaries with respect to stress axes for specimens fractured in slow tension at low temperatures. Singh et al. showed that the frequency of a 45° angle between the grain boundary and the stress axis for high-purity zinc is $\sim 30\%$ at 73 degrees Fahrenheit ($^\circ\text{F}$) and peaks at 40% at 153 $^\circ\text{F}$ for constant engineering strain-rate tensile tests [ref. 12].

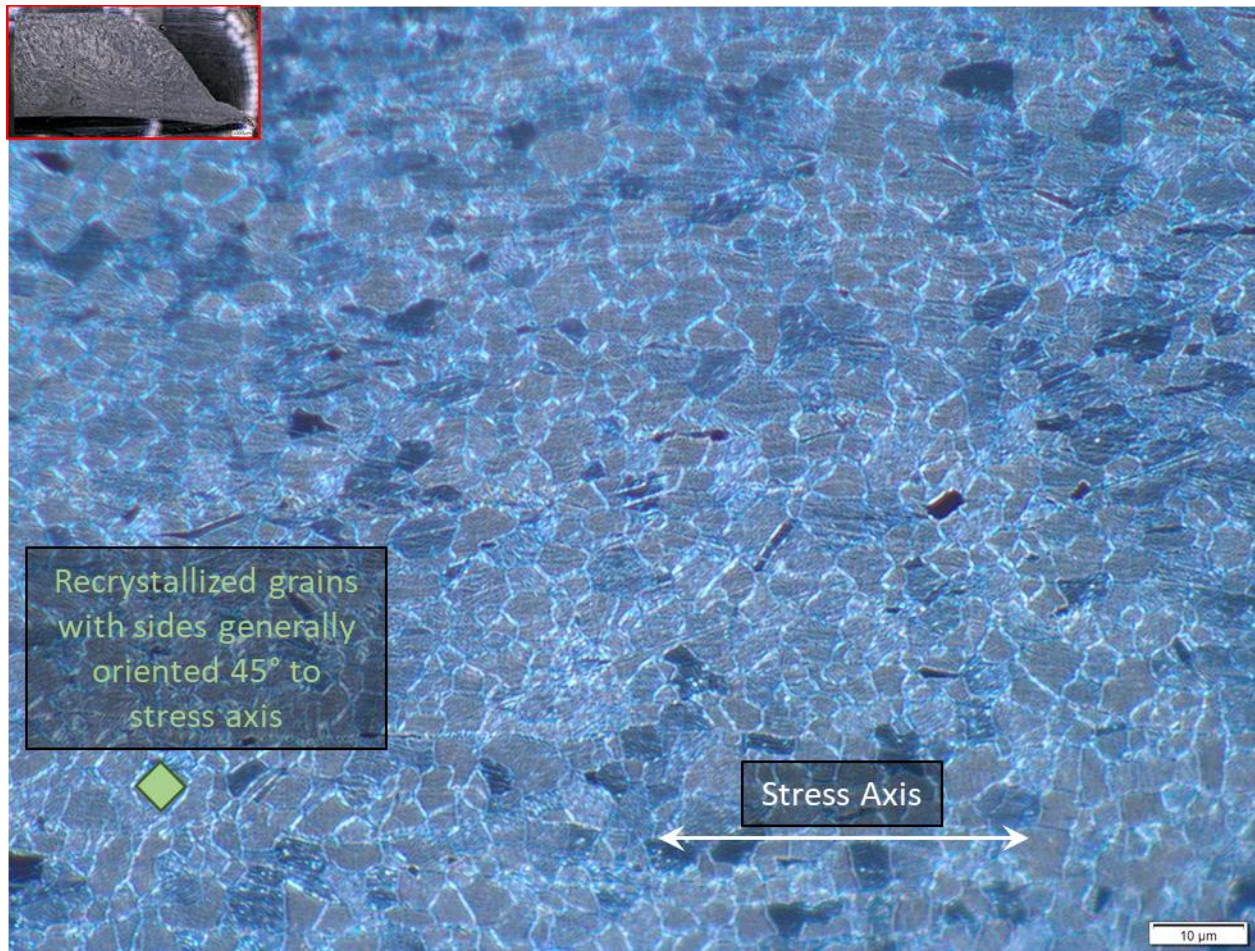


Figure 7.2.4-7 (Appendix A Figure 82). Metallograph Image of Tint Etch of Small Grains Present Near Socket Base and Cable/Zinc Slug Boundary

Creep phenomenon in stressed polycrystalline metals is generally classified as a high-temperature process, defined as ~40% of the homologous temperature (i.e., the ratio of the metal's temperature to its melting point, measured on an absolute temperature scale (i.e., Kelvin or Rankine)). Thus, creep becomes a critical design parameter for different metals at different temperatures. Commercially pure zinc has a melting point of 788 °F, ~42% of its melting point at room temperature, which is within the expected range for activating creep deformation mechanisms. Therefore, the time-dependent creep properties of zinc are a critical design parameter in a sustained load structure.

Creep deformation is a time-dependent failure mechanism, dependent on temperature and load. Over that time, creep deformation is divided into three stages: primary, secondary, and tertiary. In the primary stage, strain rate decreases with time and strain, which is due to strain hardening within the material. The secondary stage is characterized by the strain rate being relatively constant due to a balance of work hardening and annealing. This stage is typically the longest in duration, and no material strength is lost in this or the primary stage. In the tertiary stage, the strain rate increases exponentially, which is associated with internal cracking or cavitation and decreases the effective material area. This process eventually leads to failure, termed creep rupture. At low temperatures and a high speed of deformation, creep rupture tends to be

transgranular; at high temperatures and low speeds of deformation, creep rupture tends to be intergranular.

Small, non-connected cracks are present within the fully recrystallized grain region near the cable/zinc boundary (see Figures 7.2.4-1 and 7.2.4-8), running parallel with the cable-end section. These cracks are either from the tertiary stage or cavitation/voids that were squeezed closed due to continued confining pressure imposed by the cable tension and socket wall. Figure 7.2.4.8 shows the same high-magnification image of non-connected cracks in different illuminations after tint etching to see the microstructure within the grains. The cracks appear predominantly intergranular and, where not fully connected, form a continuous crack from adjacent voids spreading along grain boundaries. As stated earlier, intergranular creep rupture tends to be associated with high temperatures and low speeds of deformation.

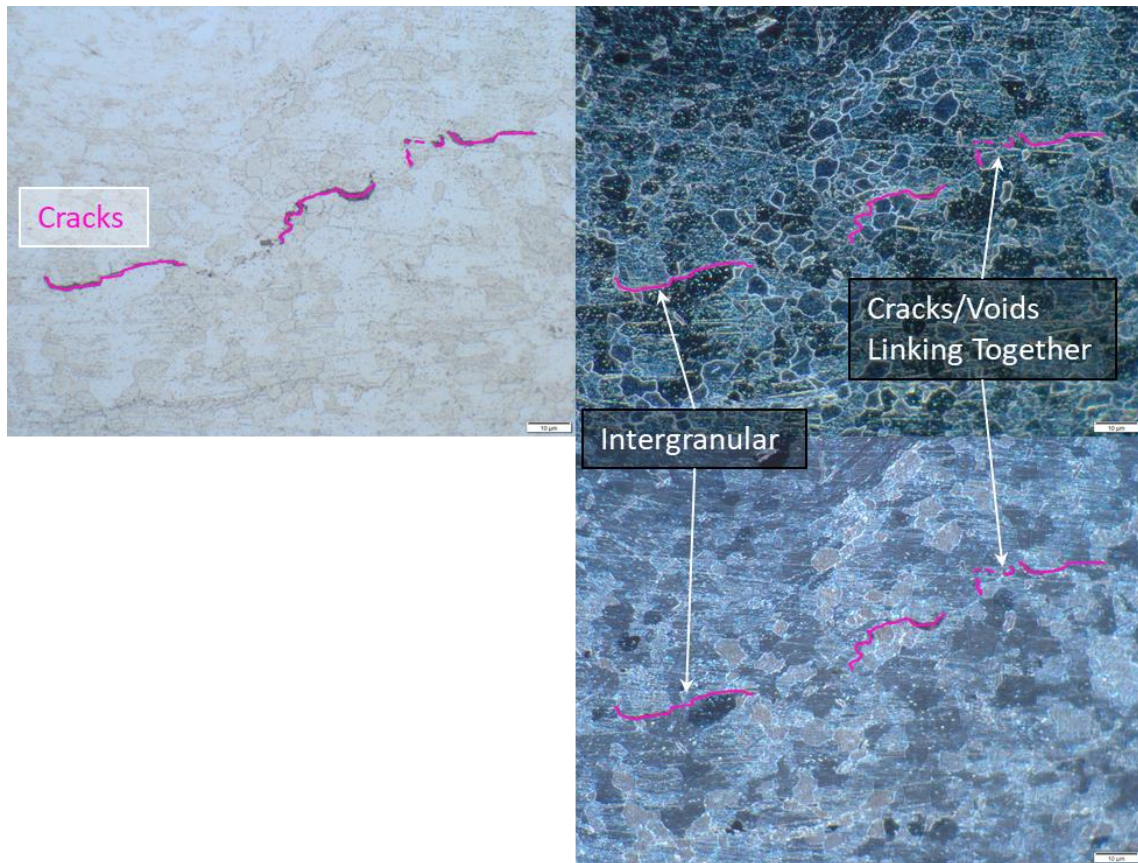


Figure 7.2.4-8 (Appendix A Figure 83). Cracks Present in Appendix A Figure 295 Adjacent to Cable/Zinc Slug Boundary

Creep deformation mechanism maps provide a way to assess the dominant deformation mechanisms at play for varying temperatures, shear stress, strain rate, and grain sizes. Because the Aux M4N primarily carries dead loads at ambient temperature, a Mohamed-Langdon map [ref. 13] could be a useful aid in understanding how variations in casting grain size and shear stresses relate to strain rate. A Mohamed-Langdon map holds the stress and temperature constant and maps the creep deformation mechanisms against grain size and shear stress. The data to use this technique were not available during this investigation but may be useful for future study.

F-17. Zinc casting was composed of elongated grains, with significant variation in both grain size and length.

F-18. Metallography shows no evidence of fatigue cracking within the zinc, but minor additional contributions of cyclic loading damage may not be discernable from the overall contributions of sustained loading damage, as both would manifest themselves in deformation mechanisms (e.g., twinning and slip bands) present within the zinc.

F-19. The zinc nearest the socket base, adjacent to the cable/zinc boundary, was determined to be in the late secondary or tertiary stage of creep.

- Zinc creep becomes a design consideration when its homologous temperature exceeds 40%, which is the case for zinc at room temperature.
- Grains near the cable/zinc boundary are fully recrystallized and have grain boundaries that are generally oriented 45° to the stress direction.
- Cracks appear predominantly intergranular, which is typically associated with creep rupture at high temperatures and low speeds of deformation.

7.2.4.1 Transgranular Bulk Cracking

Cracks were found through the bulk of the zinc. Initially, on the first longitudinal cut through the zinc casting, a crack was observed between the outer and inner diameters of the zinc casting (see Figures 7.2.4.1-1 and 7.2.4.1-2). Figure 7.2.4.1-1 shows the 12 o'clock position in the 9 o'clock half. Corrosion product, most likely zinc oxide, filled the cracks. Figure 7.2.4.1-2 shows the 12 o'clock position in the 3 o'clock half.

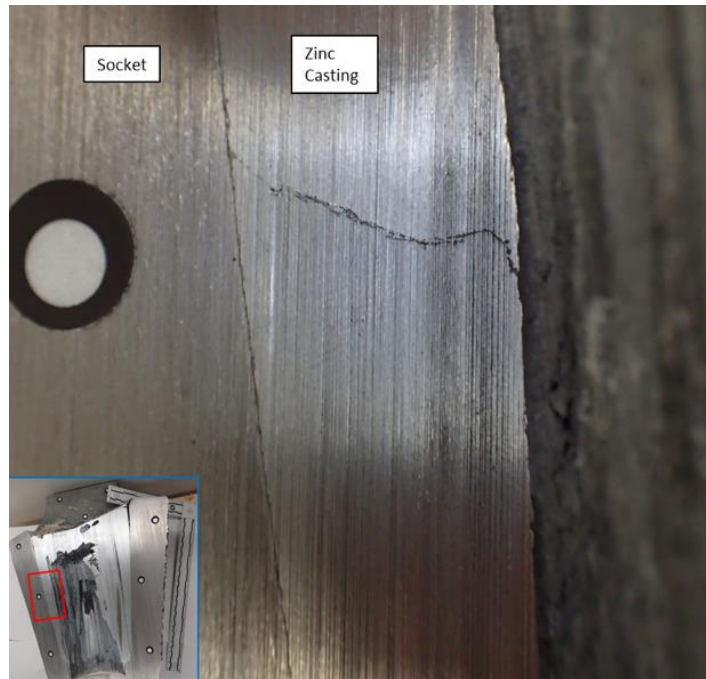


Figure 7.2.4.1-1 (Appendix A Figure 55). Close-up View of Crack Present in Zinc Casting at 12 o'clock (9 o'clock half)

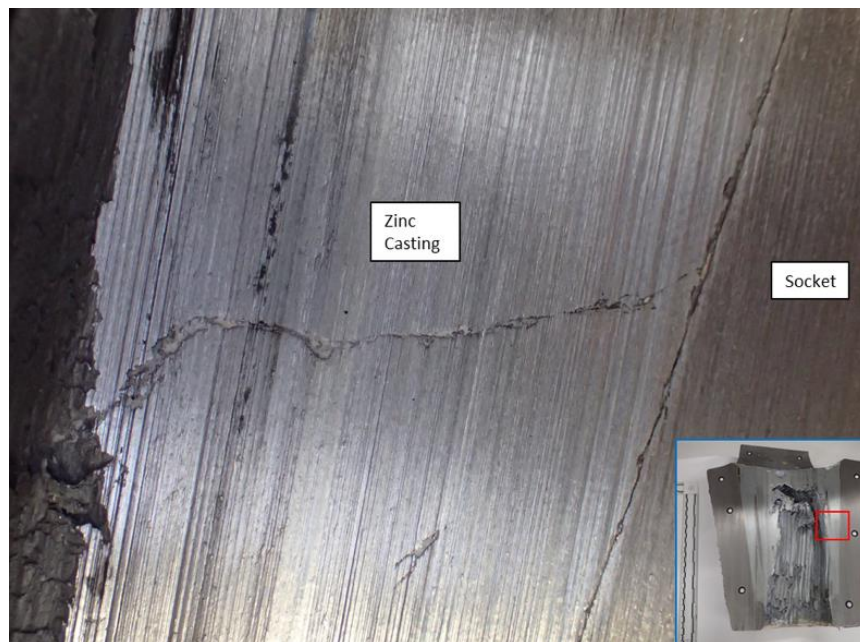


Figure 7.2.4.1-2 (Appendix A Figure 56). Close-up View of Crack Present in Zinc Casting at 12 o'clock (3 o'clock half)

Additional cracks were identified throughout the bulk zinc sectioned from approximately mid-depth into the socket (see Figures 7.2.4.1-3 through 7.2.4.1-6). These cracks did not follow grain boundaries and were not aligned in any particular orientation. The cracks varied in thickness, at times appearing to be connecting larger, irregularly shaped porosity or widening due to local grain structure or additional corrosion. The only noticeable orientation to the cracks was that

these cracks ran along or adjacent to wire surfaces. Although these cracks and the surrounding zinc were not examined in close detail, it is believed that because the cracks were completely filled with zinc oxide the cracks were present before the ultimate socket failure; however, using corrosion as a timeline indicator carries uncertainty due to the many factors and localized conditions that affect corrosion rates.

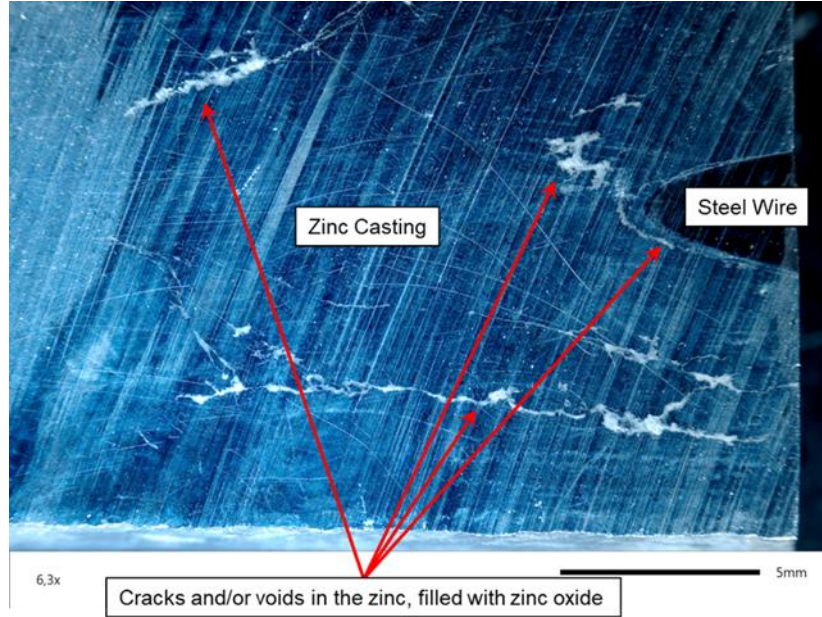


Figure 7.2.4.1-3 (Appendix A Figure 84). Cracks and Voids Found during Metallography of Slice 3c

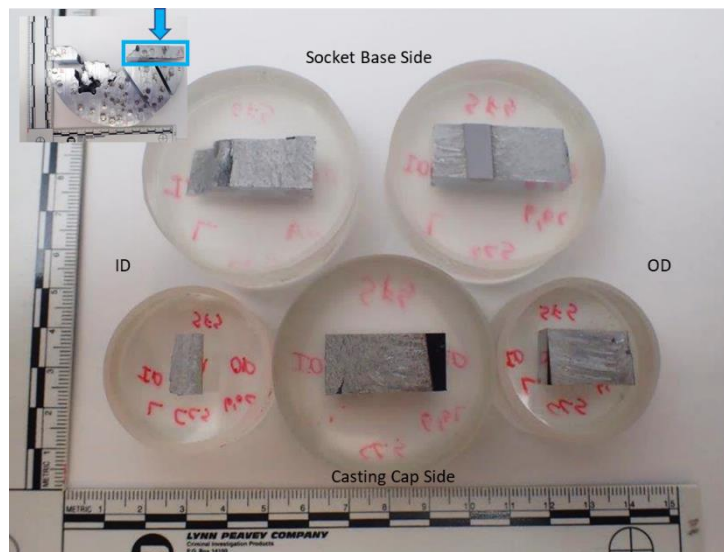


Figure 7.2.4.1-4 (Appendix A Figure 287). Metallographic Specimens of 6 o'clock Side of Longitudinal Cut Face of Slice 3c

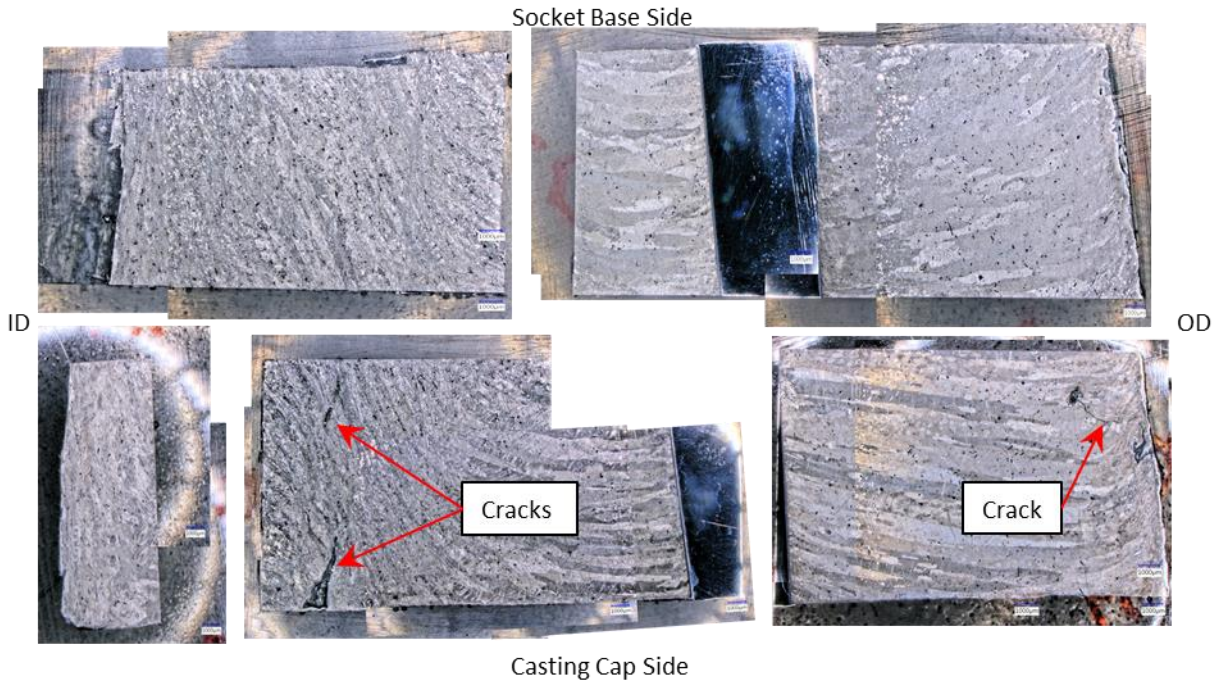


Figure 7.2.4.1-5 (Appendix A Figure 288). Metallographic Specimens of 6 o'clock Side of Longitudinal Cut Face of Slice 3c



Figure 7.2.4.1-6 (Appendix A Figure 289). Metallographic Specimen of 12 o'clock Side of Longitudinal Cut Face of Slice 3c

7.2.5 Corrosion

Chemical analysis revealed extensive amounts of zinc oxide wherever white corrosion product was encountered, and trace amounts of iron, likely iron oxide, wherever orange corrosion product was identified. The largest area of corrosion was found between the socket inner diameter wall and the zinc casting outer diameter (see Figures 7.2.5-1 through 7.2.5-3).

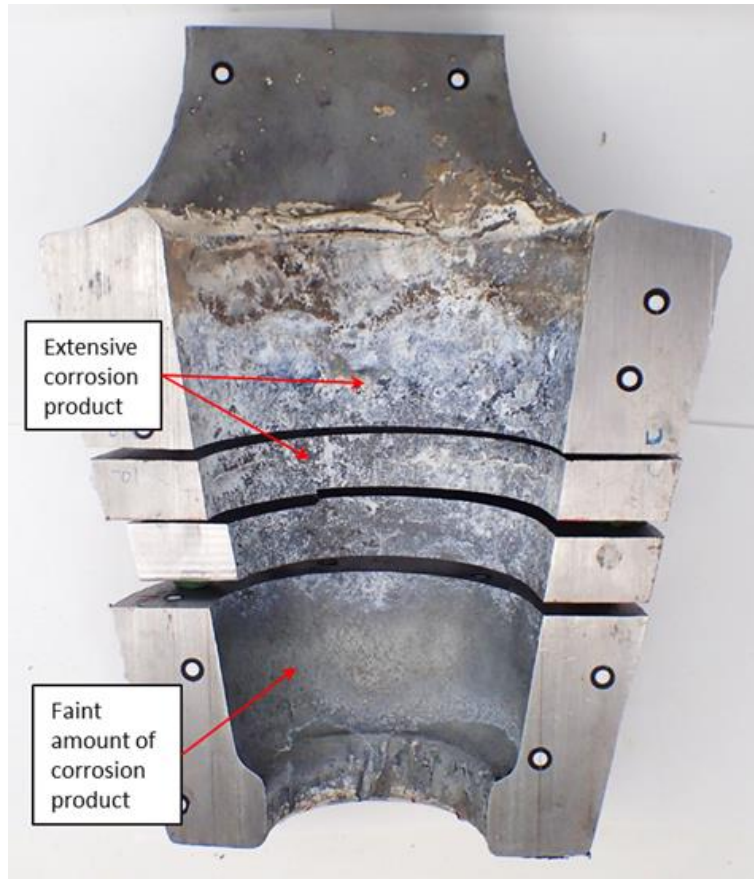


Figure 7.2.5-1 (Appendix A Figure 96). 3 o'clock Side of Inner Diameter Socket Wall, showing Surface behind Outer Diameter of Zinc Casting

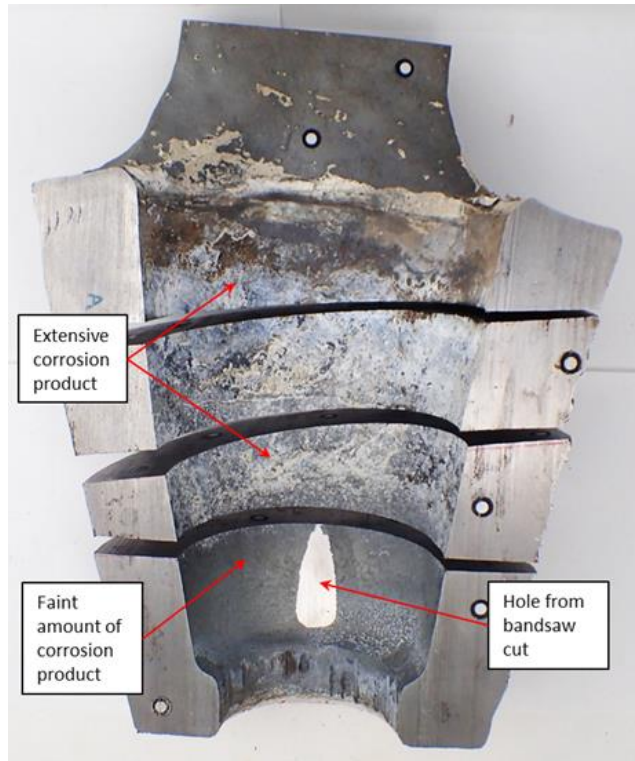


Figure 7.2.5-2 (Appendix A Figure 97). 9 o'clock Side of Inner Diameter Socket Wall, showing Surface behind Outer Diameter of Zinc Casting

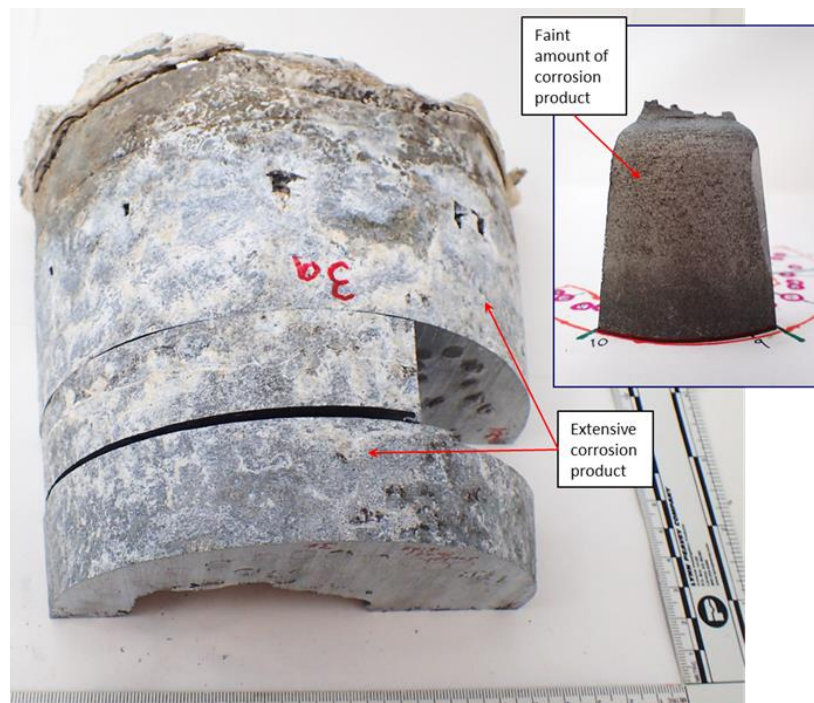


Figure 7.2.5-3 (Appendix A Figure 98). Outer Diameter of 3 o'clock Side of Zinc Casting of Slices 3a, 3c, and 3e

Inset shows outer diameter from piece of zinc casting removed from 9g between 9 and 10 o'clock.

The region between the socket inner diameter and the zinc casting outer diameter was characterized as having among the thickest areas of corrosion, but the corrosion was largely limited to the upper two-thirds of the socket wall, closest to the casting cap. Shrinkage along the outer edge of the casting cap from the casting solidification (see Figure 7.2.2.1-3 shown previously) created a gap between the zinc casting outer diameter and socket inner diameter that likely provided a pathway for moisture and/or water.

The bottom third nearest the socket base was noticeably devoid of most corrosion product, which likely occurred after the cable failure. All the wire fractures within the zinc casting were located within this bottom third, corresponding to slices 3g and 9g.

The zinc-oxide corrosion product in the lower one-third evolved through the galvanic corrosion process between the zinc and the socket cone wall, which can qualitatively be compared against other socket areas exposed to the environment post failure. The galvanic corrosion process between the steel and zinc is expected to evolve oxides faster than oxide evolution elsewhere (e.g., within zinc cracks). The electrical potential between different metals in the galvanic corrosion process drives the evolution of hydrogen and oxides.

F-20. Significant corrosion was found in the upper two-thirds region between the socket housing and the zinc casting outer diameter, while negligible corrosion was found in the lower third.

Eight wires were found to have protruded from the zinc casting to the socket wall during fabrication, located on the outer diameter of the casting in the upper third closest to the casting cap. Figure 7.2.5-4 shows the eight wire holes left by wires that were displaced from their original positions toward the socket base but remained embedded in the zinc casting, failing within the socket. Figure 7.2.5-5 shows heavy corrosion around one of the wire holes that breached the zinc casting outer diameter. The spot in the center of the hole is ambient light coming from the center of the socket cavity.

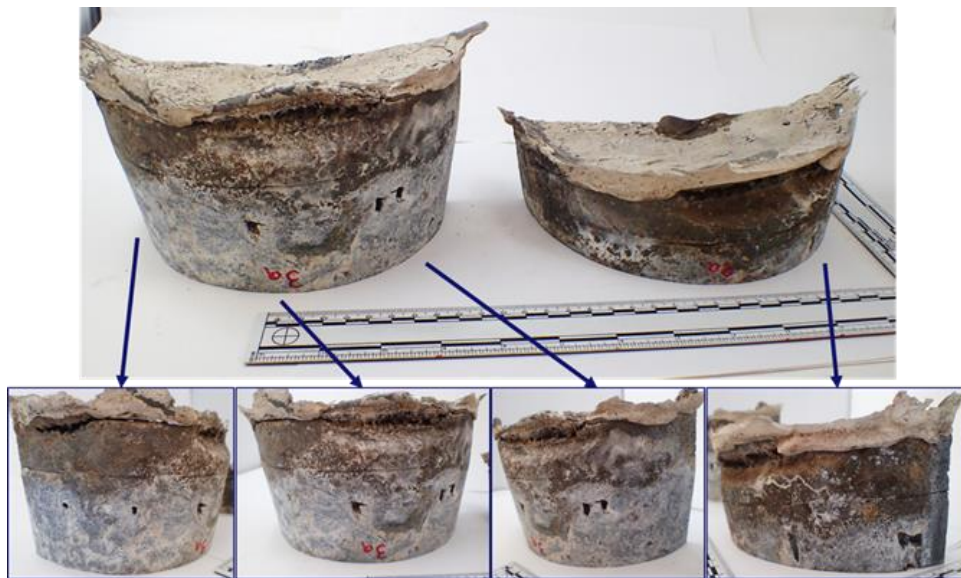


Figure 7.2.5-4 (Appendix A Figure 99). Wire Holes in Zinc Casting



Figure 7.2.5-5 (Appendix A Figure 100). Corrosion around Wire Hole

These holes were potential pathways for moisture ingress into the socket cavity. Around and within the holes, white and orange corrosion product, most likely zinc oxide and iron oxide, are present in relatively large amounts. Several of these holes were confirmed to provide pathways from the zinc casting outer to inner diameter. Cracks were identified along the boundary between the brittle fracture region and at the ends of the wire channels within the socket cavity (see Figure 7.2.3.3-11). These cracks extended out toward the zinc casting outer diameter. This appears to be the most probable pathway for moisture intrusion within the socket cavity, and the conduit between the socket wall and the zinc casting and the exposed eight wire holes were likely present for the majority of the socket's life since those features were present at the time of solidification.

The largest volumes of corrosion within the socket cavity appear on the wire imprint region at the back of the socket cavity and along the adjacent wire channels in the upper one-third of the casting (see Figures 7.2.5-6 and 7.2.5-7). This region does not exhibit the same faceted appearance as the neighboring brittle fracture region from slice 3a. Wire-end imprints and heavy amounts of probable zinc and iron oxide are seen in this area, most likely due to the galvanic corrosion cell created between the wires and the surrounding zinc in the presence of moisture.

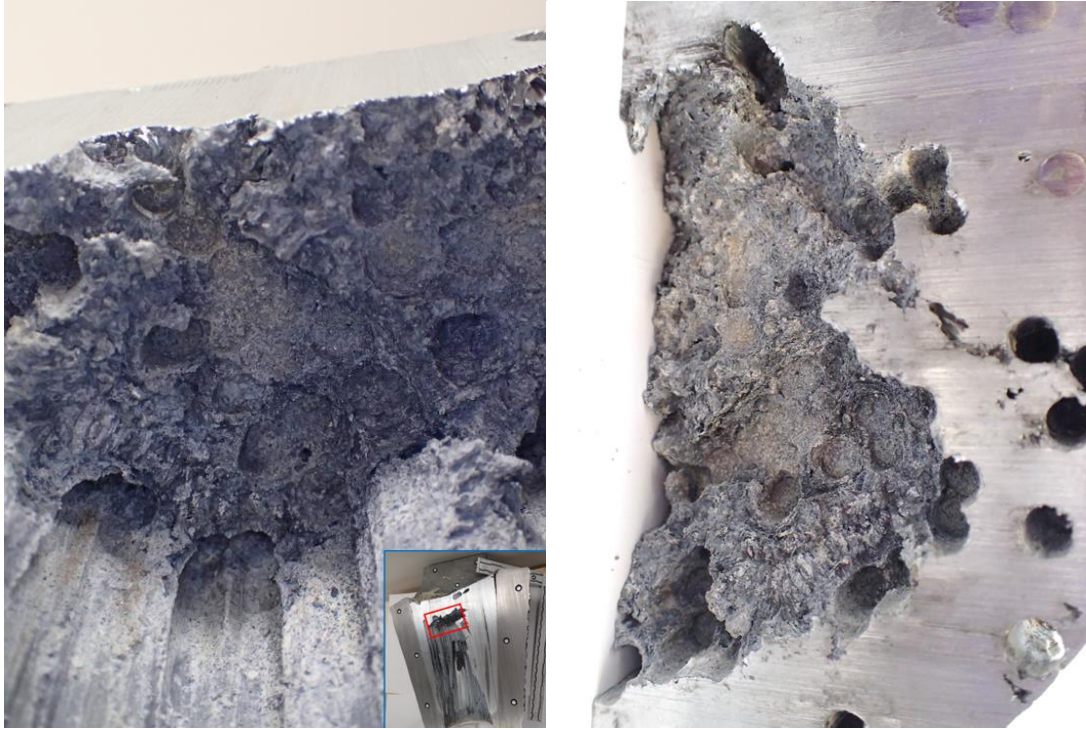


Figure 7.2.5-6 (Appendix A Figures 69 and 70). Closer View of Back of Socket Cavity on Slice 9a



Figure 7.2.5-7 (Appendix A Figure 101). Extensive and Relatively Thick Corrosion on Zinc Casting Wire Channels

Corrosion above the wire ends still embedded within the zinc is heaviest above the wire's final resting location and extends the full wire channel length above the wire end (see Figures 7.2.5-8 and 7.2.5-9). Significant corrosion is also present along the wire surface in the 3a or 9a slice that is less than the amount above the wire. The pattern of corrosion on the wire surface maps well to the pattern of corrosion on the wire channel in the zinc.

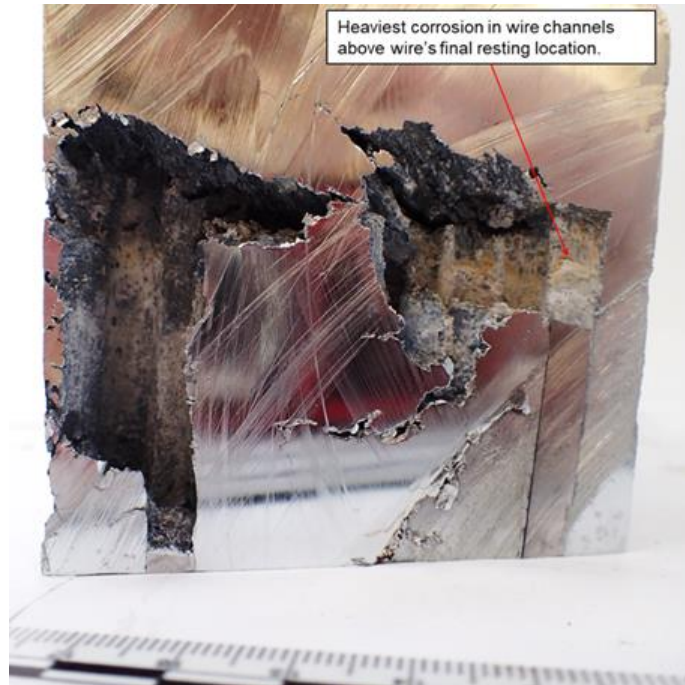


Figure 7.2.5-8 (Appendix A Figure 102). Relatively Large Volumes of Corrosion Visible in Wire Channels above Wires (wire channel for Wire AN is pointed to here)

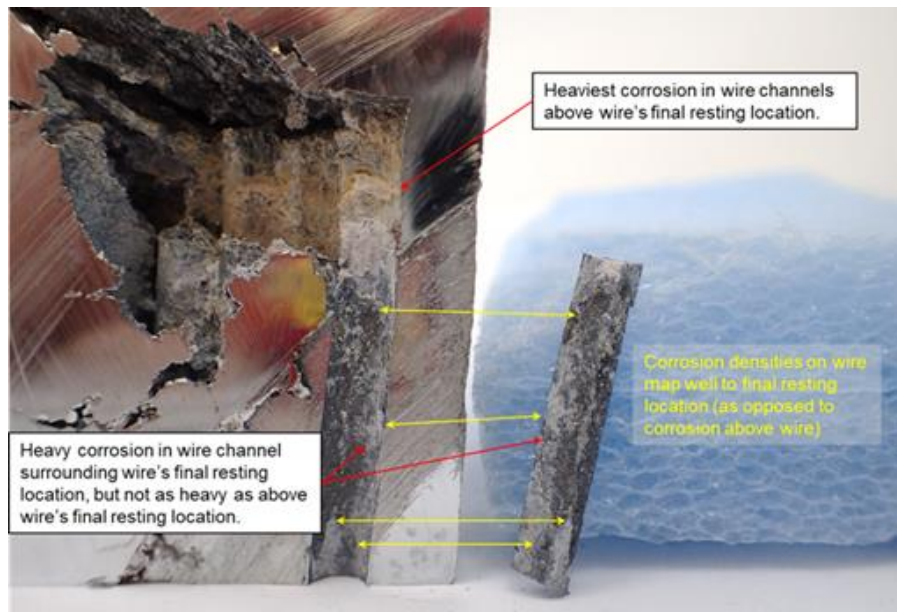


Figure 7.2.5-9 (Appendix A Figure 103). Embedded Wire (wire AN) removed from Wire Channel

While corrosion quantities vary based on localized conditions and there is uncertainty in using this approach as a time-based indicator, examination of corrosion quantities throughout the socket still inform an event timeline:

- Corrosion between the housing and zinc in the lower third is an indicator of how much zinc oxide evolved following socket failure. Figure 7.2.5-9 shows that the amount of corrosion in the back of the socket cavity, both on the surface and the wire channel of wire AN, was much

thicker. Three observations noted are (1) the heavy amount of corrosion on the wire channel surface all the way to near the top of the wire channel suggests that corrosion was occurring when the wire was near its original as-cast position, which would also suggest that very little movement of the wire occurred during proof testing; (2) the heavy amount of corrosion along the wire channel surface between the top of the wire channel and where the wire finally came to rest suggests that wire movement along this distance was slow enough for significant corrosion to build up along this full length; and (3) the significant buildup of corrosion on wire AN's surface, matching the pattern and location of corrosion on the wire channel, suggests that wire AN had either failed some time prior to socket failure or moved very little prior to socket failure.

- The surface of the brittle fracture region (Figure 7.2.3.3-9) showed minimal corrosion over the flat surfaces but exhibited an intermediate amount of corrosion on the ridges and protrusions. Corrosion in this region was away from steel wires and not due to galvanic corrosion. It is difficult to determine moisture exposure and corrosion time because there is no clear region with similar environmental conditions with a known time of exposure to that environment. The second large gas bubble is another potential time indicator, but there is also uncertainty in the exposure time. Wire AB (see Figure 7.2.3.3-3) shows significant wire displacement from its original position. However, the top of the wire shows little gap between its wire end and the top of its wire channel, part of the lower surface in the brittle fracture region. This comparison suggests that the brittle fracture region was open, or opening up, at the same time that wire AN and neighboring wires were displaced from their original positions.

Assessment of corrosion along wire surfaces showed disparities in the condition of the wire-zinc bond among the various wires. Wires AE and N (Figures 7.2.5-10 and 7.2.5-11) exhibited white corrosion product, most probably zinc oxide, along their lengths embedded within their socket base slices (3g and 9g).

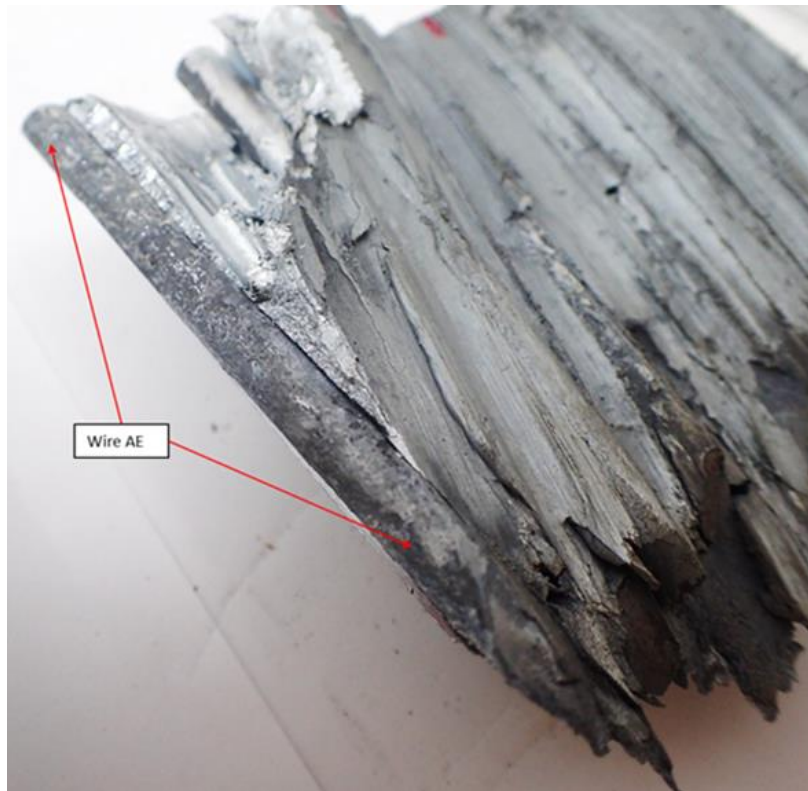


Figure 7.2.5-10 (Appendix A Figure 105). Wire AE, Mechanically Removed, showed Similar Quantity of Corrosion along Length of Wire embedded in Slice 3g, as seen on Wire AN in Figure 7.2.5-9

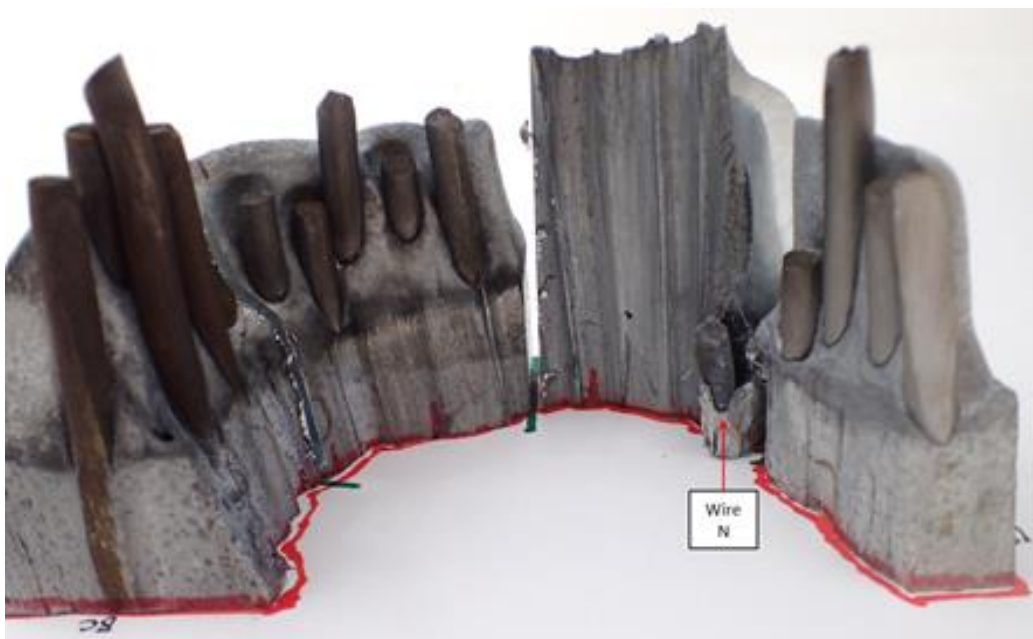


Figure 7.2.5-11 (Appendix A Figure 172). Hydrochloric Acid Wire Fracture Reveal on Slice 9g
 Note that the 9-10 o'clock piece was not acid etched, and the one wire within that piece, wire N, was mechanically removed.

The quantity of corrosion was similar to that seen on the wire end of wire AN (Figure 7.2.5-9) in the back of the socket cavity. However, wires AI and AJ have visibly good adhesion of zinc along their wire surfaces embedded in slice 3g (Figure 7.2.5-12). Thus, disparities exist in the amount of corrosion along the wire surfaces. Because all of the wires fractured within the socket, the comparison suggests that corrosion was a small factor in wire behavior within the zinc.

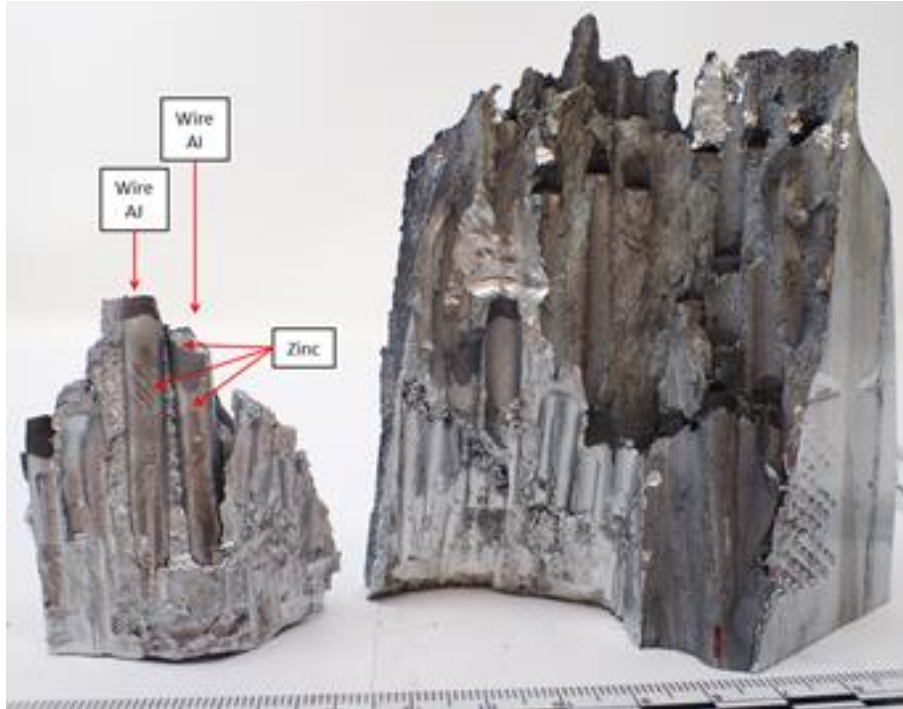


Figure 7.2.5-12 (Appendix A Figure 106). Wires AI and AJ had Visibly Good Adhesion of Zinc along Wire Surfaces that were Embedded in Slice 3g

Note that the thin layer of zinc on wire AI continues from the wire outer diameter surface onto the shear fracture surface.

The wire corrosion analysis did not evaluate all wires due to the labor-intensive method employed in extracting fractured wire ends. Therefore, there are limitations in extrapolating findings to all wires. Additional wires could be mechanically extracted to further examine corrosion features along the wires. However, there was no evidence suggesting that corrosion significantly affected the mechanical behavior at the wire-zinc interface.

F-21. Moisture intrusion, which led to zinc/wire corrosion, followed a path that included a gap between the inner socket wall and the zinc casting, wire protrusions from the zinc, cracks in the bulk zinc, and the wire surfaces of individual wires.

F-22. Evidence shows corrosion generally had a minimal effect on wire-zinc bond strength.

7.2.6 Summary and Conclusions – Failure Analysis

NASA and WJE executed a material forensics plan for the Aux M4N socket assembly. The socket was visually and nondestructively examined and then dissected for material analysis to identify and characterize the material condition and failure mechanics within the socket joint.

The as-received socket was largely unrevealing of any anomalies, meeting specifications and requirements for the housing and cable.

Defects

Internally, some casting defects were found that included porosity within the zinc, solidification gas bubbles near the casting cap surface, poor wire/zinc bonding at the wire ends, and a brittle fracture region. Forensic examination of features and additional structural analysis found them to be small potential contributors to the Aux M4N failure; promoted moisture intrusion and corrosion may have contributed to individual wire pullout in two outer wires at most.

Corrosion

Corrosion was found throughout the socket, with the primary pathway for moisture ingress through the casting cap/mastic coating and the gap between the socket housing and zinc. The steel and zinc created a galvanic couple and an accelerated corrosion environment, resulting in formation of zinc oxides and sometimes a break in the galvanic couple, which resulted in small amounts of iron oxides. The upper two-thirds region of the socket housing and zinc contained the most corrosion. The lower third of the casting, where wire fractures were located, was mostly devoid of corrosion product with the minimal amount likely due post-failure exposure.

The primary pathway for moisture ingress into the zinc was along eight wires that protruded from the casting, which exhibited corrosion. The wires and the surrounding zinc created a galvanic couple, resulting in oxidation. Moisture likely traveled along the wires and cracks along the wire ends. Heavy corrosion from moisture exposure and the galvanic couple was found along the wire imprint region and down the upper portions of the adjacent wire channels. The brittle fracture region had faceted surfaces that exposed the elongated portion of zinc grains, with the ends of the grains lifted up (i.e. a peeling failure). The brittle fracture region was only moderately to lightly corroded due to not having adjacent wires nearby to establish the accelerated galvanic corrosion and/or because this region may have opened up later in the lifespan of the socket. The heavy corrosion along the exposed wire channels in the back of the socket was limited to a few inches.

Additionally, cracks were present throughout the bulk of the zinc casting, linking up with the cracks along wires, and were filled with zinc oxide. Some of the fractured wires within the socket exhibited zinc oxide corrosion down to the socket base, while other wires that fractured within the socket exhibited good zinc adhesion near the socket base. This indicated that, despite the amount of corrosion found throughout the socket, corrosion did not significantly affect the strength capacity of the wires.

A considerable body of information was generated during the investigation and documentation of the corrosion; the analysis and commentary on the potential role of corrosion in socket failure progression is presented in Sections 7.3, 7.5, and 7.6.

Zinc Creep and Fatigue Mechanisms

Metallography revealed a zinc casting composed of elongated grains with a large degree of variation in grain size and length. This was expected but was a concern, as anisotropy in grain size and shape can play a major role in mechanical behavior of a material. Metallography shows no evidence of fatigue cracking within the zinc, but minor additional contributions of cyclic loading damage would not be expected to be discernable from the overall contributions of

sustained loading damage, as both would manifest themselves in deformation mechanisms (e.g., twinning and slip bands), which are present within the zinc.

There were indications that the zinc was in the late secondary stage, or maybe tertiary stage, of creep. Recrystallization is evident within the zinc grains. Adjacent to the zinc failure, between the socket and cable section, the zinc grains are fully recrystallized and have grain boundaries that are generally oriented 45° to the stress direction. This evidence has been documented in literature with respect to pure zinc creep at low zinc-creep temperatures. At ambient temperature, zinc is above 40% of its homologous temperature, which is a defining point for when material creep properties are an important design consideration. Intermittent, non-connected cracks were found in this recrystallized region, running parallel with the cable direction. These cracks appear predominantly intergranular. Intergranular cracking from creep deformation tends to be associated with creep rupture at high temperatures and low speeds of deformation, suggesting that the creep failure in the zinc was a slow process.

Wire Analysis and Failure Progression

Fifty-six of the 126 wires fractured in the socket, and the other 70 wires did not fracture. Although 70 wires did not fracture, no more than two of those wires could have pulled free of the socket joint individually due to inadequate zinc/wire bond strength. The zinc failed before these 70 wires, coming free from the socket attached to most of these wires and the cable-end of the failed wires in a cable/zinc slug. Forty-four of the 56 wire fracture morphologies were cup-cone fractures; 9 were shear failures, primarily from the outer ring; and the remaining 3 were mixed-mode fractures, which included a progressive failure mechanism believed to be HAC (one cup-cone/HAC and two shear/HAC). None of the wires examined by microscopy and SEM had any features of fatigue fracture except a few wires with potential HAC fractures influenced by cyclic loading.

Of the 56 wires that failed, 5 were observed to have surface defects running along their lengths. Two of those defects likely influenced the fracture, and one was an initiation site for HAC. The HAC wire with the defect was also an outer ring wire. The shear and HAC fractured wires exhibited little to no necking. The shear failures developed due to the lack of uniform compressive stresses around the wire fracture, explaining why many of these are located along the outer ring wires where limited zinc on one side may have resulted in a non-uniform compressive stress around the wire. The HAC fractures were mixed mode, with the HAC exhibiting a brittle failure and thereby reducing the cross-sectional area of the wire for the other failure mode. Necking is attributed to ductile failure, where the wire is given enough time to yield, as is typically seen in the cup-cone failures. The outer ring wires that failed typically had less necking than the failed inner ring wires.

Examination of the exposed wire channel lengths in the back of the socket showed that the inner ring wires displaced more than the outer ring wires. This was due to the progression of failure starting with the outer ring wires and moving to more inner ring wires as wires continued to fail, and possibly due to the brittle fracture region tearing open. Visual observation of the pulled-out cable section and the socket internal cavity showed a skew in the failed core versus the socket centerline. This skew reflects the progression of failure as wire loads are redistributed to the remaining wires, likely starting with an outer ring wire on one side of the socket and progressing

to more adjacent inner ring wires, while at the same time progressing around the perimeter to more heavily stressed outer ring wires.

7.2.7 Mechanical Testing

Mechanical property characterization was performed on the ASTM A586 wire and zinc from the Aux M4N failed socket assembly. In addition, mechanical property characterization was performed on ingot material for comparison purposes. The zinc ingot was 99.995% pure zinc, as reported in the analytical report from Eastern Alloys of Kentucky. Properties collected include wire tensile strength, zinc tensile strength, zinc compressive strength, zinc shear strength, and creep deformation [ref. 1]. Additionally, other details were collected to better understand the test results and support the investigation. Included in these other activities were microscopy of zinc metallurgical specimens and fracture images of crack growth in zinc. A summation of results can be found in this section (for specific details of mechanical testing, see Appendix B).

7.2.7.1 Wire Material Properties

Tension testing of the wire was performed at MSFC and WJE (see Appendix B and reference 1). Tensile properties from the ASTM A586 specification and wire from Aux M4N are shown in Table 7.2.7.1-1. The test results from MSFC include five wires cut nominally to 16-inch lengths from wires U and B (see Figure 7.2.7.1-1). Strain values were collected by an extensometer with a 2.0-inch gauge length through at least 4.3% during each test. The test results from WJE were from five wires cut from the Aux M4N. One of the five wires had a stress value at 0.7% strain, lower than the ASTM specification, but all five wires had ultimate tensile strengths and total elongation greater than the ASTM specification. Test results from each laboratory indicate wires maintained the minimum required strength properties.

Table 7.2.7.1-1. Wire Tensile Test Results

Tensile Property	ASTM Specification	MSFC Test Results	WJE Test Results
Tensile strength	220.0 ksi	240.0 ksi (4.5 std. dev.)	237.6 ksi (4.5 std. dev.)
Stress at 0.7% strain	160.0 ksi	169.3 ksi (3.0 std. dev.)	164.5 ksi (8.1 std. dev.)
Total elongation	4.0 %	Exceeds 4.3%	Exceeds 5.3%



Figure 7.2.7.1-1. Location of Wires Approximately 15 ft from Socket

F-23. Wire mechanical properties meet ASTM specification.

7.2.7.2 Zinc Material Properties

Mechanical testing of zinc was performed at MSFC. Overall, strengths appeared to be highly dependent on grain size and directionality. Metallography was performed to aid evaluation of the cast zinc microstructure and explain the differences in test data among the Aux M4N socket slug, the ingot, and previously published tensile test data for zinc. Figures 7.2.7.2-1 through 7.2.5.7-3 illustrate these findings. Figure 7.2.7.2-1 shows the grain structure taken from socket slug material in an axial orientation near steel wires. Figures 7.2.7.2-2 and 7.2.7.2-3 show larger grains in the ingot material. Figure 7.2.7.2-3 shows that in some orientations, grains are greater than 1 inch in length.

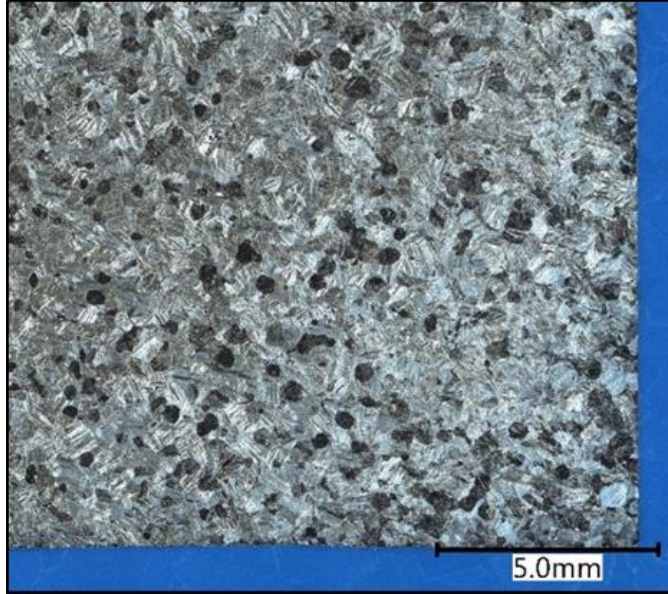


Figure 7.2.7.2-1. Metallography of Socket Slug Material

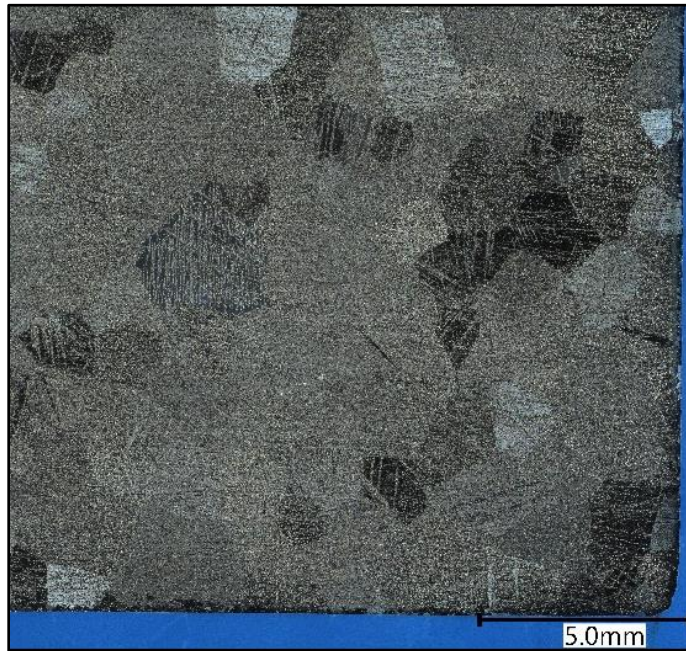


Figure 7.2.7.2-2. Metallography of Ingot Material Showing Equiaxed Grains

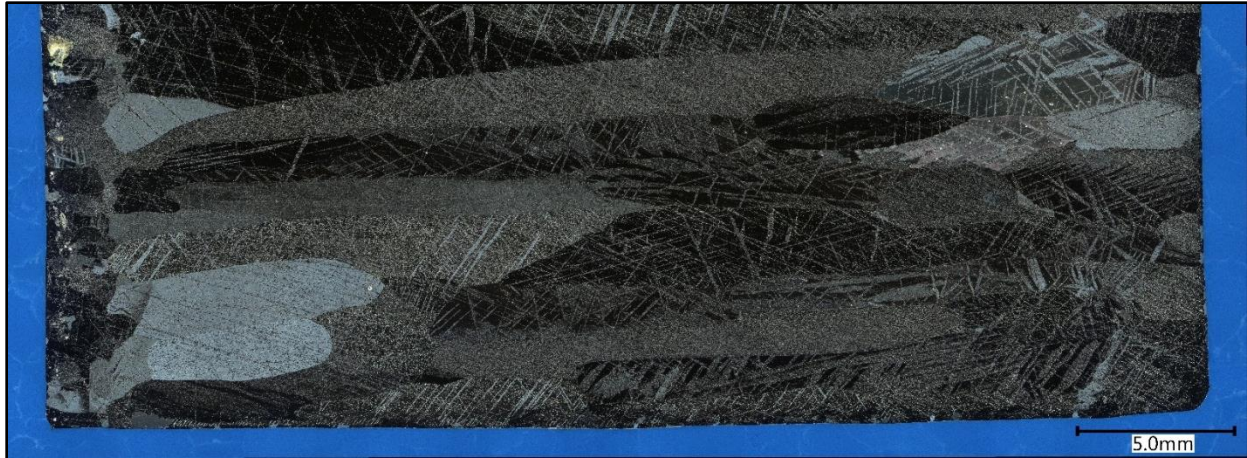


Figure 7.2.7.2-3. Metallography of Ingot Material Showing Elongated Grains

7.2.7.2.1 Zinc Tensile Properties

Small-scale tension test specimens were fabricated from zinc taken from the Aux M4N socket assembly in the axial direction and from a zinc ingot for comparison. The specimens had nominal cross-section dimensions of 0.150 inch by 0.125 inch. Among the socket slug specimens, four were successfully taken near the casting cap in close proximity to steel wires (see section 9c in Figure 7.2.1.3-2). Two were taken near the socket base with more separation from steel wires (see section 9g in Figure 7.2.1.3-2). Six specimens were taken from the comparative ingot material. Figure 7.2.7.2-4 compares the tensile strength of each of these small-scale specimens.

ASTM E8 rectangular specimens (0.500-inch by 0.625-inch cross section) were also tested using digital image correlation (DIC). Figure 7.2.7.2-5 illustrates slip bands in one of these specimens. Strength results were not significantly different between the small-scale and standard-sized specimens; only the results for the small-scale coupons are consolidated and presented here.

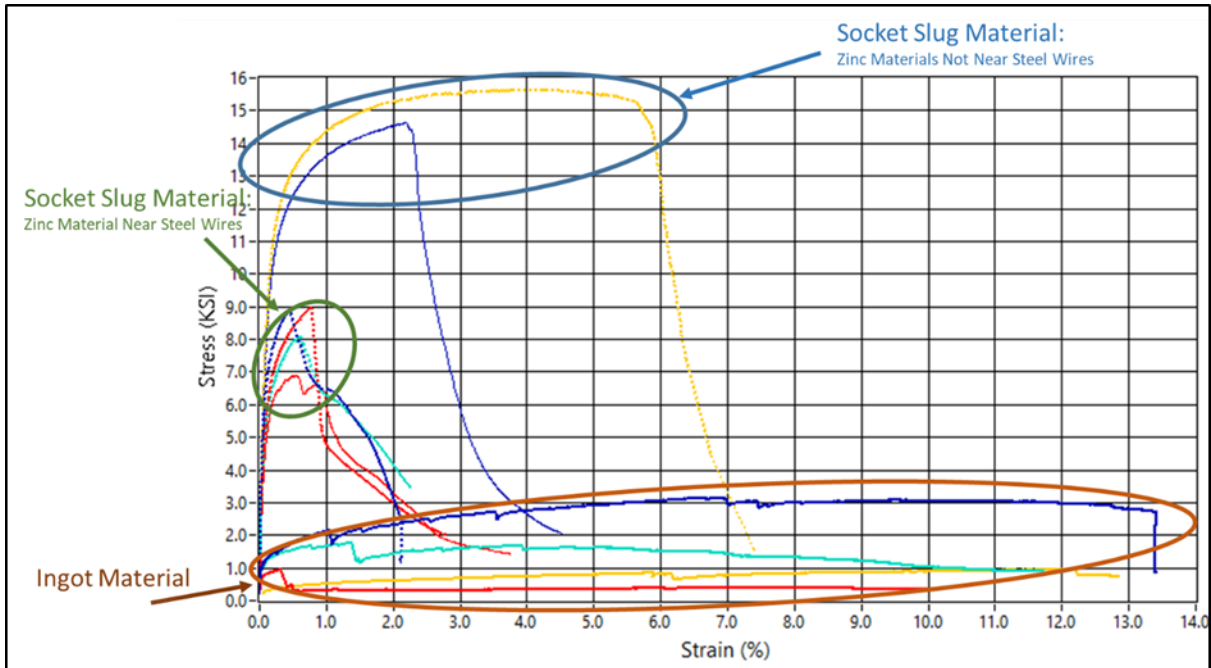


Figure 7.2.7.2-4. Comparison of Small-scale Tensile Results

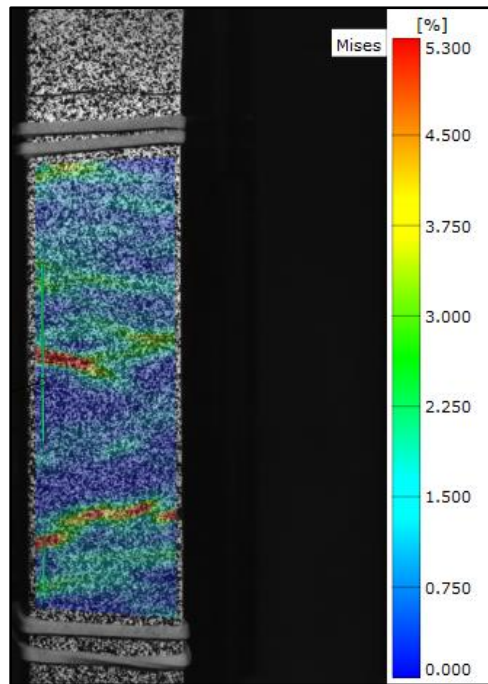


Figure 7.2.7.2-5. DIC of Standard Size Tension Specimen

7.2.7.2.2 Zinc Compression Properties

Zinc compression test specimens were made from the Aux M4N socket assembly in the axial and radial directions, in addition to specimens made from the comparative zinc ingot in three orientations 90° apart. These specimens were 0.375 inch in diameter. Additionally, large-scale specimens that were nominally 2.5 inches in diameter were taken from the ingot material. These

larger specimens were taken from the same orientation but from a different location in the ingot as a group of smaller-scale specimens (Ingot 4-6 specimens in Figure 7.2.7.2-6). Each of these specimens in this figure was compressed to 8.0% strain.

F-24. Zinc mechanical properties in the Aux M4N spelter have significant variability as a function of grain size and directionality.

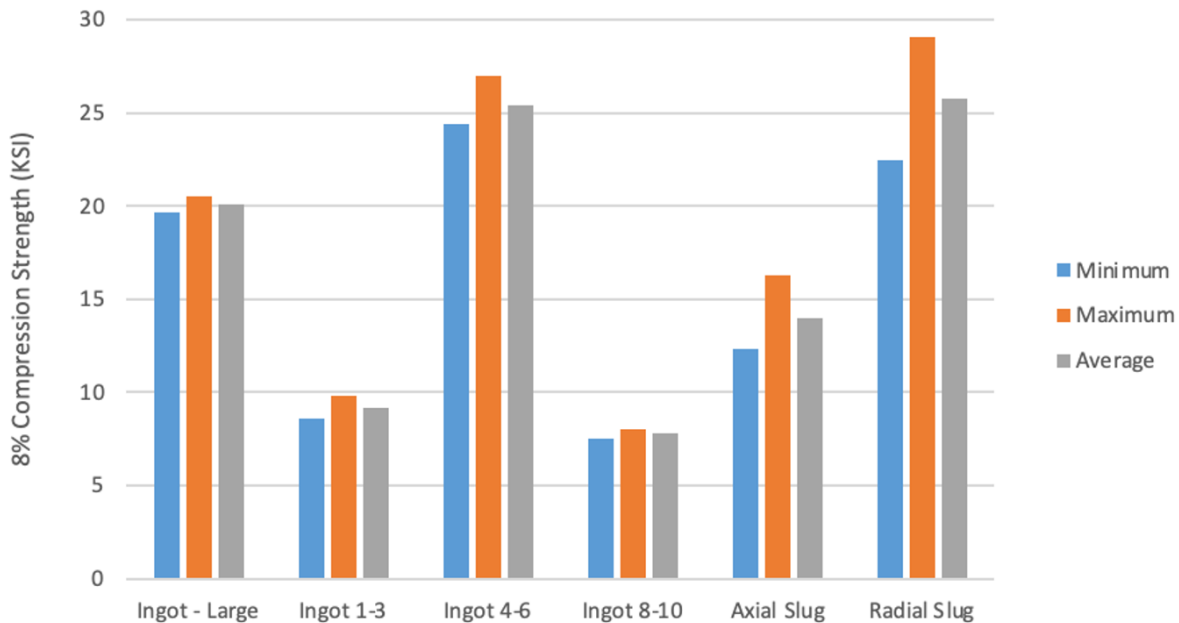


Figure 7.2.7.2-6. Comparison of Compression Strength at 8% Strain

7.3 Structural Assessment of Auxiliary Main Socket Joint

The structural assessment of the auxiliary main socket joint is provided in this section (see Appendix C for the complete analysis). Appendix C includes extended details of the model construction, relevant inputs, general mechanics of the socket loading, sensitivity studies of varying material properties and dimensions, analysis of the as-built/as-failed socket condition, evaluation of metallurgical findings, and assessment of potential contributors to the failure.

7.3.1 Finite Element Model

A detailed 3D model of the structural strand termination into the M4N socket was developed using Abaqus/CAE to investigate the individual wire, zinc, and steel socket mechanics and to support the failure investigation.

The models were developed to gain a better understanding of socket load transfer mechanics and to perform sensitivity studies to understand the effects of various parameters including the degree of brooming, zinc material properties, and voids observed during metallurgic examinations. Several separate model configurations were constructed, each containing varying levels of wire brooming, one of which represented the as-built/as-failed wire brooming specific to Aux M4N.

The interfaces between the wires and zinc were modeled one of two ways depending on the desired analytical study. In select instances, the interfaces were considered rigidly connected

(“tied” in Abaqus terminology) for convergence efficiency. Otherwise, the interfaces were modeled with a nearly infinite stiffness contact condition (“contact pair” in Abaqus terminology) to enable extraction interface shear and pressure stresses. Contact modeling with friction was implemented between the zinc and the socket casing to allow for zinc “seating” within the socket. Material nonlinearity was included for the steel wires and the zinc spelter to predict the post-yield material response. Examples of the idealized wire brooming, simplified socket model, and wedge model mesh density are shown in Figure 7.3.1-1.

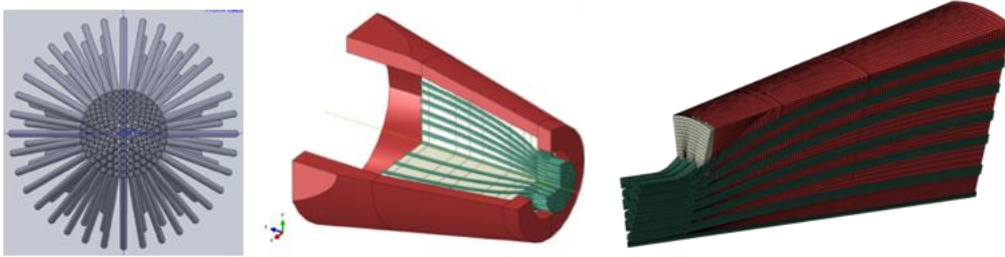


Figure 7.3.1-1. Socket is Modeled as a Simplified Version that does not consider Clevis Pin and Holes

7.3.2 Material Property Development Testing and Strength Properties

The baseline set of mechanical properties of the various constituents of the joint (i.e., wire steel, socket steel cast casing, and zinc spelter) are provided in Appendix C. While a significant body of material testing was performed on the zinc and steel constituents, the only information leveraged for the purpose of analytical model development was the tensile and compressive strength properties to estimate stress-strain curve material models using the Ramberg-Osgood method.

True stress-strain curves were generated and incorporated into the models based on NASA testing of the steel wire and the zinc (see Appendix B). Several different zinc material models were developed for use in sensitivity studies to determine socket termination capability based on the variability in material properties. These sensitivity studies were performed to mitigate concerns associated with uncertainty stemming from zinc material test data (see Appendix C). Sensitivity studies were also performed to investigate variability in the wire elastic modulus, but analysis results showed minimal sensitivity and are not reported in detail.

Commercially pure zinc is a unique structural material in structural socket terminations because its tensile capability is extremely low. However, its compressive capability is high. Grain sizes also vary significantly based on manufactured method and rates of cooling during casting (see Appendix A, Section 4.3.1). As such, it is difficult to construct a high-confidence material model that accurately reflects both tension and compression response or attempts to model progressive damage. This acknowledgment was the impetus for considering the range of zinc material properties that are discussed later in this report. Figure 7.3.2-1 shows stress-strain curves generated using the Ramberg-Osgood method based on test data for steel and zinc.

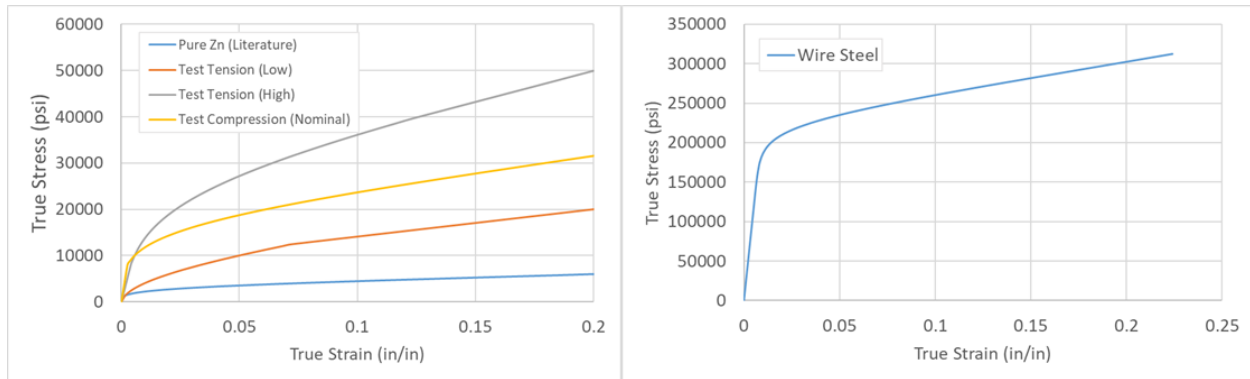


Figure 7.3.2-1. True Stress-Strain Curves for the Range of Zinc Material Properties (left) and Baseline Steel Material Property (right)

7.3.3 Boundary Conditions and Loads

Finite element analysis showed that the pin-clevis connection at the back of the open socket termination did not need to be included in the baseline finite element models, as its effects were found to be insignificant in the overall socket mechanics. The loads did not cause ovalization of the socket and were shown to behave axisymmetrically. Appendix C provides additional details of this assumption.

As stated originally in Section 7.1, the first load experienced by a newly manufactured socket is the socket proof test to 50% of the specified cable breaking strength. In the case of Aux M4N, this corresponds to a load of roughly 660 kips.

Regarding operational loads, the observatory drawings specified three relevant loading cable conditions for the Aux Main cable (see Appendix D):

Loading Condition 1: Initial tension under dead loads at 90 °F and includes all loads from modified central feed structure, the new Gregorian Dome, cables, loads due to raising the platform, loads due to tie-downs, and loads from wave guide supporting system. The final loads after initial erection is 602 kips.

Loading Condition 2: Operational loads include all loads in Condition 1 plus 50-mph wind and 90 °F: 615 kips.

Loading Condition 3: Operational loads include all loads in Condition 1 plus 100-mph wind and 90 °F: 622 kips.

WJE performed analysis using the SAP2000 software and found that cable loads were affected by routine movement of the telescope and by wind loading during “survival” events. During routine operation, the movements cause loading imbalances in the cable suspension structure, while the tie-downs counter the imbalance so the auxiliary cable tensions vary only by the proportion of the additional tie-down force and auxiliary cable angles. WJE generated envelope values for each cable in this process but only presented the maximums. During “survival” conditions, the Gregorian Dome is stowed, and tie-down forces are relaxed so that the observatory receiver is free to displace as needed with the winds. WJE’s analysis predicted a maximum cable load of 720 kips [ref. 1], nearly 100 kips higher than the value prescribed in the drawing. Dead loads were a significant portion of the maximum cable load: (602 kips/720 kips) ~84% resulting in a design factor of safety against the 1314-kip cable breaking strength of

approximately (1314 kips/720 kips) ~1.83. Finally, a proof factor of roughly 0.92 is achieved when considering a proof test of 657 kips and a survival load of 720 kips.

Fluctuating cable loads and corresponding load spectra due to wind oscillations from hurricanes, earthquakes, temperature fluctuations, and telescope movements was not fully characterized. Due to limited available data to WJE, they did not characterize the many variations in loads that could occur and did not analyze the effects of various combinations of tie-down loads with static/dynamic wind loads. However, when examining the three loading conditions per the drawings, loads caused by winds are a small percentage of the total cable loads based on a comparison of load conditions 1, 2, and 3.

Due to the uncertainty to the maximum tensile load expected in Aux M4N, all finite element analysis sensitivity studies were performed with a baseline cable load of 602 kips (load condition 1). Residual stresses from manufacturing and thermal and vibration sources were not included in the model.

F-25. Observatory dead load resulted in sustained cable tensions within 20% of the maximum expected cable tension.

7.3.4 Socket Joint Physics

Cable tensions from observatory dead load, operational loads, and survival transients are transmitted to the socket termination through the 126 individually broomed wires that are held in place by the cast zinc spelter within the steel open socket conical volume. The zinc that fills the socket cavity is bonded to the wires, and this bond creates an efficient load transfer among the wires within the socket.

A special characteristic of the socket termination is that the combination of zinc plasticity and the conical volume forces a “squeezing” effect to occur around the broomed wire bundle in the narrow part of the socket. The high confining pressures experienced at the outlet of the socket keep the broomed wires from pulling out of the zinc and allow the failure to occur in the cable outside the socket (see Figure 7.3.4-1), thus developing the cited 100% efficiency termination.

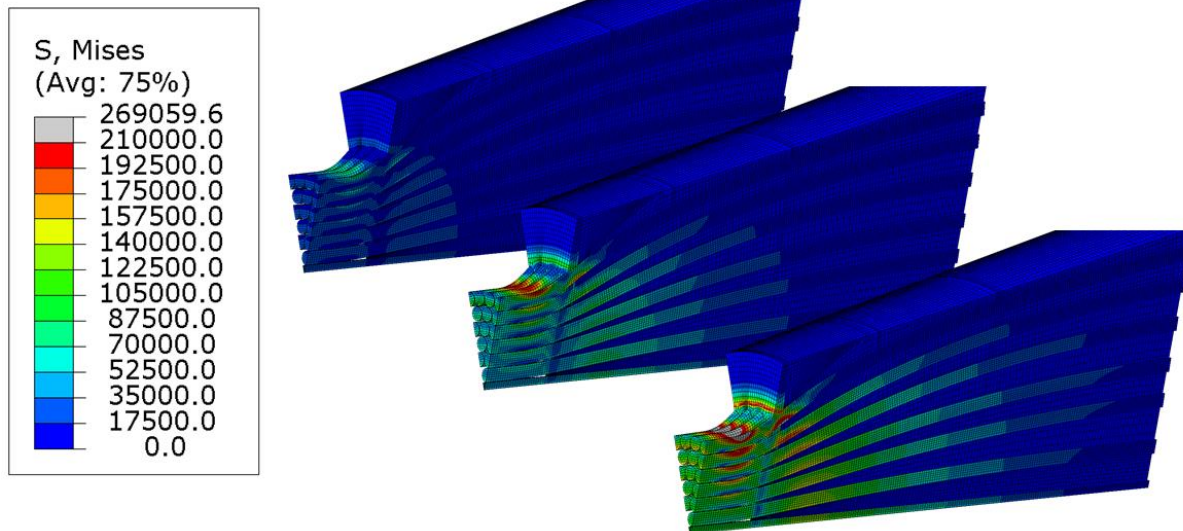


Figure 7.3.4-1. As Loading in Cables Increases (left to right), the Zinc Distributes Load amongst Wires within the Socket in a Mechanism Analogous to Metal Matrix Reinforced Composites
Note: The magnitude of the contour stress plots is not particularly relevant for this demonstration.

It is worth noting that some sockets, specifically those manufactured in the field, use a thermoset poured resin rather than molten zinc to confine the broomed wires within the socket. Functionally, the nearly incompressible resin achieves the same mechanical locking and squeezing of the wires as the zinc plasticity and conical socket shape. Reference 14 states:

“When a load is applied to the rope, the resin cone must move forward into the socket. This effect generates high wedging pressures in the resin, tightly gripping the embedded wires. This movement, and the resulting wedging process, is essential to the operation of the system...”

A properly manufactured socket termination should develop the full breaking strength of the structural strand or wire rope, meaning that the socket termination itself should not be the limiting strength factor in the capability of the whole cable. This is observed during testing when the failure mode is breakage in the cable rather than individual wire pullout of the zinc or resin casting. The exact progressive failure is complicated, and it is not obvious which individual wire fails first or where along the length of the cable the first failures should occur. Once individual wires fail, the failure mode may or may not exchange to the cast zinc or resin or may remain somewhere within the strand.

Figure 7.3.4-2 shows the distribution of plastic shear strain in the zinc for three configurations of model brooming. The effects of brooming on performance are discussed later in this report, but it is worth noting that the bands of shear strain in the middle and lower configurations show how brooming affects stress and strain level in the zinc. Better brooming traps the wires and redistributes stress to the wires, while poor brooming puts more shear stress into the zinc, which can have deleterious effects on termination performance. This is discussed in more detail later.

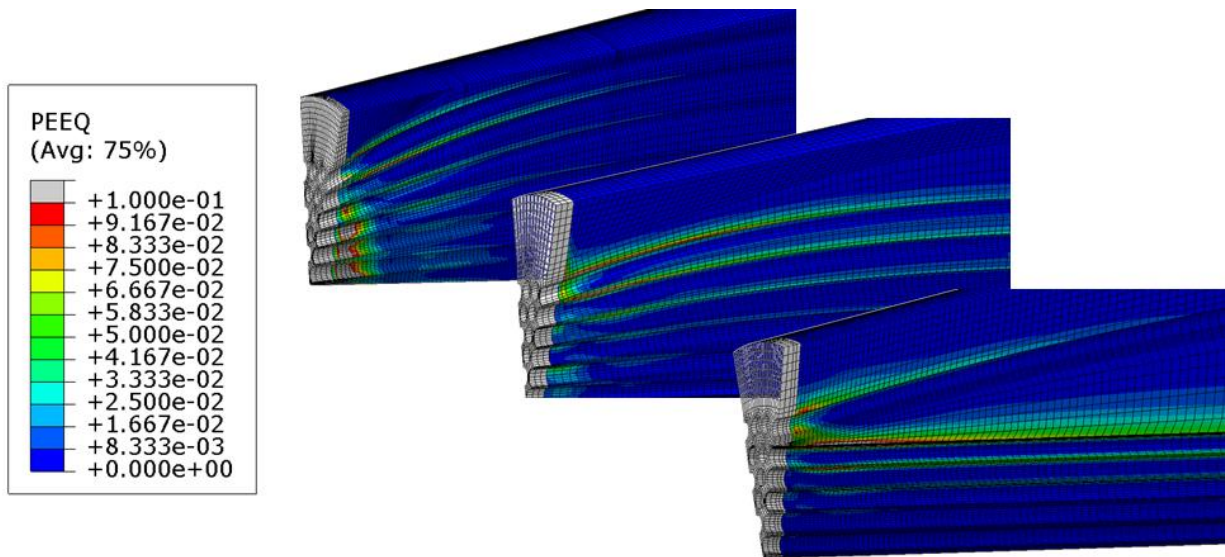


Figure 7.3.4-2. Comparison of Representative Zinc Plastic Strain Fields for Three Different Wire Brooming Configurations highlighting Bands of Significant Shear for Less-broomed Cable Ends

In reference 15, the cable fails at the far socket termination. In this failure example, it appears as though the cable core (remaining unfractured wires) would have pulled out of the socket due to zinc overload, like the Arecibo failure, had the test rig continued to move. In other tests, the structural strand has been shown to fail away from the socket, somewhere within the span of the strand length. However, it is not possible to predict which configurations fail in the strand near the socket and which would fail in span.

7.3.5 Analysis-Test Correlation

The breaking strength of the strand is rated at 1,314 kips and is consistent with hand calculations based on cross-sectional area of each wire: $A_{wire} = \pi * 0.125^2 = 0.049 \text{ in}^2$. Based on the single-wire minimum strength specification of 220 ksi, the predicted load at failure is 1,360 kips ($= 126 \text{ wires} \times A_{wire} \times 220 \text{ ksi}$).

The wedge finite element model predicted the highest stresses in the outer wires, and the ultimate strain to failure of the whole cable cross section was not predicted until the failure load was above 1,200 kips. However, the Aux M4N socket joint failed at operational loads near 600 kips. So one key question is why a socket with a rated breaking strength of more than 1,300 kips failed at near 600 kips. As stated previously, the rated breaking strength is determined in a test where the cable is loaded until total net section failure occurs. Total cable overload does not occur until most of the individual wires are yielding and collectively reaching their ultimate elongation limit. In all versions of the model, as-built and wedge models, analysis predictions showed that at 600 kips the entire row of outer wires has begun to yield and plastically elongate, albeit not grossly. As intended, this causes a load redistribution to the inner rows of wires, which eventually yield next, and the process continues. All analyses show agreement that the breaking strength of the full strand would not occur at 600 kips of applied load for a pristine, newly constructed cable termination of this design.

The finite element analyses were helpful in understanding the basic mechanisms of failure for such designs. A qualitative comparison to the failed socket shows that the finite element model predicts the “stepped” pattern wire failures observed during forensic examination, as shown in

Figure 7.3.5-1. The highest stresses were not predicted to be planar from wire to wire, rather the failure surface followed the surface of a rough spheroid, matching the stepped patterns seen from forensic examination. The outer wires were predicted to fail closer to the socket base cable outlet region, while the inner wires failed slightly inboard to the socket, as seen in the forensic evidence identified (see Appendix A, Section 4.2.2). The stress field suggested that the wires failed adjacent to the greatest confining pressure within the zinc. The zinc plastic flow and the shape of the socket create a region of confining pressure in the shape of a half spheroid, which causes the highest wire stresses adjacent to the boundary of the highest confining pressure. The red output, showing interface contact pressure (“CPRESS”) in Figure 7.3.5-1, reflects the area of highest confining pressure at the zinc/wire interface, which would squeeze the individual wires and suggest the fracture location to be ahead of this region (near the cable outlet of the socket).

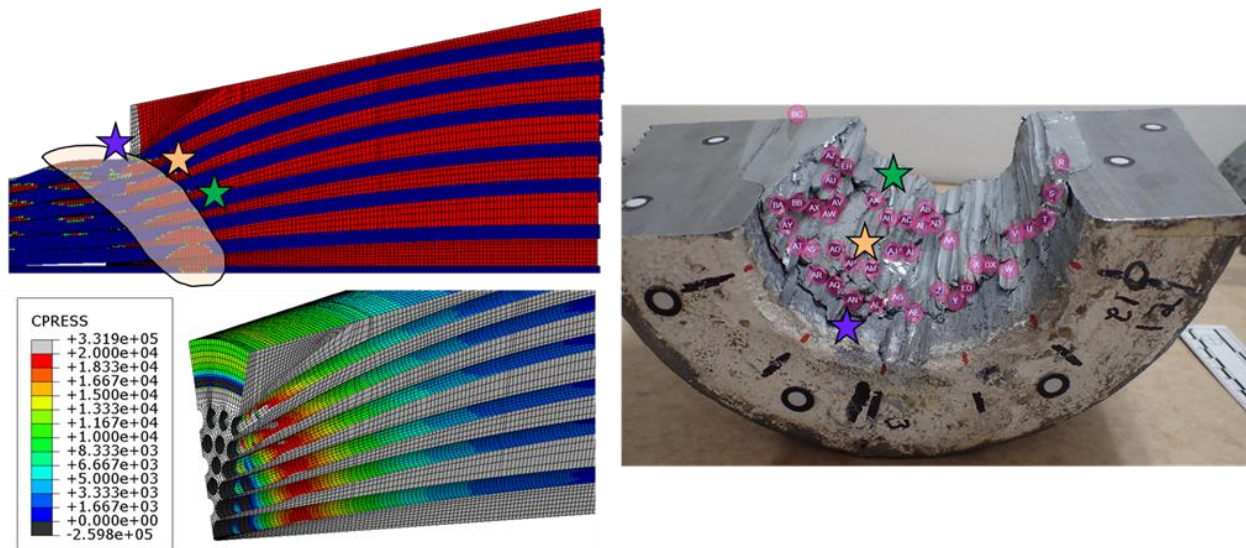


Figure 7.3.5-1. Highest Stresses were not Predicted to be Planar; Failure Surface followed a Spheroid Shape, matching Stepped Patterns seen in Forensic Investigation
Regions of colored stars show the different "steps" of failure in the socket. Note that the yellow shading in the top left figure and the red high stress zones in the lower left figure match the shape of the failure surfaces in the right figure.

Model predictions were qualitatively consistent with the observed wire failure modes from the Aux M4N socket. Forensics identified that the majority of wires failed in cup-cone fracture, although a select number of outer wires failed in shear. Analysis shows that the inner wires are under significant confining pressure, thus increasing elongation capability and resulting in a “ductile” cup-cone failure mode. The outermost wires have unbalanced confining pressure and are geometrically more broomed, which increases the likelihood of a shear failure mode.

F-26. Finite element modeling predictions quantitatively agree with rated/measured wire breaking strength.

F-27. Finite element modeling predictions were qualitatively in agreement with the NASA forensic analysis:

- Maximum wire stresses predicted followed the stepped pattern observed in the forensic analysis.
- Outer wires were predicted to fail in a shear failure.
- Inner wires were predicted to fail in a cup-cone failure mode due to the compression effects of the zinc on the wires.

7.3.6 Strength Assessment

Due to uncertainty in the zinc material properties, sensitivity analyses were performed with a suite of zinc material models ranging from “soft” to “stiff” that envelope NASA independent test data of the zinc spelter and ingot, as indicated by Figure 7.3.2-1.

For an applied load of 600 kips, the range of zinc material models resulted in outer wire stress predictions ranging from 220 to 230 ksi, yielding in all cases. With a factor of safety of unity, this corresponds to structural margins ranging from +15% to -4% when considering a range of wire ultimate strengths of 220 to 250 ksi. Margins are considerably lower with the maximum cable load of 720 kips predicted by WJE’s analysis.

For typical aerospace applications, structures with highly complicated stress distributions are analyzed and compared not only against the breaking strength of the joint but also for constituent stresses against their respective material strengths. Regardless of the zinc material model, the wires support the majority of the sustained load, and the outermost wires are stressed near the ultimate strength of the wire steel material, even at 600 kips of applied load, which is well below the rated breaking strength of the structural strand. The yielding of the outer wires results in load transfer to inner wires that can more readily accommodate the further increases in load before full cable failure. This can be understood by examining Figure 7.3.6-1.

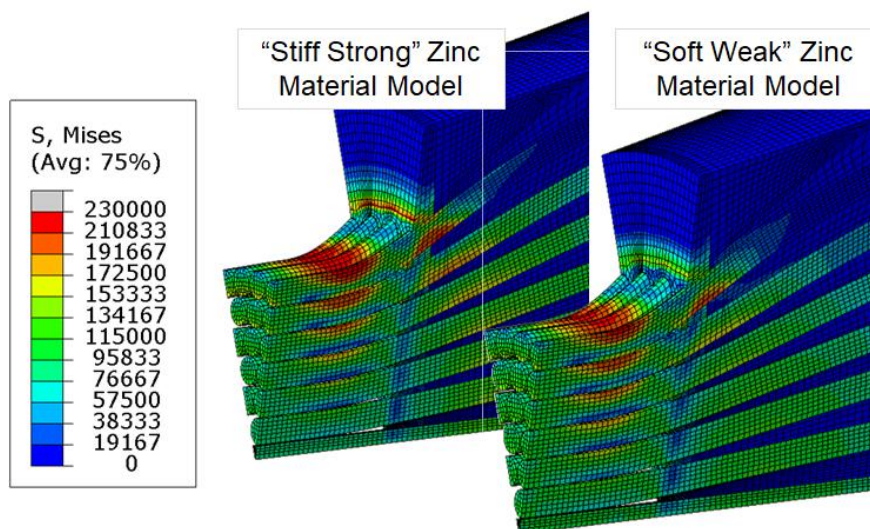


Figure 7.3.6-1. Wire Stresses are Highest in Outer Wires; Wire Stress was Relatively High Compared with the Material Capability, Regardless of Zinc Material Model

F-28. For a large range of realistic zinc material properties, all models predict that outer wire stresses are near ultimate strength of individual wires, even at operational observatory loads, demonstrating low or even negative margins of safety for the Aux M4N socket.

7.3.7 Cumulative Damage

The topic of cumulative damage arises when considering structures with long lifetimes, structures subject to significant loading transients, or structures with minimal design margin. In the Aux M4N socket termination, the low structural margin and long lifetime create a condition where it is theoretically unable to accommodate loading transients, creep, and other time-dependent factors ad infinitum. The topic of damage accumulation was explored in a basic assessment of creep and fatigue for the joint.

Socket Corrosion Discussion: Forensic analysis and associated microstructural studies found corrosion within the zinc casting, at the wire-zinc interfaces, and at the zinc-socket interface. Finite element analysis was leveraged to assess the potential role of each forensic finding in the failure progression.

Corrosion was found in the upper two-thirds region between the socket housing and the zinc casting outer diameter, while negligible corrosion was found in the lower third. A finite element analysis sensitivity study examined the influence of corrosion between the zinc casting and socket housing. The analyses varied the coefficient of friction from 0.3 to 0.8 and then as permanently affixed between the zinc casting and socket housing, and found minimal effects on the wire stresses. The findings are consistent with understood socket physics that pulling wires also pulls the zinc against the socket housing. A high-compression zone then develops between the socket housing and zinc during this process, and any presence of corrosion has a low influence on wire stresses because the load transfer mechanism remains intact.

Finite element analysis also evaluated the corrosion findings that eight wire ends were cast protruding from the zinc outer diameter and found corroded. Analysis showed that wires are not stressed highly in the wider region of the socket compared with those in the front and that the as-identified corroded interfaces should not be detrimental to the load transfer mechanism. Separately, analysis evaluated voids and defects within the casting near the wider socket casting region and found negligible effects on the maximum predicted wire stress located adjacent to the cable outlet from the socket.

Corrosion throughout the zinc casting was also evaluated for potential degradation of zinc mechanical properties and potential influence on wire stresses. Results of this sensitivity study did not change the conclusion that individual outer wire stresses are near ultimate strength at operational observatory loads.

Finally, the analysis showed that the highest stresses were near the narrow diameter of the socket, where corrosion was less pervasive. While corrosion was present in smaller quantities, the potential influence on wire stresses was significantly lower than the role of low structural margins at operational loads and the influence of long-term sustained loading.

Zinc Creep: The cast zinc is under a large amount of shear and compression stress in this design due to the wires shearing the zinc at the bonded interface and the overall compression that develops once the volume of zinc flows and becomes compressed by the narrow end of the

socket. Literature of zinc spelter sockets suggests that the zinc is susceptible to creep behavior at a higher rate than steel wires. Shear stresses vary throughout the cast spelter volume, with the highest stressed regions being in the narrow half of the socket and sufficiently high in magnitude to expect the occurrence of creep. The significant stress and strain levels in the zinc are evident in the plastic strain field shown in Figure 7.3.4-2. This is also confirmed by WJE testing, which subjected samples to constant loading and resulted in creep behavior [ref. 1].

Rather than modeling the creep behavior, a sensitivity study was performed for cases that considered zinc linear, zinc nonlinear with a “medium level” of softening, and zinc nonlinear with a “higher level” of softening. More softening contributes to more plastic flow and higher stresses in the outer wires. Analysis with “soft” zinc properties mimicking creep suggests that plastic flow is likely to occur over time and will continuously redistribute load into the outer wires as the inner wires and core continue to mobilize. This is similar in spirit to the findings associated with the variability in zinc material models described earlier. The hydrostatic effects that develop in the zinc are key to developing load transfer to the wires due to the pinching mechanism that occurs in the regions of high compression near the outlet of the socket. *Due to a lack of reliable creep failure criteria, no attempt was made to predict the creep failure of the zinc, but the assessment demonstrates qualitative relevance.*

Steel Wire Surface Defects: Forensic analysis revealed wire surface defects on five fractured wires and indicated that defects influenced the failure of two of the wires. From the structural assessment perspective, surface defects can cause local stress risers that decrease the strength capability of those respective wires. The negative structural margins predicted with a factor of safety of 1.0 at limit load further deteriorate when the stress riser due to the surface defect is considered.

Steel Wire Creep: Adjacent to the socket termination, the brooming of the wires and the geometric stress concentration results in the outer wires being stressed to a significant percentage of their strength capability. As such, there is limited structural margin remaining that can accommodate overloading events or reduction of capacity due to “time-dependent” failure mechanisms for infinite durations. Steel wire is known to exhibit creep response [refs. 16-18] under sustained loading and, as the stress increases relative to the strength of the wire, the creep strain rate also increases.

Strain loading was sufficiently high that it could not accommodate creep and cyclic loading. The creep mechanism is therefore a credible phenomenon, particularly on the heavily stressed outer wires of the socket joint. Increasing the strain level in the wire also results in decreasing elongation capability. *Due to the lack of reliable stress rupture failure criteria, no attempt was made to predict creep failure of the wire, but the assessment demonstrates qualitative relevance.*

Cyclic Loading of Socket Joint: A finite element model was constructed to understand the zinc and wire mechanical behavior due to proof testing followed by fluctuating cable loads. A six-step analysis process was performed: (1) socket proof test to 50% rated breaking strength (660 kips), (2) unload (<12 kips), (3) load to initial operational load (624 kips), (4) reduce to low operation load (500 kips), (5) increase to survival load (720 kips), (6) return to original operational load (624 kips). In reference to Figure 7.3.7-1, it was confirmed that cyclic loading beyond proof test loading progressively increases strain in wires, progressively increases plastic flow in zinc, and exhibits structural hysteresis. During subsequent loading events at lower magnitudes, the response in outer wires remains linear.

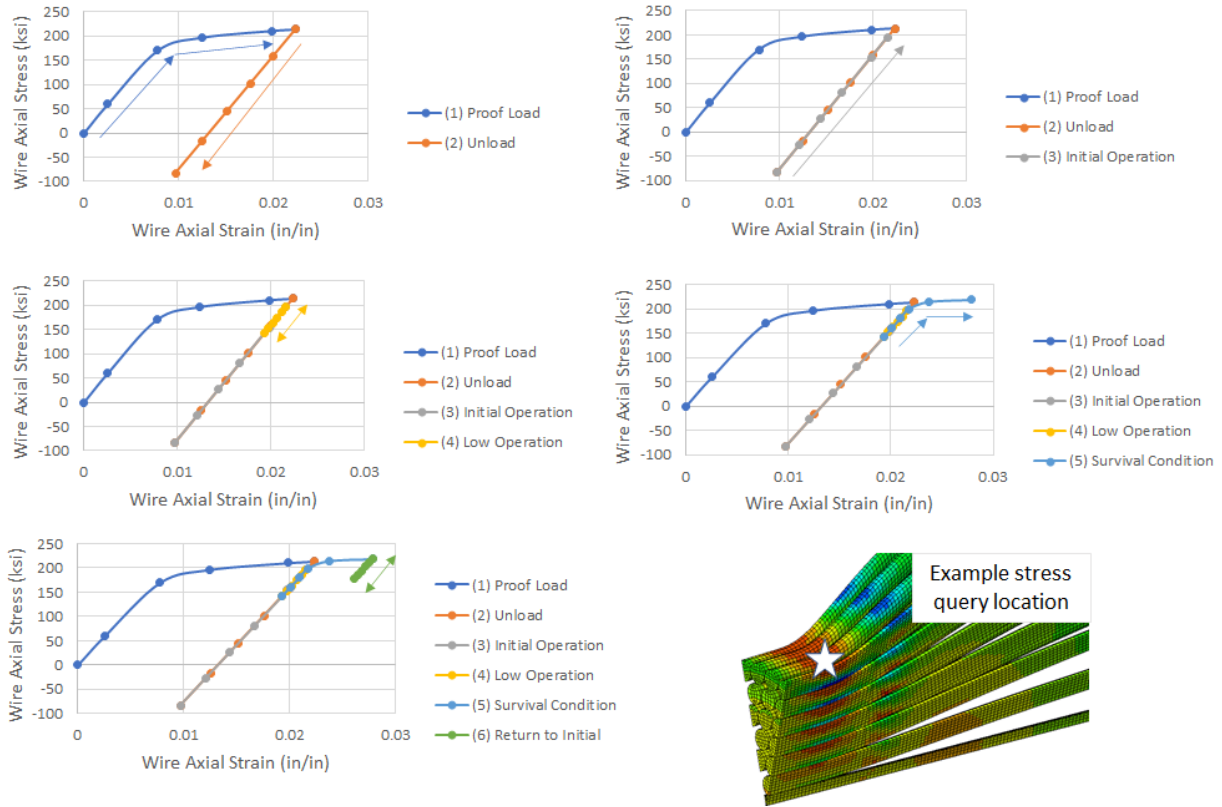


Figure 7.3.7-1. Stress History and Hysteresis from Repeated Loading above Proof Load Level
Stresses Shown from Starred Location in Bottom Right Graphic.

Comparing field output plots of the yield state in each step confirms that the majority of the structure responds linearly for loading below previously achieved loads (from proof test, initial operations, or survival conditions). Figure 7.3.7-2 shows the yielding portions of the socket in red for each of the six analysis steps. Subsequent elevated loading or loading reversal results in yielding of both zinc and wire steel, although the zinc repeatedly yields in compression during load removal while the wires do not yield.

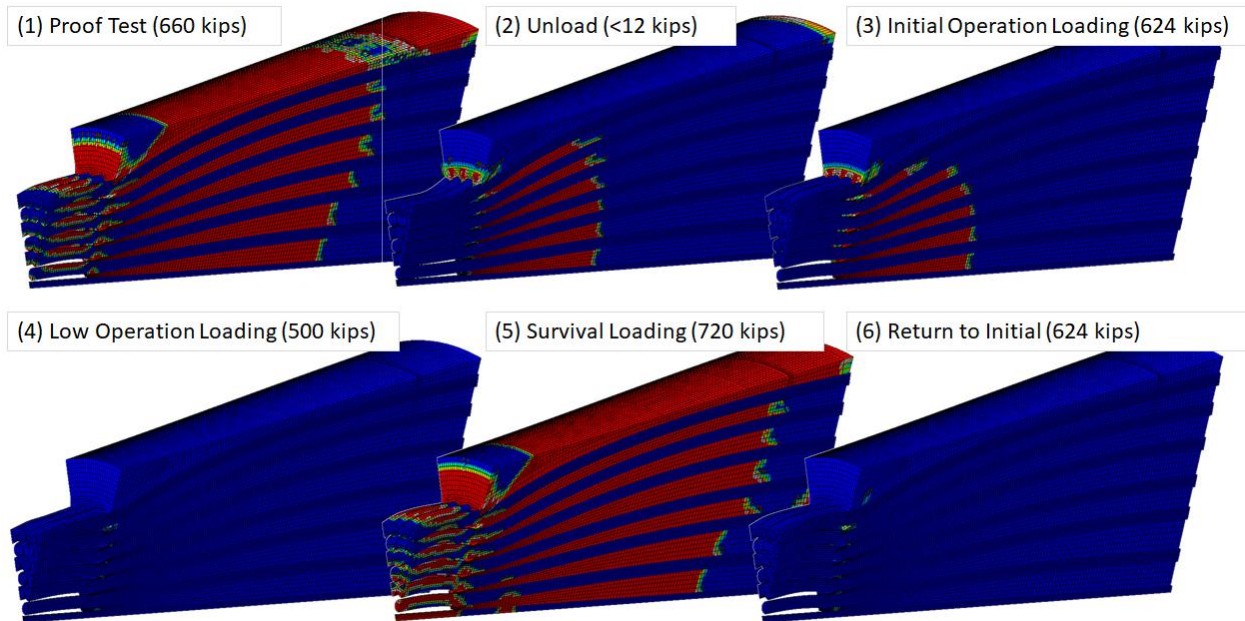


Figure 7.3.7-2. Yield State Shown in Red for Zinc and Wires for each Analysis Step

Fatigue Life Characterization of Steel Wires: The observatory receiver suspension cables were subject to load fluctuations from temperature cycles, winds from tropical storms, routine daily winds, and earthquakes. *Due to lack of available information relative to the load spectra, it was not possible to predict damage accumulation with high degree of confidence.* Rather, a qualitative assessment was performed, illustrating that the design will accumulate damage from cyclic loading, preventing the structure from possessing an infinite life.

The concept of a modified Goodman diagram can be employed to demonstrate the relationship between mean stress offset, cyclic stresses, and their combined effect on expected life. Qualitatively, the modified Goodman diagram gives information on whether the design space (mean and alternating stress combination) possesses effectively infinite life or whether some finite life failure is expected. The diagram is constructed by establishing axes for mean stress (horizontal) and alternating stress (vertical) and drawing one line between ultimate tensile strength and endurance limit strength and another line between yield strength on both axes. The conservative inner envelope of yield strength and endurance limit stress is the region where effectively infinite life would exist for combinations of mean and alternating stresses existing within that region. Outside this envelope, some finite lifetime is expected, dependent upon the exact load history, material capability, susceptibility to environmental degradation, etc. The modified Goodman diagram for the highly loaded outer wires at the Aux M4N socket termination is shown by the yellow oval in Figure 7.3.7-3. The diagram indicates finite life due to cyclic loading conditions. The diagram was constructed for specification yield and ultimate strengths of the individual wires, but the concept can be extended to nominal strengths, design minimum strengths, or those specified by a customer.

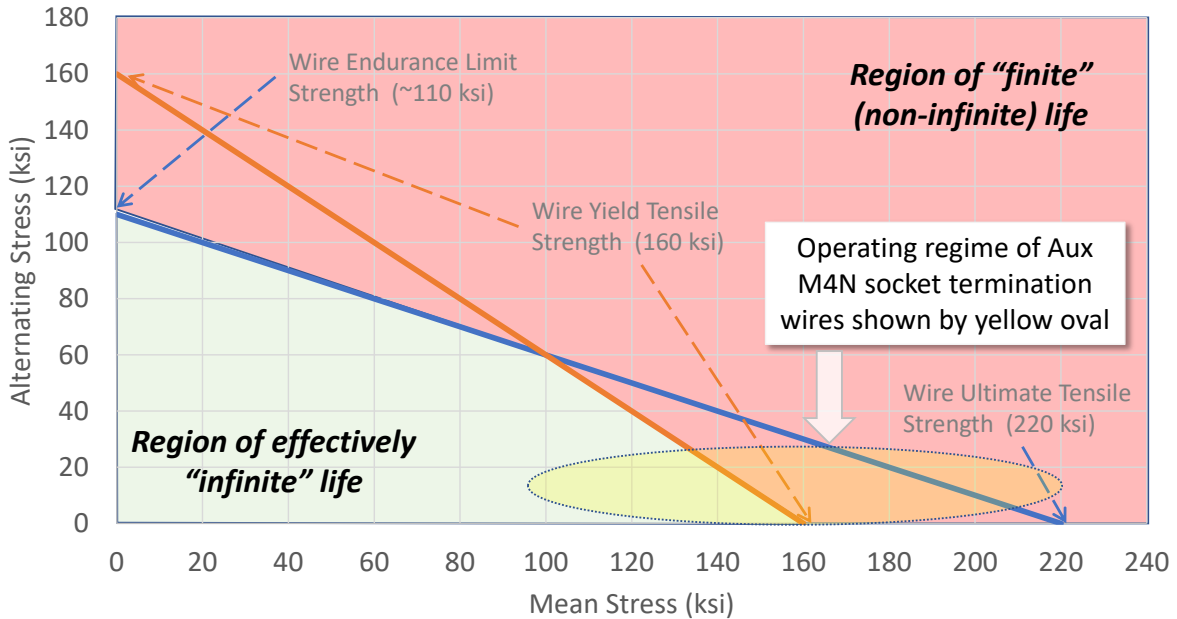


Figure 7.3.7-3. Modified Goodman Diagram showing Separation of Finite and Infinite Life Regions with Annotations for Aux M4N Operational Space

The modified Goodman equation was used to qualitatively conclude that the number of cycles to failure can vary drastically depending on the assumptions made. The modified equation is as follows:

$$N = \left(\frac{\sigma_a}{\frac{(f \sigma_u)^2}{\sigma_e} \left(1 - \frac{\sigma_m}{\sigma_u} \right)} \right)^{1/b} ; \quad b = - \left(\frac{1}{3} \right) \log \left[\frac{f \sigma_u}{\sigma_e} \right]$$

where a mean stress correction is necessary due to sustained cable tension from observatory dead loads. Here, σ_a is stress amplitude due to fluctuating loads, σ_u is wire ultimate strength, σ_m is the mean stress in the wire, f is the fatigue strength adjustment factor (typically 0.9), b is the Basquin coefficient (approximately -0.1 for metals), and σ_e is the endurance limit. In the above equation, it can be seen that the ability to accommodate alternating stresses is reduced as the mean stress approaches the strength of the material.

The prediction for mean stress related to the sustained loading condition (e.g., dead loads) was estimated for the purpose of calculating a range of allowable cycles. However, because the load spectra defining the alternating cable load and stress spectra was not fully characterized, a quantitative prediction with high confidence could not be performed. Since the sustained loads are roughly 80% to 90% of the total cable load (per Section 7.3.3), the remaining percentage of the load can be assigned to transient effects. Given the uncertainties in load spectra, the range of predicted cycles to failure showed anywhere from 100 to 1 million cycles, which is instructive because a finite life is predicted but the range is too big to draw conclusive statements on the amount of accumulated damage due to cyclic loading. Given the nature of the Arecibo Observatory operation, it is known that the Aux M4N successfully endured a significant number of cycles. Nonetheless, every cycle does generally contribute to accumulation of damage.

In conclusion, a qualitative cumulative damage analysis considering cable load fluctuations shows that cumulative damage occurs during operation, but the total accumulation of damage is unknown due to uncharacterized load spectra.

Creep and Cyclic Loading: Generally, materials incur cumulative damage due to both sustained loading and cyclic loading, as structures are not likely operating in conditions where one of the contributors is totally absent. Per American Society of Mechanical Engineers (ASME) Section III Division 5, accumulation of damage occurring due to sustained loading and cyclic loading can be linearly combined using Miner’s rule. This is illustrated by the interaction diagram in Figure 7.3.7-4. Here, n and N_d are the number of cycles and the allowable number of cycles for the loading condition j ; t and T_d are the actual time at stress level k and the allowable time at that stress level. D is the allowable combined damage fraction. The point of this diagram is to illustrate that time-dependent degradation modes are not only due to sustained loading, but cyclic loading can accelerate creep-related failure modes. The graphic shows an example exchange rate between cyclic and time-dependent contributors to total accumulated damage.

In the Arecibo Observatory Aux M4N application, sustained loads are due to observatory dead loads, which make up most of the total cable load envelope (in the range of 80% to 90% per Section 7.3.3 and WJE supporting analysis [ref. 1]). Comparing the alternating cable load with the mean cable load (sustained) demonstrates that the failure event was influenced by creep mechanisms. Considering creep to be a dominating factor is consistent with metallurgical observations that revealed no evidence for typical fatigue failures (e.g., beach marks and striations). However, contributions from cyclic loading cannot be entirely dismissed, as they can be masked by the occurrence of creep, can accelerate creep-dominated failure modes, and can contribute to the total cumulative damage of the hardware.

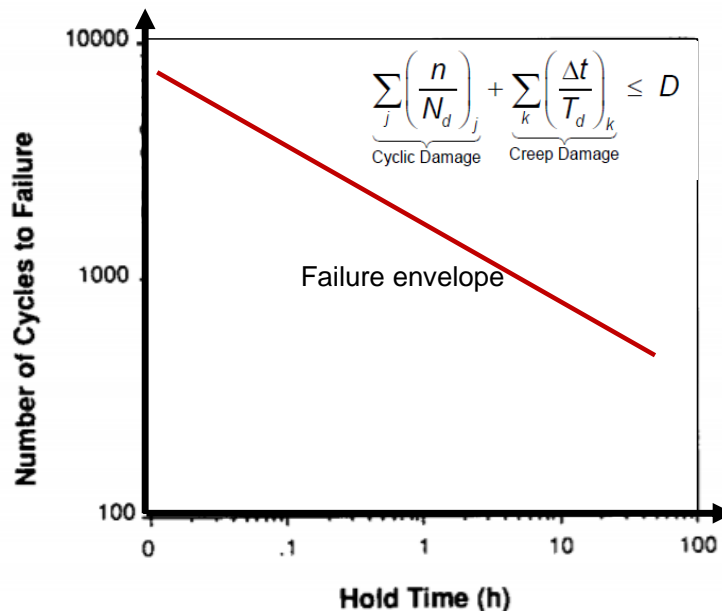


Figure 7.3.7-4. Cumulative Damage Can Occur due to Combination of Cyclic Loading and Sustained Loading

F-29. The socket design had low wire structural margins and a large percentage of sustained loading, which made the design susceptible to a creep-dominated failure, likely accelerated by fluctuating cable loads.

7.3.8 Discussion on Transient Loading (e.g., Hurricane Maria, earthquakes)

Structural elements cannot easily endure both near-ultimate static sustained load and large alternating loads for long periods of time. In the Aux M4N design, at operational observatory loads, the outer wires of the cable adjacent to the socket termination experience significant stresses and local yielding and possess limited structural margin. While the transient loading of the Arecibo Observatory may be comparably small to the sustained dead load, it is recognized that cyclic loading only accelerated the creep-dominated failure mechanism. Environments such as hurricanes, earthquakes, and temperature fluctuations can increase creep, per the ASME interaction curve, and reduce the life of the socket joint.

According to WJE, Arecibo collected wind data every 15 seconds to determine peak velocity. For Hurricane Maria, the peak recorded wind velocity was 110 mph, while the average wind speed over 15 minutes peaked at about 70 mph. It is worth reflecting on the original design that considered the “survival” condition to be 100 mph winds.

During normal daily operations, one body of data collected at 200 Hz did not show evidence of significant cable load oscillations due to wind or temperature transients. No data were provided for conditions during Hurricane Maria or for those reflective of tropical storms, hurricanes, or earthquakes. Therefore, no correlation between measured values and significant transient environments can be made. As such, the real structural response due to wind gusts or vortex shedding during transient environments is unknown and can only be qualitatively assessed as a general contributor to the accumulation of damage.

7.3.9 Effects of As-built Wire “Brooming”

All results presented so far were based on a representation of the brooming condition that enables the development and use of a reasonable finite element model. At the time of the analysis, the reconstruction of the as-built condition was not available. Subsequently, the team developed several representations of brooming where the wire distribution is axisymmetric around the cross section. The model version containing the largest degree of brooming is referred to as the “ideal brooming condition,” although it is recognized that such a brooming would not materialize in actual socket manufacturing. Nevertheless, analyses with various brooming conditions can provide insight into the sensitivity of brooming quality to the critical stress of the socket joint and help develop a more thorough understanding of socket termination mechanics.

The brooming operation ensures that the wires are as evenly distributed as possible within the socket so that the load distribution is efficient. Since the brooming operation is a manual operation, no two sockets are exactly alike. The exact brooming geometry and the quality of the wire-to-zinc bond are affected by the manual operations.

Multiple models were developed that assumed various “qualities” of brooming in attempt to bound the problem. Specifically, three levels of broomed models were created: “ideal,” “medium,” and “poor.” The “medium” brooming resembled the “ideal” configuration in terms of relative distribution of wires, but they were broomed to a small final footprint. The “poor” brooming only broomed the outer-most row of wires and did not significantly broom the inner

rows. It is recognized that the terminology assigned to each condition is in name and not an explicitly and optimized “ideal” or “poor” condition in practice.

Analysis results suggest that a more uniform distribution of wires within the zinc matrix leads to the development of better confining pressure on the broomed wires, reduced excessive extrusion of the zinc, and a more predictable failure wire mode outside the socket termination. The more non-uniform the density distribution of wires over a cross section of the zinc matrix, the “worse” the brooming is considered. Based on Figure 7.3.9-1, it is visually apparent that the as-built configuration falls somewhere between an “ideal” and a “poor” brooming, as expected. It should be noted that when making this qualitative assessment the brooming in the socket that failed could be similar to other socket “brooming,” while the “ideal” brooming configuration modeled may never be achieved in practice.

Further, the interviews with two industry subject matter experts (see Section 6.4) confirmed the as-built brooming to be visually consistent with their experience of structural strand socket termination brooming.

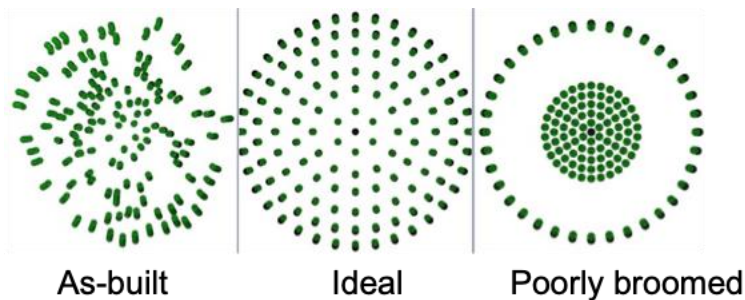


Figure 7.3.9-1. As-built Wire Distribution compared with Ideal Brooming Configuration and Poorly Broomed Configuration

Analysis shows that, for marginal designs like the M4N socket, brooming quality becomes more important than designs with robust structural margin. A sensitivity analysis was performed comparing the outer wire stresses for the three brooming configurations with decreasing levels of quality of brooming. The plastic strains and tensile stresses in the outer wires increased with decreasing quality of brooming. The proposed explanation for this phenomenon is that more brooming leads to better development of confining pressure in the narrow end of the socket, which results in a more distributed load across the cable cross section. Better brooming prevents excessive zinc seating extrusion and time-dependent extrusion due to the distribution of wires through the zinc volume, resulting in a composite system that uses the entire embedded wire surface to resist flow. When there is a lesser degree of brooming, there is more zinc plastic flow, and the mechanical response exhibits a softening phenomenon (i.e., a reduction of tangent modulus), which leads to a distribution of load into the outer wires as the wire and zinc continue to experience excessive seating extrusion. For poorly broomed configurations, a lower volume of high triaxial compression is predicted, which is directly correlated to the effects of confining pressure on the wires that keeps the wire-zinc bond intact; more brooming redistributes load into wires across the cross section.

F-30. Decreasing brooming quality results in increasing stresses in the outer-row wire and reduces margin for designs operating near their strength capacity.

7.3.10 Effects of Defects within Zinc Spelter

Forensic evidence indicated that zinc voids were from the manufacturing process (See Appendix A, Section 4.3). Corrosion products were also observed in the some of the zinc surfaces (see Appendix A, Section 4.4). An analytical study was pursued to study whether zinc voids could have accelerated the failure of the outer wires. Three analytical models were developed, one with a void toward the socket base side, one with a void midway down the length of the socket, and one with a void toward the casting cap side of the socket. The voids were simulated by deleting elements representative of the zinc material. Analyses predicted negligible effects on the outer wire stresses due to the presence of these voids. All effects of the voids were limited to the local area adjacent to the voids within the socket volume and did not affect the overall stress distribution of the wires outside the socket. This is because the most highly stressed wires occur near the socket base and remain unaffected by the existence of voids a substantial distance away in the zinc. However, the analysis cannot rule out the effects of voids on time-dependent effects, local zinc damage, or damage to the wire/zinc interface that would have progressively contributed to an increase in plastic flow and affected wires elsewhere.

A separate model configuration was run where 20% of the zinc volume was removed from the casting-cap side of the socket to mimic the existence of the cavity tear that was observed just under the casting cap. The loss of zinc away from the cable outlet of the termination indicated no change in critical wire stress level and did not indicate a difference in termination capacity. Termination capacity is influenced significantly by the zinc in the narrow side of the conical volume but is largely unaffected by the zinc at the open end of the socket.

F-31. Analysis predicts that stresses in the zinc and wires are not affected by the zinc voids identified in the forensic examination of the Aux M4N socket.

7.3.10 Analysis Progression of Failure

An analytical exercise was undertaken to examine the load redistribution and stress concentration effects of progressively failing wires adjacent to the socket termination. The intent of the study was to quantify the stress increase of failure on adjacent wires, determine a failure pattern assuming select failed outer row wires, and qualitatively compare to results from forensics evidence. Figures 7.3.10-1 and 7.3.10-2 graphically show the first configuration considering three failed wires at the 3 o'clock side of the cross section.

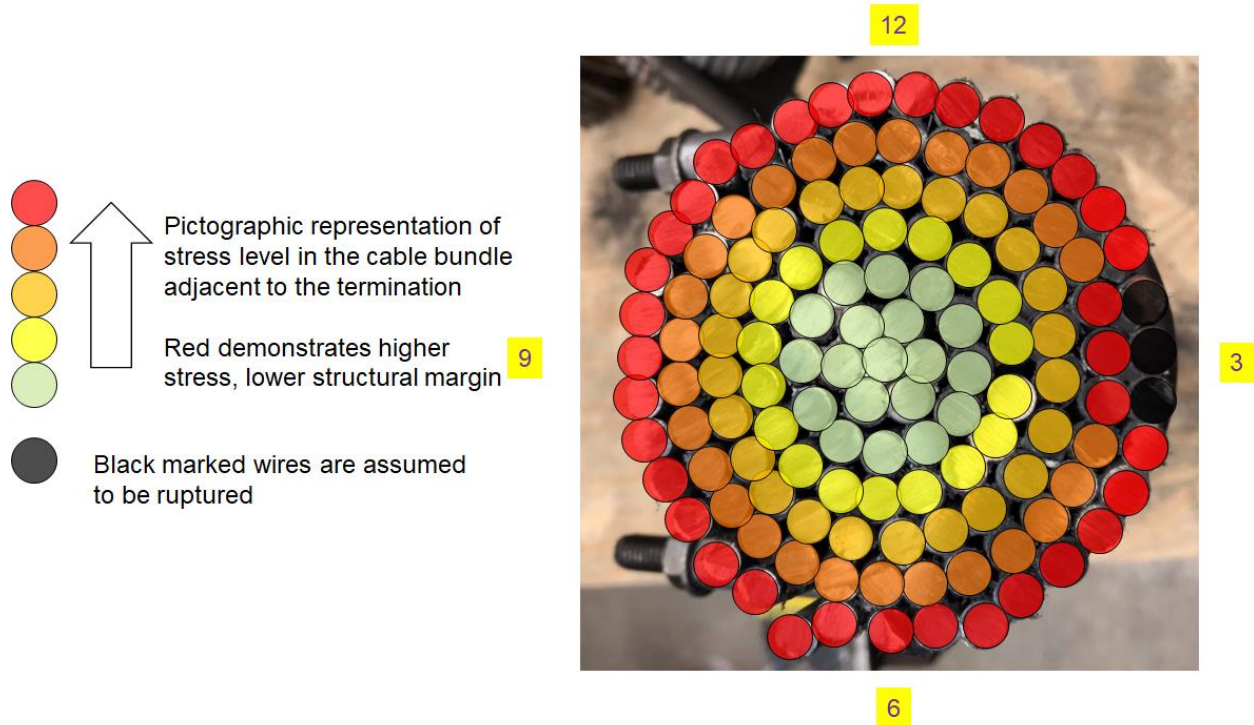


Figure 7.3.10-1. Pictographic Representation of Wire Stress over Cross Section and Initially Failed Wires at 3 o'clock Side

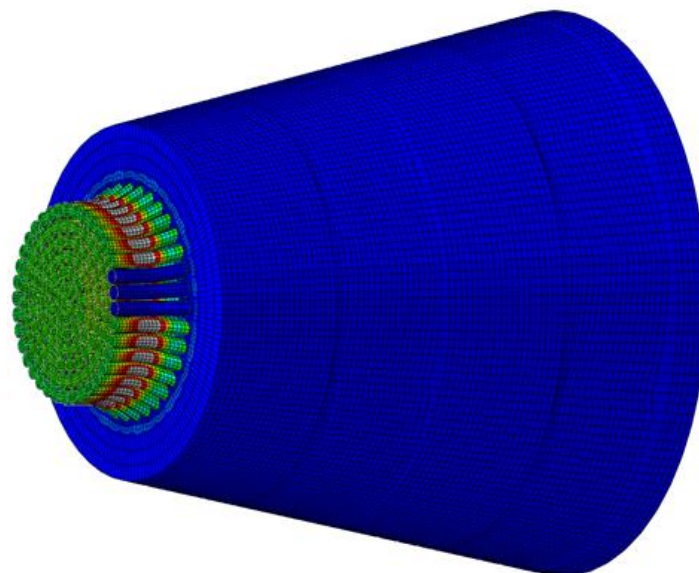


Figure 7.3.10-2. Finite Element Model Visualization of Three Initially Failed Wires

Six finite element analyses were conducted, each with differing number of failed wires. Models containing 3, 9, 15, 21, 31, and 38 disconnected wires representing post-fracture configuration were leveraged for the purpose of this study. Figure 7.3.10-3 shows a representative change in stress distribution across the cross section when considering the increasing number of failed wires. For the first configuration of three failed wires, the adjacent wire stresses increase by

roughly 5%. The stress increase changes with the number of failed wires, with more load transfer and stress increase occurring for increasing numbers of failed wires. Note the cross-sectional stress distribution shown in Figure 7.3.10-3 is for a specific distance away from the socket face and that there are complicated 3D effects not captured by this two-dimensional (2D) image.

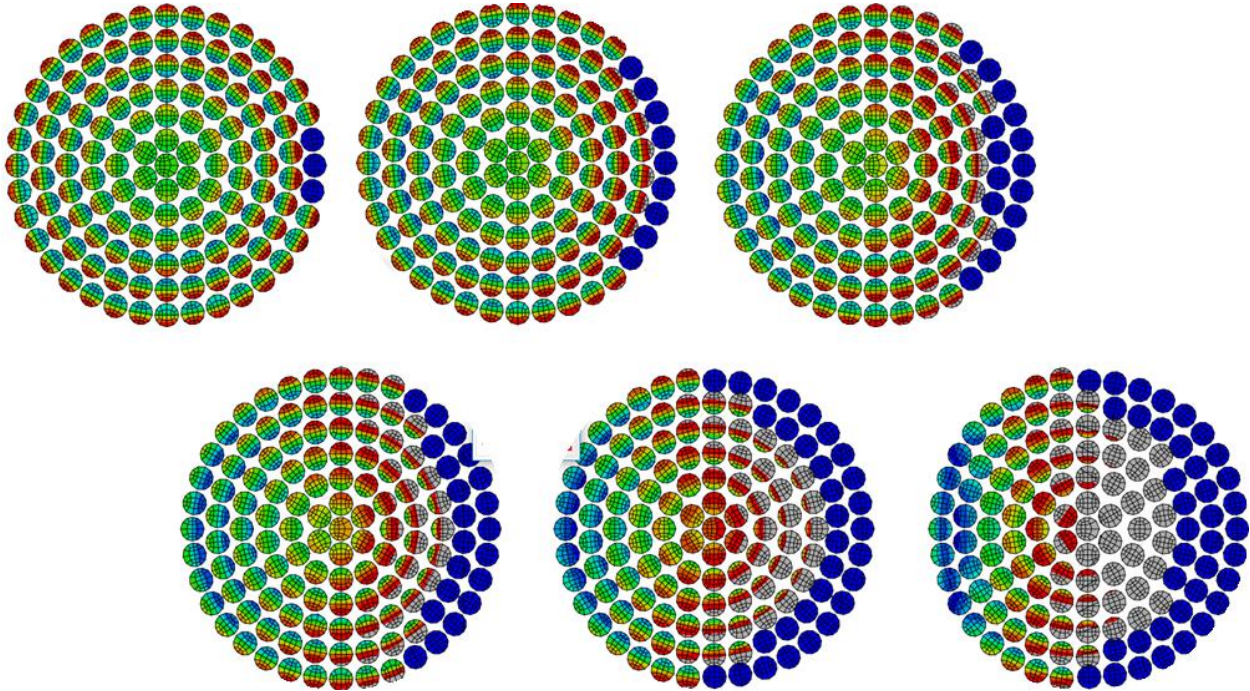


Figure 7.3.10-3. Model Cross-sectional Stresses for Differing Numbers of Failed Wires showing Stress Redistribution Radially and Circumferentially

The forensic analysis identified which wires in the cross section remained intact and pulled out of the socket with the core of the cable versus those which fractured in the socket. There was a clear bias of the wire failures to one side of the socket with a distribution of wire failures emanating radially and circumferentially from the 3 o'clock side of the socket. This is shown in Figure 7.2.3.1-1 but is shown again in the composite image in Figure 7.3.10-4. The red arrows show the theme of failure progression radially and circumferentially overlaid on the forensics cross-sectional naming and fracture type.

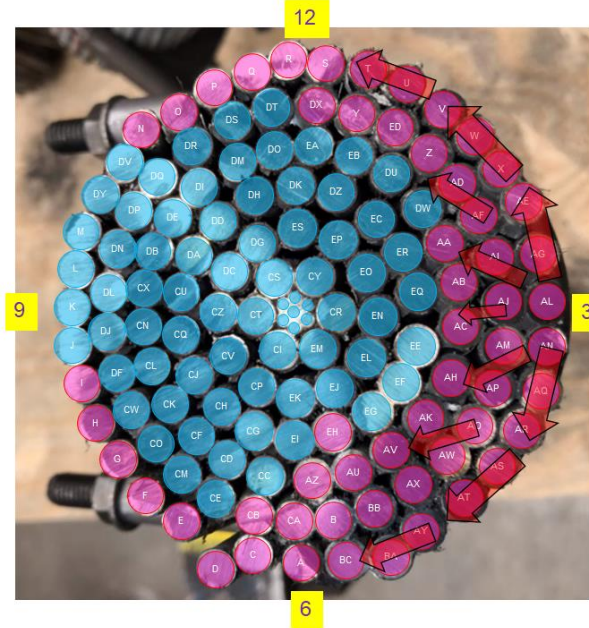


Figure 7.3.10-4. Pictographic Representation of Failure Progression Overlaid on Forensics Failure Mode Coloring

Lastly, the strain distribution within the zinc is markedly different when considering only three failed wires versus 38 failed wires. The shape and magnitude of strain is compared in Figure 7.3.10-5, which shows that peak plastic strains are greater than four times the pristine design when considering 38 failed wires. Note that, qualitatively, the shape of the zinc strain field is roughly similar to the cross section or cable that pulled from the socket during the failure event.

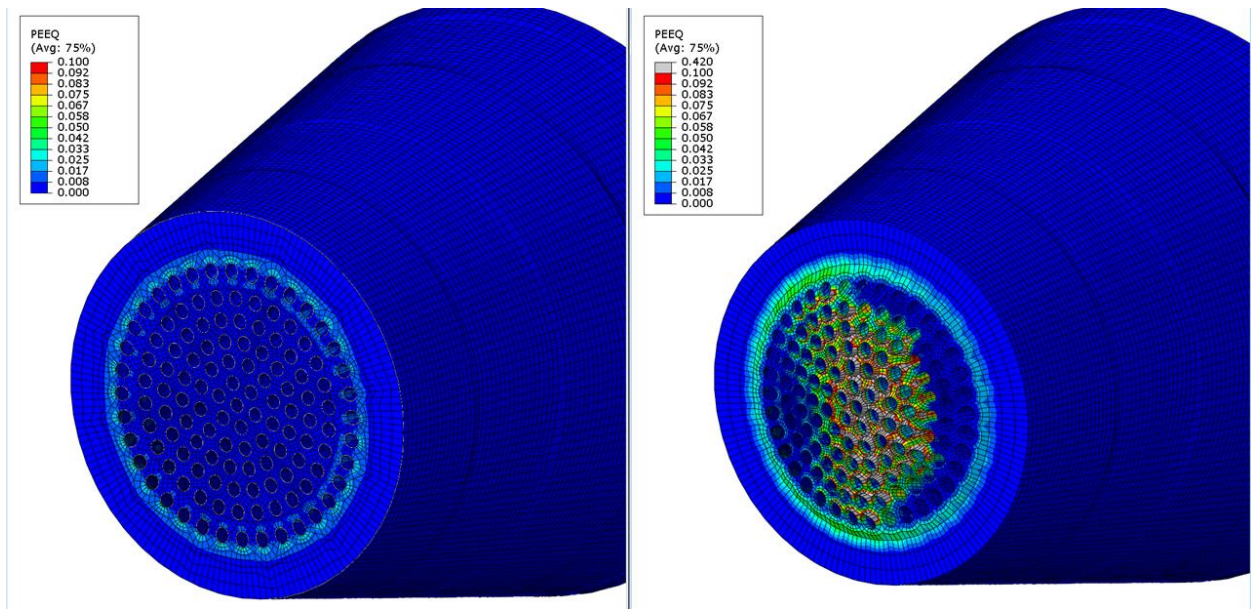


Figure 7.3.10-5. Plastic Strain Field Comparison between Three Failed Wires (left) and 38 Failed Wires (right)

7.3.11 Summary Based on Analysis Predictions

A combination of the design factors of safety, local socket mechanics, and high dead load resulted in small or negative margins of safety for the critical outer wires adjacent to the failed socket termination. There was no structural margin to accommodate time-dependent mechanisms under sustained loading, additional loads from dynamic environments (e.g., thermal fluctuations, hurricanes, earthquakes), or degradation mechanisms (e.g., corrosion). A hypothetical use case with a higher factor of safety (e.g., 4.0) predicts wire stresses below yield and reduced zinc yielding. In this case, the design is more accommodating of time-dependent degradation mechanisms and less sensitive to socket fabrication variability.

A key question in this study examines why this socket failed versus others at Arecibo or across the industry. While many designs exist in industry that could potentially use similar factors of safety, the Arecibo Observatory application required that most of the tension load in the cable was dead load due to constant suspension of the receiver. Fluctuating loads do occur from wind and temperature, but these are a relatively small relative to the magnitude of dead load. In contrast, other civil structural applications of structural strand socket terminations (e.g., bridges) are designed for conditions where there are live loads and dead loads and the dead load is a smaller percentage of the peak load condition. Therefore, in those applications, the strength margins are effectively larger for a longer period of the hardware life and provide comparably more margin to resist time-dependent failure mechanisms.

Despite the socket termination receiving a dedicated proof test, the intent of socket proof tests is not to screen for time-dependent degradation mechanisms such as creep, but rather test gross manufacturing intactness by demonstrating an adequate bond between the wires and the zinc at the individual interfaces within the socket. Due to the low margins in this application, the design was less accommodating of time-dependent mechanisms (e.g., the creep-dominated failure mode) and the multitude of environments over 25 years that combined to erode already low margins until the point of failure.

Finally, analyses were leveraged to investigate the possible sequences for progression of failure based on progressively increasing the number of failed wires. Results show qualitative congruence with forensic examination of the failed wires in the socket termination cross section. Failures of outer row wires lead to stress increases in the adjacent radial and circumferential wires, which propagate around the cross section until final zinc overload.

7.4 Design Factors and Standards

7.4.1 Insufficient Design Factor of Safety

The design factors of safety and their role in the failure of socket joint are discussed in this section. The Aux M4N socket has a defined minimum rated breaking strength of the cable (1,314 kips) compared with the maximum survival cable load predicted by WJE's analysis of 720 kips. This results in an effective design factor of safety of less than 1.83. Because insight into the exact factors of safety targeted in the original design and the original design analyses were unavailable, this section will reference the effective safety of 1.83, acknowledging that the actual safety factor targeted in the design could have been different. The following sections consider the Aux M4N socket in the context of design standards, live load to dead load ratio, factors of safety, analysis results, nonlinearity, and redundancy. It is postulated here that a 1.83 design factor of safety for the cable in question was insufficient to protect for time-

dependent creep-dominated failure modes and application in environments subject to hurricanes, earthquakes, and moisture.

7.4.2 Design Standards

The design upgrades involving the failed socket joint predated ASCE 19-96 [ref. 19], which was the requirements document governing the design of steel cables for buildings. Further, SEI/ASCE 7-02 [ref. 20] amends ASCE 19-96 steel cable design requirements. ASCE 19-96 was superseded by ASCE 19-10 [ref. 21]. While the inapplicability of ASCE 19-10 to the failed socket design is recognized, it is useful to discuss how current governing standards compare against this design. In the observatory application, the effective design factor was 1.83 or less, while current civil engineering design standards evaluate various combinations of loads (e.g., live, dead load) against a design factor of approximately 2.2.

According to reference 22, there is open debate concerning the structural redundancies of cable-stayed bridges (CSBs) and to what extent these structures are structurally sound under various extreme loading conditions. Table 7.4.2-1, reproduced from reference 22, shows factors of safety for cables.

Table 7.4.2-1. Design Factors of Safety from Various Industry Standards [ref. 22]

Standards	Design Factor of Safety for Stay cables of CSBs
Japan Road Association. Specifications for highway bridges: part II, steel bridges. Tokyo: Japan Road Association; 2017. Japanese.	2.5
EN 1993-1-11: Eurocode—3. Design of steel structures—Part 1–11: Design of structures with tension components. European standard. Brussels: European Committee for Standardization; 2006.	2.2
Post-Tensioning Institute. Recommendations for stay-cable design, testing and installation. 5th ed. Farmington Hills: Post-Tensioning Institute; 2007.	2.22
Service d'Etudes Techniques des Routes et Autoroutes. Cable stays—recommendations of French interministerial commission on prestressing. Bagnaux Cedex: Service d'Etudes Techniques des Routes et Autoroutes; 2001. French.	2.174
International Federation for Structural Concrete. Acceptance of stay cable systems using prestressing steels. Report. Lausanne: International Federation for Structural Concrete; 2005.	2.2

The selection of an appropriate design factor of safety for stayed cables is discussed in the literature, and it is argued that their selection depends on the ratio of live load to dead load stress and occurrence frequency of live load stress, fatigue, and corrosion, among other factors [ref. 22].

7.4.3 Qualification Methodology Discussion

Correspondence with subject matter experts indicated that the only testing performed at the time of Aux M4N design was a single pull test to failure that demonstrated a breaking strength in excess of the required rated breaking strength of the structural strand. Subsequently, builds were production units for Arecibo, receiving only socket proof tests and no additional qualification-type tests. No documentation of this qualification strength test was available for review.

While zinc spelter sockets are not specifically aerospace structures, it is insightful to examine the recommended design/build process of the socket as if it were aerospace hardware. Aerospace industry standards such as SMC-S-016 and NASA-STD-5001 recommend the following:

1. Fatigue/fracture testing demonstrating that the design is robust to the minimum detectable flaw size to at least four times the service life.
2. Thermal cyclic tests.
3. Vibration tests.
4. Creep tests.
5. Static strength tests.
6. Acceptance tests (e.g., proof test).

This comprehensive verification methodology is of high importance in aerospace applications because factors of safety are typically lower than in civil engineering applications.

Larger structural margins generally reduce the potential for fatigue and creep failure modes. In the Arecibo Observatory socket verification, the static strength qualification test did not explicitly consider other failure modes. Comparing the minimum breaking strength specified in the drawing (1,314 kips) and WJE limit load calculation (720 kips), the effective test factor of safety was calculated as:

$$\text{Effective Qualification Strength Factor} = (1314 \text{ kips}) / (720 \text{ kips}) = 1.82$$

The acceptance test is performed at half the breaking strength, so the effective proof test factor is calculated as follows:

$$\text{Effective Proof Test Factor} = (657 \text{ kips}) / (720 \text{ kips}) = 0.91$$

In aerospace applications, the proof test factor is typically required to be >1.0 to demonstrate the capability of the hardware to endure greater than limit-load-level loading. In some instances, specifically where fatigue and creep want to be exonerated, the qualification test and proof test factors are significantly greater than 1.0 to show how significant design margin for the production build is against the limit load condition. For the Aux M4N socket in question, a proof test factor of 0.91 may demonstrate that no grossly unacceptable manufacturing conditions exist, but no credit can be taken for demonstrating margin to life or other deleterious failure modes.

Potential shortfalls of Aux M4N design/build verification:

1. Proof test factor was <1.0.
2. Incomplete identification of failure modes associated with the Aux M4N socket. Potential failure scenarios include intra-material (e.g., adhesive failure between steel rope and zinc) or inter-material (e.g., crack propagation within the zinc itself). An analog to the design can be found with structural composites, particularly those that include face sheets bonded to a core material. In such cases, qualifying the design for life may entail dedicated subcomponent tests.
3. Socket joint fabrication is sensitive to workmanship. Testing just a single unit, as is often done for aerospace hardware, may not be appropriate. Instead, the sample size should be large enough to account for lot-to-lot variability considering material, human, and process elements. In the aerospace community, manufacturers often establish expected strength based on multiple specimens pulled from multiple builds. For such process-sensitive components,

workmanship testing is critical. It may be the case that the socketing community possesses an additional body of data related to this topic, but nothing specific was made available to the authors of this investigation.

7.4.4 Redundancy

Per ASCE 19-10 Section 3.1.1, cable system structures should be configured to maximize structural redundancy, and failure or malfunction of any one local component should not result in structural collapse. For example, in one structural application, the City of Chicago Department of Buildings required that structural engineers review the redundancy of a structure, and the city established criteria requiring the investigation of instantaneous cable failure and associated effects [ref. 23]. It is argued here that the concept of redundancy must be demonstrated for sufficient durations that corrective actions can be implemented to prevent total collapse. Failure of a single element delaying Arecibo Observatory collapse by several weeks or months is not sufficiently redundant for corrective action to occur.

While reference 22 was not peer reviewed by NASA or The Aerospace Corporation, there are some conclusions worth noting relative to structural redundancies and factors of safety of CSBs. In reference 22, simplified finite element models of bridges were developed and static analyses were conducted to study redundancy through a parametric study of the safety factor. The effects of overloading, cable loss, and corrosion on the structural redundancy of both bridges were investigated. Reference 22 indicates that CSBs are sufficiently redundant at a safety factor of 2.5, and that a safety factor of 2.2 yields minimum structural redundancy for a CSB under normal loading conditions. However, it is noted that a CSB can lose its redundancy significantly at 2.2 in the case of an unexpected rupture/collapse of a stay cable.

Despite the Arecibo Observatory load ratios being proportionally different than CSB designs, the conclusions in reference 22 point to a potential deficiency in the Arecibo Observatory design due to lack of structural redundancy, especially considering the observatory's comparably low safety factor (~1.83) and exposure to extreme conditions (e.g., hurricanes, earthquakes). Failure of the main cable in the Arecibo Observatory application resulted in an eventual catastrophic collapse, indicating lack of structural redundancy.

7.4.5 Live Load to Dead Load (LL/DL) Ratio

In typical design, dead loads are much more certain and predictable than live loads. In the observatory application, the source for most of the cable load was from dead loads. Live loads from operation and thermal transients were a small percentage of the total cable load. Apart from live loads, extreme environments (e.g., winds and earthquake loads) contribute to the total cable load and had to be considered in the observatory's cable upgrade designs. The LL/DL ratio, its relationship to the factor of safety 1.83, and the role in the observatory failure event are further explored.

While the observatory was not designed per ASCE 19-10 [ref. 21], it is instructive to understand how the observatory design bodes with this design standard. ASCE 19-10 indicates that temperature effects on cables, vibrations, deflections, and erection analysis must be evaluated for cable structures. The ASCE standard also states the minimum breaking strength of cables shall always be at least twice the maximum cable design loads, including the envelope of loading combinations of cable self-weight, structure dead load, cable pre-stress forces, and live load and environmental load combinations. Cables also should maintain a minimum tensile force under all

loading conditions to minimize visible cable sag and the potential for induced cable vibrations. Table 7.4.5-1 describes five of nine examples of various load combinations required in the evaluation.

Table 7.4.5-1. Load Factors required in Evaluation of Load Combinations

Combination	Dead Load	Live Load	Pretension	Wind	Earthquake	Erection	Rain
T ₁	1.0	0	1.0	0	0	0	0
T ₂	1.0	1.0	1.0	0	0	0	0
T ₃	1.0	0	1.0	0	0	0	1
T ₄	1.0	0.75	1.0				0.75
T ₅	1.0		1.0	0.6 (OR)	0.7 (OR)		

There are four other combinations in ASCE 19-10 not listed in Table 7.4.5-1. The largest load combination multiplied by 2.2 should not exceed the cable nominal breaking strength. Other reduction factors may be applicable that require consideration per ASCE 19-10, but these are not discussed here.

The observatory's cable final load is 602 kips for dead loads and potentially includes pre-tension. Under operational conditions (e.g., live load) the cable tension load is 615 kips. Survival cable load, which presumably includes loads from hurricanes and earthquakes, is 622 kips. Based on these loads, it is not possible to meet the ASCE 19-10 design factor of 2.2. With the WJE maximum predicted cable load of 720 kips, the gap is even wider against this standard.

Further, based on The Aerospace Corporation's finite element model, the operational loads of the observatory cause the outer wire stress to approach the strength capacity of the wire at nearly half the rated cable breaking strength of 1,314 kips and remain high for the service life (+20 years). The zinc within the socket is also under sustained shear loads that continuously cause the outer wire stresses to increase. Per ASCE 19-10 [ref. 21], creep in cables can occur even after pre-stretching. High stress levels relative to the breaking strength will result in a creep rate that can increase the wire strains over time, thus limiting the ability to accommodate other environmental effects stemming from cyclic loading and corrosion.

This analysis postulates that the observatory design was susceptible to creep more so than a CSB design. This will be illustrated via an example that considers roughly the same cable design load as the observatory but apportions a greater live load percentage of the total cable load compared with the observatory. In many CSB designs, live load tends to be a sizeable portion of the (LL+DL), for example, in reference 22 an LL/DL ratio of 0.45 was used in the analysis of the bridge design, while an LL/DL of 0.67 was used in reference 24.

Adapting the dead load ratio for the sake of example, consider a hypothetical socket design application where the dead load and pretension cable load is 350 kips, live loads are 150 kips, and the survival loads due to wind are 170 kips. The only sustained loading is the dead load and pre-tension of the cable. Based on the socket joint finite element model, this results in an outer wire stress level of 175 ksi, which is near the yield strength of the individual wires without significant yielding observed. Creep due to sustained loading at this level will result in a lower creep rate than in the Arecibo Observatory application and leave more capability in the wires to accommodate other time-dependent effects (e.g., creep). In this example, the design load combination per T₅ is still 620 kips, similar to the Arecibo Observatory application.

F-32. Socket joints in the Arecibo Observatory application were subjected to a relatively higher percentage of sustained cable load versus total load compared with a survey of bridge designs, increasing susceptibility to creep.

7.4.6 Cable Nonlinearity

Cables exhibit both geometric and material nonlinearities during operation. Cables are inelastically prestretched until individual wires settle into their final positions at a high percentage of their minimum breaking strength, which allows them to behave more predictably. Gossen [ref. 25], an expert in cable design, discusses the incongruity of how factors of safety are used in conjunction with the working stress design (WSD), where the stress, force, and deformation behaviors are assumed to be linear even though the behavior of the cable is nonlinear. Gossen reports that the factor of safety is intended to account for accidental overloads, material variability, and fabrication imperfections. *Note: the intent of what the factor of safety provides coverage against is not consistent across industries, and the aerospace community assigns coverage to different topics.* The argument made by Gossen is that due to the nonlinear nature of the cable, the structural margins remaining against overload can vary significantly and remain indeterminate unless the structure is analyzed beyond nominal conditions. In most standards, the loads effects are superimposed with varying amplification factors, but this is not applicable for nonlinear cables.

To illustrate this point, an independent finite element model of the socket joint was developed to understand the relationship between stress and the load applied for two zinc material models. The rated breaking strength of the cable is 1,314 kips, so at half the breaking strength a linear stress response of the wire is expected. However, due to the complexity in the geometry and the nonlinear behavior of the zinc and the wires, the outer wire stress approaches the ultimate strength at half the cable breaking strength and exhibits a nonlinear response at one-fourth of the breaking strength of the cable, as shown in Figure 7.4.6-1. The model illustrates a nonlinear scaling of outer wire stress to load applied.

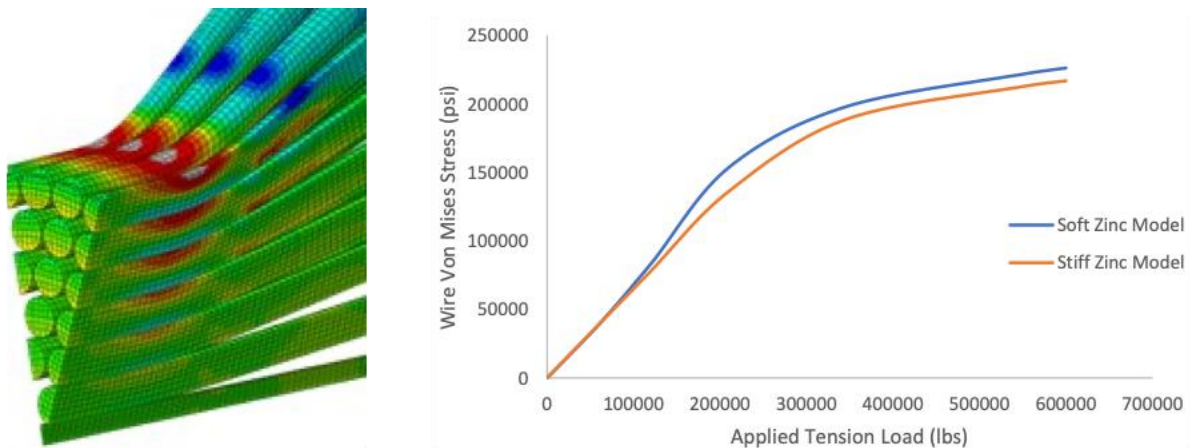


Figure 7.4.6-1. Stress Response in Wire is Nonlinear with Increasing Applied Tension Load

The finite element results confirm the thesis by Gossen [ref. 25] that “the ultimate load approach may result in individual cables stressed beyond their accepted level under service loads, while still satisfying the ultimate load design requirements. It is apparent that the analysis and design of

these structures can be much more laborious than what is common in the design and analysis of conventional structures.”

7.4.7 Design Factors of Safety

ASCE 19-10 [ref. 21] requires a minimum design factor of safety of 2.2 for steel cables. WJE [ref. 1] conducted a survey of the factors of safety required by other standards and stated:

AASHTO [American Association of State Highway and Transportation Officials] Movable Bridge Specifications provides for cable factors of safety of between 4 and 8 depending on the function of the cable, while the U.S. Department of the Interior Bureau of Reclamation suggested a factor of safety of 5 for hoisting ropes due to the expected application of frequent dynamic loads and possible abrasion during normal service applications.

The Crosby Group design manual for socket designs indicates a factor of safety ranging between 3 and 5 depending on the specific application [refs. 26-28].

Returning to the finite element model of the Aux M4N socket, one-fifth of the rated breaking strength of the cable is 262 kips, and the outer wire stress at this load is well below the yield strength of the wire. The nonlinearity in the stress response at this cable load is associated with the zinc behavior and is unrelated to material plasticity. At one-third of the rated cable breaking strength, the outer wire stress exhibits mild yielding. *This further supports the use of a factor of safety higher than the 1.83 used for this application.*

In typical design, dead loads are much more certain and predictable than live loads. In the observatory application, the source for most of the cable load was from dead loads. Live loads from operation and thermal transients were a small percentage of the total cable load. Apart from live loads, extreme environments (e.g., winds and earthquake loads) contribute to the total cable load and had to be considered in the observatory’s cable upgrade designs.

Wire stress does not scale linearly with increasing cable load, so applying standard factors of safety to cable designs results in uncertainty on whether the cable is structurally robust. The complexity in this evaluation is compounded by the known socket-to-socket fabrication variability.

Design standards and literature point to the importance of designing in structural redundancy when employing stayed-cable socket designs. It is recognized, however, that the level of redundancy to which Arecibo was intentionally designed is unknown, and it is possible that the observatory was never meant to be redundantly designed in the first place. Nevertheless, a study of bridges found that a factor of safety of 2.5 can yield sufficient redundancy in CSBs. The observatory application used a value of 1.83 against maximum cable load, but as soon as one socket failure occurred, other cables eventually failed. The collapse of the structure indicates the lack of structural redundancy and is consistent with the use of a lower factor of safety.

The 1.83 factor of safety in the observatory application is below cable factor of safety recommendations in the AASHTO Movable Bridge Specifications [ref. 29], The Crosby Group design manual [ref. 26], and various ASME standards. If the recommended higher factors had been used in the observatory cable designs, then the outer wires stress would have been below the yield strength of the material and would have been more likely to accommodate creep, fatigue, and corrosion failure mechanisms.

Finally, the dead loads in the Arecibo application were a significant percentage of the total cable load compared with CSBs, where live loads can be a larger percentage of the total cable load. For the same cable load, the observatory application has higher sustained load over 25 years compared with a bridge design, resulting in higher creep rates and leaving no structural margin for cyclic loading from hurricanes and earthquakes. Further, the observatory application has lower structural margins to ASCE 19-10 [ref. 21] compared with a generic bridge design.

F-33. The Arecibo Observatory had an effective design factor of safety of ≤ 1.83 , which is significantly less than the minimum suggested by literature (i.e., >2.1) to ensure structural redundancy in the event of cable failure.

7.5 Root Cause Analysis and Failure Progression

As discussed in Section 6.3, the NASA and The Aerospace Corporation teams developed a best-effort systematic fishbone and evaluated supporting and refuting evidence for each potential causal factor of the Auxiliary M4N cable. Assessments for each potential factor, considering all available evidence, are presented in this section under these categories: (1) design, (2) loads and environments, (3) build variability, (4) maintenance, (5) environmental assisted degradation, and (6) failure mechanisms. The joint investigative team developed a most probable root cause scenario within practical limitations using available data taken from NASA/Aerospace independent testing/analysis, referenced data from the WJE investigation, and other external referenced sources.

7.5.1 Design

Insufficient Design Criteria

Finite element analyses predict significant yielding of outer wires and negative structural margins at the maximum predicted cable loads, as discussed in Section 7.3. The effective design factor of safety was calculated as 1.83, which is lower than typical industry standards (see Section 7.4). The low factor of safety reduced tolerance to time-dependent degradation mechanisms. Furthermore, analysis considering a hypothetical 3.0 factor of safety predicted no wire yielding and produced limited zinc yielding. Therefore, insufficient design criteria was identified as significant contributor to the failure event.

Material Incompatibility

While some corrosion protective measures were put in service during the life of the socket (e.g., a mastic coating on the casting cap), these measures were put in place after corrosion had begun and were not adequately maintained to provide continued corrosion protection over the life of the socket. This resulted in pervasive quantities of corrosion product, particularly zinc oxide, throughout the socket along various identified moisture pathways. Where steel and zinc were present, heavy amounts of zinc oxide were present with trace amounts of iron oxide. This imbalance in corrosion product is largely due to the cathodic protection of the steel created by the zinc acting as a sacrificial anode in the galvanic corrosion process. Stress analysis found that the corrosion of the zinc casting was largely inconsequential to the strength of the joint. The galvanic protection of the steel likely aided in allowing the wires to realize their ultimate strength in spite of the amount of time exposed to a corrosive environment. The conclusions on corrosion are discussed in Section 7.5.5, but in general, corrosion was assessed as a low contributor to the overall failure of events based on extensive finite element analyses.

Wire mechanical properties met specification. Measured zinc mechanical properties varied significantly, although some of this can be attributed to size effects of the samples excised from the socket; however, there was a large amount of zinc grain anisotropy that, although expected due to the casting process, can create significant variability in mechanical properties based on grain size and orientation. Finite element analysis predicted negative margins of the outer wires regardless of the zinc material properties. In conclusion, material incompatibility was assessed as a low contributor to the progression of failure events.

Insufficient Acceptance Criteria

While the drawing did not specify acceptance criteria or characteristics for brooming, NASA/Aerospace reconstruction of the brooming was reviewed by “socket joint experts” and found to be in-family to their experience base. NDEs were not performed prior to entering the socket joint in service, but forensic examination of the failed socket showed dimensions to be within specifications and without notable defects (e.g., voids/cracks) that appreciably affected wire stresses based on finite element analysis. Methods for socket joint construction are well-established in industry, and gross build defects are verified through proof test. However, the proof test is not intended to screen for time-dependent failure modes and was below 1.0 times limit load. Finally, it is noted that the socket joint survived 20+ years in service.

7.5.2 Loads and Environments in Service

Characterization of Nominal Loads

“Nominal loads” refers to overall observatory receiver mass, total dead load, nominal winds, temperature loads, and expected environments except hurricanes and earthquakes. Strain-gage and load cell data collected over a multi-day window demonstrated that typical wind and temperature fluctuations produced small cable loads in comparison with the sustained loads from dead weight of the various Arecibo radio telescope structures.

Full observatory system loads models were employed by multiple design firms (WSP, TT) to establish quasi-static load distribution within the cable architecture. Cable loading distribution is sensitive to many factors including the local stiffness of the cable, position of the receiver and Gregorian Dome, tie-down tension, and environmental transients. Per WJE, an independent analysis of observatory load distribution demonstrated the possibility of higher tensile loads than shown on the original design drawing for the operational condition of the Aux M4N cable. Per WJE, analysis estimates of cable load through observatory lifetime based on cable sag survey data indicate the possibility for increasing tensile loads through time, indicating that the design did not differentiate between a beginning-of-life load and an end-of-life load. The higher loads predicted by WJE exceeded those specified in the drawing and resulted in a lower factor of safety (1.83) compared with the intended value for the design.

Improper Characterization of Survival Loads

Analysis of this factor focused on whether improperly characterized survival loads (e.g., earthquake, hurricane, extreme temperatures) caused the hardware to be used beyond its design capability. Analysis methods used to analyze survival conditions do not incorporate dynamic amplification, resonance, vortex shedding, etc. to establish the survival load requirement. Arecibo experienced several hurricane and earthquake events after which damage was identified in portions of the facility, including other cables, that required repair. The real structural response due to wind gusts or vortex shedding during transient environments is unknown and can

only be qualitatively assessed as a general contributor to the accumulation of damage. Per the discussion in Section 7.3.8, it is recognized that cyclic loading only accelerated the creep-dominated failure mechanism. Environments such as hurricanes, earthquakes, and temperature fluctuations can increase creep, per the ASME interaction curve, and reduce the life of the socket joint. Further, the Aux M4N cable failure occurred on a day with benign wind/thermal environments and without operation of the observatory receiver. Due to the significant dead loads compared with transient loads in this design, improper characterization of survival loads was deemed a low but still notable factor in the failure event.

Improper Moisture Characterization

Failure analysis showed pervasive corrosion associated with moisture within the socket joint. Structural qualification of the cable was for a pristine configuration rather than being derated for decades of moisture exposure, corrosion, and weather events. Actions were taken over the service life to prevent observed water intrusion, indicating conditions were not adequately considered during the design process. Despite these observations, excised wire segments were found to be in-family with nominal strengths. The conclusions on corrosion found within the zinc are further discussed in Section 7.5.5, but in general, corrosion was assessed as a low contributor to the overall failure of events based on extensive finite element analyses.

7.5.3 Build Variability

Wires

Independent mechanical testing of excised/recovered wire material from the Aux M4N socket shows conformance in both dimensions and mechanical properties (see Section 7.2). Failure analysis of the socket verified that the cross section met drawing and had the correct number of wires. Two wires had surface defects that likely contributed to wire fractures. The negative structural margins in the outer wires likely deteriorated further by the surface defects, as these act as stress risers.

Socket Outer Casing

No cracks were identified from dry powder magnetic particle examination of the socket's outer cone. Finite element analysis shows large structural margins for the outer casing, and robustness to any out-of-tolerance conditions. Dimensions of the socket cone were measured during failure analysis to be within drawing dimensions. Socket joint metrology measurements differed by up to about 0.25 inch based on NASA KSC metrology measurements of the socket and pin dimensions. The variability in final dimensions is expected due to the nature and precision in the casting process. Variability was considered acceptable based on structural analysis demonstrating robust structural margins of the steel casting.

Wire Brooming

Finite element analysis showed that decreasing brooming quality leads to increased creep rates and, consequently, higher outer wire strains. Relatively poorly broomed sockets are predicted to distribute loads unequally into the critical outer wires, decreasing the overall capability of the design. Therefore, fabrication variability of wire brooming may affect wire stress.

The Aerospace Corporation and NASA KSC reconstructed the geometric distribution of the wires within the socket (i.e., wire brooming). It is recognized that non-uniform wire brooming is an inherent characteristic of these socket joints as it is a manual operation, not controlled in

uniformity by drawing, and is primarily verified for build quality through inspection prior to spelter pour and proof testing, which the Aux M4N socket successfully passed prior to installation. Discussion with industry experts indicates that wire brooming is not out of family/atypical with experience and that the likelihood of significantly poor fabrication/brooming propagating through the build/proof/inspection process to in-service is highly unlikely. Interviewed experts were unaware of any process escapes in industry where a socket of this type passed proof test but subsequently failed due to poor build/brooming quality.

Zinc Spelter

Zinc spelter was destructively examined to evaluate both dimensions and material properties of the zinc and wire. Dimensions conformed to the drawing (see Section 7.2). Results confirm the presence of gas bubbles, intermittent porosity, large regions in the back of the socket that are uncharacteristic of castings, cracks throughout the bulk zinc, and inhomogenous anisotropic grain structure determined through microscopy, grain study, and mechanical testing. Finite element modeling evaluated the potential effects of varying zinc mechanical properties and gas bubbles/voids on the observed failure progression; these analyses indicated high wire stresses regardless of zinc properties. The analysis specifically predicted insensitivity of wire stress to the presence of gas bubbles.

Poor Wire-Zinc Bond Strength

Fifty-six of the 126 wires fractured in the socket. The other 70 wires did not fracture; the zinc failed before these wires, coming free from the socket attached to most of these wires and the cable-end of the failed wires in a cable/zinc slug. Although 70 wires did not fracture, up to two outer ring wires could have pulled free of the socket joint individually due to inadequate wire/zinc bond strength. Of the wires that fractured within the socket and were mechanically removed, some exhibited zinc oxide corrosion product along their wire surfaces down to the wire fracture location, while others exhibited no corrosion with good zinc/metal adhesion along their wire surfaces near the wire fracture location. This led to the conclusion that the wire-zinc bond strength was not a factor amongst the wire failures and likely not the reason those two wires were found separated from the cable/zinc slug.

7.5.4 Inspections

Inspection limitations prevent the ability to characterize defects within the zinc casting of a particular build, thus preventing the qualification test from accounting for worst-case build conditions without some other destructive process of determining expected variability. Further, inspection criteria during the life of the socket joint were not traceable to the qualification program, despite easily observable and measurable zinc extrusion at the socket joint base. Finally, the qualification test target load did not explicitly consider stress levels of the constituent components within the socket joint but rather was based on a generic, load-based design criterion.

In-service inspections conducted over the socket life shows evidence of zinc extrusion and moisture intrusion/corrosion. Records and socket failure analysis show that corrosion mitigations were employed, and that the zinc extrusion showed evidence of progression between 2003 (0.5 inch) and 2019 (1 3/8 inches). Although no pass/fail criteria were known to exist, AASHTO M277-06 states that seating extrusion should be less than one-sixth of the cable diameter, or <0.6 inch for the Aux M4N. The inspection process did not couple the qualification/design

process to a pass/fail criterion to trigger a replacement. Data were not provided to explain the decision process after the 2019 photos were taken.

7.5.5 Environmental Assisted Degradation

No evidence of stress corrosion cracking was found during metallurgical studies using visual and SEM inspections. The majority of the wires exhibited a cup-cone ductile failure mode demonstrating that the wires were able to realize their ultimate tensile strengths.

Hydrogen-assisted Cracking HAC

HAC is caused by diffused hydrogen accumulating at stress concentrations and further decreasing strength capacity of the wires, and can lead to wire cracking. Forensic analysis identified three failed wires within the socket that contained evidence of progressive failure, likely HAC. One wire had a surface defect at the crack initiation site where the fracture surface exhibited characteristics of HAC. HAC can accelerate failure of a wire, especially when subject to sustained loading with negative structural margins over the entire service life.

Corrosion

The presence of zinc and steel in a humid environment enabled corrosion mechanisms throughout the socket, including accelerated corrosion of the zinc due to galvanic coupling with adjacent steel. This was evidenced by significant formation of zinc oxide coincident with conduits for moisture intrusion, as well as heavy accumulations of zinc oxide and sometimes trace accumulations of iron oxide along these conduits where both zinc and steel were present. The moisture was able to penetrate into the zinc casting through various pathways identified in and around the zinc casting cap, through wires protruding the zinc casting outer diameter, and then along cracks in the zinc, wire surfaces, and casting defects present within the zinc casting, leading to a pervasive amount of corrosion evidence. The corrosion, while pervasive, was mostly limited to the upper two-thirds of the socket, nearest the casting cap. Of the wires that fractured within the socket and were mechanically removed, some exhibited zinc oxide corrosion product along their wire surfaces down to the wire fracture location, while others exhibited no corrosion, with good zinc/metal adhesion along their wire surfaces near the wire fracture location. Because of this, the forensic evaluation concluded that corrosion played a minimal role in the ultimate failure of the socket.

A finite element study indicated minimal effects on the wire stresses based on a sensitivity study of varying conditions between the socket housing and the zinc. The large compression zone that develops at this interface causes a small sensitivity of the surface conditions on the wire stresses. Analysis extensively evaluated voids within the casting and defects near the casting cap side of the socket and found negligible effects on the maximum predicted wire stress located toward the socket base. This finding was used to assess that corroded wires protruding from the zinc outer diameter were not a factor to the overall progression of failure. Finally, while corrosion was found throughout the zinc, analysis showed a larger role of wire negative margins at operational loads and sustained loading due to dead loads, compared with the corrosion in the zinc.

7.5.6 Failure Mechanisms

Strength

Of the 56 wires that failed, five were observed to have surface defects running along their lengths. Two of those defects likely influenced the fracture, and one was an initiation site for a progressive failure, probably HAC, on an outer ring wire. The shear and HAC fractured wires exhibited little to no necking. Necking is attributed to ductile failure where the wire is given enough time to yield, as is typically seen in the cup-cone failures. The outer ring wires that failed typically had less necking than the inner ring wires that failed.

Examination of the exposed wire channel lengths in the back of the socket showed that the inner ring wires displaced more than the outer ring wires. This was due to the progression of failure, starting with the outer ring wires and moving to inner ring wires as wires continued to fail, and possibly due to the brittle fracture region tearing open. Visual observation of the pulled-out cable section and the socket internal cavity showed a skew in the failed core versus the socket centerline. This skew reflects the progression of failure as wire loads were redistributed to the remaining wires, likely starting with an outer ring wire on one side of the socket and progressing to more adjacent inner ring wires, while at the same time progressing around the perimeter to more heavily stressed outer ring wires.

In summary, (1) failure in the outer wires occurred prior to total cable collapse, (2) the outer wires were critical in maintaining function of the socket joint, and (3) outer wires were highly stressed with minimal structural margins of safety at nominal observatory.

Cumulative Damage

The forensic investigation of the examined failed wire surfaces (see Section 7.2) found no evidence of fatigue striations (fatigue crack propagation), beach marks (macroscopic appearances), or pearlitic steel fracture surfaces that resemble fatigue fracture even without beach marks or striations. Fatigue striations are correlated to crack advancement per loading cycle, while macroscopic beach marks generally represent some changes in the fatigue loading conditions. The only wire fracture forensic evidence that may be attributable to cyclic loading were the HAC wire fractures, and all of those were mixed-mode, indicating that any cyclical contribution was only a partial contributor. Additionally, forensic inspection found no evidence of fatigue within the zinc, but minor additional contributions of cyclic loading damage may not be discernable from the overall contributions of damage within the zinc casting due to sustained loading. Finite element analysis could not rule out the potential of accumulation of damage due to cyclic loading caused by transient events. However, the contributions of the cyclic damage were assessed to be small compared with the accumulation of damage from sustained loads from dead loads. Forensic analysis showed clear evidence of creep within the zinc. Analysis of the loads also supports a higher percentage of dead loads compared with transient loads. Finite element analysis predicted high stresses within the zinc caused by sustained loading, and as the zinc crept the outer wire stresses were predicted to increase. The negative structural margins further deteriorated over time due to the creep setting within the zinc, until wire failure occurred.

7.6 Failure Progression

- Design criteria had a 1.83 factor of safety on rated breaking strength without consideration for constituent stress margins. Loads predictions reviewed after the failure indicate up to 15% higher than design criteria, and < 2.0 factor of safety. Additionally, the sustained dead load versus total load is significantly higher than for typical open socket terminations in bridges, hoists, etc. **(F-23, F-25, F-26, F-28, F-29, F-30)**
- Design verification lacked specific testing of creep, cyclic loading, and worst-case workmanship conditions. Credible failures modes were unqualified in the Arecibo Observatory application. *Note: A robust qualification program also establishes inspection techniques, inspection success criteria, and repair actions needed for specific service life definitions and inspection intervals.* **(F-3, F-18, F-19, F-28 F-29, F-32, F-33)**
- As the casting cooled and solidified, shrinkage occurred between the casting cap and the socket cone inner diameter, leaving a gap along the sides of the zinc casting nearest the casting cap. Additionally, eight wire ends were found to touch the socket cone inner diameter, which provided a pathway for moisture intrusion. **(F-15, F-16, F-20, F-21)**
- During the zinc spelter fabrication process and subsequent proof testing, wires reached their full loading capacity as zinc flowed to develop the confining pressure, which resulted in less than 0.5 inch of zinc seating extrusion from the socket base. **(F-1, F-2)**
- Finite element modeling predicts local yielding of outer wires adjacent to the socket base during pre-stretching events and possible repeated yielding during operation depending on observatory use and survival events. Additionally, failure analysis shows a progressive failure starting with outer wire failure, consistent with predictions on lowest margin wires. **(F-13, F-25, F-28)**
- Analysis indicates that zinc flow primarily due to creep caused stress redistribution to the outer wires, further decreasing their capability. An increase in outer wire stresses was shown when replicating a high creep condition versus a condition with no creep. At ambient temperature, the high shear stress and strain rate caused the zinc to creep, which was further confirmed by metallography. **(F-19, F-29, F-32)**
- Periodic inspections found progressive zinc extrusion in several sockets before the Aux M4N failure, in 2003 and 2019, increasing from 0.5 to 1 3/8 inches. Although no pass/fail criteria existed, AASHTO M277-06 [ref. 29] states that seating extrusion should be less than one-sixth of the cable diameter, or less than 0.6 inch for the Aux M4N. Interviewed industry experts also confirmed that extrusion of 1 3/8 inches is evidence of likely socket damage. **(F-1, F-2)**
- Significant transient loading events, including hurricanes and earthquakes, damaged portions of the observatory over its life and may have contributed to cumulative damage through cyclic loading. **(F-29)**
- Wire build defects and probable HAC were found on a few wires and were possible contributors to the initial failed wires. Over time, a few outer wires fractured due to local overload, causing load transfer to adjacent wires (e.g., circumferentially and radially). Progressive failure analysis simulating wires fractures shows that if a few outer wires fail, adjacent wires are subjected to ~5% increase in stress. **(F-11, F-12, F-13, F-27, F-28)**

- Wires progressively fractured circumferentially and radially through the cross section. Progressive failure analysis simulating wire fractures indicates circumferential fractures first, followed by fractures of the adjacent inner ring of wires. The stresses increased significantly in the adjacent wires. (F-12, F-13, F-27, F-28)
- As wire fractures moved inward or adjacent to the first fractures, the fracture failure mode changed. Due to zinc confining pressure, inner wires had more elongation capability compared with outer wires and exhibited ductile cup-cone fracture behavior. The confining pressure, as predicted by the analysis, acted on the inner core wires. Compression increases wire ductility, also confirmed by forensic evidence showing primarily cup-cone failures. (F-12, F-13)
- After approximately half of the wires failed, there was insufficient confining pressure and ability of the zinc to sustain increasing shear. The socket-level failure exchanged to zinc “core” overload. Significant zinc plastic strains then developed and transferred load internal to the socket. Finally, the zinc core with unfractured wires pulled out, resulting in cable failure. (F-16)

7.7 Summary of Findings

The NASA/Aerospace team concludes that the most probable cause of the Aux M4N cable failure was a socket joint design with insufficient design criteria that did not explicitly consider socket constituent stress margins or time-dependent damage mechanisms. The socket attachment design was found to have an initially low structural margin, notably in the outer socket wires, which degraded primarily due to long-term zinc creep effects that were activated by long-term sustained loading and exacerbated by cyclic loading. Additionally, wire defects and probable HAC were found in a few wires that may also have contributed to initial wire failures.

F-34. The Aux M4N design had insufficient design criteria and a low structural margin, which were insufficient to accommodate time-dependent damage mechanisms.

The design did not explicitly consider the time-dependent effects of creep and cyclic loading on design capability, nor did it explicitly set service life inspection intervals with pass/fail inspection criteria. It also did not specify an end-of-life capability requirement associated with service life degradation. Verification did not account for a worst-case build condition that was traceable to in-service inspection of features (e.g., zinc creep/extrusion). In-service inspections showed evidence of progressive zinc extrusion on several Arecibo sockets, which in hindsight was evidence of cumulative damage and in effect a missed opportunity to prevent cable failure.

F-35. The Aux M4N socket joint design did not explicitly consider time-dependent mechanisms for the Arecibo application to establish an end-of-life capability.

A combination of low socket design margin and high percentage of sustained loading revealed an unexpected vulnerability to zinc creep and environments, and to long-term cumulative damage, which led to progressive zinc/wire failure. The resulting core-pullout failure mode that preceded observatory collapse was found to be (1) unique compared with other industry applications, (2) insufficiently addressed within existing standards, and (3) a potential risk for similar designs and, therefore, should be characterized and mitigated. The effective design factor of safety was significantly less than the minimum necessary to ensure structural redundancy in the event of a cable failure. After the Aux M4N failure and before the main cable failure, additional loads

analyses incorrectly asserted acceptable positive margin of the remaining structure despite no understanding of why a cable had failed at half the rated breaking strength.

F-36. Low socket design margin and atypical operating conditions revealed an unexpected vulnerability to zinc creep and to long-term cumulative damage, which led to progressive zinc/wire failure of the socket.

F-37. The effective design factor of safety was significantly less than the minimum suggested by literature and was insufficient to ensure structural redundancy in the event of a cable failure.

8.0 Findings, Observations, and NESC Recommendations

8.1 Findings

The following findings were identified for the Aux M4N socket:

- F-1.** The Aux M4N socket build process and original construction was typical of zinc spelter open-socket terminations.
- F-2.** Zinc extrusion of Aux M4N socket as documented in 2019 indicated an unquantified degree of damage and a nonconformance.
- F-3.** Creep behavior of the zinc spelter socket termination constituents (zinc or broomed wires) is not a failure mode typically evaluated for these sockets.
- F-4.** Socket housing dimensions were within wire rope catalog specifications.
- F-5.** The Aux M4N cable met drawing requirements for a 3.25-inch diameter cable (see Appendix D).
- F-6.** The Aux M4N cable end section and socket cavity are skewed compared with the socket's longitudinal centerline axis.
- F-7.** Gas bubbles located above wire ends were trapped during the solidification process.
- F-8.** Smaller-sized porosity inherent to the casting process was found intermittently throughout the bulk zinc.
- F-9.** Fifty-six of 126 wires fractured in the socket.
- F-10.** Seventy of the 126 wires did not fracture; the zinc failed before the remaining wires failed.
- F-11.** Wire surface defects were found on five fractured wires. Defects on two wires likely influenced the fracture, one of which was an initiation site for probable HAC.
- F-12.** Forty-four of the 56 wire fracture morphologies were cup-cone fractures, nine were shear fractures primarily from the outer ring, and the remaining three were mixed-mode fractures, which included a progressive failure mechanism believed to be HAC (one cup-cone/HAC and two shear/HAC).
- F-13.** Outer ring wires typically had less necking than inner ring wires and are expected to have failed first.

- F-14.** Excluding the HAC fractures, none of the wires examined by microscopy and SEM exhibited fatigue fracture.
- F-15.** Wire imprint region of the zinc in the back of the socket cavity is heavily corroded and poorly bonded to the wire ends.
- F-16.** The brittle fracture region of the zinc in the back of the socket cavity is corroded, with faceted surfaces that expose the elongated portion of the grains (i.e., cleavage fracture), and the ends of the grains have lifted up (i.e., a peeling failure).
- F-17.** Zinc casting was composed of elongated grains, with significant variation in both grain size and length.
- F-18.** Metallography shows no evidence of fatigue cracking within the zinc, but minor additional contributions of cyclic loading damage may not be discernable from the overall contributions of sustained loading damage, as both would manifest themselves in deformation mechanisms (e.g., twinning and slip bands) present within the zinc.
- F-19.** The zinc nearest the base, adjacent to the cable/zinc boundary, was determined to be in the late secondary or tertiary stage of creep.
- Zinc creep becomes a design consideration when its homologous temperature exceeds 40%, which is the case for zinc at room temperature.
 - Grains near the cable/zinc boundary are fully recrystallized and have grain boundaries that are generally oriented 45° to the stress direction.
 - Cracks appear predominantly intergranular, which is typically associated with creep rupture at high temperatures and low speeds of deformation.
- F-20.** Significant corrosion was found in the upper two-thirds region between the socket housing and the zinc casting outer diameter, while negligible corrosion was found in the lower third.
- F-21.** Moisture intrusion, which led to zinc/wire corrosion, followed a path that included a gap between the inner socket wall and the zinc casting, wire protrusions from the zinc, cracks in the bulk zinc, and the wire surfaces of individual wires.
- F-22.** Evidence shows corrosion generally had a minimal effect on wire-zinc bond strength.
- F-23.** Wire mechanical properties meet ASTM specification.
- F-24.** Zinc mechanical properties in the Aux M4N spelter have significant variability as a function of grain size and directionality.
- F-25.** Observatory dead load resulted in sustained cable tensions within 20% of the maximum expected cable tension.
- F-26.** Finite element modeling predictions quantitatively agree with rated/measured wire breaking strength.
- F-27.** Finite element modeling predictions were qualitatively in agreement with the NASA forensic analysis:
- Maximum wire stresses predicted followed the stepped pattern observed in the forensic analysis.

- Outer wires were predicted to fail in a shear failure.
 - Inner wires were predicted to fail in a cup-cone failure mode due to the compression effects of the zinc on the wires.
- F-28.** For a large range of realistic zinc material properties, all models predict that outer wire stresses are near ultimate strength of individual wires, even at operational observatory loads, demonstrating low or even negative margins of safety for the M4N socket.
- F-29.** The socket design had low wire structural margins and a large percentage of sustained loading, which made the design susceptible to a creep-dominated failure, likely accelerated by fluctuating cable loads.
- F-30.** Decreasing brooming quality results in increasing stresses in the outer-row wire and reduces margin for designs operating near their strength capacity.
- F-31.** Analysis predicts that stresses in the zinc and wires are not affected by the zinc voids identified in the forensic examination of the Aux M4N socket.
- F-32.** Socket joints in the Arecibo Observatory application were subjected to a relatively higher percentage of sustained cable load versus total load compared with a survey of bridge designs, increasing susceptibility to creep.
- F-33.** The Arecibo Observatory had an effective design factor of safety of ≤ 1.83 , which is significantly less than the minimum suggested by literature (i.e., >2.1) to ensure structural redundancy in the event of cable failure.
- F-34.** The Aux M4N design had insufficient design criteria and a low structural margin, which were insufficient to accommodate time-dependent damage mechanisms.
- F-35.** The Aux M4N socket joint design did not explicitly consider time-dependent mechanisms for the Arecibo application to establish an end-of-life capability.
- F-36.** Low socket design margin and atypical operating conditions revealed an unexpected vulnerability to zinc creep and to long-term cumulative damage, which led to progressive zinc/wire failure of the socket.
- F-37.** The effective design factor of safety was significantly less than the minimum suggested by literature and was insufficient to ensure structural redundancy in the event of a cable failure.

8.2 Observations

The following observations were identified:

- O-1.** NASA's investigation would have been more efficient with improved coordination between engineering firms overseen by the NSF. Additional data and hardware were available to the NSF and were requested by this team but were not made available.
- O-2.** After the Aux M4N failure and before the main cable failure, loads analysis was performed that incorrectly asserted acceptable positive margin of the remaining structure despite no explanation for why a cable had failed at half its rated breaking strength.

8.3 NESC Recommendations

The following NESC recommendations were identified and are directed toward the NSF:

- R-1.** The NSF should section and examine additional Arecibo sockets, including auxiliary sockets and backstays, to understand whether the Aux M4N had unique features versus other sockets and to understand why backstays had zinc extrusion but did not fail. This will increase the understanding of progressive failure mechanisms in sockets similar to Aux M4N and inform guidance on best practices for spelter socket design and usage.
(*F-1, F-2, F-3, O-1*)

9.0 Alternative Viewpoint(s)

There were no alternative viewpoints identified during the course of this assessment by the NESC team or the NRB quorum.

10.0 Other Deliverables

Failure analysis, materials testing, and finite element modeling results generated during this investigation were provided to WJE.

11.0 Lessons Learned

No lessons learned were identified during the course of this assessment.

12.0 Recommendations for NASA Standards and Specifications

No recommendations for NASA standards and specifications were identified as a result of this assessment.

13.0 Definition of Terms

Aux M4N	The north-side auxiliary cable on Tower 4 that failed on August 10, 2020.
Brooming	The act of or end state due to unraveling and straightening out of the end section of a cable that interfaces with the zinc spelter inside the socket.
Cable	A construction of wire strands, twisted helically around a core to form a tension member of a symmetrical cross section.
Casting Cap	Additional protective casting on the open side of a socket termination.
Corrective Actions	Changes to design processes, work instructions, workmanship practices, training, inspections, tests, procedures, specifications, drawings, tools, equipment, facilities, resources, or material that result in preventing, minimizing, or limiting the potential for recurrence of a problem.
Design Factor	The ratio between the limit load (maximum load during service) and break strength.

Failure Analysis	Analytical investigation in pursuit of identifying the cause of failure and determining corrective action to avoid similar failures.
Finding	A relevant factual conclusion and/or issue that is within the assessment scope and that the team has rigorously based on data from their independent analyses, tests, inspections, and/or reviews of technical documentation.
Forensic Analysis	Analytical investigation of material evidence in pursuit of identifying why a material failed.
Homologous Temperature	The ratio of the absolute temperature of a metal to its melting point.
Inner Wires	Cable wires not located on the exterior ring of wires. The Aux M4N cable contained 90 inner wires positioned along five concentric rings of wires, containing 30, 24, 18, 12, and 6 wires moving progressively toward the center. Each successive ring of wires was helically wound opposite its surrounding concentric rings.
Lessons Learned	Knowledge, understanding, or conclusive insight gained by experience that may benefit other current or future NASA programs and projects. The experience may be positive, as in a successful test or mission, or negative, as in a mishap or failure.
Observation	A noteworthy fact, issue, and/or risk, which may not be directly within the assessment scope, but could generate a separate issue or concern if not addressed. Alternatively, an observation can be a positive acknowledgement of a Center/Program/Project/Organization's operational structure, tools, and/or support provided.
Outer Wires	Cable wires located on the exterior ring of wires. The Aux M4N cable contained 36 outer wires helically wound around all the other wires to form the exterior ring of wires.
Problem	The subject of the independent technical assessment.
Proximate Cause	The event(s) that occurred, including any condition(s) that existed immediately before the undesired outcome, directly resulted in its occurrence and, if eliminated or modified, would have prevented the undesired outcome.
Rated Breaking Strength	Maximum amount of tensile stress that a material can withstand before failure as specified by the manufacturer. The actual breaking strength is likely higher, and rated breaking strength tends to be a minimum value.
Recommendation	A proposed measurable stakeholder action directly supported by specific finding(s) and/or observation(s) that will correct or mitigate an identified issue or risk.
Root Cause	One of multiple factors (events, conditions, or organizational factors) that contributed to or created the proximate cause and subsequent

	undesired outcome and, if eliminated or modified, would have prevented the undesired outcome. Typically, multiple root causes contribute to an undesired outcome.
Seating	Wedging of the zinc cone along the entire inner wall of the socket basket by proof loading the socket to plastically deform the zinc cone along the socket wall.
Seating Extrusion	Plastic zinc flow outside the socket base during seating and proof testing.
Socket	Structural steel casting into which a cable terminates to provide load transfer and attachment into adjacent structures.
Socket Base	The narrow end of the socket from which the cable extends out from the socket joint.
Structural Strand	Type of cable construction most commonly used in structural applications that offers an economical combination of strength and stiffness in static structures.
Supporting Narrative	A paragraph, or section, in an NESC final report that provides the detailed explanation of a succinctly worded finding or observation. For example, the logical deduction that led to a finding or observation; descriptions of assumptions, exceptions, clarifications, and boundary conditions.
Termination	The end attach point of a cable (i.e., socket termination versus crimp termination).
Wire	Individual elements that make up the cable construction.
Zinc Extrusion	Plastic flow of zinc outside the socket base.
Zinc Spelter	Cast zinc material that occupies the volume between the structural strand wires and the socket internal faces to confine the wires and prevent the cable from pulling out of the socket.

14.0 Acronyms and Nomenclature List

°C	degrees Celsius
°F	degrees Fahrenheit
2D	Two-dimensional
3D	Three-dimensional
AASHTO	American Association of State Highway and Transportation Officials
ASCE	American Society of Civil Engineers
ASME	American Society of Mechanical Engineers
ASTM	American Society for Testing and Materials
CSB	Cable-stayed Bridge
DIC	Digital Image Correlation
HAC	Hydrogen-assisted Cracking
HCl	Hydrochloric
kip	1000 pounds-force

KSC	Kennedy Space Center
ksi	kilopounds per square inch
lb	pound
LIDAR	Light Detection and Ranging
LL/DL	Live Load to Dead Load
M&P	Materials and Processes
MCV	Microvoid Coalescence
mm	millimeter
mph	miles per hour
MSFC	Marshall Space Flight Center
NAIC	National Astronomy and Ionospheric Center
NDE	Nondestructive Evaluation
NESC	NASA Engineering and Safety Center
NSF	National Science Foundation
SEM	Scanning Electron Microscopy
SMD	Science Mission Directorate
TDT	Technical Discipline Team
TT	Thornton Tomasetti
UCF	University of Central Florida
WJE	Wiss, Janney, Elstner Associates, Inc.
WSD	Working Stress Design

15.0 References

1. “Auxiliary Main Cable Socket Failure Investigation,” Wiss, Janney, Elstner Associates, Inc., WJE No. 2020.5191, June 2021.
2. “Standard Specification for Metallic-Coated Parallel and Helical Steel Wire Structural Strand,” ASTM Standard A586-91.
3. “Wirerope Works, Inc.,” URL: <http://www.wireropeworks.com>.
4. “Standard Specification for Zinc (Hot-Dip Galvanized) Coatings on Iron and Steel Products,” ASTM A123.
5. “Standard Specification for Zinc,” ASTM B6.
6. Klein, T. W., “Wire Rope and Strand Assemblies in Bridge Applications,” Wire Rope Corporation of America, Inc., Saint Joseph, MO, 2017.
7. “Standard Guidelines for the Structural Applications of Steel Cables for Buildings,” ASCE Standard 19-16, 2016.
8. “Structural Strand and Wire Rope Catalog,” Wirerope Works, Inc., 2007.
9. Lambrighs, K., “Fatigue Properties of Heavily Drawn Steel Wires,” November 2010. ISBN 978-94-6018-273-0.
10. Toribio, J., et al., “Tensile Fracture Behavior of Progressively Drawn Pearlitic Steels,” *Metals*, Vol. 6, No. 5, p. 114.
11. Li et al., “Compressive and Fatigue Damage Behavior of Commercially Pure Zinc,” *Materials Science and Engineering A*, Vol. 466, 2007, pp. 38-46.
12. Singh et al. “On the Role of Grain-Boundary Migration during the Creep of Zinc,” *Journal of Materials Science*, Vol. 8, 1973, pp. 373-381.

13. Mohamed, F. A., and Langdon, T. G., Deformation Mechanism Maps based on Grain Size, *Metallurgical Transactions*, Vol. 5, Issue 11, November 1974, pp. 2339-2345.
14. Bradon, J. Chaplin, C., and Ridge, I., "Analysis of Resin Socket Termination for a Wire Rope," *Journal of Strain Analysis for Engineering Design*, January 2001.
DOI: 10.1243/0309324011512621
15. https://youtu.be/Jj_K6bGQIfM?t=26, "hilifting.com - 76 mm Impressive Wire Rope Break Test," August 12, 2010, last accessed June 16, 2021.
16. Vinet, R., and Roberge, R., "Evaluation of the Creep Resistance of Wire Rope End Attachments," *Transactions of ASME*, 1987.
17. Zhang, W., Yuan, X., Yang, L., and Deng, "Research on Creep Constitutive Model of Steel Cables," *Construction and Building Materials*, Vol. 246, 2020.
18. Nakai, M., Sato, S., and Aida, T., "On the Creep and the Relaxation of Spiral Ropes," *Bulletin of the JSME*, Vol. 18, No. 125, November 1975.
19. "Structural Applications of Steel Cables for Buildings," ASCE 19-96, 1996 Edition, 1996.
20. "Minimum Design Loads for Buildings and Other Structures," SEI/ASCE 7-02, Second Edition.
21. "Standard Guidelines for the Structural Applications of Steel Cables for Buildings," ASCE 19-10, 2010 Edition, 2010.
22. Ali, K., Katsuchi, H., and Yamada, H., "Comparative Study on Structural Redundancy of Cable-Stayed and Extradosed Bridges through Safety Assessment of Their Stay Cables," *Engineering*, Volume 7, Issue 1, January 2021, pp. 111-123.
23. Kloiber, L. A., Eckmann, D. E., Meyer, T. R., and Hautzinger, S. J., "Design Considerations in Cable-Stayed Roof Structures," Modern Steel Construction - North American Steel Construction Conference, March 2004.
24. Lonetti, P., Pascuzzo, A., and Davanzo, A., "Dynamic Behavior of Tied-Arch Bridges under the Action of Moving Loads," *Mathematical Problems in Engineering*, Article ID 2749720, 2016.
25. Gossen, P. "Design with Cables," *Structure Magazine*, November 2004. URL: <https://www.structuremag.org/wp-content/uploads/2014/09/DesignWithCables.pdf>, last accessed June 16, 2021.
26. "Crosby Wire Rope End Terminations: User's Manual," 2014. URL: https://www.thecrosbygroup.com/wp-content/uploads/2014/01/9992320_Termination_Manual_With_Cover_LoRes.pdf, last accessed June 16, 2021.
27. "Safety Standard for Cableways, Cranes, Derricks, Hoists, Hooks, Jacks, and Slings," ASME B30.9.
28. "Mobile and Locomotive Cranes," ASME B30.5-2004, 2004.
29. "Standard Specification for Wire Rope and Sockets for Movable Bridges," AASHTO M277-06, January 1, 2006.

Appendix A. KSC Failure Analysis Report

NASA-04710
Rev: Basic
6/15/2021

NASA-04710
Rev: Basic

Arecibo Observatory Aux M4N Cable and Socket Failure Investigation

Engineering Directorate
Laboratories, Development and Testing Division

National Aeronautics and
Space Administration

John F. Kennedy Space Center

KSC FORM 16-12 06/95 (1.0) PREVIOUS EDITIONS MAY BE USED
KDP-T-1793 Rev Basic



Table of Contents

1.	ABSTRACT	1
2.	FOREWORD.....	1
3.	PROCEDURES.....	20
3.1	Metrology	20
3.2	Three-Dimensional (3D) Laser Scan	21
3.3	3D Print.....	21
3.4	NDE	21
3.4.1	Magnetic Particle Inspection	21
3.4.2	Gamma Source Computed Radiography (CR)	21
3.5	Chemical Analysis.....	21
3.6	Sectioning	27
3.7	Microscopy.....	31
3.8	Metallography	31
4.	RESULTS	32
4.1	As-Received.....	32
4.1.1	Metrology	32
4.1.2	3D Laser Scan	32
4.1.3	3D Prints	33
4.1.4	NDE	33
4.2	Wires.....	37
4.2.1	Wire Labeling and Tracing	37
4.2.2	Fractography.....	38
4.3	Zinc Casting.....	52
4.3.1	Metallography	69
4.3.2	Transgranular Bulk Cracking.....	79
4.3.3	Brittle Fracture Region	80
4.4	Corrosion	90
5.	DISCUSSION AND/OR RECOMMENDATIONS.....	100
6.	EQUIPMENT.....	101
6.1	Metrology	101
6.2	3D Laser Scan	101
6.3	3D Print.....	101
6.4	Chemical Analysis.....	101
6.4.1	OES	101
6.4.2	XRF Spectroscopy	101
6.5	Microscopy.....	101
6.5.1	Stereomicroscopy	101
6.5.2	SEM/EDS.....	101
APPENDIX A.	AS-RECEIVED SOCKET.....	104

APPENDIX B.	AS-RECEIVED CABLE-END SECTION	143
APPENDIX C.	TEST OF CATHODIC PROTECTION OF STEEL FRACTURE SURFACE.....	157
APPENDIX D.	HCL ZINC REMOVAL.....	165
APPENDIX E.	3D LASER SCAN	173
APPENDIX F.	3D PRINTS	182
APPENDIX G.	WIRE LABELING AND TRACING.....	187
APPENDIX H.	STEREOMICROSCOPY OF WIRE FRACTURES	223
APPENDIX I.	SEM OF WIRES.....	264
APPENDIX J.	STEREOMICROSCOPE NECKING MEASUREMENTS	282
APPENDIX K.	METALLOGRAPHY	283
APPENDIX L.	CHEMICAL SAMPLE ANALYSIS.....	318
APPENDIX M.	ACCELERATED ZINC CORROSION TEST	327

SUBJECT: Arecibo Observatory M4N AUX Cable and Tower T4 Socket Failure Investigation

TO: NASA Engineering and Safety Center (NESC); Wiss, Janney, Elstner Associates, Inc. (WJE); University of Central Florida (UCF); and National Science Foundation (NSF)

1. ABSTRACT

This failure investigation is for the structural cable failure of the Arecibo Observatory, M4N AUX cable, which failed at the Tower T4 socket location on August 10, 2020 at 2:35 AM. The investigation detailed in this report is focused on material failure of the socket and cable. The analysis involved nondestructive and destructive evaluation techniques to uncover metallurgical evidence of primary and contributory mechanisms that may have led to the failure of this socket/cable system. While the evidence presented here is mentioned because it may have significant relevance to the failure mechanics of this socket/cable system. This report feeds into a NESC report that will provide a fault-tree analysis, so discussion and conclusions drawn from the evidence presented in this report are meant to be limited to factual statements of the evidence found.

2. FOREWORD

The Arecibo Observatory (AO) is a radio astronomy, solar system radar and atmospheric physics facility of the National Science Foundation (NSF), operated under cooperative agreement by the University of Central Florida (UCF). The facility was home to a giant telescope that was uniquely capable at characterization and orbital refinement of planets, comets, and asteroids; detecting optically invisible gas and revealing areas of interstellar space obscured by cosmic dust through its detection capability in the radio spectrum; studying the earth's upper atmosphere through the combination of incoherent scatter radar and optical Light Detection and Ranging (LIDAR); and a source of economic and social development, inspiration, and pride to Puerto Rico, all Americans, and everyone inspired to discover the mysteries of the universe in which we live.

Table 1 is an excerpt of significant events from a timeline of events provided by WJE.

Table 1. Timeline of significant events excerpted from a timeline of events provided by WJE.

Date	Event
1960	Design and construction begins for the Arecibo Ionospheric Observatory
Nov 1, 1963	Opening of the Arecibo Ionospheric Observatory
1992-1997	Design and construction of Gregorian Dome upgrade and ionospheric radar line feed completed
Apr 4, 2003	Condition survey performed by Ammann & Whitney. Towers T-4 and T-12 aux main cable sockets noted as having ½ inch separation from socket base.
2003	Cable sag measurements and cable tension analysis performed by Ammann & Whitney
Sep 15, 2004	Tropical Storm Jeanne impacts observatory with maximum wind speeds of 70 mph
Aug 29, 2006	Cable sag measurements and cable tension analysis performed by Ammann & Whitney
Feb 3, 2010	Crack in feed platform vertical truss member identified
Sep 2010 - Feb 2011	Strengthening repairs to feed platform trusses completed. Telescope to operate under new dome movement limits.
Jan 13, 2014	Magnitude 6.4 earthquake centered approximately 50 miles north of Arecibo in the Atlantic Ocean
Mar 11, 2014	M8-4 Jumper system installed to bypass upper splice box cable with 9 broken wires observed after earthquake
Jun 13, 2016	LIDAR cable scan completed to measure tension
Sep 20, 2017	Hurricane Maria impacts observatory with peak winds of 105 mph. Line feed falls into reflector.
Feb 18, 2019	Inspection of M4N Aux showing separation of zinc varying from ¾ in. to 1 3/8 in.
Jan 7, 2020	Magnitude 6.4 earthquake centered approximately 50 miles southwest of Arecibo in Indios
Jul 20, 2020	Tropical Storm Isaias impacts observatory with peak winds of 45 mph
Aug 10, 2020	Cable M4N Aux failed
Aug 11, 2020	Gregorian dome moved to stowed position
Nov 6, 2020	Cable M4-4 failed
Dec 1, 2020	Cable M4-2 failed resulting in collapse of the telescope

On August 10, 2020, a structural cable failed at 2:35 AM during normal observatory operations. The failed 3.25-inch diameter cable was a primary component of the system used to suspend a large, steel-framed platform (Feed Platform) above the telescope reflector dish by cabling extending to three towers, located at 4, 8, and 12 o'clock, with the 12 o'clock tower due north of the dish (Figure 1). The north auxiliary suspension cable in the 4-o'clock tower's cable set failed (M4N AUX cable). The mode of failure involved the tower end separating from the zinc-filled spelter socket in the clevis that connected the cable to Tower T4. The failed cable was one of twelve auxiliary cables installed as part of a 1992-designed modification to the observatory (Figures 2-11).

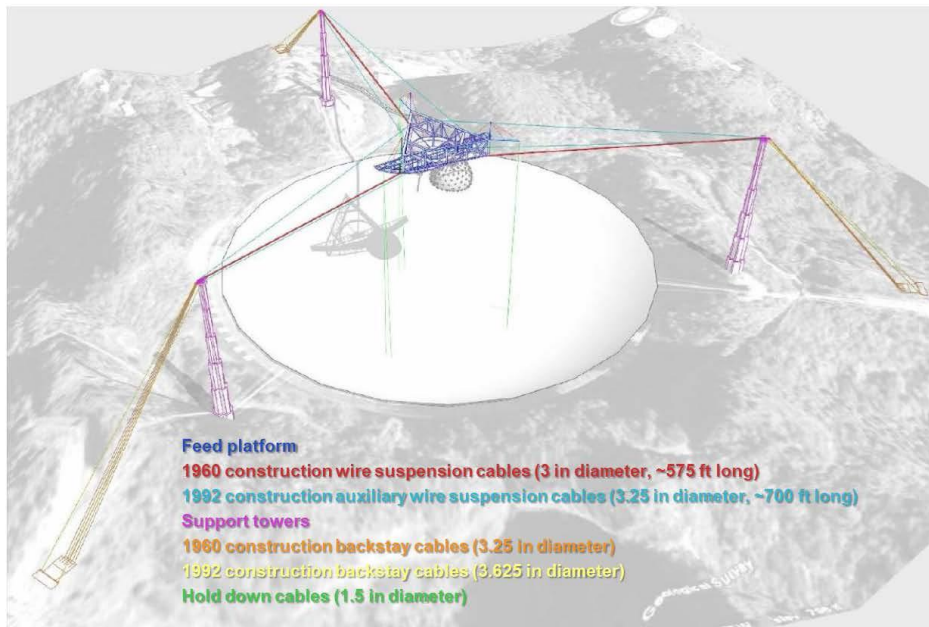


Figure 1. Color-coded diagram of the Feed Platform support structure.¹

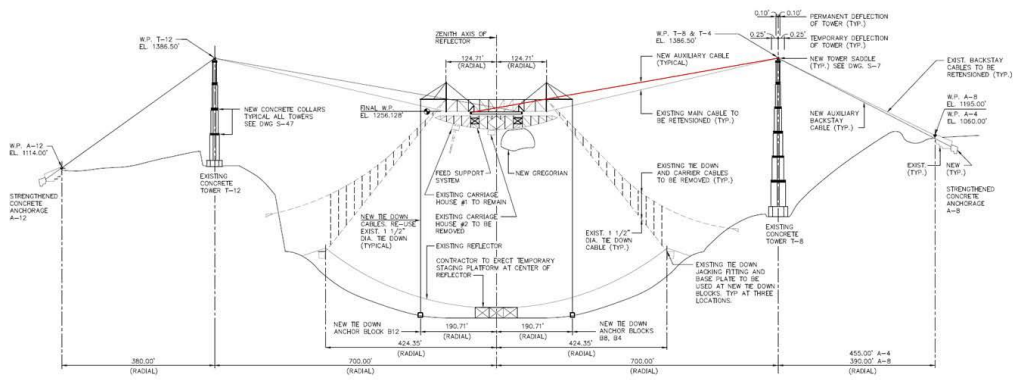
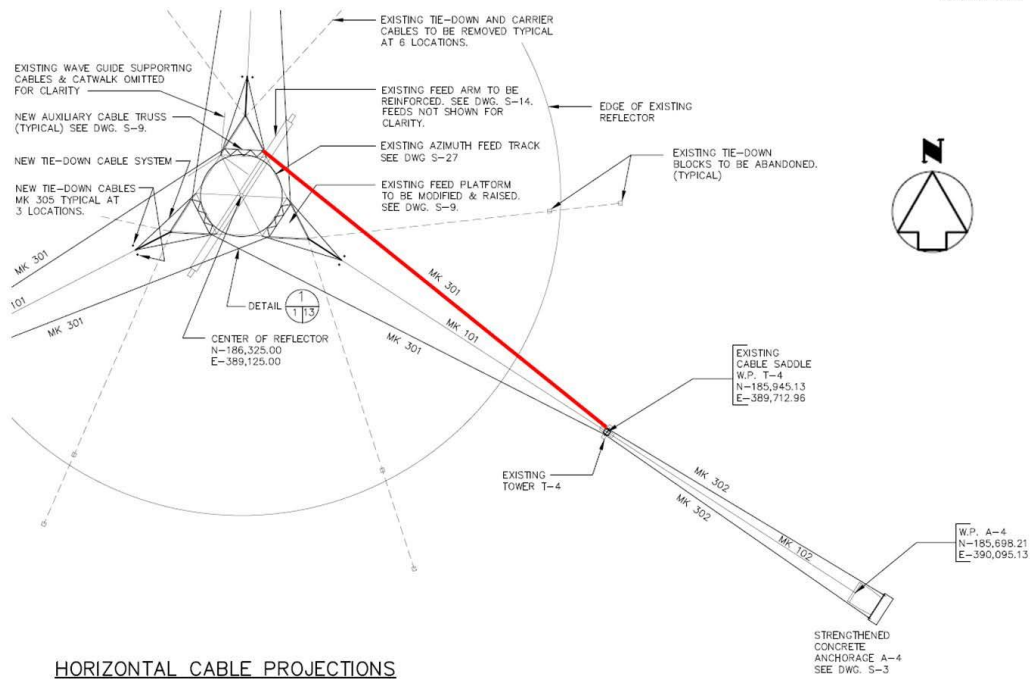
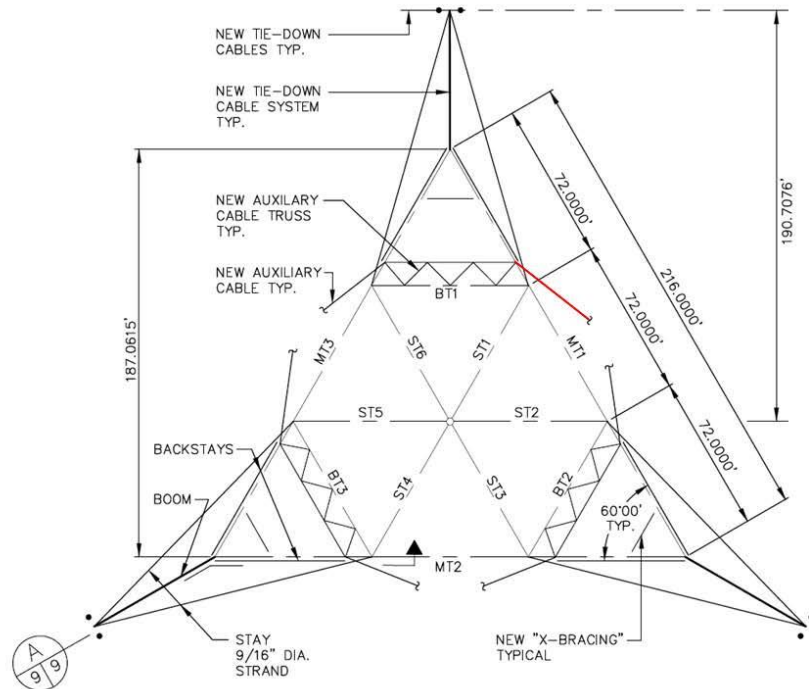


Figure 2. Elevation Drawing S-2, highlighting the failed M4N auxiliary cable in red.²



HORIZONTAL CABLE PROJECTIONS

Figure 3. Horizontal cable projections, drawing S-1, highlighting the failed M4N auxiliary cable in red.²



FEED PLATFORM PLAN

LEGEND

- MT - EXISTING MAIN TRUSS
- BT - EXISTING BRACING TRUSS
- ST - EXISTING SECONDARY BRACING TRUSS

Figure 4. Feed Platform plan, drawing S-9, highlighting the failed M4N auxiliary cable in red.²

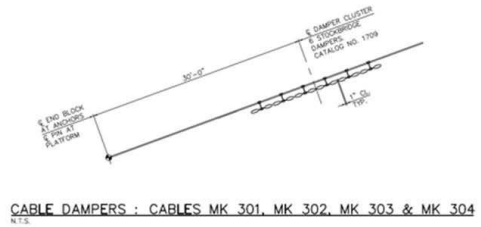
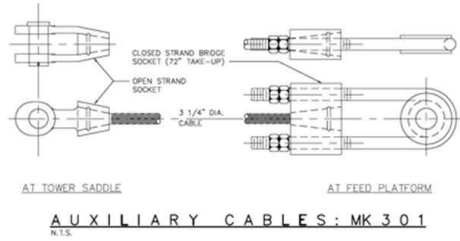


Figure 5. Cable details, drawing S-13, specific to the failed M4N auxiliary cable.²

CABLE TENSIONS – STRENGTHENED CABLE SYSTEM	
CABLES MK	301
NO.	6
DIAMETER	3 1/4"
MINIMUM BREAKING STRENGTH (KIPS)	1314
TENSION PER CABLE	
(I) INITIAL TENSION UNDER ALL DEAD LOADS EXISTING *	—
INITIAL ERECTION FINAL	450 602
(II) OPERATIONAL LOADS	615
(III) SURVIVAL CONDITION	622
DESCRIPTION	AUX. CABLES
	NEW

GENERAL NOTES

(UNLESS OTHERWISE SHOWN OR NOTED)

1. ELEVATIONS ARE IN FEET AND BASED ON THE USGS DATUM FOR PUERTO RICO, FOR WHICH MEAN SEA LEVEL IS 0.00 FT.
2. WORK POINT COORDINATES OF THE EXISTING STRUCTURE ARE IN FEET AND BASED ON THE PUERTO RICO DATUM, LAMBERT PROJECTION, PUERTO RICO ZONE.
6. STEEL CASTINGS SHALL CONFORM TO ASTM STANDARD A148 GRADE 90-60.
10. STRUCTURAL STRAND SHALL CONFORM TO ASTM STANDARD A586 PREMIUM GRADE WITH CLASS A GALVANIZED COATING ON ALL WIRES.
11. PIN HOLES SHALL BE REAMED WITH PLATES FULLY ASSEMBLED.
14. ALL CABLE END FITTINGS, END BLOCKS RODS, PINS AND ACCESSORIES SHALL BE GALVANIZED IN ACCORDANCE WITH ASTM A123 OR A153, AS APPLICABLE.
15. ALL PINS SHALL BE FORGED STEEL CONFORMING TO ASTM A521 CLASS AG. SEE TYPICAL DETAIL ON DRAWING S-13.
16. FOR ALL PAINTING SYSTEMS REFER TO SPECIFICATIONS.
21. CABLE END FITTINGS SHALL BE PROOF LOADED TO 50% OF THE SPECIFIED BREAKING STRENGTH.

* FROM ORIGINAL CONTRACT DRAWINGS.
 ACTUAL VALUES ARE SLIGHTLY LOWER.

Figure 6. General notes from drawing S-1, specific to the failed M4N auxiliary cable.²



Figure 7. Photo, provided by WJE, of the failed M4N socket, prior to removal from Tower T4. The socket was retrieved prior to the observatory's ultimate collapse.

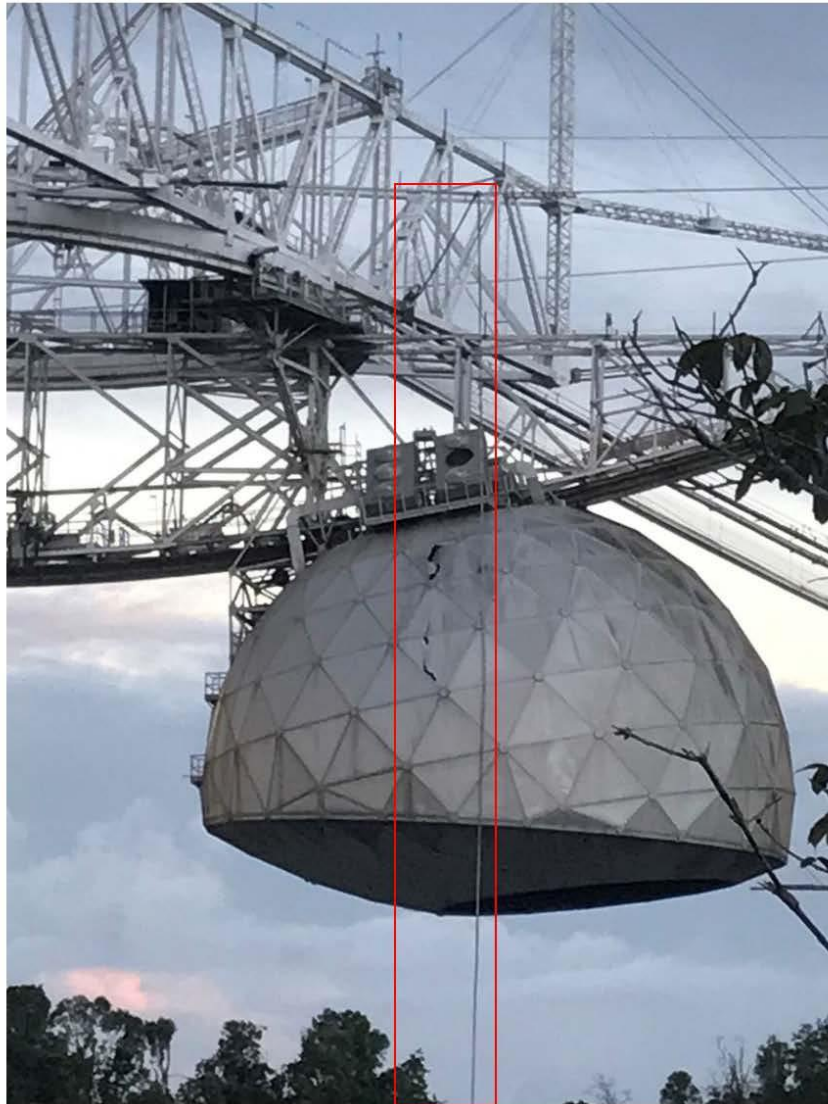


Figure 8. Photo of the failed M4N auxiliary cable, where it remained connected to the Feed Platform. This photo was taken prior to the ultimate collapse of the observatory. Photo provided by WJE.



Figure 9. Photo of the failed M4N auxiliary cable, where the Tower T4 connection came to rest on the observatory dish below the Feed Platform. This photo was taken prior to the ultimate collapse of the observatory. Photo provided by WJE.



Figure 10. Close up photo of the failed M4N auxiliary cable, where the Tower T4 connection came to rest on the observatory dish below the Feed Platform. This photo was taken prior to the ultimate collapse of the observatory. Photo provided by WJE.



Figure 11. Photos of the failed M4N auxiliary cable-end from the Tower T4 socket connection. These photos were taken prior to the ultimate collapse of the observatory. The cable was not retrieved from the observatory site until after the ultimate collapse of the observatory. Photos provided by WJE.

Kennedy Space Center (KSC) Engineering was contacted mid-August by UCF for failure analysis and nondestructive evaluation (NDE) expertise and support with respect to the failed M4N AUX cable and socket. KSC Engineering agreed to provide support, working in conjunction with the NASA Engineering and Safety Center (NESC), Marshall Space Flight Center (MSFC), Aerospace Corporation, and Wiss, Janney, Elstner Associates, Inc. (WJE), the structural engineering firm UCF/NSF had contracted to coordinate the M4N AUX cable and socket failure investigation.

Background documentation and material specification data was provided by WJE.^{1, 2, 3} Figure 12 describes the nomenclature used to describe the various parts of the socket. Figure 13 displays the clock positions used to describe the locations of the wire fractures within the socket, with 12 o'clock associated with the top of the socket. Figures 14-18 show the as-received socket. More photos of the as-received socket can be found in Appendix A.

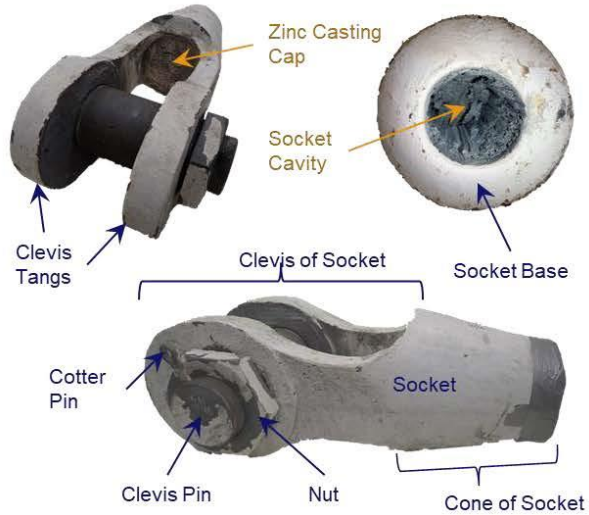


Figure 12. Nomenclature used to describe the parts of the failed spelter socket joint.

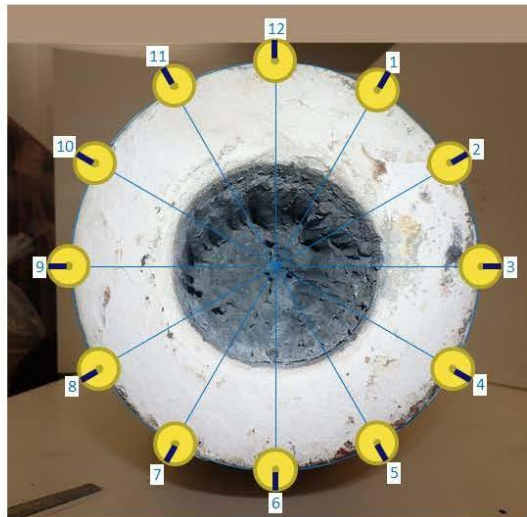


Figure 13. Clock positions used to describe the locations of the wire fractures within the socket, with 12 o'clock associated with the top of the socket.



Figure 14. The as-received socket. Note that the gray material around the socket base on the right-side of the image is tape, meant to protect the socket cavity during transport. Scale in inches and centimeters.



Figure 15. Top view of the as-received socket. Note that the protective tape around the socket base had been removed prior to this photo. Scale in inches and centimeters.

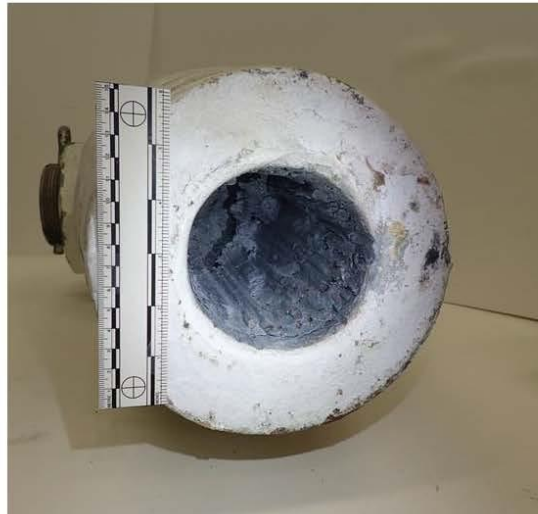


Figure 16. Oblique angle looking into the as-received socket cavity. Scale in inches and centimeters.



Figure 17. View looking mostly straight into the as-received socket cavity. Scale in inches and centimeters.

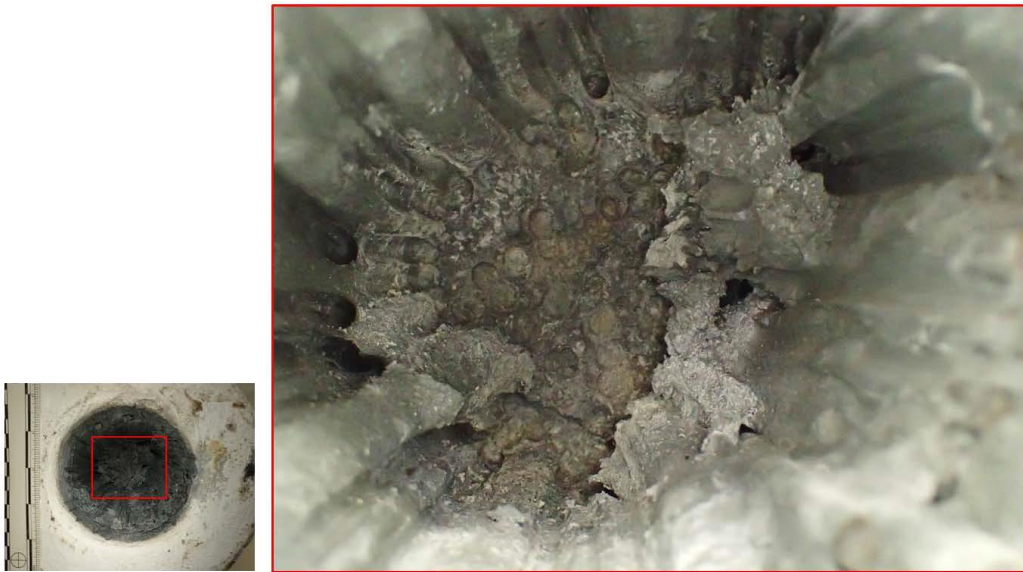


Figure 18. Close up photo of the back of the as-received socket cavity. Scale in inches and centimeters.

Figure 19 shows the cable cross-section. There are 126 0.25-in diameter wires, plus a center wire which is composed of 7 smaller diameter wire strands. The wires in the cable are arranged in concentric rings, from outside to inside, consisting of 36-30-24-18-12-6 wires. Each ring helically rotates around the ring inside of it in the opposite direction (either clockwise; counterclockwise). Figures 19-22 show the cable-end section received at KSC. The region of this cable-end section that consists of both wires and zinc is referred to as the cable/zinc slug. As seen in the right image of Figure 22, not all of the wires were present in the cable-end section received. 32 of the 36 outer ring wires were missing. These wires came free of the cable/zinc slug at some point during or after the failure of the socket. The 126 wires were labeled alphabetically A-Z, AA-AZ, BA-BC, CA-CZ, DA-DZ, and EA-ES. More photos of the as-received cable-end section can be found in Appendix B.



Figure 19. Cable cross-section. The cable is comprised of 126 0.25-in diameter wires, plus a center wire which is composed of 7 smaller diameter wire strands. The wires are arranged in concentric rings, from outside to inside, consisting of 36-30-24-18-12-6 wires.



Figure 20. Photo of the 6 o'clock side of the as-received cable-end section (right) next to the 6 o'clock side of the 3D print made from the 3D laser scan of the socket cavity (left). Scale in inches and centimeters.



Figure 21. Photos of the as-received cable-end section. From left to right, the 11 o'clock side, 4 o'clock side, and 7 o'clock side. Scale in inches and centimeters.

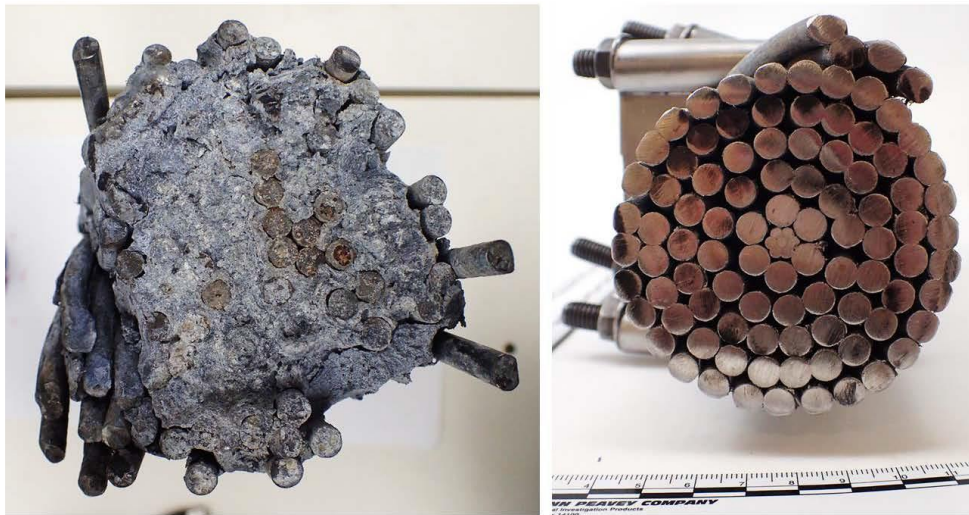


Figure 22. Photos of the as-received cable-end section. The top of the cable-end section is on the left, which would have been the end of the cable embedded in the socket, prior to failure. The top of the left image roughly corresponds with 12 o'clock, and 9 o'clock on the right-side of the left image. The bottom of the cable-end section is on the right, which is a cross-sectional cut taken a few inches outside of the socket base, towards the Feed Platform. The top of the right image roughly corresponds with 2 o'clock, and 5 o'clock on the right-side of the right image. Scale in centimeters.

3. PROCEDURES

The M4N socket, clevis pin, and cable-end were visually inspected and photo documented, as-received. Hardware condition was photo documented throughout the sectioning process. Chemical sampling was generally performed first, once accessibility was established to the area of interest. Metrology and nondestructive examination were also performed prior to sectioning. Three-dimensional (3D) laser scanning was performed prior to sectioning and then after each sectioning step to attempt to improve the surface topography captured from within the socket cavity and to aid in the construction of an as-built finite element model. 3D prints were made as forensic support aids from the 3D laser scans. Finally, sectioning began with a longitudinal cut, dividing the clevis in half and then subsequent transverse cuts were made from back to front to trace the wire brooming back to their locations at the fractured ends near the socket base. The zinc casting was removed from the steel socket with a press. From there areas of interest in the zinc were sectioned and removed by mechanical means and wire fracture-ends were removed by either mechanical means or galvanic cell reaction.

3.1 Metrology

Caliper measurements of the clevis and clevis pin were taken and compared against the data published for typical open strand sockets, with a strand diameter of 3.25-inches, in Table 6 of the Wire Rope Works Structural Strand and Wire Rope Catalog.⁴ Note that, per WJE, other drawings show the dimension “Q”, circled in Figure 23, as the socket opening dimension, which is how it was measured here.

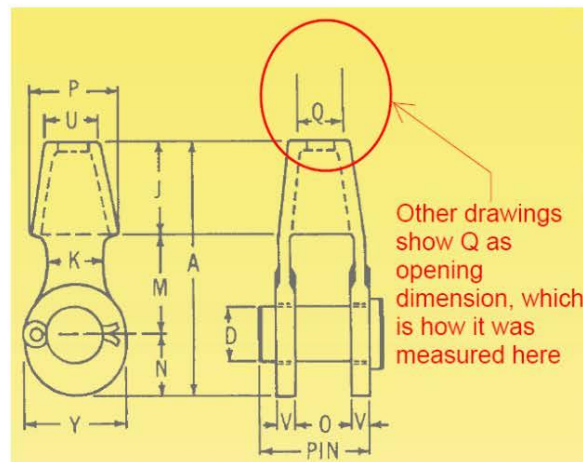


Figure 23. Dimensional feature identification for typical open strand socket measurements from Table 6 of the Wire Rope Works Structural Strand and Wire Rope Catalog.⁴ The red text overlay was added to note that dimension Q was measured as the socket opening dimension, in spite of the drawing’s visually indicated measurement.

3.2 Three-Dimensional (3D) Laser Scan

A Creaform HandySCAN BLACK Elite laser scanner was used per NASA KSC-PLN-2322 PDL-ALC-001 version B Section 4.2.6 to generate 3D surface topography data of the socket before and after each section cut into the socket cavity.⁵ The topographic data was cleaned up and aligned using the 3D Systems Geomagic Wrap software.

3.3 3D Print

The topographic data from the laser scan was converted into .stl and .stp files using ANSYS SpaceClaim software, which then were used for creating positive and negative surface 3D prints of the socket using a Stratsys Objet 500 C3 printer.

3.4 NDE

3.4.1 Magnetic Particle Inspection

The socket internal cavity was protected and then the exterior socket cone was magnetic particle inspected in accordance with ASTM E1444 using the dry magnetic particle application, continuous method.⁶

3.4.2 Gamma Source Computed Radiography (CR)

The socket cone and internal cavity were inspected by CR. A double-wall exposure radiographic inspection was performed with a Co-60 radioactive isotope gamma-ray source and four single-wall exposure radiographic inspections, rotated around the socket, were performed with an Ir-192 radioactive isotope gamma-ray source in accordance with ASTM E1742.⁷

3.5 Chemical Analysis

Chemical samples were taken with carbon tape (Figure 24). Sample locations are identified in Figures 25-29.



Figure 24. Chemical samples were taken with carbon tape.

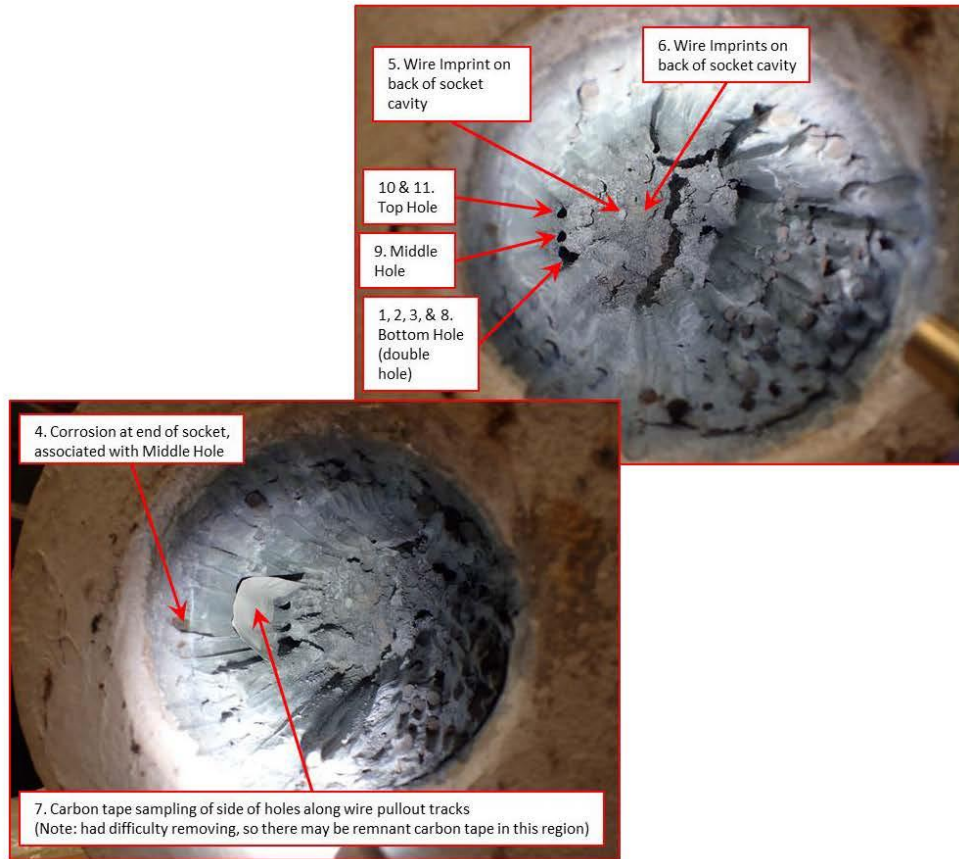


Figure 25. Chemical sample locations 1 through 12 from within the socket cavity.



Figure 26. Chemical sample location 13 from Wire AX.



Figure 27. Desk Sample 1. Sampled wet black product at 7 o'clock, between the socket cone inner wall and the zinc casting outer wall, near the zinc casting cap. Scale in inches.



Figure 28. Desk Sample 2. Sampled white product at 9 o'clock, between the socket cone inner wall and the zinc casting outer wall, near the zinc casting cap. Scale in inches.



Figure 29. Desk Sample 3. Sampled discoloration from wire end P. The wire end was exposed after a transverse band-saw cut, made with no cutting fluid. The wire end was previously fully enclosed within the zinc casting at the 11 o'clock position. Scale in inches.

The clevis pin, socket clevis, and cable wire were analyzed by OES in accordance with ASTM E415.⁸ The clevis pin was expected to be a forged steel conforming to ASTM A521 Class AG that was galvanized in accordance with ASTM A123 or ASTM A153.^{9,10,11} The socket clevis was expected to be a casting conforming to ASTM A148 Grade 90-60 that had been hot-dip galvanized in accordance with ASTM A123.^{10,12} The cable wire was expected to be structural strand conforming to ASTM A586, 91 premium grade with Class A galvanized coating; however, the galvanized coating was expected to have been stripped at installation and a flux applied to allow it to bond to the zinc casting that was subsequently poured over top it circa 1992/1993.¹³ The zinc casting was analyzed using a benchtop XRF technique in accordance with the Original Equipment Manufacturer (OEM) operating instructions.

Material samples taken from the socket were analyzed by Fourier-transform infrared spectroscopy (FTIR) in accordance with ASTM E1252, Raman spectroscopy, X-ray powder diffraction (XPD), and scanning electron microscopy with energy dispersive spectroscopy (SEM/EDS).¹⁴

3.6 Sectioning

A bandsaw was used to initially begin sectioning the socket. After sectioning off the clevis tangs, the socket cavity was masked to provide protection and the socket cone was media blasted to remove the paint coating prior to magnetic particle inspecting the socket cone outer diameter. Subsequent bandsaw cuts were made with no cutting lubricant and feed rates were slow to avoid overheating. A longitudinal cut was made along the 5:30 to 11:30 clock positions, creating the 3 and 9 o'clock halves of the socket cone (Figure 30). Prior to that cut, replet material was applied to some of the closest exposed wires to the cut, in an attempt to protect those fracture surfaces from cutting debris. Additionally, the cut was made with the socket cone resting on the socket base, so the socket cavity opening would be down on the table, and a vacuum was applied to the underside of the table to attempt to minimize the amount of cutting debris that could be trapped and contaminate the socket cavity forensic evidence. Then transverse slices of each half of the socket were made, starting near the casting cap and moving towards the socket base with each subsequent cut. Each slice was named 3a, 3c, 3e, and 3g for the 3 o'clock half and 9a, 9c, 9e, and 9g for the 9 o'clock half (Figure 31). Sections 3a and 9a are the transverse slices that include the casting cap and 3g and 9g are the transverse slices that include the socket base. While the zinc casting easily separated from the socket in slices 3a and 9a, a three-point bend was applied with a hydraulic press on the other slices to separate the zinc casting from the socket. Additionally, a longitudinal cut was made on the socket in slices 3g and 9g, to thin the center portion of the steel socket, to avoid bending the zinc casting during the hydraulic press operation.

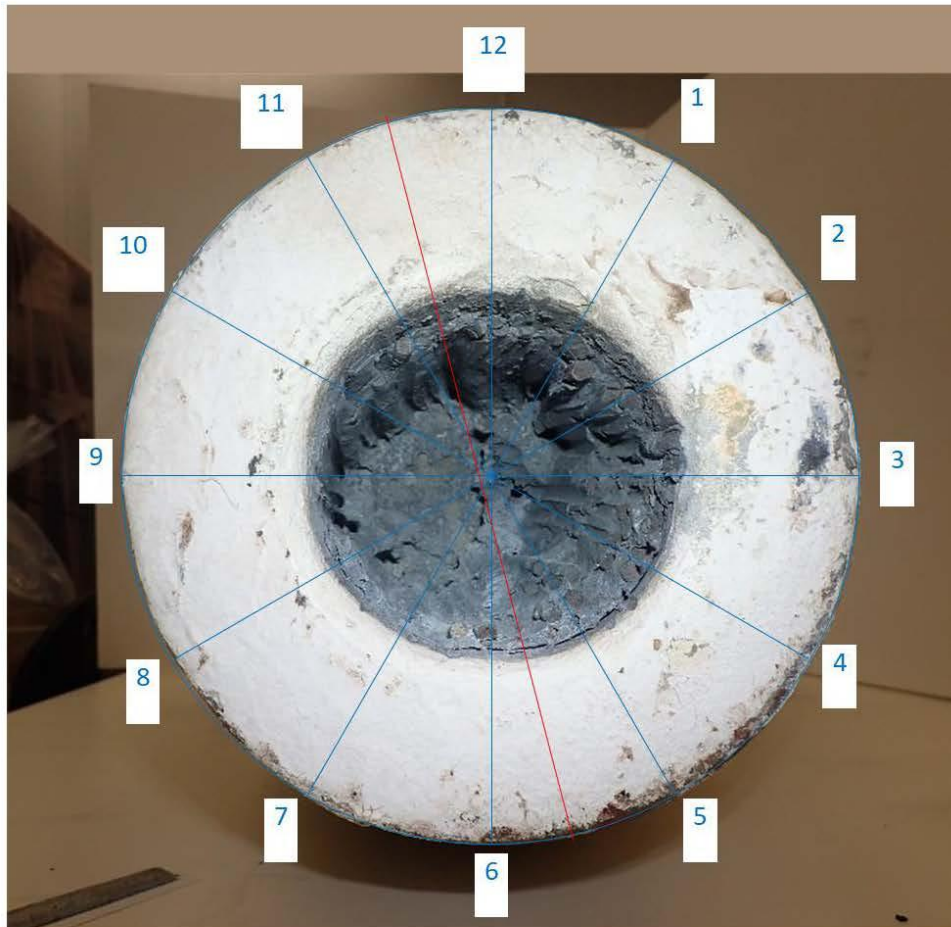


Figure 30. Photo of the socket base with the top of the socket at the top of this image. The 12 o'clock position around the socket base is associated with the top of the socket. The 3 o'clock is associated with the right side of the socket, as if viewing the socket from the feed platform, facing towards the tower. The red line identifies the intended plane for the initial longitudinal cut of the socket cone. Note that the cut was intended to be slightly off center, to attempt to avoid any visually identifiable fracture surfaces. Unfortunately, the fracture surface of wire R was partially cut.

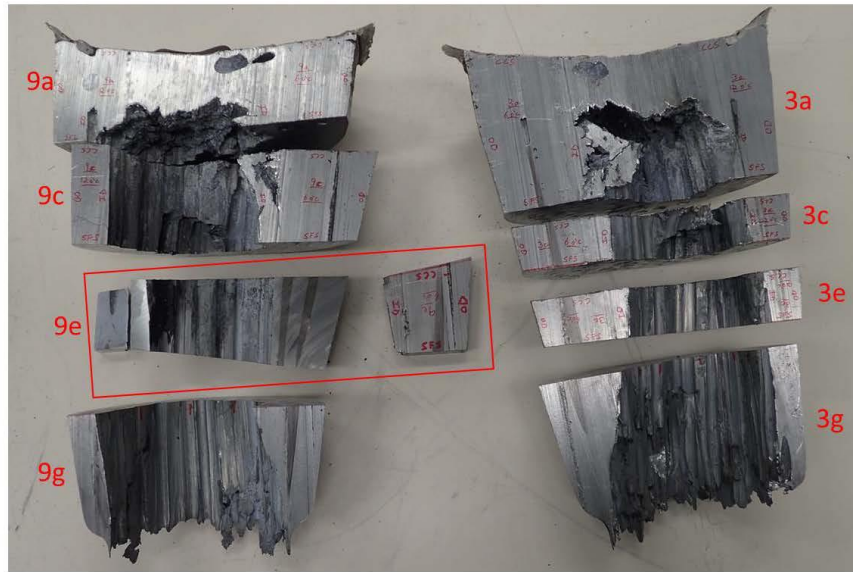


Figure 31. The zinc socket cavity transverse section labeling.

In between each cutting step, visual inspection was performed to examine the sections for forensic evidence. When accessible, microscopy was also performed.

The wire fracture surfaces embedded in the socket zinc casting were in various states of accessibility, with some protruding from the casting, others along the concave surfaces of the casting inner diameter along the slice, and still others completely buried in zinc and not visible, except that the band saw cut revealed that a wire was present somewhere within the zinc casting volume.

Initially, the wire fracture surfaces were attempted to be removed via mechanical means. A Dremel tool was used with abrasive cutoff discs to cut out zinc surrounding the wire and/or cut through the wire, away from the fracture surface. The process was very slow and difficult due to the limited reach with the Dremel tool. At one location, where there was insufficient room to traverse a path between wires on the backside of the slice, an end mill was used to hog out some zinc material. While much of the zinc was removed with the end mill, it was unclear how the wires changed direction deeper into the zinc, extensive care was utilized as excavation proceeded.

When a sufficient gap was present to insert a chisel, the slice was placed in a vice and a hammer and chisel were carefully used to break the fractured wire end or a group of fractured wires from the surrounding zinc. The chisel was most successful when it could be placed between a wire and the zinc. Even when the wire had visible corrosion product consistent with zinc oxide present on its exposed surface, the zinc adhered fairly well to the non-visible side of the wire before the wire would pop free of its channel. Where the zinc was cleanly adhered to the wire and no zinc oxide was visible, the wire had to be "peeled" free of the zinc by the chisel with subsequent hammer blows.

Abrasive cutoff wheels were used to cut the slices into smaller more manageable pieces to gain better access to the individual fractured wire ends during dissection, hydrochloric (HCl) acid zinc removal, and for cutting samples for SEM analysis, mechanical testing, and metallography.

In order to perform fractography analysis of the wires in the socket removal of the zinc surrounding the wires was required to expose any fracture surfaces that had become encased by the zinc as a result of the overall socket failure. The left image in Figure 32 shows one of the removed sections of zinc from the socket with varying amounts of zinc encasement around the wires and the fracture surfaces. To expose the fracture surfaces of all wires for analysis, the zinc was removed via dissolution in hydrochloric acid. The right image in Figure 32 shows the same section of zinc after exposure revealing any encased wires and their associated fracture surface. This method was chosen as it was the quickest and easiest procedure to remove the zinc from around the wires with minimal damage to the wires. Mechanical removal is possible but would be very time consuming due to the amount of zinc and depth of some wires within it. One downside to the acid removal method, is the reaction of the steel wires with the acid and removal of iron from the fracture surfaces. This was mitigated to an extent due to the cathodic nature the steel will take on relative to the zinc leading to the zinc-acid reaction being preferable and its rate higher than the steel causing minimal loss of iron from the fracture surface. This was confirmed via an analysis of a control sample before and after removal documenting the qualitative nature of the fracture surface. Comparison SEM images of the control can be found in Appendix C and

further images of the HCl-exposed wire fracture surfaces from the socket can be found in Appendix D.



Figure 32. Section of zinc with encased wires before removal of the zinc (left) and after removal (right) via dissolution in acid. Scale in centimeters.

3.7 Microscopy

Throughout the sectioning process, pieces of the socket were analyzed with stereomicroscopes. The stereomicroscopes provide a three-dimensional magnified view of the specimen, enabling greater visibility of microscopic features, such as grains, cracks, and fracture surfaces.

Once all zinc had been removed that encased the wires and fracture surfaces, portions of the wires containing the fracture surfaces were sectioned mechanically from the bulk sample to observe each individual fracture surface via a scanning electron microscope (SEM). This microscope allows the microstructure of the fracture to be evaluated to determine the cause of the fracture. Representative wires were analyzed in the SEM where the wire fracture displayed qualitatively a known failure mode for high strength steel. There were also a few selected wires where the cause of the fracture could not be determined macroscopically and required further analysis via the SEM. Likewise, sections of zinc were also investigated with the SEM.

3.8 Metallography

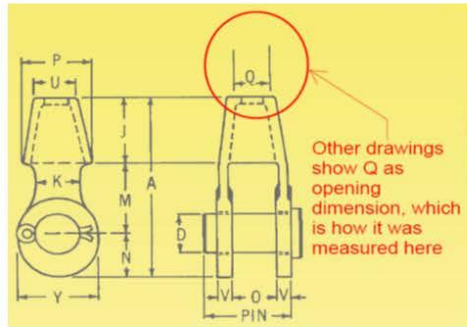
Metallography was performed on several zinc specimens. Samples were mechanically sectioned, mounted, ground, polished, and either macroetched with hydrochloric (HCl) acid or microetched with Klemm's 1 Reagent tint etchant. Metallography allowed for greater visibility of cracks in the zinc and revealed the casting grain structure.

4. RESULTS

4.1 As-Received

4.1.1 Metrology

Figure 33 shows the structural strand and wire rope catalog specified dimensions in the first row and the as-measured metrology measurements of the socket and clevis pin underneath (in gold).⁴ The measurements were in-family, but varied by as much as a 0.25 in.



	A (in)	J* (in)	K (in)	M* (in)	N (in)	O (in)	P (in)	Q (in)	U (in)	V (in)	Y (in)	Pin Bore Diameter (in)	Pin Outer Diameter (in)
Specification	3 1/2	10 1/2	6 1/8	13 1/4	7 3/4	6 3/4	11 3/4	3 3/4	7 1/2	2 3/4	11 1/4	6 1/2	6 1/2
As Measured	31.509	10.915 10.515	6.258	12.711 13.111	7.727	6.538	11.788	3.847	7.504	2.755	11.501	6.533	6.466

*Draft allowance for mold release produces a taper at J-M interface. Measurements were made at inner edge of cone which gives a larger number (~0.4 in greater than minimum material condition). Numbers come in if draft allowance is ignored which is shown in the lower column.

Figure 33. The dimension diagram and the Specification row come from the structural strand and wire rope catalog.⁴ The as-measured metrology measurements for the socket and clevis pin are underneath (in gold).

4.1.2 3D Laser Scan

Image renders made from the 3D laser scan of the socket can be found in Appendix E.

The imaging of the socket internal cavity was limited in these scans due to accessibility. Laser scanning requires line-of-site by the multiple lasers on the scanning equipment. The cavity was not large enough to place the scanner into the socket cavity. Plus, the laser scanner requires a stand-off distance to accurately measure variations along a surface. Additionally, the metallic surfaces are reflective, which can cause difficulties in obtaining accurate topographic data where the laser light may reflect off more than one surface before returning to the scanner detectors.

All measurements taken from the 3D laser scan data should be considered approximations to less precision than shown. Not only is the topographic data of the socket cavity limited, but the

cavity is an irregularly-shaped volume that is approximately described as a skewed-cylinder only for descriptive purposes. Additionally, the socket is a casting with surface irregularity that leads to difficulty in defining a surface plane or point from which to draw a measurement from and to.

Measurements taken from the 3D laser scan data are seen in Figures 182 and 183. It is noted that there is an approximately 5° skew of the socket cavity towards 9 o'clock, from the socket base towards the casting cap, and an approximately 5° skew of the socket cavity towards 12 o'clock, from the socket base towards the casting cap. The casting cap thickness was measured at about 30-35 mm (1.2-1.4 in) thick. The clevis tangs were also measured as not being parallel, each tang angled slightly (~1° or less) away from the center line, as measured from the casting cap side of the clevis pin to the opposite side of the clevis pin. In spite of this, the clevis pin was able to be rotated and removed by hand with no difficulty or noted impingement.

4.1.3 3D Prints

4.1.3.1 Negative 3D Print of Socket Cavity

Images of the negative 3D print of the socket cavity can be found in Appendix F. Smooth areas of the 3D print are where topographic data had to be interpolated due to those areas being inaccessible to the laser scan.

4.1.3.2 Positive 3D Print of Socket Steel Base and Zinc Casting

Images of the positive 3D print of the socket cavity can be found in Appendix F.

4.1.4 NDE

4.1.4.1 Magnetic Particle Inspection

The magnetic particle inspection of the exterior socket cone revealed no magnetic particle indications. Results were reported in LASSO NDE Report 01 for WON Y1019673.¹⁵

4.1.4.2 Gamma Source CR

The double-wall exposure radiographic inspection of the socket, as seen in Figure 34, was unable to penetrate the socket with sufficient energy to discern any of the internal features of the socket cavity. Vertical streaking in the CR image are processing artifacts, and not features present in the actual socket.



Figure 34. CR image of the double-wall radiographic exposure of the socket. Note that the vertical streaking are CR processing artifacts. No internal features of the socket cavity were discernable from this exposure.

The single-wall exposure radiographic inspection images and images of each side of the socket wall examined by each exposure can be seen in Figures 35-38. Density variations due to the zinc thickness and/or the wires are discernable in the images; however, distortion in the CR image plate made correlating wire locations from the CR image to the physical socket difficult. No cracks or voids were visible in the CR images, but due to the density of the socket material, the technique would likely only be able to detect large voids or cracks, and large cracks only with close alignment between the source, crack-face planes, and the detector.



Figure 35. CR image of the single-wall radiographic exposure of the socket, position 0. The blue markers indicate the direction of gamma-rays (“x” is going into the page and “dot” is coming out of the page) and where around the perimeter the source was aligned (approximately through the socket base’s 12 o’clock position).



Figure 36. CR image of the single-wall radiographic exposure of the socket, position 1. The blue markers indicate the direction of gamma-rays (“x” is going into the page and “dot” is coming out of the page) and where around the perimeter the source was aligned (approximately through the socket base’s 9 o’clock position).



Figure 37. CR image of the single-wall radiographic exposure of the socket, position 2. The blue markers indicate the direction of gamma-rays (“x” is going into the page and “dot” is coming out of the page) and where around the perimeter the source was aligned (approximately through the socket base’s 5 o’clock position).

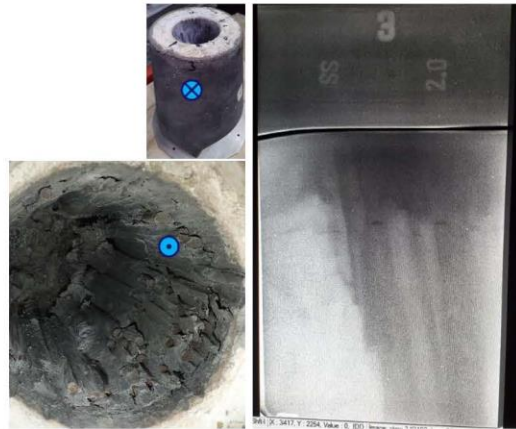


Figure 38. CR image of the single-wall radiographic exposure of the socket, position 3. The blue markers indicate the direction of gamma-rays (“x” is going into the page and “dot” is coming out of the page) and where around the perimeter the source was aligned (approximately through the socket base’s 2 o’clock position).

4.2 Wires

4.2.1 Wire Labeling and Tracing

The fractured wires were identified by labeling the wires cut through on the first transverse cuts of each half of the socket cone. Those wires were then traced through each subsequent transverse cut, and their labels carried forward, until the socket base was reached. Final identification of the fractured wires was then determined after sufficient zinc was removed from the socket base sides of the slices 3g and 9g. The intact wires were identified by labeling the wire imprints left in the back of the zinc socket cavity as well as the wire channels left along the zinc socket cavity walls. Only 113 wires are identified and labeled on the socket side, but the cable is comprised of 126 wires, plus the center wire which is composed of 7 smaller diameter strands. After determining how the cable/zinc slug mated with the socket cavity and a transverse slice was made approximately 1 inch down from the cable/zinc slug end, the remaining wires were labeled. The wire labeling and tracing results can be found in Appendix G.

Wire labeling and tracing was important for understanding wire brooming, fractography, and for finite element modeling the as-built joint configuration. As such, it is also important to note that the wire labeling settled on at the time of this report was imperfect. Three different configurations were determined, with minor changes between each. And it is important to understand where discrepancies between the labels identified here and the actual wire positions within the socket. Because the wire labeling began from the back of the socket and traced its way forward to the front, the wire labels for each of the wire fractures in the socket are considered to be most accurate and, with relatively small differences between wire orientations between each slice, there is not much likelihood of error in those wire label traces. The identification of the mating fractures in the cable-end section were generally clear based on the locations of wires compared to their neighboring wire fractures and how that matched with the socket wire-fracture locations compared to their neighboring wire fractures; however, sometimes the correlation between the socket regions and the cable-end regions was not very clear. Some amount of variation in individual wire movement likely occurred with the wires in the cable-end, socket, or both, which results in a reduced confidence in particular wire label arrangements within small regions of the cable-end section. Additionally, some wires in the cable-end section were completely encased in zinc, but only identified by their proximity to the zinc surface for detection with a magnet. Tracing the intact wires resulted in still less confidence. The process started with labeling wire imprints identified in the back of the socket cavity zinc. Those wires were matched with patterns in the wire ends as seen in the end of the cable-end section or the transverse cut made about 1 inch down. As stated earlier, this led to being able to place a label on all but 13 wires, which were identified through the 1 inch down transverse slice into the cable-end section.

While all 126 wires were able to be labeled, the known issues with the labeling and orientation then manifested through various additional analytical work. One discrepancy was noted when tracing the fractures back from the cable-end section. Twenty-six fractures were identified within the cable/zinc slug. Sixty-eight intact wires were identified across the cable/zinc slug transverse slice, made 1 inch down from the top of the cable-end section. Ninety-four wires were identified across the transverse slice on the bottom of the cable-end section, which matches the accounting of 26 fractures and 68 intact wires. Thirty-two wires are unaccounted for in the

cable-end section. Additionally, from the bottom view of the cable-end section, those 32 wires are all outer diameter wires. Since the socket has 56 wire fractures, and the cable-end section has 26, 30 of those 32 missing wires are mating fractures to the socket and 2 wires should be intact wires. The discrepancy was trying to identify where the 2 intact wires are positioned around the outer diameter ring. The initial trace suggested DY and DV were the outer diameter intact wires and were located near wires DW, DU, EB, and DT, but the socket wire fractures suggest that the 2 intact outer diameter wires should be adjacent to wires J, K, L, and M. Because the socket wire fractures did not present any evidence that the 2 intact outer diameter wires could be anywhere but adjacent to wires J, K, L, and M, placing DY and DV in this region is believed to be more accurate. However, there is no space or identifying feature in the back of the socket to allow for these wires to be positioned here. Another discrepancy was encountered when the finite element model was attempting to be built using the wire mapping from the socket slices. Wires AA and AD were intersecting one another between their socket wire fracture locations and the arrangement just outside of the socket base. This was most easily remedied by swapping their positions in the arrangement just outside of the socket base; however, their identified locations on the cable/zinc slug suggests the original arrangement is correct or they must swap positions within the cable-end section.

4.2.2 Fractography

From the wire tracing process, 70 of the 126 wires did not fracture, but instead pulled free of the socket joint. 68 of these 70 wires were recovered still embedded within their surrounding zinc, having pulled free of the socket as a slug of wires and zinc. The remaining 56 of the 126 wires fractured within the socket – between the casting cap and the socket base. 26 of the mating fractured wires were also recovered still embedded within their surrounding zinc along with the 68 intact wires. Table 2 sums up the split between fractured and intact wires, and provides a key to which wire labels are classified under these two categories.

Table 2. Identification of fractured and intact wires

A	AA	BA	CA	DA	EA	Fractured	56
B	AB	BB	CB	DB	EB		
C	AC	BC	CC	DC	EC	Total Wires (not including center wire)	
D	AD		CD	DD	ED	126	
E	AE		CE	DE	EE		
F	AF		CF	DF	EF		
G	AG		CG	DG	EG		
H	AH		CH	DH	EH		
I	AI		CI	DI	EI		
J	AJ		CJ	DJ	EJ		
K	AK		CK	DK	EK		
L	AL		CL	DL	EL		
M	AM		CM	DM	EM		
N	AN		CN	DN	EN		
O	AO		CO	DO	EO		
P	AP		CP	DP	EP		
Q	AQ		CQ	DQ	EQ		
R	AR		CR	DR	ER		
S	AS		CS	DS	ES		
T	AT		CT	DT			
U	AU		CU	DU			
V	AV		CV	DV			
W	AW		CW	DW			
X	AX		CX	DX			
Y	AY		CY	DY			
Z	AZ		CZ	DZ			

Appendix H contains the stereomicroscopy images of each of the fractured wires. Some thin localized melting of the zinc was evident in zinc spatter across the wires, as seen in Figure 39.

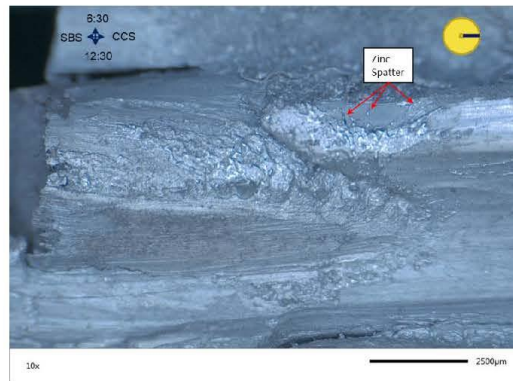


Figure 39. Inner diameter side of wire AH, exhibiting zinc spatter, from a thin layer of localized melting of the zinc. Note that the direction of flow of this layer of zinc is perpendicular to the wire channels.

Four of the wire fractures had surface defects running lengthwise along the wire, all similar in appearance to machining or tooling marks (see Figures 40 and 41). Only one of these four

surface defects appeared to be influential in the fracture surface (wire AN). Another one of these four surface defects was located away from the fracture surface (wire AR). Another surface defect, with a different appearance to the four described above, was found on wire BA (see Figure 42). This defect was a scribe-like groove, running lengthwise along the wire. This defect is located at the initiation site of the hydrogen assisted cracking morphology of the wire BA fracture surface.

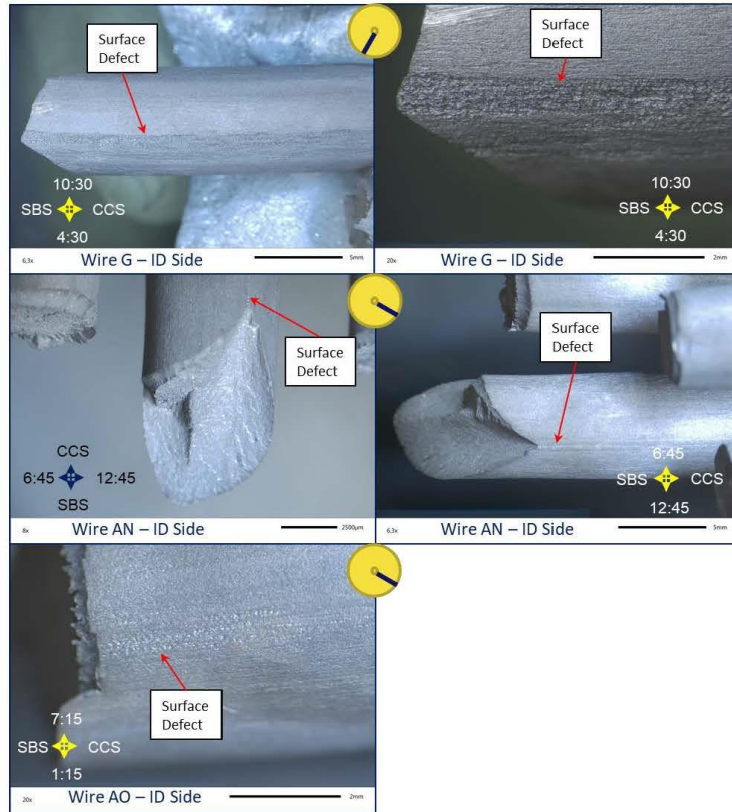


Figure 40. Stereomicroscope images of similar surface defects found on wires G, AN, and AO.

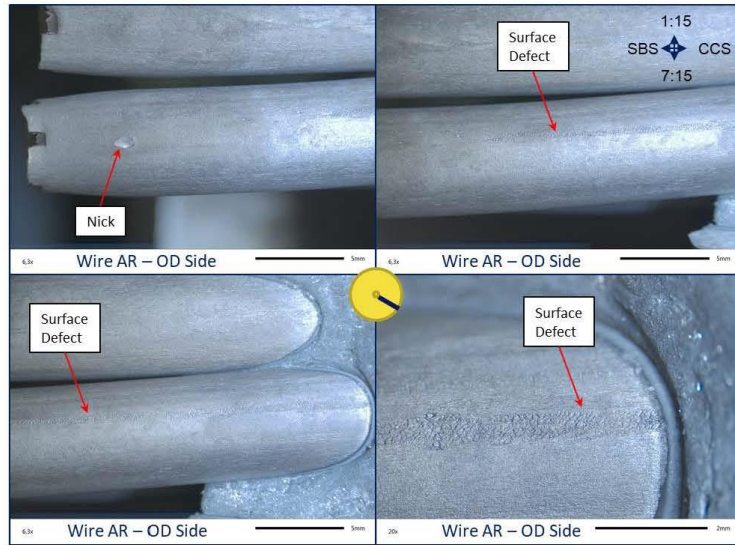


Figure 41. Stereomicroscope images of a surface defect found on wire AR. The nick visible in the top row left image was likely from sectioning.

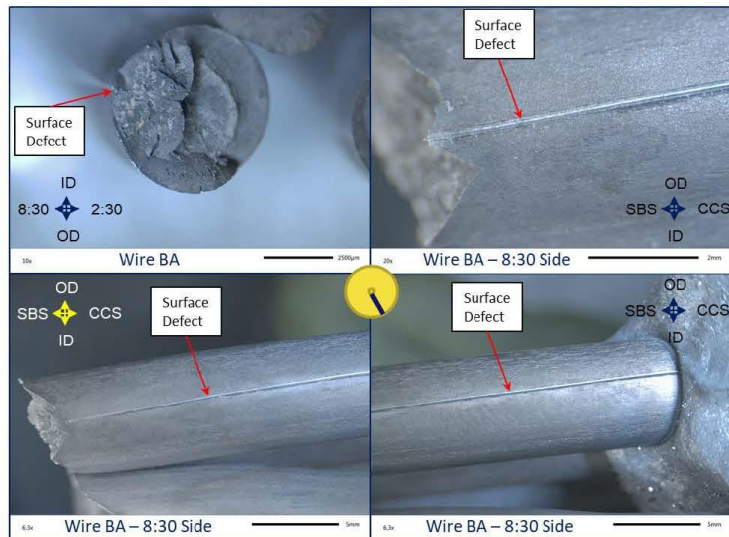


Figure 42. Stereomicroscope images of a surface defect found on wire BA.

Appendix I contains SEM images of select fractured wires. Three distinct macrostructures were observed via optical microscopy with one being the cup-cone structure indicative of a tensile ductile fracture. Another structure was an angled flat structure that is indicative of a shear failure. The last one was unable to be identified via its macrostructure so further analysis was needed to observe the fracture surface. Through the use of the scanning electron microscopy (SEM), microstructure of the fracture surface was observable to confirm the two known fractures and identify the unknown fracture.

Figure 43 shows an overview of the fracture surface displaying the cup-cone structure with observable and known features such as the smooth tensile failure area in the center with the shear lip around the outer circumference. The higher magnification images display various areas within the tensile failure fracture surface showing microstructure that has both microvoid coalescence (MVC) and cleavage fracture features that correspond to tensile failure in high strength steel with a pearlite microstructure these wires have. The first image was taken near the center of the fracture where the failure initiates and is representative of a higher amount of MVC than all other areas of the fracture. The second image was taken in the intermediate area between the center area and the outer shear lip. This area shows more cleavage fracture than the center along with a good amount of MVC still being present leading to more a combination of the two fracture features. The third image shows the beginning of the shear lip area.

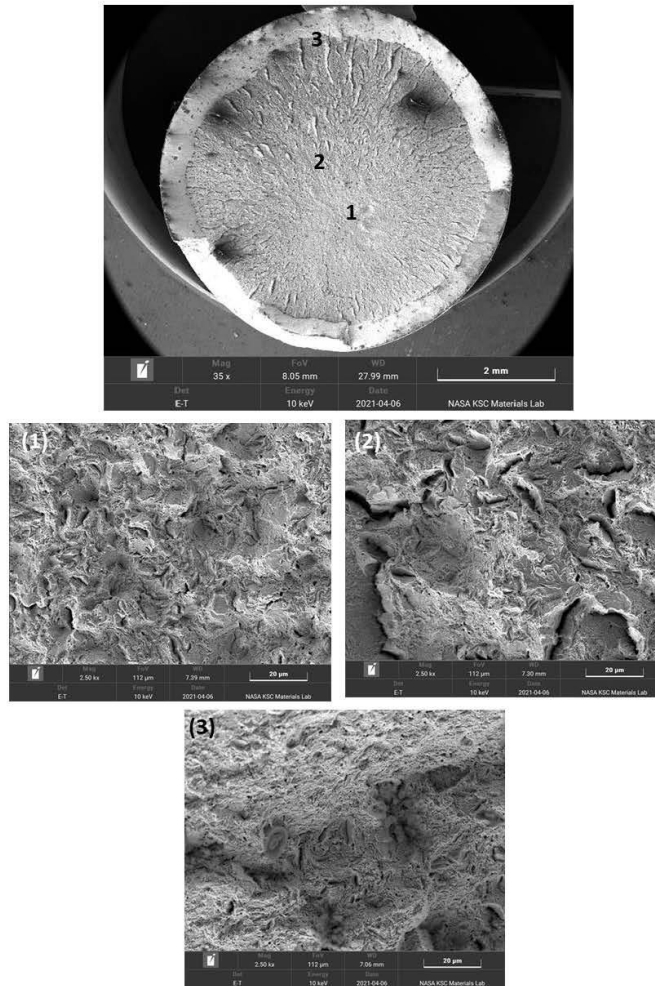


Figure 43. SEM images of a wire fracture surface displaying tensile failure (top) with higher magnification images displaying MVC and cleavage fracture (1,2) leading to a shear lip (3).

Figure 44 shows the overview of the shear failure fracture surface with the observable complete smooth surface at an angle across the diameter of the wire. The higher magnification images display various areas over the shear failure fracture surface. These images show microstructure features that are distinctive to shear type failures in high strength steel.

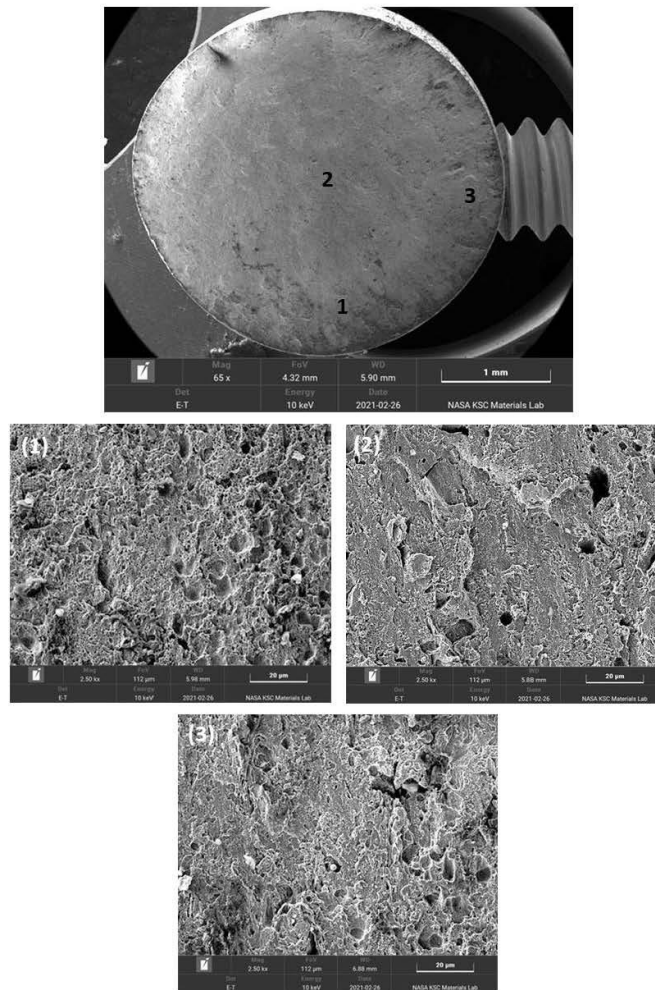


Figure 44. SEM images of a wire fracture surface displaying shear failure (top) with higher magnification images displaying the shear failure microstructure.

Figure 45 shows an overview of a more complex fracture surface consisting of a flat area with ridging on the left going into a shear failure area to the right. In the flat area, the macroscopic features point to initiation of the fracture occurring on the left side of the wire as oriented in the overview image and then proceeding to the final shear failure occurring on the right. To identify the fracture features the microstructure that was within the flat area was closely observed under the SEM to determine the cause of the fracture. The higher magnification areas show no indications of MVC and upon closer examination the features are attributed to being a function

of hydrogen assisted cracking (HAC) leading to the fracture. This microstructure correlates well with similar images shown in literature that display HAC. The high strength steel of the wire is also susceptible to HAC from manufacturing, the galvanization process these wires underwent, and the corrosive environment the wires were in. With respect to corrosion evidence on or in the vicinity of these HAC wires, wire AF and AI were mechanically removed and did not have corrosion evidence on their surfaces and wire BA was chemically removed and any corrosion evidence on its surfaces was lost from the cleaning action of the acid during the chemical removal process. HAC was limited in its impact to the few wires that did not exclusively exhibit tensile or shear failure.

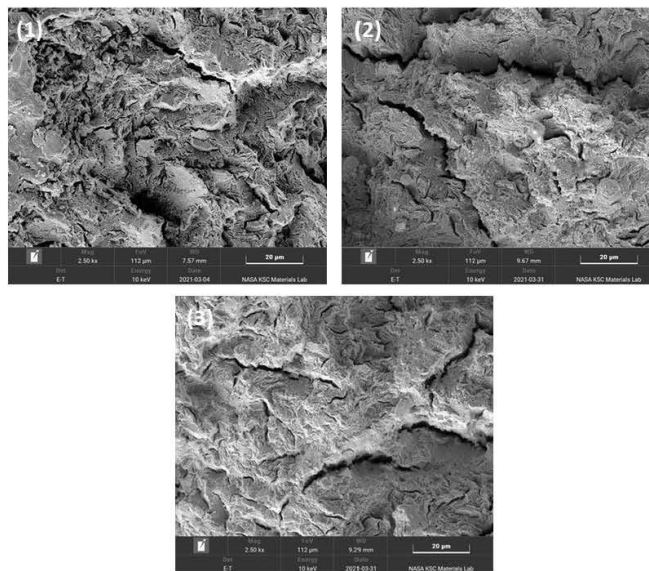
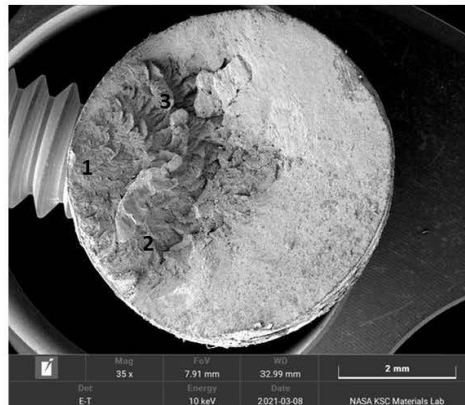


Figure 45. SEM images of a wire fracture surface displaying microstructure in the higher magnification images of HAC in the flat area of the fracture leading to a shear failure area (top).

The vast majority of the 56 wire fracture morphologies were cup-cone fractures (44). Nine were shear fractures. The remaining three of the 56 wire fractures were mixed-mode fractures which included a progressive failure mechanism, likely HAC; one was a cup-cone/HAC fracture and two were shear/HAC fractures –. Table 3 sums up the morphologies of the fractured wires.

Table 3. Identification of fracture morphology

A	AA	BA	CA	DA	EA
B	AB	BB	CB	DB	EB
C	AC	BC	CC	DC	EC
D	AD		CD	DD	ED
E	AE		CE	DE	EE
F	AF		CF	DF	EF
G	AG		CG	DG	EG
H	AH		CH	DH	EH
I	AI		CI	DI	EI
J	AJ		CJ	DJ	EJ
K	AK		CK	DK	EK
L	AL		CL	DL	EL
M	AM		CM	DM	EM
N	AN		CN	DN	EN
O	AO		CO	DO	EO
P	AP		CP	DP	EP
Q	AQ		CQ	DQ	EQ
R	AR		CR	DR	ER
S	AS		CS	DS	ES
T	AT		CT	DT	
U	AU		CU	DU	
V	AV		CV	DV	
W	AW		CW	DW	
X	AX		CX	DX	
Y	AY		CY	DY	
Z	AZ		CZ	DZ	

Cup cone	44
Cup cone, possible HAC	1
Shear	9
Shear, possible HAC	2
Intact	70
Total Wires (not including center wire)	126

Almost all of the fractured wires in the outer ring of the cable fractured. The other fractured wires came from progressively more inner rings, between about 2 o'clock and 7 o'clock. Outer ring wires generally fractured closest to the socket base opening, and wires from more inner rings failed progressively further away from the socket base opening, back into the socket, towards the casting cap. Most of the shear fractures also appear to have been from outer ring wires (Figures 46-49).

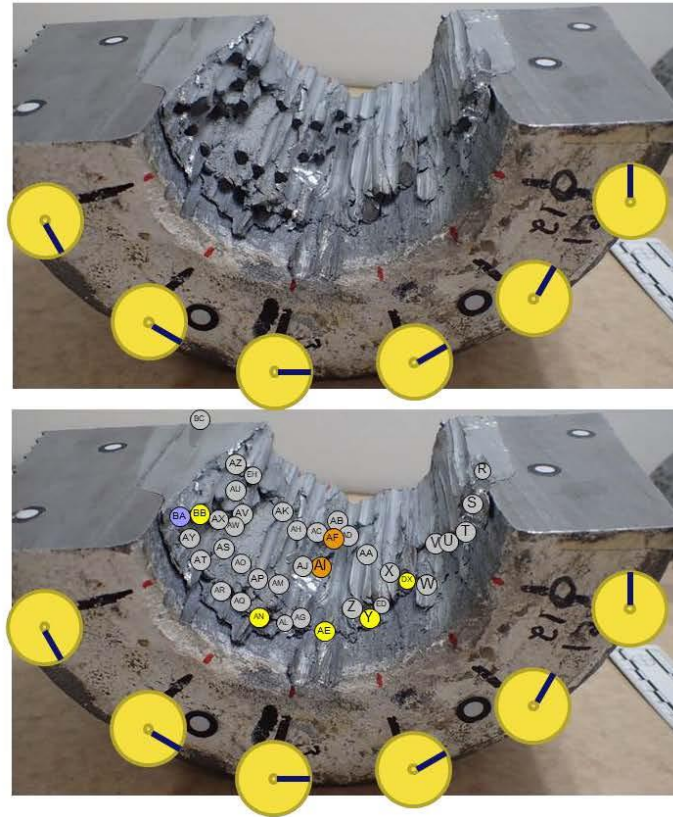


Figure 46. Slice 3g. The lower image is the same as the upper image, but with wire label overlays that correspond to the color-coding in Table 3. The wire fractures are successively stacked the further they are located within the socket.

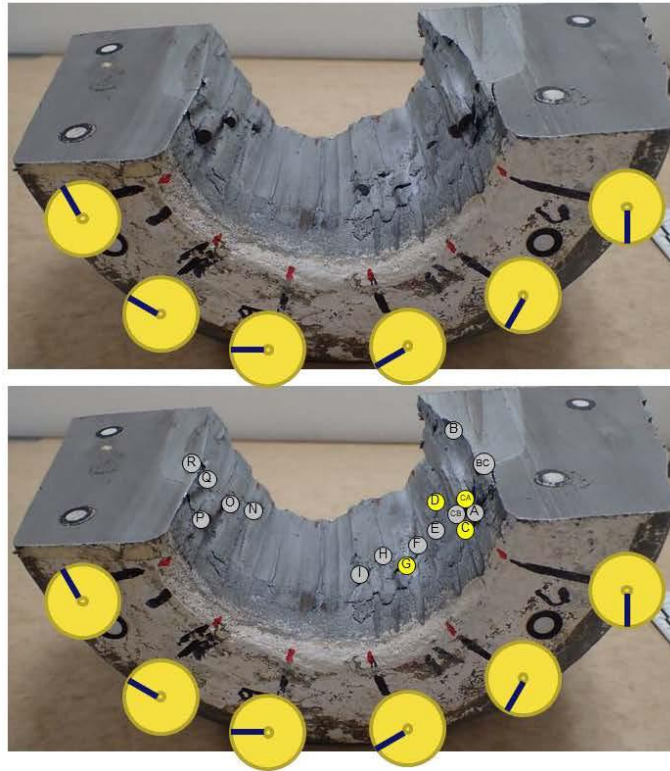


Figure 47. Slice 9g. The lower image is the same as the upper image, but with wire label overlays that correspond to the color-coding in Table 3.

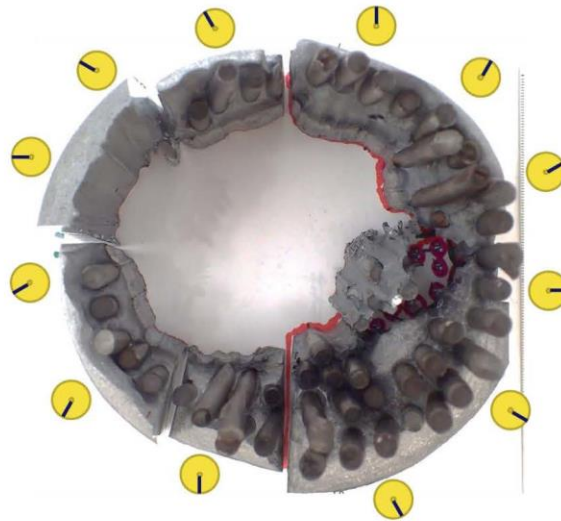


Figure 48. Rearrangement of the pieces from slices 3g and 9g back into their approximate as-built configuration, after the acid bath zinc removal process. Note that the outer diameter wires almost complete a full circle.

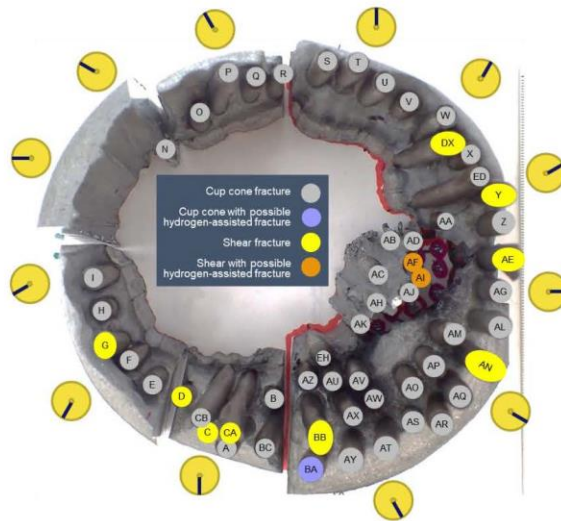


Figure 49. Rearrangement of the pieces from slices 3g and 9g back into their approximate as-built configuration, after the acid bath zinc removal process with wire label overlays that correspond to the fracture morphology identified.

Stereomicroscope measurements of the fractured wire necking were made with either the circle tool or the line measurement tool, typically depending on whether the measurement was to be made looking down on the fracture surface or looking at the side profile of the wire. When visible, additional measurements were made away from the fracture surface and necked region, to get an unnecked measurement value. The wires are known to be 0.25 in diameter, but, because the stereomicroscope was not calibrated prior to taking the measurements, the arithmetic mean was taken from the unnecked measurement values and used as the comparative value for necked measurement values obtained for each individual wire. Table 5, in Appendix J, tabulates these data and sorts them from most necked to least. Table 4 pulls the summary data from Table 5. Figure 50 overlays the percent necking color coding from Table 4 onto the approximate as-built arrangement from Figure 49. The amount of necking was predominantly greater on wires that failed closer to the center and further into the socket (i.e., inner ring wires). The three wires with possible HAC exhibited little necking, with two of those wires (wire AI and AF) as part of the inner ring wires and one (wire BA) an outer ring wire.

Table 4. Summary data from Table 5 in Appendix J.

Wire	Grouping	% Necked	Rank (1 = most necked)
AH	Cup Cone	23.07%	1
EH	Cup Cone	22.68%	2
AJ	Cup Cone	22.48%	3
AZ	Cup Cone	22.02%	4
AA	Cup Cone	21.77%	5
AB	Cup Cone	20.91%	6
AU	Cup Cone	19.61%	7
AC	Cup Cone	19.20%	8
AK	Cup Cone	17.71%	9
ED	Cup Cone	17.23%	10
AG	Cup Cone	15.78%	11
B	Cup Cone	14.73%	13
AV	Cup Cone	14.73%	13
AR	Cup Cone	13.41%	14
BC	Cup Cone	13.35%	15
AQ	Cup Cone	13.07%	16
CB	Cup Cone	12.80%	17
P	Cup Cone	12.63%	18
AT	Cup Cone	11.92%	19
O	Cup Cone	11.75%	20
BB	Shear	11.50%	21
AY	Cup Cone	11.47%	22
AD	Cup Cone	10.54%	23
AL	Cup Cone	9.65%	24
AO	Cup Cone	9.60%	25
AM	Cup Cone	9.51%	26
Q	Cup Cone	8.94%	27
AP	Cup Cone	8.77%	28
R	Cup Cone	8.60%	30
AW	Cup Cone	8.60%	30
Z	Cup Cone	8.11%	31
F	Cup Cone	7.50%	32
D	Shear	7.11%	33
T	Cup Cone	6.56%	34
N	Cup Cone	5.04%	35
S	Cup Cone	4.36%	36
W	Cup Cone	4.80%	37
U	Cup Cone	4.63%	38
E	Cup Cone	4.05%	39
X	Cup Cone	3.64%	40
H	Cup Cone	3.06%	41
AN	Shear	2.73%	42
A	Cup Cone	1.65%	43
V	Cup Cone	1.48%	44
BA	Cup Cone/HAC	0.82%	45
AI	Shear/HAC	0.10%	46
I	Cup Cone	-0.34%	47
CA	Shear	-1.00%	48
AF	Shear/HAC	-1.77%	49
G	Shear	-2.16%	50
AS	Cup Cone	-2.32%	51
Y	Shear	-2.65%	52
AE	Shear	-40.98%	
C	Shear		
AK	Cup Cone		
DX	Shear		

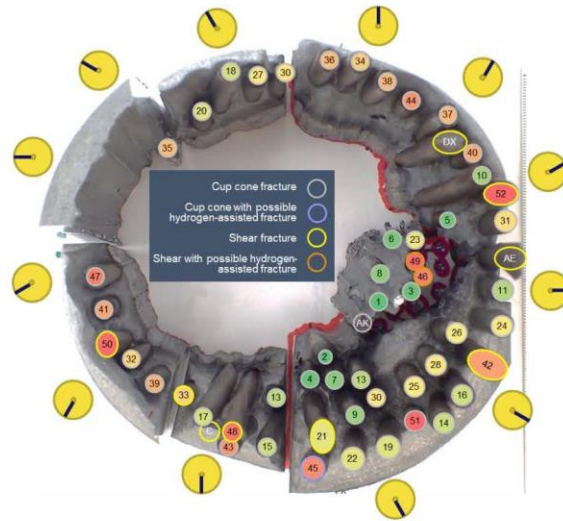


Figure 50. Rearrangement of the pieces from slices 3g and 9g back into their approximate as-built configuration, after the acid bath zinc removal process with wire label overlays that correspond to both the fracture morphology identified (outline color of the overlay) and the percent necking from Table 4 (fill color of the overlay).

4.3 Zinc Casting

Figures 51 and 52 show each half of the socket cavity, after the first longitudinal cut opening up the socket cavity to view.



Figure 51. 3 o'clock side of the socket cavity after the longitudinal cut, but before any transverse cuts. The socket base is aligned with the bottom of the image. Scale in inches and centimeters.

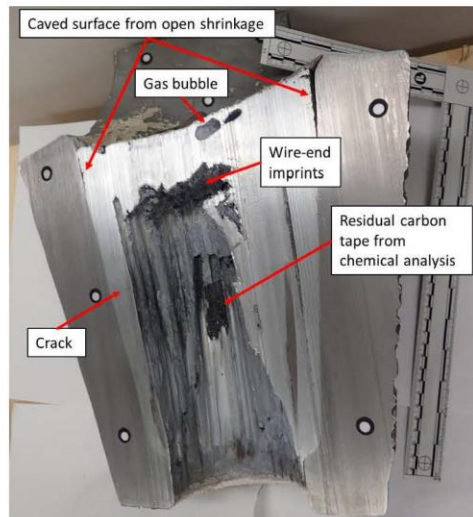


Figure 52. 9 o'clock side of the socket cavity after the longitudinal cut, but before any transverse cuts. The socket base is aligned with the bottom of the image. Scale in inches and centimeters.

Between the inner diameter of the socket cone and the outer diameter of the zinc casting, at the socket base, a tight gap can be seen. Figure 53 show a closer view.

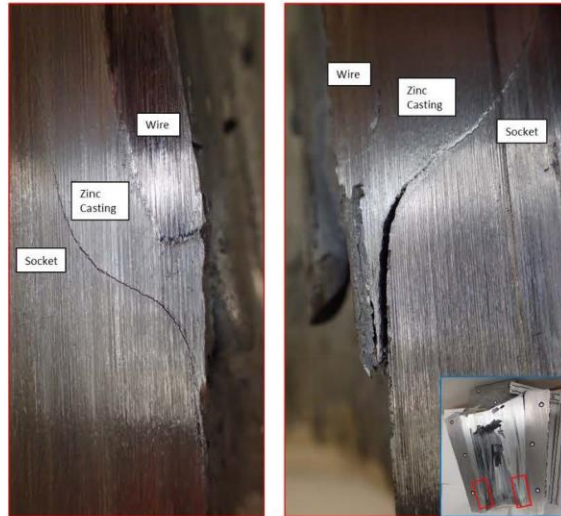


Figure 53. Close up view of the tight gap present between the socket wall inner diameter and the zinc casting outer diameter, just inside the socket base. These images were taken from the 9 o'clock half – 12 o'clock is on the left and 6 o'clock is on the right.

Figure 54 show a larger gap between the inner diameter of the socket cone and the outer diameter of the zinc casting, at the casting cap. This larger gap is a caved surface due to open shrinkage of the zinc casting during solidification. Approximately mid-way down a crack is identified in each half of the socket.



Figure 54. Close up view of the larger gap present between the socket wall inner diameter and the zinc casting outer diameter, at the casting cap. These images were taken from the 9 o'clock half – 12 o'clock is on the left and 6 o'clock is on the right.

Figures 55 and 56 show a closer view of the crack. Note that, this is one crack and is only seen in both halves because it was cut through during the longitudinal bandsaw cut. White corrosion product, probably zinc oxide, is seen within the crack.

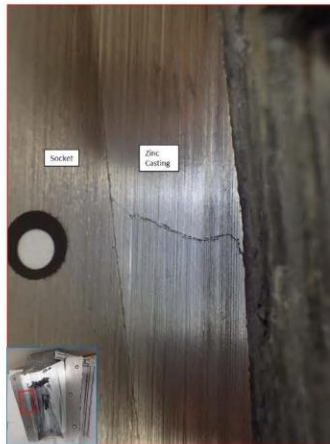


Figure 55. Close up view of the crack present in the zinc casting, running between the inner diameter of the zinc casting, where the cable/zinc slug pulled out, and the outer diameter of the zinc casting. This image was taken from the 9 o'clock half at 12 o'clock.

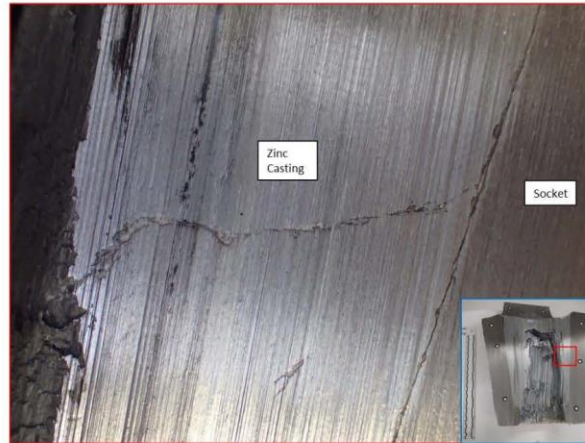


Figure 56. Close up view of the crack present in the zinc casting, running between the inner diameter of the zinc casting, where the cable/zinc slug pulled out, and the outer diameter of the zinc casting. Corrosion product, most likely zinc oxide, has completely filled the crack space. This image was taken from the 3 o'clock half at 12 o'clock.

Figure 57 shows the gas bubble located just below the casting cap. The bubble is filled with white corrosion product, most probably zinc oxide. The gas bubble identified in each half of the socket cavity is a single gas bubble, split open from the longitudinal bandsaw cut. The gas bubble has cracks that appear to span from the casting cap surface to the gas bubble surface. Additionally, there may have been a pathway from the gas bubble surface to the brittle fracture region that lies immediately below it, but that connection is at least filled with white corrosion product, most probably zinc oxide.



Figure 57. Close up view of the gas bubble in the zinc casting, just under the casting cap. Corrosion product, most likely zinc oxide, built up within the walls of the gas bubble. This image was taken from the 9 o'clock half.

Figures 58 and 59 provide a measurement and show a close up of the gap from a wire displacement. This cavity behind the wire also appears to have white product on its surface, which would most probably be zinc oxide. A crack appears to be present on the casting cap side of the cavity. Several pores can also be seen next to the wire cross-section in the same local area.

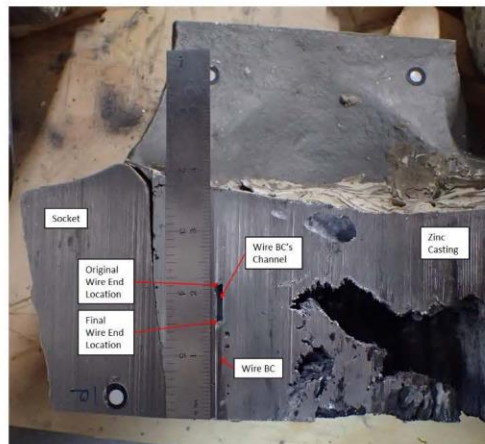


Figure 58. Measurement of wire-end displacement of wire BC within the zinc casting. This image was taken from the 3 o'clock half. Scale in inches.

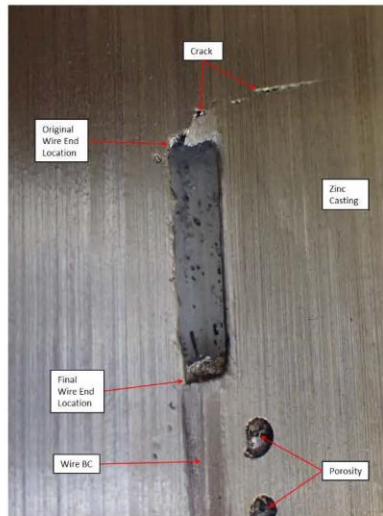


Figure 59. Close up view of the wire-end displacement of wire BC within the zinc casting. A crack appears evident on the casting cap, which would be a potential ingress route for moisture. Additionally, several pores can be seen adjacent to the wire. This image was taken from the 3 o'clock half.

Figures 60 and 61 show close up views of the wire channels left in the zinc.

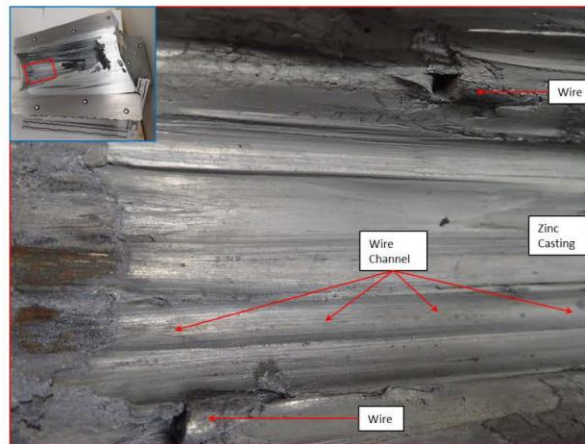


Figure 60. Close up view of the wire channels left in the zinc on the 9 o'clock side of the socket cavity. The socket base is towards the left-side of this image.

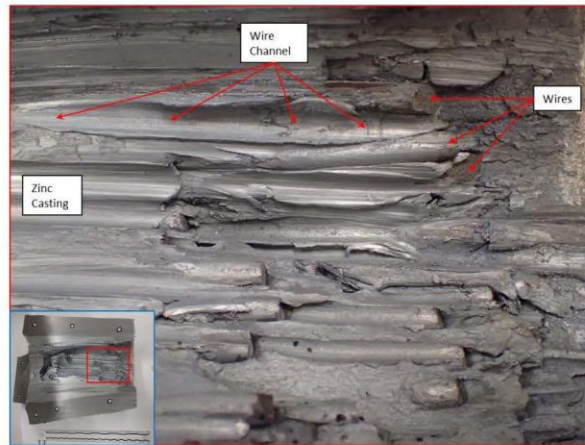


Figure 61. Close up view of the wire channels left in the zinc on the 3 o'clock side of the socket cavity. The socket base is towards the right-side of this image.

Figure 62 provides a close up view of slice 9c, within the socket cavity near the casting cap side of the slice, where some of the zinc between wires shows a brittle fracture surface. The wire channels in this image also appear to show a significant amount of corrosion product, most likely zinc oxide, on their surface.

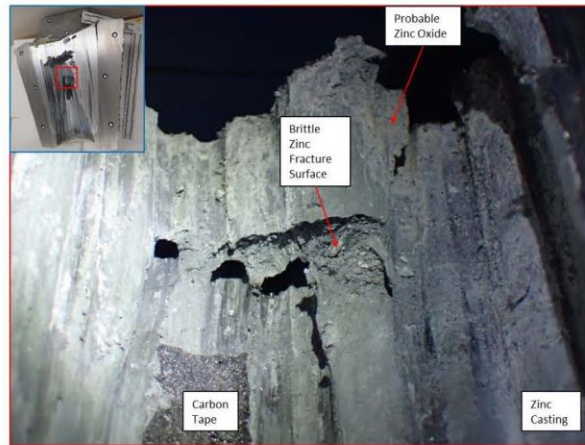


Figure 62. Close up view of slice 9c, within the socket cavity near the casting cap side of the slice, where some of the zinc between wires shows a brittle fracture surface. The wire channels in this image also appear to show a significant amount of corrosion product, most likely zinc oxide, on their surface. The black rectangular piece at the bottom left of the image is remnant carbon tape from chemical sampling.

Figure 63 arranges slice 9a onto the 3 o'clock half and Figure 64 arranges slice 9a onto slice 3a, both as a visual aid for how the back of the socket cavity looked prior to sectioning.

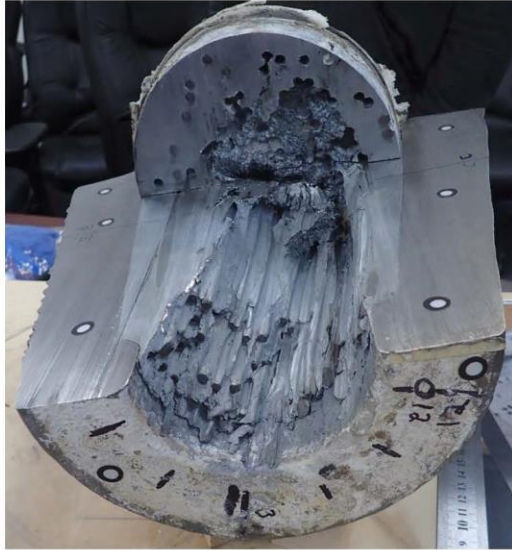


Figure 63. Slice 9a on top of the 3 o'clock half, providing a visual on how the back of the socket cavity was at the time of failure.



Figure 64. Slice 9a on top of slice 3a, providing a visual on how the back of the socket cavity was at the time of failure.

After having removed part of the socket base side of the brittle fracture region in the back of the socket cavity, Figures 65-67 provide a better view of the casting cap side of the brittle fracture region in the back of the socket cavity on slice 3a. The surfaces of the brittle fracture region forms a cone-shape that comes to a point just behind the gas bubble. White corrosion product can be seen on the surface, predominantly along ridges and protrusions. Additionally, Figure 68 shows the ends of many elongated grains lifted from the surrounding surface.

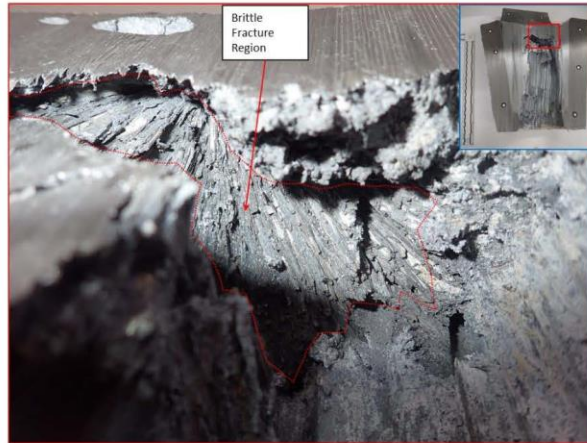


Figure 65. View of the casting cap side of the brittle fracture region in the back of the socket cavity on slice 3a. The fracture surface can be seen extending from the wire channels from the outer diameter of the cable-end section that pulled free of the socket during the ultimate failure up to a point just below the gas bubble. The gas bubble can be seen at the top left of the image.



Figure 66. View of the casting cap side of the brittle fracture region in the back of the socket cavity on slice 3a. The fracture surface can be seen extending from the wire channels from the outer diameter of the cable-end section that pulled free of the socket during the ultimate failure up to a point just below the gas bubble. The gas bubble can be seen at the bottom right of the image.



Figure 67. View of the casting cap side of the brittle fracture region in the back of the socket cavity on slice 3a, after some additional abrasive saw cuts on the left and right of this image and a third cut along the outer diameter of the zinc casting to remove the socket base side of the remaining piece. The fracture surface can be seen converging to a point just below the gas bubble (refer to Figure 66 for the location of the gas bubble).

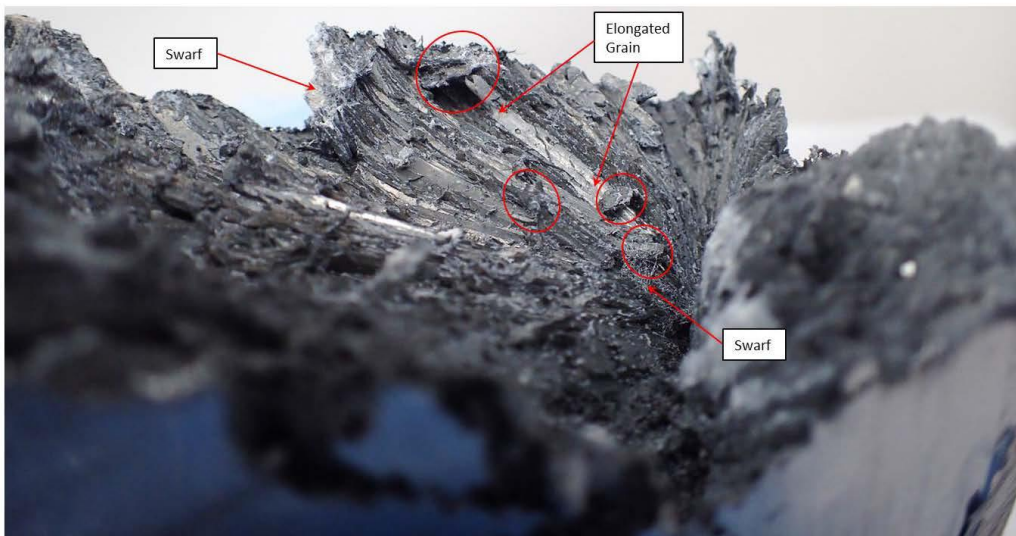


Figure 68. View of the casting cap side of the brittle fracture region in the back of the socket cavity on slice 3a. Many ends of the elongated grains appear lifted up from the surface (some have been circled in the image). Note that there is a substantial amount of swarf from the cutting process that is visibly stuck along edges and protrusions within the image.

Figures 69 and 70 provide a closer view of the back of the socket cavity on slice 9a. This region does not exhibit the same faceted appearance as the neighboring brittle fracture region of the back of the socket cavity. Instead, it is covered in a large volume of corrosion, identified by chemical analysis as being predominantly zinc oxide, with trace amounts of iron (the orange coloration is likely caused by the presence of iron oxide). Additionally, wire-end imprints are clearly identifiable on the surface. Large volumes of corrosion are also noticeable along the wire channel, coming towards the socket base from the back of the socket cavity.



Figure 69. Closer view of the back of the socket cavity on slice 9a. This region does not exhibit the same faceted appearance as the neighboring side of the back of the socket cavity from slice 3a. Wire-end imprints and heavy amounts of probable zinc oxide and iron oxide corrosion can be seen in this area.

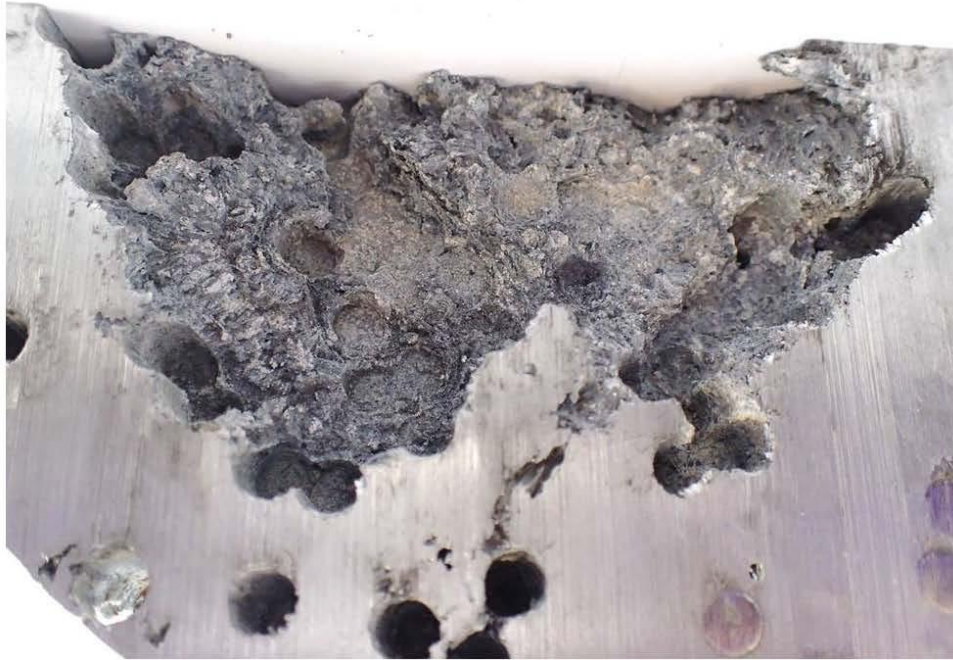


Figure 70. Closer view of the back of the socket cavity on slice 9a. This region does not exhibit the same faceted appearance as the neighboring side of the back of the socket cavity from slice 3a. Wire-end imprints and heavy amounts of probable zinc oxide and iron oxide corrosion can be seen in this area.

Figures 71-73 reveal a second gas bubble uncovered during sectioning slice 3a. This gas bubble showed no pathway into the socket cavity, but a network of cracks are visible above the gas bubble, leading to the casting cap. A mastic coating was applied to the casting cap at some point in its service history, but cracks can be seen in the mastic above this second gas bubble. Large volumes of white corrosion product, most likely zinc oxide, were present within the second gas bubble, immediately below the network of cracks, and the entire interior showed some amount of corrosion.

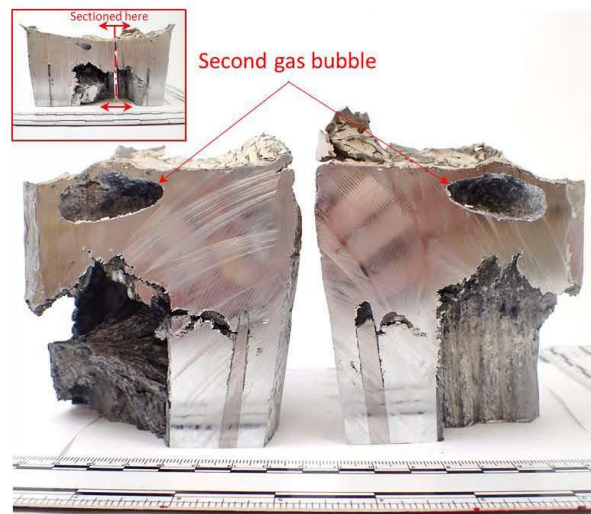


Figure 71. Slice 3a was sectioned longitudinally, revealing a second gas bubble below the casting cap.

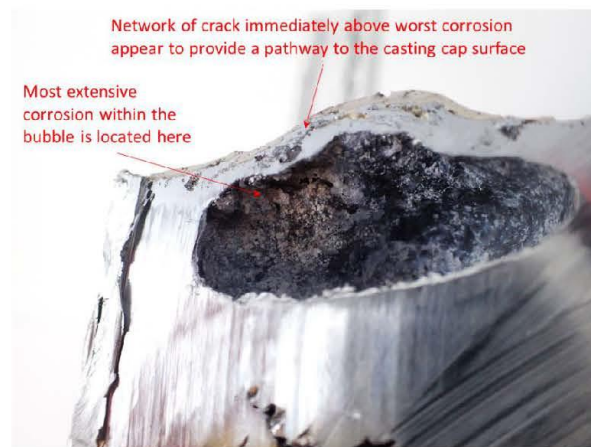


Figure 72. Close up image of the second gas bubble from Figure 71. The interior of the gas bubble is heavily corroded with white corrosion product, most probably zinc oxide, particularly just below the network of cracks between the bubble and the casting cap.



Figure 73. Oblique view of the casting cap immediately above the second gas bubble revealed in Figure 71.

4.3.1 Metallography

Appendix K details the metallography results from samples taken and etched from the upper, casting cap, region of the zinc casting; middle, slice 3c, region of the zinc casting; and lower, socket base region of the zinc casting. An HCl etchant revealed an elongated grain structure, with predominantly large grains, but a great amount of variation in the size and length of those grains depending on their location within the zinc casting. While these grains are pure zinc, EDS revealed a fine dispersion of zinc iron sodium (Zn-Fe-Na) constituents throughout the casting that is highly reflective after etching, appearing either dark or bright depending on the viewing angle (e.g., see dark constituents in Figure 294). Smaller finer elongated grains solidified outwards from the individual wire outer diameters. Those grains were shorter in length than the elongated grains that solidified inwards from the inner diameter of the socket wall. The thickest and longest grains solidified inwards from the socket cone wall and grew at an angle upward towards the casting cap. A thin layer of elongated grains solidified downward from the casting cap. The first gas bubble lies at the boundary between the zinc grains that grew down from the casting cap and the other zinc grains that solidified inward and upward from the socket wall and upward from the cable wire ends (see Figure 283).

The grains closest to the socket base, along the boundary of the cable/zinc slug that pulled free of the socket, appear to be very fine grains. Moving away from that boundary towards the outer diameter of the zinc casting, once the grain orientation becomes evident in the socket, it appears to be approaching parallel to the wires, and changes angle to perpendicular to the wires as you get to the zinc casting outer diameter. Looking at the zinc grains near the casting cap end of the socket, the grain orientation is closer to perpendicular to the wires between the cable/zinc slug interface and the inner cone wall of the socket. Figure 74 shows the directional changes in the elongated grain direction from the grains analyzed in slice 3c. Figure 75 shows the directional changes in the elongated grain direction from the grains analyzed in slice 9g. Figures 76-78 are measurements taken from the plane adjacent to the cable/zinc slug that pulled free of the socket to the approximate location where the grains noticeably begin to have an elongated orientation.

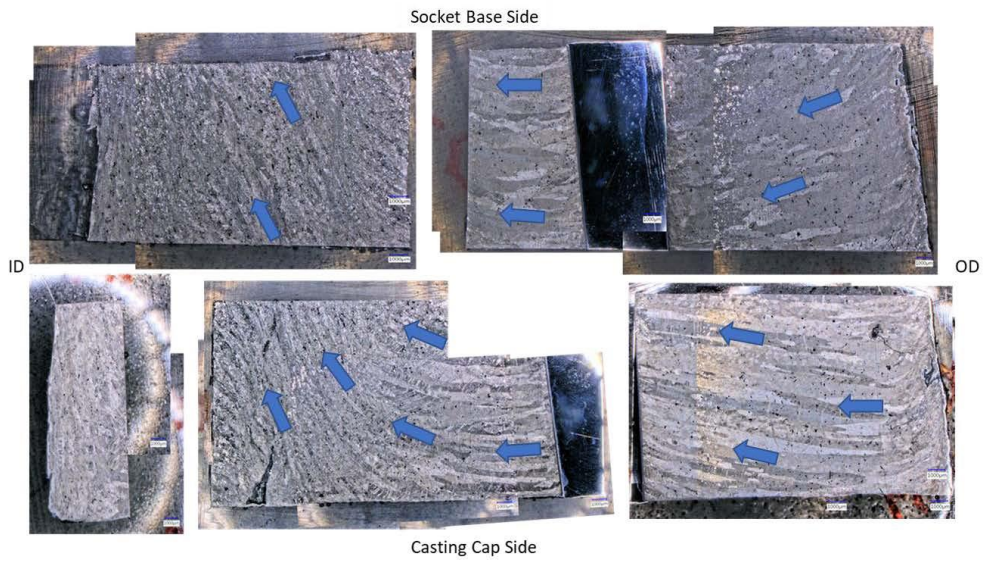


Figure 74. Directional changes in the elongated grain direction from the grains analyzed in slice 3c, from Figure 288.



Figure 75. Directional changes in the elongated grain direction from the grains analyzed in slice 9g, from Figure 293. Note that, at the cable/zinc slug boundary (bottom of image), the grains had no discernable elongated orientation. Refer to the tint etch images in Figures 307-310.

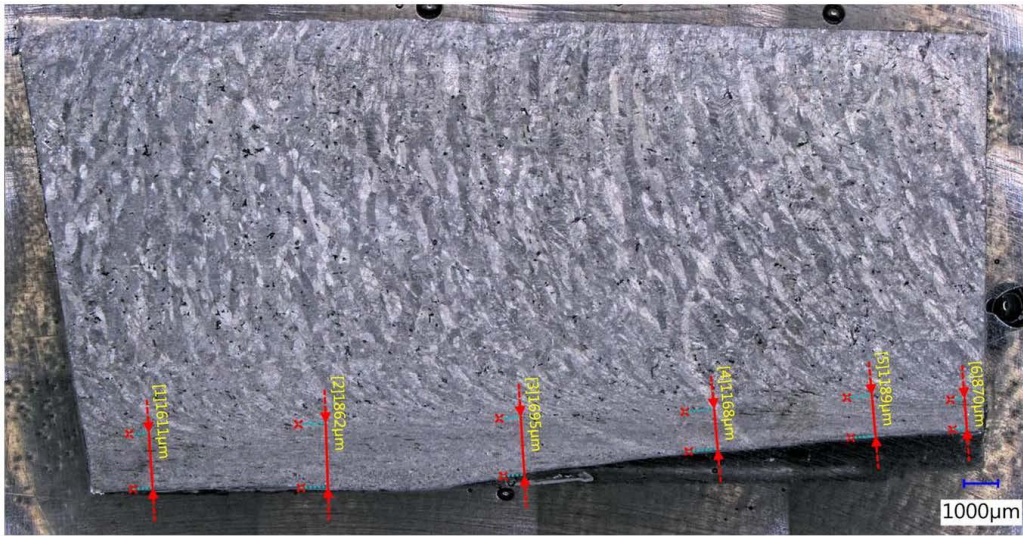


Figure 76. Measurements taken on Figure 293 from the plane adjacent to the cable/zinc slug that pulled free of the socket to the approximate location where the grains orientation begins to noticeably change from parallel to that interface.

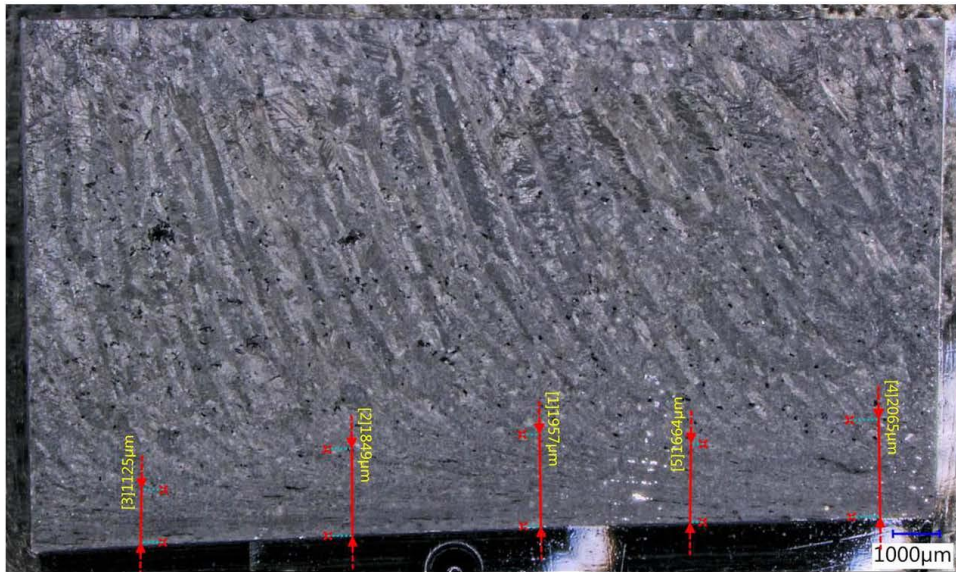


Figure 77. Measurements taken on Figure 294 from the plane adjacent to the cable/zinc slug that pulled free of the socket to the approximate location where the grains orientation begins to noticeably change from parallel to that interface.

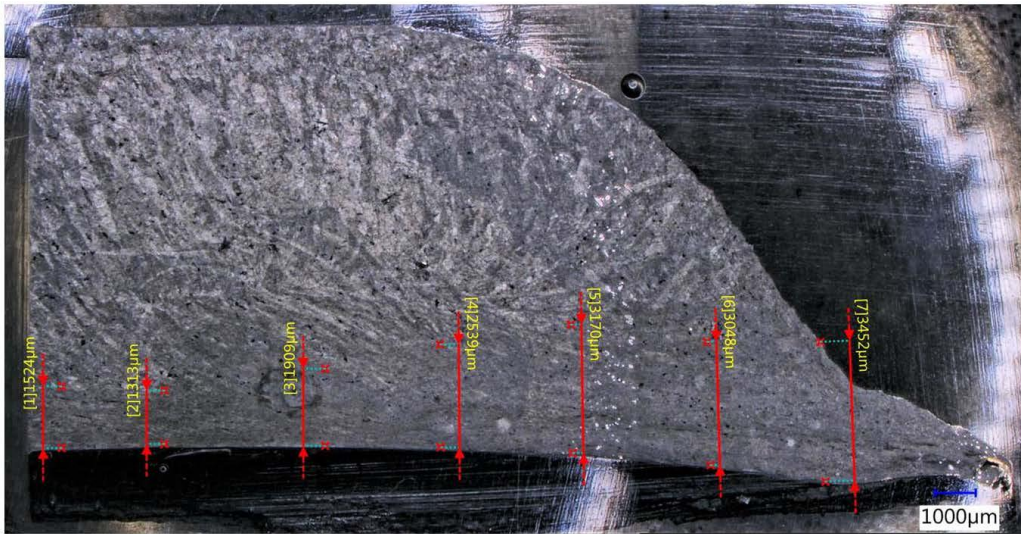


Figure 78. Measurements taken on Figure 295 from the plane adjacent to the cable/zinc slug that pulled free of the socket to the approximate location where the grains orientation begins to noticeably change from parallel to that interface.

Figure 79 shows the zinc grain structure adjacent to the cable/zinc slug that pulled free of the socket near the socket base at 50X magnification. In the image, intermittent cracking is visible running parallel with the cable/zinc slug boundary plane.

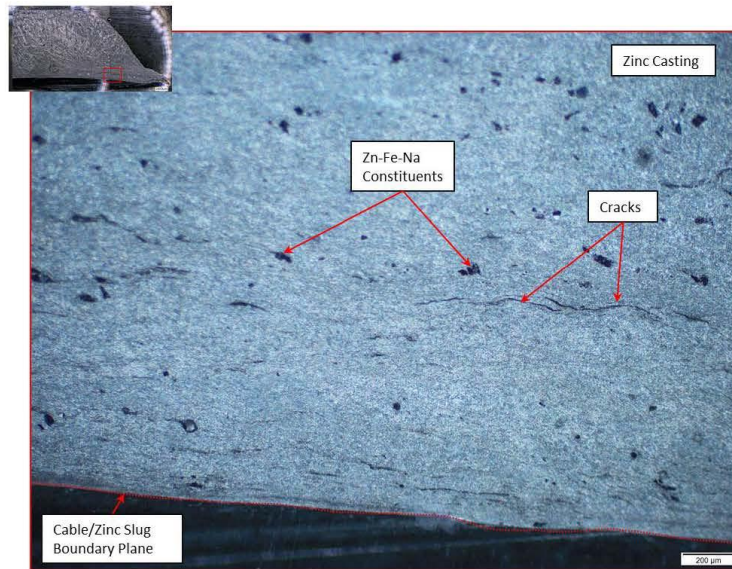


Figure 79. Zinc grain structure adjacent to the cable/zinc slug that pulled free of the socket near the socket base. Intermittent cracks are visible, running parallel with the cable/zinc slug boundary plane. (50X magnification)

The metallographic specimen from Figure 78 was microetched with Klemm's 1 Reagent tint etchant. The tint etch revealed zinc metallurgical structure within the grains. Figures 80 and 81 shows some of the grain structure features in the larger grains, near the zinc casting outer diameter. Figure 82 shows the microstructure near the cable/zinc slug boundary. These tint etches reveal internal grain features associated with deformation mechanisms such as slip planes and twin boundaries, that would be expected in a highly stressed zinc. The grain boundaries, partially outlined, are difficult to identify because the grains were recrystallizing. Note that the individual deformation mechanisms occurring within the original grains appear to be confined within their original grains, and are not traversing across their original grain boundaries. The recrystallizing grain boundaries are generally aligned 45° to the stress axis, running parallel to the cable/zinc slug boundary. This is particularly evident closer to the cable/zinc slug boundary, which would be the expected response of zinc undergoing creep deformation around ambient temperature.

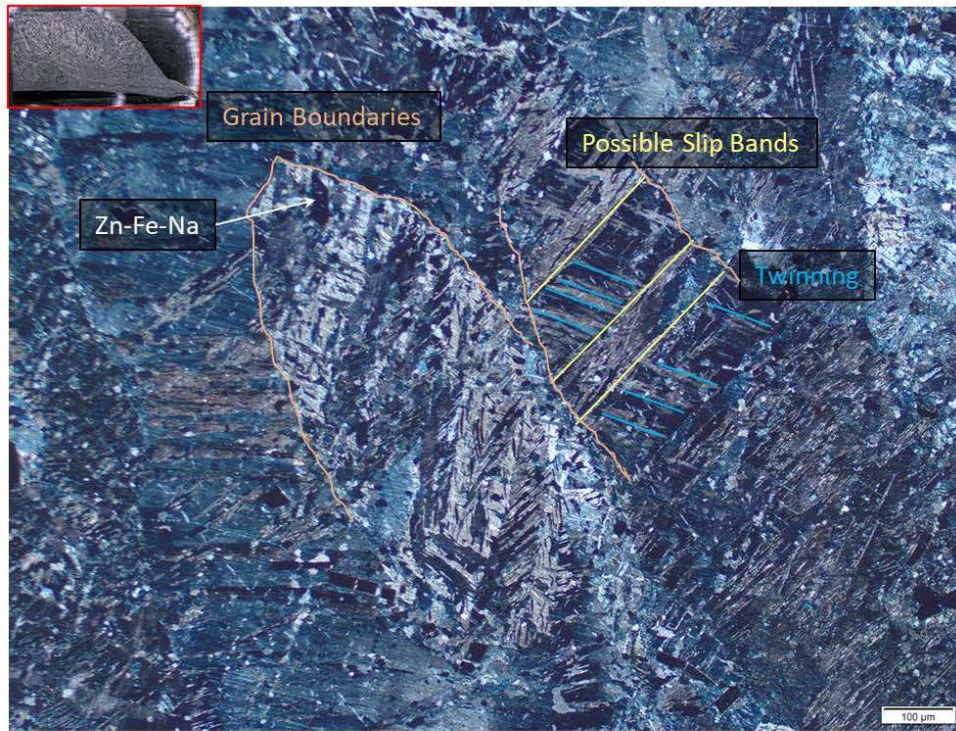


Figure 80. Metallograph image of the large grains present in Figure 78 close to the zinc casting outer diameter. Tint etch at 100X.

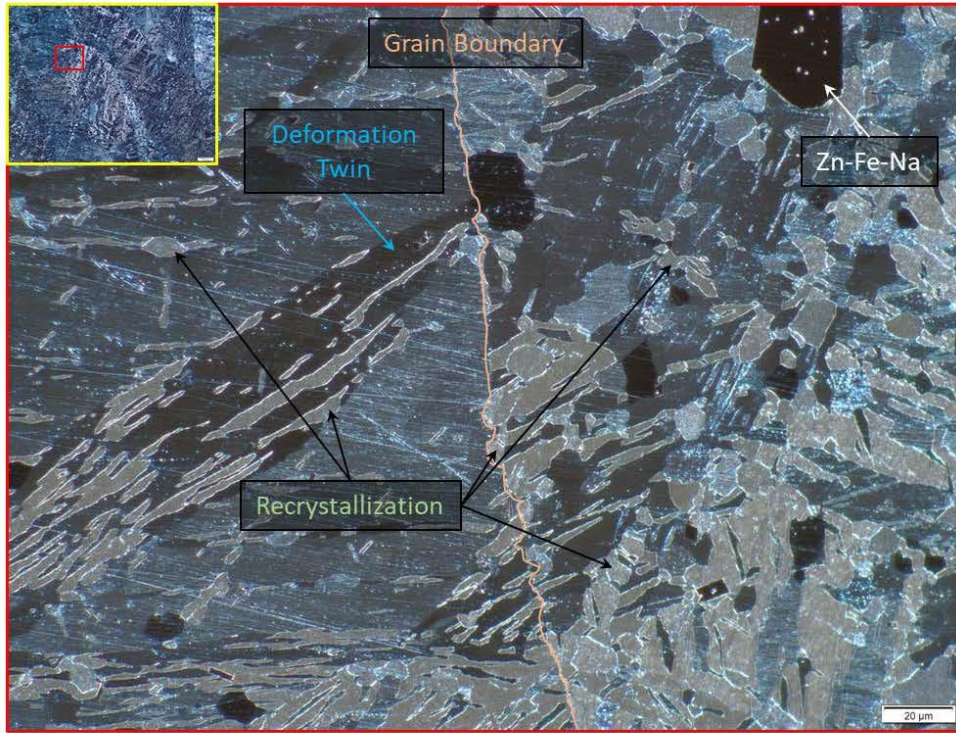


Figure 81. Metallograph image of the large grains present in Figure 78 close to the zinc casting outer diameter. Tint etch at 500X.



Figure 82. Metallograph image of the small grains present in Figure 78 adjacent to the cable/zinc slug boundary. Tint etch at 1000X.

Figure 83 looks at the cracks adjacent to the cable/zinc slug boundary near the socket base opening in closer detail with various illumination techniques. The more developed lengths of these cracks appear to be, at least, predominantly intergranular and the less developed lengths appear to have been opening up at their adjacent grain boundaries and in the process of linking up with adjacent cracks opening up at their adjacent grain boundaries. Some regions along the length, where the crack-like feature appears very broken up or "dotted", may be more appropriately characterized as individual voids.

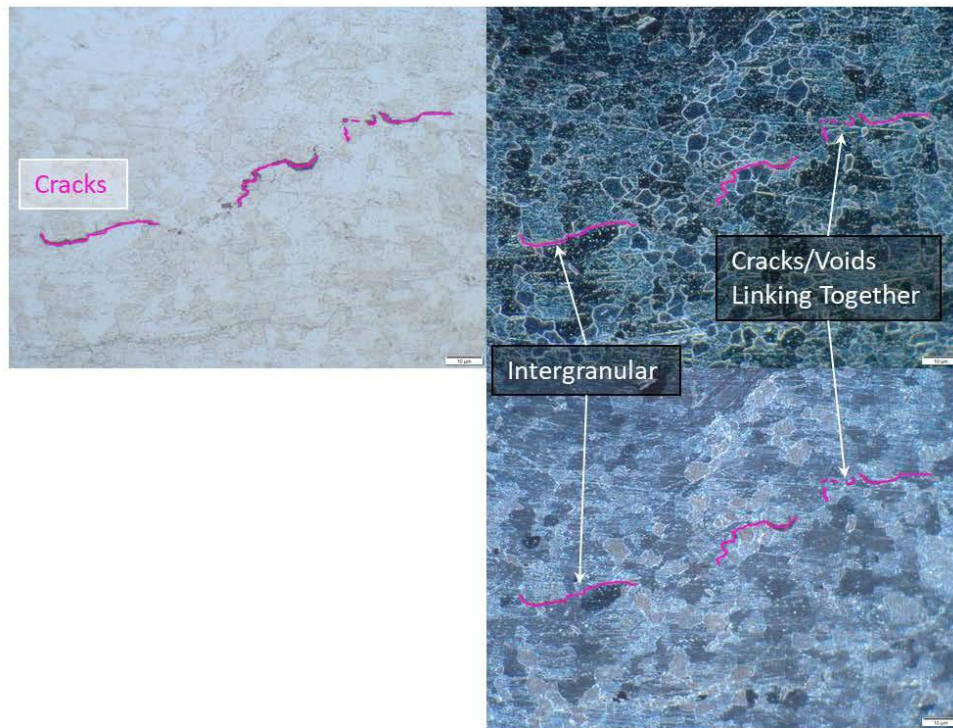


Figure 83. Close up metallograph images of cracks present in Figure 295 adjacent to the cable/zinc slug boundary. Tint etch at 1000X.

4.3.2 Transgranular Bulk Cracking

Metallographic analysis revealed cracking and voids through the bulk of the zinc. See Figure 84. The cracks and voids are meandering in appearance and varying in their gap opening along their length. They appeared interconnected and crossed through grains (transgranular), but had no particular orientation with respect to the overall socket. These cracks and voids were completely filled with zinc oxide corrosion product. Additional similar cracks can be seen in Figures 288 and 289.

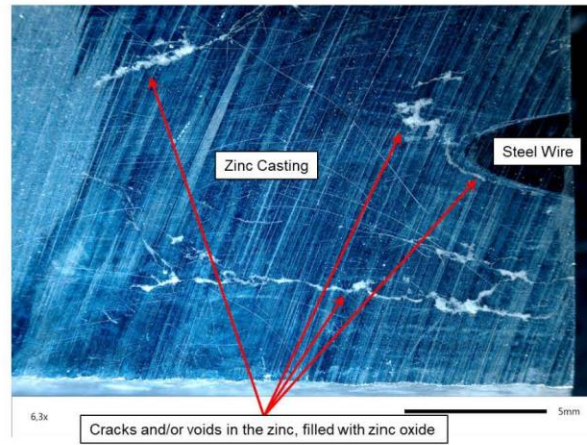


Figure 84. Cracks and voids found during metallography of slice 3c. The cracks do not follow grain boundaries, but do follow the edges of the wires. Also, the cracks and voids are filled with zinc oxide corrosion product.

4.3.3 Brittle Fracture Region

As described in Figures 63-70, the back of the socket cavity exhibits two distinct regions. One region is the heavily corroded area with wire imprints. The other region has opposing faceted surfaces, characteristic of brittle metal cleavage fracture. Further sectioning was performed to analyze this faceted structure further. Figure 85 shows the surface of an additional longitudinal cut made on slice 3a. Cracks from the faceted structure can be seen to extend along the cut surface to an embedded wire and then past the wire on towards the outer diameter of the zinc casting. Figure 86 shows how that crack joins to the central socket cavity region and connects along the tops of the wire channels from the cable-end section, just below the faceted surface. The cracks extend from the socket cavity to within an inch of the zinc casting outer diameter.

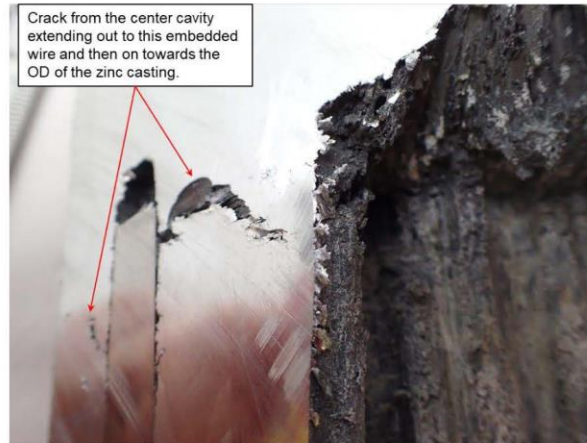


Figure 85. Surface of an additional longitudinal cut made on slice 3a. Cracks from the faceted structure can be seen to extend out from the tops of the wire channels, left from the outer diameter of the cable-end section that pull free of the socket, along the abrasive saw cut surface to an embedded wire. The crack extends past the wire, on a different transverse plane, on towards the outer diameter of the zinc casting.

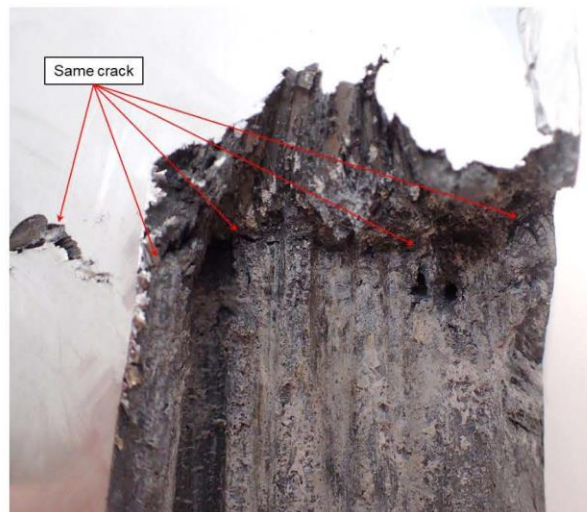


Figure 86. The crack from Figure 85 physically connects with the crack that extends around the cable-end section's interface between the faceted surface and the tops of the wire channels.

The center lower piece of the socket cavity (the piece closest to the socket base, with one side of the faceted surface feature located on the casting cap side of the piece) has wire channels that bend where the wire ends were positioned at one time (see Figure 87). The wires that were in those channels – wires EE, EF, and EG – pulled free of the socket with the cable-end section while remaining embedded in the cable/zinc slug. It is not clear whether the bending occurred when the wires were in the socket or after those wires had already been displaced from that location. Wires EE, EF, and EG in the cable/zinc slug do exhibit bending at the ends, but they also appear to have incurred additional bending, likely occurring after separating from the socket.

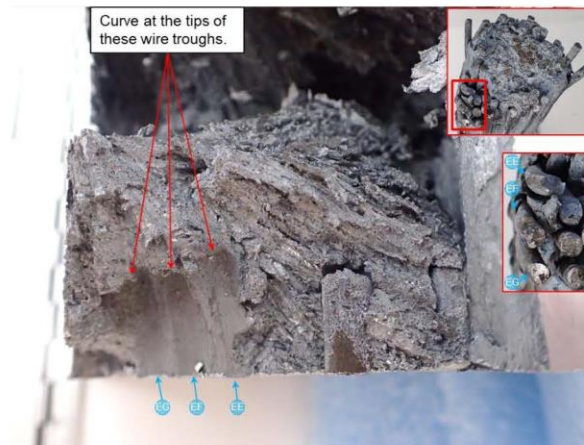


Figure 87. The center lower piece of the socket cavity (the piece closest to the socket base, with one side of the faceted surface feature located on the casting cap side of the piece) has wire channels that bend at where the wire ends were positioned at one time. The wires EE, EF, and EG, that filled those channels are seen in the inset images as-received with the cable-end section.

Figure 88 shows two of the wires embedded in the center lower piece of the socket cavity (wires AC and AB) have little to no gap between the top of the wire-ends and the zinc. Looking closer at wire AB in Figure 89, its wire channel is also visible, showing that the wire has been displaced along the wire channel, towards the socket base. This movement must have occurred at some point in time after solidification.



Figure 88. The center lower piece of the socket cavity has still embedded wires, wires AB and AC identified here, with little to no gap between the top of the wire and the surrounding zinc.



Figure 89. The center lower piece of the socket cavity has still embedded wires, with little to no gap between the top of the wire and the surrounding zinc, that have traveled an inch or more down their original wire channels towards the socket base at some point in time after solidification of the zinc casting. Wire AB and its channel are identified with arrows here.

Figures 90-94 examine a small piece of the center lower piece of the socket cavity that was broken off and labeled piece 3-1. Examination of the faceted surface revealed a number of stepped surfaces, characteristic of brittle zinc fracture (see Figure 95), and white corrosion product, most probably zinc oxide, in varying concentrations throughout.

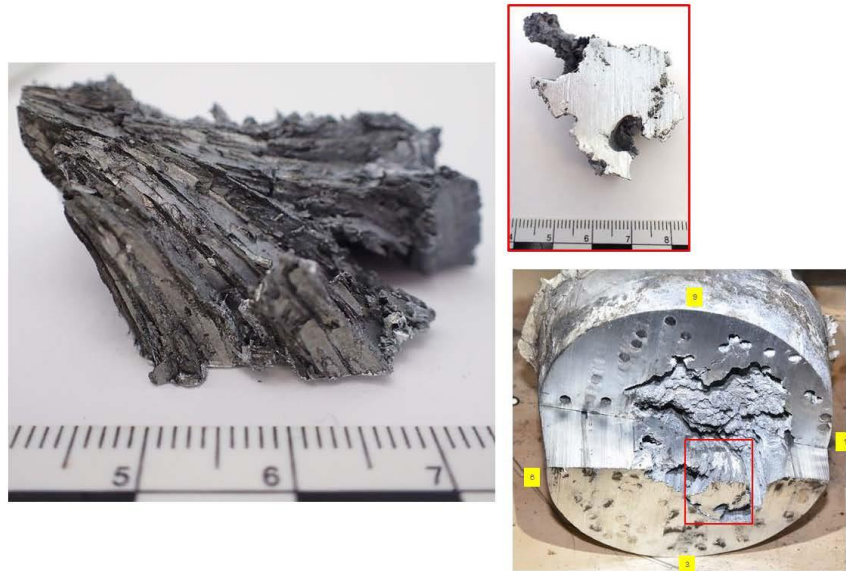


Figure 90. A small piece of the center lower piece of the socket cavity was broken off, labeled piece 3-1, and examined more closely.

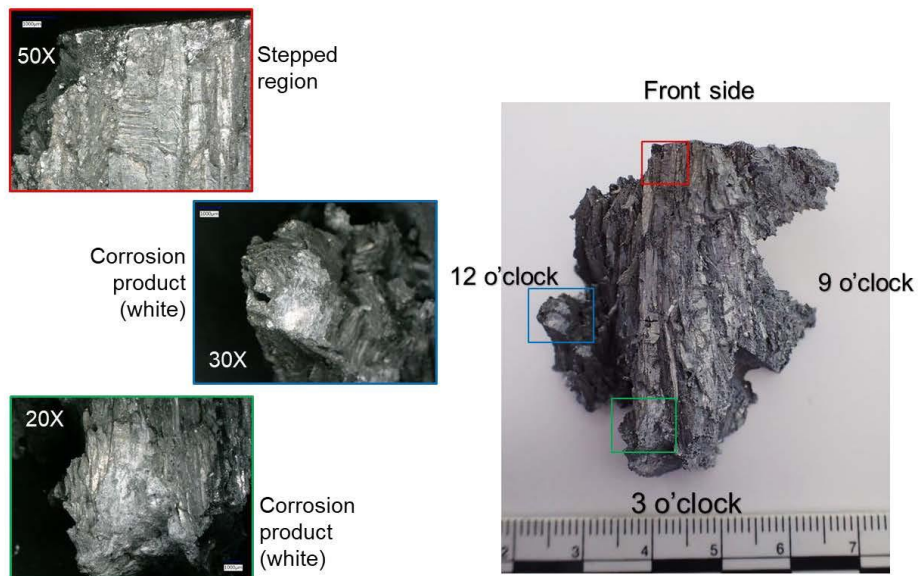


Figure 91. Examining the faceted surface on the casting cap side of Piece 3-1 by stereomicroscopy, revealed a stepped region, characteristic of zinc brittle fracture, along with lots of white corrosion product, most probably zinc oxide.

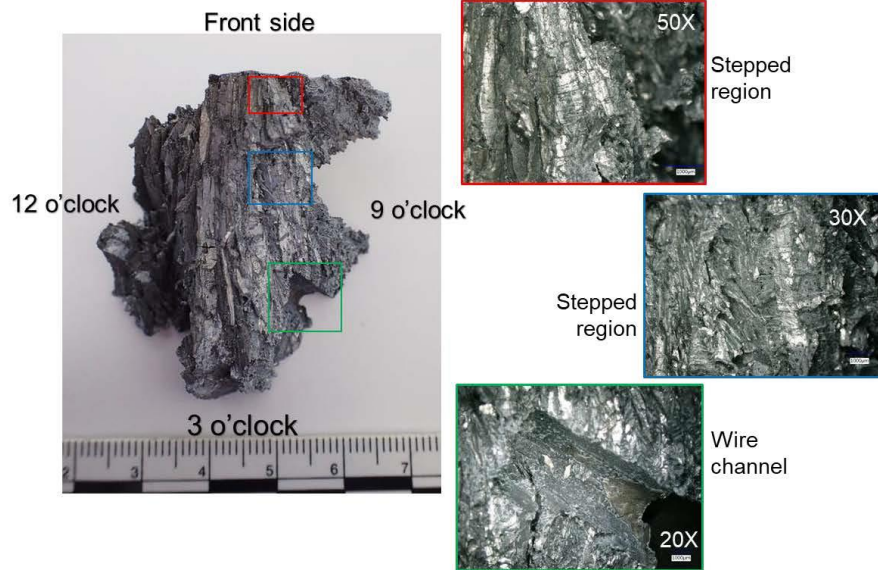


Figure 92. Additional stereomicroscope images of the faceted surface of Piece 3-1, identifying more stepped regions, characteristic of zinc brittle fracture.



Figure 93. A wire channel located on Piece 3-1 in both bright field and dark field illumination, showing the presence of white corrosion product along the wire channel.

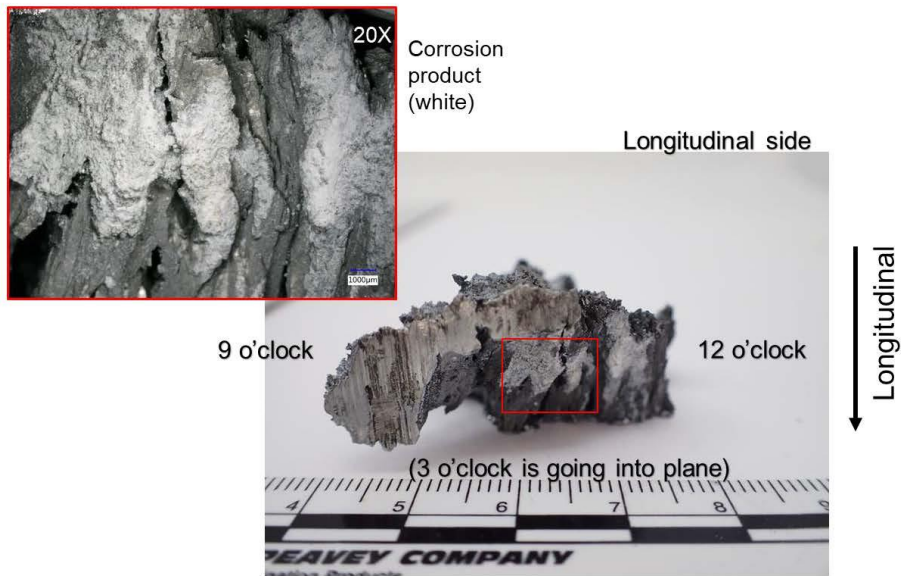


Figure 94. A location on Piece 3-1 with heavy white corrosion, likely zinc oxide. Scale in centimeters.

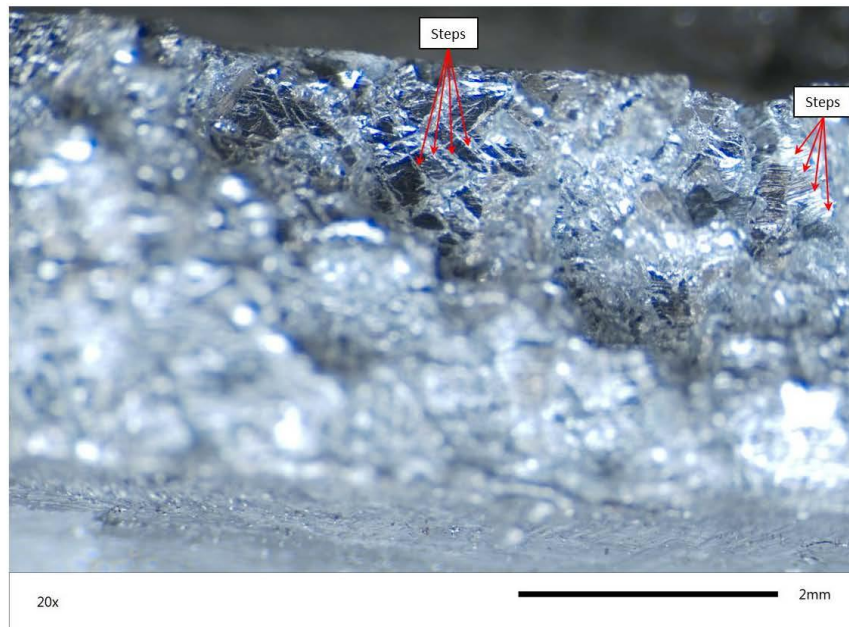


Figure 95. An exemplar that was made by applying a bending force at wire AE. The force was a non-cyclical overload force. The characteristic brittle zinc fracture surface exhibits similar stepped region features as seen on the faceted surface in Figures 91 and 92.

4.4 Corrosion

Appendix L includes the detailed results of the chemical analysis samples taken from the locations in Figures 25-29. Chemical analysis of Samples 1-3, taken from the bottom hole at the 9 o'clock position within the socket cavity, revealed zinc oxide and zinc metal, with minor amounts of zinc hydroxide. Analysis of Samples 4-13 taken from within the socket cavity, revealed trace amounts of iron, with Sample 4 – the orange-colored smear near the front of the socket base and associated with the wire that pulled out of the middle hole at the 9 o'clock position, having the highest percentage. Desk Sample 1, taken from the wet black product located at 7 o'clock between the zinc casting outer diameter and the socket cone inner diameter wall, revealed aluminum silicates. Desk Sample 2, taken from the white product located at 9 o'clock between the zinc casting outer diameter and the socket cone inner diameter wall, revealed zinc oxide and Desk Sample 3, taken from wire-end P at 11 o'clock that was embedded within the zinc but was exposed on a transverse bandsaw cut near the casting cap, revealed zinc oxide with trace amounts of iron.

Extensive zinc oxide corrosion is found between the socket inner diameter wall and the zinc casting outer diameter (see Figures 96-98). The corrosion is nearly entirely limited to the upper two-thirds of the socket wall, closest to the casting cap. The bottom third, nearest the socket base, is noticeably devoid of most corrosion product – almost perfectly aligned with the bandsaw cuts made to section off 3g and 9g. Note that all the wire fractures were located in slice 3g and 9g.

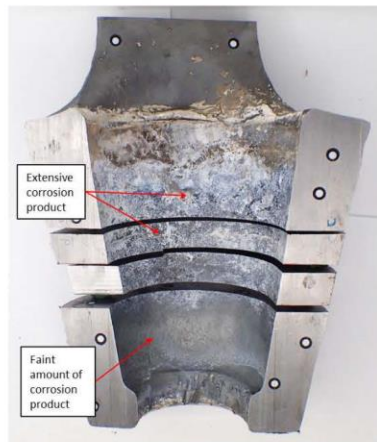


Figure 96. 3 o'clock side of the inner diameter socket wall, showing the surface behind the outer diameter of the zinc casting.

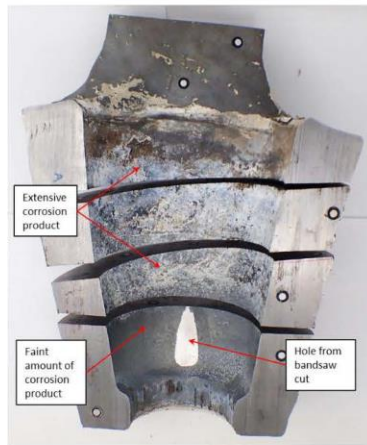


Figure 97. 9 o'clock side of the inner diameter socket wall, showing the surface behind the outer diameter of the zinc casting. Note, the bright teardrop shape in the center of the slice that was adjacent to 9g is a hole from a transverse bandsaw cut made on that socket slice. The cut passed a little too close to the inner diameter wall, leaving a hole.

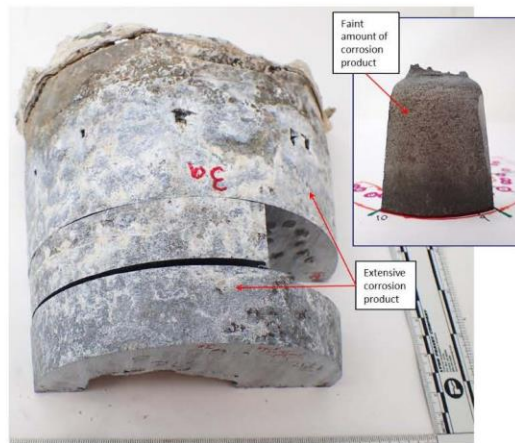


Figure 98. Outer diameter of the 3 o'clock side of the zinc casting (slices 3a, 3c, and 3e). Inset is the outer diameter from a piece of the zinc casting removed from 9g, between 9 and 10 o'clock.

Figure 99 reveals 8 wires left holes in the zinc casting outer diameter wall in slices 3a and 9a. These holes were extensively corroded, with white corrosion that is most probably zinc oxide

and orangish brown corrosion that is most probably iron oxide. Figure 100 shows a closer image of one of the wire holes, where light can be seen passing through from the inner diameter of the socket cavity. Additionally, the flow of compressed air could be felt when applied through a different hole to the inner diameter side of the zinc casting. All 8 wires of these wires fractured within the socket; none pulled free of the socket with the cable/zinc slug.



Figure 99. 8 wire holes left by wires that were broomed out and touching the inner socket wall at one time, before being displaced from their original positions towards the socket base. All 8 wires remained embedded in the zinc casting, failing within the socket. Scale in inches and centimeters.



Figure 100. Heavy corrosion around one of the wire holes that breached the zinc casting outer diameter. The bright light in the center of the hole is light coming from the center of the socket cavity.

Relatively large volumes of corrosion are found extensively along wire channels in the back of the socket cavity, as shown in Figure 101. The build up of corrosion is comparable to the densities of corrosion seen on the wire imprints in the back of the socket (see Figures 69 and 70), within the gas bubbles (see Figure 57 and Figure 72), and on the upper two-thirds of the outer wall of the zinc casting / inner wall of the socket (see Figures 96-98).



Figure 101. Extensive and relatively thick corrosion on the zinc casting wire channels.

Figures 102 and 103 look more closely at the corrosion within the wire channels. The heaviest corrosion is located along the wire channel above the wires' final resting locations. As seen in Figure 103, behind the wire is a relatively large quantity of corrosion, but not as much as is located above the wire, along the wire channel. The visible corrosion densities on the wire surface map well to the visible corrosion densities within the wire channel at the wire's final resting location.

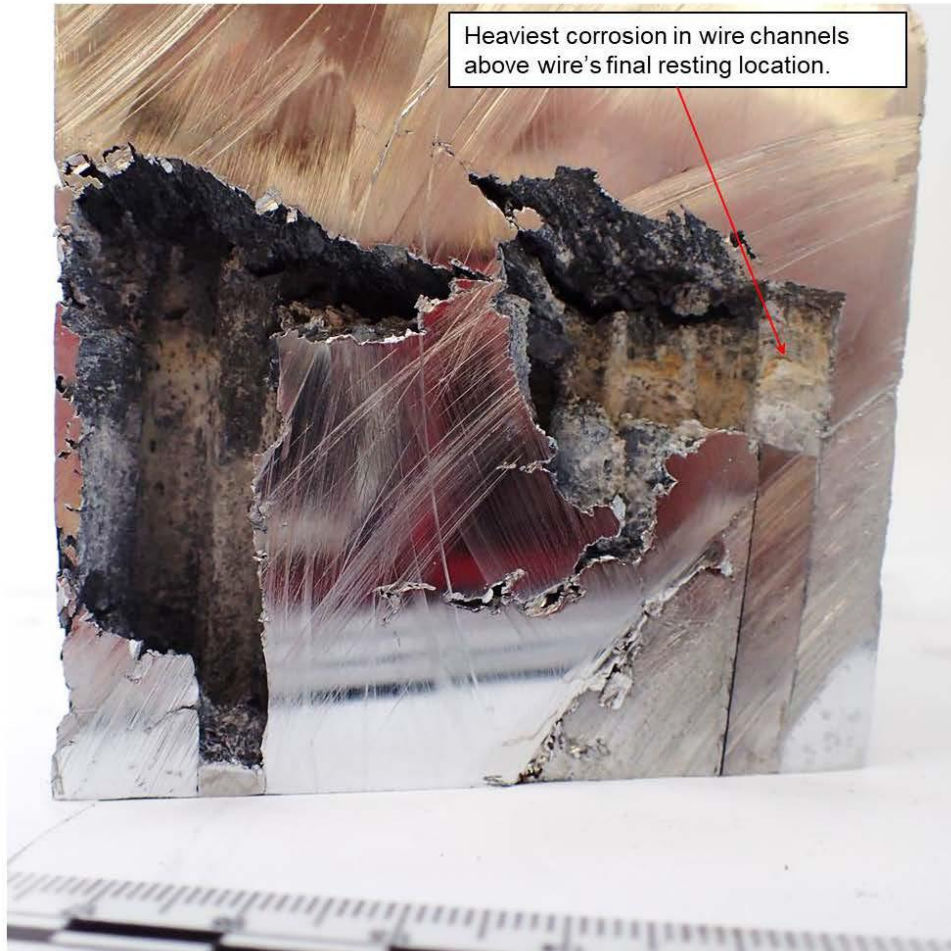


Figure 102. Relatively large volumes of corrosion were visible in the wire channels above the wires (the wire channel for Wire AN is pointed to here).

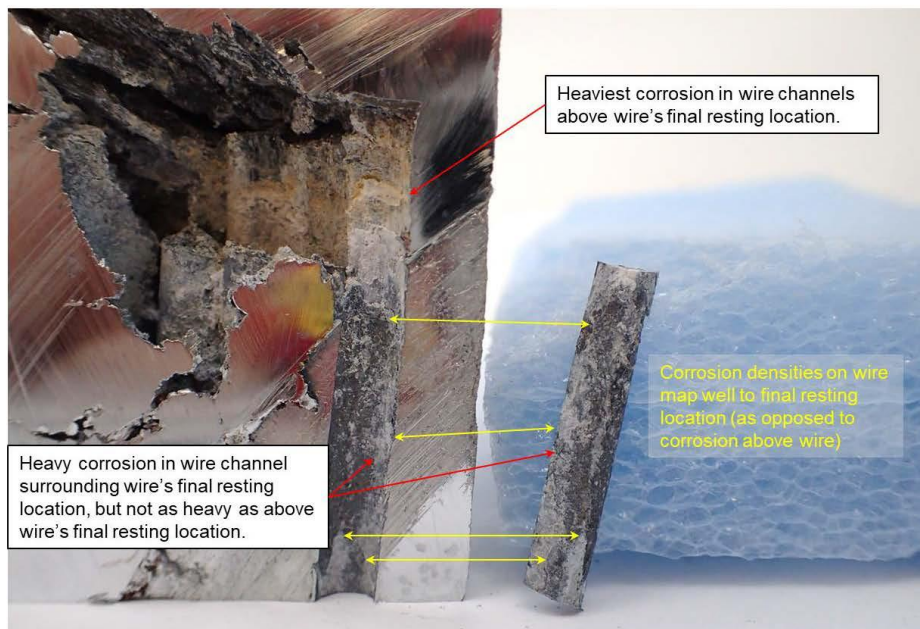


Figure 103. One of the embedded wires (wire AN) was removed from the wire channel. Behind the wire was a heavy amount of corrosion, but not as great as the quantity of corrosion above the wire, along its wire channel. The corrosion densities on the wire surface mapped well to the mating wire channel surfaces.

Looking more closely at the brittle fracture surface feature within the socket cavity, Figure 104 identifies varying amounts of corrosion. As stated earlier, there is heavy corrosion along the wire channels. Along the flat surfaces of the brittle fracture feature, there is minimal corrosion, but it does reveal a dull gray appearance and pieces taken from this region became bright and shiny after ultrasonic cleaning. The ridges and protrusions along the faceted feature exhibit an intermediate amount of corrosion product. Appendix M details an accelerated corrosion test that was performed in the coastal marine environment at KSC with a piece of the Arecibo socket from this region.

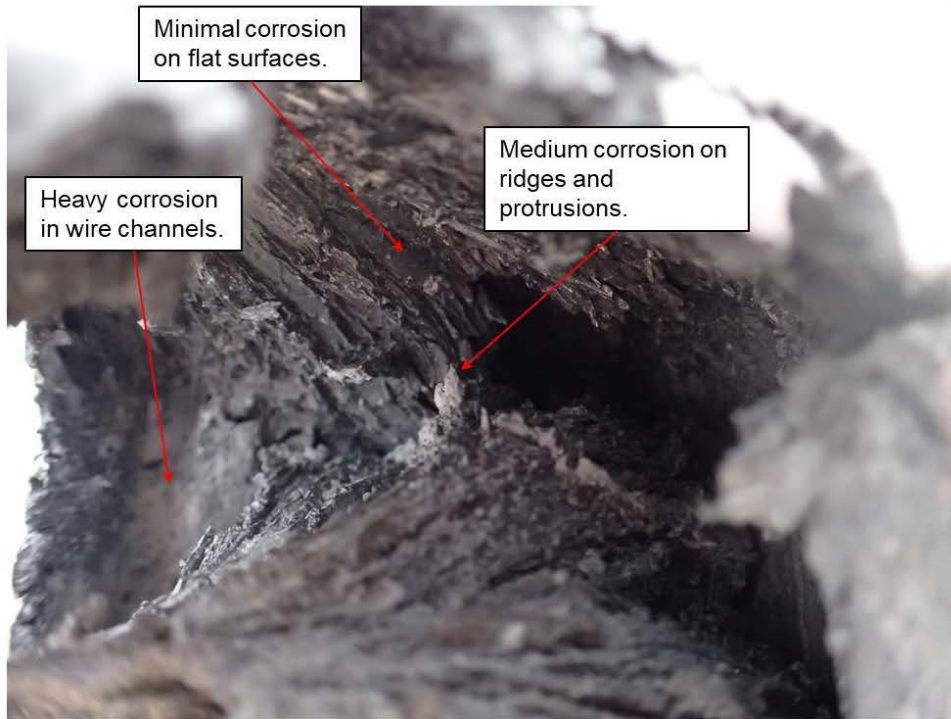


Figure 104. Image of the brittle fracture surface within the socket cavity, showing varying amounts of corrosion build up on different surfaces. The largest amounts of corrosion were seen along the wire channels. Along the faceted surface, the most corrosion build up was on ridges and protrusions, while the flat surfaces exhibited a dull gray appearance, having only a relatively light amount of corrosion.

Figures 105 and 106 show the variation in wire surface conditions encountered near the socket base. Wire AE had white corrosion product, most probably zinc oxide, along its entire length embedded within slice 3g. The quantity of corrosion was similar to what was seen on the wire

AN's wire-end in Figure 103. Wires AI and AJ both have visibly good adhesion of zinc along their wire surfaces that were embedded in slice 3g. While there is a great disparity in the corrosion product, consistent with zinc oxide, present along the surface between these two wires, all these wires failed within the socket. It should also be noted that wire AI and AJ are both inner ring wires that showed good zinc adhesion to the wires, while wire AE, along with wire N (see the fifth from the right wire in Figure 172), are both outer ring wires that showed similar quantities corrosion on the exterior of the wires. Not enough wires were examined by mechanical removal to determine if there was a pattern of outer ring wires having more corrosion product present along their lengths compared to inner ring wires.

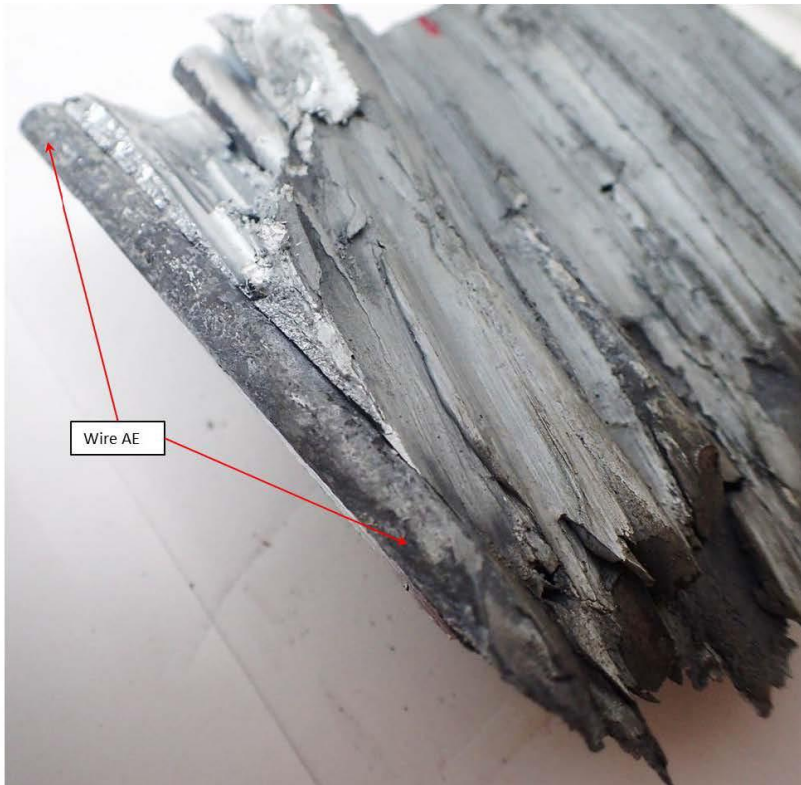


Figure 105. Wire AE, mechanically removed, showed a similar quantity of corrosion along the length of wire embedded in slice 3g as seen on wire AN in Figure 103.

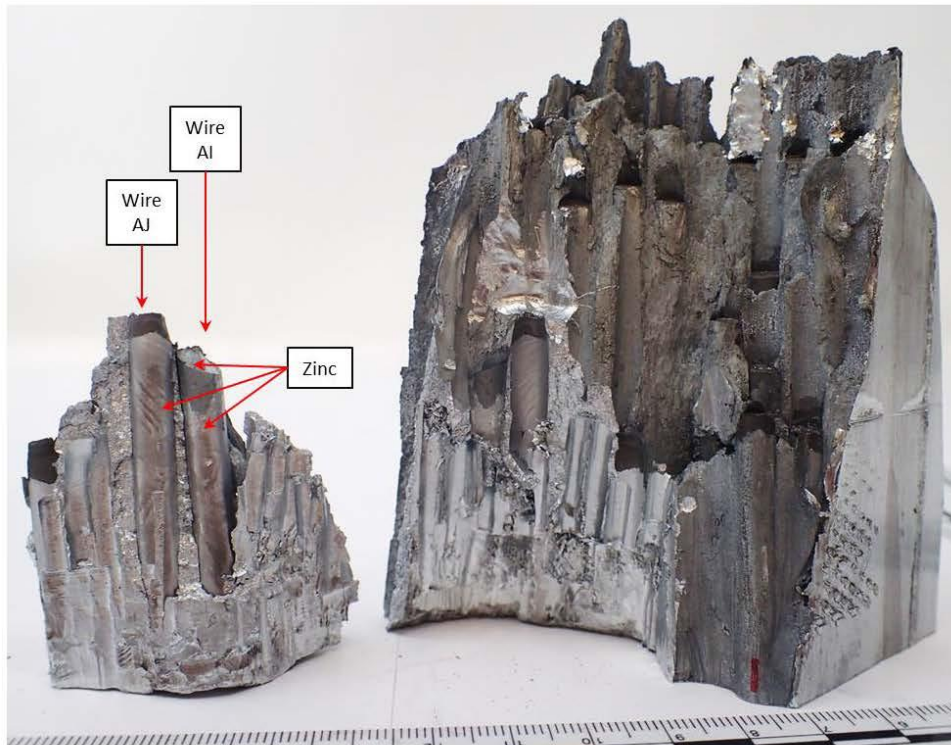


Figure 106. Wires AI and AJ both have visibly good adhesion of zinc along their wire surfaces that were embedded in slice 3g. Note that the thin layer of zinc on wire AI continues from the wire outer diameter surface onto the shear fracture surface. Scale in centimeters.

5. DISCUSSION AND/OR RECOMMENDATIONS

Due to the number of organizations collaboratively or independently performing failure analysis on the Arecibo Observatory failure, the purpose of this report is to catalog the forensic investigation results performed by KSC for reference in any comprehensive analytical reports. NASA is aggregating evidence and analysis obtained from collaborative efforts made towards this failure investigation among NESC, KSC, MSFC, WJE, and Aerospace Corporation into a comprehensive analytical NESC Report 20-01585.

6. EQUIPMENT

6.1 Metrology

40-inch Caliper (M71220)

24-inch Caliper (M71219)

12-inch Caliper (M78398)

6.2 3D Laser Scan

Creaform HandySCAN BLACK Elite (S/N 9270968)

Creaform VXElements, Version 8

3D Systems Geomagic Wrap, Version 2021

6.3 3D Print

Stratasys Objet500 C3 (S/N 570517)

ANSYS SpaceClaim, Version 2020R2

6.4 Chemical Analysis

6.4.1 OES

Bruker Q4 Tasman Spark Optical Emission Spectrometer

6.4.2 XRF Spectroscopy

Bruker S1 Titan X-ray Fluorescence Spectrometer

6.5 Microscopy

6.5.1 Stereomicroscopy

Keyence VHX-5000 Digital Microscope, S/N 8B410382

Leica MZ95 Stereoscope, S/N 4415571

6.5.2 SEM/EDS

TESCAN AMBER S8252G FIB-SEM, S/N 119-0215

Oxford ULTIM MAX 100 ESD, S/N 41055

RELATED DOCUMENTATION

- ¹ *McGormley, Jonathan C, and Brian J Santosuosso of Wiss, Janney, Elstner Associates, Inc. "Response Plan for the Arecibo Observatory Cable Failure." Received by Mr. Ramon Lugo of University of Central Florida, 12354 Research Parkway, Orlando, Florida, 1 Sept. 2020.*

- ² *Contract No. 92.146, National Astronomy and Ionosphere Center, Cornell University, Arecibo Radio Observatory, Gregorian Upgrading Engineering Drawing, Ammann & Whitney, Consulting Engineers, New York, New York, Dwg No. S-1A through S-47.*
- ³ *WJE No. 2020.5191, Wiss, Janney, Elstner Associates, Inc., Auxiliary Main Cable Socket Failure Investigation Plan, 330 Pfingsten Road, Northbrook, Illinois, 9 Oct. 2020.*
- ⁴ *Structural Strand and Wire Rope Catalog, Wire Rope Works, Inc., 2007.*
- ⁵ *KSC-PLN-2322_PDL-ALC-001 Authorized Laboratory Capability, Prototype Development Laboratory, Manufacturing and Testing, Revision B.*
- ⁶ *ASTM E1444 Standard Practice for Magnetic Particle Testing.*
- ⁷ *ASTM E1742 Standard Practice for Radiographic Examination.*
- ⁸ *ASTM E415 Standard Test Method for Analysis of Carbon and Low-Alloy Steel by Spark Atomic Emission Spectrometry.*
- ⁹ *ASTM A521 Standard Specification for Steel, Closed-Impression Die Forgings for General Industrial Use.*
- ¹⁰ *ASTM A123 Standard Specification for Zinc (Hot-Dip Galvanized) Coatings on Iron and Steel Products.*
- ¹¹ *ASTM A153 Standard Specification for Zinc Coating (Hot-Dip) on Iron and Steel Hardware.*
- ¹² *ASTM A148 Standard Specification for Steel Castings, High Strength, for Structural Purposes.*
- ¹³ *ASTM A586 Standard Specification for Metallic-Coated Parallel and Helical Steel Wire Structural Strand.*
- ¹⁴ *ASTM E1252 Standard Practice for General Techniques for Obtaining Infrared Spectra for Qualitative Analysis.*
- ¹⁵ *LASSO Nondestructive Evaluation Surface Examination Report 01 for WON Y1019673, 10 Nov. 2020.*

REVISION HISTORY

Revision	Description	Date
Basic	Basic issue	6/15/2021

Primary Investigator:


Nathan Trepal, NE-L7

Contributors:

Nicole Bolado, LASSO
Jerry Buhrow, NE-L7
Brian Cheshire, NE-L7
Dan Dupuy, LASSO
Athela Frandsen, NE-L3
Phil Howard, NE-L3
John Ivester, MSFC-EM42
Michael Lane, NE-L2
Dave Lubas, NE-L7
David McLaughlin, NE-L2
Eliza Montgomery, NE-L7
Macy Mullen, NE-L3
Michelle Pierre, NE-L7
Eric Roesler, NE-L2
Jeffrey (Jeff) Sampson, NE-L3
Jack Strieter, NE-L3
Dennis Taylor, LASSO
Elizabeth (Liz) Tomsik, NE-L7
Monroe Willis, NE-L7
Clara Wright, NE-L7

APPENDIX A. AS-RECEIVED SOCKET



Figure 107. As-received socket, clevis pin, nut, and cotter pin. Tape to protect the socket cavity during shipping is still on the socket base, on the right side of the image. Scale in inches and centimeters.



Figure 108. Top view of the socket, clevis pin, nut, and cotter pin. Scale in inches and centimeters.



Figure 109. Socket base view of the as-received socket, with the threads of the clevis pin, nut, and cotter pin visible in the back left of the image. Scale in inches and centimeters.



Figure 110. View into the socket cavity of the as-received socket. Scale in inches and centimeters.

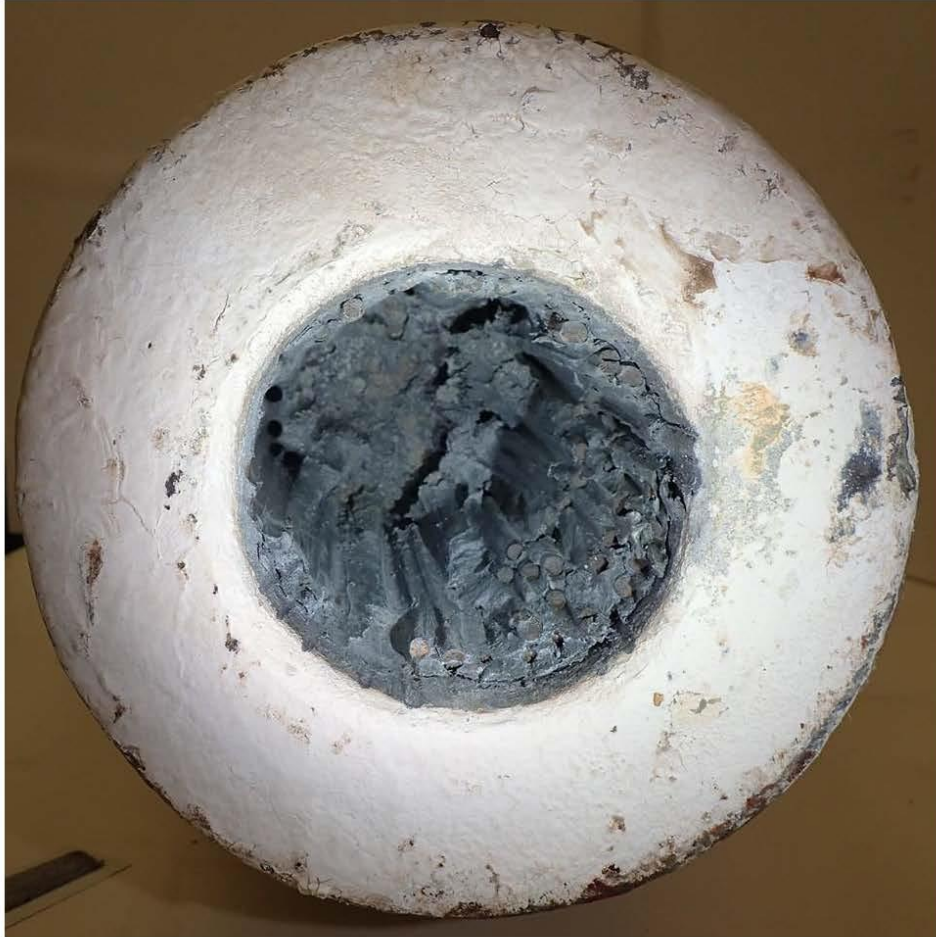


Figure 111. View into the socket cavity of the as-received socket.



Figure 112. View into the socket cavity of the as-received socket. Scale in inches and centimeters.



Figure 113. View into the back of the socket cavity of the as-received socket.



Figure 114. View of the casting cap of the as-received socket. Scale in inches and centimeters.



Figure 115. View of the casting cap of the as-received socket. Scale in inches.



Figure 116. View of the 9 o'clock side of the as-received socket, including the clevis pin, nut, and cotter pin. Note, tape on the front of the socket base is visible on the right side of the image, which was there to protect the cavity during shipment. Scale in inches and centimeters.



Figure 117. Close up view, from the socket base side of the socket, of the nut and outside of the 9 o'clock clevis tang of the as-received socket.



Figure 118. Close up view, from the casting cap side of the socket, of the nut and outside of the 9 o'clock clevis tang of the as-received socket.



Figure 119. Close up view of the clevis pin and inside of the 9 o'clock clevis tang of the as-received socket.



Figure 120. Close up view, from the socket base side of the socket, of the clevis pin and inside of the 9 o'clock clevis tang of the as-received socket.



Figure 121. Close up view, from the casting cap side of the socket, of the clevis pin and inside of the 9 o'clock clevis tang of the as-received socket.



Figure 122. Close up view, from the casting cap side of the socket, of the clevis pin and inside of the 9 o'clock clevis tang of the as-received socket.



Figure 123. Close up view, from the socket base side of the socket, of the clevis pin and inside of the 3 o'clock clevis tang of the as-received socket.



Figure 124. Close up view, from the socket base side of the socket, of the clevis pin and inside of the 3 o'clock clevis tang of the as-received socket.



Figure 125. Close up view, from the casting cap side of the socket, of the clevis pin and inside of the 3 o'clock clevis tang of the as-received socket.



Figure 126. Close up view, from the casting cap side of the socket, of the clevis pin and inside of the 3 o'clock clevis tang of the as-received socket.



Figure 127. View, from the socket base side of the socket, of the clevis pin and outside of the 3 o'clock clevis tang of the as-received socket.



Figure 128. Close up view, from the socket base side of the socket, of the clevis pin and outside of the 3 o'clock clevis tang of the as-received socket.



Figure 129. Close up view, from the socket base side of the socket, of the clevis pin and outside of the 3 o'clock clevis tang of the as-received socket.



Figure 130. Close up view, from the casting cap side of the socket, of the clevis pin and outside of the 3 o'clock clevis tang of the as-received socket.



Figure 131. Close up view, from the casting cap side of the socket, of the clevis pin and outside of the 3 o'clock clevis tang of the as-received socket.



Figure 132. View, from the casting cap side of the socket, of the clevis pin and outside of the 3 o'clock clevis tang of the as-received socket.



Figure 133. View, looking towards the casting cap, of the bottom of the 3 o'clock side of the as-received socket. Scale in inches and centimeters.



Figure 134. View, looking towards the casting cap, of the 9 o'clock side of the as-received socket.



Figure 135. View, looking towards the casting cap, of the bottom of the 9 o'clock side of the as-received socket. Scale in inches and centimeters.



Figure 136. View of the 9 o'clock clevis tang hole of the as-received socket.



Figure 137. View of the 9 o'clock clevis tang hole of the as-received socket.



Figure 138. View of the 9 o'clock clevis tang hole of the as-received socket.



Figure 139. View of the 9 o'clock clevis tang hole of the as-received socket.



Figure 140. View of the 3 o'clock clevis tang hole of the as-received socket.



Figure 141. View of the 3 o'clock clevis tang hole of the as-received socket.



Figure 142. View of the clevis pin, nut, and cotter pin of the as-received socket.



Figure 143. View of the clevis pin, nut, and cotter pin of the as-received socket.



Figure 144. View of the clevis pin, nut, and cotter pin of the as-received socket.



Figure 145. View of the clevis pin, nut, and cotter pin of the as-received socket.

APPENDIX B. AS-RECEIVED CABLE-END SECTION



Figure 146. 6 o'clock side of the as-received cable-end section. Scale in inches and centimeters.



Figure 147. 7 o'clock side of the as-received cable-end section. Scale in inches and centimeters.



Figure 148. 11 o'clock side of the as-received cable-end section. Scale in inches and centimeters.



Figure 149. 4 o'clock side of the as-received cable-end section. Scale in inches and centimeters.



Figure 150. Top of the as-received cable-end section, which would have been the end of the cable embedded in the socket, prior to failure. The top of the image roughly corresponds with 12 o'clock, and 9 o'clock on the right-side of the image.



Figure 151. Top of the as-received cable-end section. The top of the image roughly corresponds with 12 o'clock, and 9 o'clock on the right-side of the image.



Figure 152. Close up view of the top of the as-received cable-end section. The top of the image roughly corresponds with 12 o'clock, and 9 o'clock on the right-side of the image.

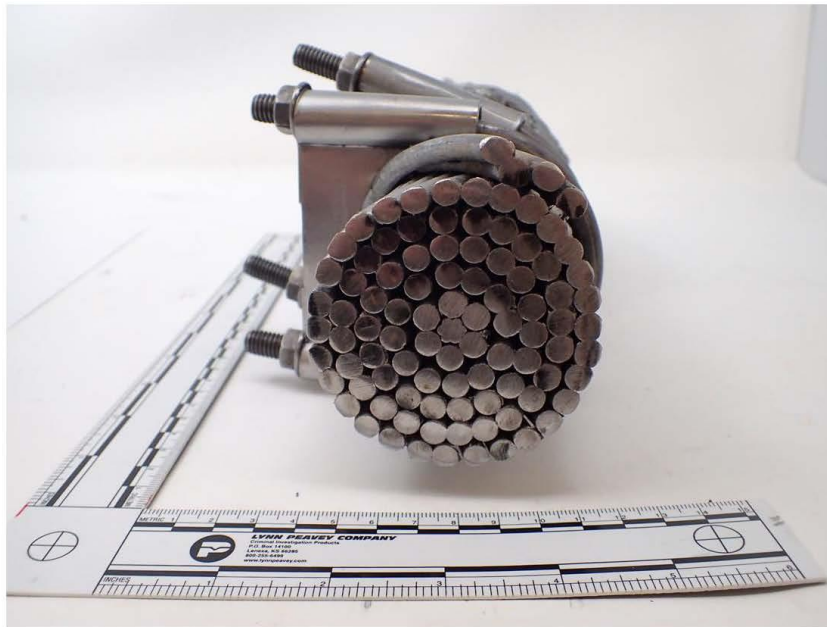


Figure 153. Bottom of the cable-end section, which is a cross-sectional cut taken a few inches outside of the socket base, towards the Feed Platform. The top of the image roughly corresponds with 2 o'clock, and 5 o'clock on the right-side of the image. Scale in inches and centimeters.



Figure 154. Close up view of a couple wire fractures on the 12 o'clock side of the cable-end section.



Figure 155. View looking down the 12 o'clock side of the cable-end section, towards the Feed Platform end.
Scale in inches and centimeters.



Figure 156. Close up view of a wire fracture on the 2 o'clock side of the cable-end section.



Figure 157. Close up view of wire fractures on the 3 o'clock side of the cable-end section.



Figure 158. Close up view of wire fractures on the 4 o'clock side of the cable-end section.



Figure 159. Close up view of wire fractures on the 5 o'clock side of the cable-end section.

APPENDIX C. TEST OF CATHODIC PROTECTION OF STEEL FRACTURE SURFACE

A wire test specimen was created by taking an intact wire from the cable-end section and tensile testing the wire to create a fracture surface. The wire end opposite the fracture surface was cut into a V-shape and then laid into a V-groove channel cut into a piece of zinc, taken from the mid-depth within the socket. The wire was secured to the zinc with a thin stainless steel wire and laid horizontally into the beaker with the HCl acid, such that, as the zinc was corroded by the HCl acid, the wire end laying in the zinc V-groove would stay in electrical contact due to its own gravitational weight. The following before and after images were taken to observe how well the fracture surface was cathodically protected after a couple hours of immersion. The images were taken on two different scanning electron microscopes and the before images were not as sharp as the after. Each before and after were taken in approximately the same location; matching macroscopic features are highlighted in each set of images. Overall assessment is that there may have been some pitting that occurs on the fracture surface, but it is not evident until at least 2,500X magnification.

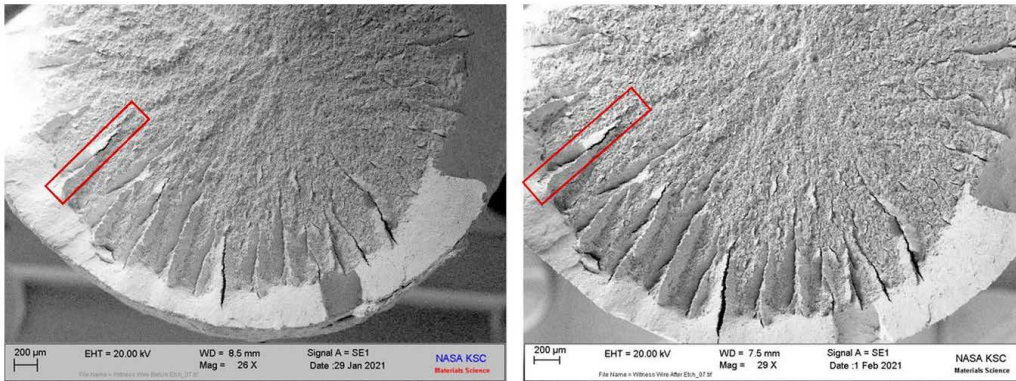


Figure 160. SEM images of the cathodic protection test specimen examined before (left) and after (right) HCl acid immersion. Note the magnifications are slightly different in these two images: 26x on the left and 29x on the right. The red boxes identify a matching feature in both images as an aid for comparing the images.

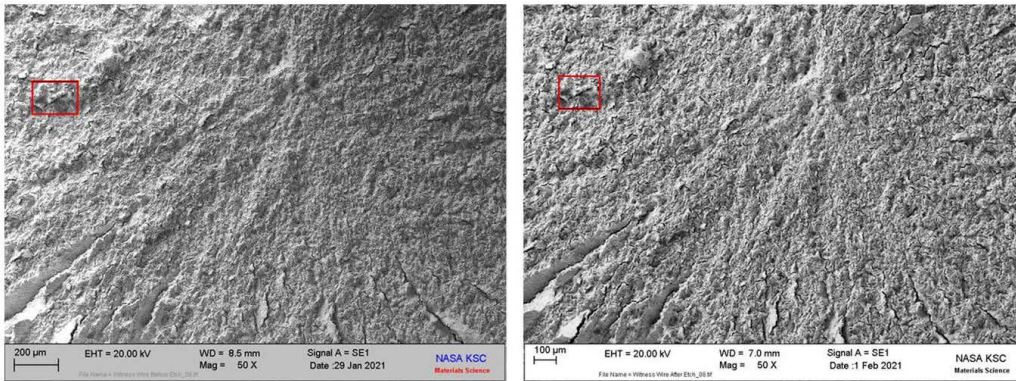


Figure 161. SEM images of the cathodic protection test specimen examined before (left) and after (right) HCl acid immersion at 50X magnification. The red boxes identify a matching feature in both images as an aid for comparing the images.

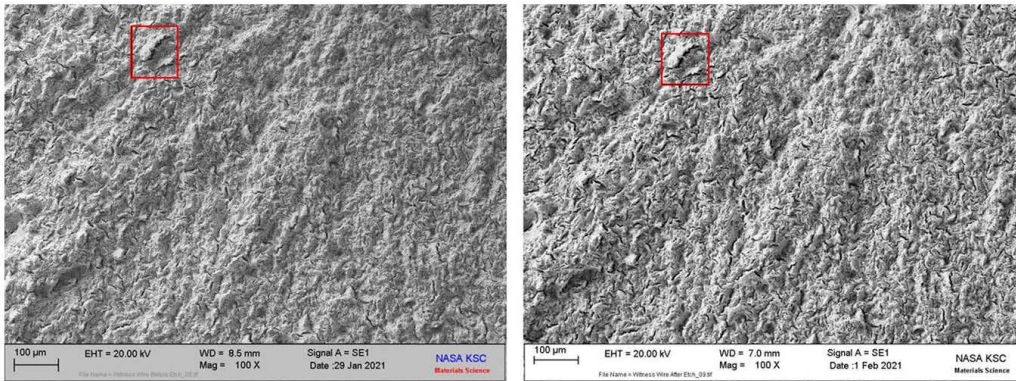


Figure 162. SEM images of the cathodic protection test specimen examined before (left) and after (right) HCl acid immersion at 100X magnification. The red boxes identify a matching feature in both images as an aid for comparing the images.

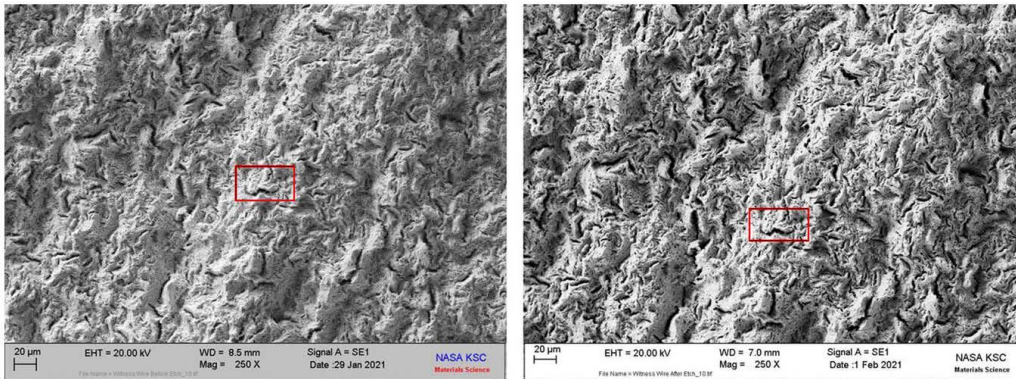


Figure 163. SEM images of the cathodic protection test specimen examined before (left) and after (right) HCl acid immersion at 250X magnification. The red boxes identify a matching feature in both images as an aid for comparing the images.

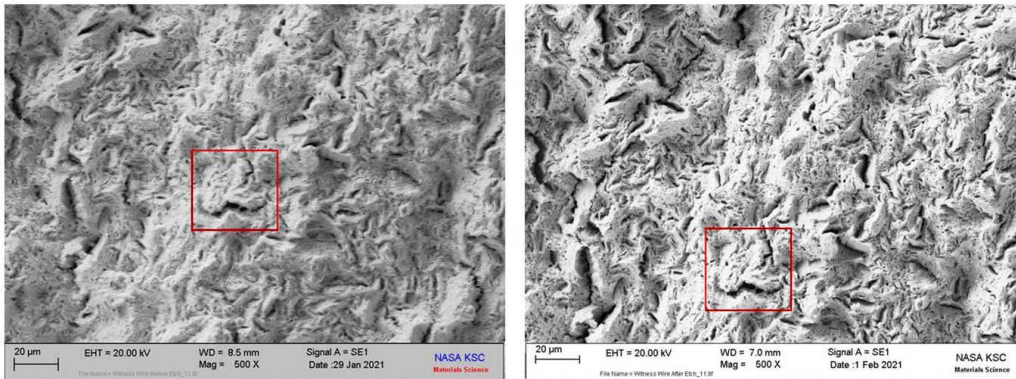


Figure 164 SEM images of the cathodic protection test specimen examined before (left) and after (right) HCl acid immersion at 500X magnification. The red boxes identify a matching feature in both images as an aid for comparing the images.

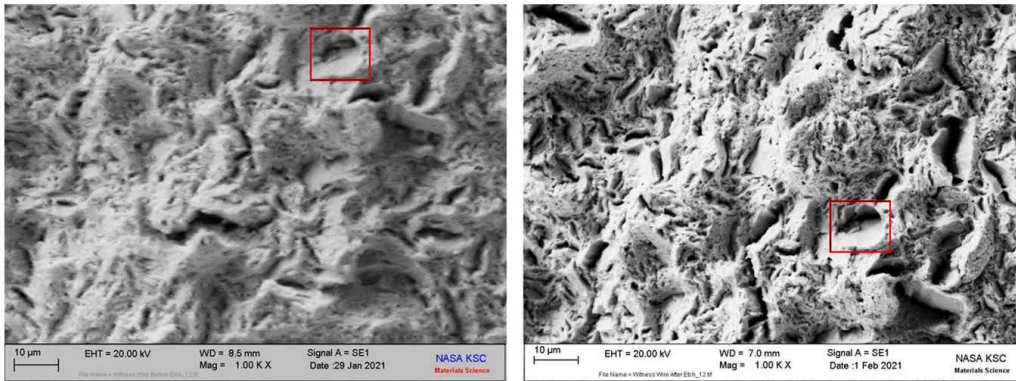


Figure 165. SEM images of the cathodic protection test specimen examined before (left) and after (right) HCl acid immersion at 1,000X magnification. The red boxes identify a matching feature in both images as an aid for comparing the images.

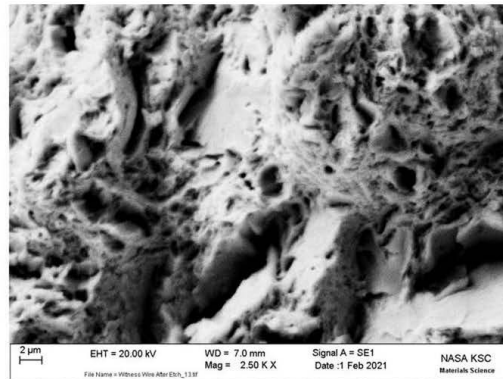


Figure 166. SEM image of the cathodic protection test specimen examined after HCl acid immersion at 2,500X magnification. No before HCl acid immersion image was made.

APPENDIX D. HCL ZINC REMOVAL

D.1 Slice 3g



Figure 167. HCl acid wire fracture reveal on slice 3g. Note that the wire oxidation is from flash rusting between removal from the acid bath, cleaning, and then drying. For comparison, the small piece in the center front was mechanically removed, rather than being partially immersed in the acid like the remaining sections.



Figure 168. HCl acid wire fracture reveal on slice 3g.



Figure 169. HCl acid wire fracture reveal on slice 3g.



Figure 170. HCl acid wire fracture reveal on slice 3g.



Figure 171. HCl acid wire fracture reveal on slice 3g.

D.2 Slice 9g

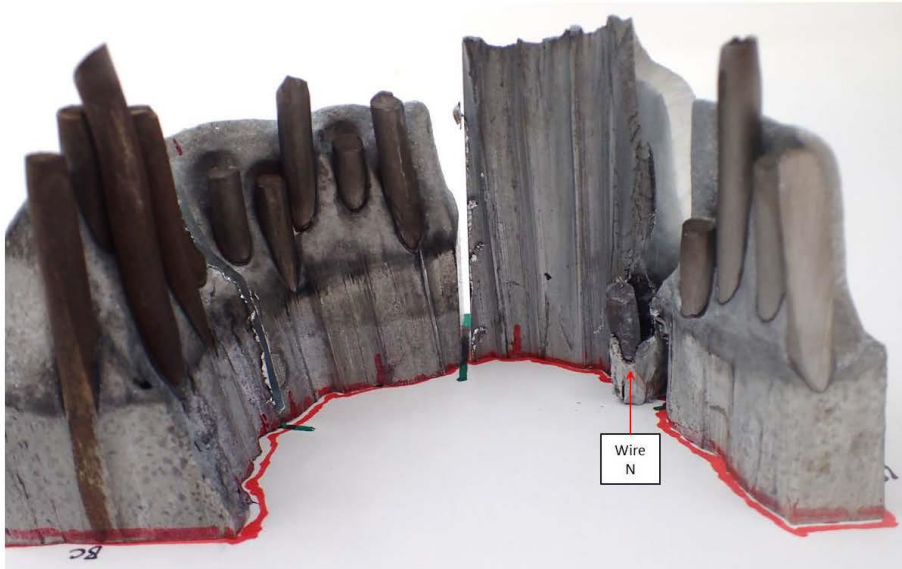


Figure 172. HCl acid wire fracture reveal on slice 9g. Note that the 9-10 o'clock piece was not acid etched and the one wire within that piece, wire N, was mechanically removed.

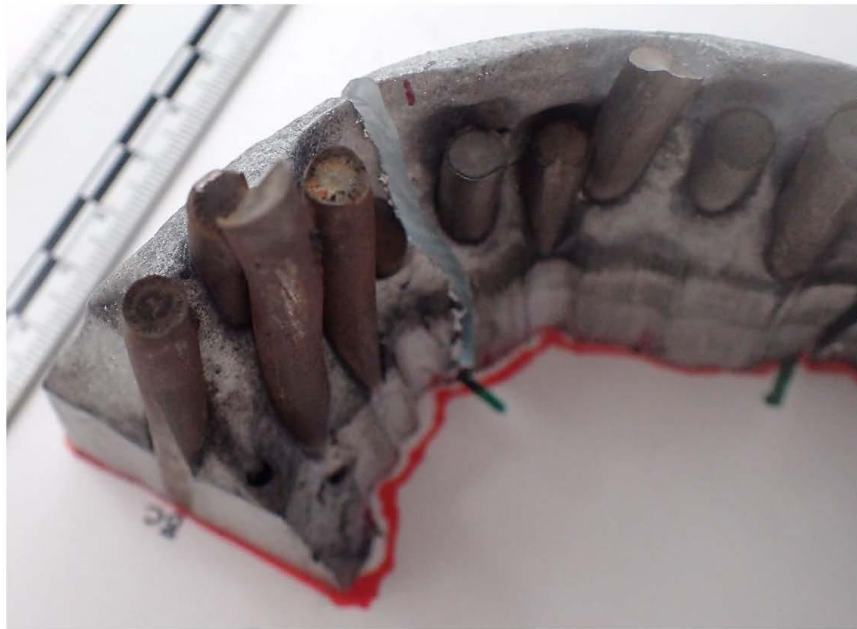


Figure 173. HCl acid wire fracture reveal on slice 9g.



Figure 174. HCl acid wire fracture reveal on slice 9g.

APPENDIX E. 3D LASER SCAN

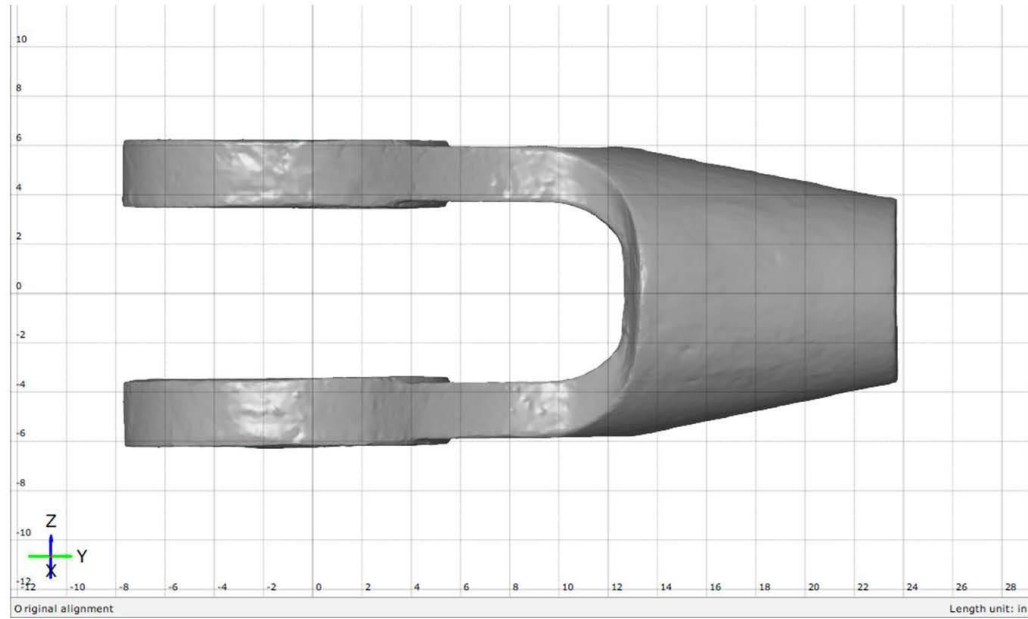


Figure 175. Laser scan of the as-received M4N socket, top view.

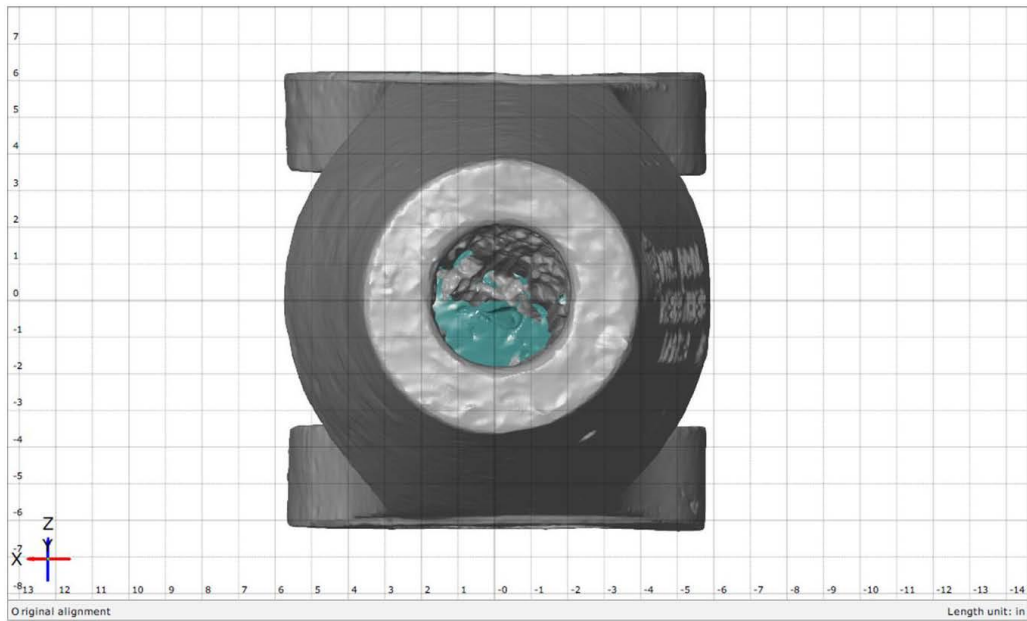


Figure 176. Laser scan of the as-received M4N socket, socket base view with the top of the socket on the left side of this image.

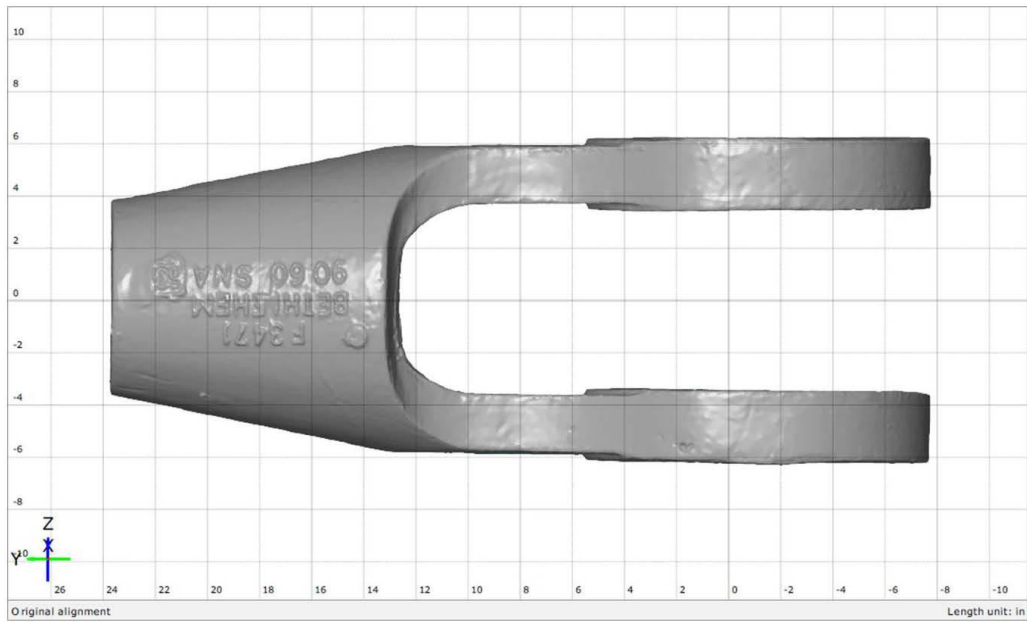


Figure 177. Laser scan of the as-received M4N socket, bottom view.

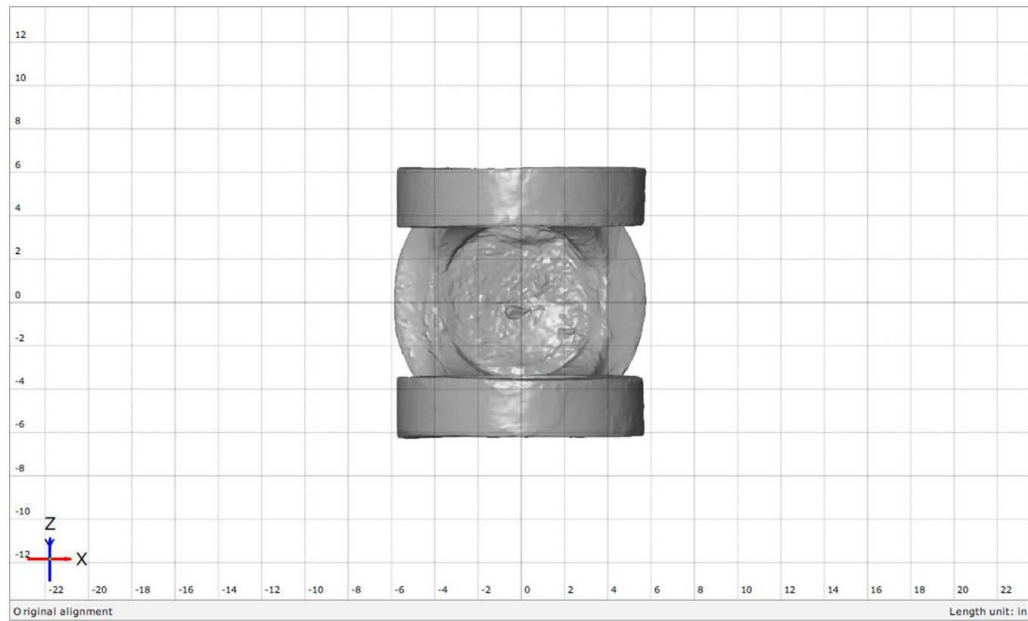


Figure 178. Laser scan of the as-received M4N socket, casting cap view with the top of the socket on the right side of this image.

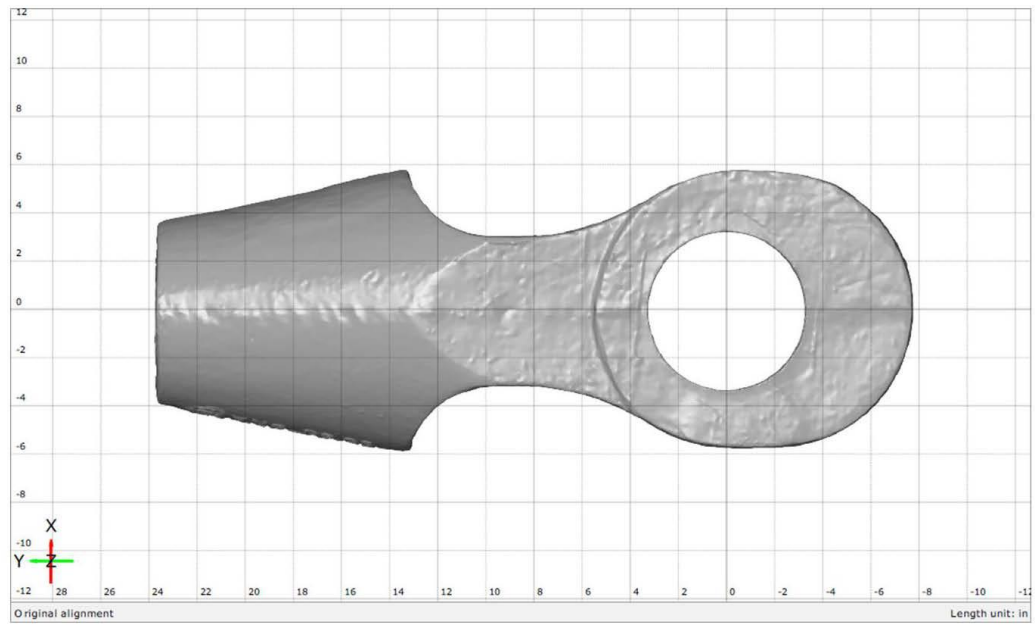


Figure 179. Laser scan of the as-received M4N socket, 3 o'clock side view with the top of the socket on the top side of this image.

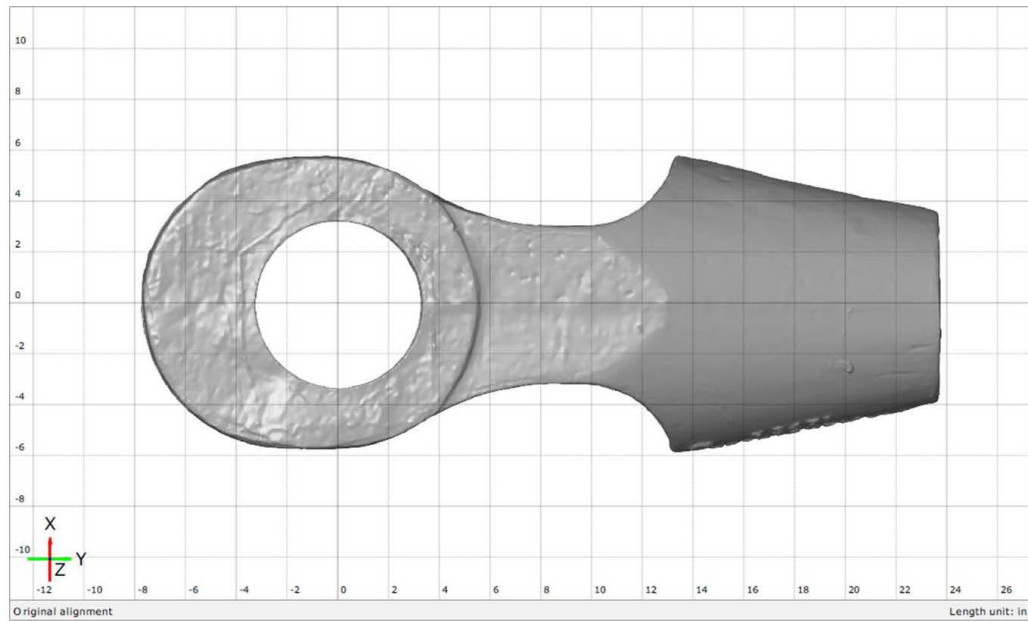


Figure 180. Laser scan of the as-received M4N socket, 9 o'clock side view with the top of the socket on the top side of this image.

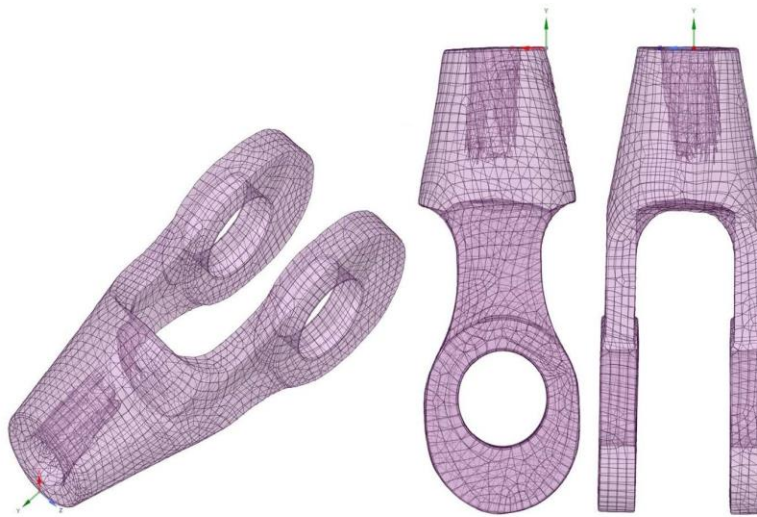


Figure 181. Wire-frame view of the laser scan of the as-received M4N socket. From left to right are an isometric projection, 9 o'clock view with the top on the left side of the wire-frame, and bottom view. Note that the imaging of the socket internal cavity was limited in these scans due to accessibility. Laser scanning requires line-of-site by the multiple lasers on the scanning equipment. The cavity was not large enough to place the scanner into the socket cavity. Plus, the laser scanner requires a stand-off distance to accurately measure variations along a surface. Additionally, the metallic surfaces are reflective, which can cause difficulties in obtaining accurate topographic data where the laser light may reflect of more than one surface before returning to the scanners detectors.

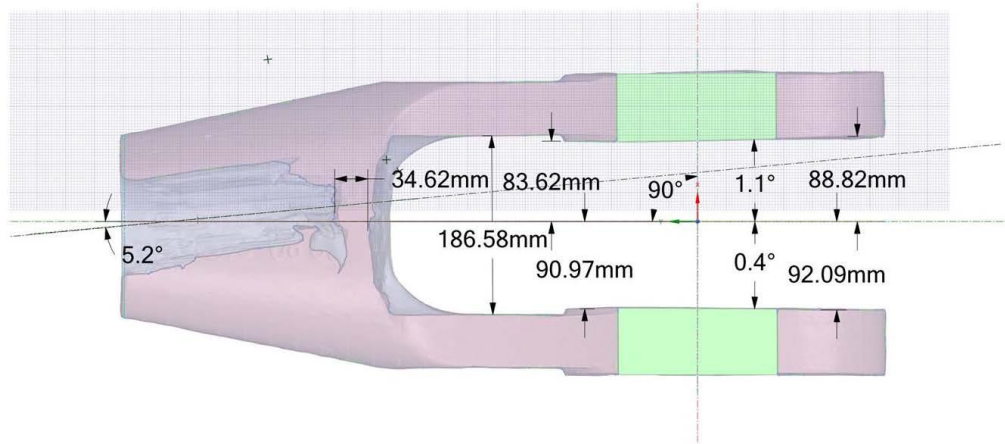


Figure 182. Some measurements taken from the 3D laser scan of the as-received M4N socket. Top view is shown. Note that, all these measurements should be considered approximations to less precision than shown. Not only is the topographic data of the socket cavity limited, but the cavity is an irregularly-shaped volume that is approximately described as a skewed-cylinder only for descriptive purposes. Additionally, the socket is a casting with surface irregularity that leads to difficulty in defining a surface plane or point from which to draw a measurement from and to.

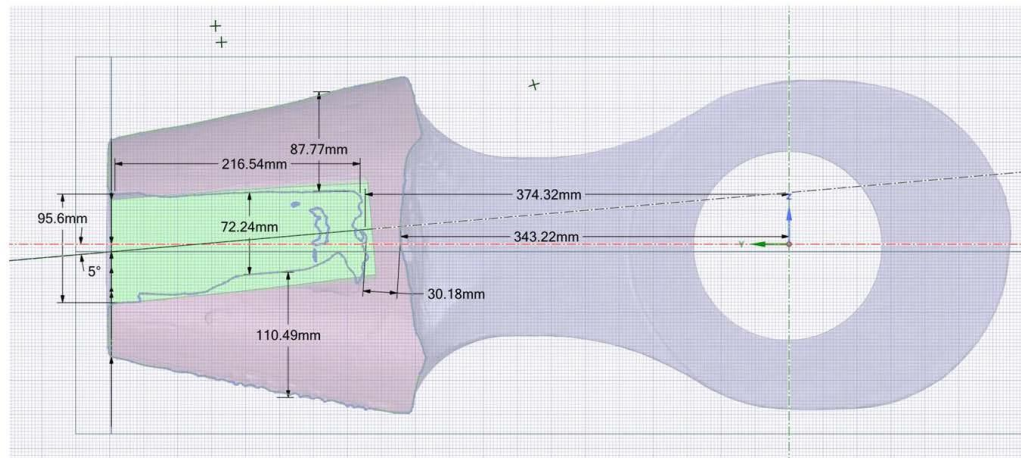


Figure 183. Some measurements taken from the 3D laser scan of the as-received M4N socket. 3 o'clock view is shown. Note that, all these measurements should be considered approximations to less precision than shown. Not only is the topographic data of the socket cavity limited, but the cavity is an irregularly-shaped volume that is approximately described as a skewed-cylinder only for descriptive purposes. Additionally, the socket is a casting with surface irregularity that leads to difficulty in defining a surface plane or point from which to draw a measurement from and to.

APPENDIX F. 3D PRINTS

F.1 Negative 3D Print of Socket Cavity



Figure 184. Side photographs of the negative 3D print of the socket cavity generated from the 3D laser scan of the socket. The back of the socket cavity is at the top of these images. The front of the socket cavity, in plane with the socket base, is at the bottom of these images.

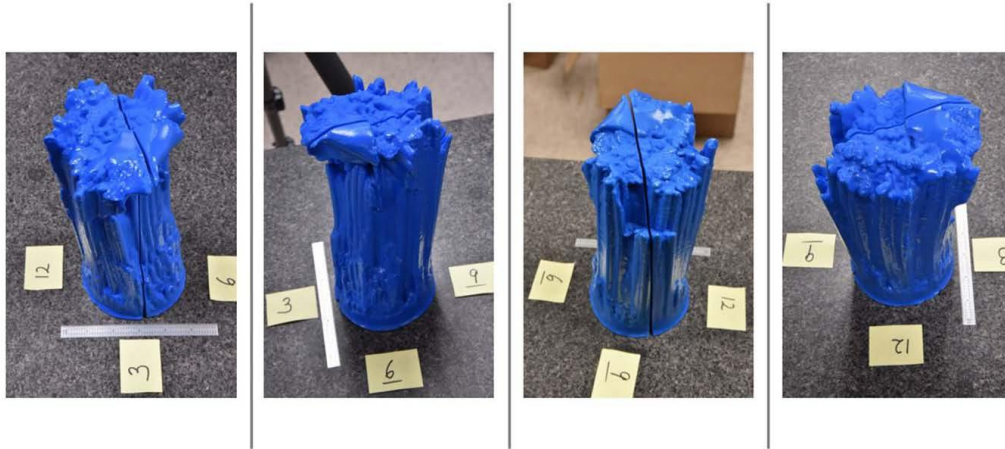


Figure 185. Oblique angle photographs of the negative 3D print of the socket cavity. The back of the socket cavity is at the top of these images. The front of the socket cavity, in plane with the socket base, is resting on the table.

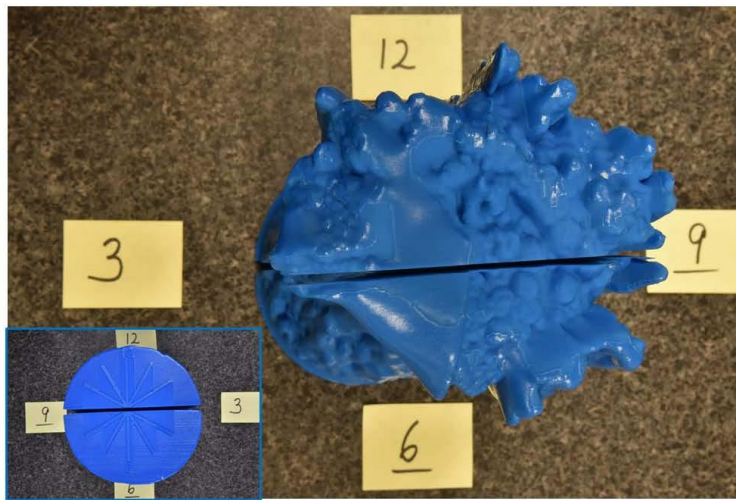


Figure 186. Top down photograph of the negative 3D print of the socket cavity, which is the back of the socket cavity. Inset is the opposite side of the 3D print, which is the front of the socket cavity, in plane with the socket base.

F.2 Positive 3D Print of Socket Cavity



Figure 187. Photographs of the positive 3D print of the socket cavity, zinc casting, and portion of the socket base generated from the 3D laser scan of the socket. The left image is looking into the cavity from the socket base side and 12 o'clock is at the top of the image. The right image is looking at the bottom of the socket, with 9 o'clock on the left side of the image and the socket base at the top of the image. Scale in inches.



Figure 188. Interior view of the socket cavity of the positive 3D print. The socket base is at the top of the image. Scale in inches.

APPENDIX G. WIRE LABELING AND TRACING

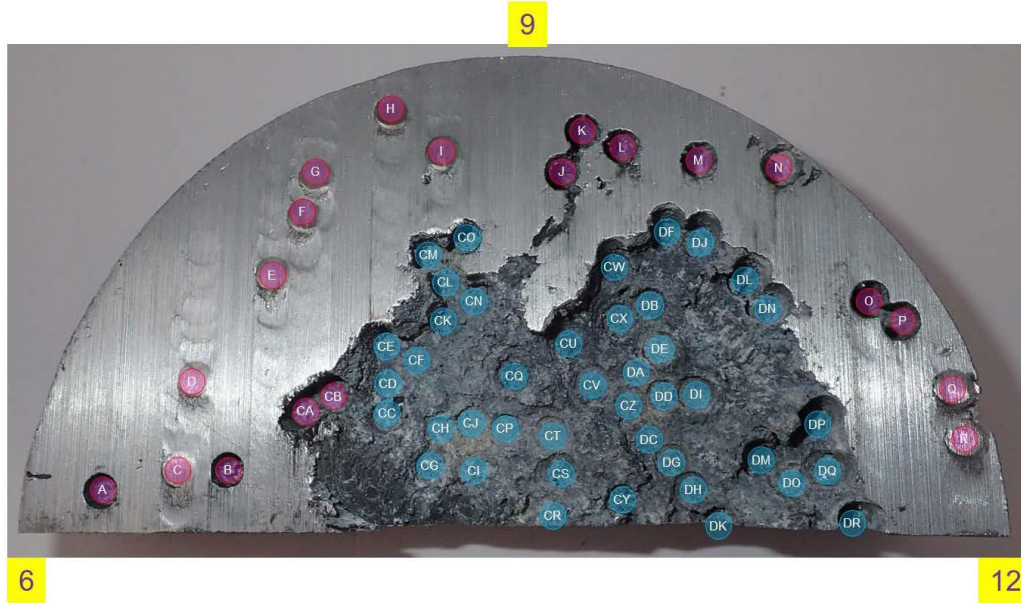


Figure 189. Wire map of the socket base side of slice 9a. Pink wire labels are wires that fractured within the socket and blue wire labels are wires that remained intact.

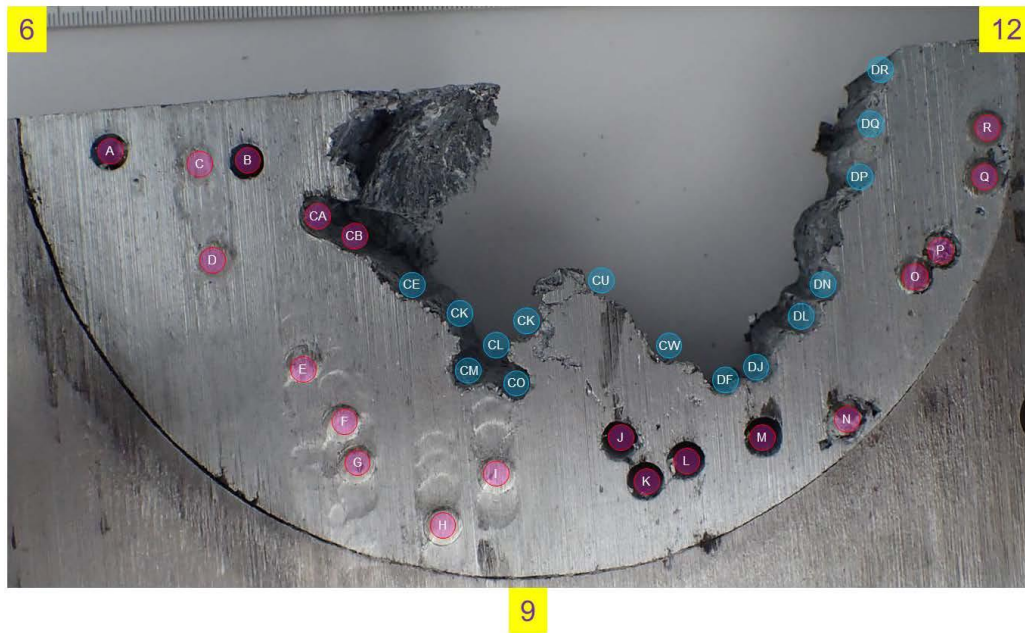


Figure 190. Wire map of the casting cap side of slice 9c. Pink wire labels are wires that fractured within the socket and blue wire labels are wires that remained intact.

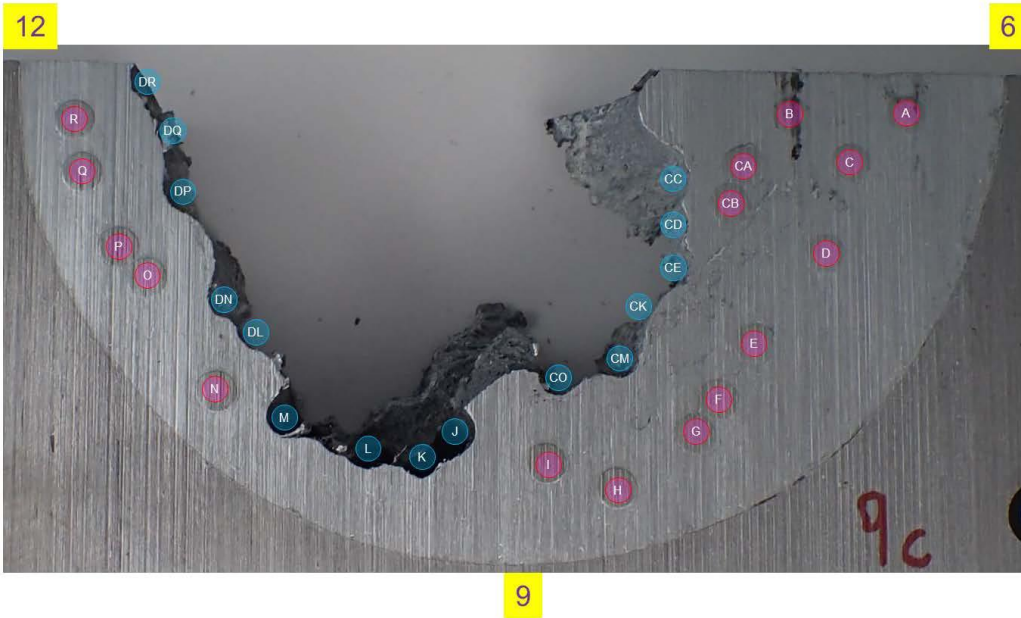


Figure 191. Wire map of the socket base side of slice 9c. Pink wire labels are wires that fractured within the socket and blue wire labels are wires that remained intact.



Figure 192. Wire map of the casting cap side of slice 9e. Pink wire labels are wires that fractured within the socket and blue wire labels are wires that remained intact.

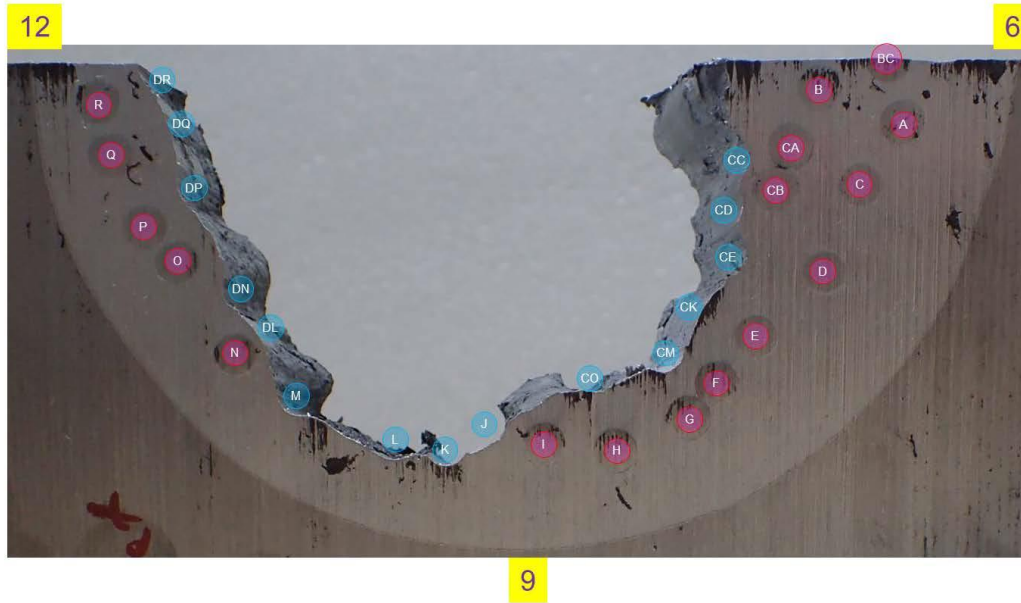


Figure 193. Wire map of the socket base side of slice 9e. Pink wire labels are wires that fractured within the socket and blue wire labels are wires that remained intact.

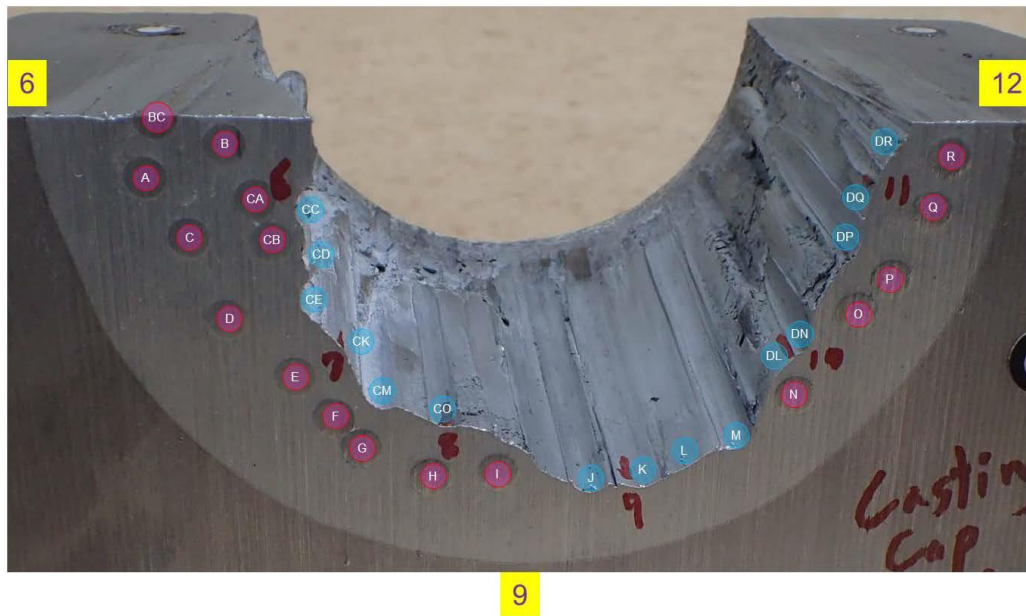


Figure 194. Wire map of the casting cap side of slice 9g. Pink wire labels are wires that fractured within the socket and blue wire labels are wires that remained intact.

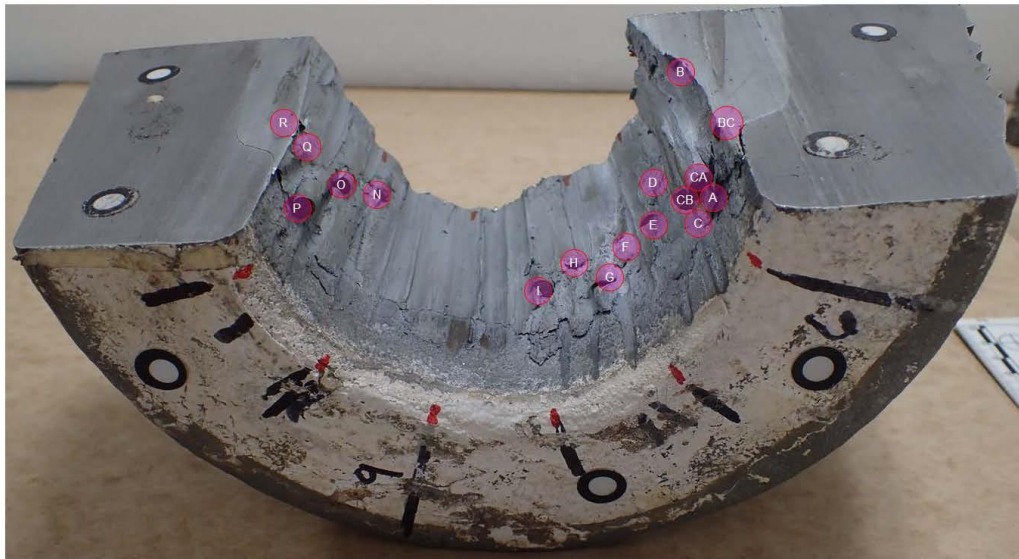


Figure 195. Wire map of the socket base side of slice 9g. Pink wire labels are wires that fractured within the socket.

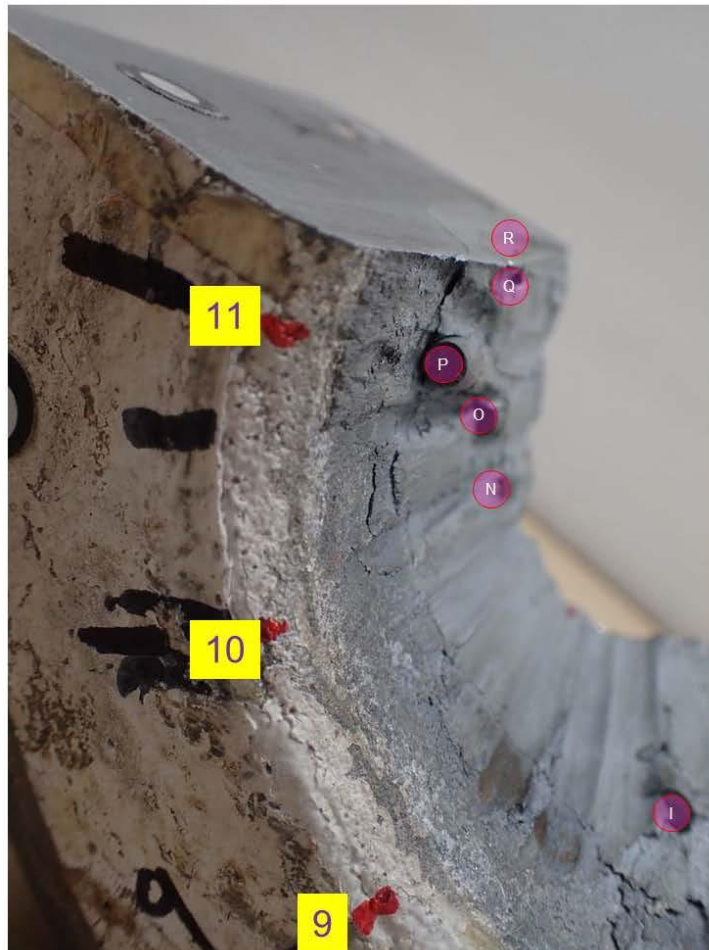


Figure 196. Wire map of the socket base side of slice 9g, from 9 o'clock to 11 o'clock. Pink wire labels are wires that fractured within the socket.



Figure 197. Wire map of the socket base side of slice 9g, from 8 o'clock to 11 o'clock. Pink wire labels are wires that fractured within the socket.



Figure 198. Wire map of the socket base side of slice 9g, from 7 o'clock to 10 o'clock. Pink wire labels are wires that fractured within the socket.



Figure 199. Wire map of the socket base side of slice 9g, from 7 o'clock to 8 o'clock. Pink wire labels are wires that fractured within the socket.

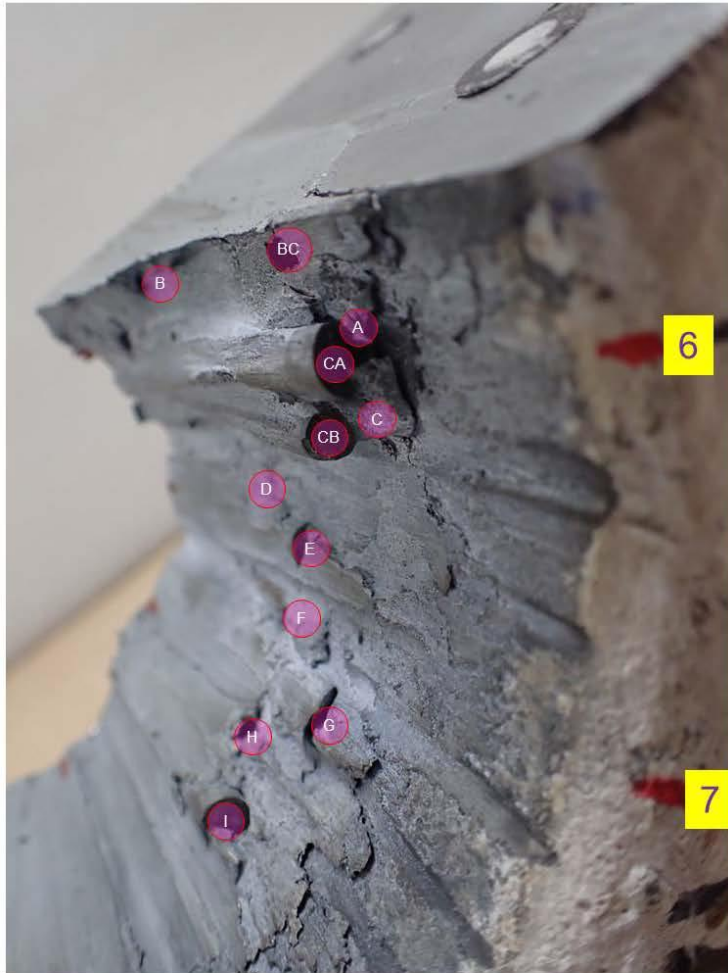


Figure 200. Wire map of the socket base side of slice 9g, from 6 o'clock to 7 o'clock. Pink wire labels are wires that fractured within the socket.

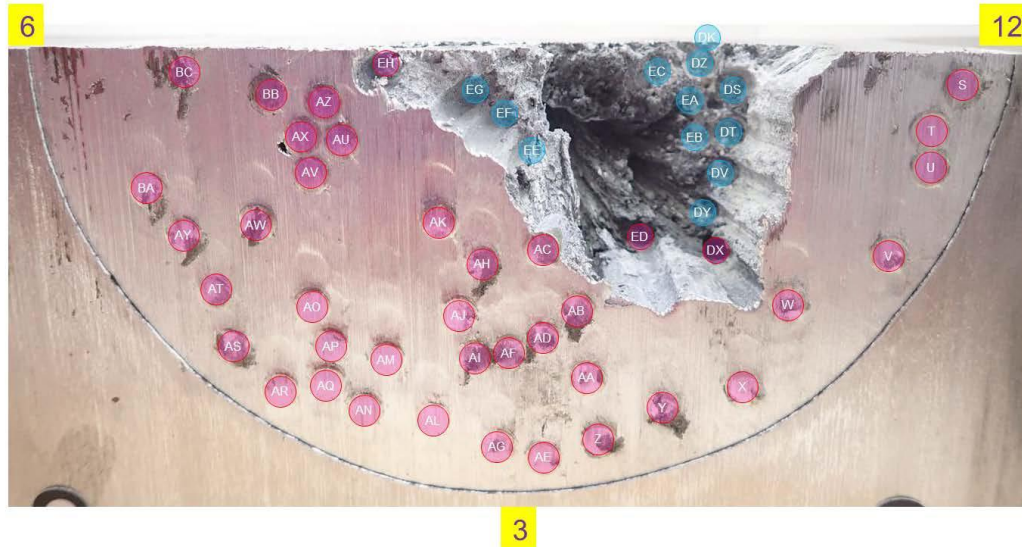


Figure 201. Wire map of the socket base side of slice 3a. Pink wire labels are wires that fractured within the socket and blue wire labels are wires that remained intact.



Figure 202. Wire map of the casting cap side of slice 3c. Pink wire labels are wires that fractured within the socket and blue wire labels are wires that remained intact.



Figure 203. Wire map of the socket base side of slice 3c. Pink wire labels are wires that fractured within the socket and blue wire labels are wires that remained intact.



Figure 204. Wire map of the casting cap side of slice 3e. Pink wire labels are wires that fractured within the socket and blue wire labels are wires that remained intact.



Figure 205 Wire map of the socket base side of slice 3e. Pink wire labels are wires that fractured within the socket and blue wire labels are wires that remained intact.

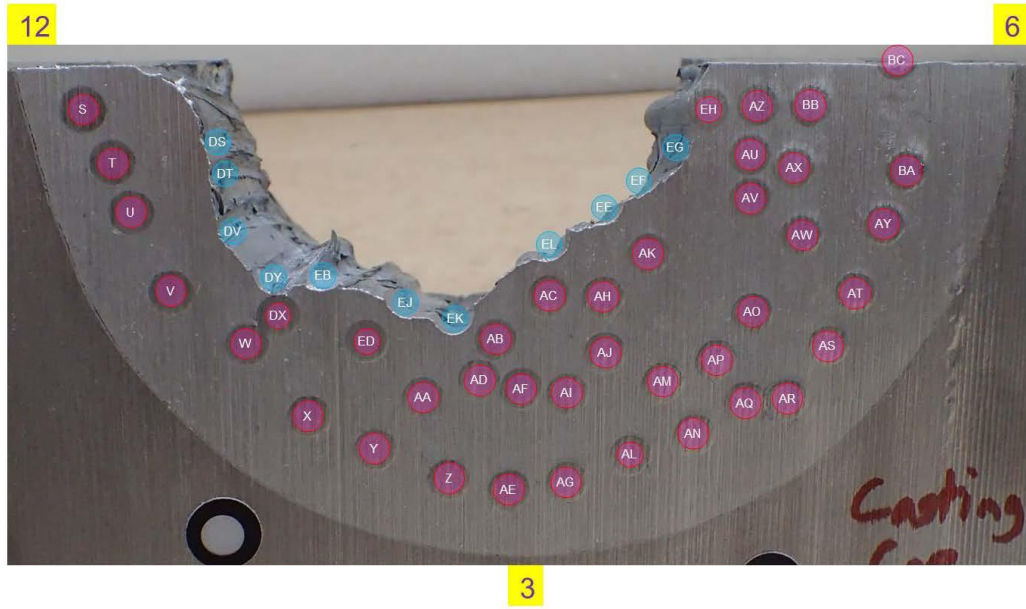


Figure 206. Wire map of the casting cap side of slice 3g. Pink wire labels are wires that fractured within the socket and blue wire labels are wires that remained intact.

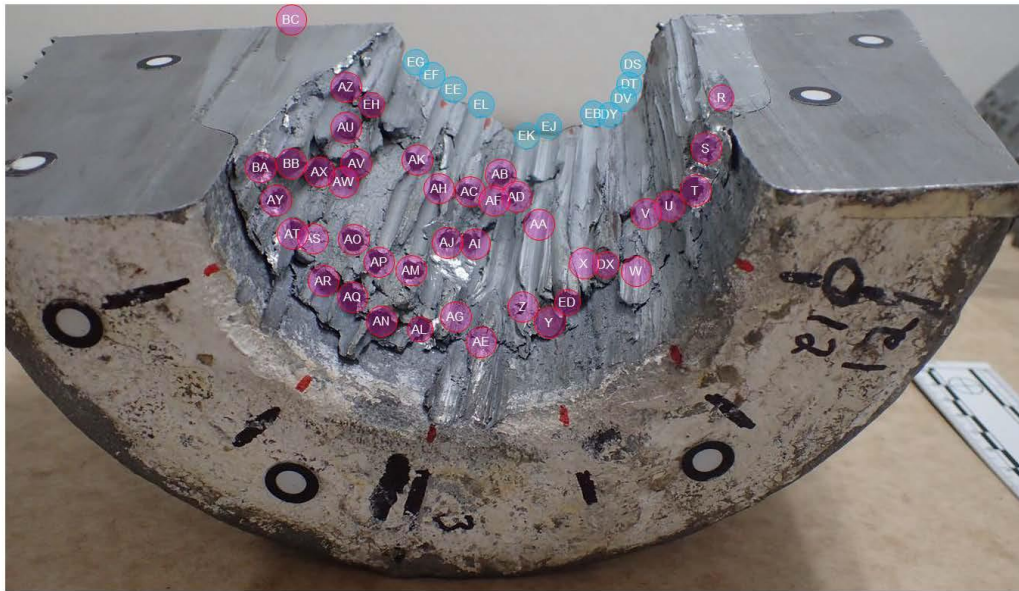


Figure 207. Wire map of the socket base side of slice 3g. Pink wire labels are wires that fractured within the socket and blue wire labels are wires that remained intact.

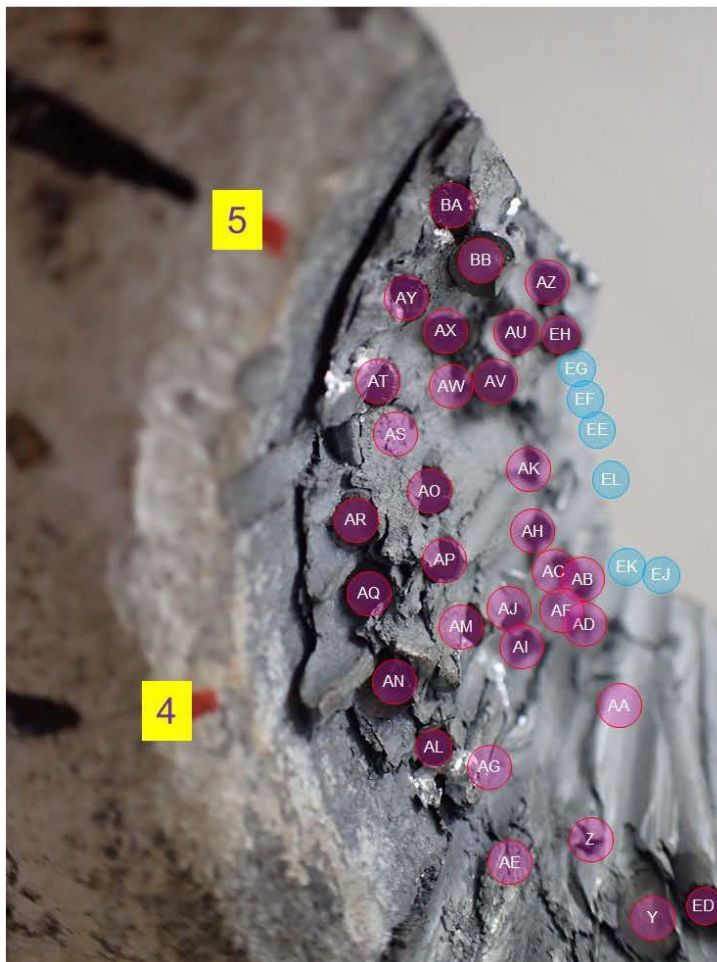


Figure 208. Wire map of the socket base side of slice 3g, from 4 o'clock to 5 o'clock. Pink wire labels are wires that fractured within the socket and blue wire labels are wires that remained intact.

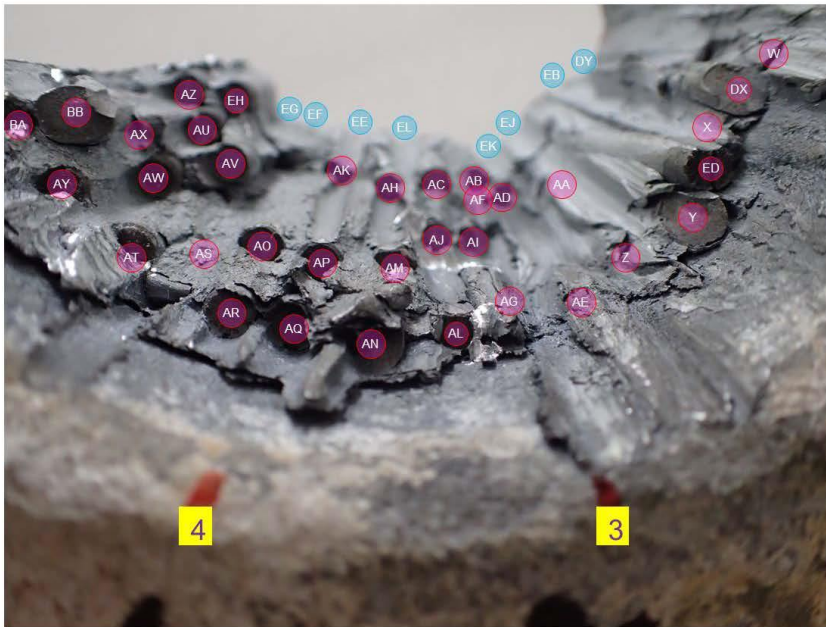


Figure 209. Wire map of the socket base side of slice 3g, from 3 o'clock to 4 o'clock. Pink wire labels are wires that fractured within the socket and blue wire labels are wires that remained intact.

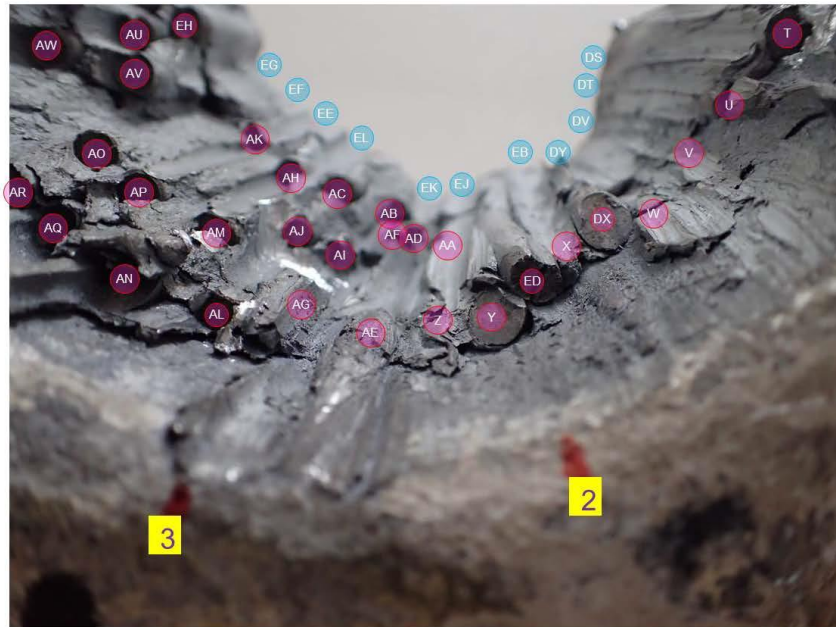


Figure 210. Wire map of the socket base side of slice 3g, from 2 o'clock to 3 o'clock. Pink wire labels are wires that fractured within the socket and blue wire labels are wires that remained intact.

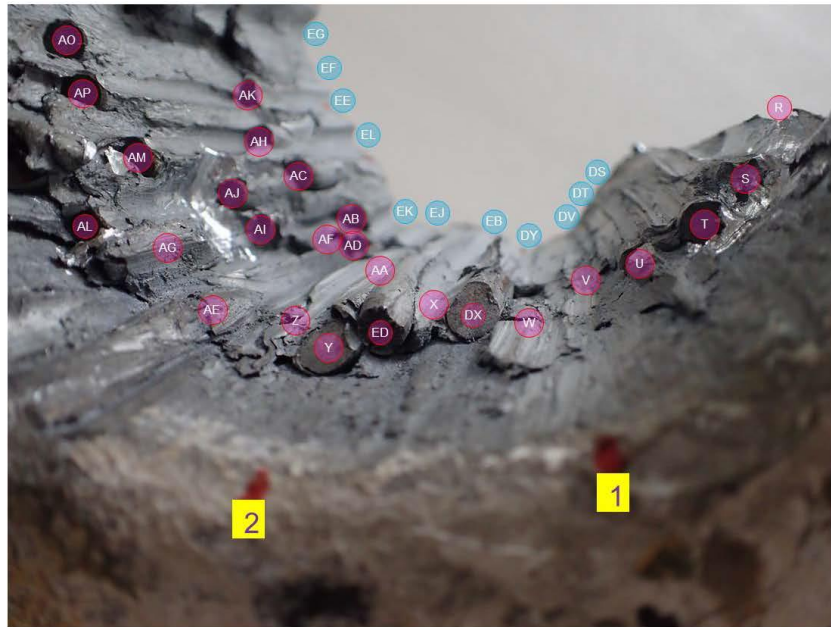


Figure 211. Wire map of the socket base side of slice 3g, from 1 o'clock to 2 o'clock. Pink wire labels are wires that fractured within the socket and blue wire labels are wires that remained intact.

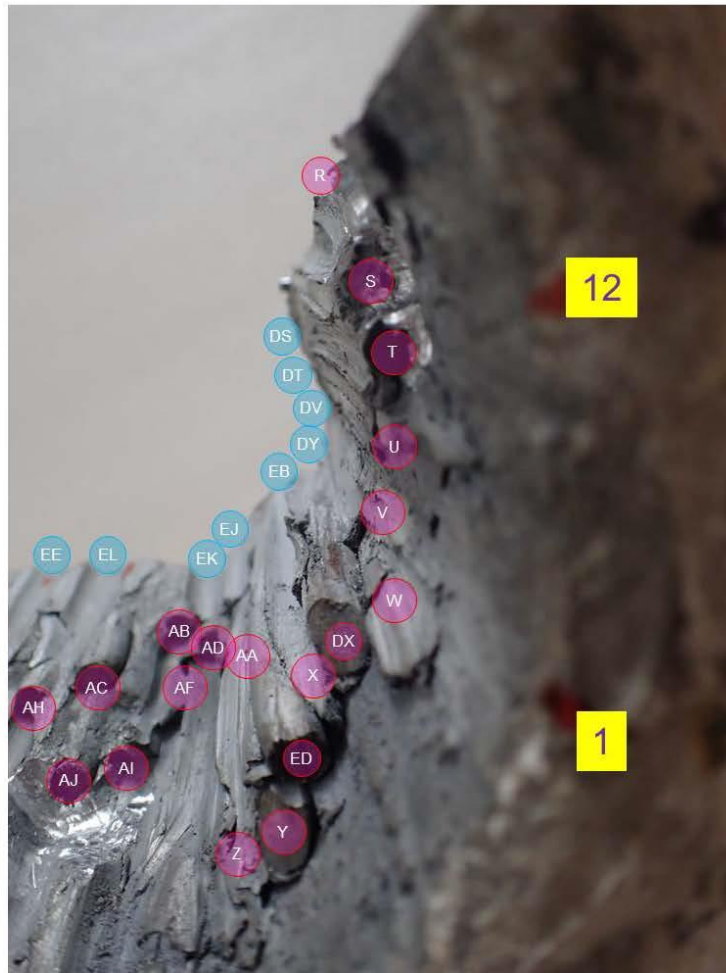


Figure 212. Wire map of the socket base side of slice 3g, from 12 o'clock to 1 o'clock. Pink wire labels are wires that fractured within the socket and blue wire labels are wires that remained intact.

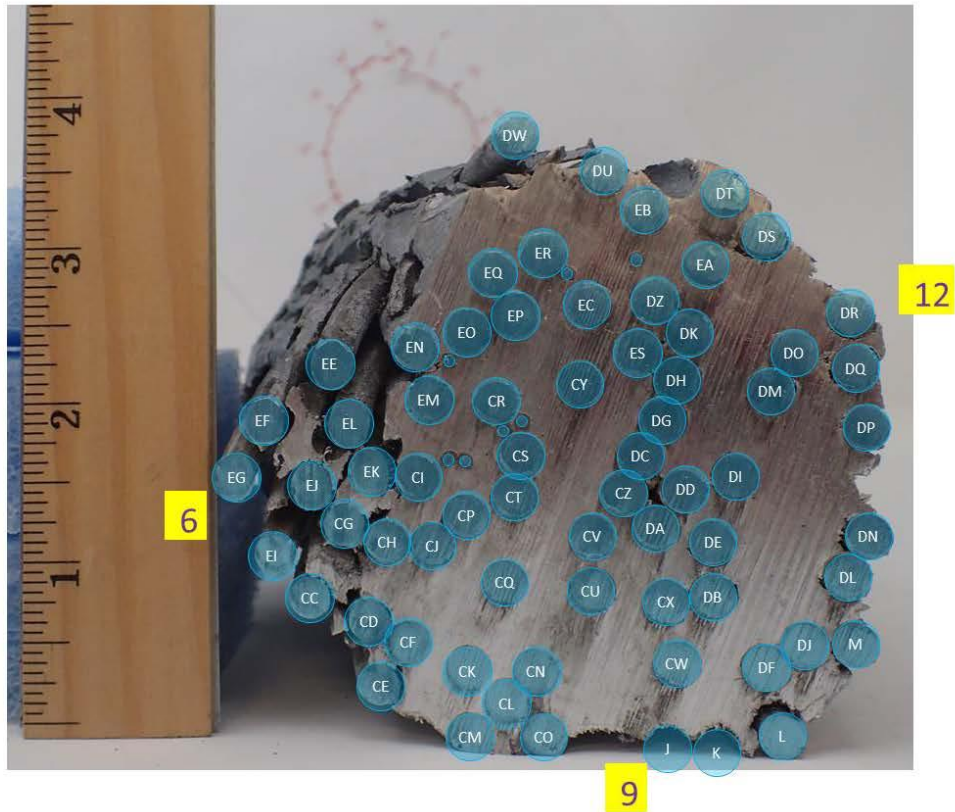


Figure 213. Wire map of the cable-end section transverse slice, 1 inch down from the top. Blue wire labels are wires that remained intact. Scale in inches.

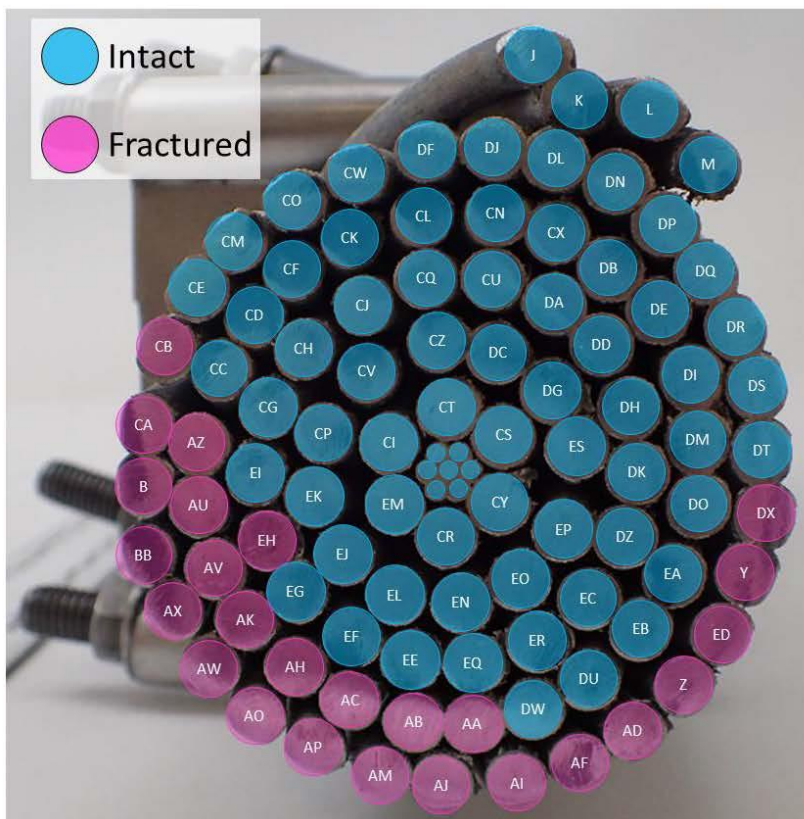


Figure 214. Wire map of the bottom of the cable-end section. Note that this is a representation of the wire configuration at approximately the socket base. The actual wire configuration will vary with distance from the socket base, since each concentric ring of wires rotates in the opposite direction as the adjacent concentric rings of wires. Pink wire labels are wires that fractured within the socket (although these would be the Feed Platform side of those wire fractures) and blue wire labels are wires that remained intact.

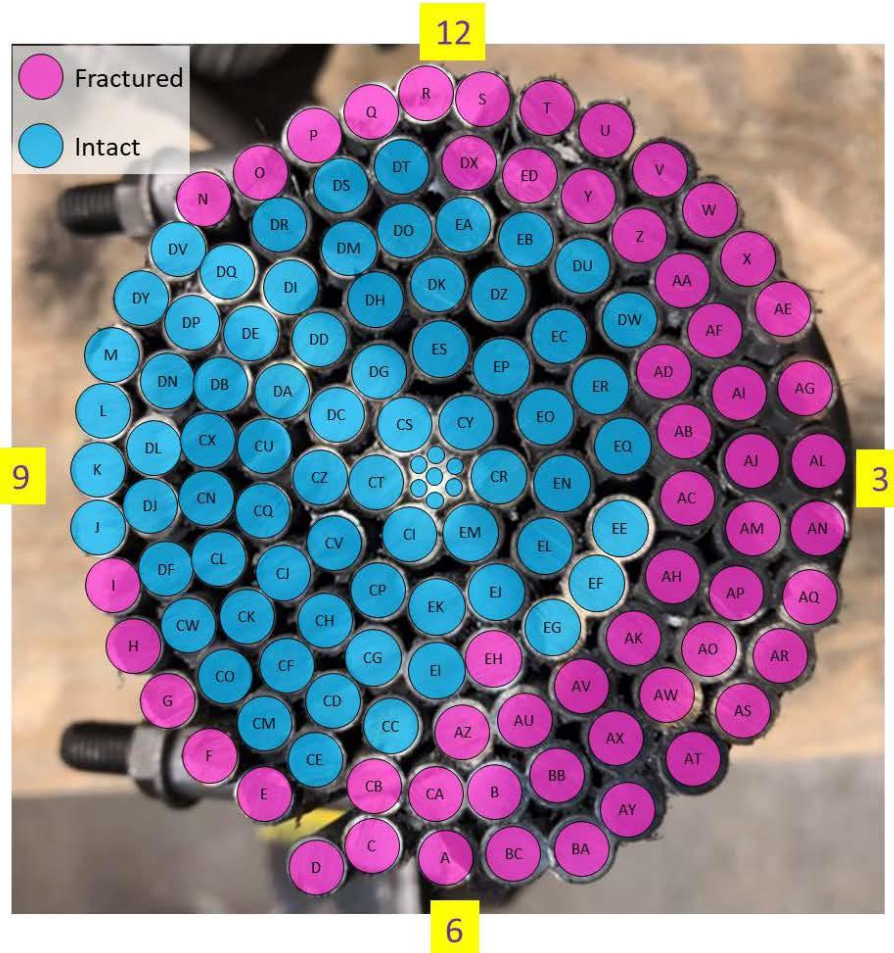


Figure 215. Wire map of the cable. Note that this is a representation of the wire configuration at approximately the socket base. The actual wire configuration will vary with distance from the socket base, since each concentric ring of wires rotates in the opposite direction as the adjacent concentric rings of wires. Pink wire labels are wires that fractured within the socket (although these would be the Feed Platform side of those wire fractures) and blue wire labels are wires that remained intact.

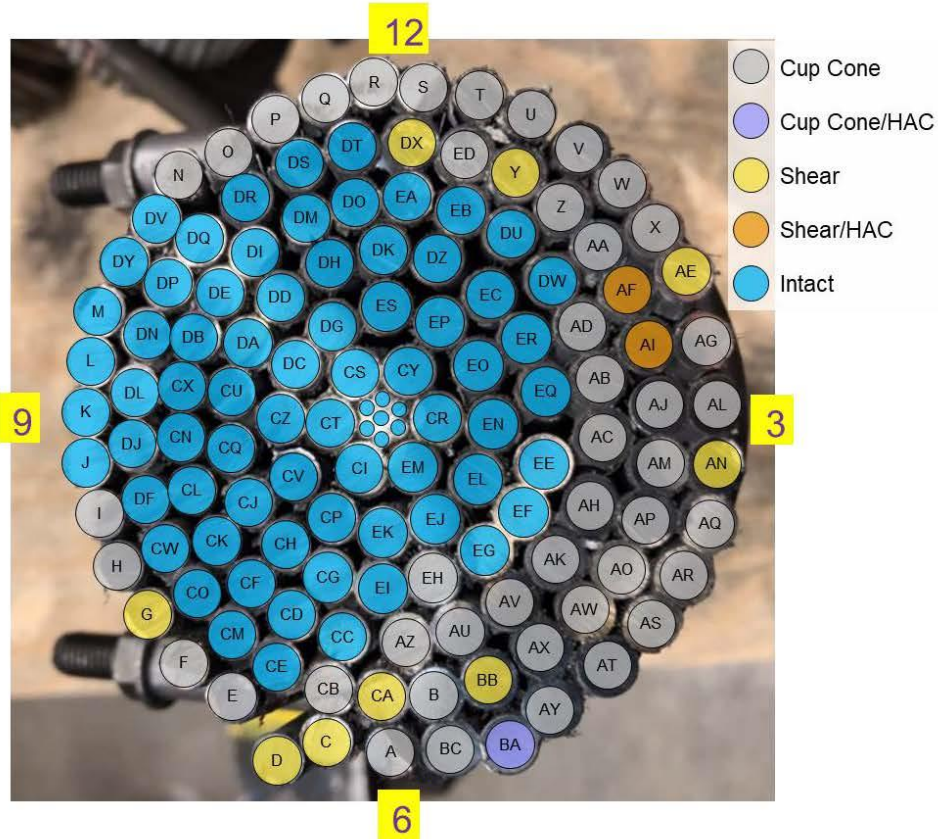


Figure 216. Wire map of the cable by fracture classification. Note that this is a representation of the wire configuration at approximately the socket base. The actual wire configuration will vary with distance from the socket base, since each concentric ring of wires rotates in the opposite direction as the adjacent concentric rings of wires. Gray, purple, yellow, and orange wire labels are wires that fractured in the socket and the color corresponds to the predominant fracture mechanism classified for that wire and blue wire labels are wires that remained intact.

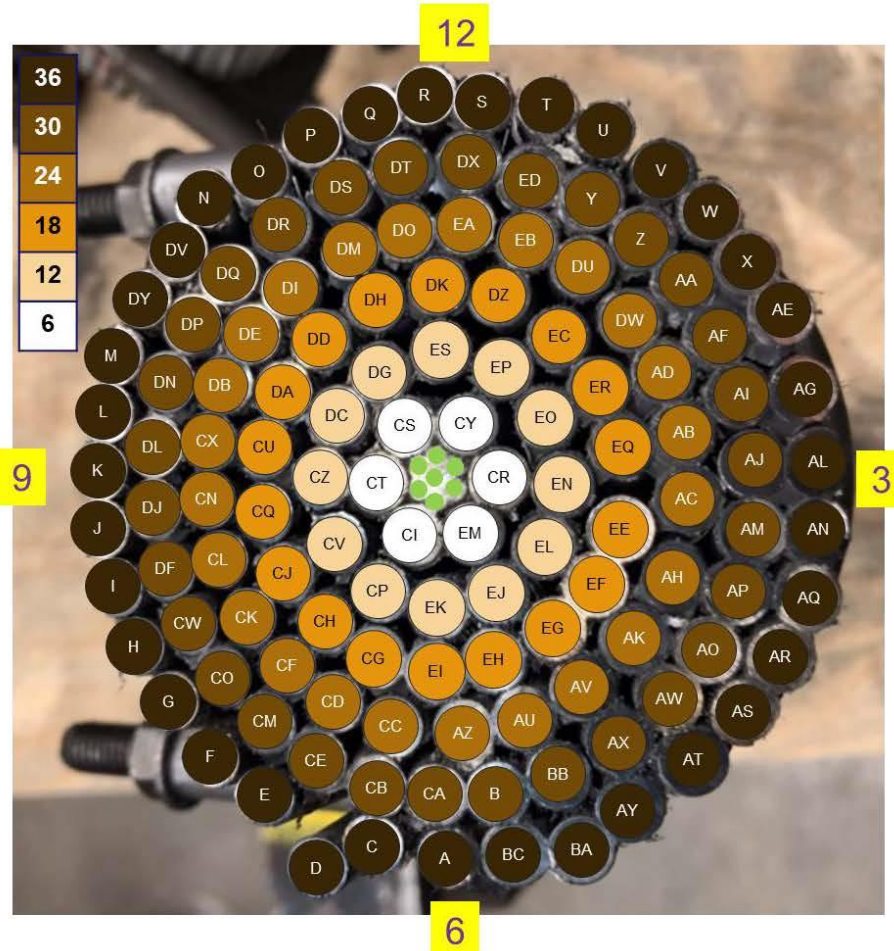


Figure 217. Wire map of the cable by rings. Note that this is a representation of the wire configuration at approximately the socket base. The actual wire configuration will vary with distance from the socket base, since each concentric ring of wires rotates in the opposite direction as the adjacent concentric rings of wires. The color range (white-tan-orange-light brown-brown-dark brown), with the white wires being the inner ring of wires and the dark brown representing the outer diameter wires.



Figure 218. Wire map of the cable-end section transverse slice, 1 inch down from the top, by rings. The color range (white-tan-orange-light brown-brown-dark brown), with the white wires being the inner ring of wires and the dark brown representing the outer diameter wires. Scale in inches.



Figure 219. Wire map of the 12 o'clock side of the cable-end section by rings. The color range (white-tan-orange-light brown-brown-dark brown), with the white wires being the inner ring of wires and the dark brown representing the outer diameter wires.



Figure 220. Wire map of the 3 o'clock side of the cable-end section by rings. The color range (white-tan-orange-light brown-brown-dark brown), with the white wires being the inner ring of wires and the dark brown representing the outer diameter wires.

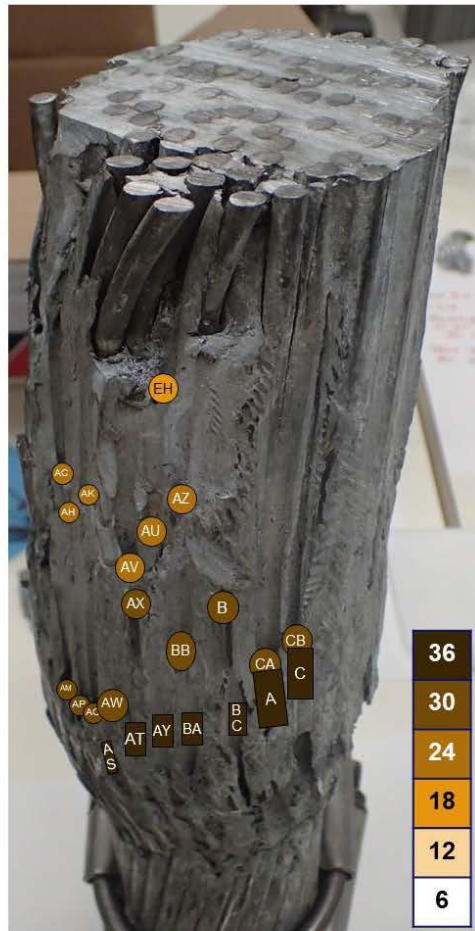


Figure 221. Wire map of the 6 o'clock side of the cable-end section by rings. The color range (white-tan-orange-light brown-brown-dark brown), with the white wires being the inner ring of wires and the dark brown representing the outer diameter wires.



Figure 222. Wire map of the 9 o'clock side of the cable-end section by rings. The color range (white-tan-orange-light brown-brown-dark brown), with the white wires being the inner ring of wires and the dark brown representing the outer diameter wires.

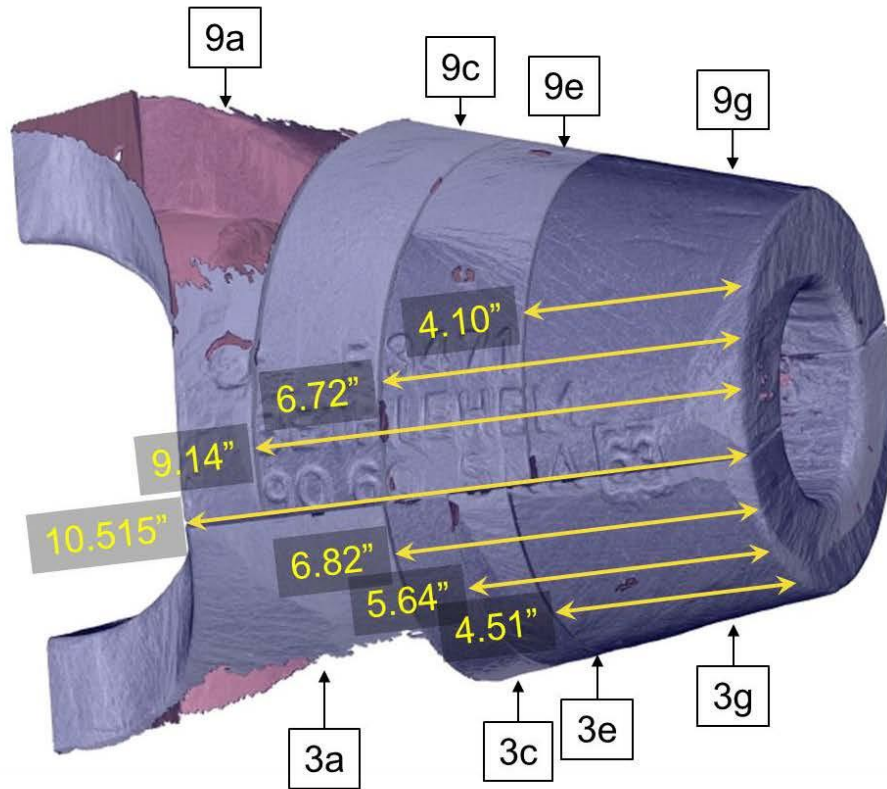


Figure 223. Distance measurements between the socket base and the transverse cuts, provided for the as-built finite element model.

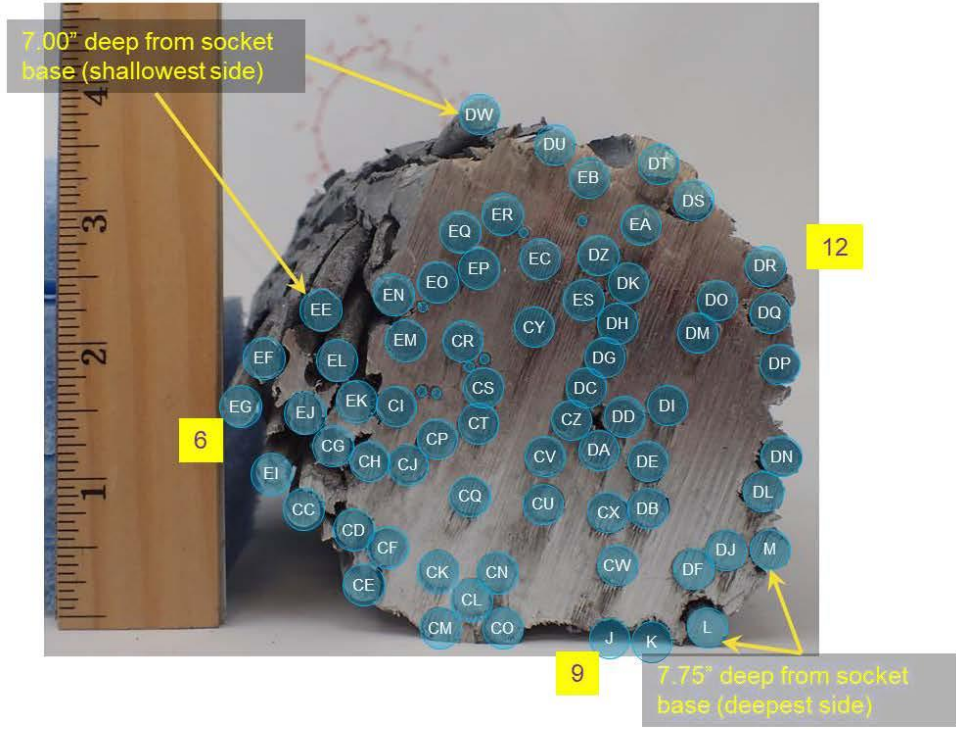


Figure 224. Distance measurements between the expected location of the socket base along the cable-end section and the shown transverse cut, provided for the as-built finite element model. Scale in inches.

APPENDIX H. STEREOMICROSCOPY OF WIRE FRACTURES

Stereomicroscope images of the wire fractures appear below. Inner diameter (ID) is the side facing the center of the socket cavity. Outer diameter is the side facing the outer diameter of the zinc casting. Socket base side (SBS) is the side facing the socket base opening. Casting cap side is the side facing the casting cap. Numbers represent clock position around the socket base, as described in Figure 13, and, when used with the direction indicator, represent 3 hours left or right of the wire's clock position (e.g., a wire at 6 o'clock will have direction indicators of 9 o'clock and 3 o'clock when referring to the left and right sides of the wire, when looking at the wire's socket base side). A yellow circle hour-clock indicates each wire's approximate hour position around the socket cavity. A closer approximation of each wire's location, within 15 minutes, is stated in the caption.

The wires are split up into the identified fracture morphologies (cup-cone, shear, and hydrogen assisted cracking) and then in alphabetical order.

H.1 Cup-Cone Fracture Morphology

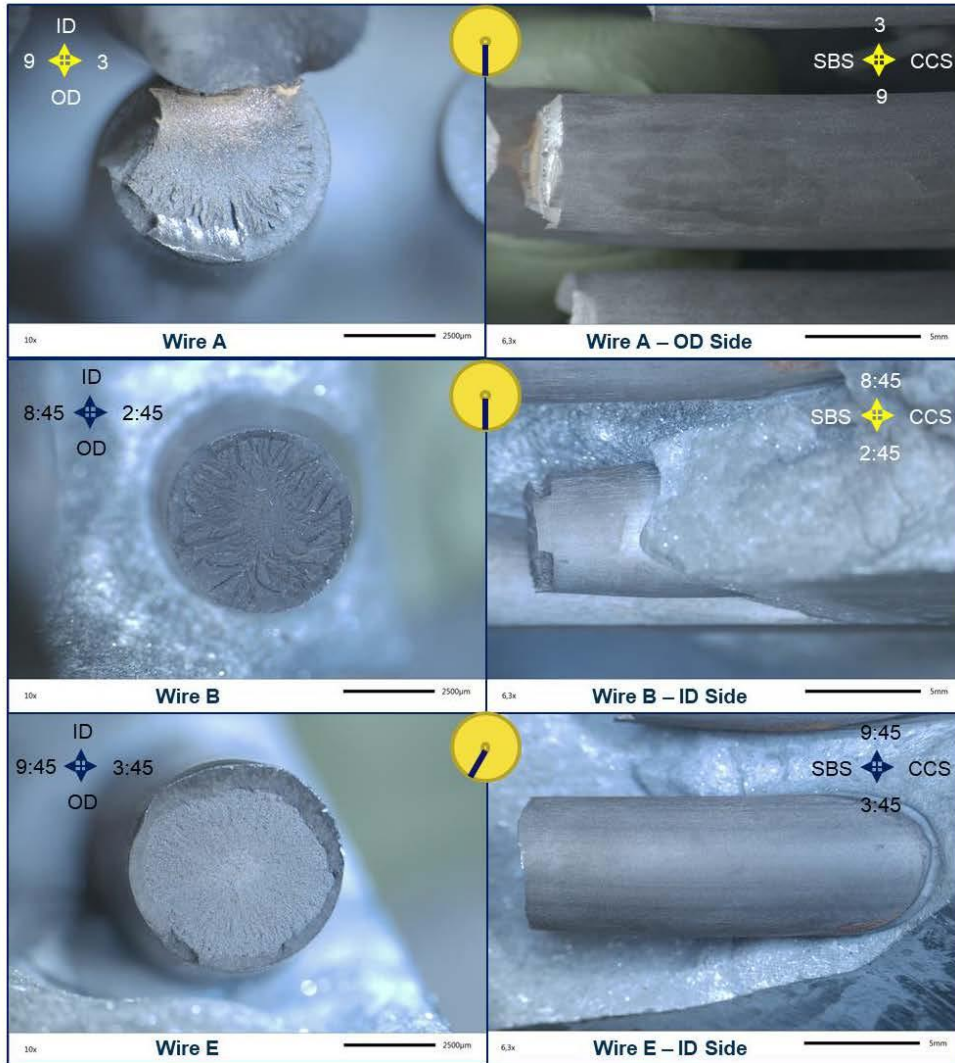


Figure 225. Stereomicroscope images of wire A (6:00), wire B (5:45), and wire E (6:45).

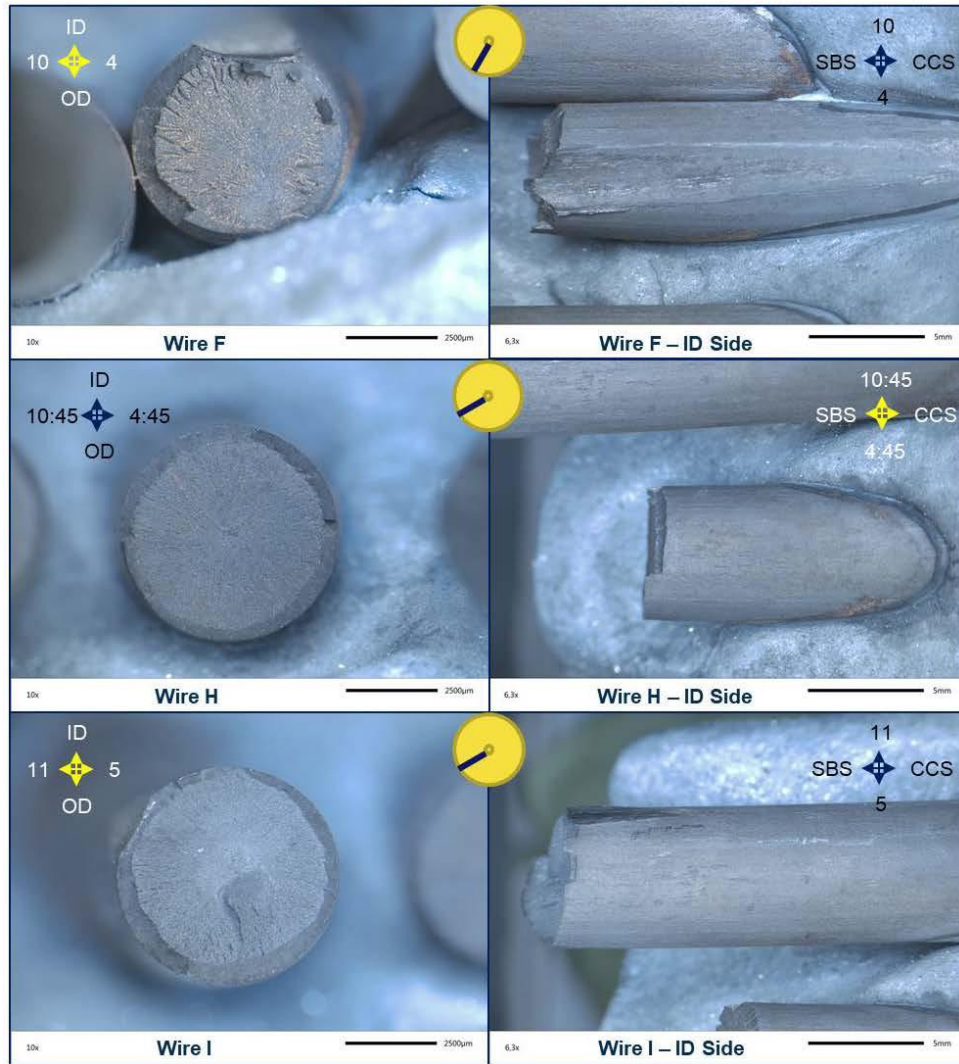


Figure 226. Stereomicroscope images of wire F (7:00), wire H (7:45), and wire I (8:00).

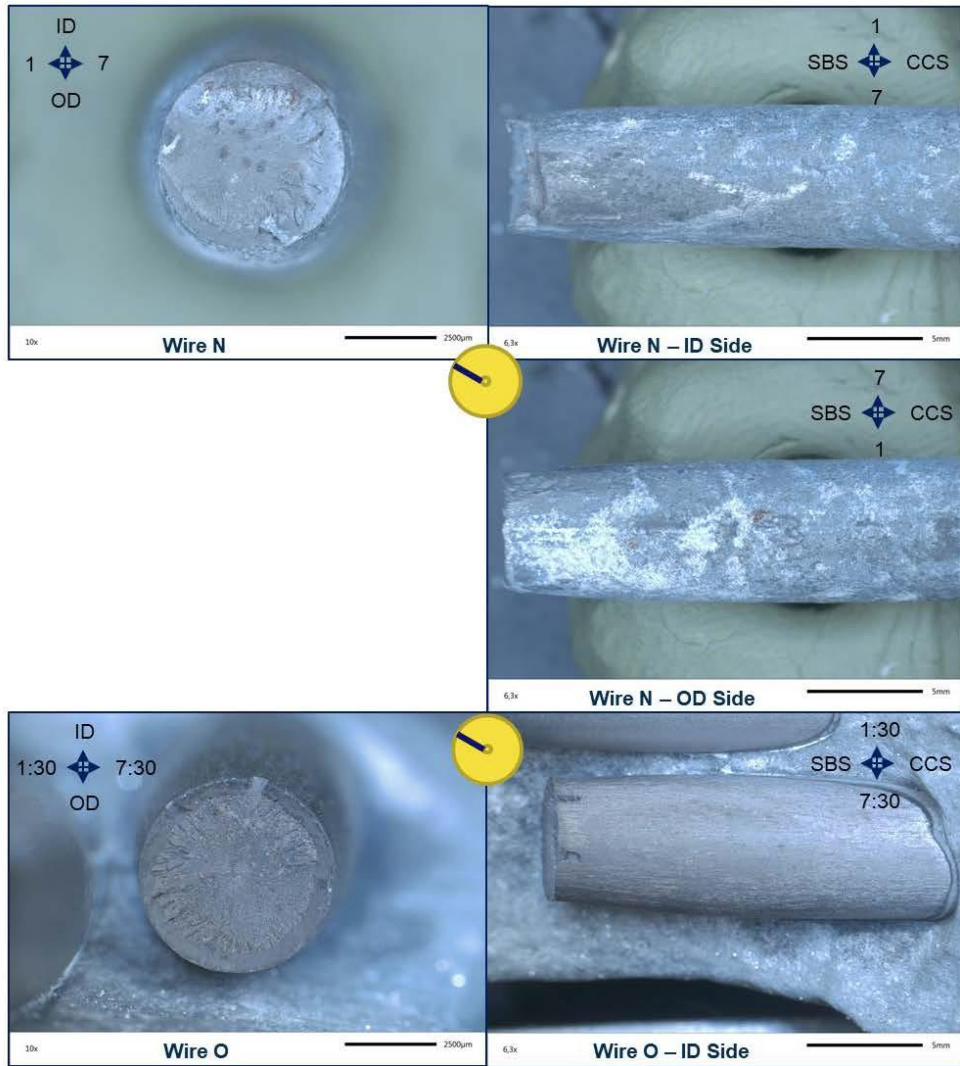


Figure 227. Stereomicroscope images of wire N (10:00) and wire O (10:30).

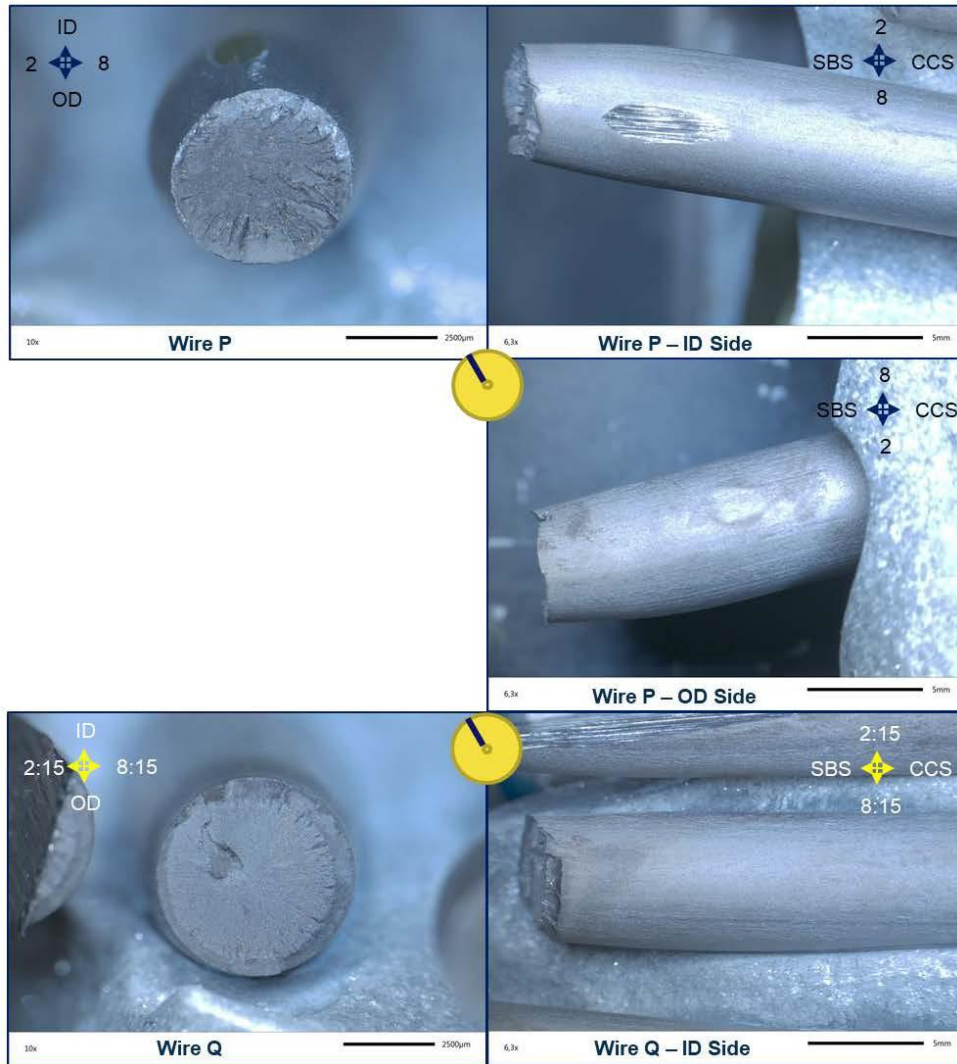


Figure 228. Stereomicroscope images of wire P (11:00) and wire Q (11:15). The nick on the inner diameter side of wire P may have occurred during sectioning.

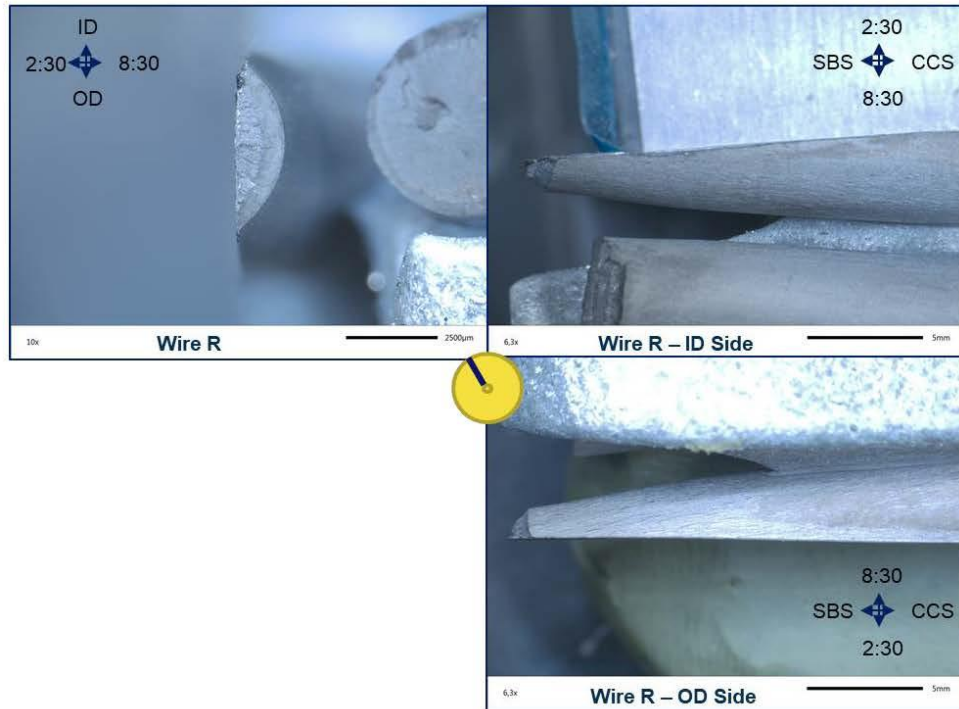


Figure 229. Stereomicroscope images of wire R (11:30). The fracture surface of wire R was cut through during the initial longitudinal cut of the socket cavity.

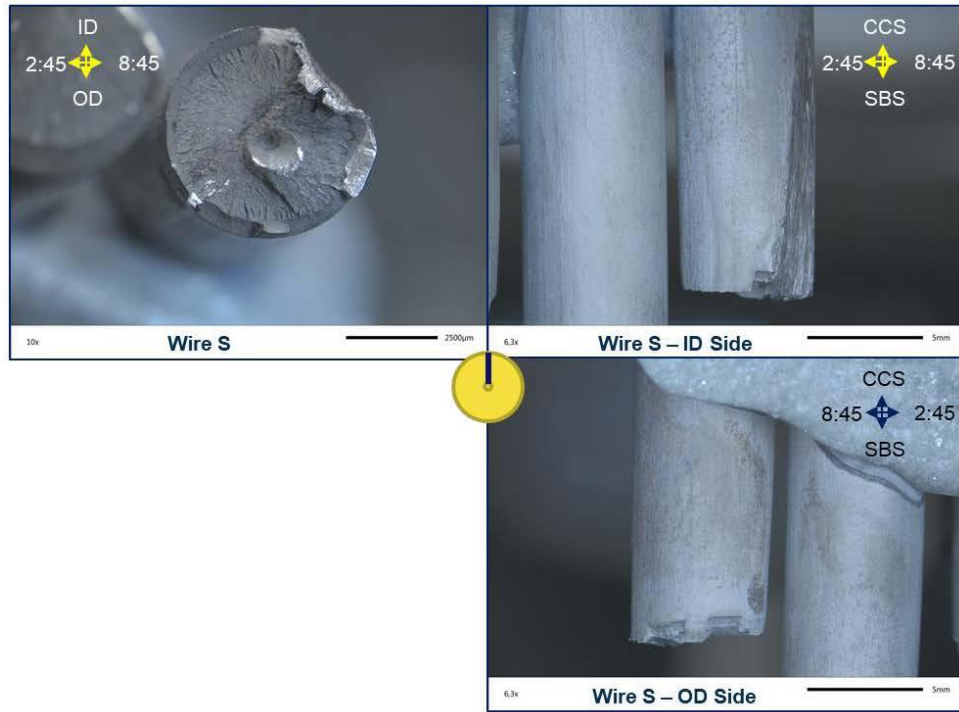


Figure 230. Stereomicroscope images of wire S (11:45).

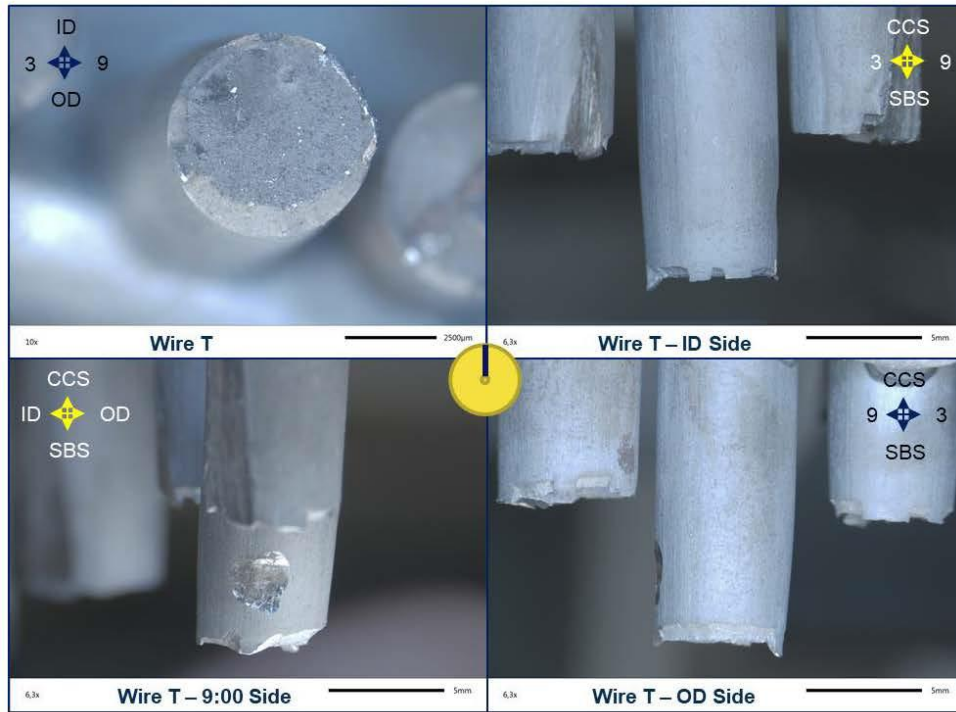
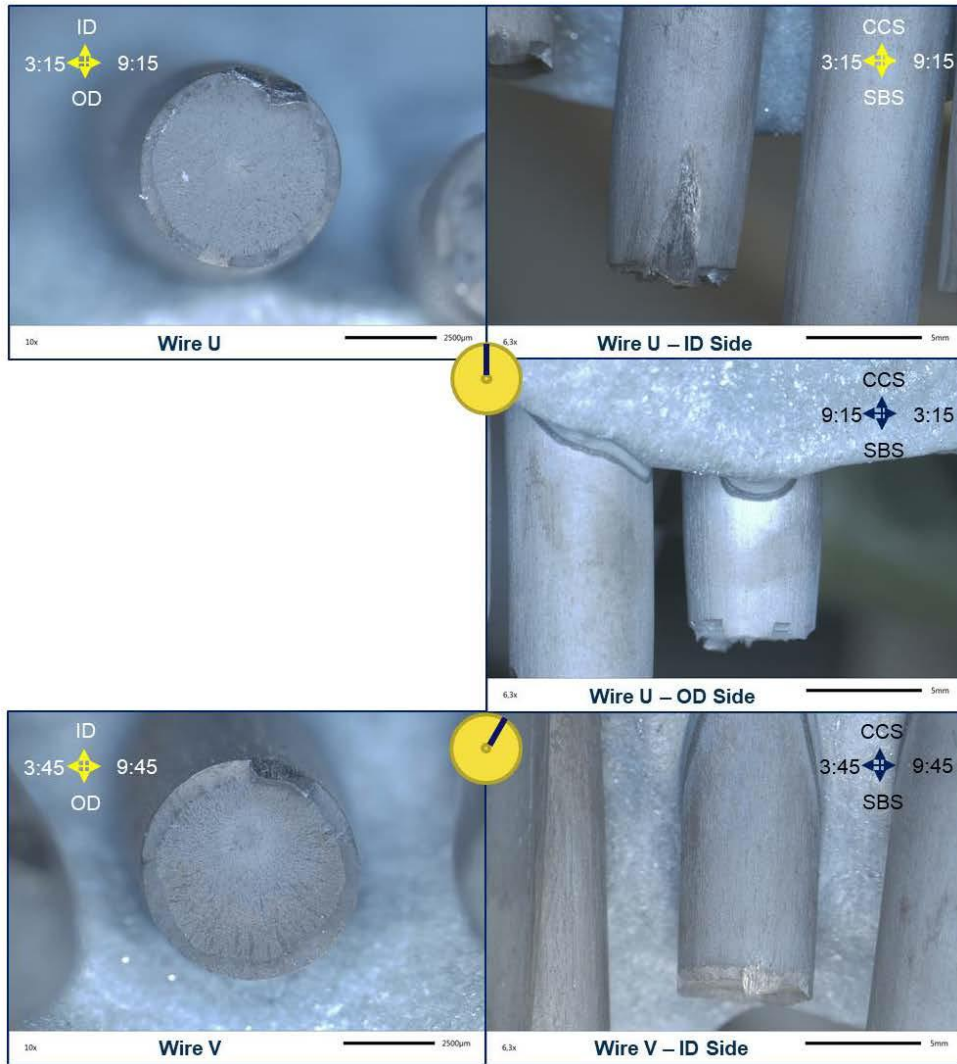


Figure 231. Stereomicroscope images of wire T (12:00). The nick on the 9 o'clock side of wire T occurred during sectioning.



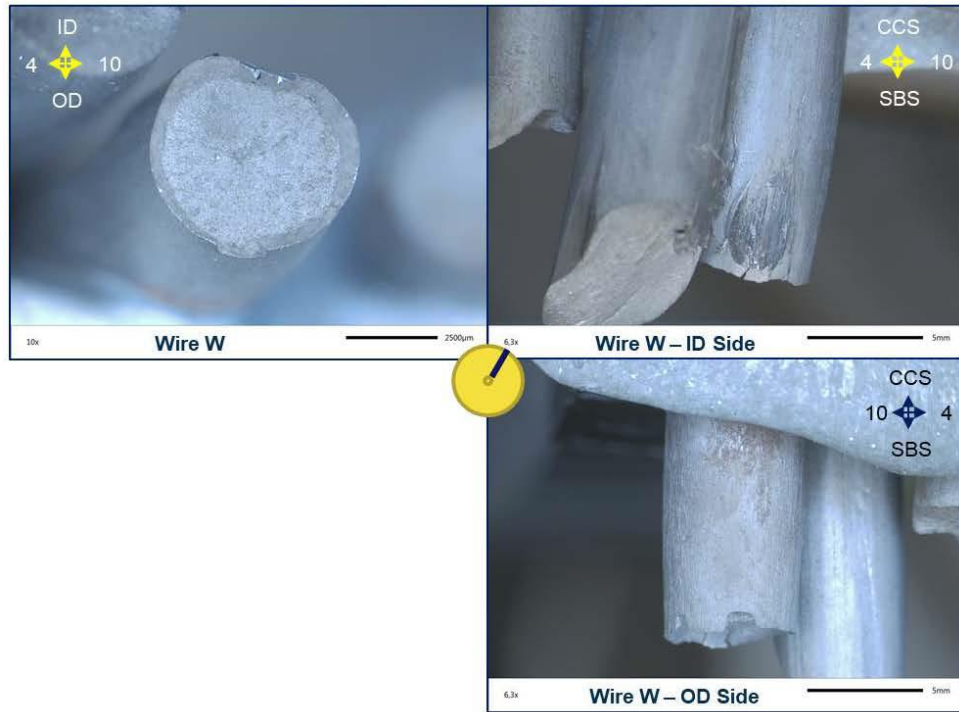


Figure 233. Stereomicroscope images of wire W (1:00).

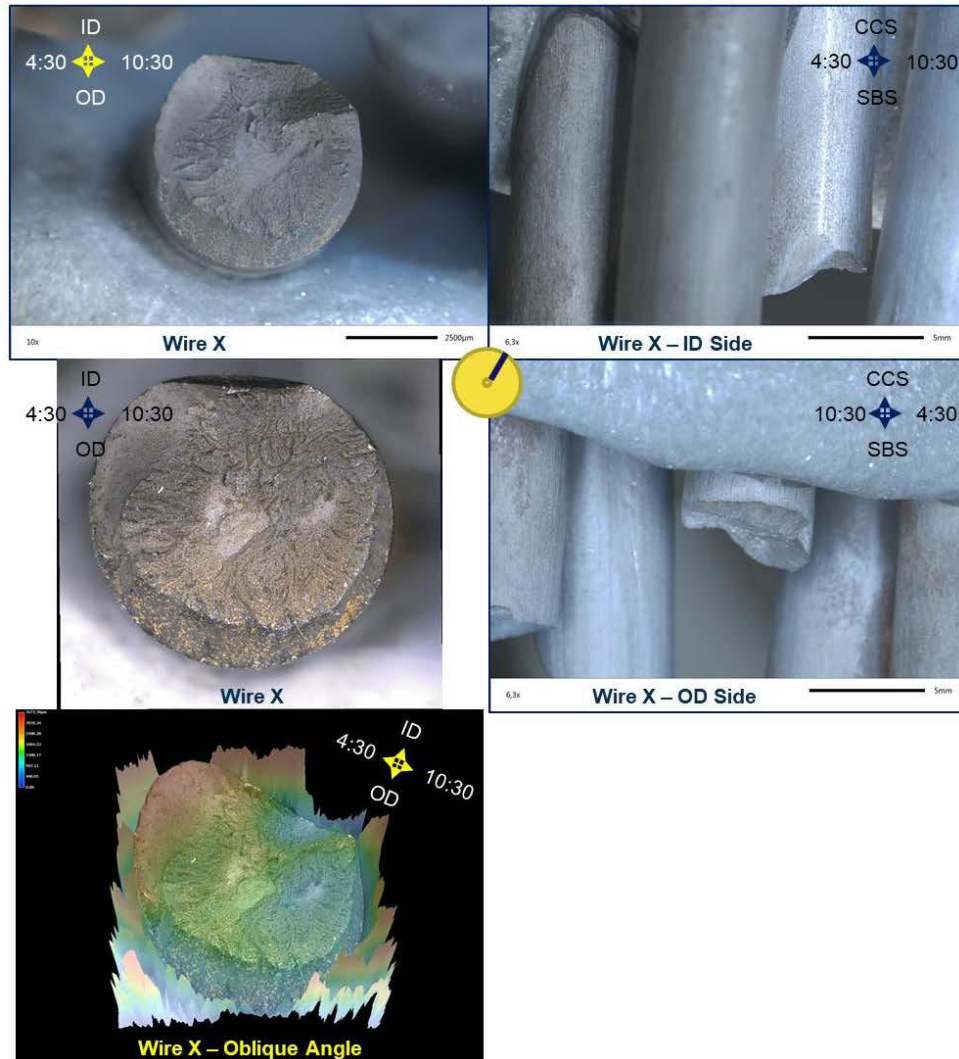


Figure 234. Stereomicroscope images of wire X (1:30). The bottom row left image is a digitally enhanced 3D view of the fracture topography with a color-coded height map.

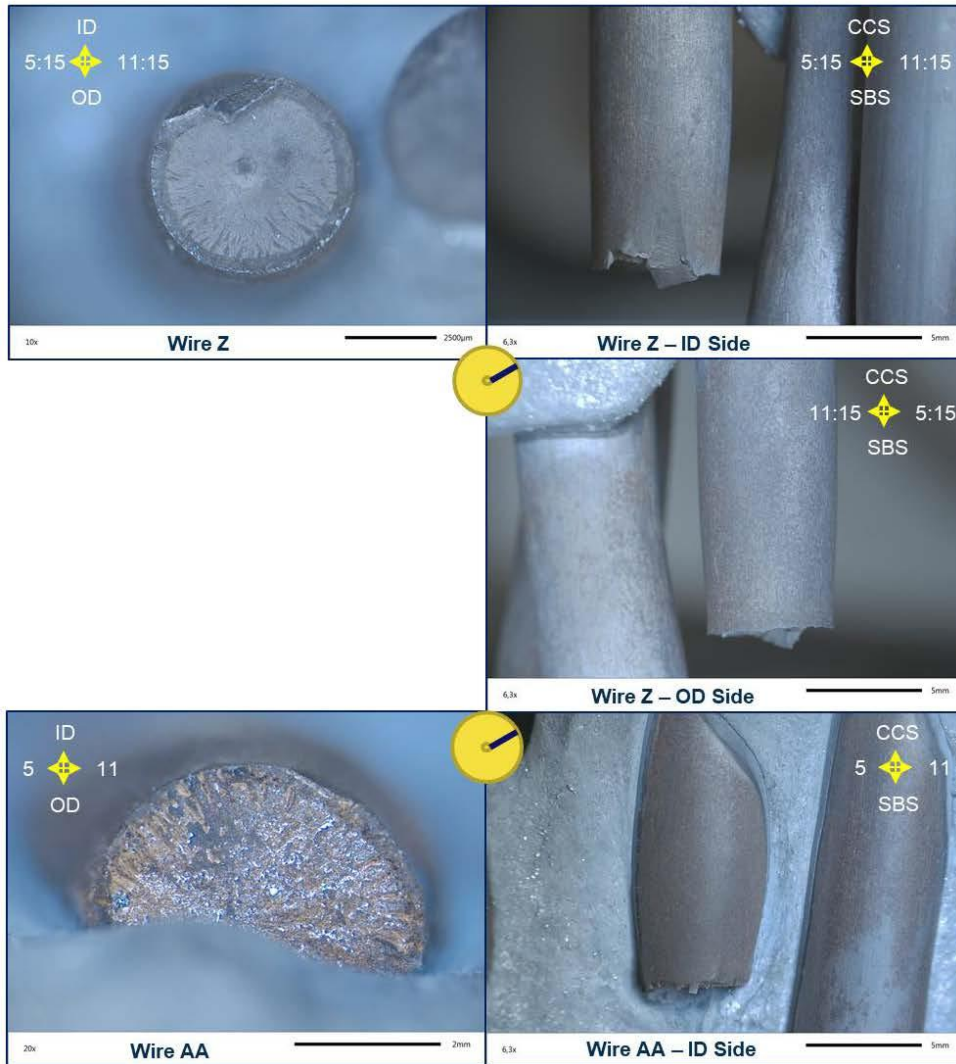


Figure 235. Stereomicroscope images of wire Z (2:15) and wire AA (2:00).

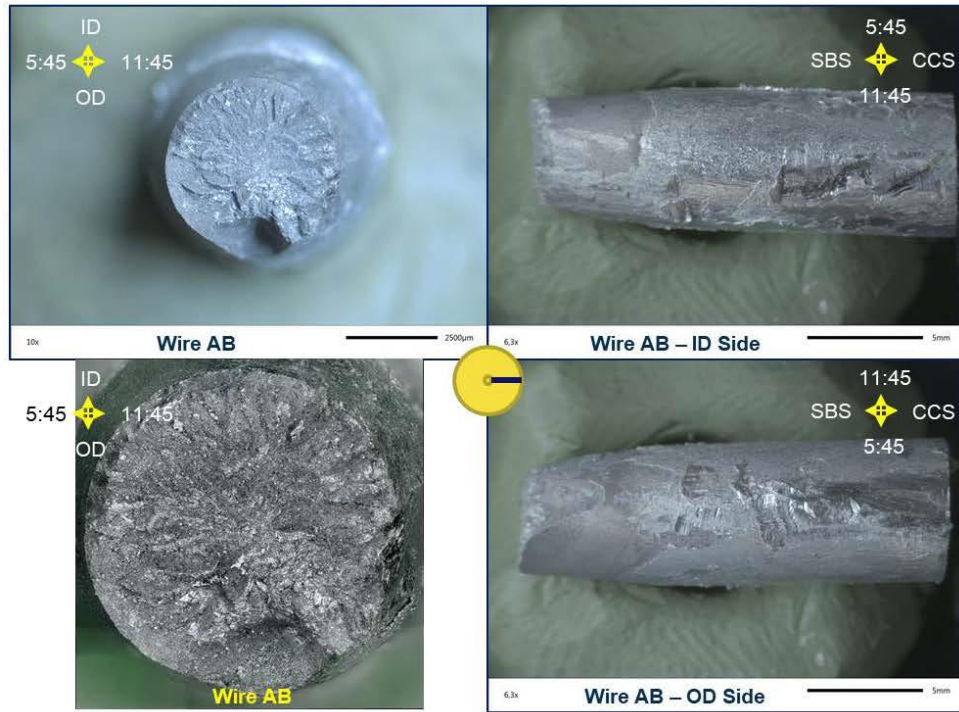


Figure 236. Stereomicroscope images of wire AB (2:45).

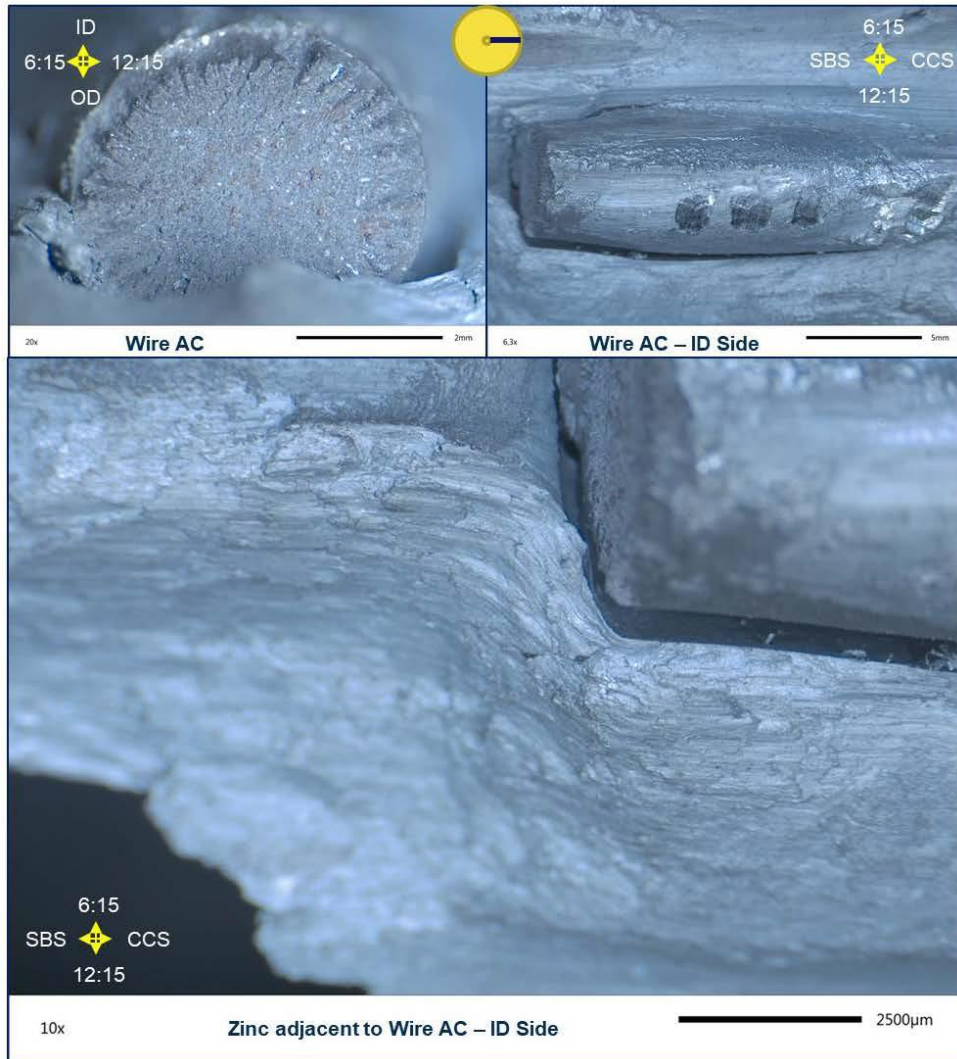


Figure 237. Stereomicroscope images of wire AC (3:15). The nicks on the inner diameter side if wire AC were from the sectioning process.

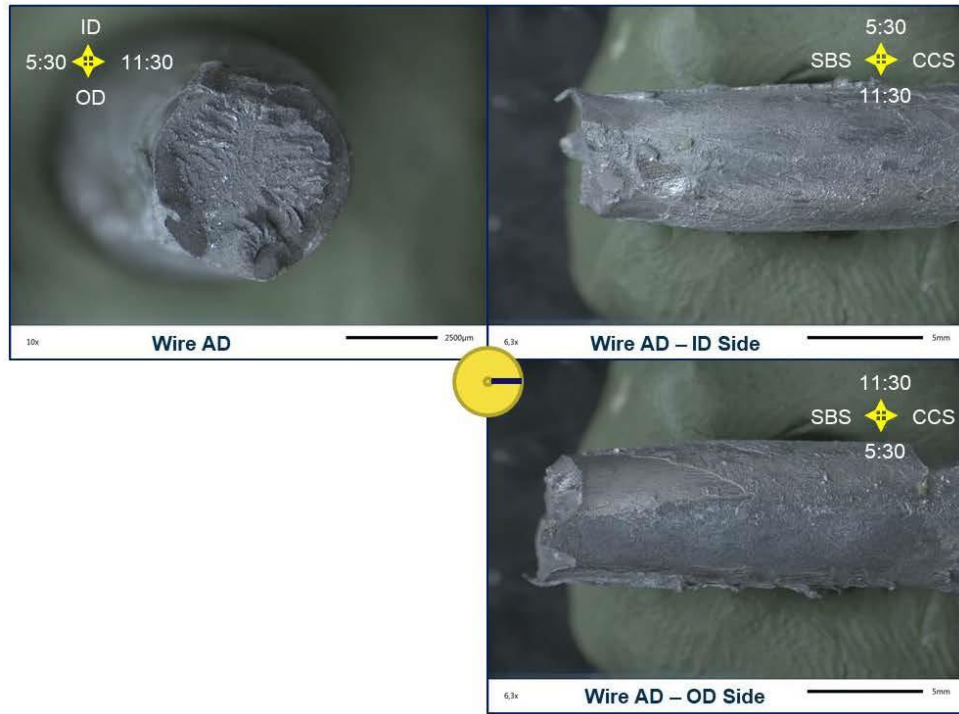


Figure 238. Stereomicroscope images of wire AD (2:30).

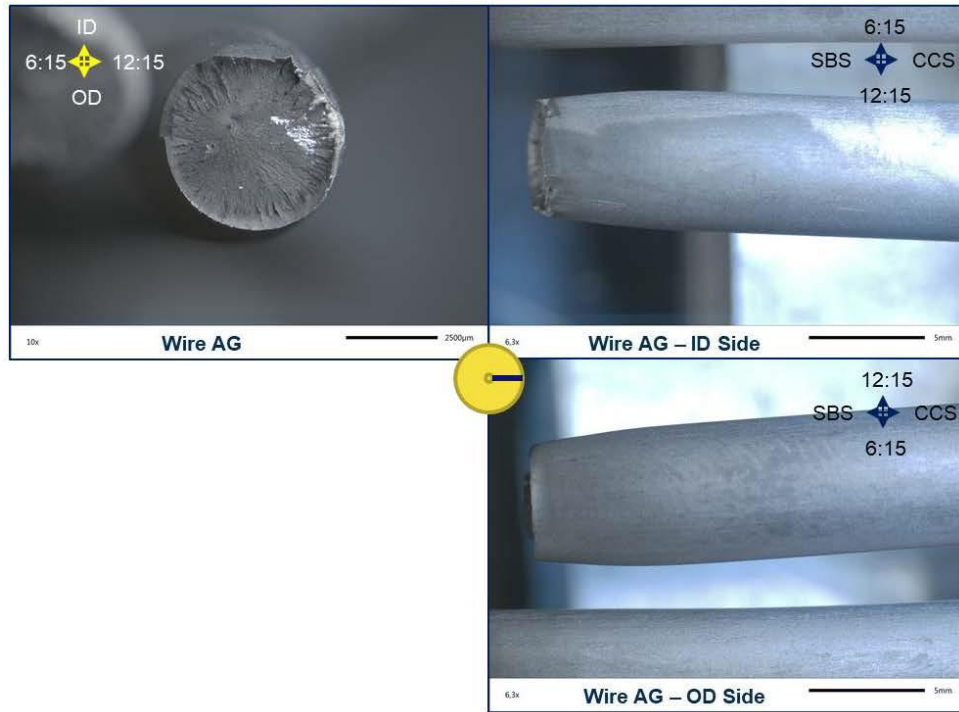


Figure 239. Stereomicroscope images of wire AG (3:15).

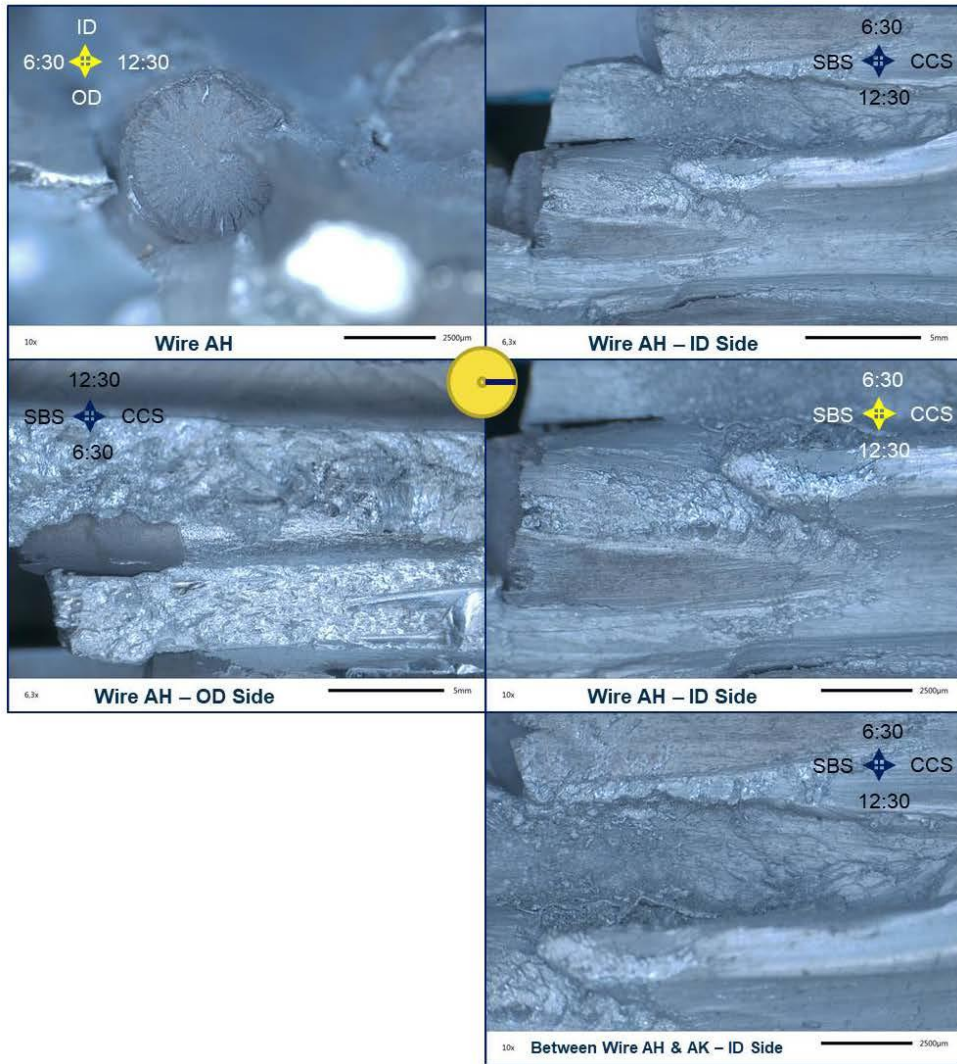


Figure 240. Stereomicroscope images of wire AH (3:30). Close up images of the zinc show a thin layer of molten zinc spatter that occurred when the cable/zinc slug was displaced from the socket during the ultimate failure of the joint.

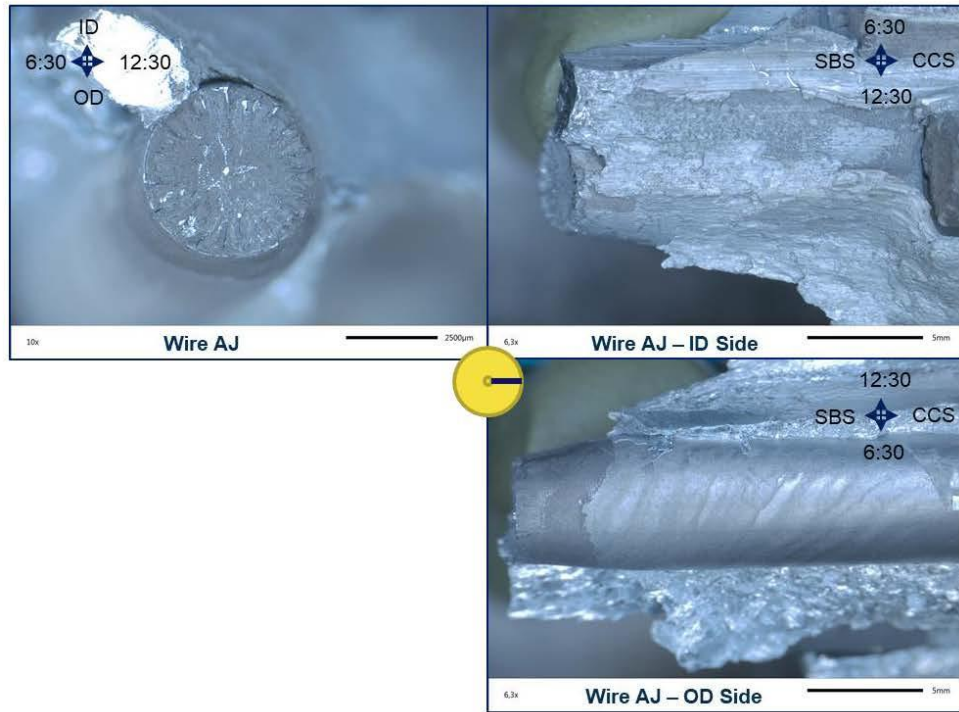


Figure 241. Stereomicroscope images of wire AJ (3:30).

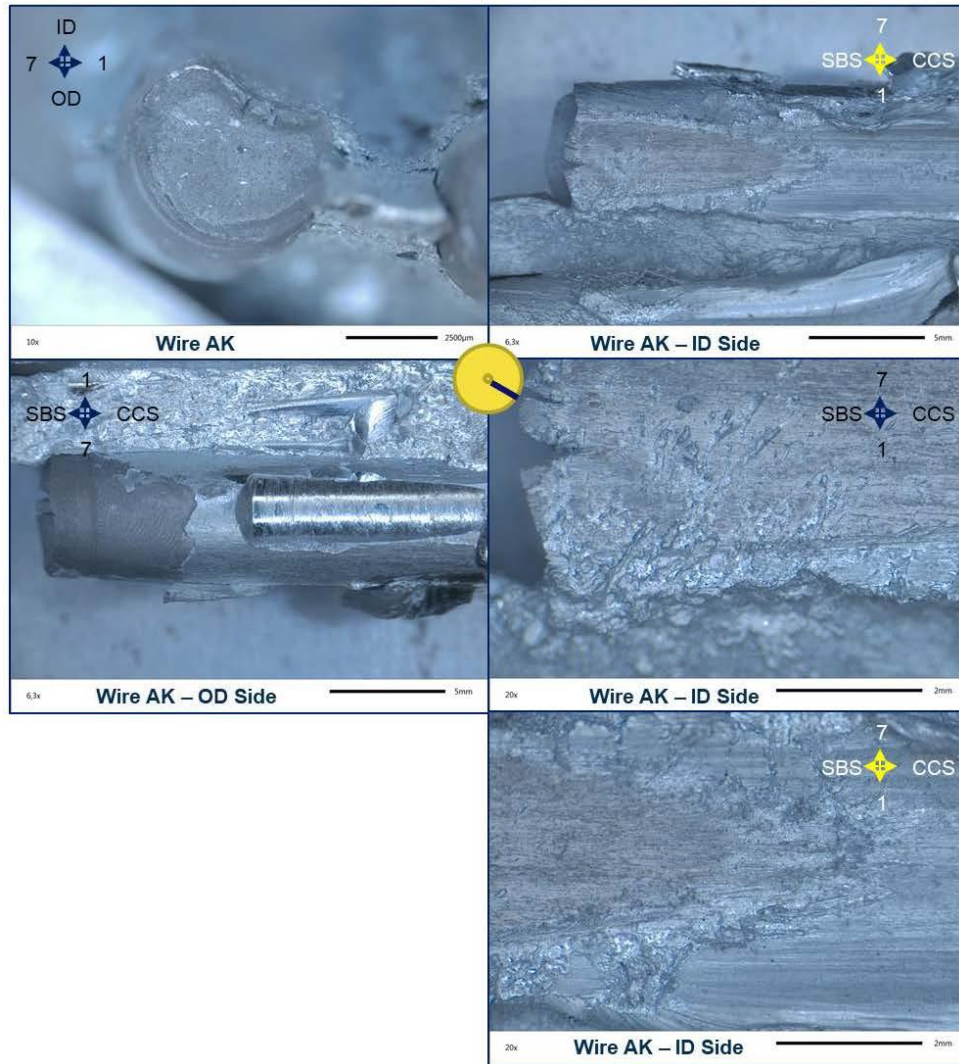


Figure 242. Stereomicroscope images of wire AK (4:00). Close up images of the zinc show a thin layer of molten zinc spatter that occurred when the cable/zinc slug was displaced from the socket during the ultimate failure of the joint.

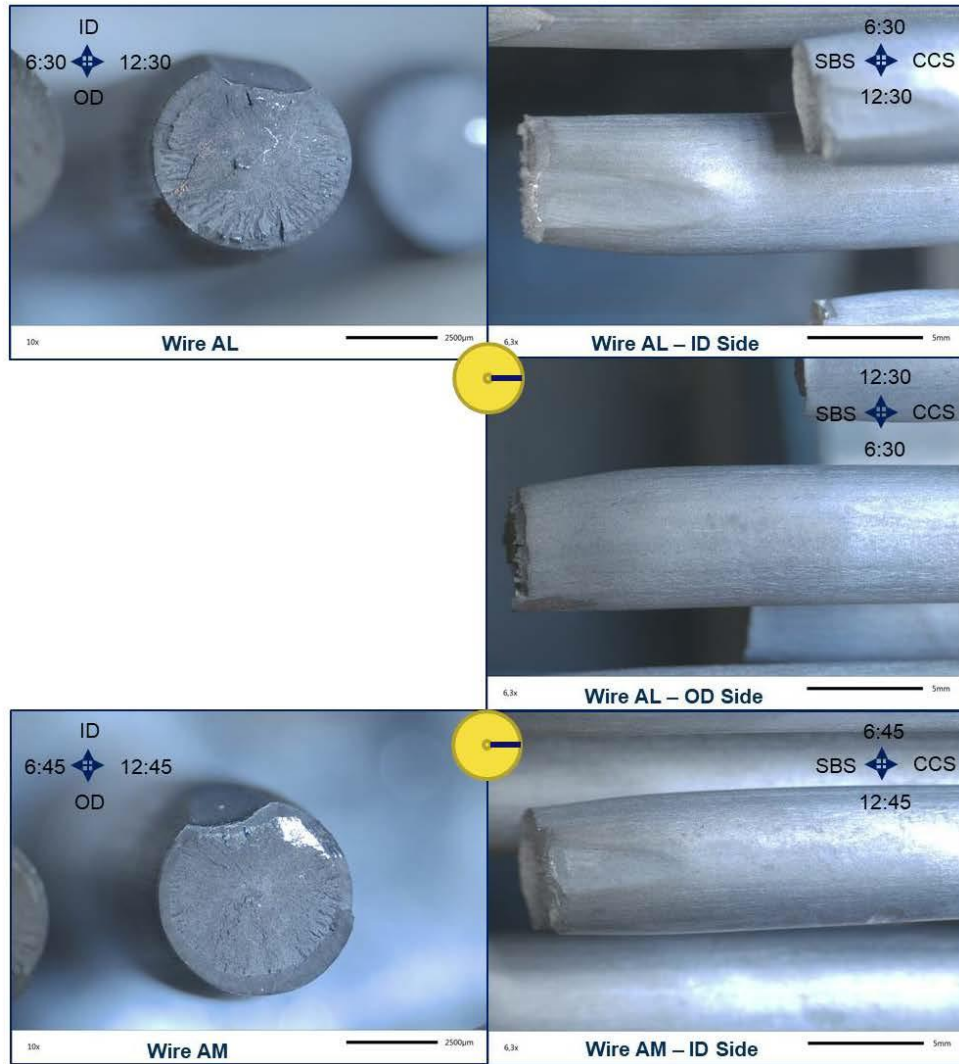


Figure 243. Stereomicroscope images of wire AL (3:30) and wire AM (3:45).

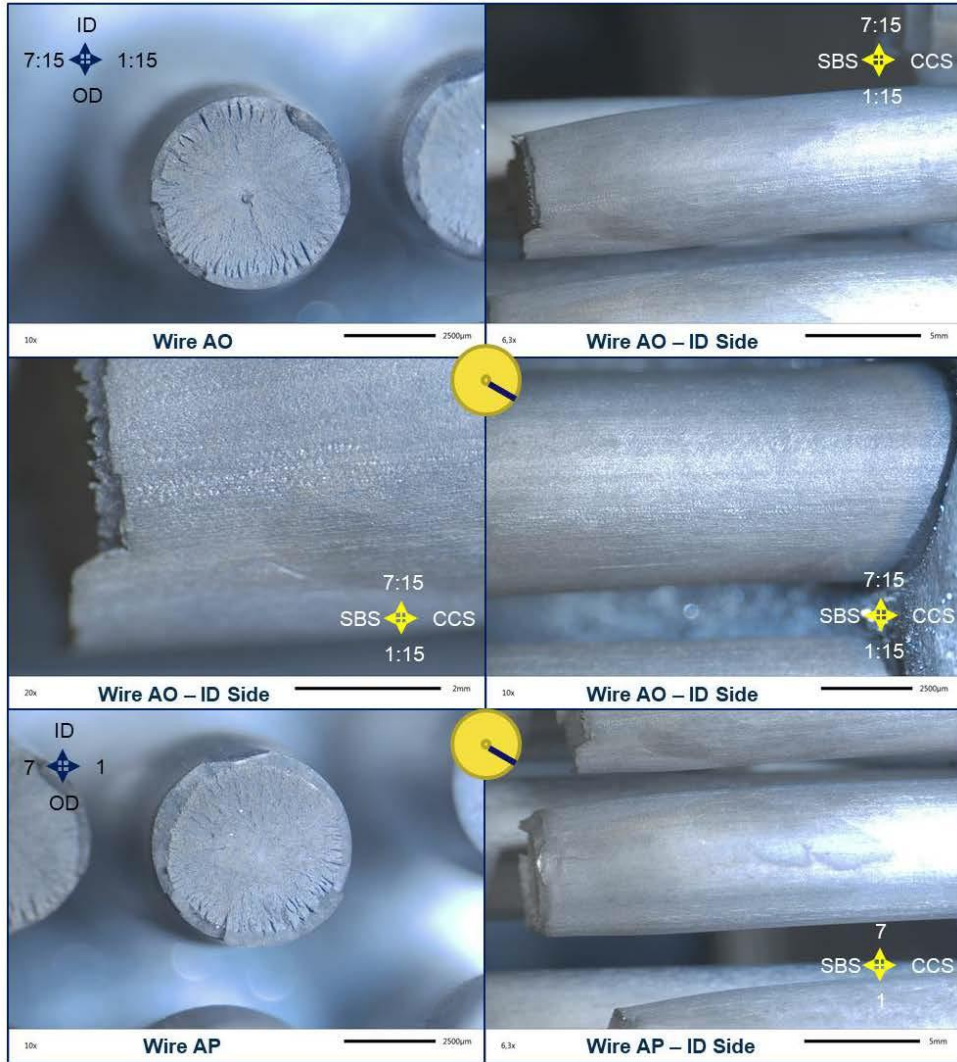


Figure 244. Stereomicroscope images of wire AO (4:15) and wire AP (4:00). Wire AO has a defect running in a line down the length of visible wire, that appears to have been created by a machine or tool.

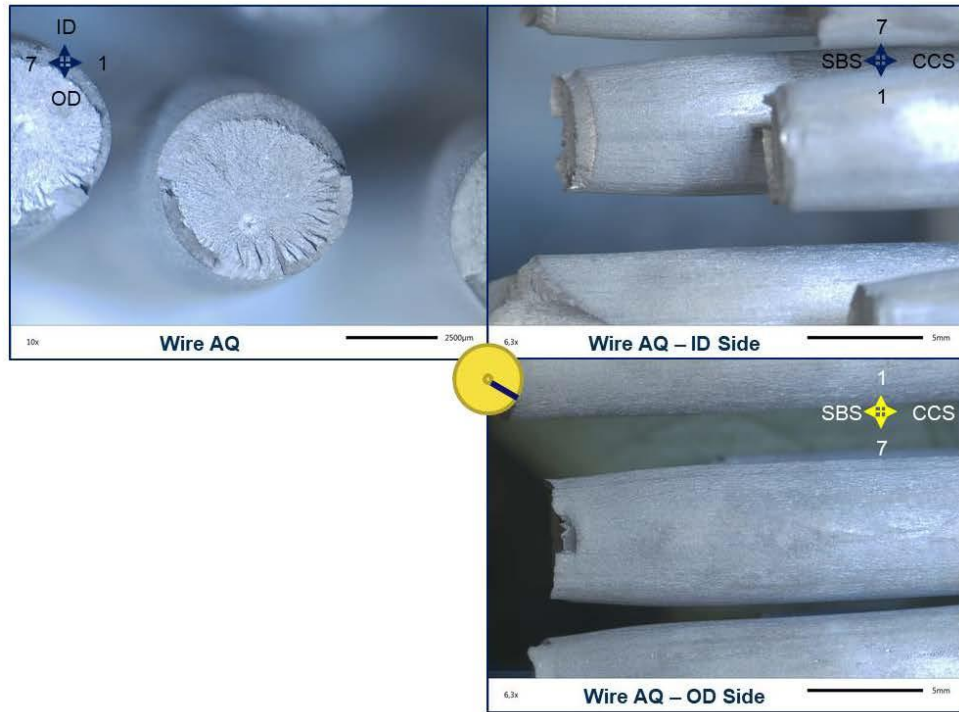


Figure 245. Stereomicroscope images of wire AQ (4:00).

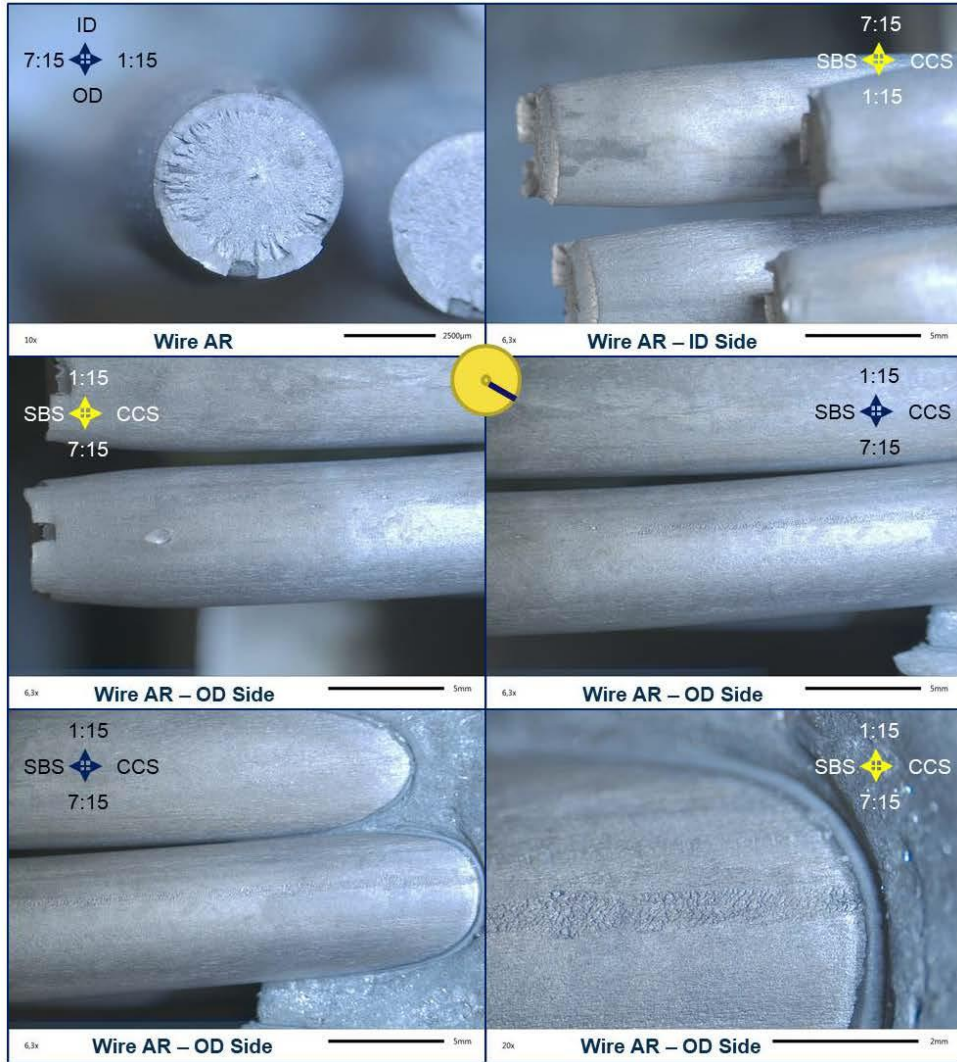


Figure 246. Stereomicroscope images of wire AR (4:15). Wire AR has a defect running in a line down most of the length of visible wire, but not to the fracture surface, that appears to have been created by a machine or tool. The nick seen on the outer diameter side in the middle row left image likely occurred during sectioning.

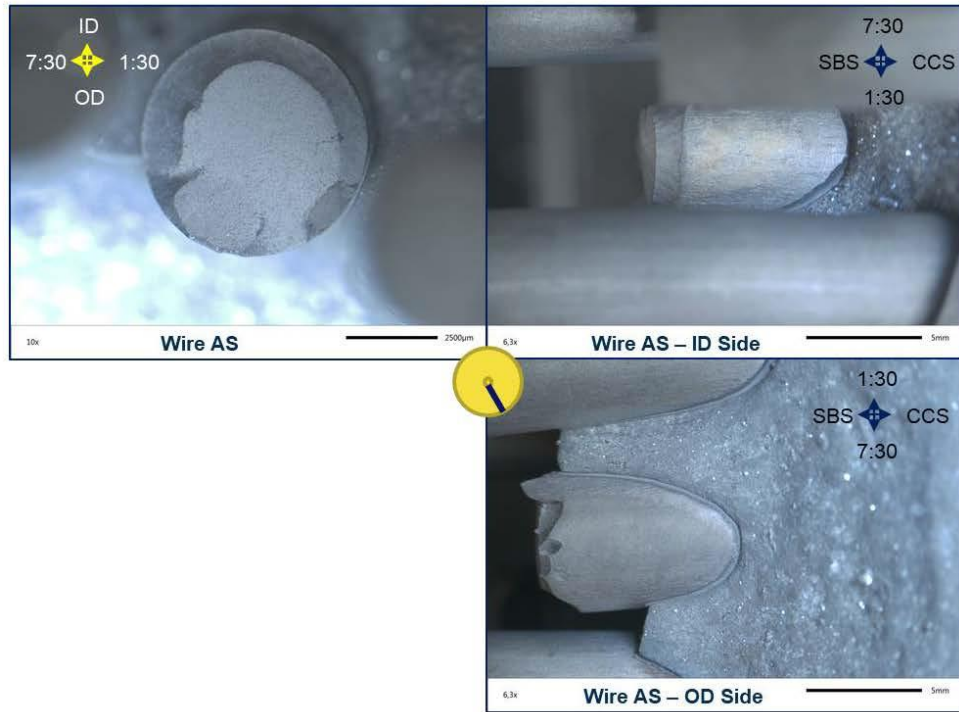


Figure 247. Stereomicroscope images of wire AS (4:30).

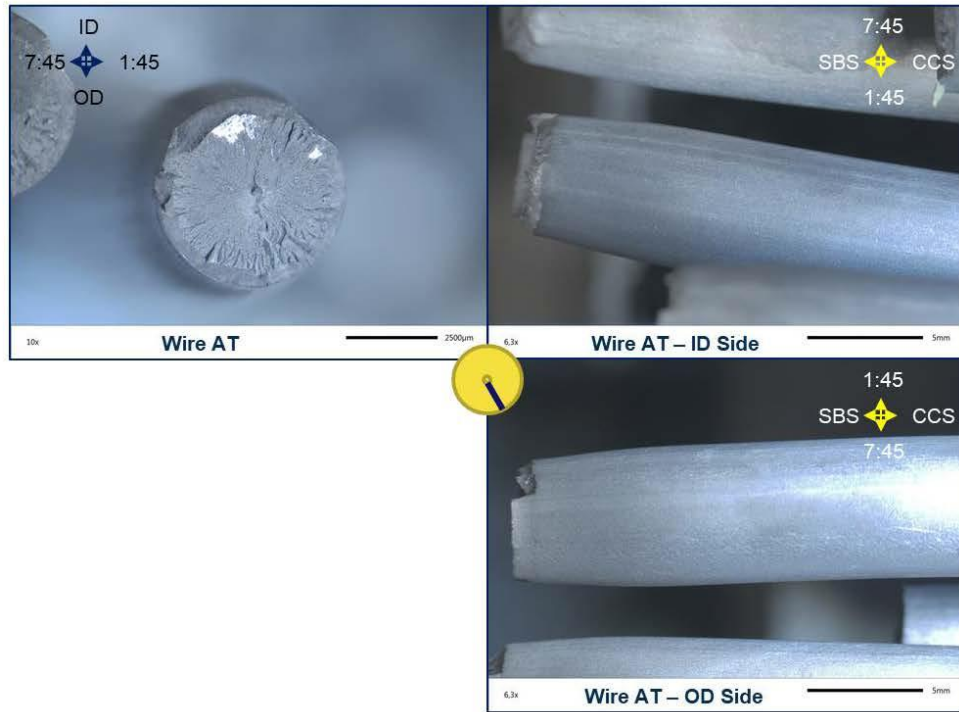


Figure 248. Stereomicroscope images of wire AT (4:45).

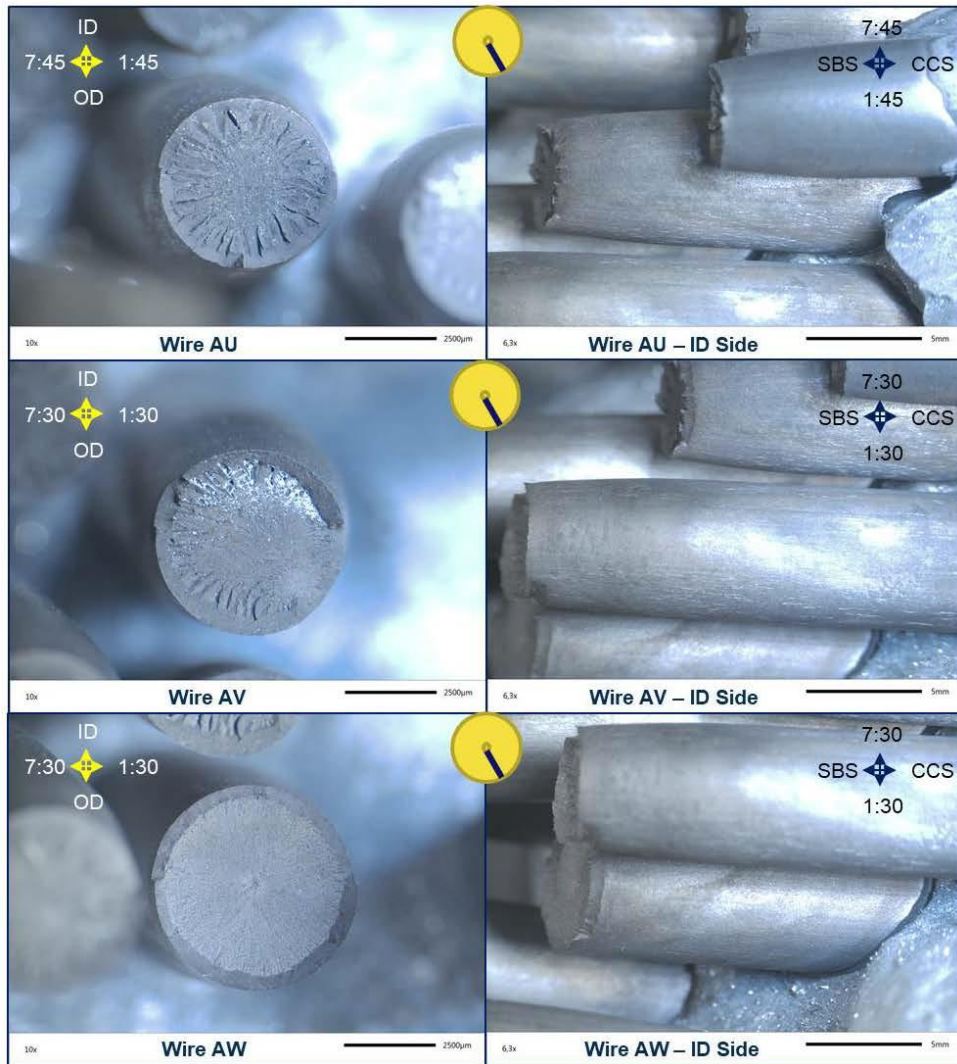


Figure 249. Stereomicroscope images of wire AU (4:45), wire AV (4:30), and wire AW (4:30).

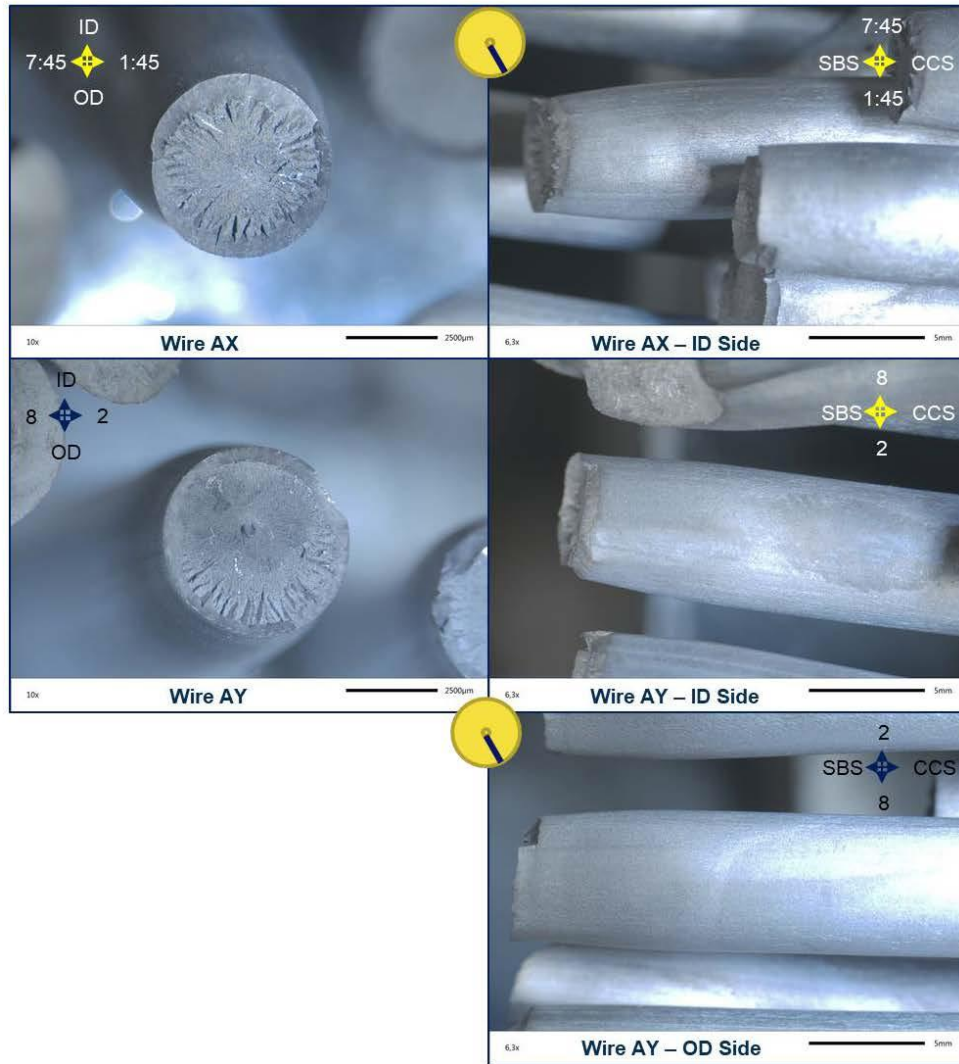


Figure 250. Stereomicroscope images of wire AX (4:45) and wire AY (5:00).

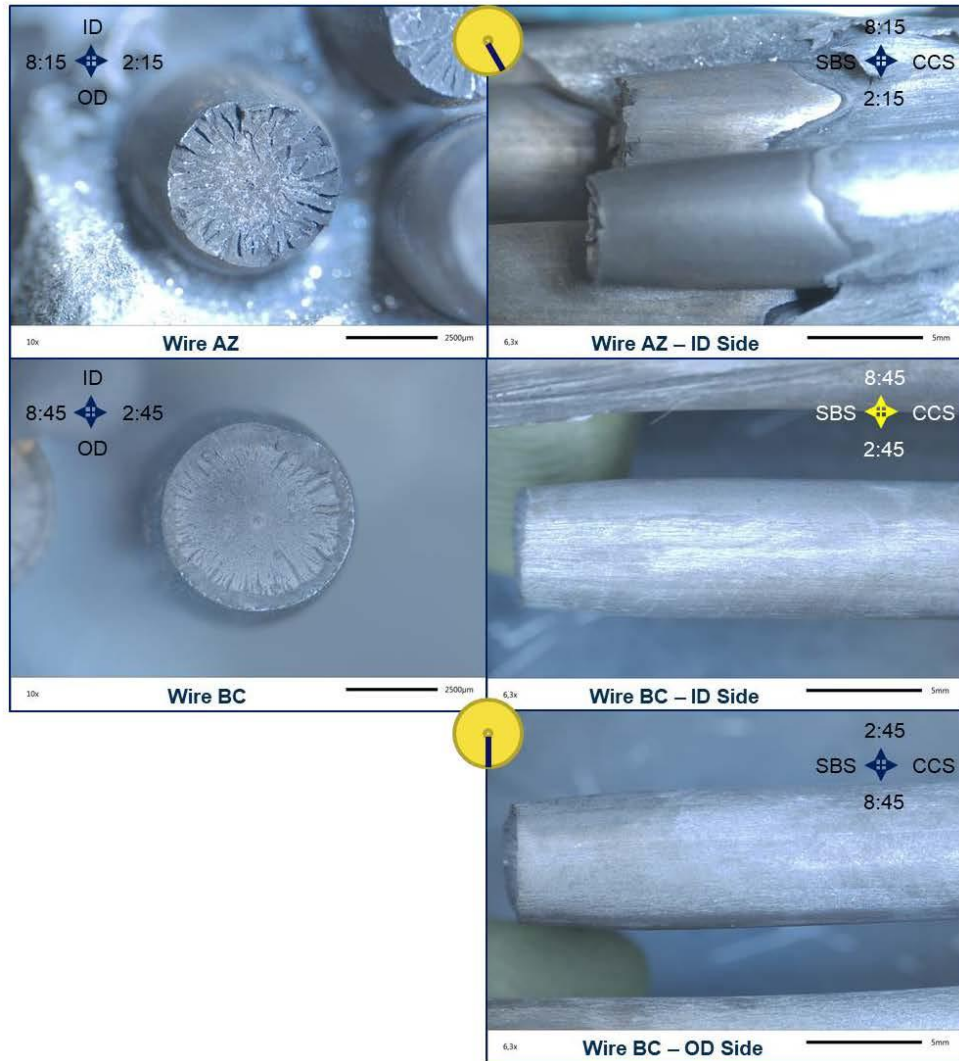


Figure 251. Stereomicroscope images of wire AZ (5:15) and wire BC (5:45).

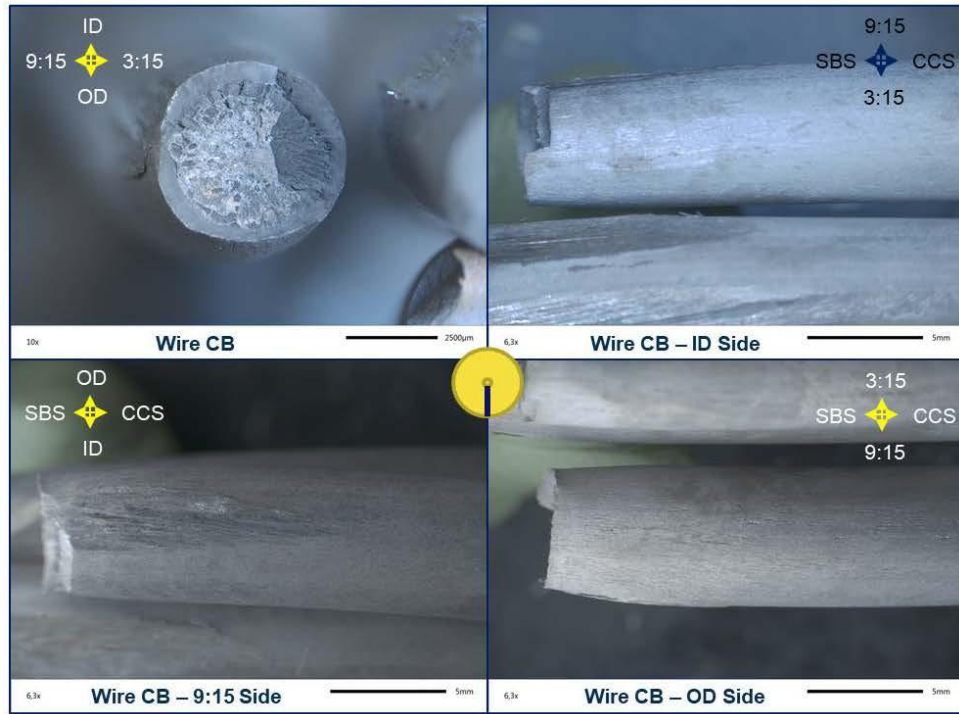


Figure 252. Stereomicroscope images of wire CB (6:15).

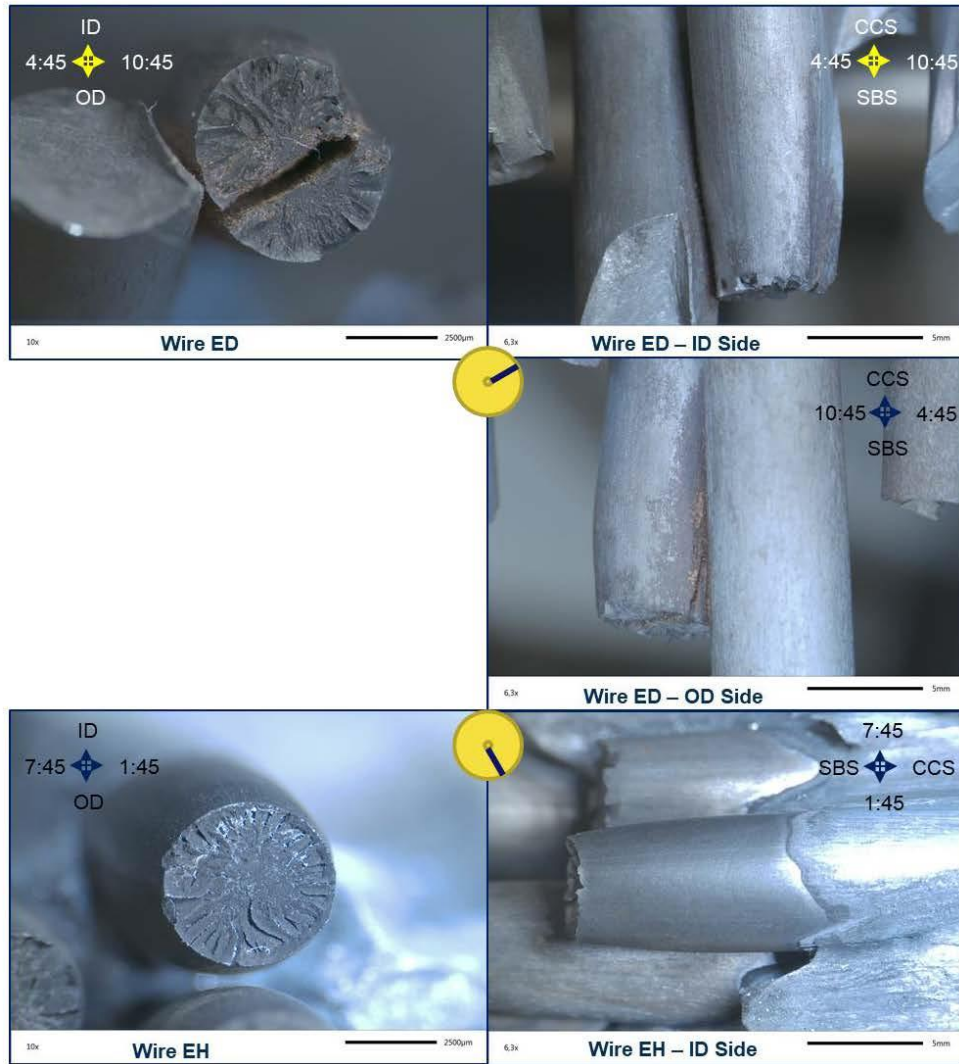


Figure 253. Stereomicroscope images of wire ED (1:45) and wire EH (4:45).

H.2 Shear Fracture Morphology

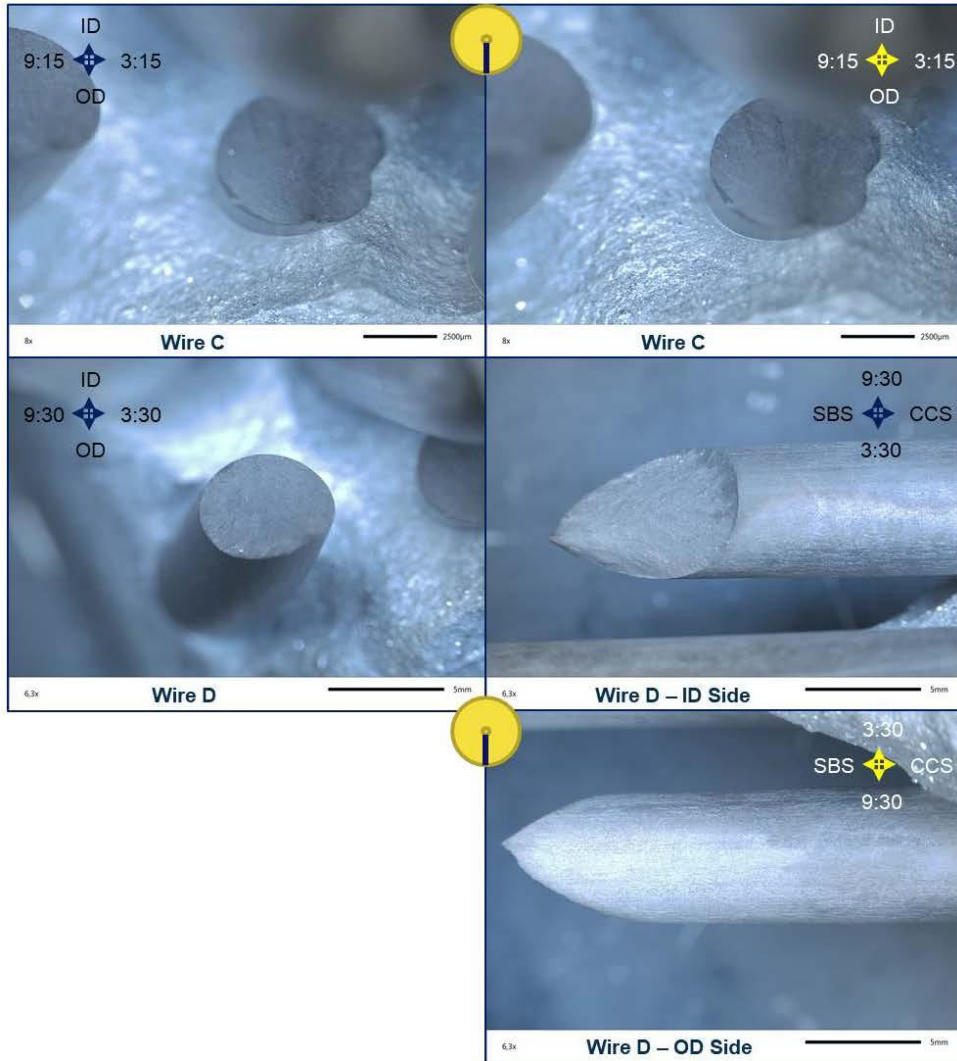
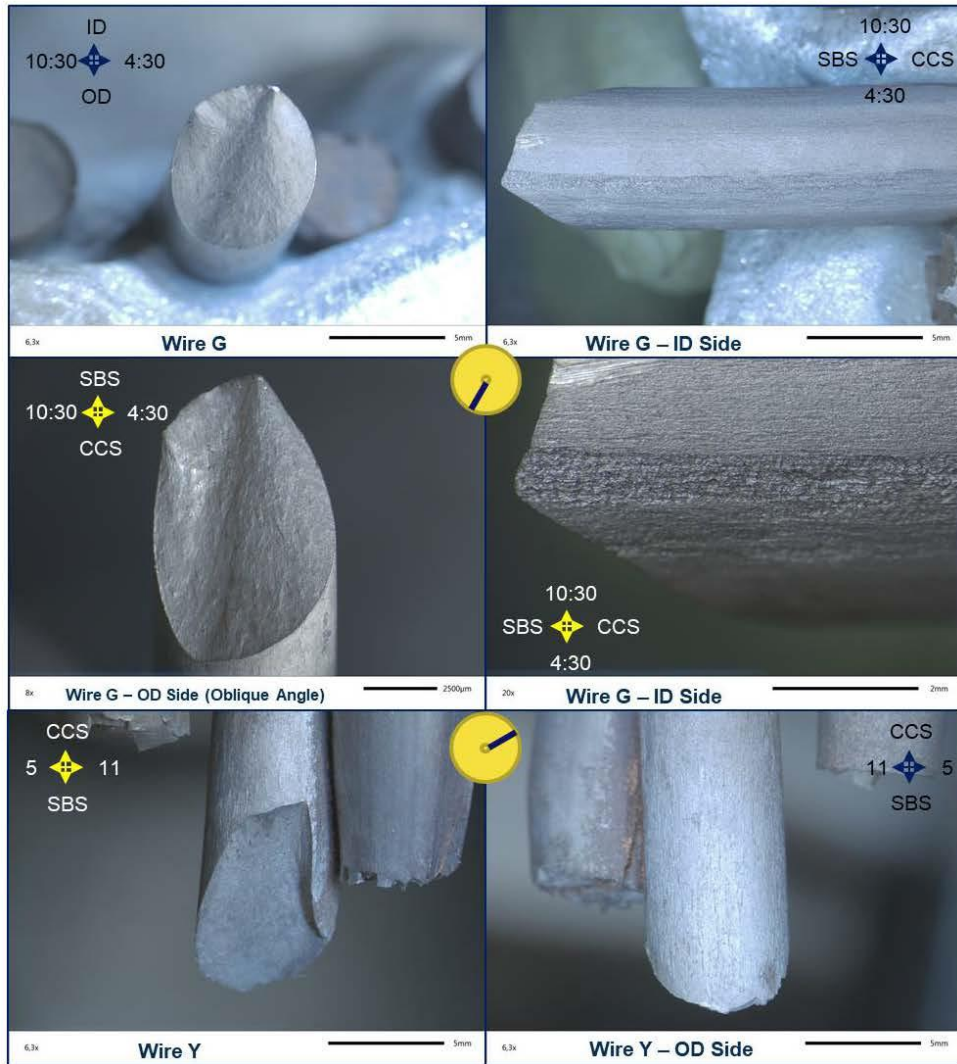


Figure 254. Stereomicroscope images of wire C (6:15) and wire D (6:30).



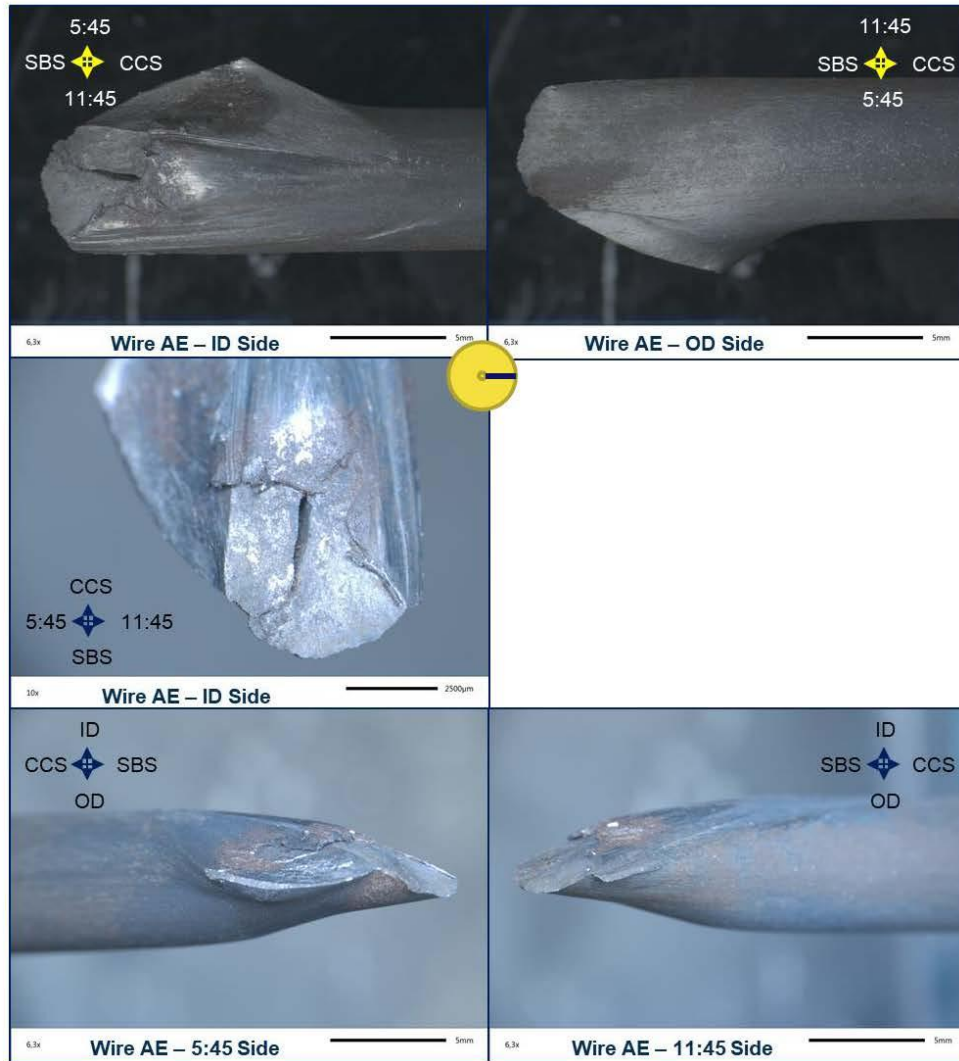


Figure 256. Stereomicroscope images of wire AE (2:45).

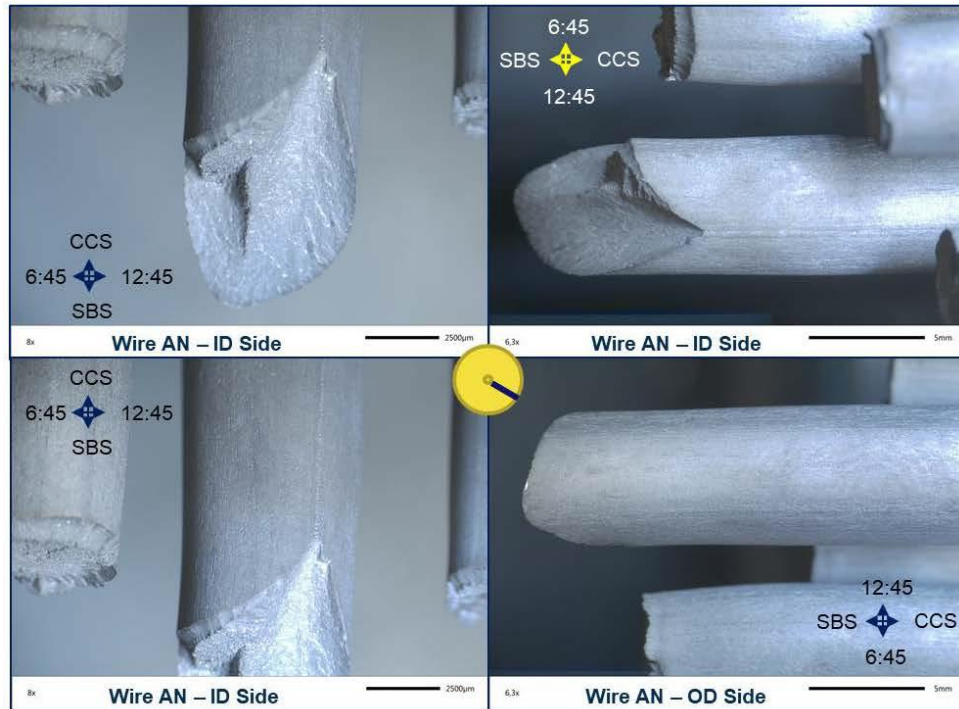


Figure 257. Stereomicroscope images of wire AN (3:45). Wire AN has a defect running in a line down the length of visible wire, that appears to have been created by a machine or tool.

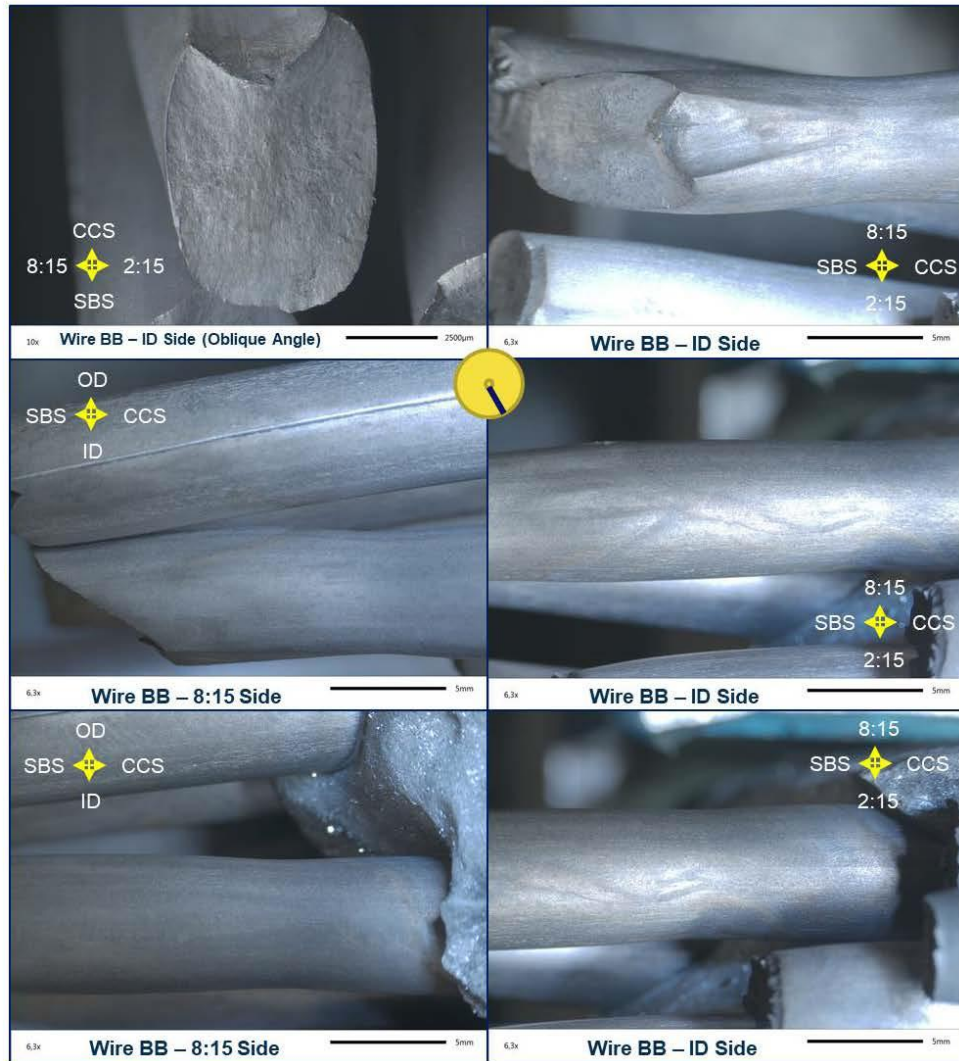


Figure 258. Stereomicroscope images of wire BB (5:15). Wire BB had two necked regions behind the fracture surface.

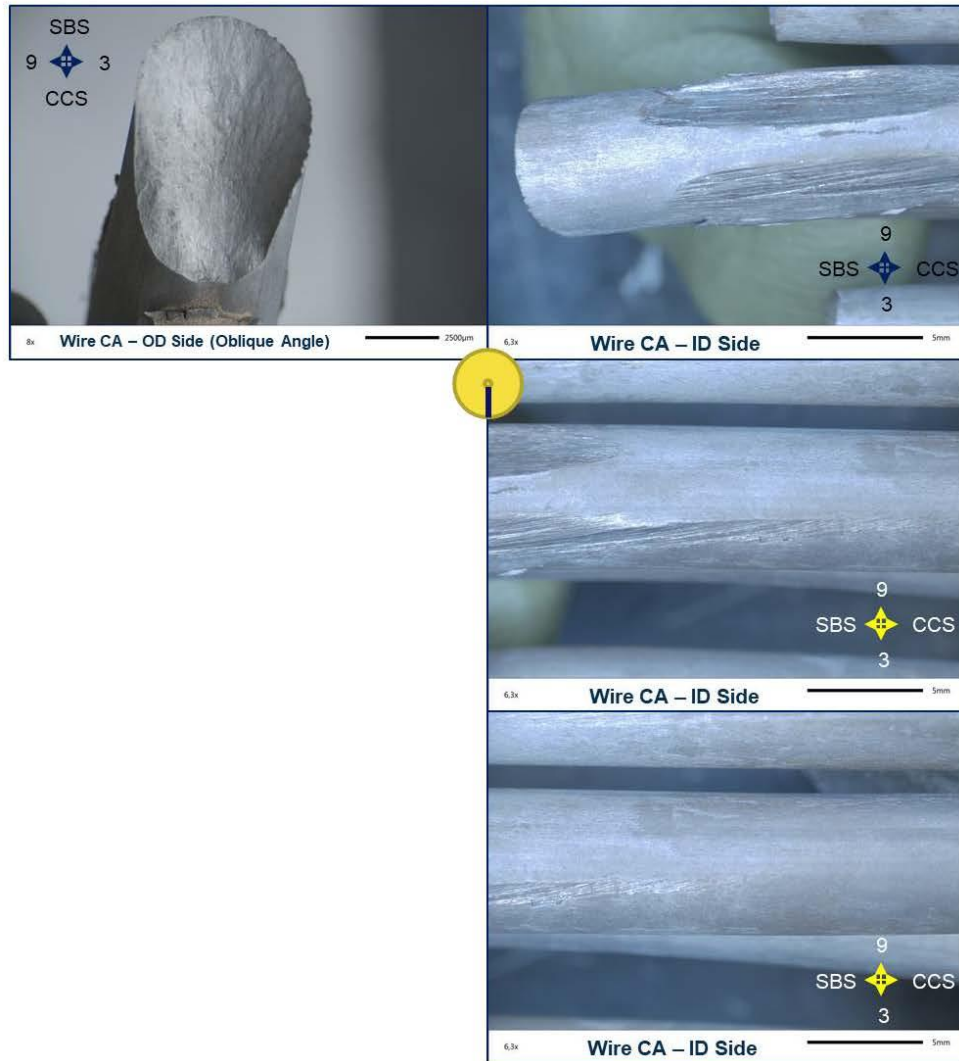


Figure 259. Stereomicroscope images of wire CA (6:00).

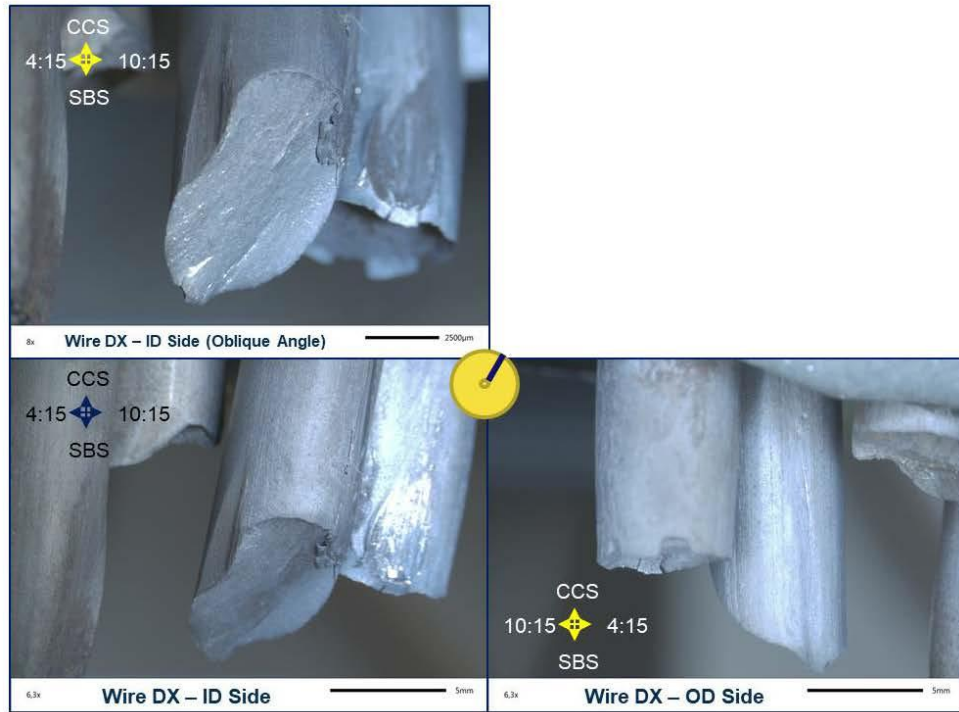


Figure 260. Stereomicroscope images of wire DX (1:15).

H.3 Hydrogen Assisted Cracking Morphology

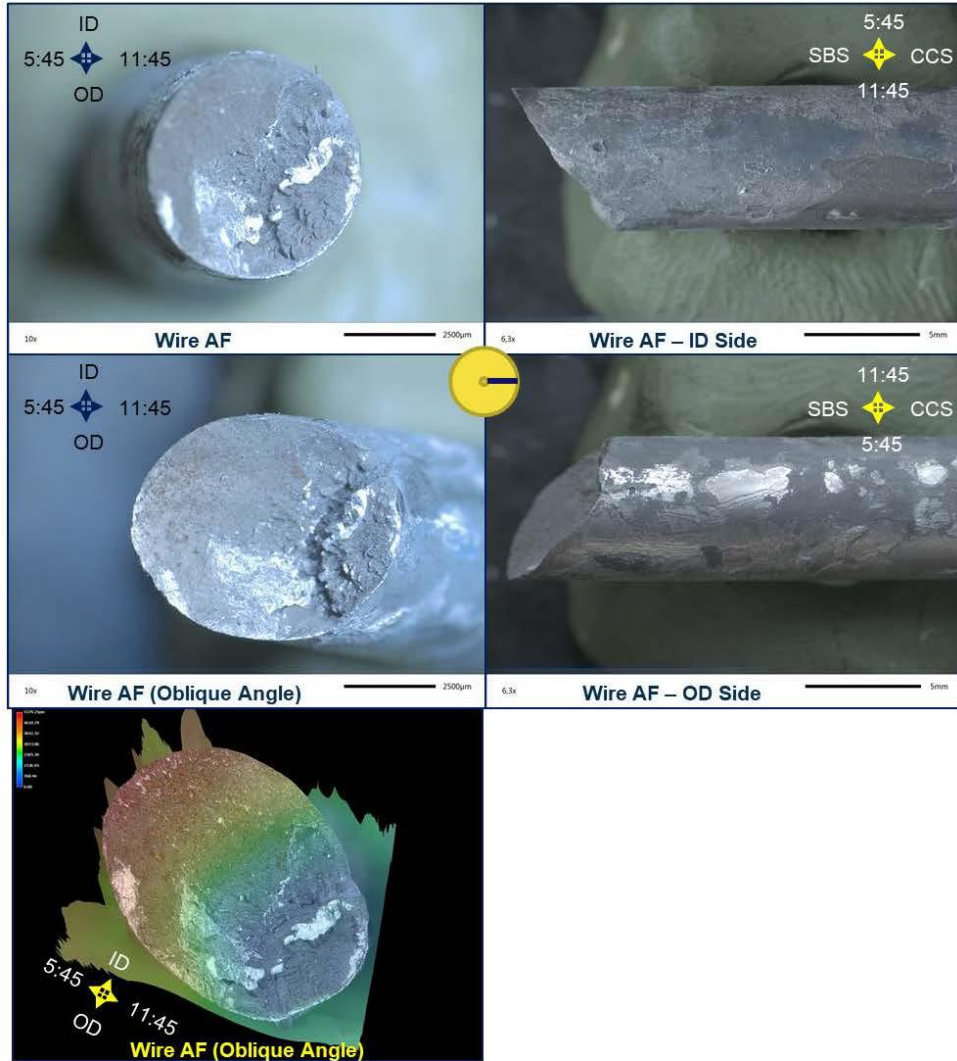


Figure 261. Stereomicroscope images of wire AF (2:45). The bottom row left image is a digitally enhanced 3D view of the fracture topography with a color-coded height map.

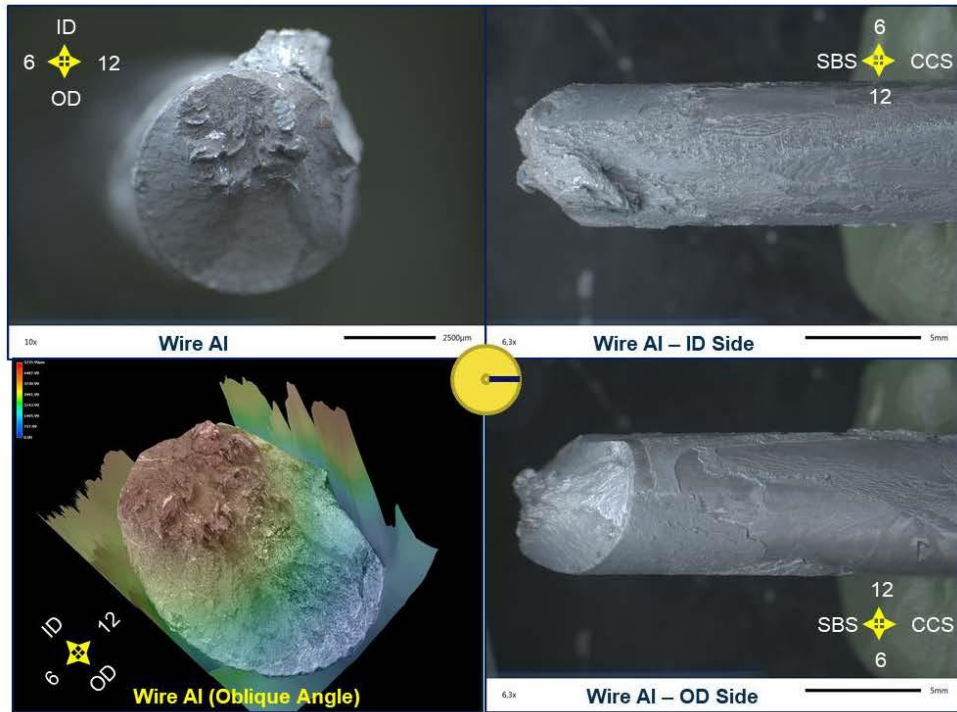


Figure 262. Stereomicroscope images of wire AI (3:00). The bottom row left image is a digitally enhanced 3D view of the fracture topography with a color-coded height map.

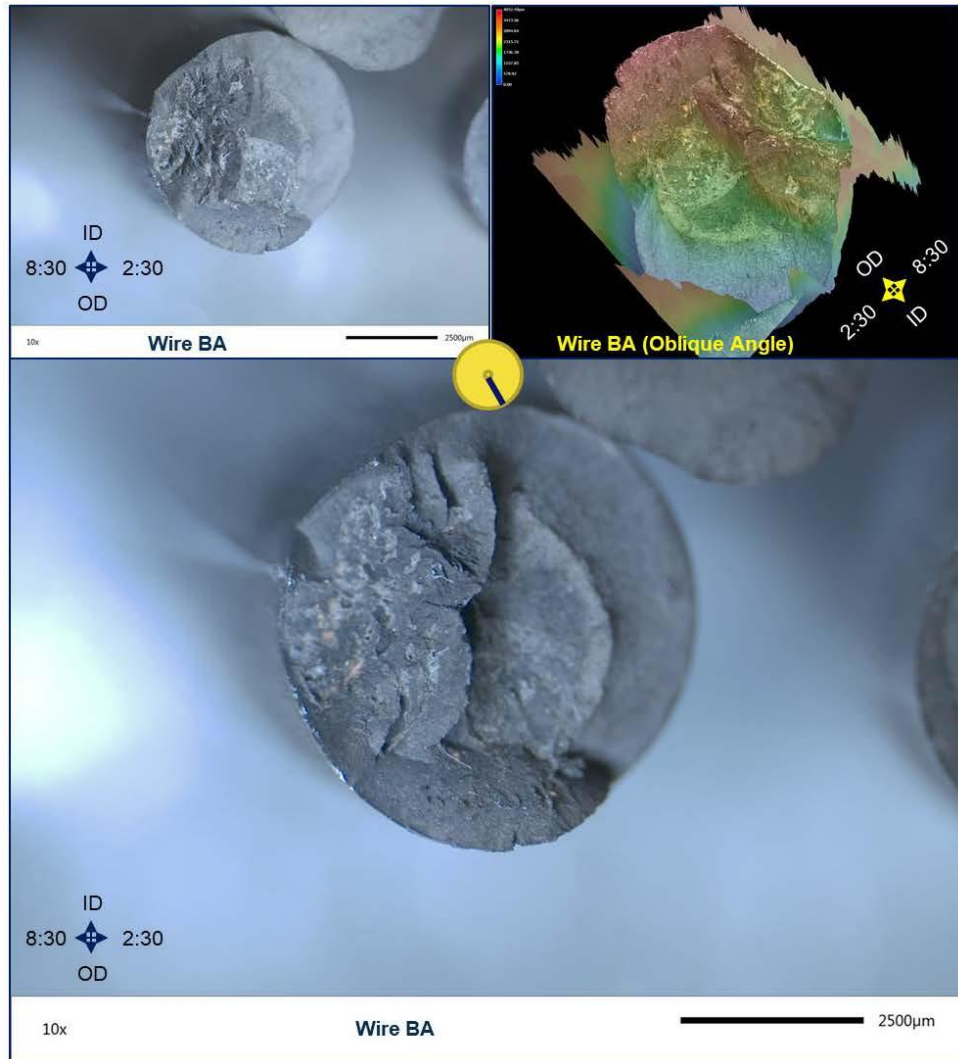


Figure 263. Stereomicroscope images of wire BA (5:30). The top row right image is a digitally enhanced 3D view of the fracture topography with a color-coded height map.

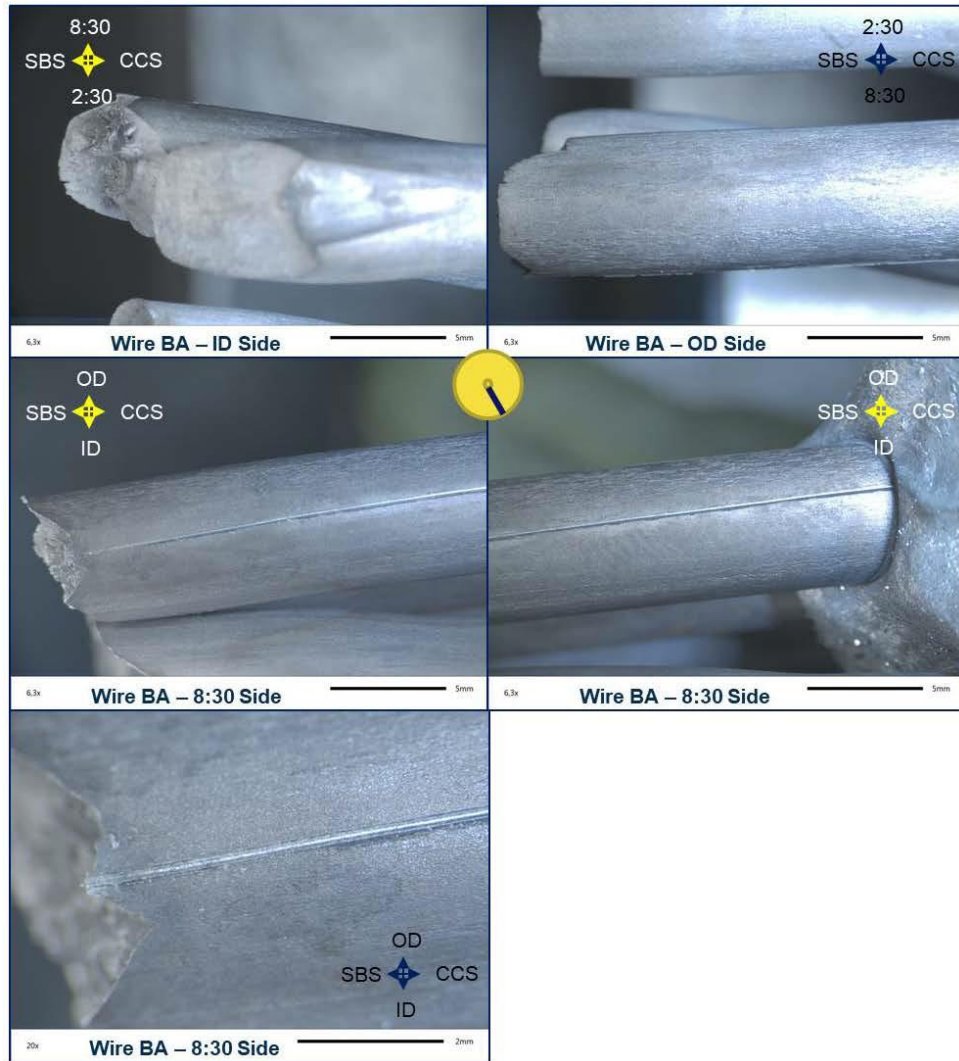


Figure 264. Stereomicroscope images of wire BA (5:30). Wire BA has a defect running in a line down the length of visible wire, that appears like a smooth but deep scribe line.

APPENDIX I. SEM OF WIRES

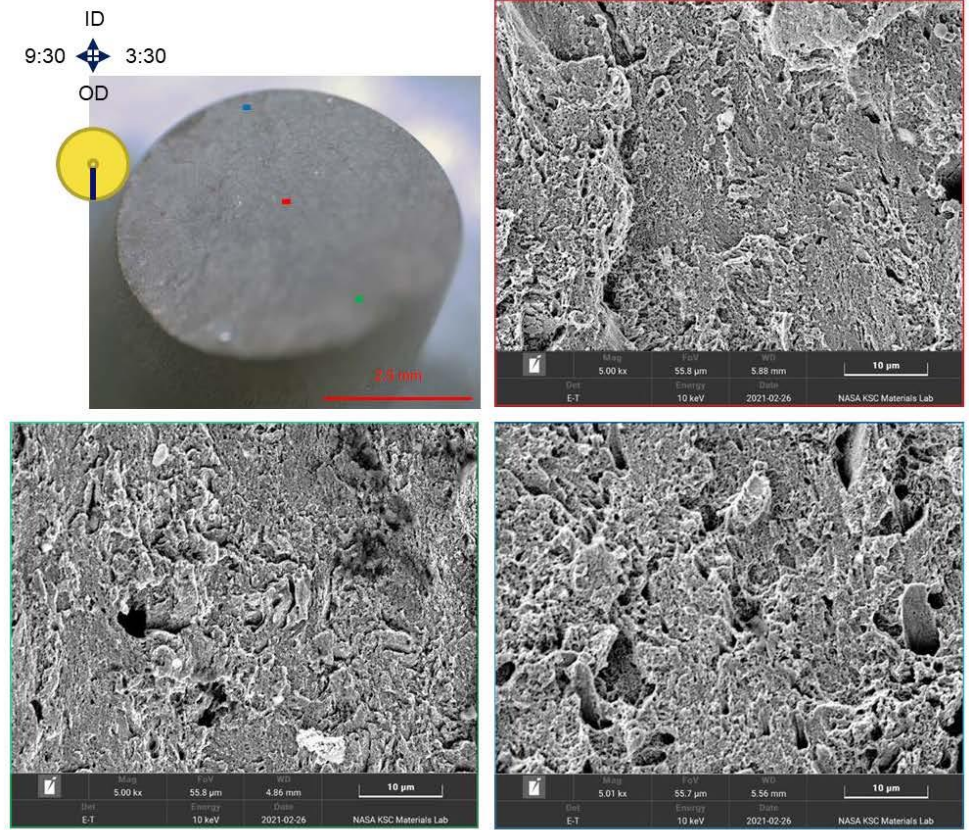


Figure 265. SEM images of wire D.

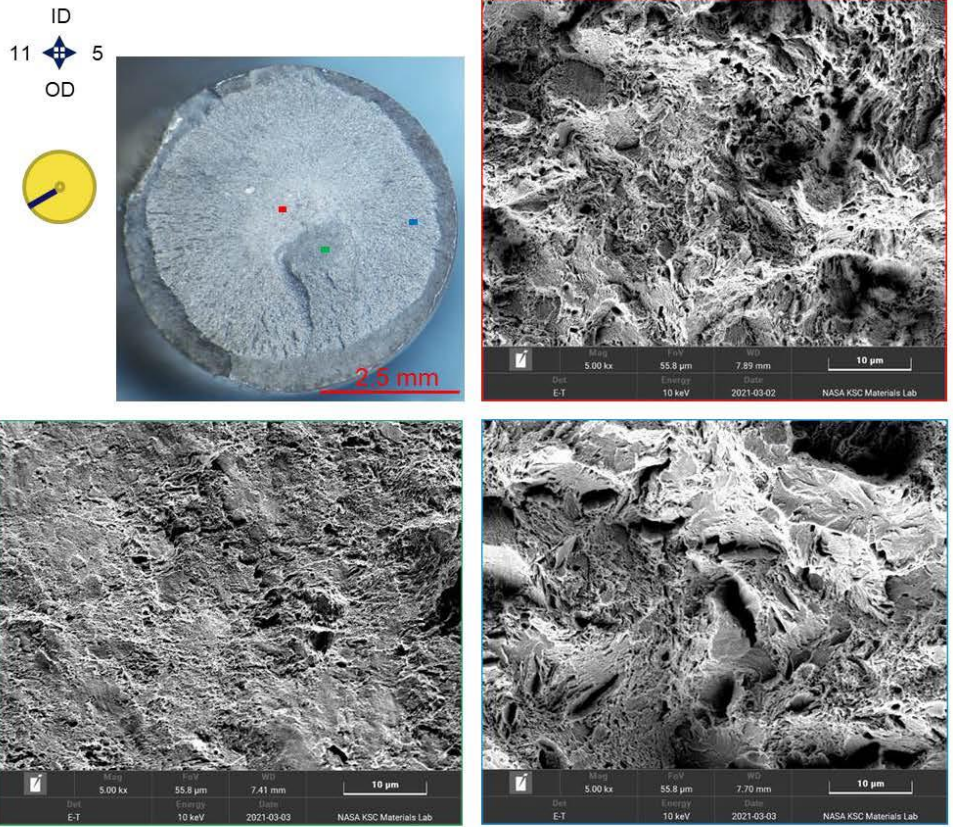


Figure 266. SEM images of wire I

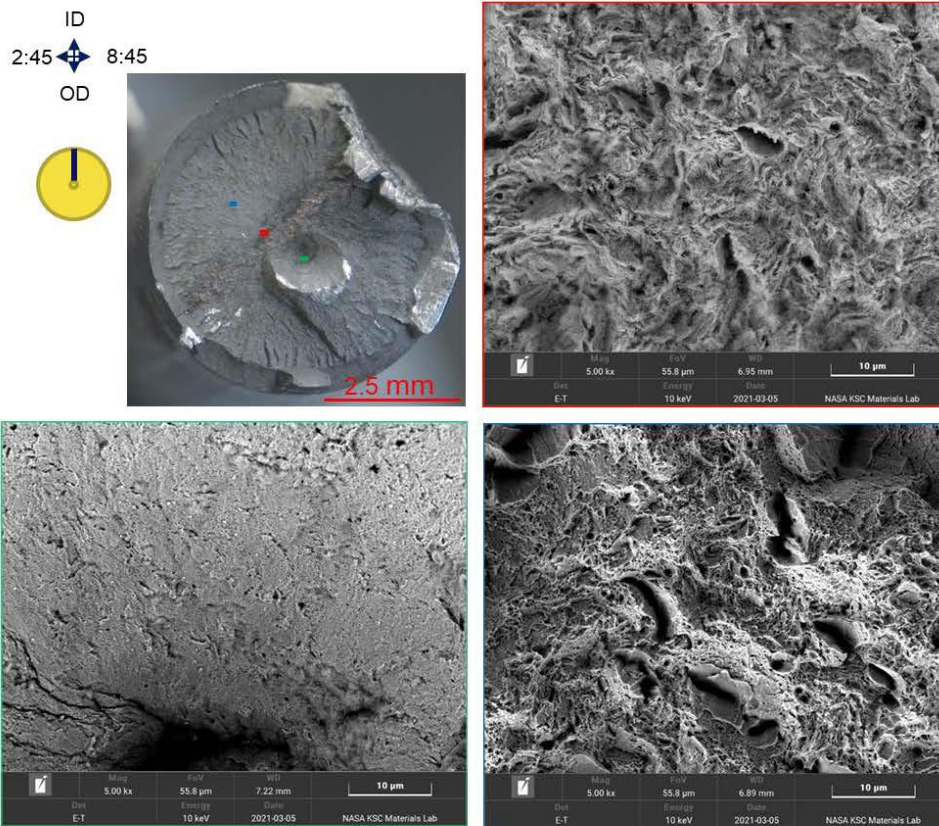


Figure 267. SEM images of wire S.

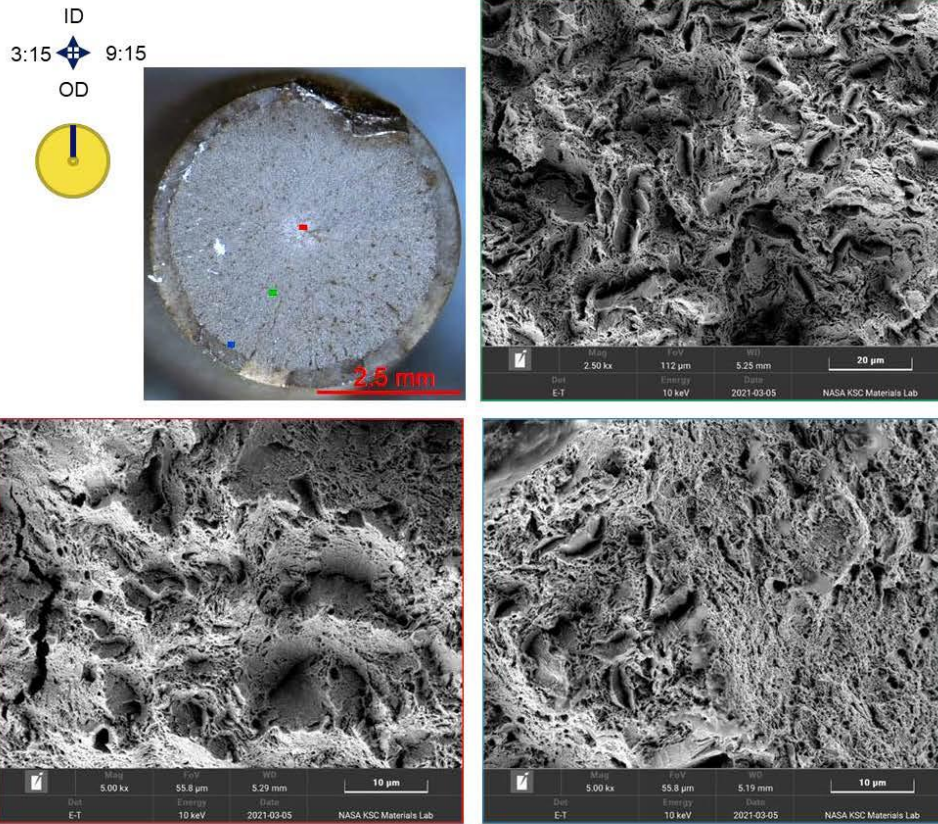


Figure 268. SEM images of wire U.

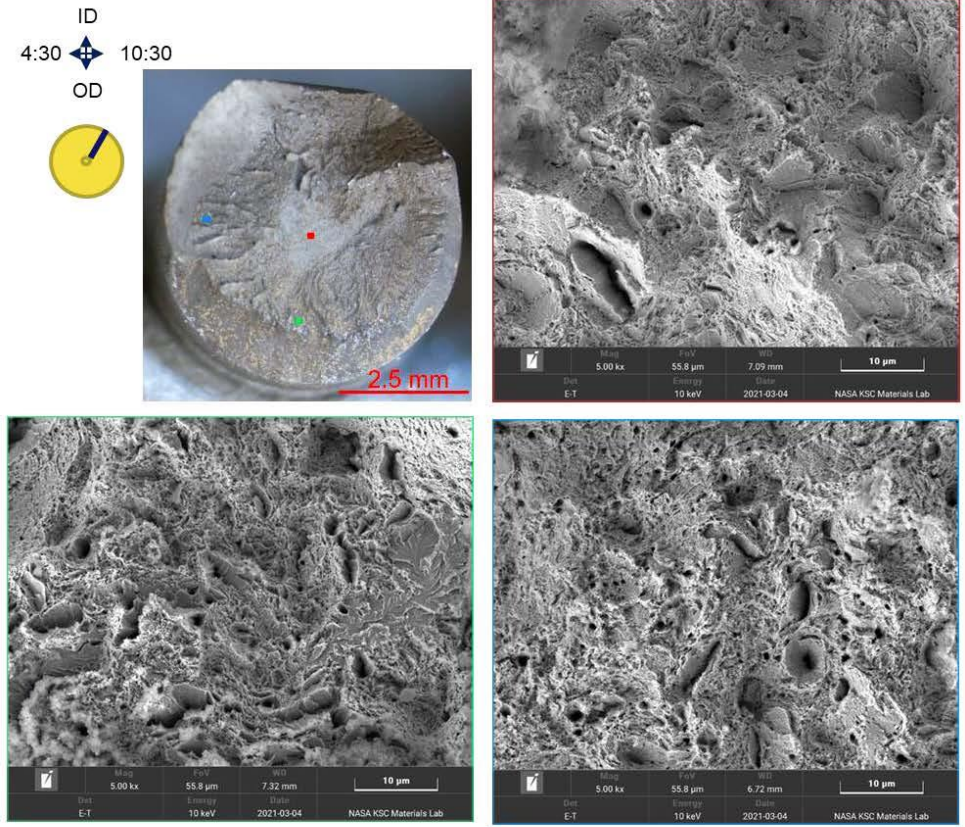


Figure 269. SEM images of wire X.

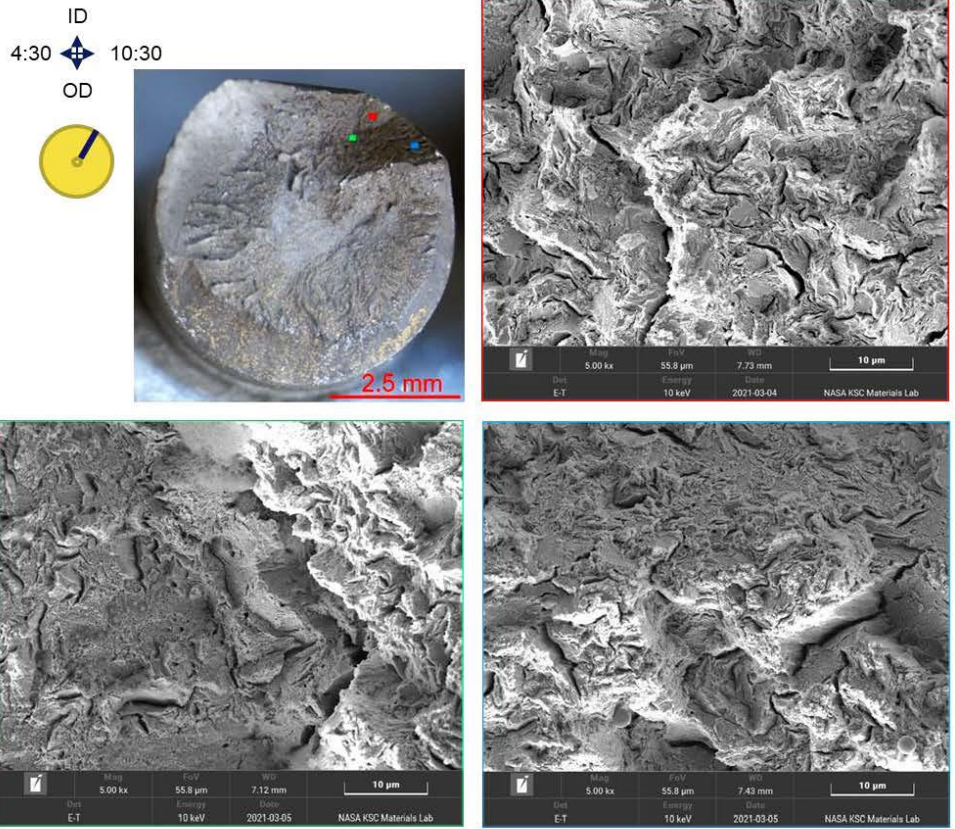


Figure 270. SEM images of the notch area of wire X.

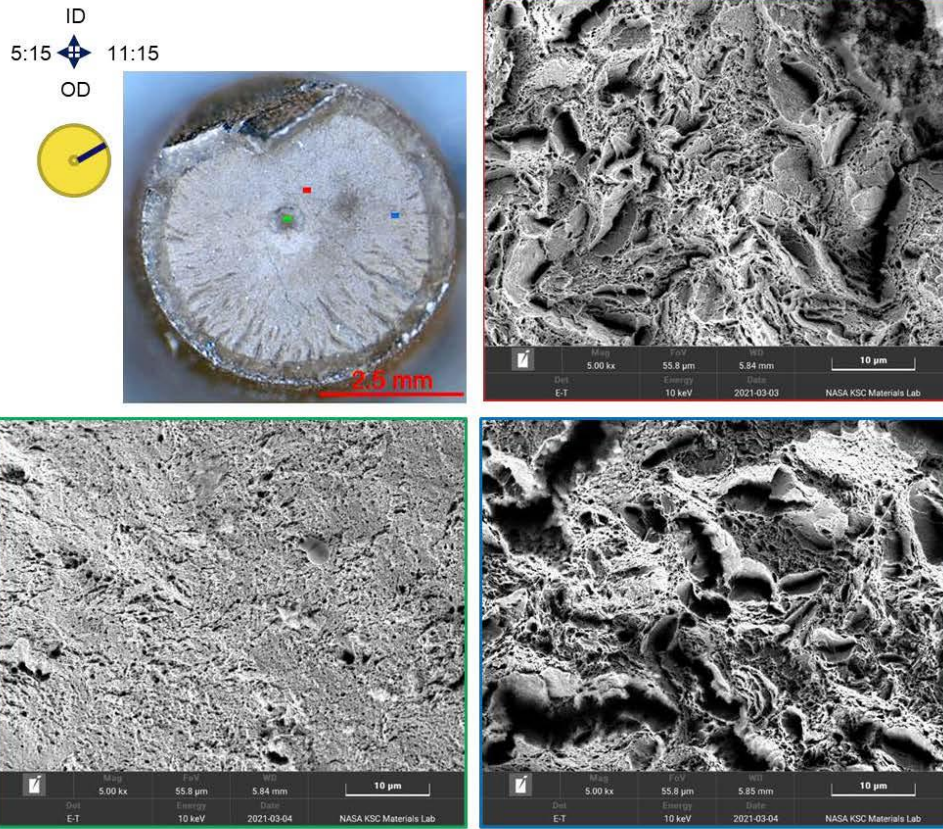


Figure 271. SEM images of wire Z.

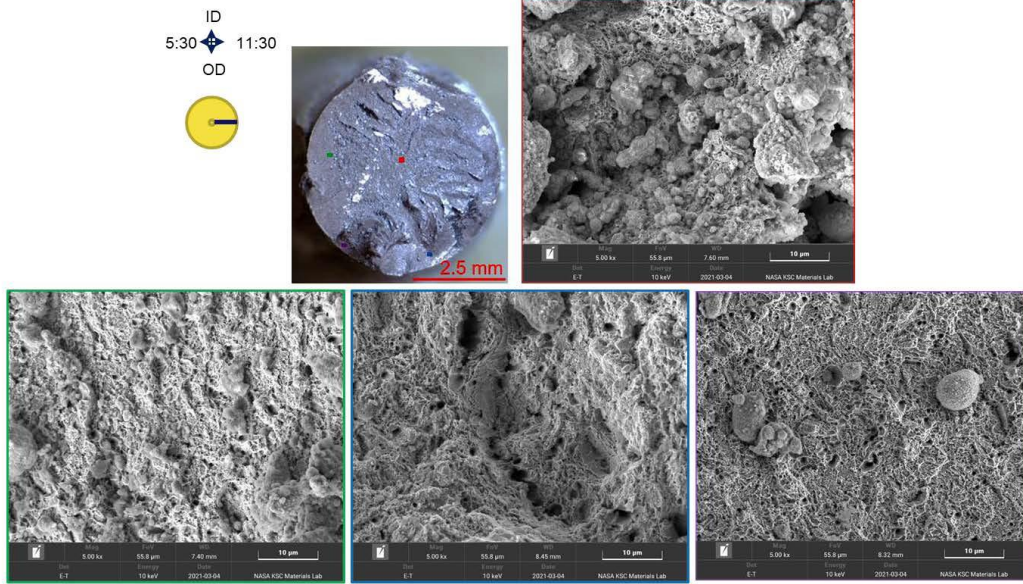


Figure 272. SEM images of wire AD.

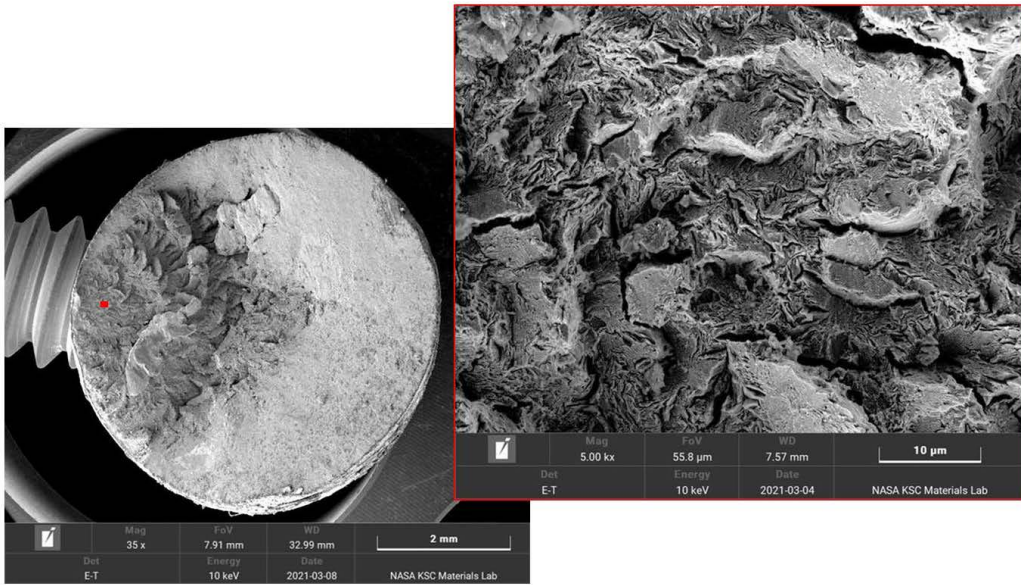


Figure 273. SEM images of wire AF.

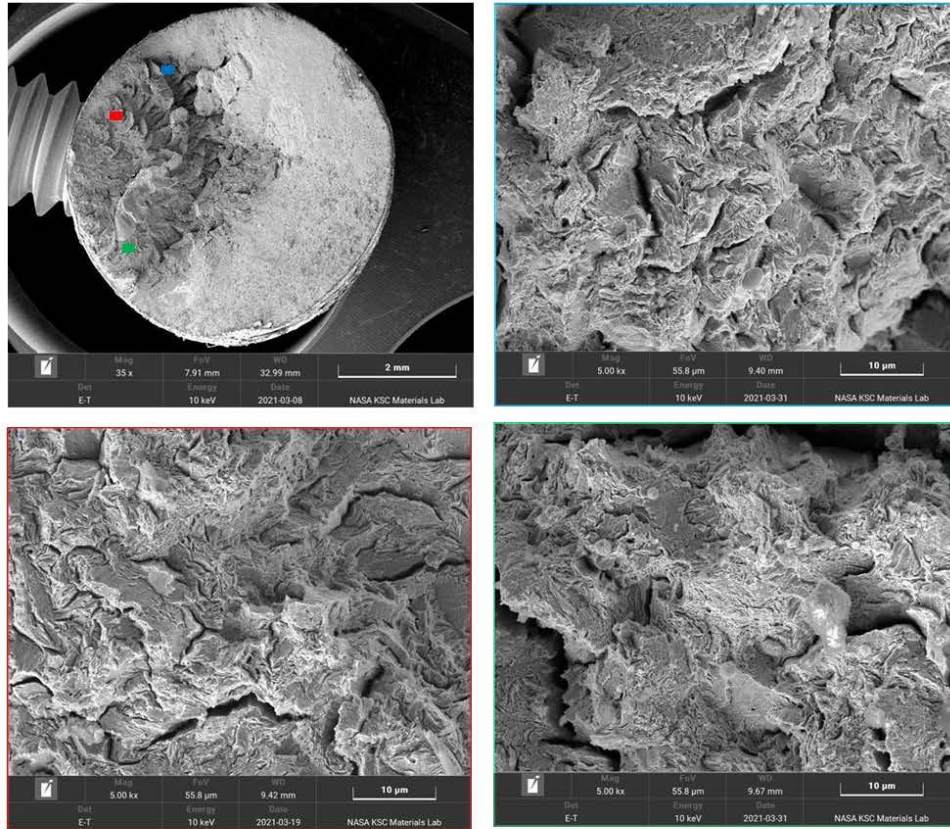


Figure 274. SEM images of wire AF.

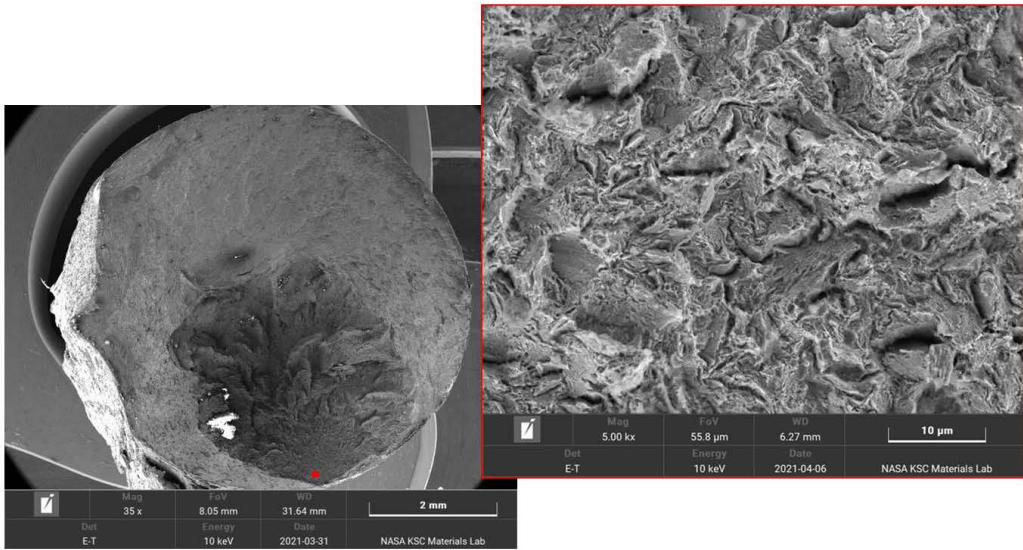


Figure 275. SEM images of wire Al.

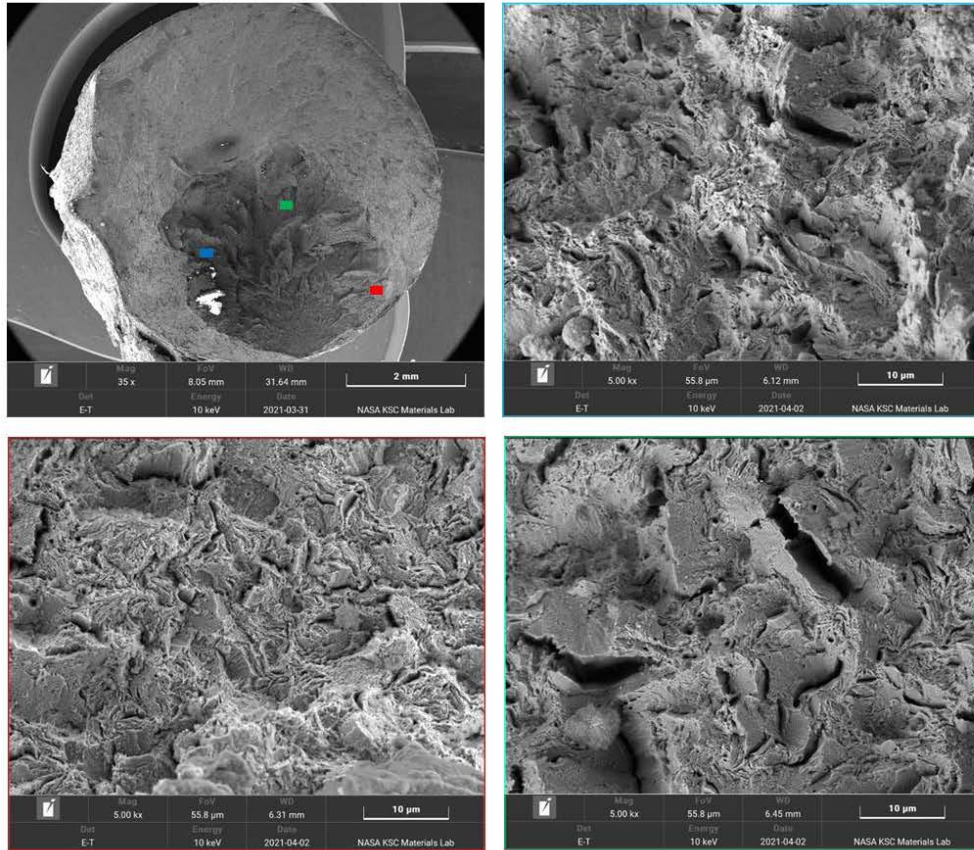


Figure 276. SEM images of wire Al.

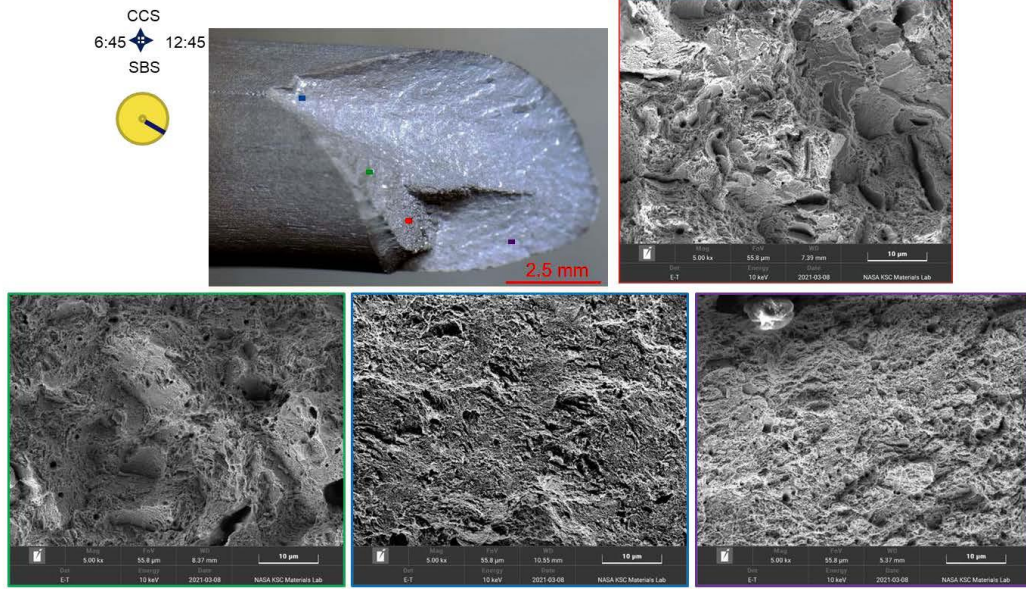


Figure 277. SEM images of wire AN, looking top down.

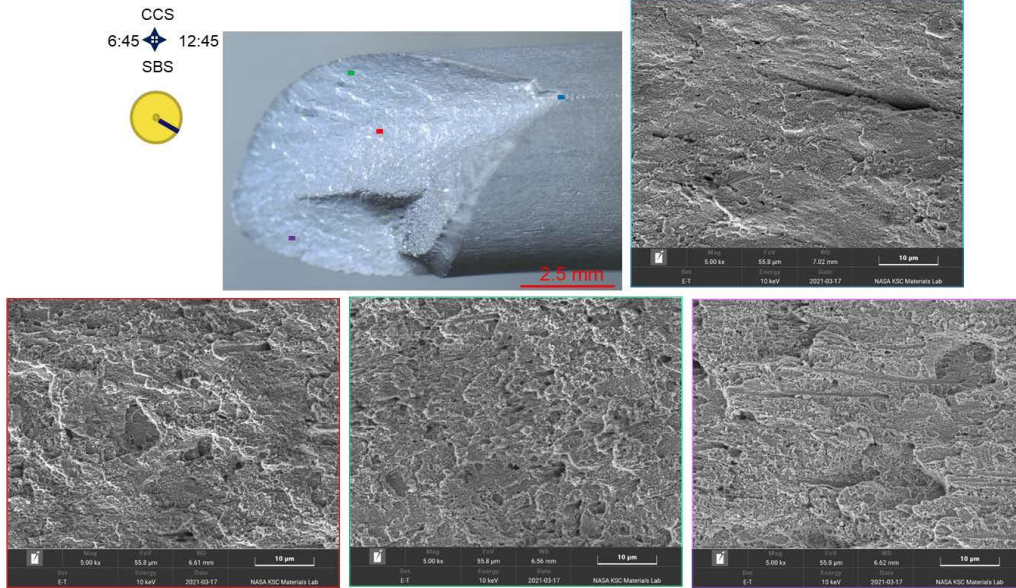


Figure 278. SEM images of wire AN, with the shear surface flat.

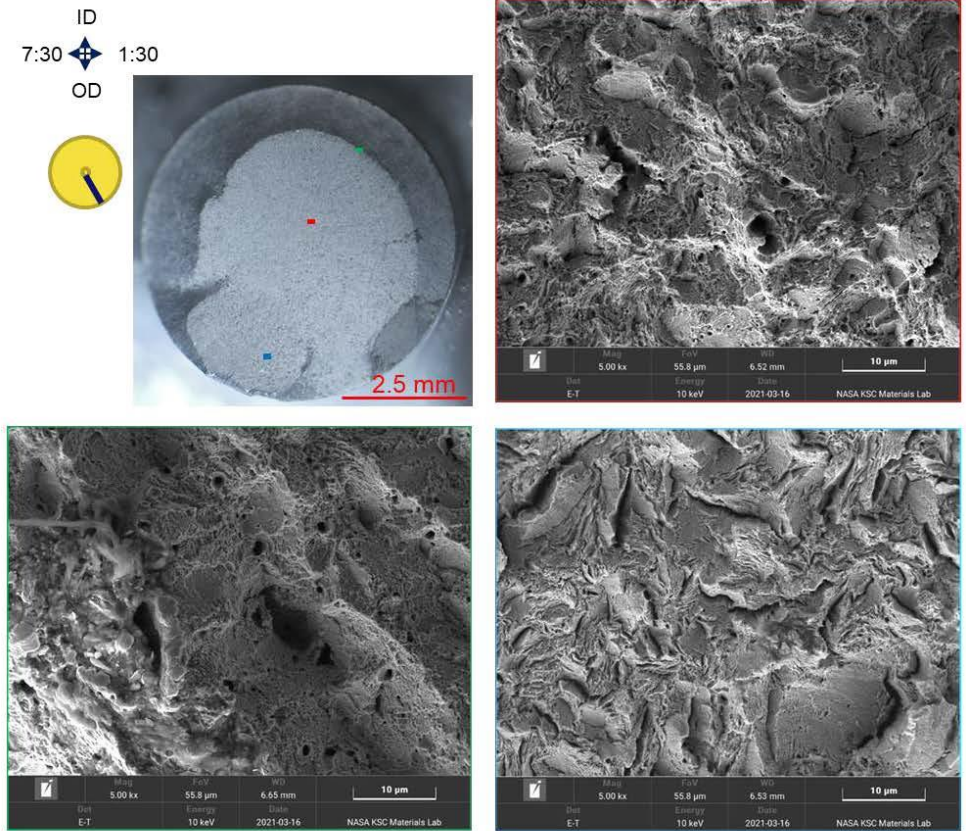


Figure 279. SEM images of wire AS.

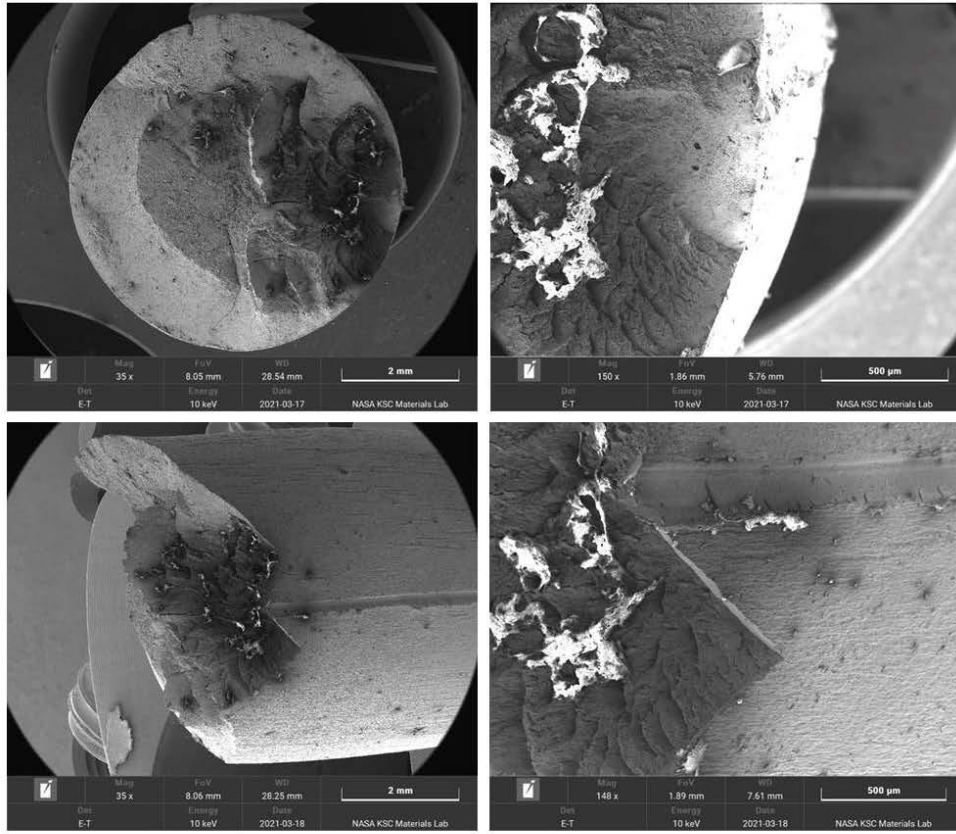


Figure 280. SEM images of the notch on wire BA.

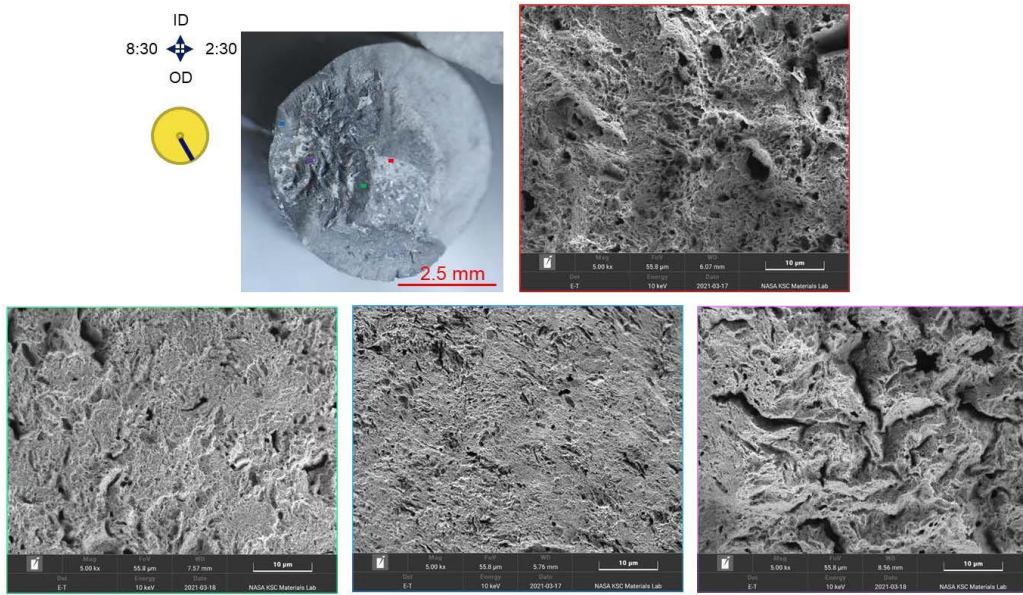


Figure 281. SEM images of wire BA, looking top down.

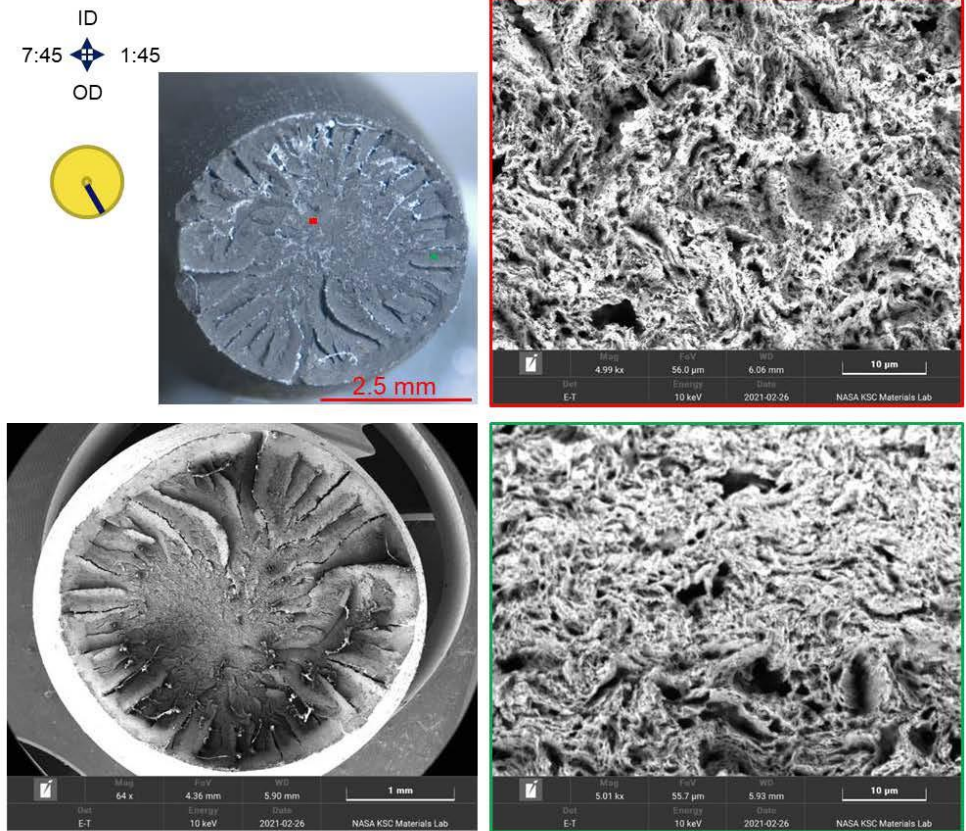


Figure 282. SEM images of wire EH.

APPENDIX J. STEREOMICROSCOPE NECKING MEASUREMENTS

Table 5. Necking measurements taken on the stereomicroscope. Note, these measurements were not initially calibrated, so the numerical value may not be accurate, but these values can be compared against one another.

Wire	Orientation	Neck Dia. (mm)	Neck Dia. (microns)	Neck Dia. (microns)	Neck Dia. (microns)	Neck Dia. (microns)	Neck Dia. (microns)	Mean Neck Dia., mm	Rank (1 = most necked)	Dia. Assy From Fracture (microns)	Dia. Assy From Fracture (microns)	Neck 2 Dia. (microns)	Neck 1 Dia. (microns)	Mean Neck 2 Dia., mm	% Necked	Expected Dia., mm ± 0.10	
AM	Cup Cone		4.69					4.69	1								
AM	Cup Cone		4.68					4.67	2	5.98							
AJ	Cup Cone		4.68					4.70	3								
AZ	Cup Cone		4.71					4.71	4								
AA	Cup Cone		4.70					4.70	5								
AB	Cup Cone	4.80		4.70		4.80		4.78	6	6.26	6.30						
AU	Cup Cone		4.84					4.86	7	5.94							
AC	Cup Cone		4.88					4.88	8								
AX	Cup Cone		4.84			5.00		4.87	9	5.03							
ED	Cup Cone		5.00	4.87				5.00	10								
AG	Cup Cone		4.99		5.18	5.09		5.08	11	6.05	6.09						
B	Cup Cone	unavailable (S-43, where x = 0, 0.07)															
AV	Cup Cone		5.15			5.15		5.15	12	5.83							
AK	Cup Cone		5.18		5.13	5.18		5.15	13	6.06	6.07						
BC	Cup Cone		5.22		5.22	5.23		5.23	14	5.98	6.07						
AG	Cup Cone		5.28		5.27	5.20		5.25	15	6.14	6.05						
CB	Cup Cone		5.11		5.39	5.30		5.27	16	6.18	6.08						
F	Cup Cone		4.89		4.96	4.02		5.28	17	4.95	6.16						
AT	Cup Cone		5.28		5.37	5.31		5.33	18	6.10	6.10						
C	Cup Cone		5.32		5.34			5.33	19	6.06							
BP	Shear		5.37		5.32	5.35		5.35	20	5.96	5.57	5.58	5.58	5.68	7.68%		
AV	Cup Cone		5.36		5.40	5.35		5.37	21	6.10	6.06						
AD	Cup Cone	5.32		5.37		5.32		5.40	22	6.23	6.22						
AL	Cup Cone		5.37		5.50	5.50		5.46	23	6.26	5.97						
AD	Cup Cone		5.37		5.35			5.46	24	5.96							
AM	Cup Cone		5.40		5.33			5.47	25	5.85							
CG	Cup Cone		5.40		5.35			5.40	26	5.84							
AP	Cup Cone		5.44		5.38			5.51	27	6.09							
E	Cup Cone		5.52					5.52	28								
AW	Cup Cone		5.52					5.52	29								
Z	Cup Cone		5.59		5.60	5.46		5.55	30	6.21	6.11						
F	Cup Cone		5.68	5.34		5.74		5.66	31	6.04							
D	Shear		5.67		5.65	5.61		5.64	32	5.81							
T	Cup Cone		5.65		5.68	5.61		5.64	33	6.09	6.14						
H	Cup Cone		5.63		5.62	5.74		5.66	34	5.83	6.19						
S	Cup Cone		5.64		5.64			5.74	35	6.12							
W	Cup Cone		5.70		5.60			5.70	36	6.10							
U	Cup Cone		5.67		5.61	6.19		5.74	37	6.10	6.09						
F	Cup Cone		5.81		5.79			5.80	38	6.13							
X	Cup Cone		5.82					5.82	39								
H	Cup Cone		5.89		5.82			5.88	40	6.03							
AN	Shear		5.86		5.89			5.88	41	6.06	6.06						
A	Cup Cone		6.08		5.80			5.94	42	6.08							
V	Cup Cone		6.02		5.88			5.95	43	6.00							
BA	Cup Cone/MAC				5.89			5.89	44	6.09							
AI	Shear/MAC	6.14		5.95		6.01		6.00	45	6.19	6.11						
I	Cup Cone		5.94		6.15			6.06	46	6.12							
CA	Shear				6.10			6.10	47								
AP	Shear/MAC	5.89		6.10		6.23		6.13	48	6.11	6.23						
G	Shear				6.17			6.17	49	6.13							
AS	Cup Cone		6.18					6.18	50	6.04							
Y	Shear				6.20			6.20	51	6.11	6.11						
AT	Shear				6.21			6.21	52	6.10	6.11						
C	Shear				6.22			6.22	53								
AK	Cup Cone				6.23			6.23	54								
DX	Shear				6.24			6.24	55								
Mean																6.04	

APPENDIX K. METALLOGRAPHY



Figure 283. Top image shows slice 3a on the left and 9a on the right. Bottom image is a closer view of the etch of the longitudinal cut face of slice 9a. The boundary between the zinc grains that solidified up from the cable wires and socket inner diameter wall meet at the gas bubble with the zinc grains that solidified down from the casting cap surface. Scale in inches and centimeters.



Figure 284. Oblique view of the slice 9a etch, revealing how the brittle fracture region is associated with grains elongated in the direction of the gas bubble near the casting cap.



Figure 285. Oblique view of the slice 9a etch, revealing the solidification boundary between the zinc grains that grew out from the wires and the grains that grew inward from the socket inner diameter wall. Note the cone-shape of the zinc surface above where the wire-end was originally within the wire channel.

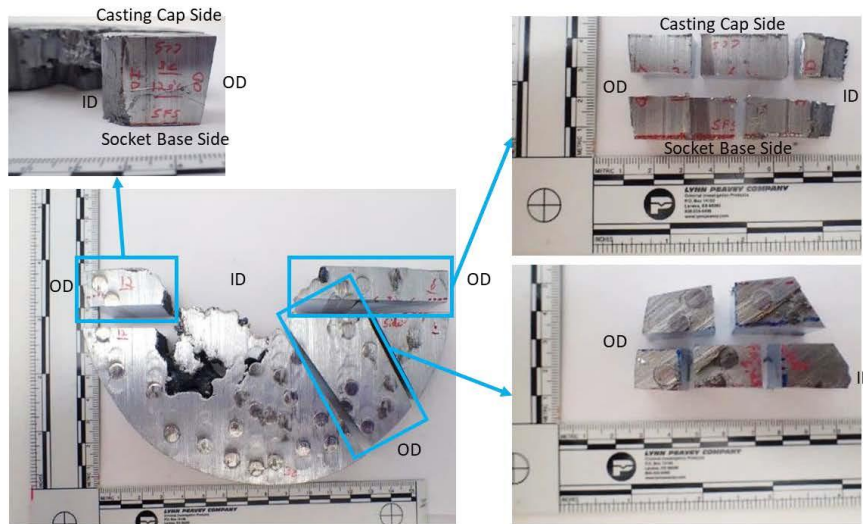


Figure 286. Metallographic cut plans for the two orthogonal orientation views of slice 3c – two looking at the longitudinal cut face on each side of the slice and one looking at the transverse cut face. Scale in inches and centimeters.

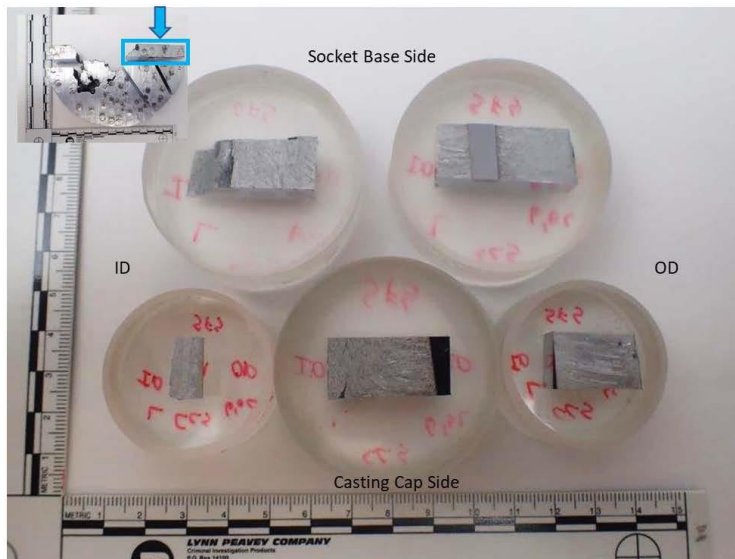


Figure 287. Metallographic specimens of the 6 o'clock side of the longitudinal cut face of slice 3c. Scale in centimeters.

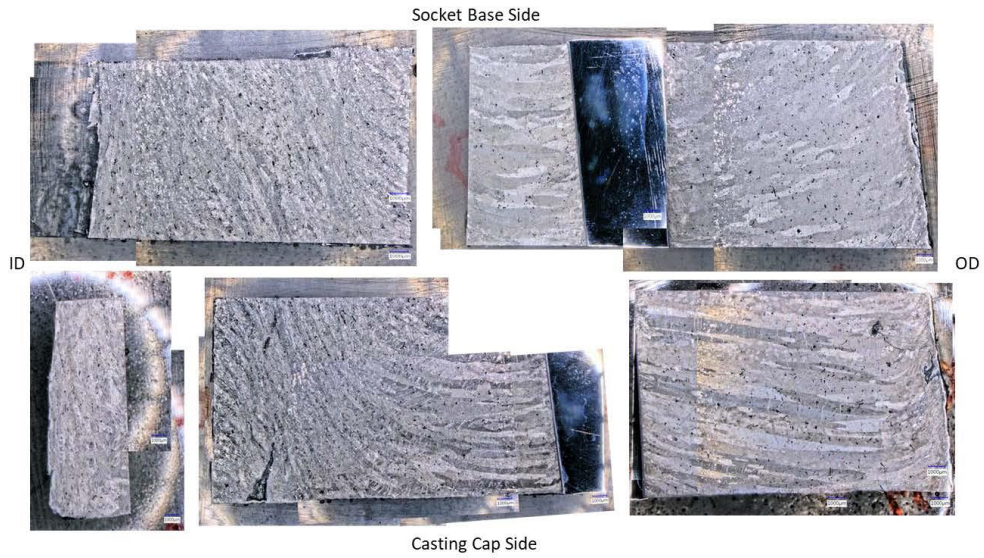


Figure 288. Metallographic specimens of the 6 o'clock side of the longitudinal cut face of slice 3c.



Figure 289. Metallographic specimen of the 12 o'clock side of the longitudinal cut face of slice 3c.

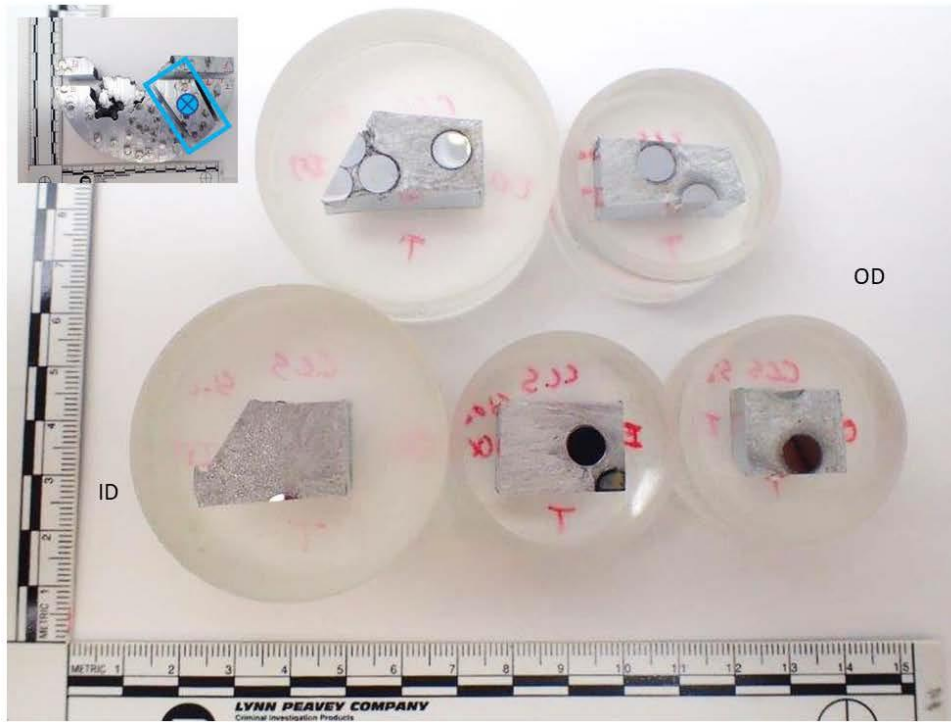


Figure 290. Metallographic specimens of the transverse cut face of slice 3c.
Scale in centimeters.

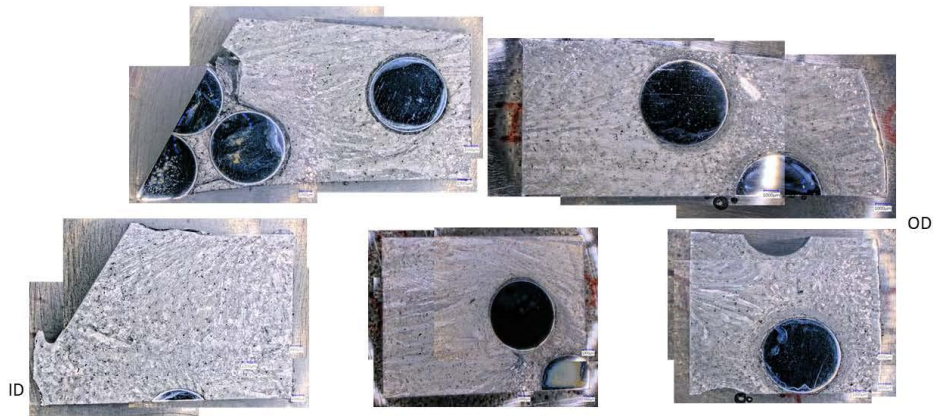


Figure 291. Metallographic specimens of the transverse cut face of slice 3c.

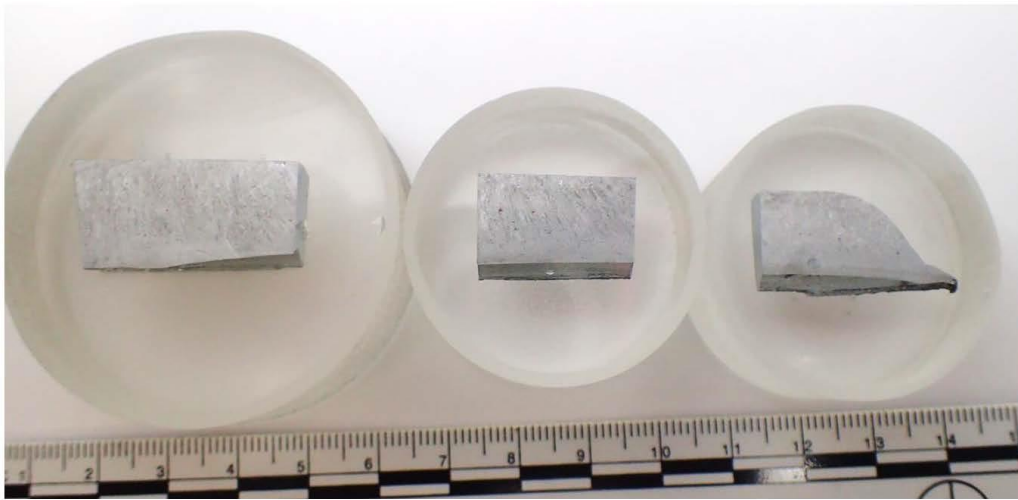


Figure 292. Metallographic specimens of the longitudinal cut face along the 9 o'clock position of slice 9g, as seen in Figure 172. The right side of the specimens is at the socket base edge of the zinc casting. The left side of the specimens is at the transverse cut between 9g and 9e. The bottom side of the specimens is against the cable/zinc slug. The top side of the specimens is against the socket inner diameter wall. Scale in centimeters.



Figure 293. Metallographic specimen of the longitudinal cut face along the 9 o'clock position of slice 9g. This specimen is the leftmost specimen from Figure 292.

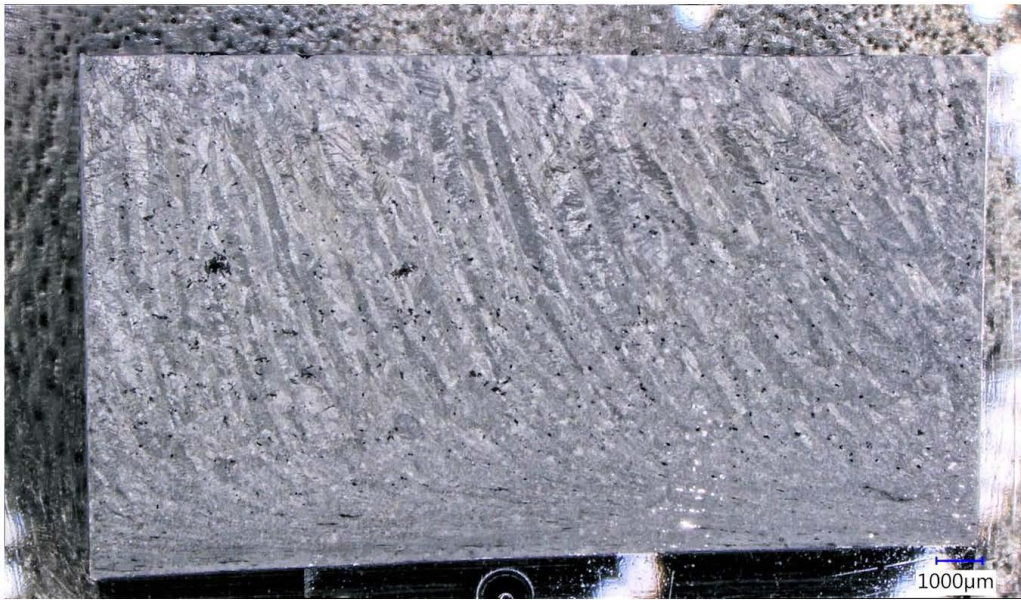


Figure 294. Metallographic specimen of the longitudinal cut face along the 9 o'clock position of slice 9g. This specimen is the center specimen from Figure 292.



Figure 295. Metallographic specimen of the longitudinal cut face along the 9 o'clock position of slice 9g. This specimen is the rightmost specimen from Figure 292.

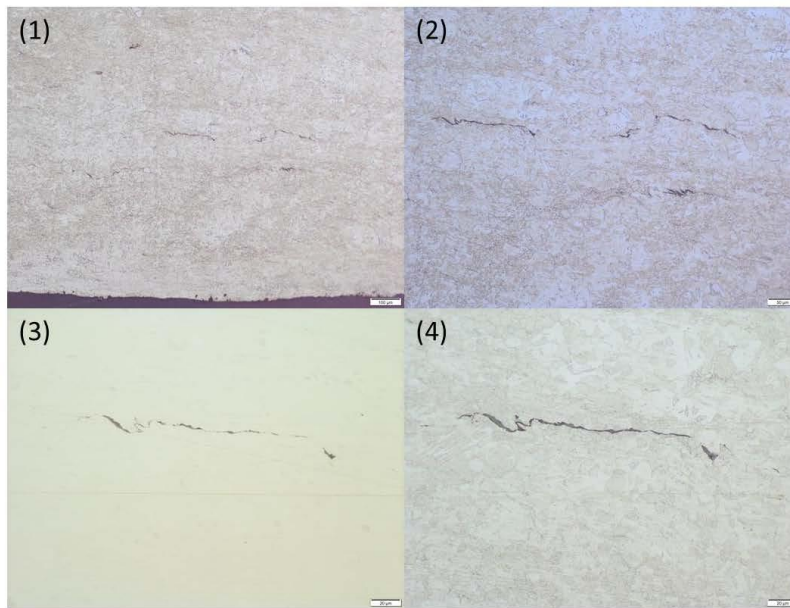


Figure 296. Close up metallograph images of some of the cracks present in Figure 295 adjacent to the cable/zinc slug boundary. (1) Tint etch at 100X. (2) Tint etch at 200X. (3) As polished at 500X. (4) Tint etch at 500X.

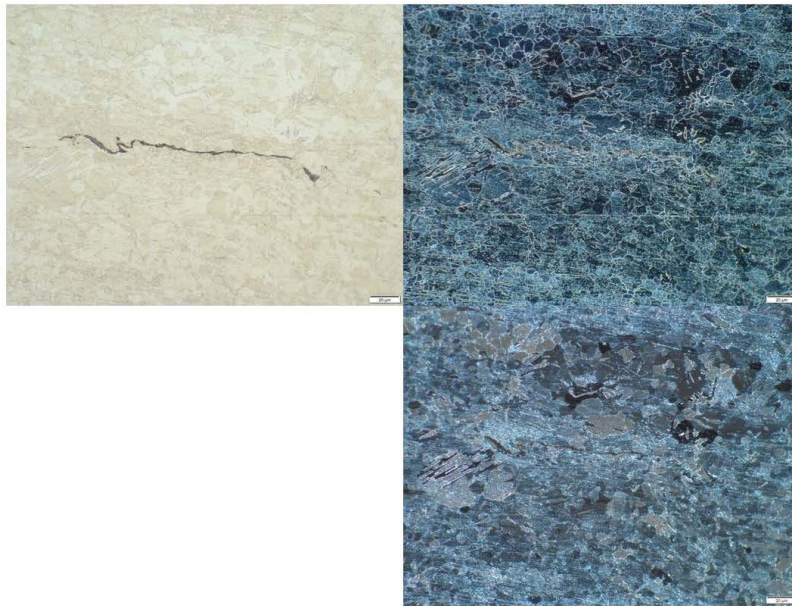


Figure 297. Close up metallograph images of the crack in Figure 296 3) and 4) in brightfield, dark field, and cross-polarized illumination. Tint etch at 500X.

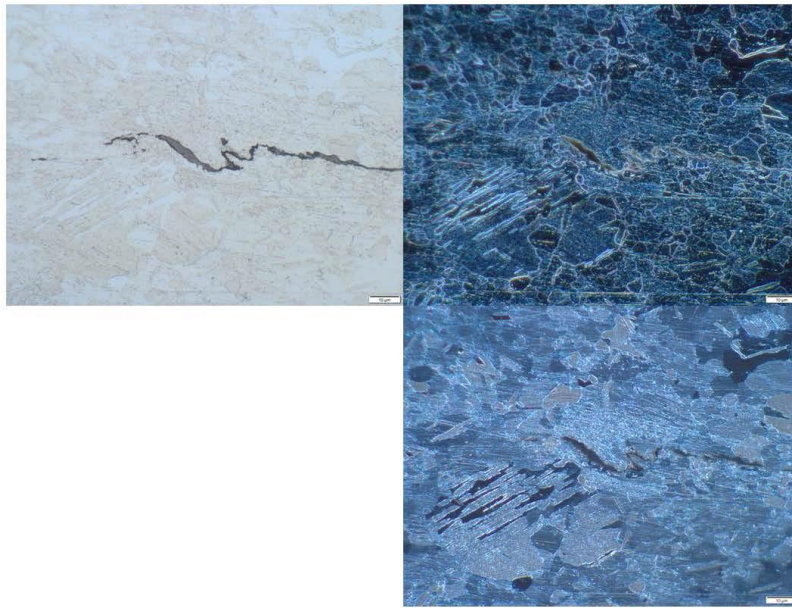


Figure 298. Close up metallograph images of the crack in Figure 297 in brightfield, dark field, and cross-polarized illumination. Tint etch at 1000X.

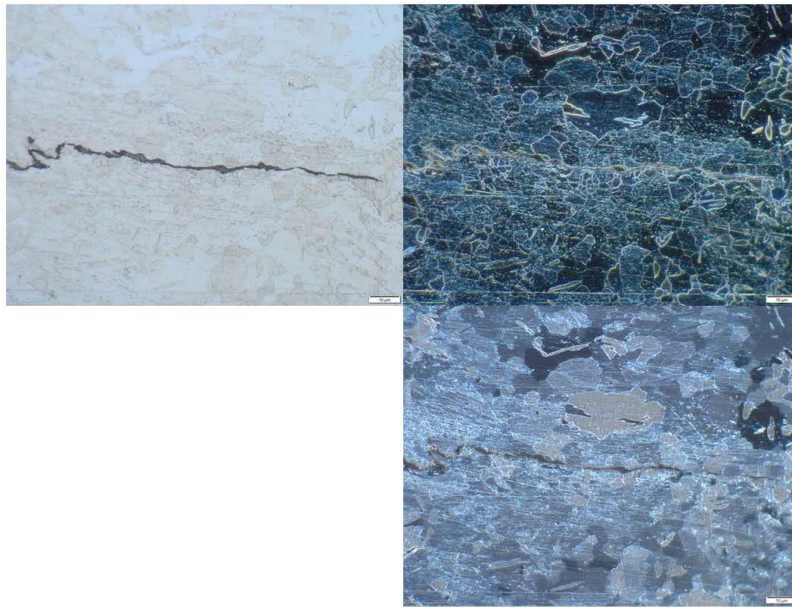


Figure 299. Close up metallograph images of the crack in Figure 297 in brightfield, dark field, and cross-polarized illumination. Tint etch at 1000X.

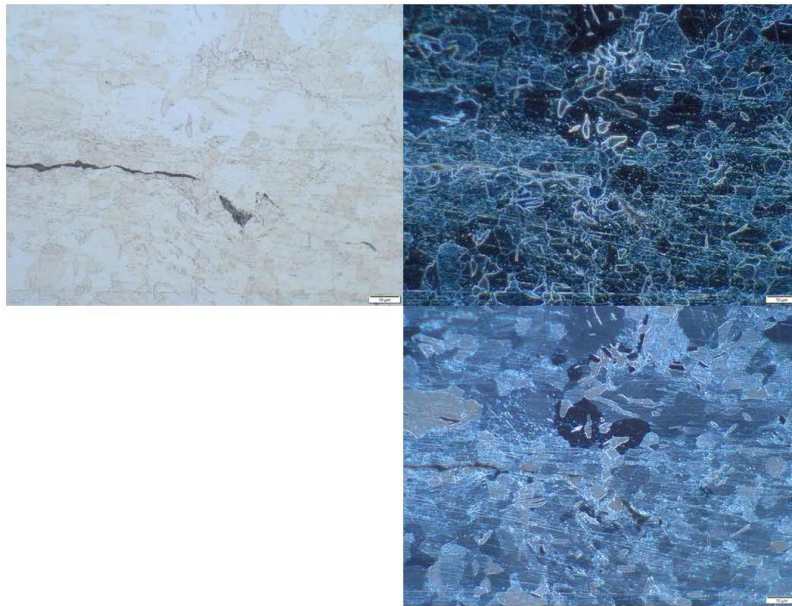


Figure 300. Close up metallograph images of the crack in Figure 297 in brightfield, dark field, and cross-polarized illumination. Tint etch at 1000X.

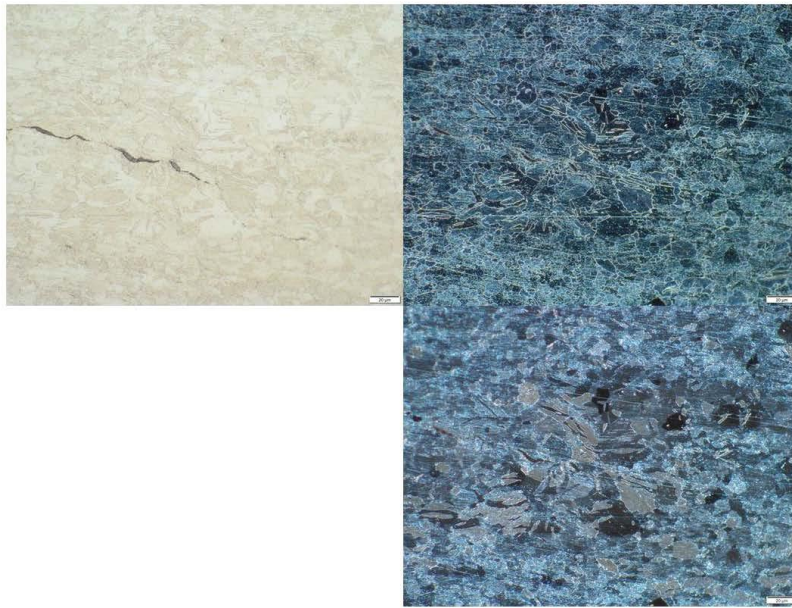


Figure 301. Close up metallograph images of a crack present in Figure 295 adjacent to the cable/zinc slug boundary. Tint etch at 500X.

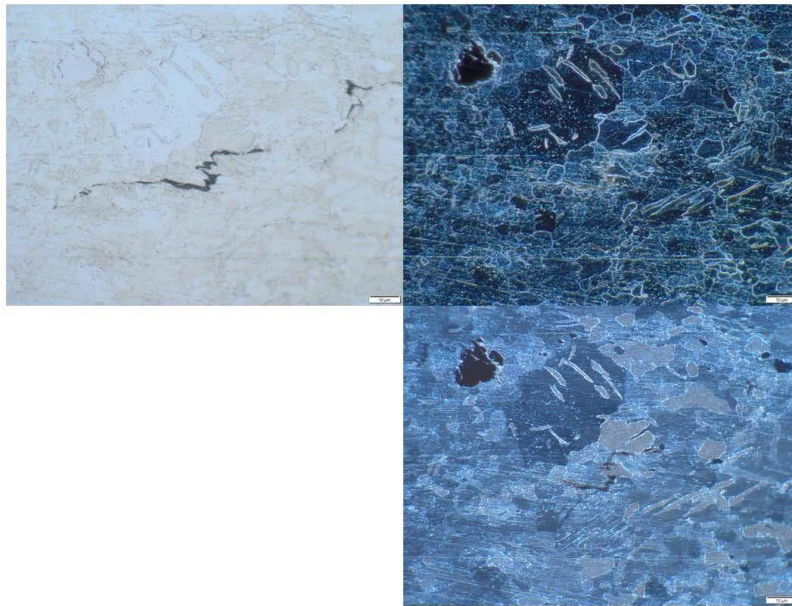


Figure 302. Close up metallograph images of a crack present in Figure 295 adjacent to the cable/zinc slug boundary. Tint etch at 1000X.

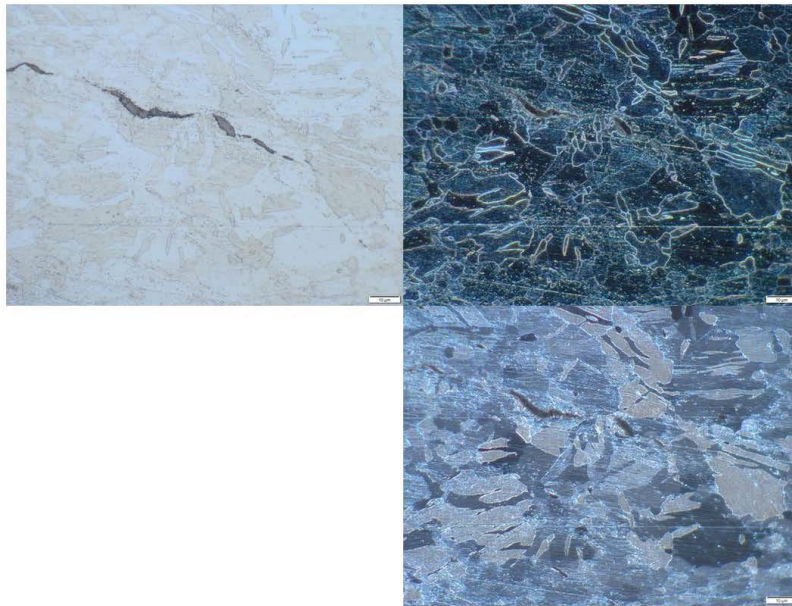


Figure 303. Close up metallograph images of a crack present in Figure 295 adjacent to the cable/zinc slug boundary. Tint etch at 1000X.

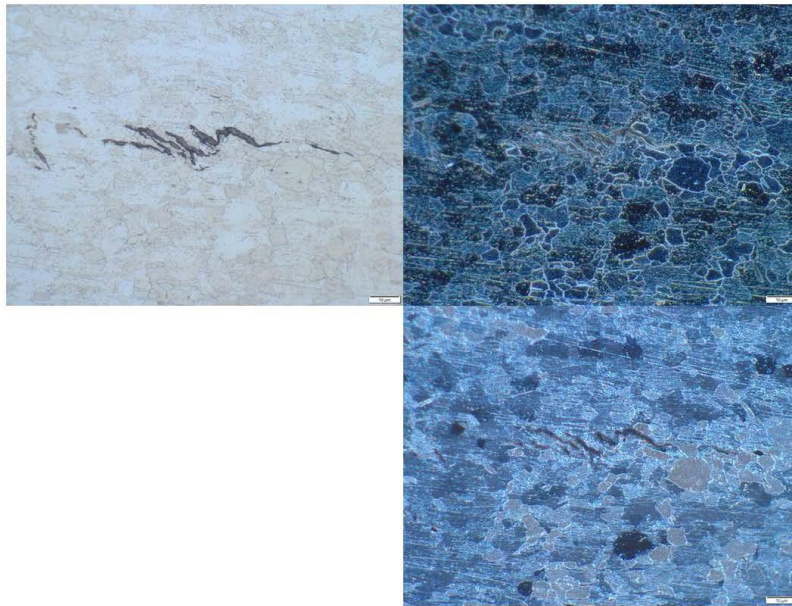


Figure 304. Close up metallograph images of a crack present in Figure 295 adjacent to the cable/zinc slug boundary. Tint etch at 1000X.

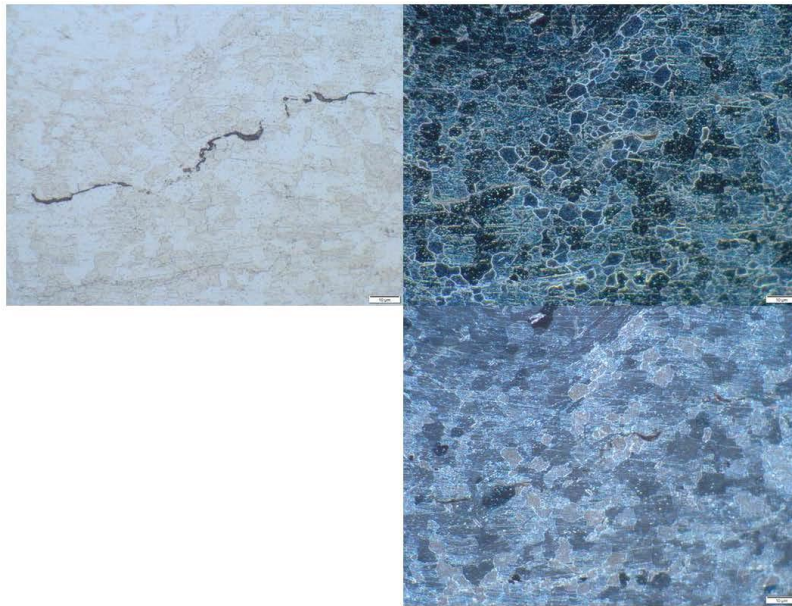


Figure 305. Close up metallograph images of a crack present in Figure 295 adjacent to the cable/zinc slug boundary. Tint etch at 1000X.

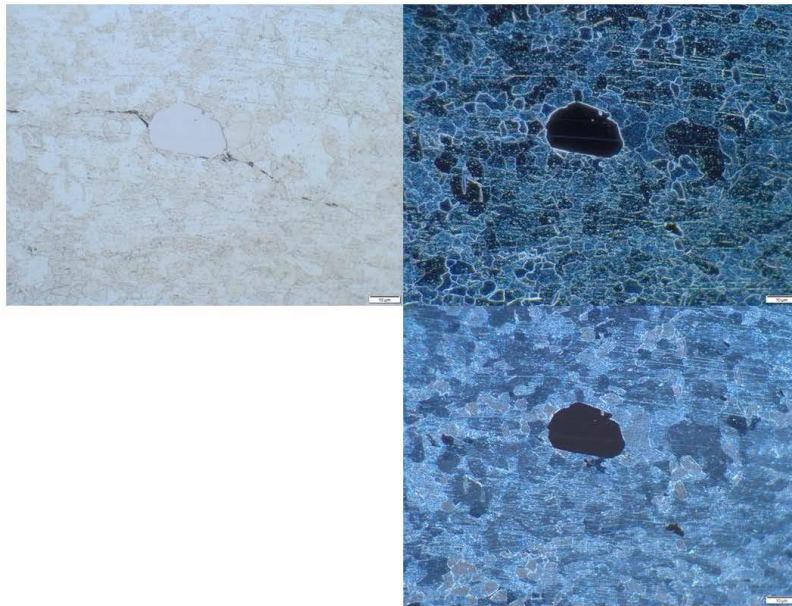


Figure 306. Close up metallograph images of a crack present in Figure 295 adjacent to the cable/zinc slug boundary. Tint etch at 1000X.

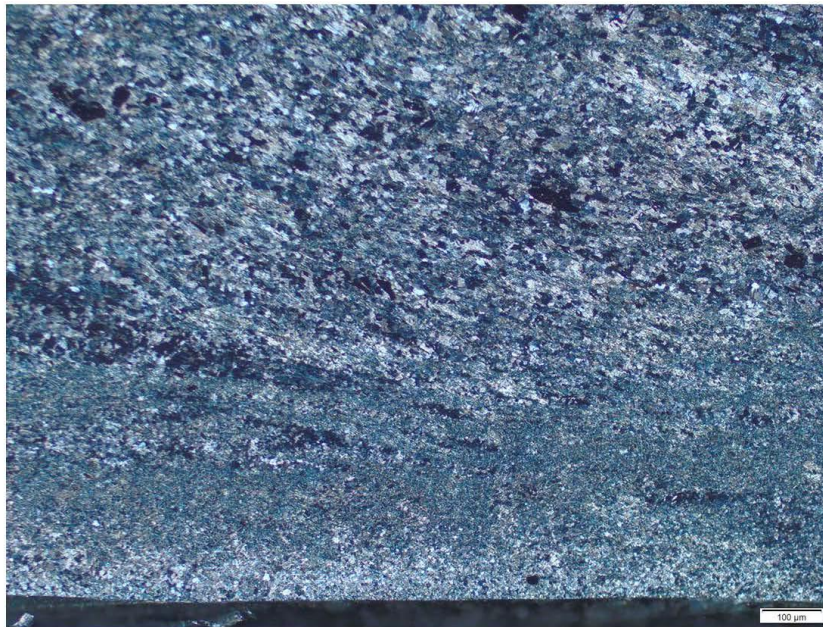


Figure 307. Metallograph image of the small grains present in Figure 295 adjacent to the cable/zinc slug boundary. Tint etch at 100X.

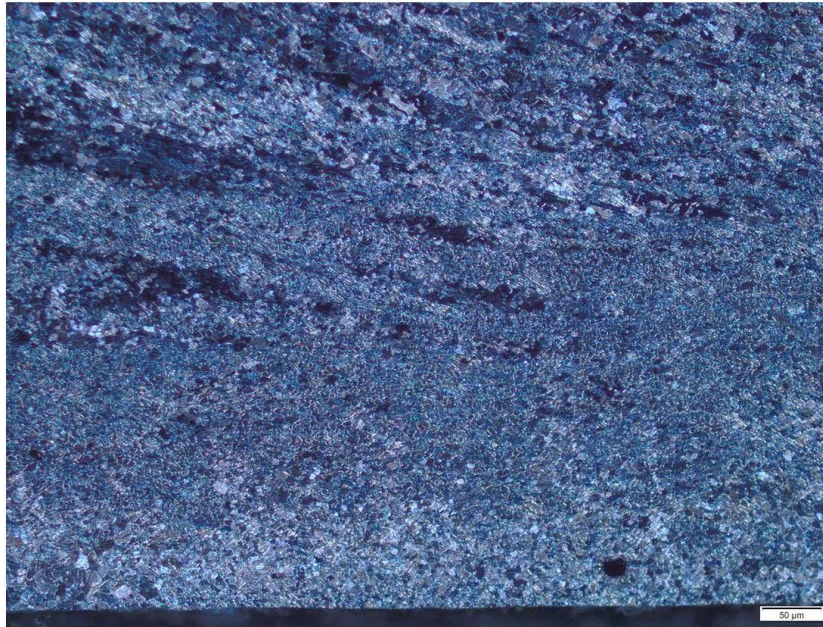


Figure 308. Metallograph image of the small grains present in Figure 295 adjacent to the cable/zinc slug boundary. Tint etch at 200X.

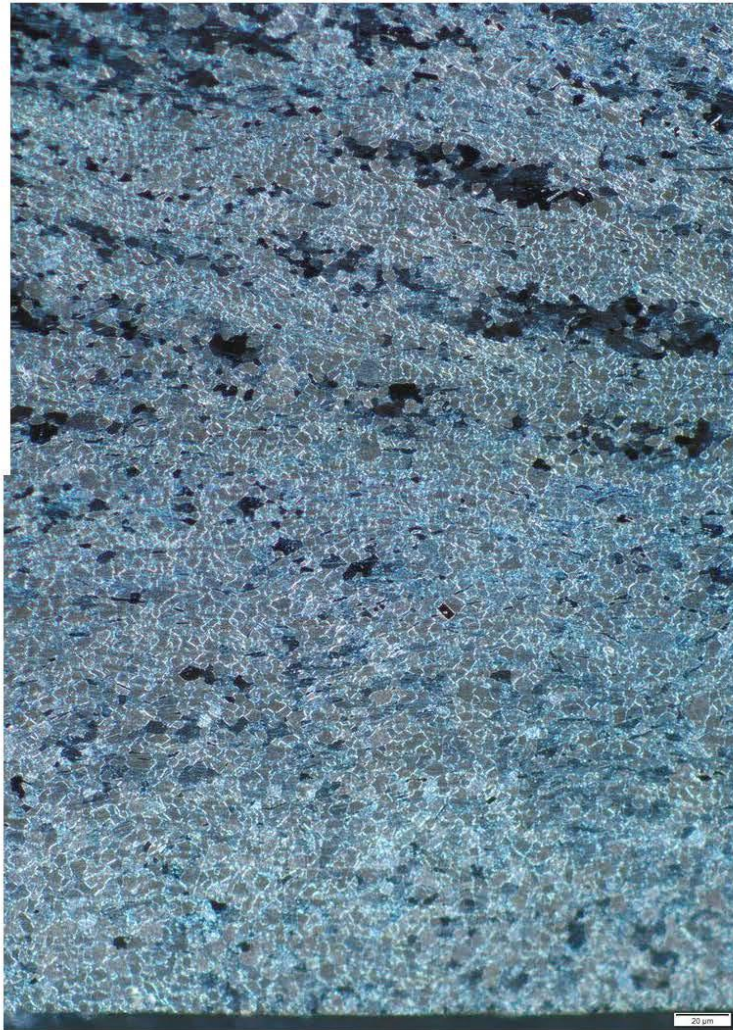


Figure 309. Metallograph image of the small grains present in Figure 295 adjacent to the cable/zinc slug boundary. Tint etch at 500X.

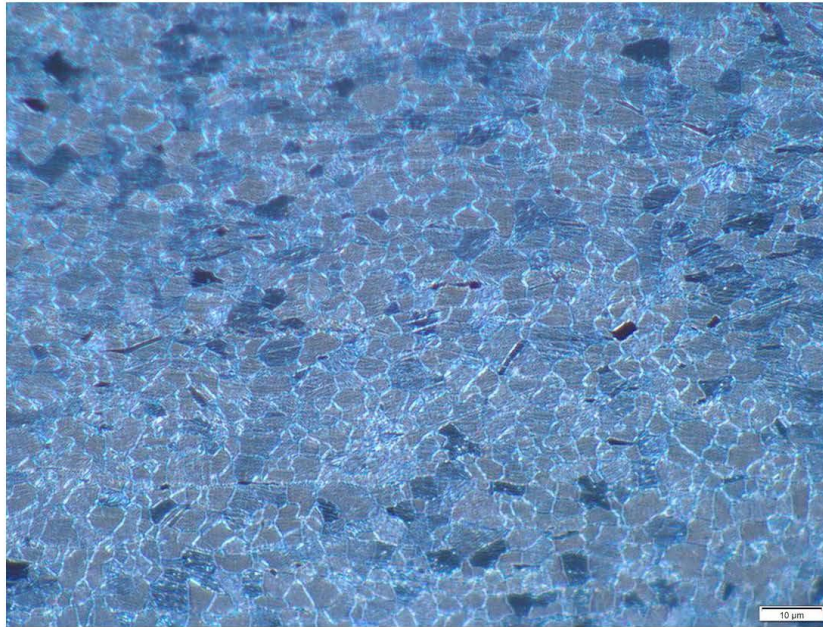


Figure 310. Metallograph image of the small grains present in Figure 295 adjacent to the cable/zinc slug boundary. Tint etch at 1000X.

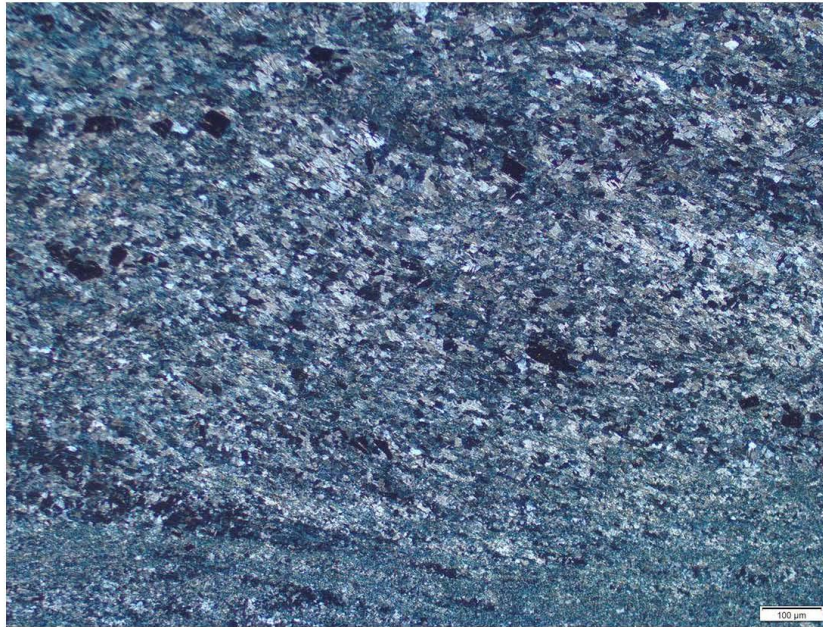


Figure 311. Metallograph image of the medium grains present in Figure 295 between the cable/zinc slug boundary and the zinc casting outer diameter. Tint etch at 100X.

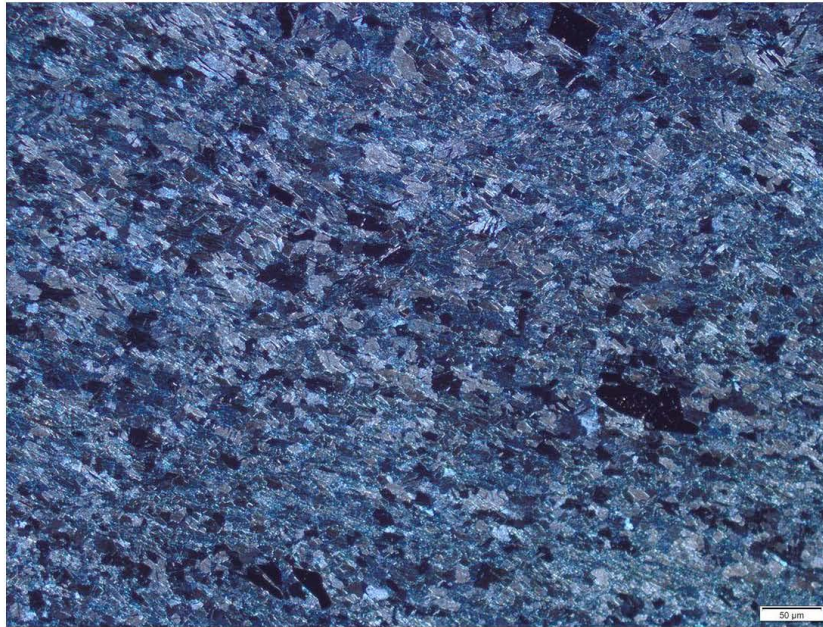


Figure 312. Metallograph image of the medium grains present in Figure 295 between the cable/zinc slug boundary and the zinc casting outer diameter. Tint etch at 200X.

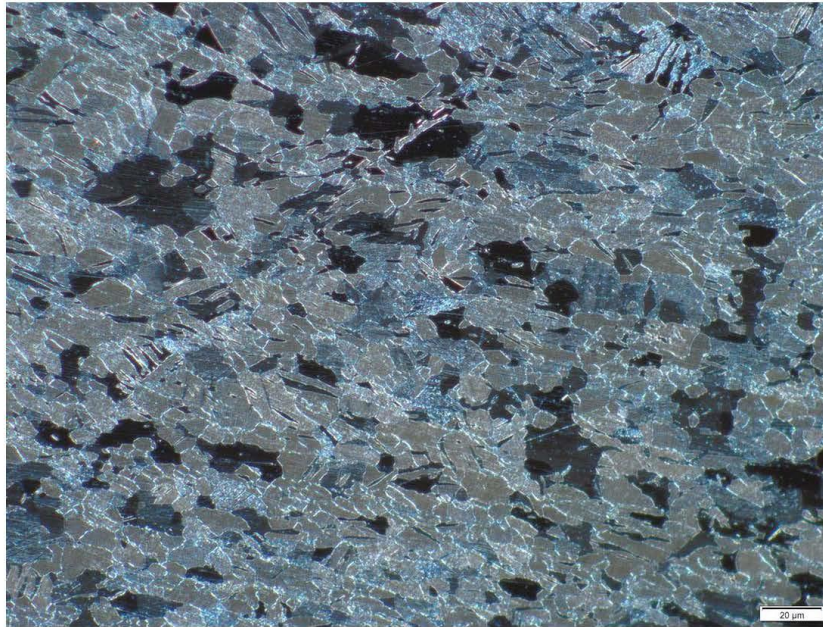


Figure 313. Metallograph image of the medium grains present in Figure 295 between the cable/zinc slug boundary and the zinc casting outer diameter. Tint etch at 500X.

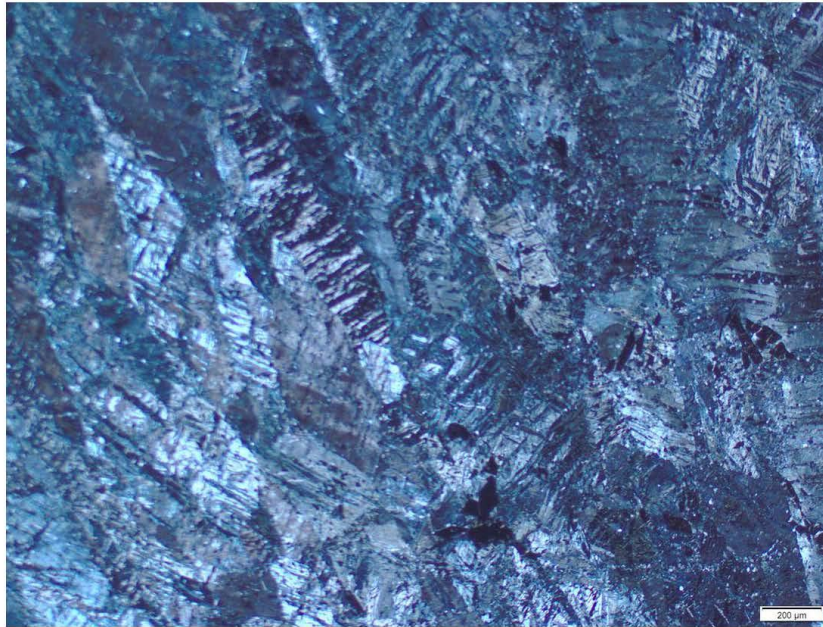


Figure 314. Metallograph image of the large grains present in Figure 295 close to the zinc casting outer diameter. Tint etch at 50X.

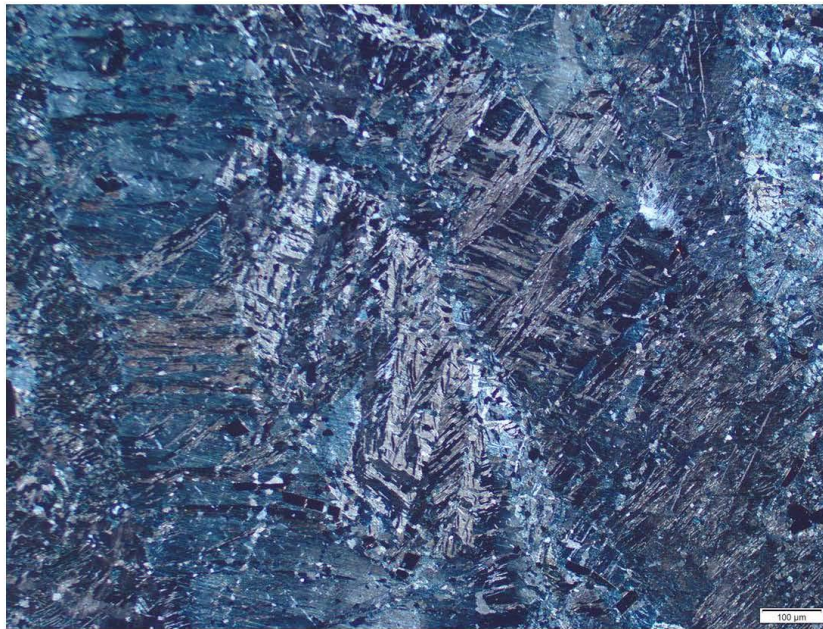


Figure 315. Metallograph image of the large grains present in Figure 295 close to the zinc casting outer diameter. Tint etch at 100X.

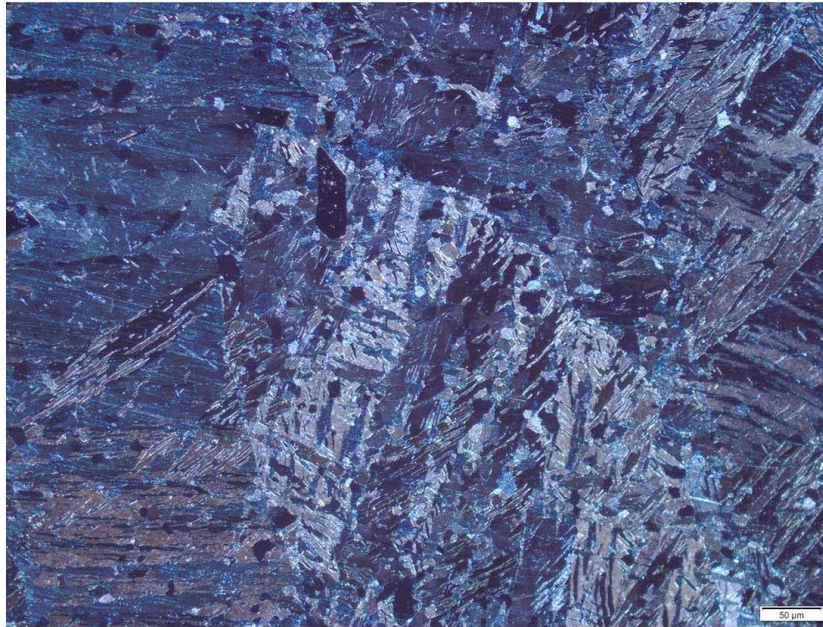


Figure 316. Metallograph image of the large grains present in Figure 295 close to the zinc casting outer diameter. Tint etch at 200X.

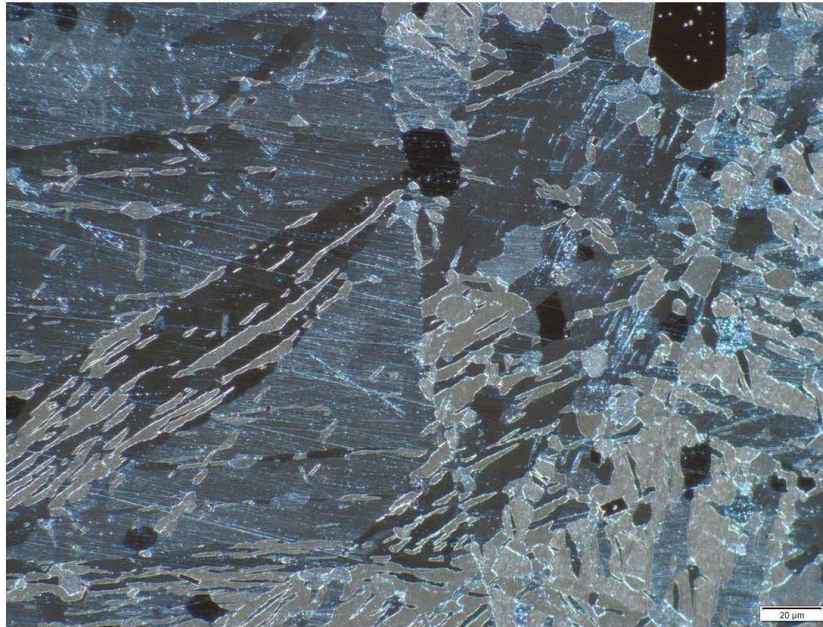


Figure 317. Metallograph image of the large grains present in Figure 295 close to the zinc casting outer diameter. Tint etch at 500X.

APPENDIX L. CHEMICAL SAMPLE ANALYSIS

L.1 Socket Component Chemical Analysis Results

Table 6. Clevis pin OES measurements.

NASA-04710- Areco Alloy Chemistry
 Equipment: Bruker Q4 Tasman Spark Optical Emission Spectrometer (Spark-OES)
 Component Specifications: ASTM A521 Class A5 (normalized, quenched, and tempered)
 Material Specification Requirements: ASTM A521 or A576 Carbon Steel Bar
 For nonresulfurized Carbon Steels, Mn is <1.0% and Cu can be specified when required at 0.20 % minimum

Alloy chemistry values in weight percent (wt %). * Cu values exceeded >0.228% calibration, results from XRF method

Element:	C	Mn	P	S	Si	Cu*	Ni	Cr	Mo	Al	As	Ca	Co	Sn	V	B	Bi	Ce	N	Nb	Pb	Sb	Ta	La	Ti	W	Zr	Fe	
1) wt %	0.448	0.785	0.012	0.029	0.259	0.2918	0.132	0.08	0.039	0.028	0.008	0	0.019	0.015	0.0018	0.00031	<0.0070	0	0.0077	0.0023	0	0	0	0	0	0.0018	0.015	0	97.88
2) wt %	0.451	0.792	0.012	0.028	0.256	---	0.129	0.081	0.039	0.028	0.008	0	0.017	0.014	0.0012	<0.0020	<0.0070	0	0.0083	0.002	0	0	0	0	0	0.002	0.0056	0	97.89
3) wt %	0.45	0.774	0.01	0.024	0.252	---	0.13	0.079	0.036	0.025	0.009	0	0.019	0.012	0.0011	<0.0020	<0.0070	0	0.0077	0.0016	0	0	0	0	0	0.0018	<0.0090	0	97.91
4) wt %	0.455	0.778	0.011	0.023	0.257	---	0.133	0.08	0.039	0.025	0.008	0	0.018	0.014	0.0019	<0.0020	<0.0070	0	0.0083	0.0023	0	0	0	0	0	0.0019	<0.0090	0	97.91
5) wt %	0.453	0.756	0.011	0.023	0.259	---	0.134	0.08	0.039	0.03	0.006	0	0.018	0.014	0.0017	<0.0020	<0.0070	0	0.0087	0.0024	0	0	0	0	0	0.0019	0.008	0	97.89
Average	0.451	0.783	0.0112	0.0254	0.2566	0.2918	0.1316	0.08	0.0384	0.0268	0.00682	0	0.0174	0.0138	0.00146	0.00031	0.0075	0	0.00814	0.00212	0	0	0	0	0	0.0019	0.009533	0	97.9

Table 7. Socket clevis OES measurements.

NASA-04710- Areco Alloy Chemistry
 Equipment: Bruker Q4 Tasman Spark Optical Emission Spectrometer (Spark-OES)
 Component Specifications: ASTM A158 grade 60-60
 Material Specification Requirements: ASTM A158 section 7, chemical composition 7.1 The steel shall conform to sulfur and phosphorus requirements as prescribed in table 1 (grade 60-60) P < 0.005%, S < 0.005%
 7.2 The content of carbon, manganese, silicon, and alloying elements may, by agreement, be prescribed by the purchaser. If not specified, the content may be selected by the manufacturer to obtain the required mechanical properties

Alloy chemistry values in weight percent (wt %)

Element:	C	Mn	P	S	Si	Cu	Ni	Cr	Mo	Al	As	Ca	Co	Sn	V	B	Bi	Ce	N	Nb	Pb	Sb	Ta	La	Ti	W	Zr	Fe	
1) wt %	0.216	0.685	0.015	0.016	0.379	0.039	0.356	0.355	0.191	0.061	0.0029	0	0.013	0.0033	0.0034	0.00031	<0.0070	0	0.0084	0.0027	0	0	0	0	0	0.0017	0.0058	0	97.24
2) wt %	0.221	0.698	0.016	0.011	0.386	0.04	0.367	0.361	0.197	0.067	0.0035	0	0.014	0.0037	0.0038	0.00049	<0.0070	0	0.0086	0.003	0	0	0	0	0	0.0018	0.0056	0	97.18
3) wt %	0.212	0.687	0.016	0.012	0.38	0.04	0.359	0.359	0.196	0.053	0.0011	0	0.013	0.0035	0.0038	0.00035	<0.0070	0	0.008	0.0035	0	0	0	0	0	0.0016	<0.0090	0	97.14
4) wt %	0.235	0.696	0.015	0.014	0.395	0.041	0.375	0.365	0.2	0.058	0.0056	0	0.016	0.0039	0.0041	0.00056	<0.0070	0	0.0079	0.0037	0	0	0	0	0	0.0017	<0.0090	0	97.15
5) wt %	0.223	0.696	0.015	0.014	0.38	0.04	0.36	0.363	0.2	0.053	0.0056	0	0.015	0.0043	0.0041	0.00037	<0.0070	0	0.0082	0.0039	0	0	0	0	0	0.0022	0.0056	0	97.19
Average	0.2214	0.6924	0.016	0.0138	0.384	0.04	0.3634	0.3606	0.1968	0.0604	0.00354	0	0.0136	0.00374	0.00384	0.000348	ND/ND	0	0.00814	0.00356	0	0	0	0	0	0.0018	0.00533	0	97.2

Table 8. Cable wire OES measurements.

NASA-04710- Areco Alloy Chemistry
 Equipment:
 Bruker Q4 Trisman Spark Optical Emission Spectrometer (Spark-OES)
 Component Specification:
 ASTM A335
 Material Specification Requirements:
 ASTM A376 Section 6.1 (Base Metal)—The base metal shall be carbon steel made by the open-hearth, basic-oxygen, or electric-furnace process and of such quality that the finished strand and the hard-drawn individual metallic-coated wires...

Alloy chemistry values in weight percent (wt %)

Element:	C	Mn	P	S	Si	Cu	Ni	Cr	Mo	Al	As	Ca	Co	Sn	V	B	Se	Ce	N	Nb	Pb	Sb	Ta	La	Te	W	Zr	Fa
1) Wt %	0.645	0.859	0.01	0.017	0.253	0.123	0.058	0.089	0.016	0.035	0.0049	0	0.015	0.0056	0.113	<0.00020	0.02	0	0.0081	0.004	0	0	0	0	0.0016	0.015	0	97.51
2) Wt %	0.839	0.877	0.011	0.017	0.261	0.125	0.059	0.091	0.015	0.036	0.0049	0	0.013	0.0061	0.117	0.0002	0.02	0	0.0076	0.0041	0	0	0	0	0.0016	0.017	0	97.49
3) Wt %	0.824	0.858	0.01	0.017	0.255	0.121	0.058	0.088	0.016	0.036	0.0048	0	0.015	0.0058	0.115	0.00011	0.016	0	0.0072	0.0037	0	0	0	0	0.0014	0.015	0	97.54
4) Wt %	0.865	0.885	0.01	0.017	0.259	0.123	0.059	0.089	0.014	0.036	0.0051	0	0.015	0.0062	0.115	0.00011	0.018	0	0.0087	0.0035	0	0	0	0	0.0016	0.015	0	97.48
5) Wt %	0.831	0.866	0.0095	0.015	0.267	0.127	0.063	0.088	0.015	0.037	0.0045	0	0.016	0.0055	0.115	<0.00020	0.018	0	0.0085	0.0038	0	0	0	0	0.0015	0.014	0	97.49
Average	0.8306	0.8620	0.0101	0.0165	0.259	0.1238	0.0594	0.089	0.0148	0.0356	0.00472	0	0.0152	0.0058	0.115	0.00024	0.0184	0	0.00802	0.00382	0	0	0	0	0.00154	0.0148	0	97.502

Table 9. Zinc casting OES measurements.

NASA-04710- Areco Alloy Chemistry
 Equipment:
 Bruker S1 Titan X-ray Fluorescence (XRF) Spectrometer
 Component Specification:
 ASTM B5 "High Grade" Zn Spelter casting
 Material Specification Requirements:
 High Grade is a grade of zinc containing a minimum of 99.95% zinc, with controlled impurity maximum levels of lead (0.03%), iron (0.02%), cadmium (0.01%), aluminum (0.01%), copper (0.002%), tin (0.001%), and other non-zinc elements (0.05%)

Alloy Chemistry values in weight percent (wt %)

< LOD - below level of detection. The zinc method is programmed to assume these elements are in the alloy, however their values are essentially 0.0 wt%.

Element:	Al	Si	P	S	Ti	V	Cr	Mn	Fe	Co	Ni	Cu	Zn	Nb	Mo	Pd	In	Sn	W	Pb	Bi
1) Wt %	<LOD	0	0	0	0	0	0	<LOD	0.1154	0	<LOD	<LOD	99.8556	0	0	<LOD	0.0003	0.0287	0	<LOD	<LOD
2) Wt %	<LOD	0	0	0	0	0	0	<LOD	0.1167	0	<LOD	<LOD	99.8495	0	0	<LOD	0.0003	0.0287	0	<LOD	<LOD
3) Wt %	<LOD	0	0	0	0	0	0	<LOD	0.1247	0	<LOD	<LOD	99.8463	0	0	<LOD	0.0003	0.0287	0	<LOD	<LOD
Average	0	0	0	0	0	0	0	0	0.118933	0	0	0	99.85047	0	0	0	0.0003	0.0287	0	0	0

L.2 Socket Material Sample Chemical Analysis Report

L.2.1 Chemical Analysis Results

Initially, the three holes located at 270° (Figure 318) were sampled using conductive carbon adhesive tape and analyzed to determine if flux material of zinc ammonium chloride was still present at the bottom of the cable cavities in the socket using optical microscopy (OM), Fourier-transform infrared spectroscopy (FTIR), Raman spectroscopy, X-ray powder diffraction (XPD), and scanning electron microscopy with energy dispersive spectroscopy (SEM/EDS). The remainder of the samples from the other locations were also analyzed using SEM/EDS.

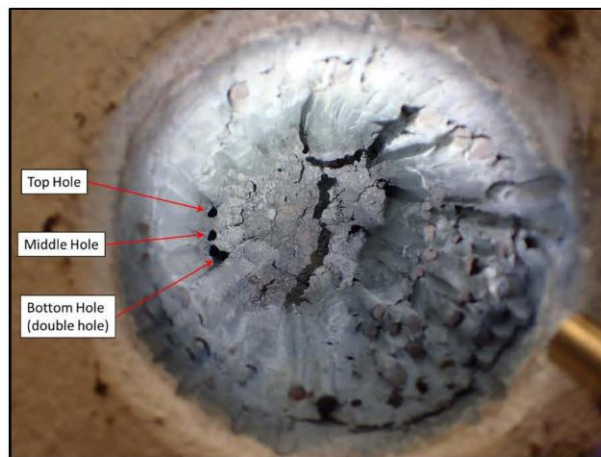


Figure 318. Image of the three holes at 270° in the socket.

OM examination of the material collected from the Top Hole was primarily powdery light gray residue (Figure 319). The Middle and Bottom Hole samples collected larger white particles, metallic gray flakes, and light gray powdery residue (Figure 320).



Figure 319. OM image at 1X magnification of the powdery light gray residue collected from the Top Hole.

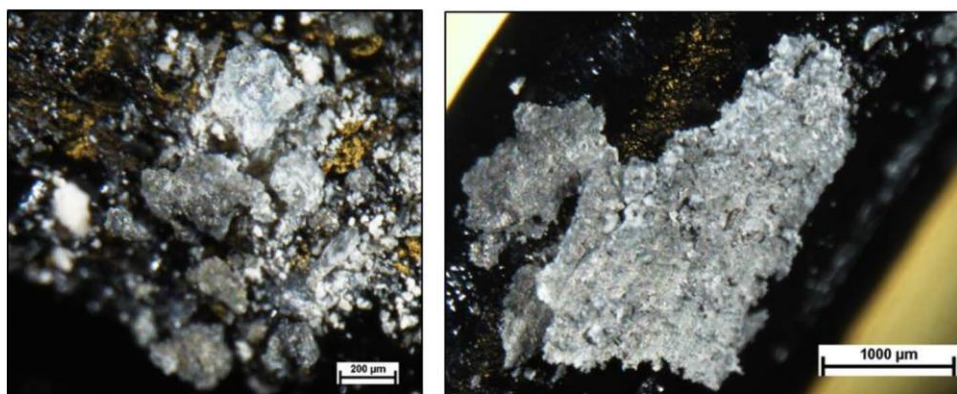


Figure 320. OM image at 4X of white and metallic gray particles from the Middle Hole (left) and an image at 1.5X of the large, gray zinc metal flake collected from the Bottom Hole (right).

FTIR analysis was performed on a white particle with a metallic gray interior which was indicated to be an inorganic hydroxide material (Figure 321). The large rounded peak around 3450cm^{-1} and the sharp peak at 850cm^{-1} are hydroxide (OH^-) signals. The large peak around 1530cm^{-1} is typically a carbonate (CO_3^-) signal.

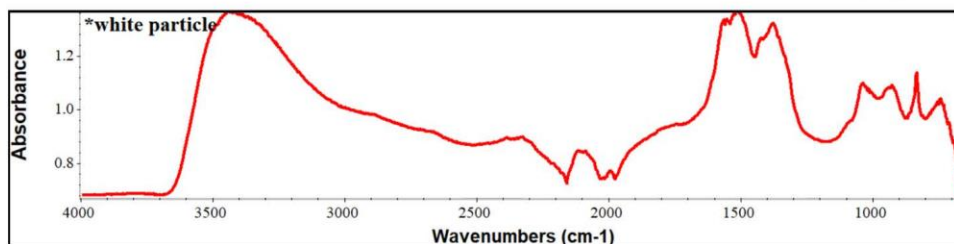


Figure 321. FTIR spectrum of the white particle with a metallic gray interior.

Raman spectroscopy indicated that neither ionic species (OH or CO₃) was present and that the particle was just zinc oxide (Figure 322). Raman analysis also confirmed that the white particle was not an ammonium chloride salt.

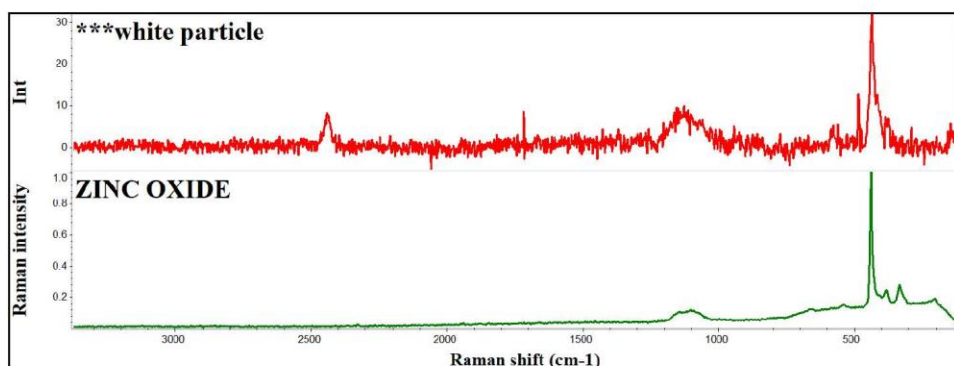


Figure 322. Raman spectroscopy of the white particle (top) and a zinc oxide reference (bottom).

XPD analysis was performed on particles that were picked off the samples from the Middle and Bottom Holes. XPD identified three species present; primarily zinc oxide and zinc metal with minor amounts of zinc hydroxide (Figure 323).

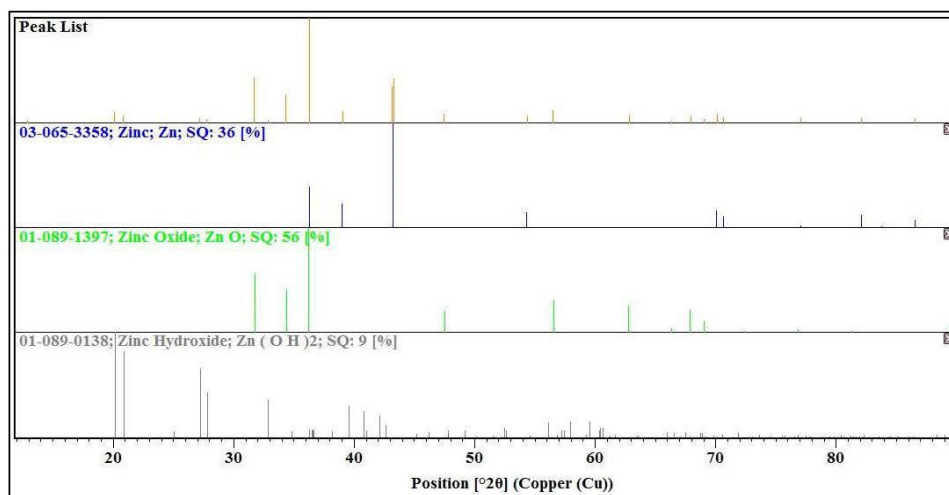


Figure 323. XRD patterns: particles from the Middle and Bottom Holes (top), zinc metal (second from top), zinc oxide (third from top), and zinc hydroxide (bottom).

SEM/EDS analysis indicated that the material was consistent across the three swabbed holes. The “rough” morphology was by far the most common (Figure 324), but the crystalline (Figure 325) and two other phases based upon morphologies (Figure 326) were also seen fairly often. The oxide content varied from ~5% to 28% (Figure 327). There was also possible trace amounts of chlorine (0.2-0.4%) on some (~20%) of the particles, though this remains unconfirmed. The chlorine peak was not 3x the height of the background noise, and was typically a shorter peak than the noise peak itself.

The other samples were then analyzed and it was discovered that Samples 4 and 12 had consistent amounts of trace iron (5.45%) throughout the entire sample. A particle in Sample 4 had the highest amount of iron (80%) and it was associated with trace manganese and chromium (Figure 328). Samples 5, 6, and 7 only had a few areas where trace iron was detected. Figure 329 shows zinc oxide (79% Zn and 21% O) in an additional crystal form taken from the socket. Desk sample 1 (7 o'clock) was primarily aluminum silicates. Desk sample 2 (9 o'clock) was primarily zinc oxide. Desk sample 3 (from wire) was also primarily zinc oxide, but did have consistent trace iron levels with some particles high in iron with trace manganese, nickel, and chromium, resembling stainless steel.

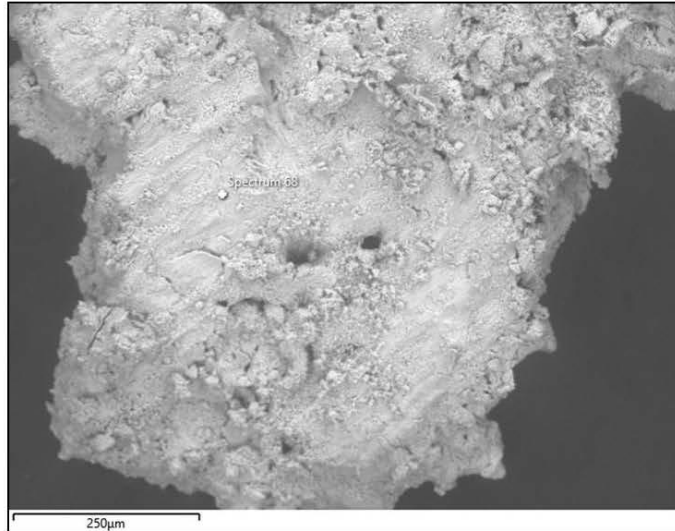


Figure 324. SEM showing most common “rough” morphology of the zinc material.

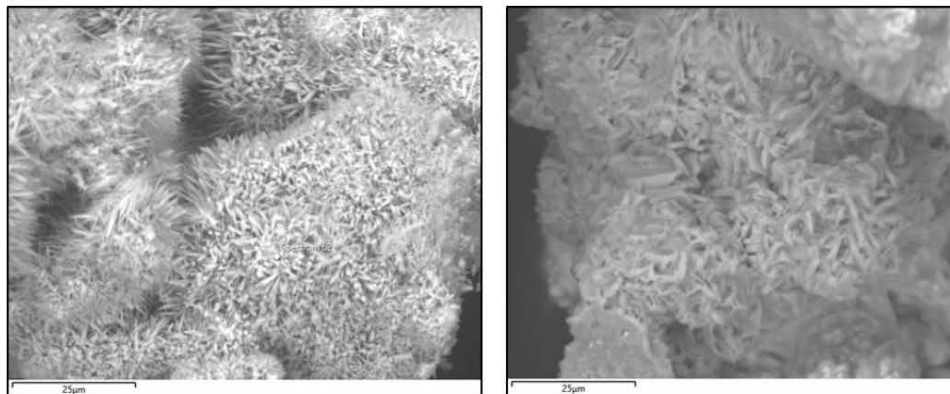


Figure 325. SEM of crystalline morphology.

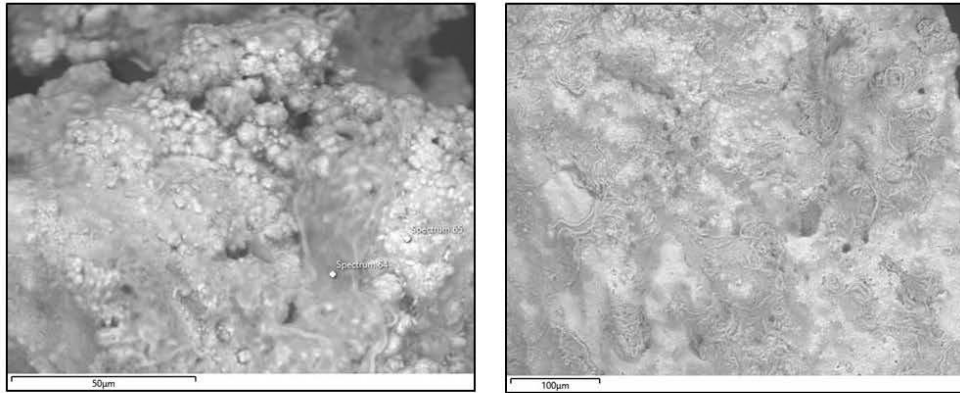


Figure 326. SEM of two-phase morphology.

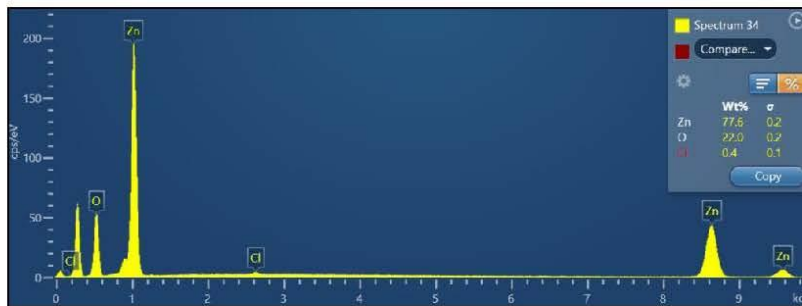


Figure 327. EDS spectrum of zinc / zinc oxide material.

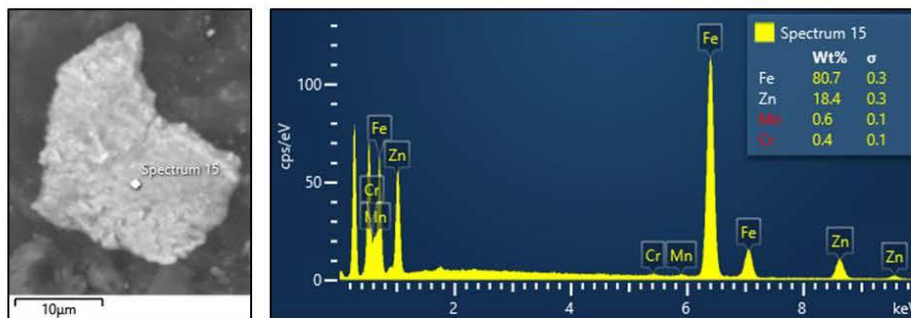


Figure 328. SEM micrograph and EDS spectrum of iron particle with manganese and chromium from Sample 4.

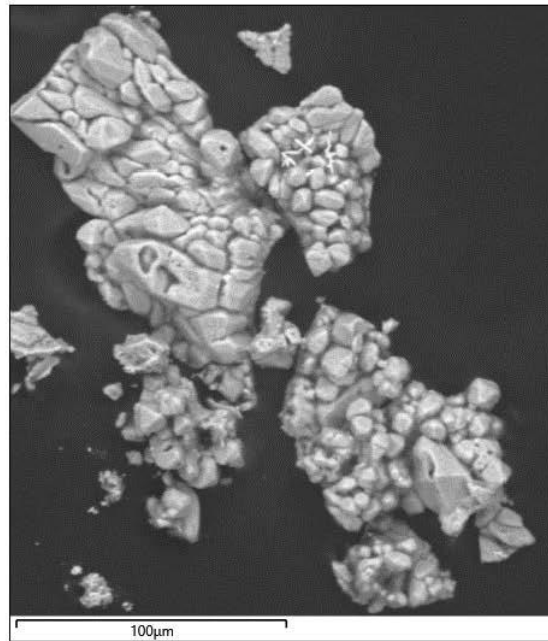


Figure 329. SEM micrograph of the additional crystal form of zinc oxide (79% Zn and 21% O).

L.2.1.1 Chemical Analysis Discussion

During manufacturing, the steel is typically subjected to degreasing and pickling to remove surface contamination and oxides. The steel then is coated with a chemical flux (such as zinc ammonium chloride) to dissolve the thin oxide layer that forms. The steel is then dipped in a molten zinc galvanizing bath to create a zinc coating. It is unlikely any of the original zinc ammonium chloride flux material survived. The decomposition temperature of the flux (644 °f boiling point, with one manufacturer stating that it decomposes at around 400 °f) is well below the temperature of the molten zinc galvanizing bath (~840 °f). The rods were also secured in place with a molten zinc pour, which was again above the melting point of the zinc ammonium chloride.

APPENDIX M. ACCELERATED ZINC CORROSION TEST

As a qualitative corrosion test, a piece of zinc was removed from the socket and, after forensic analysis, was ultrasonically cleaned and then exposed to a coastal marine environment at KSC. The piece was examined every two weeks, for a total of four weeks of exposure. The test was performed to see how certain features of the zinc would corrode (e.g., ridges compared to flat surfaces) and to see the rate of corrosion over a period similar to the time the socket remained on the tower post-failure. The coastal marine environment is more corrosive than the mountainous environment at Arecibo, so this test was expected and proved to corrode the zinc at a faster rate than exposed zinc would have at Arecibo. And, while the corrosion was extensive, the heavier amounts of corrosion were found to be along some of the sharp ridges; although there were many sharp ridges that did not have additional corrosion compared to their adjacent flat surfaces.

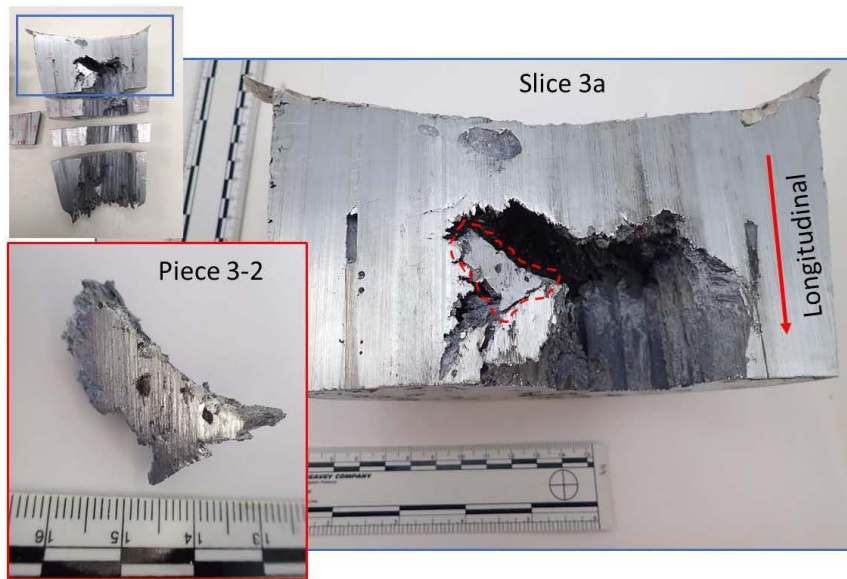


Figure 330. Piece 3-2 was taken from slice 3a and used for the accelerated corrosion test. Scale in inches and centimeters.

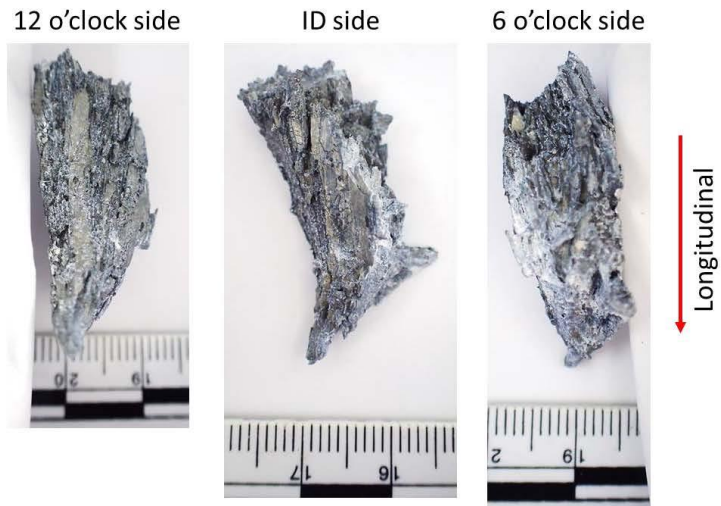


Figure 331. Piece 3-2 as-received, after removal from the socket. White areas are corrosion product. Scale in centimeters.

Transverse side – closest to socket base



Figure 332. Piece 3-2 as-received, after removal from the socket. White areas are corrosion product. Scale in centimeters.

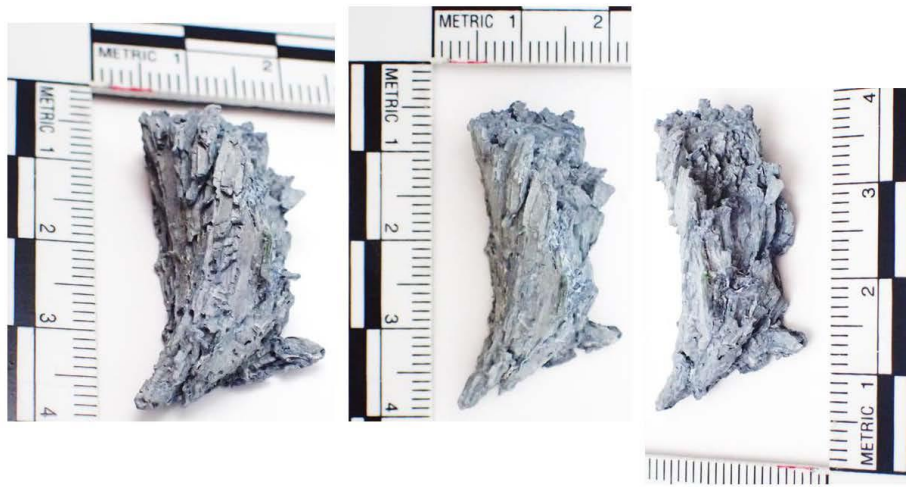


Figure 333. Piece 3-2 after two weeks of exposure to the coastal marine environment at KSC. Scale in centimeters.



Figure 334. Piece 3-2 after two weeks of exposure to the coastal marine environment at KSC. Scale in centimeters.

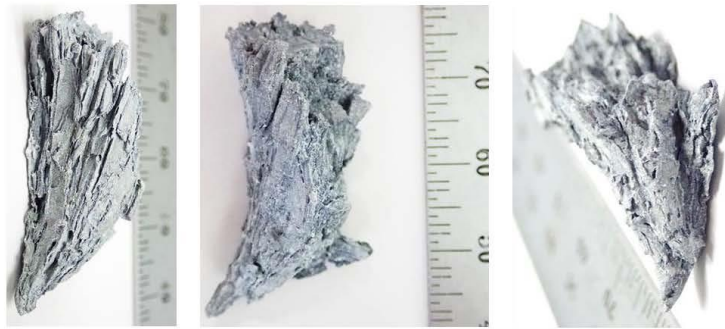


Figure 335. Piece 3-2 after four weeks of exposure to the coastal marine environment at KSC. Scale in millimeters.



Figure 336. Piece 3-2 after four weeks of exposure to the coastal marine environment at KSC. Scale in millimeters.

Appendix B. MSFC Materials Characterization Testing

B.1 Arecibo Failure Investigation Wire Tensile Testing, Work Order #2021-0110, Sequence 4



Arecibo Failure Investigation Wire Tensile Testing Work Order # 2021-0110, Sequence 4

Eric King
Test Engineer
April 20, 2021

BACKGROUND

Information in this report is in support of the Arecibo failure investigation. The Arecibo Observatory main feature was a 1000 foot diameter radio telescope collecting dish. In December 2020, the final of a series of failures occurred that caused the collecting dish and support structures to collapse. The primary failed component being investigated is a spelter socket assembly that fastens a 3.25 inch diameter steel rope to the support structure. This particular set of tests relates to the 0.25 inch wire in the steel (ASTM A586) rope. Test articles were taken from the failed test structure.

APPROACH

This report describes seven tensile tests of A586 steel wire. Segments of wire were cut and gripped using collet grips and vee wedge grips. Early attempts used hydraulic collets and then hydraulic vee wedge grips. These specimens were cut to 4-inch lengths. Each of these tests included grip failures that affected strength values. Only the test using Vee Wedge faces is included in this report. Also, six specimens cut to 16-inch lengths were tested in manual collet grips. One of these six specimens failed in the gage section. All of these are included in this report. These specimens were tested on Test Station 5 (manual collet grips) and Test Station 6 (Vee Wedge Face Grip) in building 4602 at Marshall Space Flight Center (MSFC). The environment for this testing was ambient laboratory air. The mechanical test frames consisted of servo-hydraulic actuator and reaction frame. 20,000 pound load cells were used for load and stress measurements. Linear Variable Differential Transformers (LVDTs) were used to control a 0.05 in/min ramp from a 500 pound preload to failure. These LVDTs had a total range of six inches. The image in Figure 1 to the right illustrates the setup on TS-5 using manual collet grips.

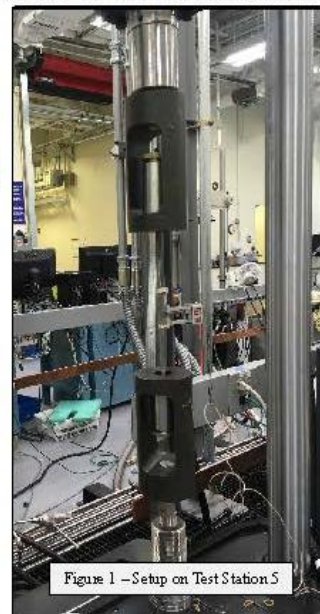


Figure 1 - Setup on Test Station 5

RESULTS

The results from these tests can be found on the following pages of this report. The pre-stressed wire from the observatory was curved or bent after the observatory failure occurred. For this reason, the wire had to be straightened under preload before testing. It required 500 pounds to straighten this wire to a reasonable point where strain values could be observed. For this reason, strain was shifted to illustrate zero strain going through zero load from 500 pounds where data could be compared. Strain was not collected on CP-701-3 (trial 4-inch length piece of wire) or CP701-14 (procedural failure). Specimen failures exhibited a classic tensile (cup/cone) failure. Since failures on all specimens except CP701-14 failed in the grip section, collected strain values after necking (ultimate strength) should not be considered. Data for these tests were uploaded into the MSFC EM Work Request System (EWRS) along with all pertinent calibration information.

Prepared By: ERIC KING Digitally signed by ERIC KING Date: 2021.04.28 07:05:49 -05'00	Reviewed By: Annette Gray Digitally signed by Annette Gray Date: 2021.04.28 09:07:00 -05'00
-------------------------------------------------------------------------------------------------------	-------------------------------------------------------------------------------------------------------------



EM22 Smooth Tensile Task Results

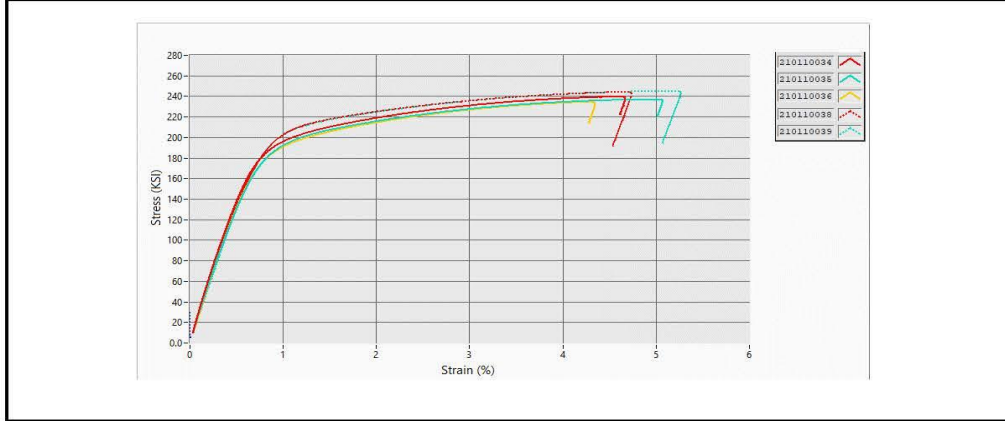
Version 4.3



M/SFC Work Order	2021-0110
Work Order Task	4
Testing Organization	EM22
Test Standard	ASTM E8

Average Data Acquisition Rate (Hz)	10
Control Mode	Stroke
Test Rate (in/min)	0.05
Extensometer Gage Length (in)	2.00

Material	A586 Steel
Nominal Temperature (°F)	70
Test Frame	TS-5 and TS-6
Pre-Load (LBS)	500



Statistics

Test Results	Maximum	Minimum	Median	Mean	Std. Deviation (sample)	Coefficient of Variation (%)
Tensile Stress (KSI)	252.74	234.43	240.87	241.98	6.03	2.49
Yield Stress (KSI)	198.78	181.63	184.99	188.20	7.24	3.84
Modulus of Elasticity (MSI)	29.95	26.57	28.33	28.23	1.28	4.53

Results

* Modulus of elasticity value is for reference only. Specific modulus tests are required for true value.

EM22 Specimen ID	Other Specimen ID	Tensile Stress (KSI)	Tensile Load (KIP)	Yield Stress (KSI)	Modulus of Elasticity (MSI)*
210110026	CP701-3	252.74	12.31	Not Available	Not Available
210110034	CP701-11	239.65	11.86	184.99	29.95
210110035	CP701-12	236.98	11.82	181.63	28.33
210110036	CP701-13	234.43	11.69	183.14	27.52
210110037	CP701-14	240.87	12.01	Not Available	Not Available
210110038	CP701-15	244.06	12.08	192.49	28.80
210110039	CP701-16	245.10	12.13	198.78	26.57



EM22
Smooth Tensile Specimen Test Results
 Version 4.3

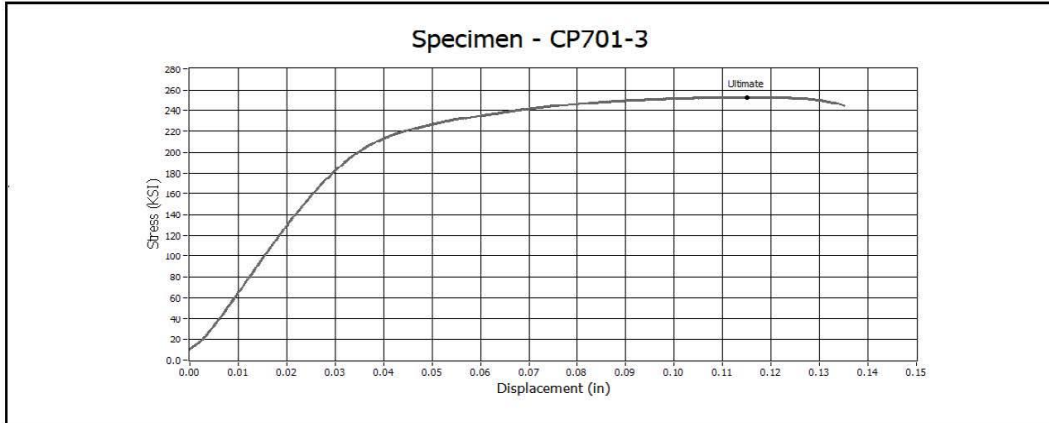


EM22 Specimen ID	210130026
Other Specimen ID	CP701-3
Operator	Eric King
Test Date	3/15/2021
Failure Location	Grip Section

Environment	Laboratory Air
Test Frame	TS-6

Modulus of Elasticity (ksi)	Not Available
Geometry	Circular
Initial Diameter (in)	0.259
Initial Cross Section Area (in ²)	0.049

	Stress (ksi)	Load (lbf)	Strain (%)
Tensile	252.74	32.31	N/A



Method File:
 EM22 Tensile Test Template_v5

Comments:
 This test was performed on a wire that was four inches in total length. No strain data was collected. Gripping was performed using hydraulic grips and vee shaped wedge faces. Failure occurred in grip section.



EM22 Smooth Tensile Specimen Test Results

Version 4.3

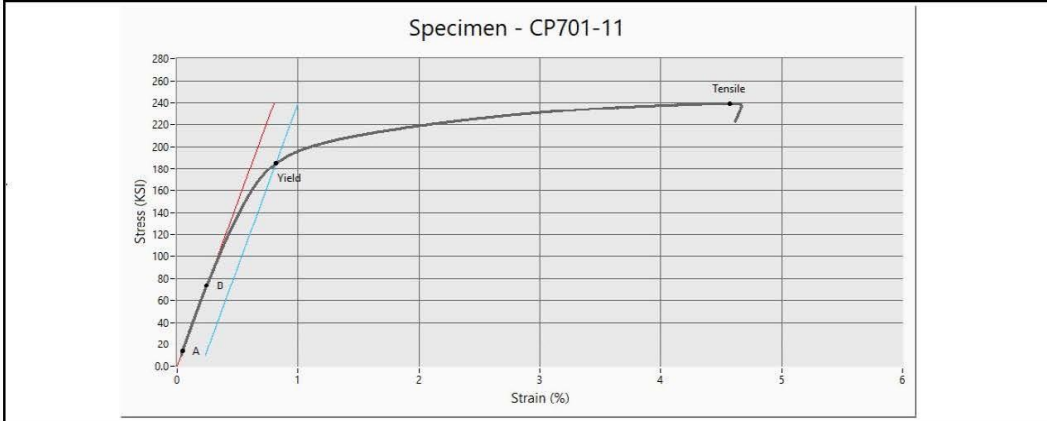


EM22 Specimen ID	210130034
Other Specimen ID	CP701-11
Operator	Eric King
Test Date	4/1/2021
Failure Location	Grip Section

Environment	Laboratory Air
Test Frame	TS-5

Modulus of Elasticity (ksi)	29.55
Geometry	Circular
Initial Diameter (in)	0.251
Initial Cross Section Area (in ²)	0.049

	Stress (ksi)	Load (lbf)	Strain (%)
Tensile	239.65	31.86	4.57
Yield	184.99	9.15	0.82



Method File:
EM22 Tensile Test Template_v5

Comments:
This test was performed on a wire that was sixteen inches in total length. Gripping was performed using manual collet grips. Failure occurred in grip section.



EM22 Smooth Tensile Specimen Test Results

Version 4.3

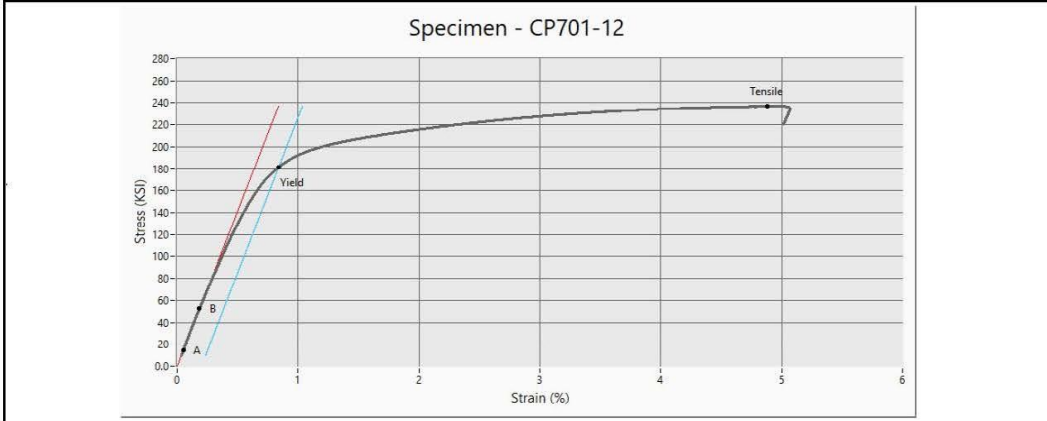


EM22 Specimen ID	210130035
Other Specimen ID	CP701-12
Operator	Eric King
Test Date	4/1/2021
Failure Location	Grip Section

Environment	Laboratory Air
Test Frame	TS-5

Modulus of Elasticity (ksi)	28.31
Geometry	Circular
Initial Diameter (in)	0.252
Initial Cross Section Area (in ²)	0.050

	Stress (ksi)	Load (lbf)	Strain (%)
Tensile	236.98	31.82	4.88
Yield	181.63	9.06	0.84



Method File:
EM22 Tensile Test Template_v5

Comments:
This test was performed on a wire that was sixteen inches in total length. Gripping was performed using manual collet grips. Failure occurred in grip section.



EM22 Smooth Tensile Specimen Test Results

Version 4.3

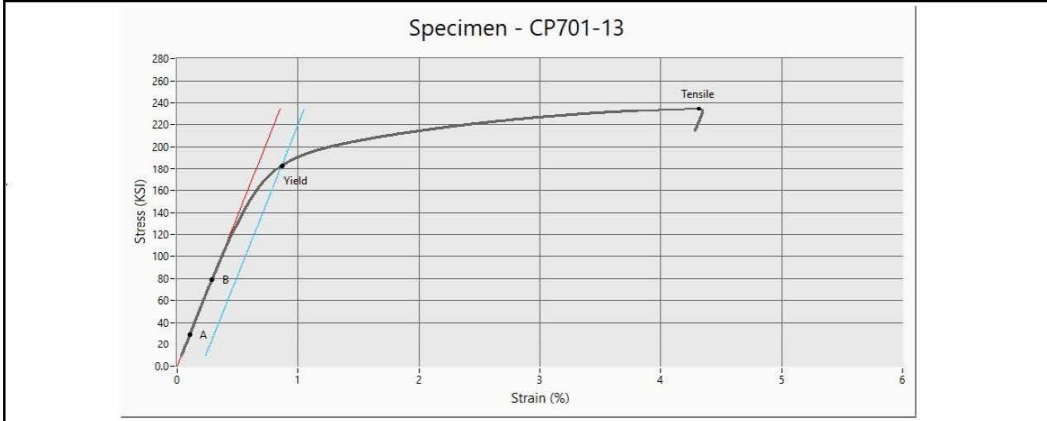


EM22 Specimen ID	210130036
Other Specimen ID	CP701-13
Operator	Eric King
Test Date	4/1/2021
Failure Location	Grip Section

Environment	Laboratory Air
Test Frame	TS-5

Modulus of Elasticity (ksi)	27.52
Geometry	Circular
Initial Diameter (in)	0.252
Initial Cross Section Area (in ²)	0.050

	Stress (ksi)	Load (lbf)	Strain (%)
Tensile	234.43	31.69	4.31
Yield	183.14	9.13	0.87



Method File:
EM22 Tensile Test Template_v5

Comments:
This test was performed on a wire that was sixteen inches in total length. Gripping was performed using manual collet grips. Failure occurred in grip section.



EM22 Smooth Tensile Specimen Test Results

Version 4.3

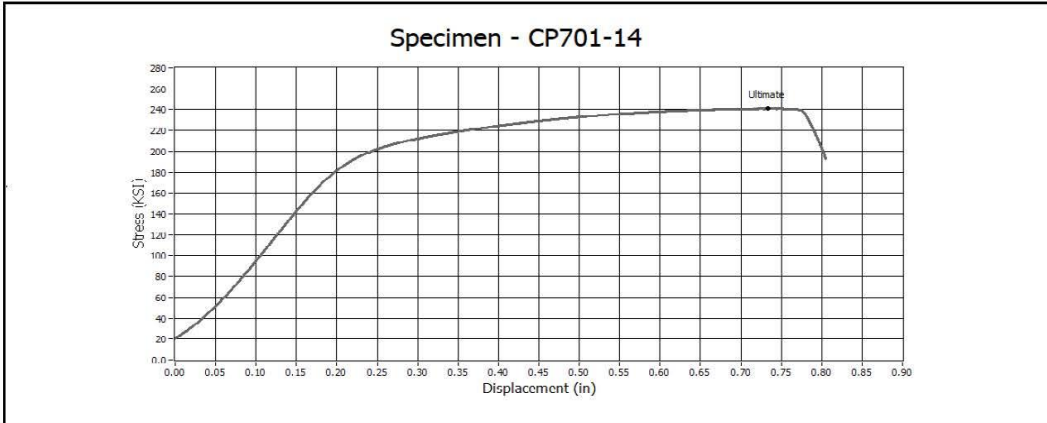


EM22 Specimen ID	210130037
Other Specimen ID	CP701-14
Operator	Eric King
Test Date	4/1/2021
Failure Location	Gage Section

Environment	Laboratory Air
Test Frame	TS-5

Modulus of Elasticity (ksi)	-946.28
Geometry	Circular
Initial Diameter (in)	0.252
Initial Cross Section Area (in ²)	0.050

	Stress (ksi)	Load (lbf)	Strain (%)
Tensile	240.87	32.01	N/A



Method File:
EM22 Tensile Test Template_v5

Comments:
This test was performed on a wire that was sixteen inches in total length. Gripping was performed using manual collet grips. No strain was collected.



EM22 Smooth Tensile Specimen Test Results

Version 4.3

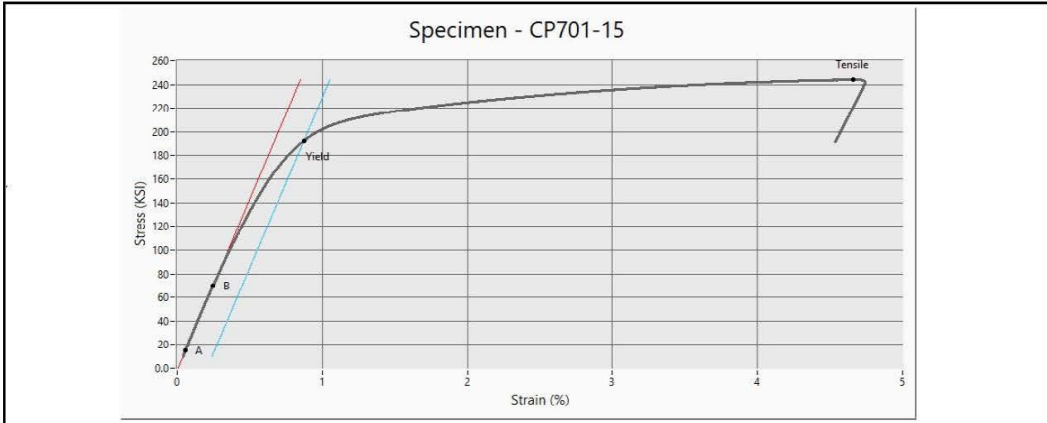


EM22 Specimen ID	210130038
Other Specimen ID	CP701-15
Operator	Eric King
Test Date	4/2/2021
Failure Location	Grip Section

Environment	Laboratory Air
Test Frame	TS-5

Modulus of Elasticity (Msi)	28.20
Geometry	Circular
Initial Diameter (in)	0.251
Initial Cross Section Area (in ²)	0.049

	Stress (ksi)	Load (lbf)	Strain (%)
Tensile	244.06	32.08	4.66
Yield	192.49	9.52	0.87



Method File:
EM22 Tensile Test Template_v5

Comments:
This test was performed on a wire that was sixteen inches in total length. Gripping was performed using manual collet grips. Failure occurred in grip section.



EM22 Smooth Tensile Specimen Test Results

Version 4.3

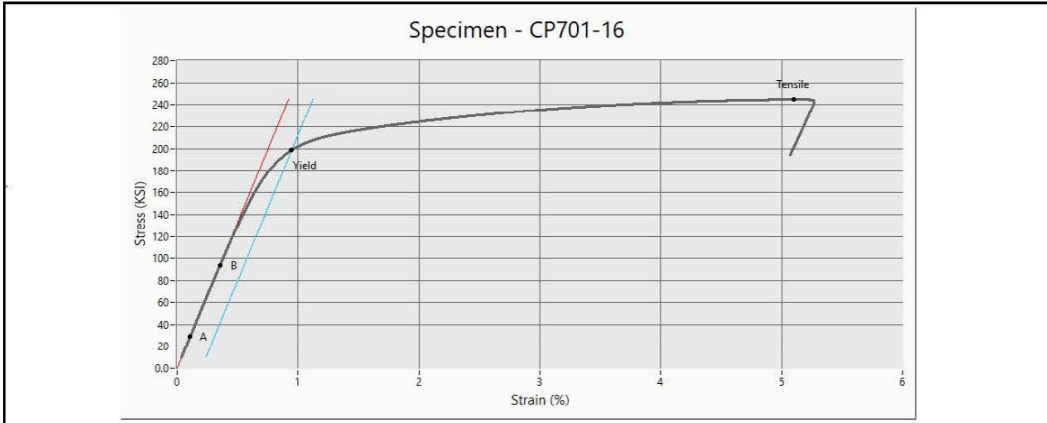


EM22 Specimen ID	210130039
Other Specimen ID	CP701-16
Operator	Eric King
Test Date	4/2/2021
Failure Location	Grip Section

Environment	Laboratory Air
Test Frame	TS-5

Modulus of Elasticity (ksi)	26.57
Geometry	Circular
Initial Diameter (in)	0.251
Initial Cross Section Area (in ²)	0.049

	Stress (ksi)	Load (lbf)	Strain (%)
Tensile	245.10	32.13	5.10
Yield	198.78	9.84	0.95



Method File:
EM22 Tensile Test Template_v5

Comments:
This test was performed on a wire that was sixteen inches in total length. Gripping was performed using manual collet grips. Failure occurred in grip section.

B.2 Arecibo Failure Investigation Compression Testing, Work Order #2021-0110, Sequence 5



Arecibo Failure Investigation Compression Testing Work Order # 2021-0110, Sequence 5

Annette Gray
Test Engineer
April 21, 2021

BACKGROUND

Information in this report is in support of the Arecibo failure investigation. The Arecibo Observatory main feature was a 1000 foot diameter radio telescope collecting dish. In December 2020, the final of a series of failures occurred that caused the collecting dish and support structures to collapse. The primary failed component being investigated is a spelter socket assembly that fastens a 3.25 inch diameter steel rope to the support structure. This particular test is to provide compression properties of a baseline zinc material and the post-failure zinc material. Test articles were taken from a cast ingot and the failed spelter socket assembly.

APPROACH

This report describes 16 compression tests of specimens machined from a cast zinc ingot and the material from the zinc slug from the failed spelter socket assembly. Testing was conducted according to ASTM E9 and specimens were a cylindrical geometry with 14 having a nominal diameter of 0.375 inches and 2 having a nominal diameter of 2.5 inches. Of the small diameter (0.375-inch), 5 are from the slug (2 in radial and 3 in axial directions), and the remaining 9 are from the ingot. All of these tests are included in this report. Three large diameter (2.5-inch) specimens were tested but a length size discrepancy that may have affected the strength value for one of the specimens and is not included in this report. All of the large diameter specimens were taken from the ingot parent material. These specimens were tested on Test Station 3 (small diameter) and Test Station 1 (large diameter) in building 4602 at Marshall Space Flight Center (MSFC). The environment for this testing was ambient laboratory air. The mechanical test frames consisted of servo-hydraulic actuator and reaction frame. A 20,000-pound load cell (small diameter) and a 200,000-pound load cell (large diameter) were used for load and stress measurements. Linear Variable Differential Transformers (LVDTs) were used to control a 0.02 in/min ramp from a 10-pound preload to 8% strain (small diameter) and a 0.01 in/min ramp from a 100-pound preload to 8% strain (large diameter). These LVDTs had a total range of six inches. The image in Figure 1 illustrates the setup on TS-3 and the image in Figure 2 illustrates the setup on TS-1 using parallel platen fixtures.

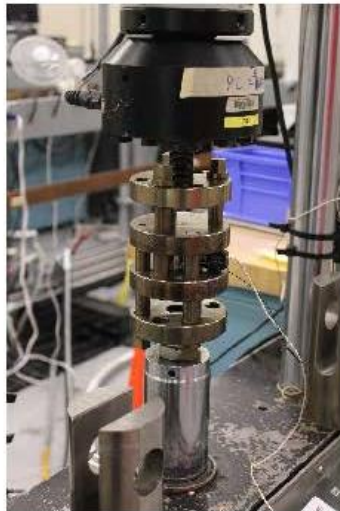


Figure 1 – Setup on Test Station 3



Figure 2 – Setup on Test Station 1



RESULTS

The results from this test can be found on the following pages of this report. The results of the small diameter specimens are separated into groups based on whether the parent material was from the ingot or the slug and then by their orientation within the parent material. Figure 3 shows the location and direction of each specimen within the parent ingot material and Figure 4 through 6 shows the location and direction of each specimen within the failed slug material. Included on each task results summary page are the locations and directions of the specimens in each grouping. Ingot material specimens within the direction groupings behaved in family with each other, with the notable exception of CP702-10. This specimen was taken from a different location within the ingot where the orientation of the grains could be different. This suggests that the mechanical properties of the zinc is orientation and location sensitive. The slug material specimens showed greater variation which could be caused by that materials loading history prior to testing. The results for the large diameter specimens are in family with each other. These results satisfy the testing requirement of the above mentioned ASTM E9 testing standard. Data for these tests were uploaded into the MSFC EM Work Request System (EWRs) along with all pertinent calibration information.

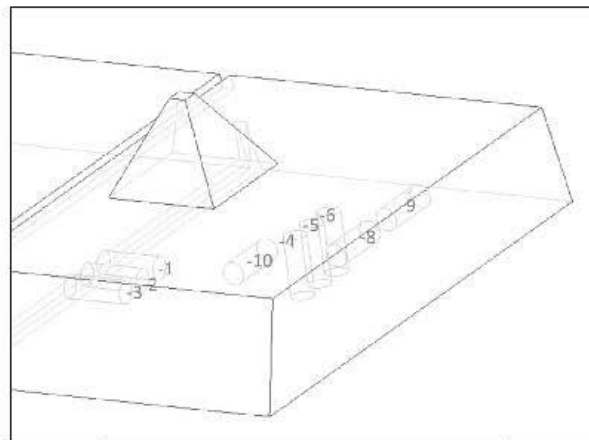


Figure 3 – Cast Zinc Ingot Diagram with Small Diameter Compression Specimen Locations and Directions

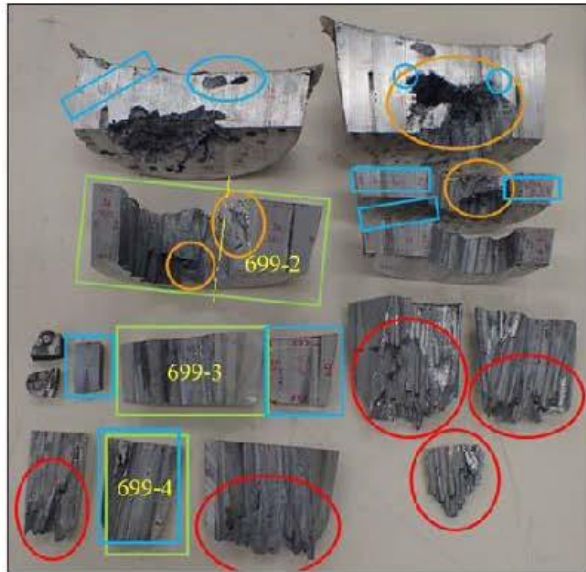


Figure 4 – Initial Dissection of Socket Shag Material
Small diameter Compression Specimens were cut from 699-2

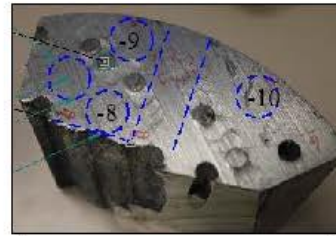


Figure 5 – Top view of Dissection of 699-2

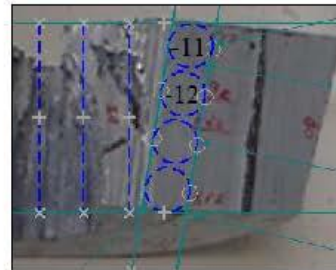


Figure 6 – Front view of Dissection of 699-2

Prepared By: Annette Gray Digitally signed by Annette Gray Date: 2021.04.27 12:41:17 -0500	Reviewed By: ERIC KING Digitally signed by ERIC KING Date: 2021.04.27 13:28:22 -0500
---------------------------------------------------------------------------------------------------------	---------------------------------------------------------------------------------------------------



EM22 Ingot Specimen 1-3 Compression Task Results

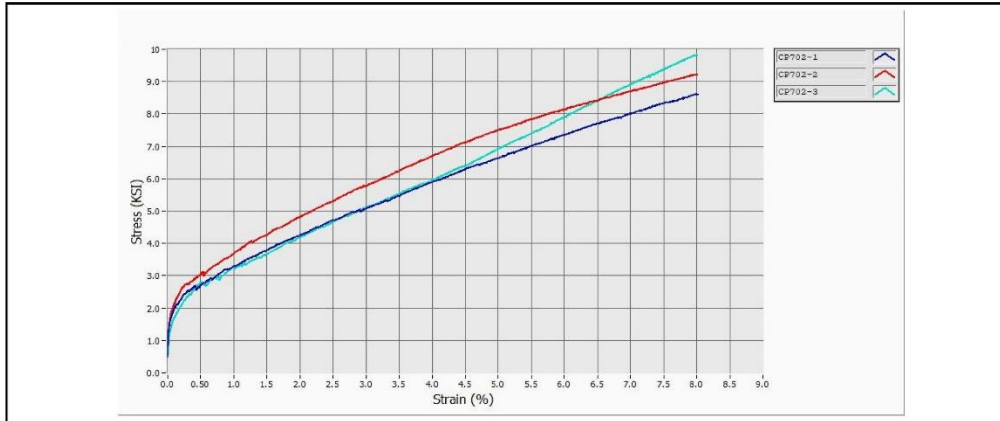
Version 4.3



MSFC Work Order	2021-0110
Work Order Task	5
Testing Organization	EM22
Test Standard	ASTM E9

Data Acquisition Rate (Hz)	10
Control Mode	Stroke
Average Test Rate (in/min)	0.02
Extensometer Gage Length (in)	0.50
Nominal Specimen Length (in)	1.00

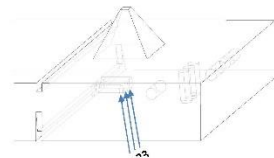
Material	Zinc
Nominal Temperature (°F)	70
Test Frame	TS-3
Drawing Number	S-1A
Pre-Load (LBS)	10



Results

* Modulus of elasticity value is for reference only. Specific modulus tests are required for true value.

EM22 Specimen ID	Other Specimen ID	Yield Stress (KSI)	8% Compression Stress (KSI)	Modulus of Elasticity (MSI)*
210110044	CP702-1	2.33	8.58	11.04
210110045	CP702-2	2.60	9.20	10.77
210110046	CP702-3	2.20	9.80	4.26





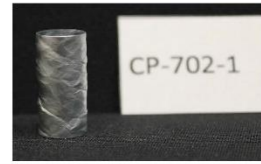
EM22
Specimen Test Results
 Version 4.3



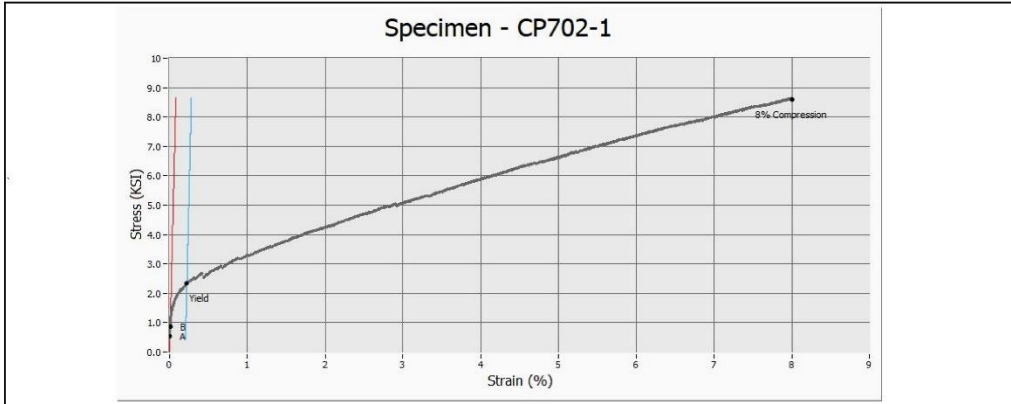
EM22 Specimen ID	210112041
Other Specimen ID	CP-702-1
Operator	Annette Gray
Test Date	3/26/2021
Geometry	Circular
Initial Diameter (in)	0.374
Initial Cross Section (in ²)	0.110

Environment Laboratory Air

Modulus of Elasticity (MSI) 11.01



	Stress (KSI)	Load (LBS)	Strain (%)
Yield	2.33	253.95	0.22
8% Compression	8.58	943.08	8.01



Method File:
 Compression Test.matic with Bi digage Fixture

Comments:



EM22 Specimen Test Results

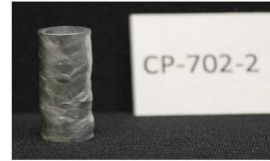
Version 1.3



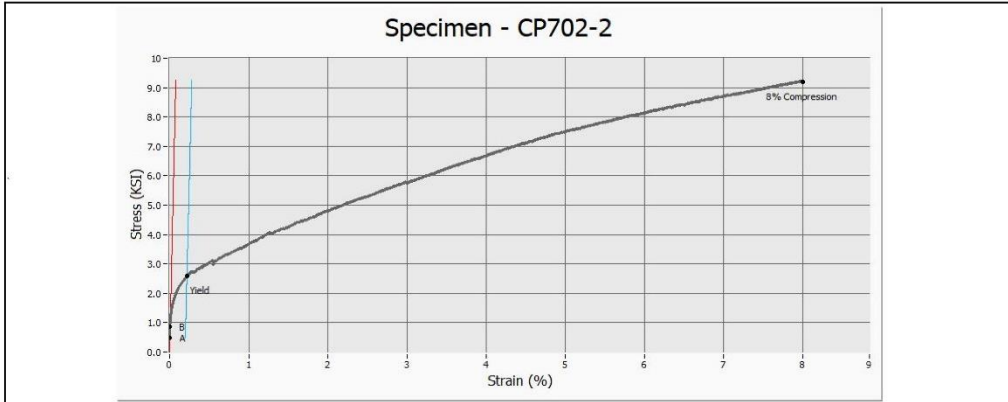
EM22 Specimen ID	210112045
Other Specimen ID	CP702-2
Operator	Annette Gray
Test Date	3/26/2021
Geometry	Circular
Initial Diameter (in)	0.374
Initial Cross Section (in ²)	0.110

Environment

Modulus of Elasticity (MS)



	Stress (KSI)	Load (LBS)	Strain (%)
Yield	2.60	285.33	0.22
8% Compression	9.20	1010.36	8.00



Method File:
 Compression Test.rpt with Bridgman Fixture
 Comments:



EM22 Specimen Test Results

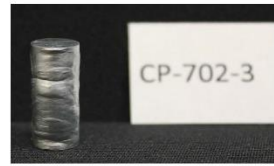


Version: 3

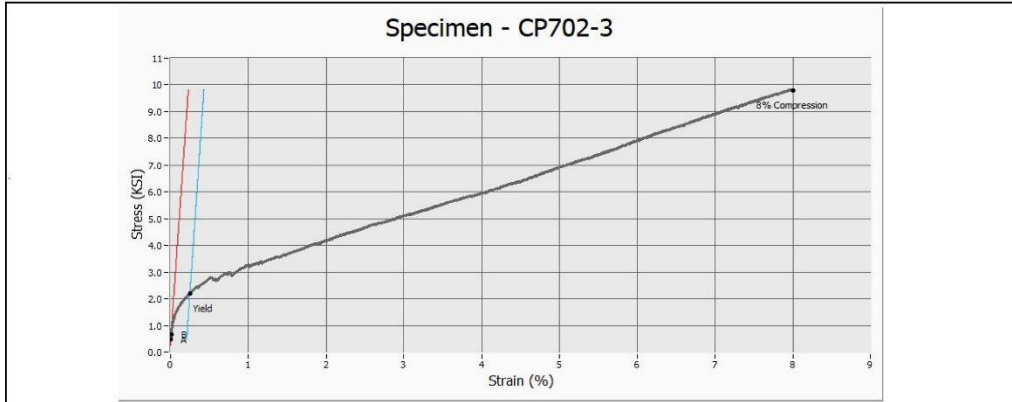
EM22 Specimen ID	210110016
Other Specimen ID	CP-702-3
Operator	Annette Gray
Test Date	3/26/2011
Geometry	Circular
Initial Diameter (in)	0.375
Initial Cross Section (in ²)	0.110

Environment: Laboratory Air

Modulus of Elasticity (MS) 1.26



	Stress (KSI)	Load (LBS)	Strain (%)
Yield	2.20	242.47	0.24
8% Compression	9.80	1082.72	8.00



Method File:
 Compression Template with Bi-Stage Fixture
 Comments:



EM22 Ingot Specimen 4-6 Compression Task Results

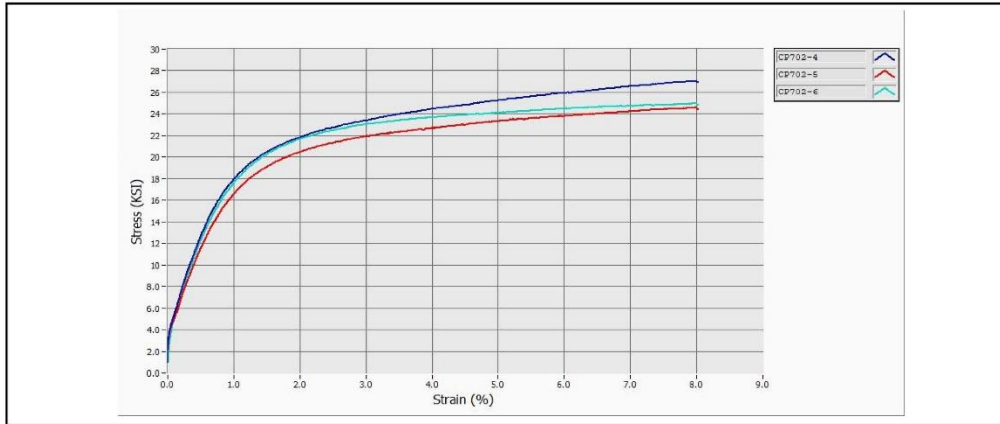
Version 4.3



MISFC Work Order	2021-0110
Work Order Task	5
Testing Organization	EM22
Test Standard	ASTM E9

Data Acquisition Rate (Hz)	10
Control Mode	Stroke
Average Test Rate (in/min)	0.02
Extensometer Gage Length (in)	0.50
Nominal Specimen Length (in)	1.00

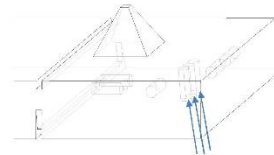
Material	Zinc
Nominal Temperature (°F)	70
Test Frame	TS-3
Drawing Number	S-1A
Pre-Load (LBS)	10



Results

* modulus of elasticity value is for reference only. Specific modulus tests are required for true value.

EM22 Specimen ID	Other Specimen ID	Yield Stress (KSI)	8% Compression Stress (KSI)	Modulus of Elasticity (MSI)*
210110047	CP702-4	17.59	26.95	1.89
210110048	CP702-5	16.29	24.43	1.71
210110049	CP702-6	17.36	24.83	1.81





EM22 Specimen Test Results



Version: 3

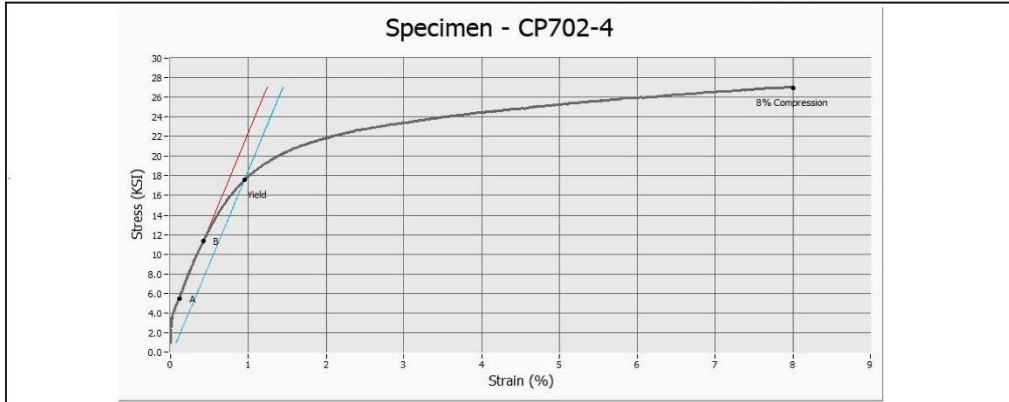
EM22 Specimen ID	210110017
Other Specimen ID	CP-702-4
Operator	FRIE King
Test Date	3/16/2013
Geometry	Circular
Initial Diameter (in)	0.376
Initial Cross Section (in ²)	0.111

Environment: Laboratory Air

Modulus of Elasticity (MSI): 1.89



	Stress (KSI)	Load (LBS)	Strain (%)
Yield	17.58	1912.59	0.95
8% Compression	26.95	2992.87	8.01



Method File:
 Compression Template with Bi-Stage Fixture
 Comments:



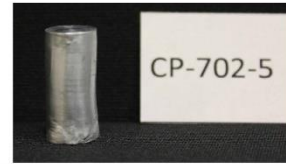
EM22
Specimen Test Results
 Version 1.3



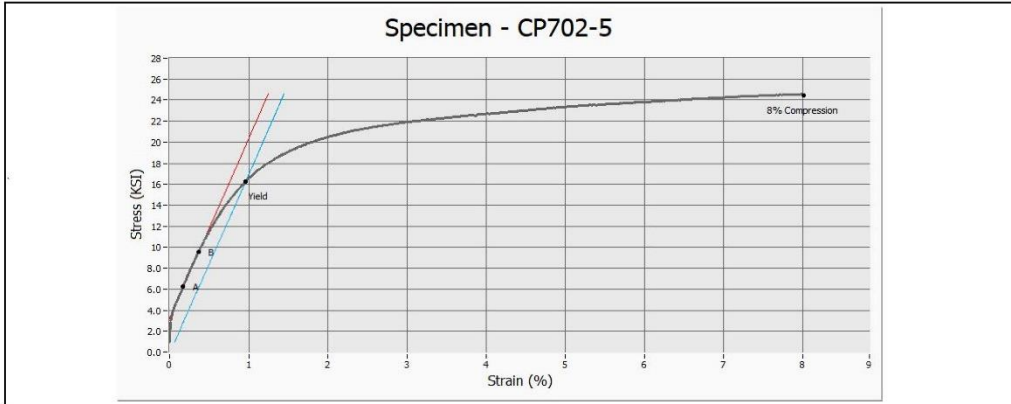
EM22 Specimen ID	210110048
Other Specimen ID	CP702-5
Operator	F.F.King
Test Date	3/16/2021
Geometry	Circular
Initial Diameter (in)	0.376
Initial Cross Section (in ²)	0.113

Environment

Modulus of Elasticity (MS)



	Stress (KSI)	Load (LBS)	Strain (%)
Yield	16.29	1808.42	0.96
8% Compression	24.43	2742.08	8.01



Method File:
 Compression Template with Bridgman Fixture
 Comments:



EM22 Specimen Test Results

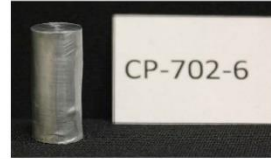
Version 1.3



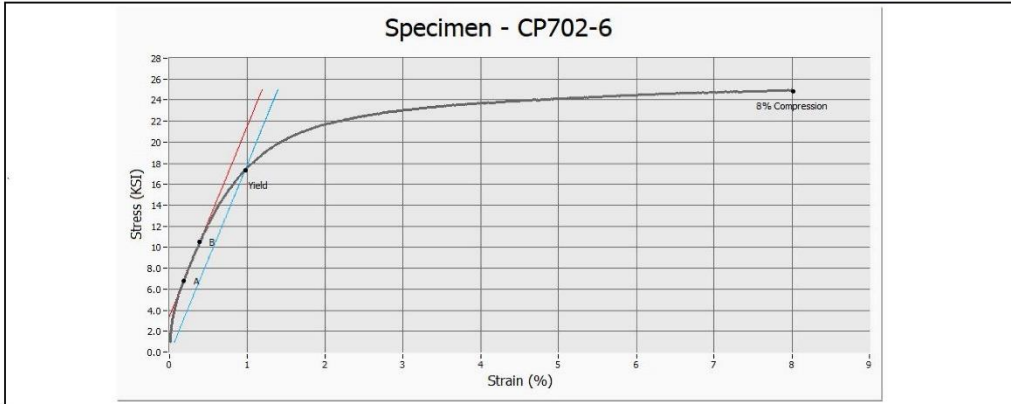
EM22 Specimen ID	210110010
Other Specimen ID	CP702-6
Operator	FRE King
Test Date	3/16/2021
Geometry	Circular
Initial Diameter (in)	0.375
Initial Cross Section (in ²)	0.110

Environment:

Modulus of Elasticity (MS)



	Stress (KSI)	Load (LBS)	Strain (%)
Yield	17.36	1916.93	0.97
8% Compression	24.83	2742.30	8.01



Method File:
 Compression Test.rpt with Bridgman Fixture

Comments:



EM22 Ingot Specimen 8-10 Compression Task Results

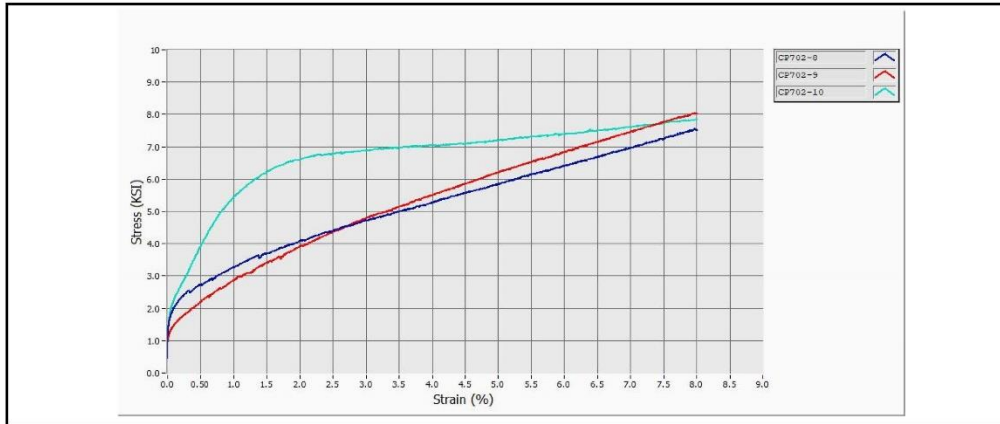
Version 4.3



MSFC Work Order	2021-0110
Work Order Task	5
Testing Organization	EM22
Test Standard	ASTM E9

Data Acquisition Rate (Hz)	10
Control Mode	Stroke
Average Test Rate (in/min)	0.02
Extensometer Gage Length (in)	0.50
Nominal Specimen Length (in)	1.00

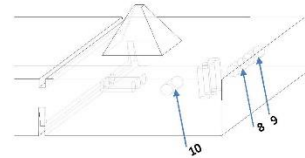
Material	Zinc
Nominal Temperature (°F)	70
Test Frame	TS-3
Drawing Number	S. 1A
Pre-Load (LBS)	10



Results

* Modulus of elasticity value is for reference only. Specific modulus tests are required for true value.

EM22 Specimen ID	Other Specimen ID	Yield Stress (KSI)	8% Compression Stress (KSI)	Modulus of Elasticity (MSI)*
210110051	CP702-8	2.39	7.51	3.61
210110052	CP702-9	1.77	8.00	2.15
210110053	CP702-10	5.76	7.83	0.39





EM22 Specimen Test Results



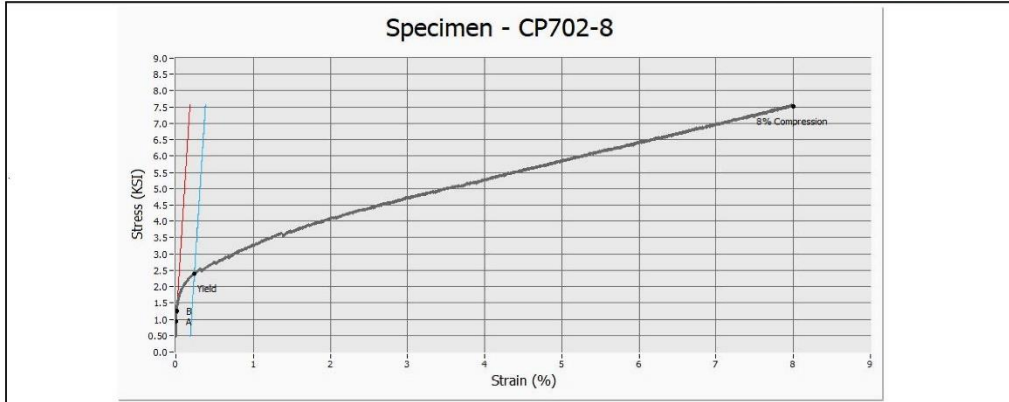
Version 1.3

EM22 Specimen ID	210110B5
Other Specimen ID	CP702-8
Operator	Annette Gray
Test Date	3/18/2021
Geometry	Circular
Initial Diameter (in)	0.375
Initial Cross Section (in ²)	0.110

Environment Laboratory Air

Modulus of Elasticity (MS) 1.61

	Stress (KSI)	Load (LBS)	Strain (%)
Yield	2.39	263.56	0.24
8% Compression	7.51	829.04	8.00



Method File:
 Compression Template with Bridgman Fixture
 Comments:



EM22
Specimen Test Results
 Version 1.3



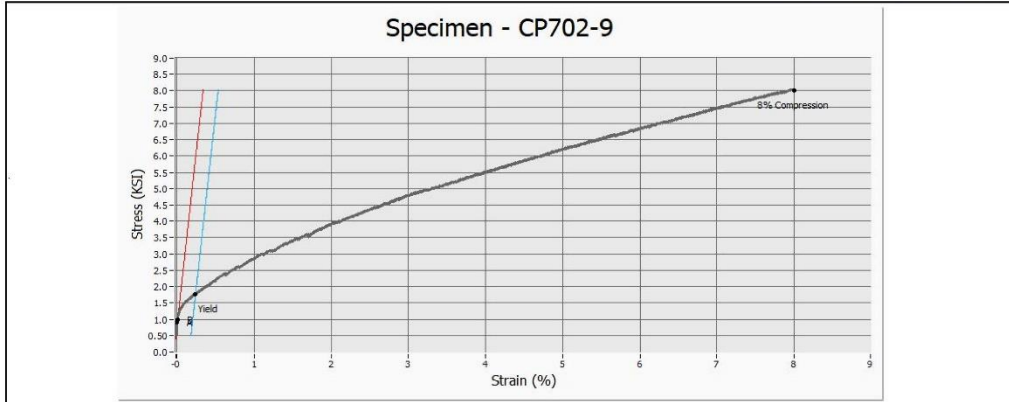
EM22 Specimen ID	210110852
Other Specimen ID	CP702-9
Operator	Annette Gray
Test Date	3/18/2021
Geometry	Circular
Initial Diameter (in)	0.375
Initial Cross Section (in ²)	0.110

Environment

Modulus of Elasticity (MS)



	Stress (KSI)	Load (lBS)	Strain (%)
Yield	1.77	195.76	0.24
8% Compression	8.00	883.46	8.00



Method File:
 Compression Template with Bridage Fixture
 Comments:



EM22 Specimen Test Results

Version - 3



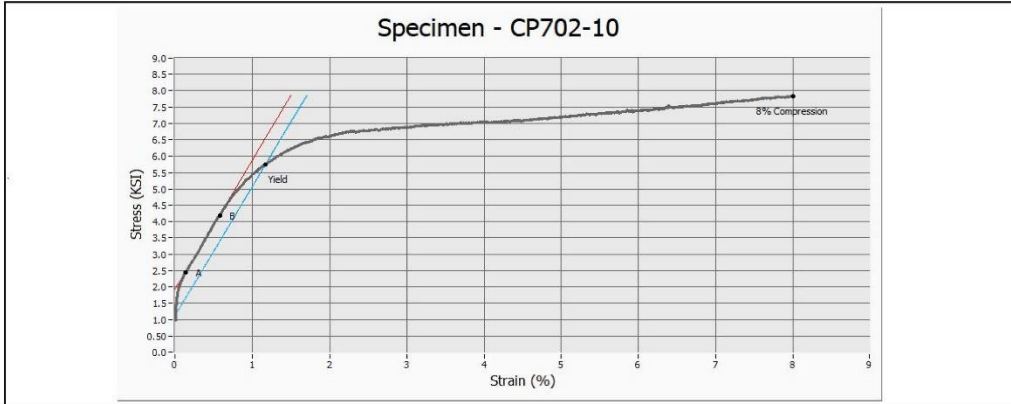
EM22 Specimen ID	710110263
Other Specimen ID	CP-702-10
Operator	Annette Gray
Test Date	3/26/2013
Geometry	Circular
Initial Diameter (in)	0.374
Initial Cross Section (in ²)	0.110

Environment Laboratory Air

Modulus of Elasticity (MS) 8.39



	Stress (KSI)	Load (LBS)	Strain (%)
Yield	5.76	632.61	1.18
8% Compression	7.83	860.03	8.00



Method File:
 Compression Template with Bi-Stage Fixture
 Comments:



EM22 Short Transverse Ingot Compression Task Results

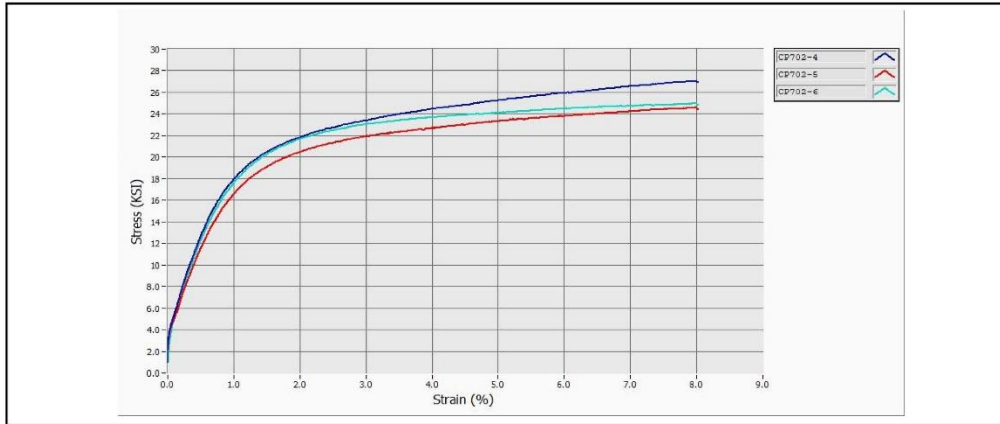
Version 4.3



MISFC Work Order	2021-0110
Work Order Task	5
Testing Organization	EM22
Test Standard	ASTM E9

Data Acquisition Rate (Hz)	10
Control Mode	Stroke
Average Test Rate (in/min)	0.02
Extensometer Gage Length (in)	0.50
Nominal Specimen Length (in)	1.00

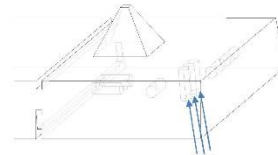
Material	Zinc
Nominal Temperature (°F)	70
Test Frame	TS-3
Drawing Number	S-1A
Pre-Load (LBS)	10



Results

* modulus of elasticity value is for reference only. Specific modulus tests are required for true value.

EM22 Specimen ID	Other Specimen ID	Yield Stress (KSI)	8% Compression Stress (KSI)	Modulus of Elasticity (MSI)*
210110047	CP702-4	17.59	26.95	1.89
210110048	CP702-5	16.29	24.43	1.71
210110049	CP702-6	17.36	24.83	1.81





EM22 Specimen Test Results



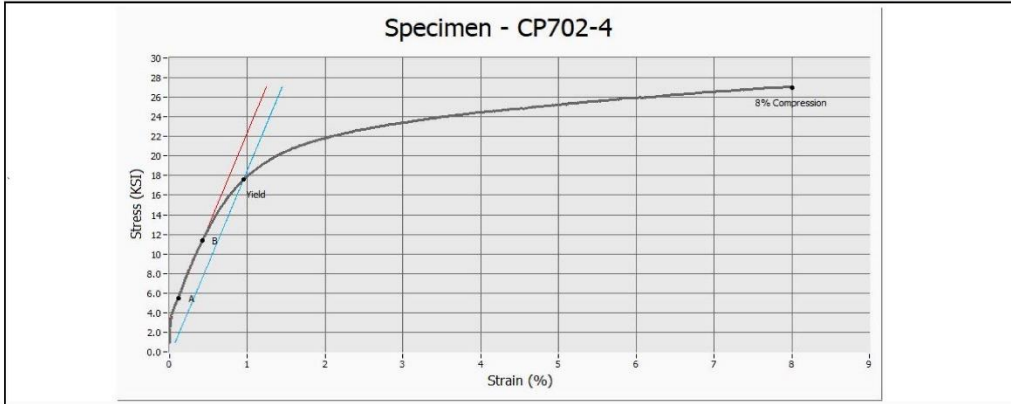
Version 4.3

EM22 Specimen ID	210112047
Other Specimen ID	CP702-4
Operator	Eric King
Test Date	3/16/2021
Geometry	Circular
Initial Diameter (in)	0.376
Initial Cross Section (in ²)	0.111

Environment Laboratory Air

Modulus of Elasticity (MS) 1.89

	Stress (KSI)	Load (LBS)	Strain (%)
Yield	17.59	1952.99	0.95
8% Compression	25.95	2902.87	8.01



Method File:
 Compression Template with Birdcage Fixture
 Comments:



EM22 Specimen Test Results

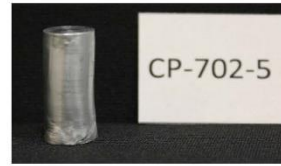
Version 4.3



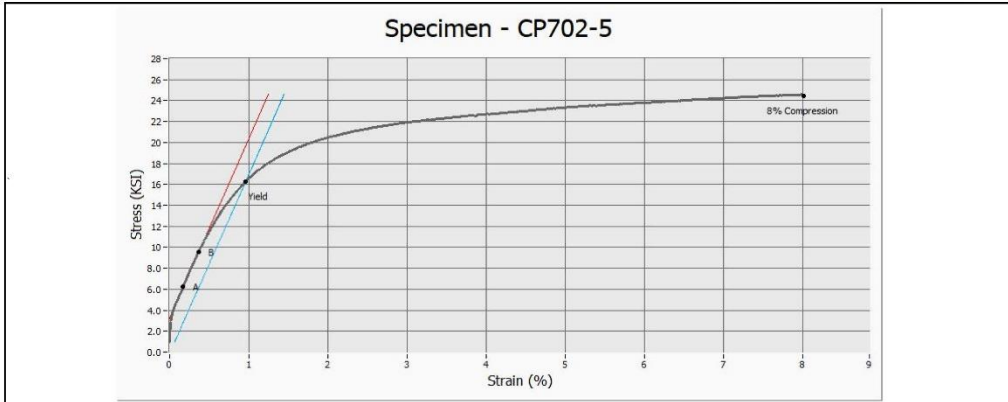
EM22 Specimen ID	210110048
Other Specimen ID	CP702-5
Operator	Eric King
Test Date	3/16/2021
Geometry	Circular
Initial Diameter (in)	0.376
Initial Cross Section (in ²)	0.111

Environment

Modulus of Elasticity (MSI)



	Stress (KSI)	Load (LBS)	Strain (%)
Yield	16.29	1808.42	0.96
8% Compression	24.43	2712.08	8.01



Method File:

 Comments:



EM22 Specimen Test Results

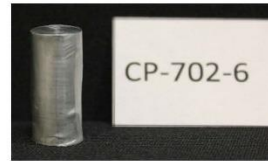
Version 4.3



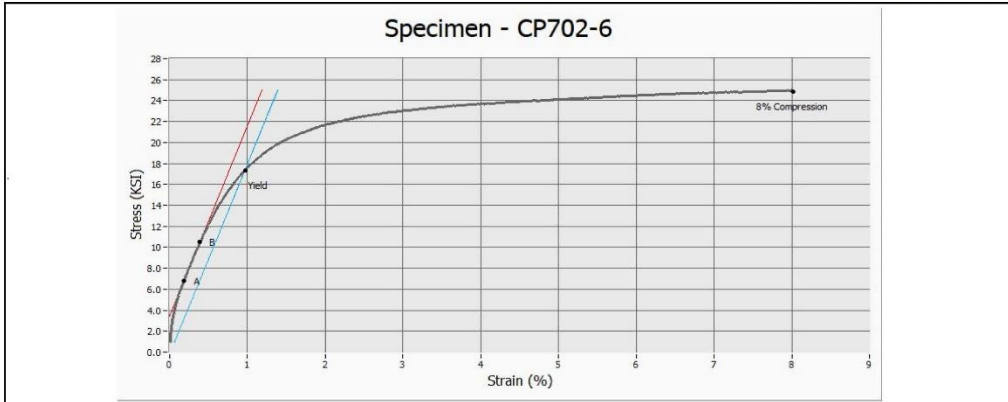
EM22 Specimen ID	210110040
Other Specimen ID	CP702-6
Operator	Eric King
Test Date	3/16/2021
Geometry	Circular
Initial Diameter (in)	0.375
Initial Cross Section (in ²)	0.110

Environment: Laboratory Air

Modulus of Elasticity (MSI): 1.81



	Stress (KSI)	Load (LBS)	Strain (%)
Yield	17.36	1916.55	0.97
8% Compression	24.83	2742.10	8.04



Method File:
 Compression Testplate with Birdcage Fixture
 Comments:



EM22 Long Transverse Ingot Compression Task Results

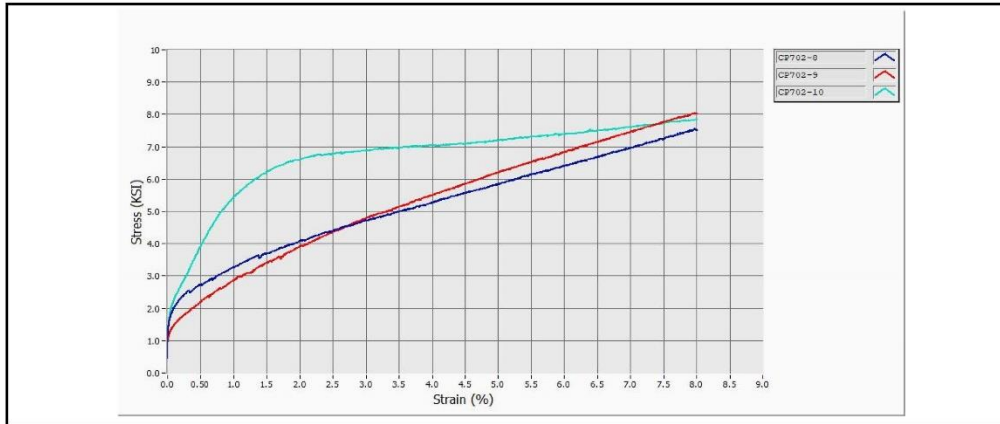
Version 4.3



MSFC Work Order	2021-0110
Work Order Task	5
Testing Organization	EM22
Test Standard	ASTM E9

Data Acquisition Rate (Hz)	10
Control Mode	Stroke
Average Test Rate (in/min)	0.02
Extensometer Gage Length (in)	0.50
Nominal Specimen Length (in)	1.00

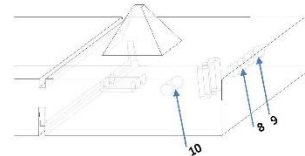
Material	Zinc
Nominal Temperature (°F)	70
Test Frame	TS-3
Drawing Number	S. 1A
Pre-Load (LBS)	10



Results

* Modulus of elasticity value is for reference only. Specific modulus tests are required for true value.

EM22 Specimen ID	Other Specimen ID	Yield Stress (KSI)	8% Compression Stress (KSI)	Modulus of Elasticity (MSI)*
210110051	CP702-8	2.39	7.51	3.61
210110052	CP702-9	1.77	8.00	2.15
210110053	CP702-10	5.76	7.83	0.39





EM22
Specimen Test Results
 Version 4.3



EM22 Specimen ID	210112051
Other Specimen ID	CP702-8
Operator	Annette Gray
Test Date	3/18/2021
Geometry	Circular
Initial Diameter (in)	0.375
Initial Cross Section (in ²)	0.110

Environment

Modulus of Elasticity (MS)

	Stress (KSI)	Load (LBS)	Strain (%)
Yield	2.39	263.56	0.24
8% Compression	7.51	829.04	8.00



Method File:
 Compression Tomplate with Birdcage Fixture
 Comments:



EM22
Specimen Test Results
 Version 4.3



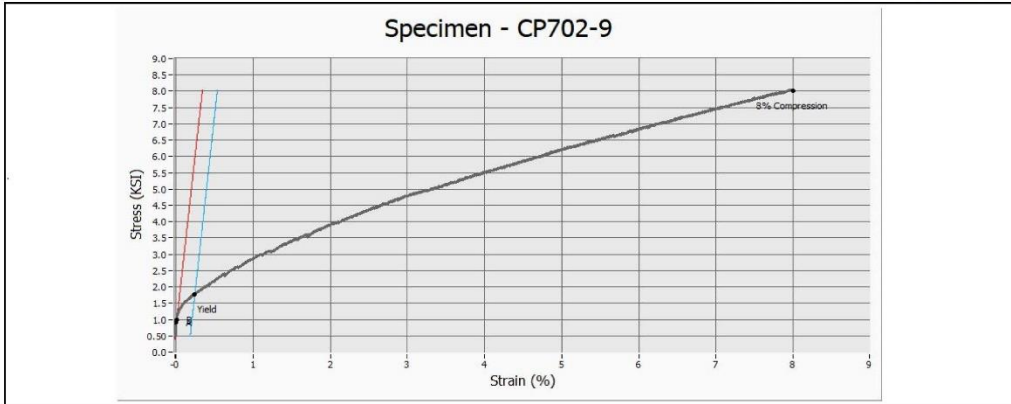
EM22 Specimen ID	210110052
Other Specimen ID	CP702-9
Operator	Annette Gray
Test Date	3/18/2021
Geometry	Circular
Initial Diameter (In)	0.375
Initial Cross Section (in ²)	0.110

Environment Laboratory Air

Modulus of Elasticity (MSI) 2.15



	Stress (KSI)	Load (LBS)	Strain (%)
Yield	1.77	195.76	0.24
8% Compression	8.00	883.46	8.00



Method File:
 Compression Template with Birdcage Fixture
 Comments:



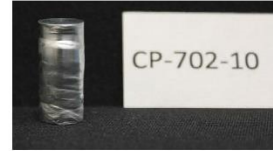
EM22
Specimen Test Results
 Version 4.3



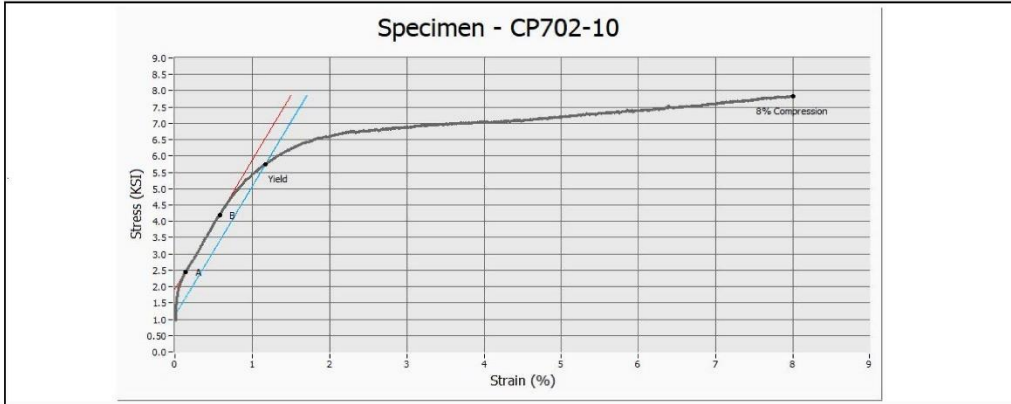
EM22 Specimen ID	210112053
Other Specimen ID	CP702-10
Operator	Annette Gray
Test Date	3/26/2021
Geometry	Circular
Initial Diameter (in)	0.374
Initial Cross Section (in ²)	0.110

Environment

Modulus of Elasticity (MSI)



	Stress (KSI)	Load (LBS)	Strain (%)
Yield	5.76	632.61	1.18
8% Compression	7.83	860.03	8.00



Method File:

 Comments:



EM22 Longitudinal Ingot Compression Task Results

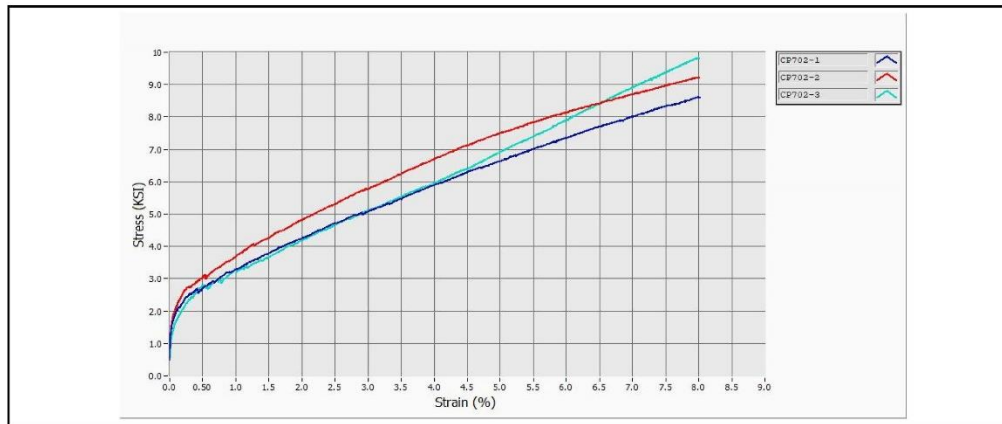
Version 4.3



M5FC Work Order	2021-0110
Work Order Task	5
Testing Organization	EM22
Test Standard	ASTM E9

Data Acquisition Rate (Hz)	10
Control Mode	Stroke
Average Test Rate (in/min)	0.02
Extensometer Gage Length (in)	0.50
Nominal Specimen Length (in)	1.00

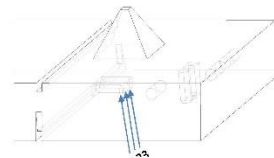
Material	Zinc
Nominal Temperature (°F)	70
Test Frame	TS-3
Drawing Number	S-1A
Pre-Load (LBS)	10



Results

* Modulus of elasticity value is for reference only. Specific modulus tests are required for true value.

EM22 Specimen ID	Other Specimen ID	Yield Stress (KSI)	8% Compression Stress (KSI)	Modulus of Elasticity (MSI)*
210110044	CP702-1	2.33	8.58	11.04
210110045	CP702-2	2.60	9.20	10.77
210110046	CP702-3	2.20	9.80	4.26





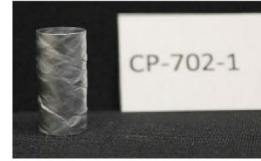
EM22
Specimen Test Results
 Version 4.3



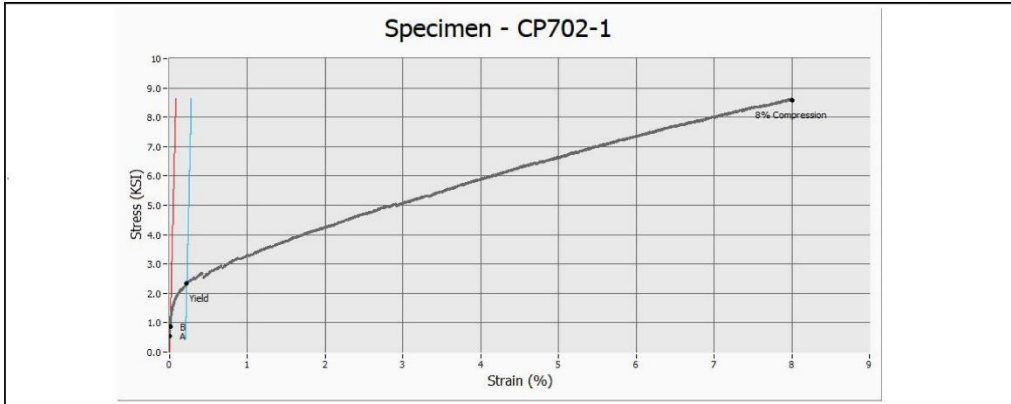
EM22 Specimen ID	210110046
Other Specimen ID	CP702-1
Operator	Annette Gray
Test Date	3/26/2021
Geometry	Circular
Initial Diameter (In)	0.374
Initial Cross Section (in ²)	0.110

Environment: Laboratory Air

Modulus of Elasticity (MSI): 11.04



	Stress (KSI)	Load (LBS)	Strain (%)
Yield	2.33	255.95	0.22
8% Compression	8.58	943.08	8.04



Method File:
 Compression Template with Birdcage Fixture
 Comments:



EM22
Specimen Test Results
 Version 4.3



EM22 Specimen ID	21011845
Other Specimen ID	CP702-2
Operator	Annette Gray
Test Date	3/26/2021
Geometry	Circular
Initial Diameter (in)	0.374
Initial Cross Section (in ²)	0.110

Environment

Modulus of Elasticity (MS)



	Stress (KSI)	Load (LBS)	Strain (%)
Yield	2.60	285.33	0.22
8% Compression	9.20	1010.16	8.00



Method File:
 Compression Test to Failure with Bridgman Fixture
 Comments:



EM22
Specimen Test Results
 Version 4.3



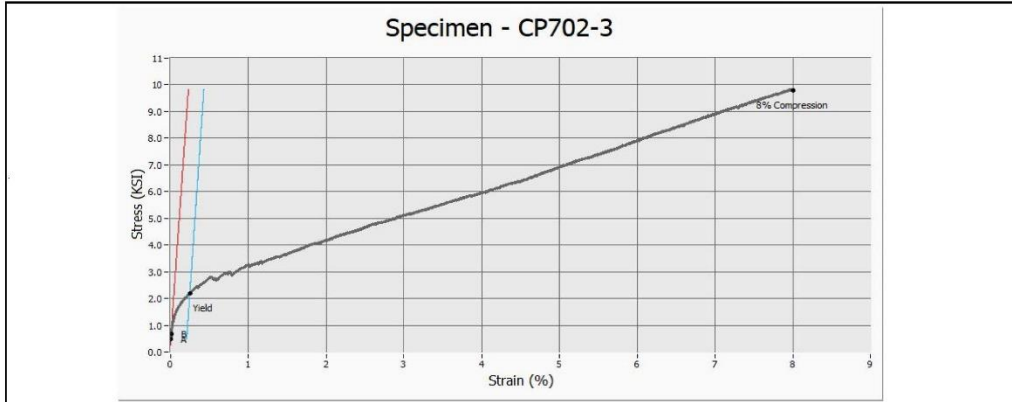
EM22 Specimen ID	210110346
Other Specimen ID	CP702-3
Operator	Annette Gray
Test Date	3/26/2021
Geometry	Circular
Initial Diameter (in)	0.375
Initial Cross Section (in ²)	0.110

Environment

Modulus of Elasticity (MSI)



	Stress (KSI)	Load (LBS)	Strain (%)
Yield	2.20	242.47	0.24
8% Compression	9.80	1062.72	8.00



Method File:
 Compression.Templates with Birdcage Fixt.un
 Comments:



EM22 Axial Slug Compression Task Results

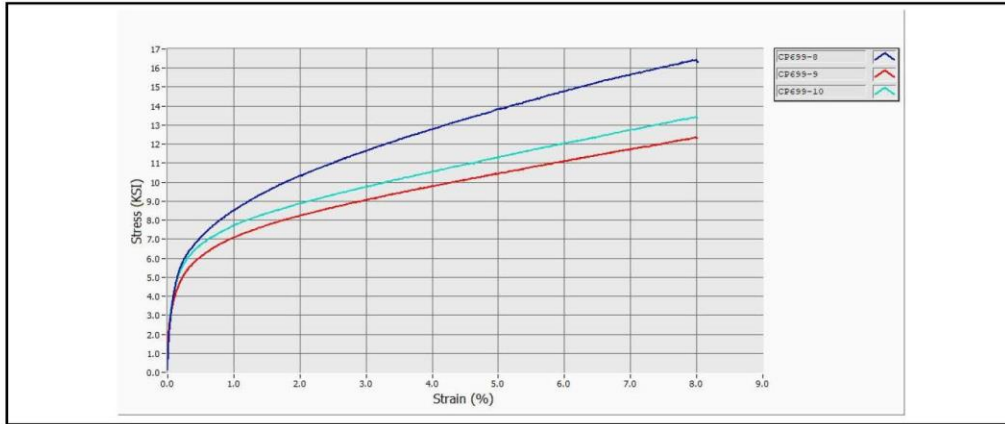
Version 4.3



MSFC Work Order	2021-0110
Work Order Task	5
Testing Organization	EM22
Test Standard	ASTM E9

Data Acquisition Rate (Hz)	10
Control Mode	Stroke
Average Test Rate (in/min)	0.02
Extensometer Gage Length (in)	0.50
Nominal Specimen Length (in)	1.00

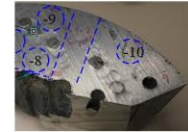
Material	Zinc
Nominal Temperature (°F)	70
Test Frame	TS-3
Drawing Number	S-1A
Pre-Load (LBS)	10



Results

* Modulus of elasticity value is for reference only. Specific modulus tests are required for true value.

EM22 Specimen ID	Other Specimen ID	Yield Stress (KSI)	8% Compression Stress (KSI)	Modulus of Elasticity (MSI)*
210110011	CP699-8	6.70	16.31	2.53
210110012	CP699-9	5.62	12.31	2.36
210110013	CP699-10	6.30	13.38	2.53





EM22
Specimen Test Results
 Version 4.3

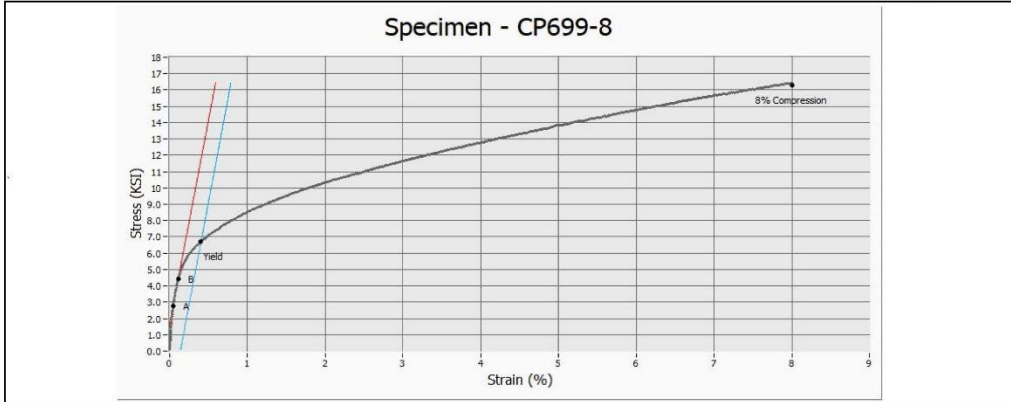
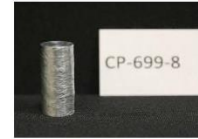


EM22 Specimen ID	2201-20011
Other Specimen ID	CP699-8
Operator	Eric King
Test Date	3/16/2023
Geometry	Circular
Initial Diameter (in)	0.376
Initial Cross Section (in ²)	0.111

Environment

Modulus of Elasticity (M50)

	Stress (KSI)	Load (LBS)	Strain (%)
Yield	6.70	743.74	0.42
8% Compression	16.31	1810.48	8.01



Method File:

 Comments:



EM22
Specimen Test Results
 Version 4.1



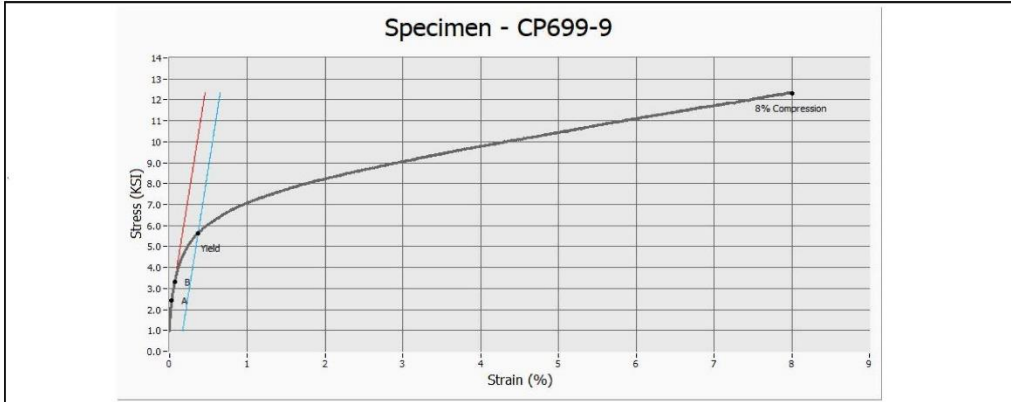
EM22 Specimen ID	210120012
Other Specimen ID	CP699-9
Operator	Annette Gray
Test Date	3/26/2021
Geometry	Circular
Initial Diameter (In)	0.376
Initial Cross Section (in2)	0.111

Environment: Laboratory Air

Modulus of Elasticity (MSI): 2.36



	Stress (KSI)	Load (LBS)	Strain (%)
Yield	5.62	624.53	0.36
8% Compression	12.31	1367.24	8.00



Method File:
 Compression Template with Bridgman Fixture
 Comments:



EM22
Specimen Test Results
 Version 1.3



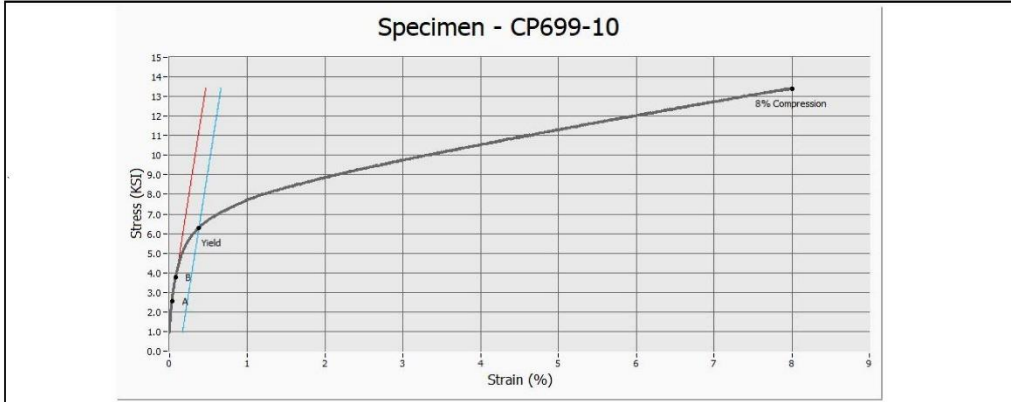
EM22 Specimen ID	210112013
Other Specimen ID	CP699-10
Operator	Amyette Gray
Test Date	3/26/2021
Geometry	Circular
Initial Diameter (in)	0.376
Initial Cross Section (in ²)	0.113

Environment

Modulus of Elasticity (MS)



	Stress (KSI)	Load (lBS)	Strain (%)
Yield	6.30	700.00	0.38
8% Compression	13.38	1486.11	8.00



Method File:
 Compression Testplate with Breakage Fixture

Comments:



EM22 Radial Slug Compression Task Results

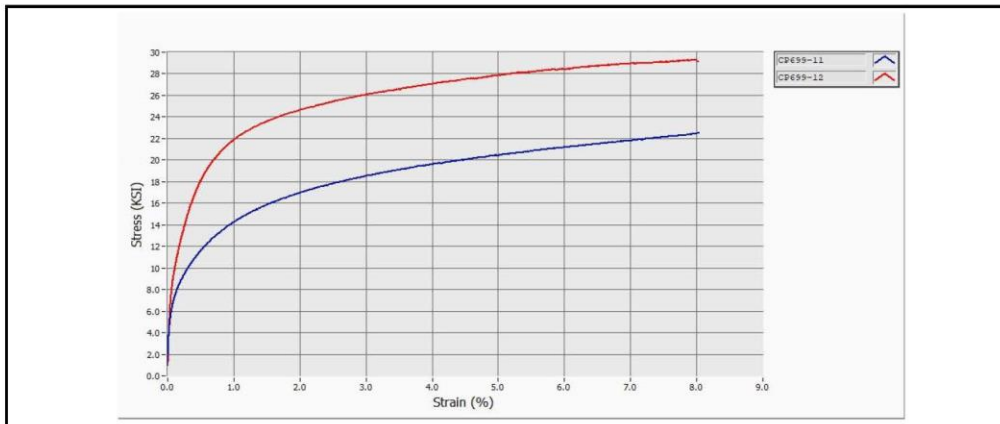
Version 4.3



MSFC Work Order	2021-0110
Work Order Task	5
Testing Organization	EM22
Test Standard	ASTM E9

Data Acquisition Rate (Hz)	10
Control Mode	Stroke
Average Test Rate (in/min)	0.02
Extensometer Gage Length (in)	0.50
Nominal Specimen Length (in)	1.00

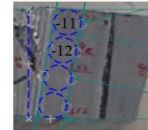
Material	Zinc
Nominal Temperature (°F)	70
Test Frame	TS-3
Drawing Number	S-1A
Pre-Load (LBS)	10



Results

* Modulus of elasticity value is for reference only. Specific modulus tests are required for true value.

EM22 Specimen ID	Other Specimen ID	Yield Stress (KSI)	8% Compression Stress (KSI)	Modulus of Elasticity (MSI)*
210110014	CP699-11	11.30	22.48	2.58
210110015	CP699-12	2.52	29.09	2.54





EM22 Specimen Test Results

Version 4.3



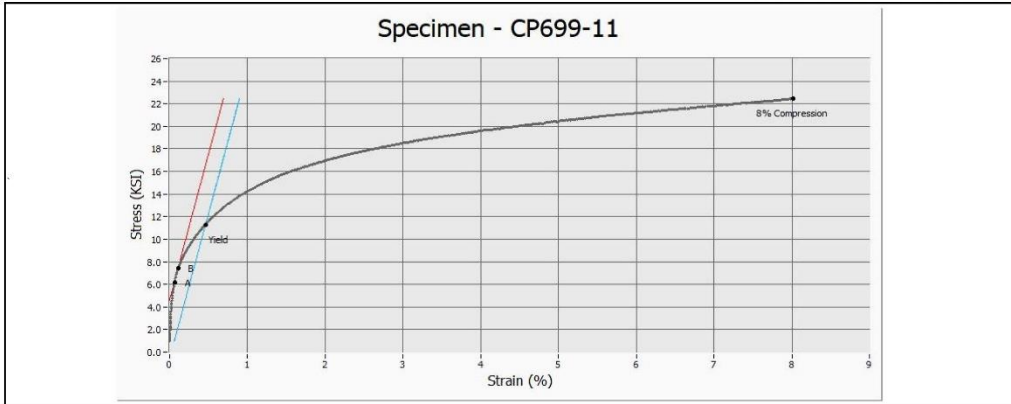
EM22 Specimen ID	210110014
Other Specimen ID	CP699-11
Operator	Eric King
Test Date	3/16/2021
Geometry	Circular
Initial Diameter (in)	0.374
Initial Cross Section (in ²)	0.110

Environment

Modulus of Elasticity (MSI)



	Stress (KSI)	Load (LBS)	Strain (%)
Yield	11.30	1241.04	0.66
8% Compression	22.48	2469.21	8.02



Method File:

 Comments:



EM22 Specimen Test Results

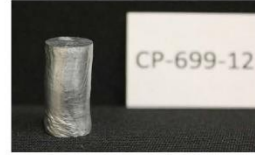
Version 4.3



EM22 Specimen ID	210112015
Other Specimen ID	CP699-12
Operator	Eric King
Test Date	3/15/2021
Geometry	Circular
Initial Diameter (in)	0.375
Initial Cross Section (in ²)	0.110

Environment

Modulus of Elasticity (MS)



	Stress (KSI)	Load (LBS)	Strain (%)
Yield	2.52	278.47	0.01
8% Compression	29.09	3213.21	8.01



Method File:

 Comments:



EM22 Large Compression Specimen Task Results

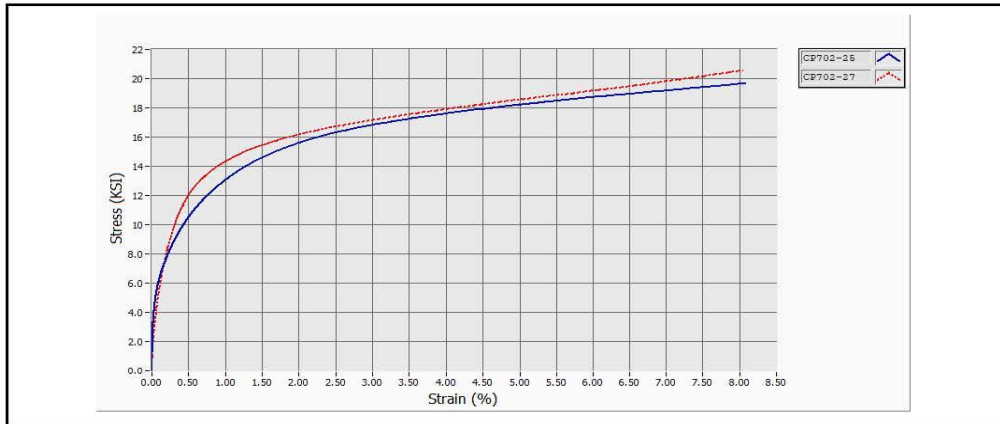
Version 4.3



MSFC Work Order	2021-0110
Work Order Task	5
Testing Organization	EM22
Test Standard	E9

Average Data Acquisition Rate (Hz)	20
Control Mode	Stroke
Average Test Rate (in/min)	0.01
Extensometer Gage Length (in)	0.50

Material	Zinc
Nominal Temperature (°F)	70
Nominal Pressure (psig)	0
Test Frame	TS-1
Drawing Number	CP702
Pre-load (lbf)	100



Results

EM22 Specimen ID	Other Specimen ID	Yield Stress (KSI)	8% Compression Stress (KSI)	Modulus of Elasticity (MSI)*
210011068	CP702-25	8.20	19.66	20.59
210011075	CP702-27	9.66	20.52	10.30

* Modulus of elasticity value is for reference only. Specific modulus is more required for true value.



EM22 Specimen Test Results

Version 4.4



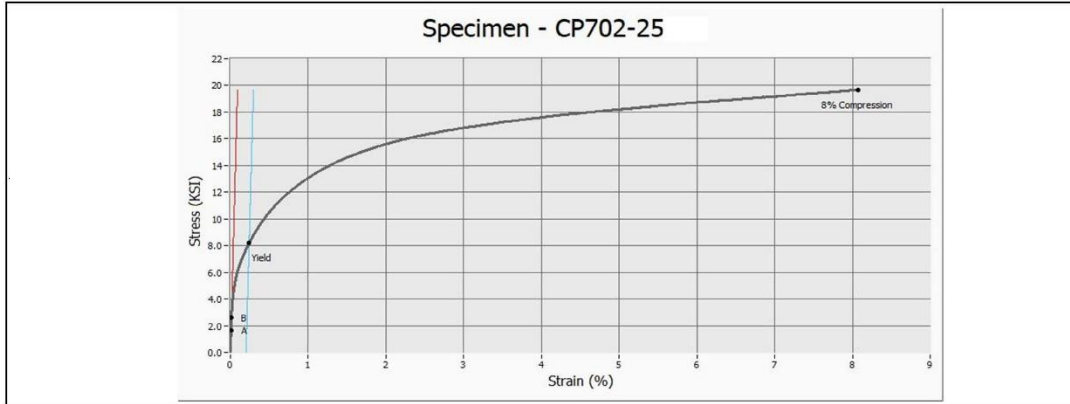
EM22 Specimen ID	210211068
Other Specimen ID	CP702-25
Operator	Lisa Shreff
Test Date	4/13/2021
Geometry	Circular
Initial Diameter (in)	2.486
Initial Cross Section (in ²)	4.854

Environment

Modulus of Elasticity (ksi)



	Stress (ksi)	Load (kIP)	Strain (%)
Yield	8.20	39.75	0.24
8% Compression	19.66	95.41	8.07



Method File:

Compression:

Comments:



EM22 Specimen Test Results

Version: 4.3



EM22 Specimen ID	212211075
Other Specimen ID	CP702-27
Operator	Lisa Sharff
Test Date	4/13/2021

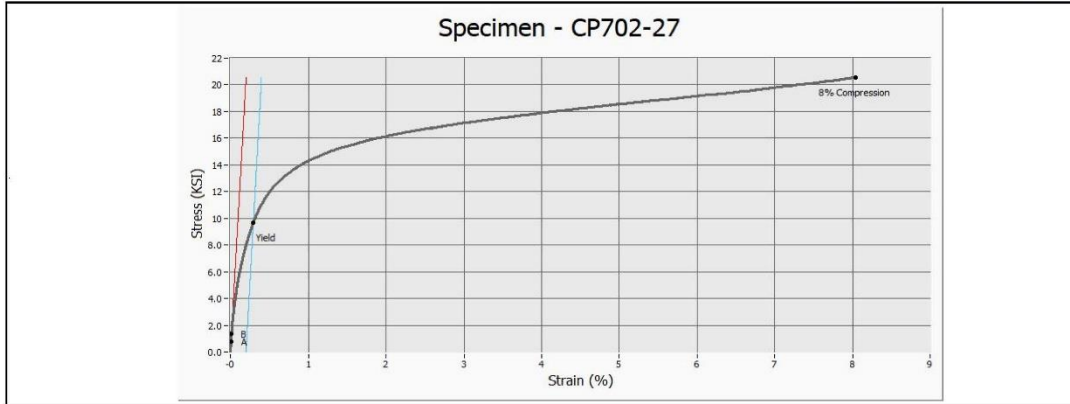
Environment

Modulus of Elasticity (KSI)

Geometry	Circular
Initial Diameter (in)	2.482
Initial Cross Section (in ²)	4.838



	Stress (KSI)	Load (KIP)	Strain (%)
Yield	9.66	46.76	0.29
8% Compression	20.52	99.29	8.04



Method File: _____

Compression: _____

Comments: _____

B.3 Arecibo Failure Investigation Smooth Tensile Testing, Work Order #2021-0110, Sequence 6



Arecibo Failure Investigation Smooth Tensile Testing Work Order # 2021-0110, Sequence 6

Eric King
Test Engineer
April 20, 2021

BACKGROUND

Information in this report is in support of the Arecibo failure investigation. The Arecibo Observatory main feature was a 1000 foot diameter radio telescope collecting dish. In December 2020, the final of a series of failures occurred that caused the collecting dish and support structures to collapse. The primary failed component being investigated is a spelter socket assembly that fastens a 3.25 inch diameter steel rope to the support structure. This particular set of tests relates the tensile properties of zinc material that was taken from the socket in the failed structure to that of the zinc taken from a cast ingot.

APPROACH

This report describes fourteen smooth tensile tests of zinc flat tension specimens. Testing was conducted according to ASTM E8. However, most specimens were much smaller than standard specimens due to the requirement of taking tensile specimens from slug material in the failed socket. Specimens taken from the slug material of the failed socket had a nominal cross-section dimensions of 0.150 inch by 0.125 inch. There were also comparative specimens taken from ingot material with these same dimensions and 0.625 inch by 0.500 inch. The images in Figures 1 through 4 illustrate where each specimen was removed from. This larger specimen is a standard ASTM E8 size specimen. The small scale specimens were tested on Test Station 26 in building 4602 at Marshall Space Flight Center (MSFC). The standard sized specimens were tested on Test Station 5 in building 4602 at Marshall Space Flight Center (MSFC). The environment for this testing was ambient laboratory air. The mechanical test frames consisted of servo-hydraulic actuator (standard specimens) or electro-mechanical actuator (small scale specimens) and reaction frame. A 2,250 pound-force load cell was used to collect load and stress data from small scale specimens. A 20,000 pound-force load cell was used on standard size test specimens. Each test consisted of a slow ramp from preload values to specimen failure. Small scale specimens were pulled at a test rate of 0.01 in/min and standard size specimens were pulled at a rate of 0.05 in/min. Specimen failure occurred.



Figure 1 - Initial Dissection of Socket Slug Material

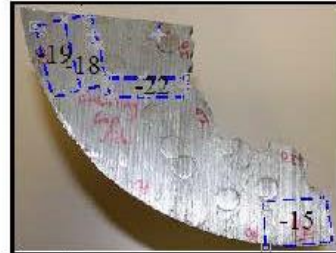


Figure 2 - Dissection of 699-3

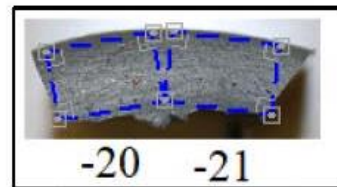


Figure 2 - Dissection of 699-4

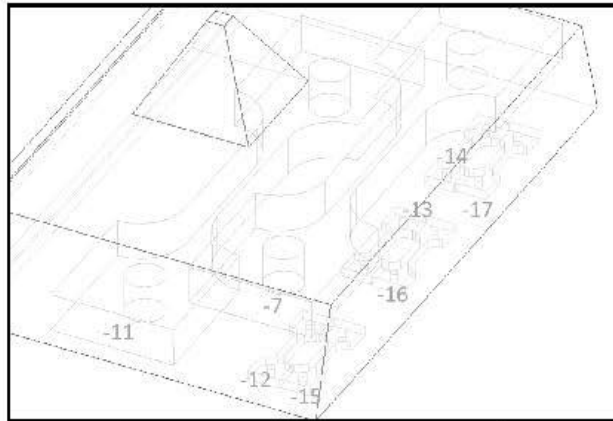


Figure 4 – Tensile Specimen Removal from Zinc Ingot

RESULTS

The results from these tests can be found on the following pages of this report. A comparison of small scale tensile specimens can be found in Figure 5. Three distinct groupings are observed from this data. The specimens taken from 699.4 (see Figure 1) are the strongest, and the specimens taken from ingot material are the weakest.

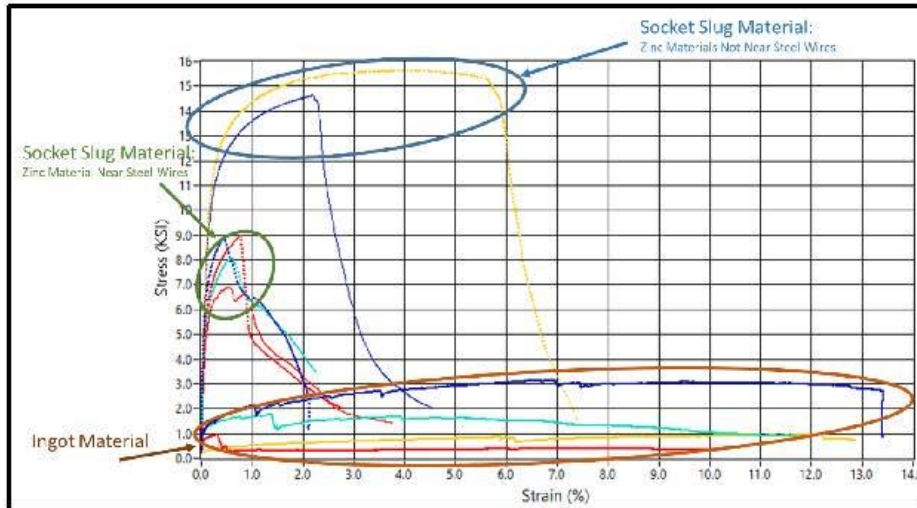


Figure 5 – Comparison of Small Scale Tensile Results



Metallography was performed to aid evaluation of cast zinc microstructure and to help explain the differences in test data among the socket slug, the ingot, and previously published tensile test data for zinc. Images in Figure 6 through 8 illustrate these findings. Figure 6 shows the grain structure taken from socket slug material in a similar orientation to the tensile specimens that were removed from the zinc near steel wires. In fact, the metallographic specimen was intended to be a tensile specimen before steel was detected in the specimen blank. Figures 7 and 8 show larger grains in the ingot material. Figure 8 shows that in some orientations, grains are over an inch in length. In this set of testing, the grain directions within each tensile specimen are not known. Figure 9 depicts digital image correlation that was performed during standard sized tensile tests from ingot material. Slip bands can be observed at several locations within the gage section.

Two specimens made from the ingot material were not included in this report because cracking began during a 5 pound-force preload. The results from the remaining specimens meet the reporting requirements in ASTM E8. Data for these tests were uploaded into the MSFC EM Work Request System (EWR.S) along with all pertinent calibration information.

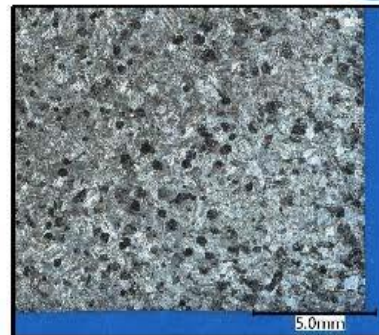


Figure 6 – Metallography of Socket Slug Material



Figure 7 – Metallography of Ingot Material Showing Equiaxed Grains



Figure 8 – Metallography of Ingot Material Showing Elongated Grains

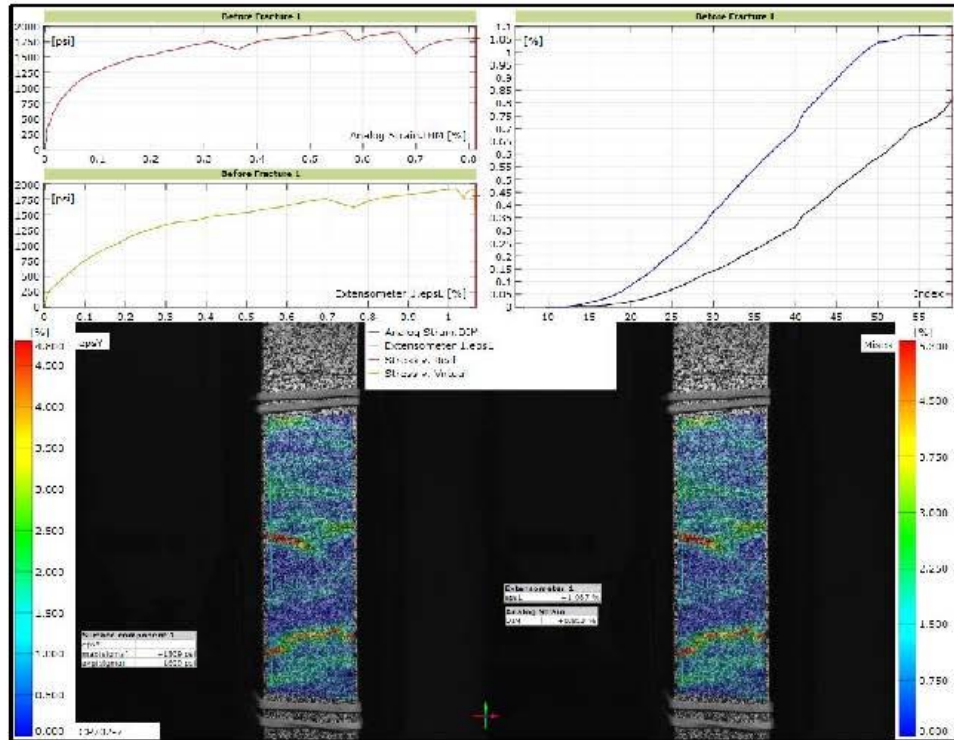


Figure 9 – Digital Image Correlation from Standard Size Tensile Test

Prepared By: ERIC KING Digitally signed by ERIC KING Date: 2021.04.28 06:45:52 -05'00'	Reviewed By: Annette Gray Digitally signed by Annette Gray Date: 2021.04.28 09:08:37 -05'00'
-----------------------------------------------------------------------------------------------------	-----------------------------------------------------------------------------------------------------------



EM22 Tensile Results - Subsize Socket Slug

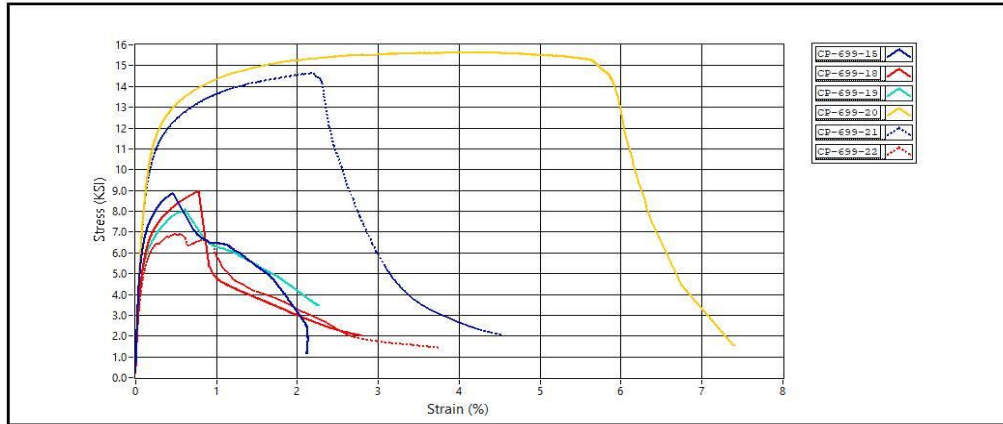


Version 4.3

MSFC Work Order	2021-0110
Work Order Task	5
Testing Organization	EM22
Test Standard	ASTM E8

Average Data Acquisition Rate (Hz)	10
Control Mode	Stroke
Test Rate (in/min)	0.01
Extensometer Gage Length (in)	0.50
Specimen Gage Length (in)	0.60

Material	Zinc
Nominal Temperature (°F)	70
Nominal Pressure (psig)	0
Test Frame	TS-26
Drawing Number	5-474



Results

EM22 Specimen ID	Other Specimen ID	Tensile Stress (KSI)	Yield Stress (KSI)	Inelastic Strain (%)	Modulus of Elasticity (MSI)*	Fracture Elongation (%)
210110018	CP-699-15	8.86	8.12	1.86	12.90	2.12
210110021	CP-699-18	8.97	7.41	2.50	9.71	2.78
210110022	CP-699-19	8.09	6.87	2.01	12.25	2.26
210110023	CP-699-20	15.64	11.97	7.10	12.49	7.40
210110078	CP-699-21	14.62	11.29	4.22	12.03	4.52
210110079	CP-699-22	6.89	6.45	3.47	9.92	3.74



EM22 Smooth Tensile Specimen Test Results



Version 4.3

EM22 Specimen ID	220110018
Other Specimen ID	CP-699-15
Operator	Lisa Sharff
Test Date	04/14/2021
Failure Location	Inside Gauge Section
Geometry	Rectangular
Initial Width (in)	0.121
Initial Thickness (in)	0.150

Environment:

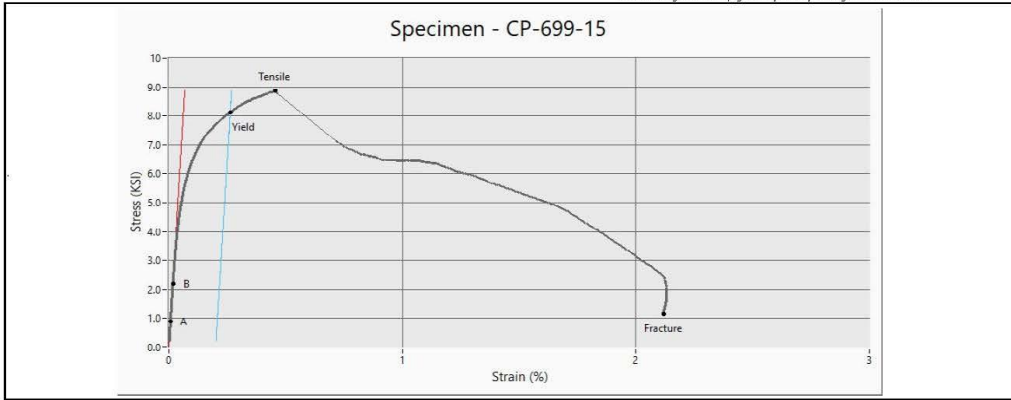
Modulus of Elasticity (MBS)	12.50
Inelastic Strain (%)	1.85

Initial Cross Section Area (in²)

	Stress (KSI)	Load (LBS)	Strain (%)
Tensile	8.85	160.85	0.45
Yield	8.12	147.50	0.26
Fracture	1.15	21.05	2.12

Elongation Method #	Initial Length (in)	Final Length (in)	Elongation (%)
Extensometer	0.50	0.51	2.12

* Fracture elongation on task page comes from the first elongation method in table.



Method File:
 C:\Users\Administrator\Desktop\Catherine\EM22 Bluehill Universal Rectangular Tensile Testing Method WITH EXTENSOMETER - SpaceX BellowW1.3.im_tens
 Comments:



EM22 Smooth Tensile Specimen Test Results

Version 4.3



EM22 Specimen ID	220110021
Other Specimen ID	CP-699-18
Operator	Lisa Sharff
Test Date	04/14/2021
Failure Location	Inside Gauge Section
Geometry	Rectangular
Initial Width (in)	0.122
Initial Thickness (in)	0.150

Environment:

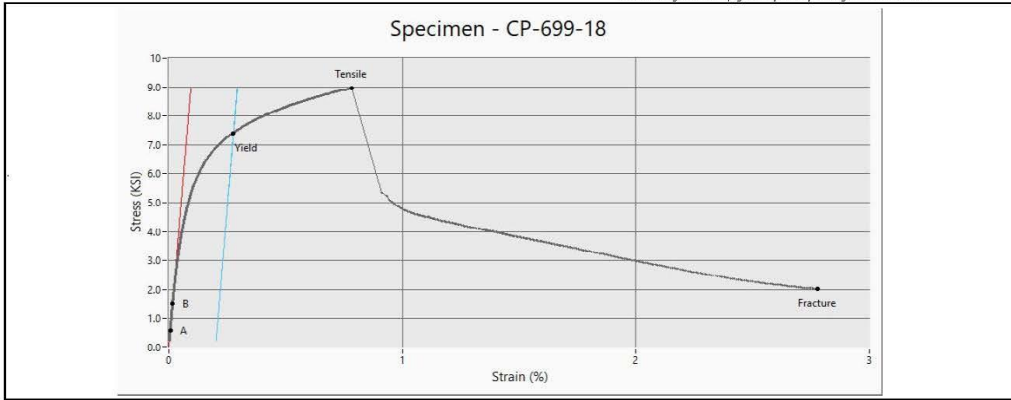
Modulus of Elasticity (MBS)	9.71
Inelastic Strain (%)	2.50

Initial Cross Section Area (in²)

	Stress (KSI)	Load (LBS)	Strain (%)
Tensile	8.97	168.68	0.78
Yield	7.41	135.64	0.28
Fracture	2.02	37.90	2.78

Elongation Method #	Initial Length (in)	Final Length (in)	Elongation (%)
Extensometer	0.50	0.51	2.78

* Fracture elongation on task page comes from the first elongation method in table.



Method File:
 C:\Users\Administrator\Desktop\Catherine\EM22 Bluehill Universal Rectangular Tensile Testing Method WITH EXTENSOMETER - SpaceX BellowW1.3.im_tens
 Comments:



EM22 Smooth Tensile Specimen Test Results

Version 4.3



EM22 Specimen ID	220110022
Other Specimen ID	CP-699-19
Operator	Lisa Sharff
Test Date	04/14/2021
Failure Location	Inside Gauge Section
Geometry	Rectangular
Initial Width (in)	0.122
Initial Thickness (in)	0.151

Environment:

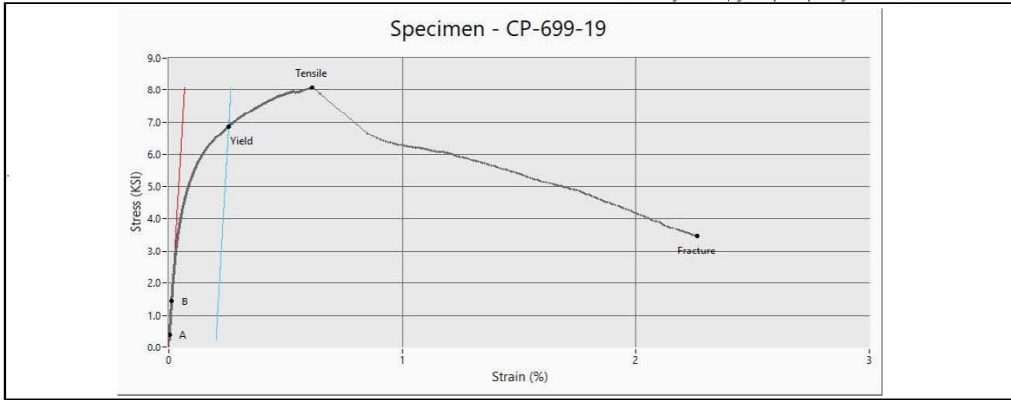
Modulus of Elasticity (MBS)	12.25
Inelastic Strain (%)	2.01

Initial Cross Section Area (in²)

	Stress (KSI)	Load (LBS)	Strain (%)
Tensile	8.09	147.85	0.61
Yield	6.27	122.69	0.26
Fracture	3.45	63.02	2.26

Elongation Method #	Initial Length (in)	Final Length (in)	Elongation (%)
Extensometer	0.50	0.51	2.75

* Fracture elongation on task page comes from the first elongation method in table.



Method File:
 C:\Users\Administrator\Desktop\Catherine\EM22 Bluehill Universal Rectangular Tensile Testing Method WITH EXTENSOMETER - SpaceX BellowW1.3.im_tens
 Comments:



EM22 Smooth Tensile Specimen Test Results



Version 4.3

EM22 Specimen ID	220110023
Other Specimen ID	CP-699-20
Operator	Lisa Sharff
Test Date	04/14/2021
Failure Location	Inside Gauge Section
Geometry	Rectangular
Initial Width (in)	0.122
Initial Thickness (in)	0.150

Environment:

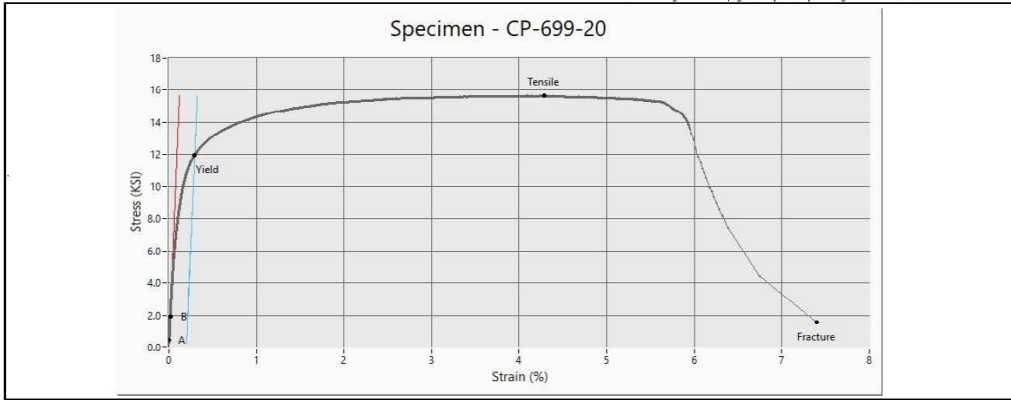
Modulus of Elasticity (Msi)	12.48
Inelastic Strain (%)	7.50

Initial Cross Section Area (in²)

	Stress (KSI)	Load (LBS)	Strain (%)
Tensile	15.64	285.02	4.28
Yield	11.87	218.23	0.50
Fracture	1.56	28.42	7.40

Elongation Method #	Initial Length (in)	Final Length (in)	Elongation (%)
Extensometer	0.50	0.54	7.40

* Fracture elongation on task page comes from the first elongation method in table.



Method File:
 C:\Users\Administrator\Desktop\Catherine\EM22 Bluehill Universal Rectangular Tensile Testing Method WITH EXTENSOMETER - SpaceX BellowW1.3.im_tens
 Comments:



EM22 Smooth Tensile Specimen Test Results

Version 4.3



EM22 Specimen ID	220110078
Other Specimen ID	CP-699-21
Operator	Lisa Sharff
Test Date	04/14/2021
Failure Location	Inside Gauge Section
Geometry	Rectangular
Initial Width (in)	0.121
Initial Thickness (in)	0.150

Environment:

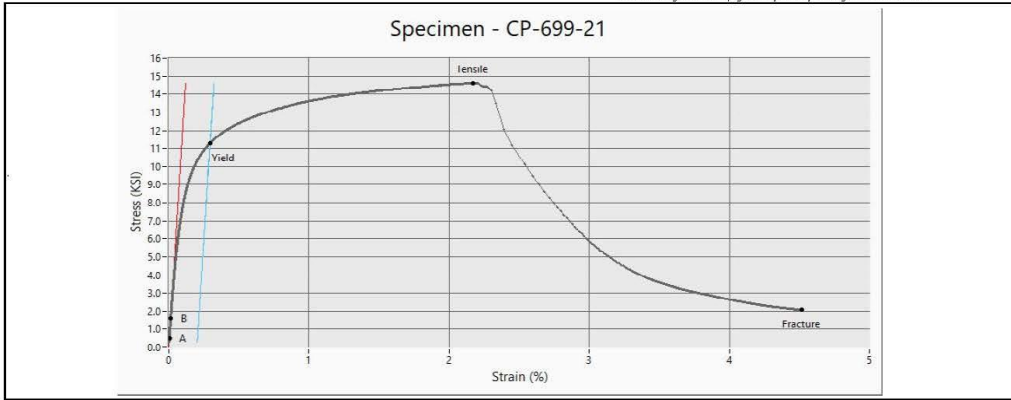
Modulus of Elasticity (MBS)	12.03
Inelastic Strain (%)	4.22

Initial Cross Section Area (in²)

	Stress (KSI)	Load (LBS)	Strain (%)
Tensile	14.62	265.40	2.17
Yield	11.39	209.95	0.29
Fracture	2.06	37.39	4.52

Elongation Method #	Initial Length (in)	Final Length (in)	Elongation (%)
Extensometer	0.50	0.52	4.52

* Fracture elongation on task page comes from the first elongation method in table.



Method File:
 C:\Users\Administrator\Desktop\Catherine\EM22 Bluehill Universal Rectangular Tensile Testing Method WITH EXTENSOMETER - SpaceX BellowW1.3.im_tens
 Comments:



EM22 Smooth Tensile Specimen Test Results

Version 4.3



EM22 Specimen ID	220110079
Other Specimen ID	CP-699-22
Operator	Lisa Sharff
Test Date	04/14/2021
Failure Location	Inside Gauge Section
Geometry	Rectangular
Initial Width (in)	0.121
Initial Thickness (in)	0.151

Environment:

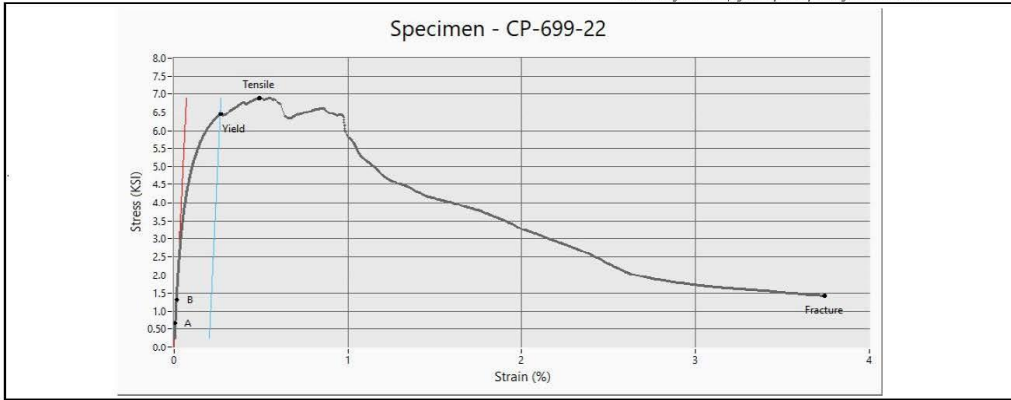
Modulus of Elasticity (MBS)	9.92
Inelastic Strain (%)	3.47

Initial Cross Section Area (in²)

	Stress (KSI)	Load (LBS)	Strain (%)
Tensile	6.88	125.96	0.49
Yield	6.45	117.80	0.27
Fracture	1.43	26.17	3.74

Elongation Method #	Initial Length (in)	Final Length (in)	Elongation (%)
Extensometer	0.50	0.52	3.74

* Fracture elongation on task page comes from the first elongation method in table.



Method File:
 C:\Users\Administrator\Desktop\C:\athena\EM22 Bluehill Universal Rectangular Tensile Testing Method WITH EXTENSOMETER - SpaceX BellowW1.3.im_tens
 Comments:



EM22 Tensile Results - Subsize Ingot

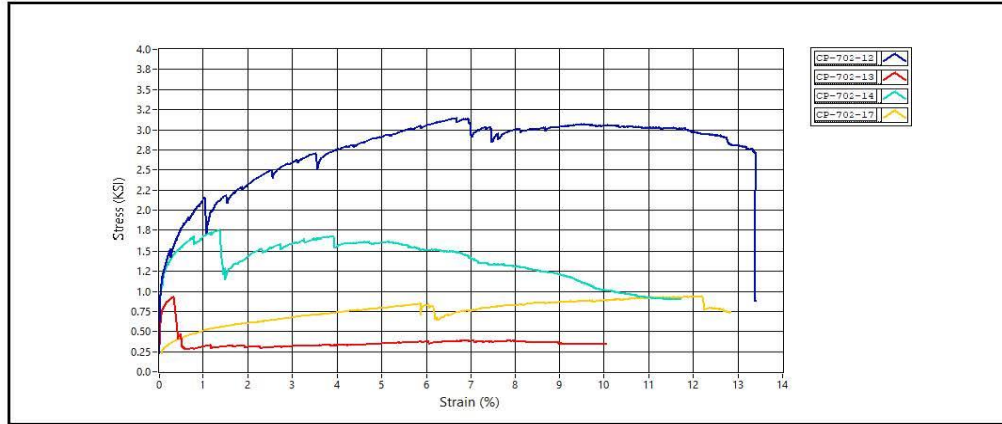


Version 4.3

MSFC Work Order:	2021-0110
Work Order Task:	5
Testing Organization:	EM22
Test Standard:	ASTM E8

Average Data Acquisition Rate (Hz):	10
Control Mode:	Stroke
Test Rate (in/min):	0.01
Extensometer Gage Length (in):	0.50
Specimen Gage Length (in):	0.60

Material:	Zinc
Nominal Temperature (°F):	70
Nominal Pressure (psig):	0
Test Frame:	TS-26
Drawing Number:	S-474



Results

EM22 Specimen ID	Other Specimen ID	Tensile Stress (KSI)	Yield Stress (KSI)	Inelastic Strain (%)	Modulus of Elasticity (MSI)*	Fracture Elongation (%)
210110035	CP-702-12	3.14	1.49	13.16	4.27	13.38
210110036	CP-702-13	0.93	0.89	9.82	3.41	10.04
210110037	CP-702-14	1.75	1.34	11.48	7.11	11.69
210110040	CP-702-17	0.93	0.91	2.06	0.39	12.82



EM22 Smooth Tensile Specimen Test Results



Version 4.3

EM22 Specimen ID	220110025
Other Specimen ID	CP-702-12
Operator	Lisa Sharff
Test Date	04/14/2021
Failure Location	Inside Gauge Section
Geometry	Rectangular
Initial Width (in)	0.122
Initial Thickness (in)	0.150

Environment:

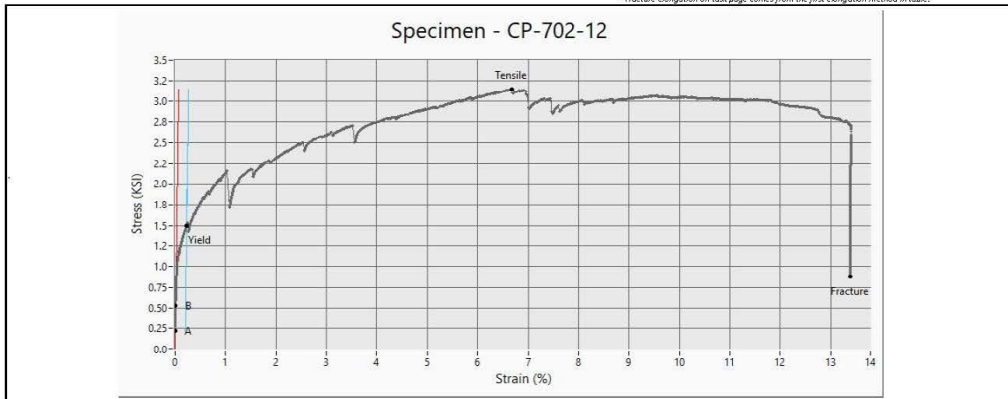
Modulus of Elasticity (Msi)	4.27
Inelastic Strain (%)	13.16

Initial Cross Section Area (in²)

	Stress (KSI)	Load (LBS)	Strain (%)
Tensile	3.14	57.93	6.67
Yield	1.49	27.51	0.25
Fracture	0.88	16.04	13.38

Elongation Method #	Initial Length (in)	Final Length (in)	Elongation (%)
Extensometer	0.50	0.57	13.38

* Fracture elongation on task page comes from the first elongation method in table.



Method File:
 C:\Users\Administrator\Desktop\C:\athena\EM22 Bluehill Universal Rectangular Tensile Testing Method WITH EXTENSOMETER.im_lens
 Comments:



EM22 Smooth Tensile Specimen Test Results

Version 4.3



EM22 Specimen ID	220110036
Other Specimen ID	CP-702-13
Operator	Lisa Sharff
Test Date	04/14/2021
Failure Location	Inside Gauge Section
Geometry	Rectangular
Initial Width (in)	0.123
Initial Thickness (in)	0.128

Environment:

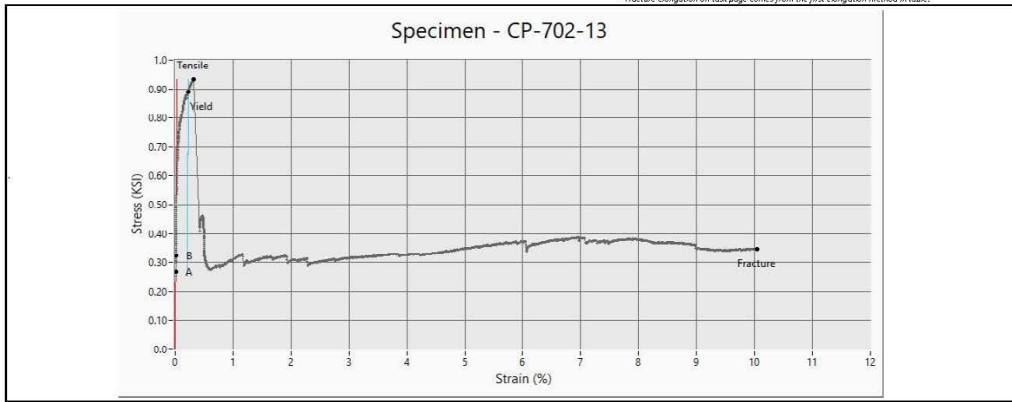
Modulus of Elasticity (MBS)	3.21
Inelastic Strain (%)	9.82

Initial Cross Section Area (in²)

	Stress (KSI)	Load (LBS)	Strain (%)
Tensile	0.93	17.13	0.92
Yield	0.29	5.59	0.23
Fracture	0.35	6.36	10.04

Elongation Method #	Initial Length (in)	Final Length (in)	Elongation (%)
Extensometer	0.50	0.55	10.04

* Fracture elongation on task page comes from the first elongation method in table.



Method File:
 C:\Users\Administrator\Desktop\Catherine\EM22 Bluehill Universal Rectangular Tensile Testing Method WITH EXTENSOMETER.in_lens
 Comments:



EM22 Smooth Tensile Specimen Test Results

Version 4.3



EM22 Specimen ID	220110027
Other Specimen ID	CP-702-14
Operator	Lisa Sharff
Test Date	04/14/2021
Failure Location	Inside Gauge Section
Geometry	Rectangular
Initial Width (in)	0.122
Initial Thickness (in)	0.150

Environment:

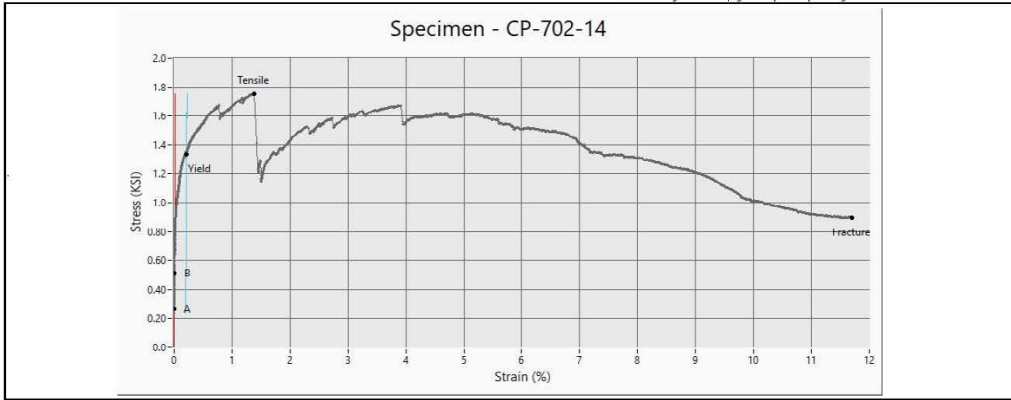
Modulus of Elasticity (MBS)	7.11
Inelastic Strain (%)	11.68

Initial Cross Section Area (in²)

	Stress (KSI)	Load (LBS)	Strain (%)
Tensile	1.75	31.97	1.37
Yield	1.24	23.25	0.22
Fracture	0.89	16.32	11.69

Elongation Method #	Initial Length (in)	Final Length (in)	Elongation (%)
Extensometer	0.50	0.56	11.69

* Fracture elongation on task page comes from the first elongation method in table.



Method File:
 C:\Users\Administrator\Desktop\Catherine\EM22 Bluehill Universal Rectangular Tensile Testing Method WITH EXTENSOMETER.in_lens
 Comments:



EM22 Smooth Tensile Specimen Test Results

Version 4.3



EM22 Specimen ID	220110040
Other Specimen ID	CP-702-17
Operator	Lisa Sharff
Test Date	04/14/2021
Failure Location	Inside Gauge Section
Geometry	Rectangular
Initial Width (in)	0.124
Initial Thickness (in)	0.151

Environment:

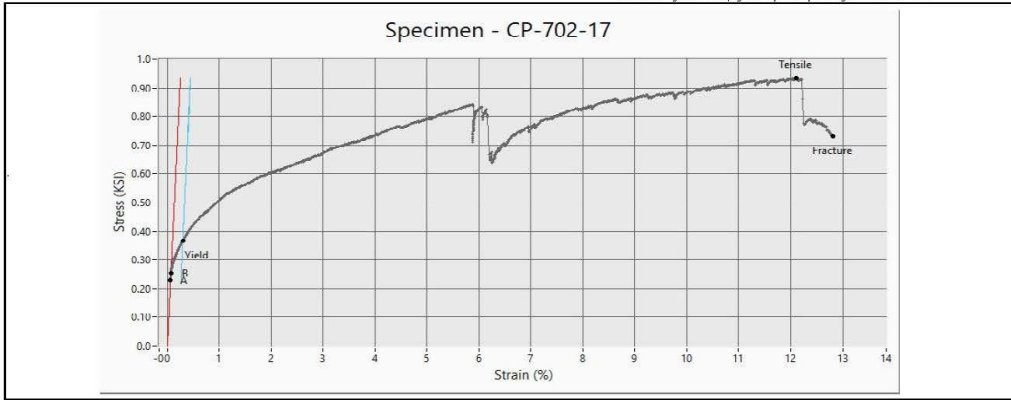
Modulus of Elasticity (Msi)	0.39
Inelastic Strain (%)	2.06

Initial Cross Section Area (in²)

	Stress (KSI)	Load (LBS)	Strain (%)
Tensile	0.93	17.40	12.11
Yield	0.27	5.05	0.29
Fracture	0.79	13.66	12.82

Elongation Method #	Initial Length (in)	Final Length (in)	Elongation (%)
Extensometer	0.50	0.56	12.82

* Fracture elongation on task page comes from the first elongation method in table.



Method File:
 C:\Users\Administrator\Desktop\C:\athena\EM22 Bluehill Universal Rectangular Tensile Testing Method WITH EXTENSOMETER.im_lens
 Comments:



EM22 Tensile Results - Standard Size Ingot

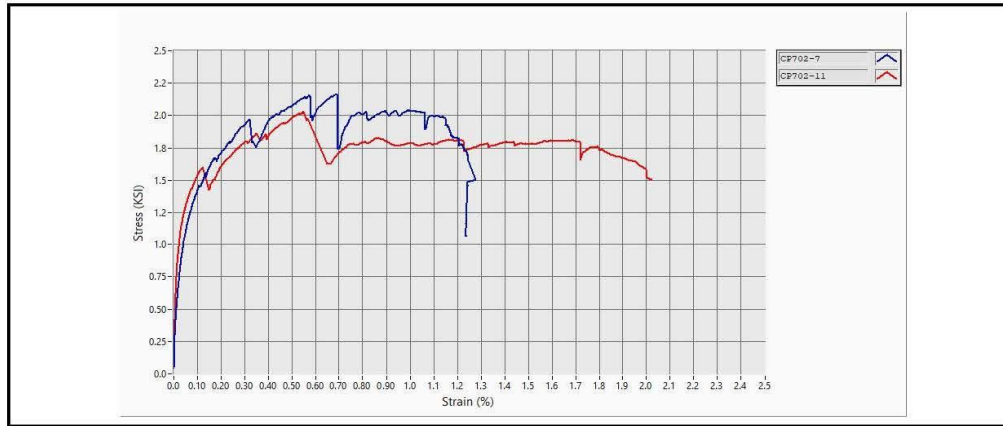


Version 4.3

MSFC Work Order	2021-0110
Work Order Task	5
Testing Organization	EM22
Test Standard	ASTM E8

Average Data Acquisition Rate (Hz)	10
Control Mode	Stroke
Test Rate (in/min)	0.05
Extensometer Gage Length (in)	2.00
Specimen Gage Length (in)	2.25

Material	Zinc
Nominal Temperature (°F)	70
Nominal Pressure (psig)	0
Test Frame	TS-5
Drawing Number	S-9 Rev D



Results

* Modulus of elasticity value is for reference only. Specific modulus tests are required for true value.

EM22 Specimen ID	Other Specimen ID	Tensile Stress (KSI)	Yield Stress (KSI)	Inelastic Strain (%)	Modulus of Elasticity (MSI)*	Fracture Elongation (%)
210110050	CP702-7	2.16	1.76	1.01	8.28	1.23
210110054	CP702-11	2.03	1.66	1.80	8.53	2.02



EM22 Smooth Tensile Specimen Test Results

Version 4.3



EM22 Specimen ID	220110056
Other Specimen ID	CP702-7
Operator	Eric King
Test Date	3/26/2021
Failure Location	Multiple Cracks Detected
Geometry	Rectangular
Initial Width (in)	0.502
Initial Thickness (in)	0.631

Environment:

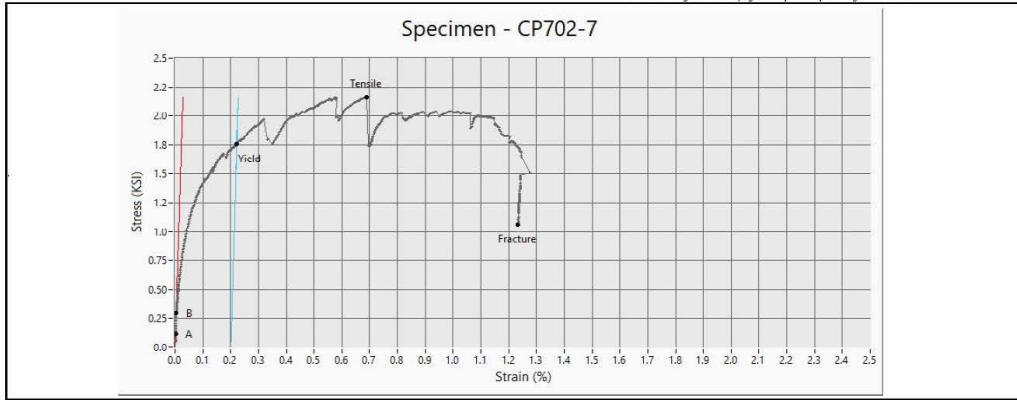
Modulus of Elasticity (ksi)	2.28
Inelastic Strain (%)	1.01

Initial Cross Section Area (in²):

	Stress (ksi)	Load (lbf)	Strain (%)
Tensile	2.16	685.24	0.68
Yield	1.75	557.50	0.23
Fracture	1.06	335.66	1.23

Elongation Method ¹	Initial Length (in)	Final Length (in)	Elongation (%)
Extensometer	2.00	2.02	1.23

¹ Fracture elongation on task page comes from the first elongation method in table.



Method File:

 Comments:



EM22 Smooth Tensile Specimen Test Results

Version 4.3



EM22 Specimen ID	2102100054
Other Specimen ID	CP702-11
Operator	Eric King
Test Date	3/26/2021
Failure Location	Multiple Cracks Detected
Geometry	Rectangular
Initial Width (in)	0.500
Initial Thickness (in)	0.635

Environment:

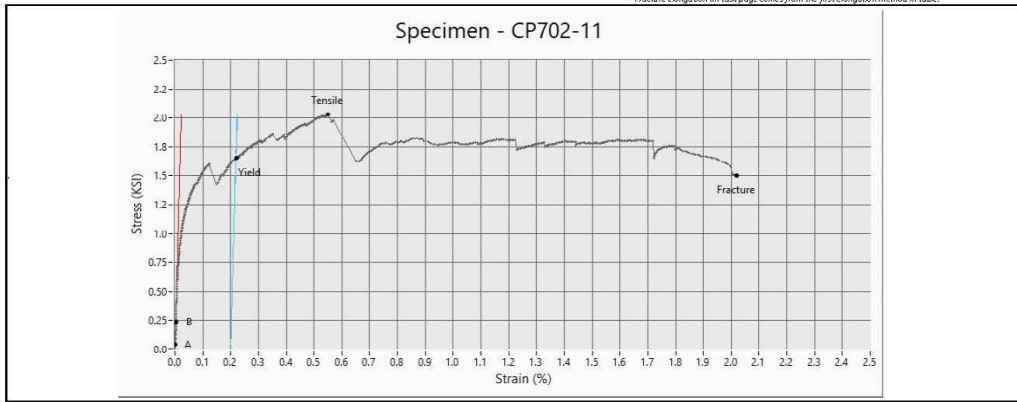
Modulus of Elasticity (MEI)	8.33
Inelastic Strain (%)	1.80

Initial Cross Section Area (in²):

	Stress (KSI)	Load (LBS)	Strain (%)
Tensile	2.03	645.90	0.55
Yield	1.65	516.33	0.22
Fracture	1.51	478.60	2.02

Elongation Method *	Initial Length (in)	Final Length (in)	Elongation (%)
Extensometer	2.00	2.04	2.02

* Fracture elongation on task page comes from the first elongation method in table.



Method File:

 Comments:

B.4 Arecibo Failure Investigation Double Shear Testing, Work Order #2021-0110, Sequence 7



Arecibo Failure Investigation Double Shear Testing Work Order # 2021-0110, Sequence 7

Annette Gray
Test Engineer
April 21, 2021

BACKGROUND

Information in this report is in support of the Arecibo failure investigation. The Arecibo Observatory main feature was a 1000 foot diameter radio telescope collecting dish. In December 2020, the final of a series of failures occurred that caused the collecting dish and support structures to collapse. The primary failed component being investigated is a spelter socket assembly that fastens a 3.25 inch diameter steel rope to the support structure. This particular test is to provide images of shear surfaces of the zinc material, but shear properties are also supplied. Test articles were taken from a cast zinc ingot used to determine baseline zinc properties.

APPROACH

This report describes three double shear tests of zinc machined from a cast zinc ingot. Testing method was adapted from ASTM B769 and specimens were a cylindrical geometry of 0.25 inch nominal diameter with a rectangular tab for placement into the test fixture. All three tests are included in this report. These specimens were tested on Test Station 26 (TS-26) in building 4602 at Marshall Space Flight Center (MSFC). The environment for this testing was ambient laboratory air. The mechanical test frames consisted of electro-mechanical actuator and reaction frame. A 2,000-pound load cell was used for load and stress measurements. An optical encoder was used to control a 0.05 in/min ramp from a 5-pound preload to at least a 10% drop below ultimate. This encoder had a total range of forty inches. The image in Figure 1 to the right illustrates the setup on TS-26 using the double shear fixture.



Figure 1 - Setup on Test Station 26

RESULTS

The results from this test can be found on the following pages of this report. After the test was stopped for CP-702-18, removal was attempted by realigning the test fixture in the test frame and pulling the specimen out. When it was determined that the specimen could not be removed this way, the fixture was reloaded into the frame and the two halves of the fixture were pulled apart to get to sections of the specimen. For the remaining two specimens, the fixture was left in the frame and immediately pulled apart post test to reach the specimens. This resulted in a slight difference in the appearance of the shear surfaces of CP-702-18. To obtain the shear stress values in accordance with ASTM B 769, the load values were divided by twice the area calculations. Data for these tests were uploaded into the MSFC EM Work Request System (EWS) along with all pertinent calibration information.

Prepared By: Annette Gray Digitally signed by Annette Gray Date: 2021.04.27 13:05:13 -0500'	Reviewed By: ERIC KING Digitally signed by ERIC KING Date: 2021.04.27 13:31:15 -0500'
----------------------------------------------------------------------------------------------------------	----------------------------------------------------------------------------------------------------



EM22 Task Results

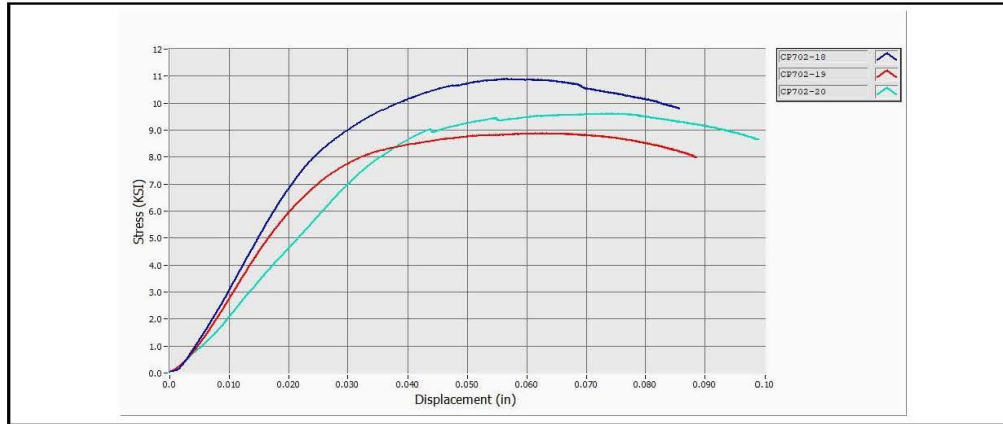
Version 4.3



MSFC Work Order	2021-0110
Work Order Task	7
Testing Organization	EM22
Test Standard	Based on ASTM B769

Average Data Acquisition Rate (Hz)	50
Control Mode	Stroke
Test Rate (in/min)	0.05
Pre-Load (LBS)	5

Material	Zinc
Nominal Temperature (°F)	72
Nominal Pressure (psig)	0
Test Frame	TS-26
Drawing Number	S-6 Rev.C



Results

EM22 Specimen ID	Other Specimen ID	Ultimate Stress (KSI)
2101.1061	CP702-18	10.88
2101.1062	CP702-19	8.88
2101.1063	CP702-20	9.60



EM22 Specimen Test Results

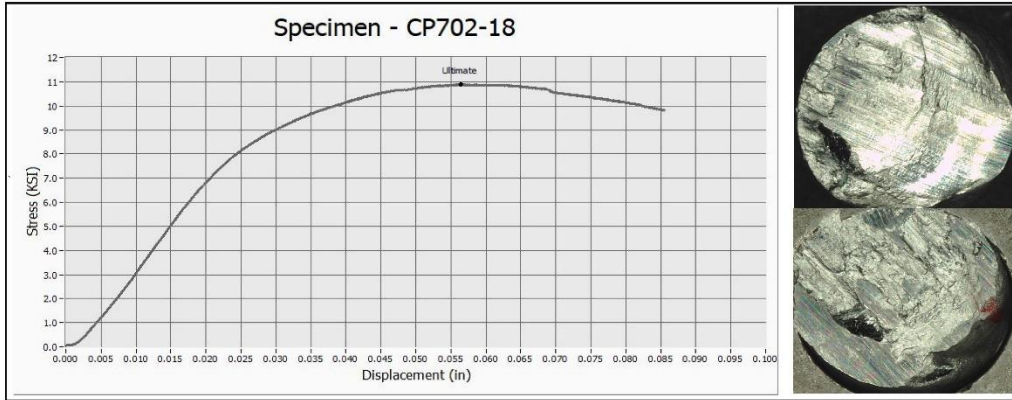
Version 4.3



EM22 Specimen ID	21011061
Other Specimen ID	CP702-18
Operator	Annette Gray
Test Date	03/31/21
Failure Location	Inside Gauge Section
Geometry	Circular
Initial Diameter (in)	0.250
Initial Cross Section Area (in ²)	0.039

Environment:

	Stress (KSI)	Load (LBS)	Displacement (in)
Ultimate	10.89	1068.02	0.06



Method File:
 C:\Data\2021\2021-0110\2021-0110 Seq 7\2021-0110 - NO EXTENSOMETER 1.im_cem
 Comments:



EM22 Specimen Test Results

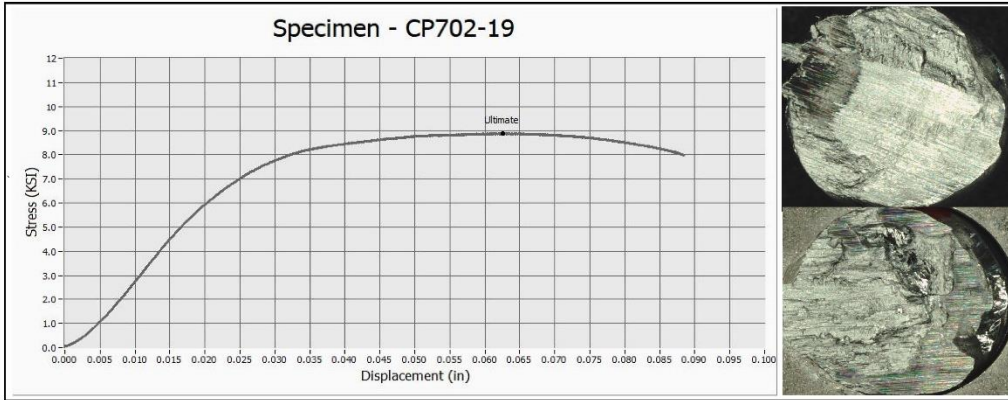
Version 4.3



EM22 Specimen ID	21011062
Other Specimen ID	CP-02-19
Operator	Annette Gray
Test Date	03/31/21
Failure Location	Inside Gauge Section
Geometry	Circular
Initial Diameter (in)	0.250
Initial Cross Section Area (in ²)	0.039

Environment:

	Stress (KSI)	Load (LBS)	Displacement (in)
Ultimate	8.88	871.35	0.06



Method file:
 C:\Data\2021\2021-0110\2021-0110 Seq 7\2021-0110 - NO EXTENSOMETER 1.im_tens
 Comments:



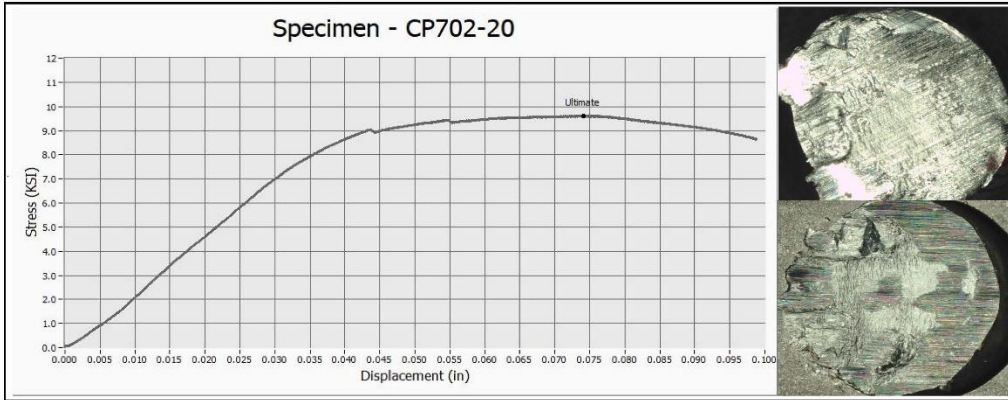
EM22
Specimen Test Results
 Version 1.3



EM22 Specimen ID	21011063
Other Specimen ID	CP702-20
Operator	Annette Gray
Test Date	03/31/21
Falure Location	Inside Gauge Section
Geometry	Circular
Initial Diameter (in)	0.250
Initial Cross Section Area (in ²)	0.098

Environment

	Stress (KSI)	Load (LBS)	Displacement (in)
URimate	9.60	947.86	0.07



Method File:
 C:\Data\2021\2021-0110\2021-0110 Seq 7\2021-0110 - NO EXTENSOMETER 1.in.tens
 Comments:

B.5 Arcibo Failure Investigation Socket Pull Testing, Work Order #2021-0110, Sequence 8



Arcibo Failure Investigation Socket Pull Testing Work Order # 2021-0110, Sequence 8

Eric King
Test Engineer
April 21, 2021

BACKGROUND

Information in this report is in support of the Arcibo failure investigation. The Arcibo Observatory main feature was a 1000 foot diameter radio telescope collecting dish. In December 2020, the final of a series of failures occurred that caused the collecting dish and support structures to collapse. The primary failed component being investigated is a spelter socket assembly that fastens a 3.25 inch diameter steel rope to the support structure. This particular set of tests relates to the 0.25 inch wire in the steel (ASTM A586) rope, zinc ingot comparative to zinc used in the Arcibo socket, and a small scale off the shelf steel socket. Only the wires from this testing were taken from the failed test structure. The goal of this testing was to better understand the bond strength between the steel wire and zinc.

APPROACH

This report describes eight tensile tests of a composite fabrication using A586 steel wire potted inside a steel socket with a zinc casting. These specimens were tested on Test Station 3 and Test Station 5 building 4602 at Marshall Space Flight Center (MSFC). The environment for this testing was ambient laboratory air. The mechanical test frames consisted of servo-hydraulic actuators and reaction frames. 20,000 pound-force load cells were used for load and stress measurements. Linear Variable Differential Transformers (LVDTs) were used as feedback to control a 0.05 in/min ramp from a 200 pound preload to failure. These LVDTs had a total range of six inches. The image in Figure 2 illustrates the setup on TS-5 using manual collet grips.

Two rounds of testing were implemented to attempt achieving the desired bond strength. Differences between the first and second round of testing included the following during the spelter process:

Table 1: Specimen Fabrication Differences

First Round	Second Round
Fabricated Specimens Composite7 through Composite10	Fabricated Specimens Composite17 through Composite20
Degalvanized wire in in hydrochloric acid prior to spelter	Degreased wire using Solstice K1016A solvent prior to spelter
Melted zinc at 875°F	Melted zinc at 950°F
N/A	Attempted to remove dross from melted zinc prior to pouring
Applied flux and heated	Applied flux and heated prior to wiping clean with wet rag and letting dry
Filled zinc to top of socket	Overfilled socket

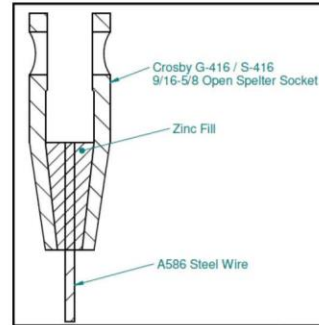


Figure 1 - Specimen Design



Figure 2 - Setup on Test Station 5

Prepared By: ERIC KING Digitally signed by ERIC KING Date: 2021.04.27 13:33:39 -05'00'	Reviewed By: Annette Gray Digitally signed by Annette Gray Date: 2021.04.27 13:13:22 -05'00'
--------------------------------------------------------------------------------------------------------	--------------------------------------------------------------------------------------------------------------

RESULTS

The results from these tests can be found on the following pages of this report. The intended bond strength was never achieved and images from failed specimens indicate mostly non-cohesive failures between the zinc and steel. Figures 3 and 4 illustrate this. Also, ultimate load comparisons can be found in Figure 5. Data for these tests were uploaded into the MSFC EM Work Request System (EWRS) along with all pertinent calibration information.

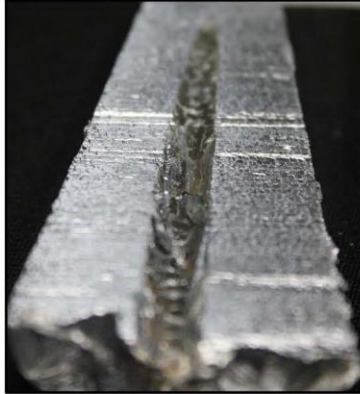


Figure 3 – Bisected Zinc Slug from Composite8 Specimen



Figure 4 – Composite8 Wire after Pullout and Time to Allow Corrosion of De-galvanized Surfaces.

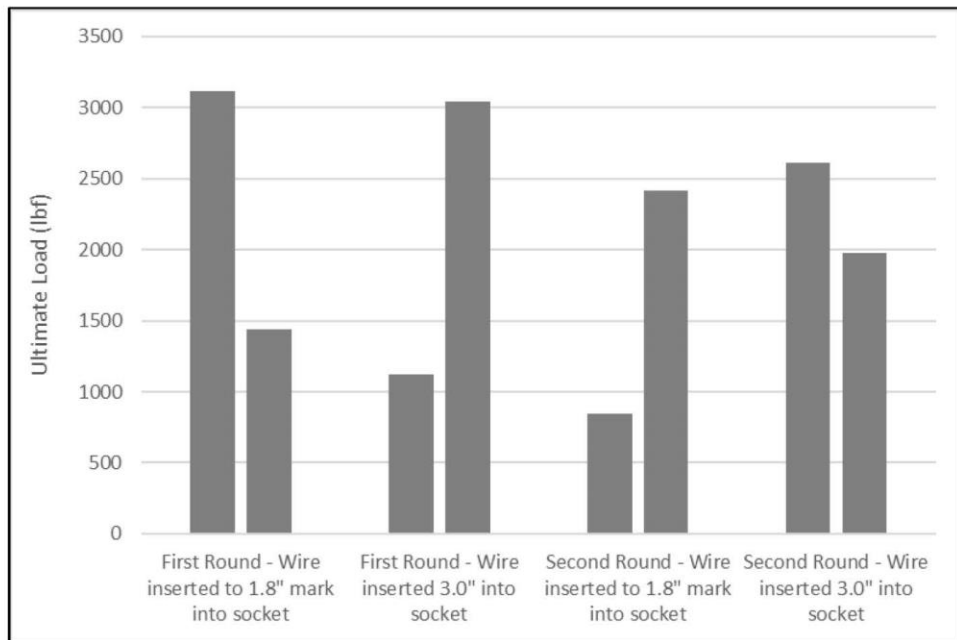


Figure 5 – Ultimate Load Comparison



EM22 Zinc Socket / Wire Tensile Task Results

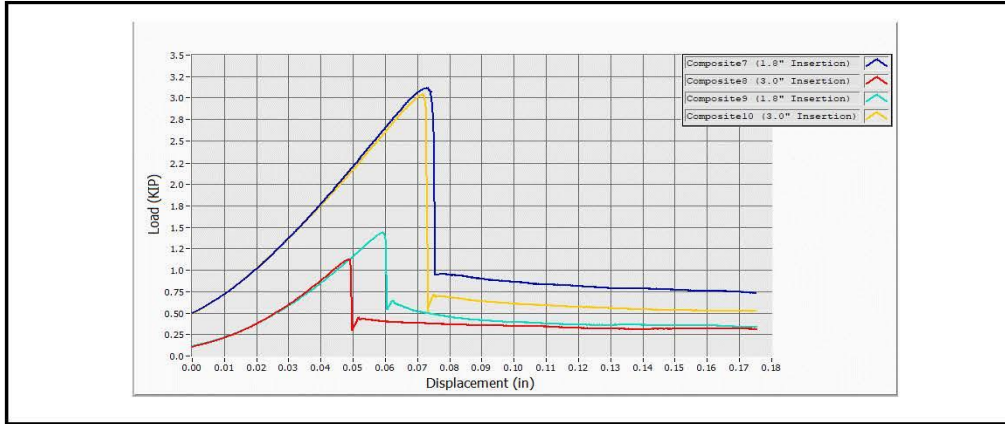


Version 4.3

MSFC Work Order	2021-0110
Work Order Task	8
Testing Organization	EM22

Average Data Acquisition Rate (Hz)	10
Control Mode	Stroke
Test Rate (in/min)	0.05

Material	A586 Steel / Zinc
Nominal Temperature (°F)	70
Test Frame	TS-3
Drawing Number	S-475
Pre-Load (LBS)	200



Results

EM22 Specimen ID	Other Specimen ID	Ultimate Stress (KSI)	Ultimate Load (KIP)	Comments
210110064	Composite7	64.99	3.11	A586 Wire Inserted to 1.75\"/>
210110065	Composite8	23.65	1.12	A586 Wire Inserted through 3\"/>
210110066	Composite9	30.04	1.44	A586 Wire Inserted to 1.75\"/>
210110067	Composite10	63.44	3.04	A586 Wire Inserted through 3\"/>



EM22 Specimen Test Results

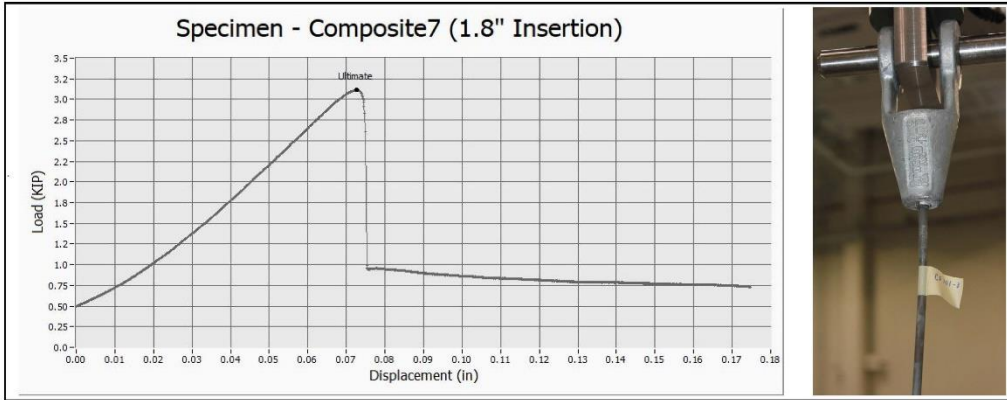
Version 4.3



EM22 Specimen ID	210110064
Other Specimen ID	Composite7
Operator	Eric King
Test Date	4/2/2023
Failure Location	Wire to Zinc Bond
Geometry	Circular
Initial Diameter (in)	0.247
Initial Cross Section Area (in ²)	0.048

Environment

	Stress (KSI)	Load (KIP)	Displacement (in)
Ultimate	64.99	3.11	0.07



Method File:
 [EM]0 Tensile Test Template_v4
 Comments:



EM22 Specimen Test Results

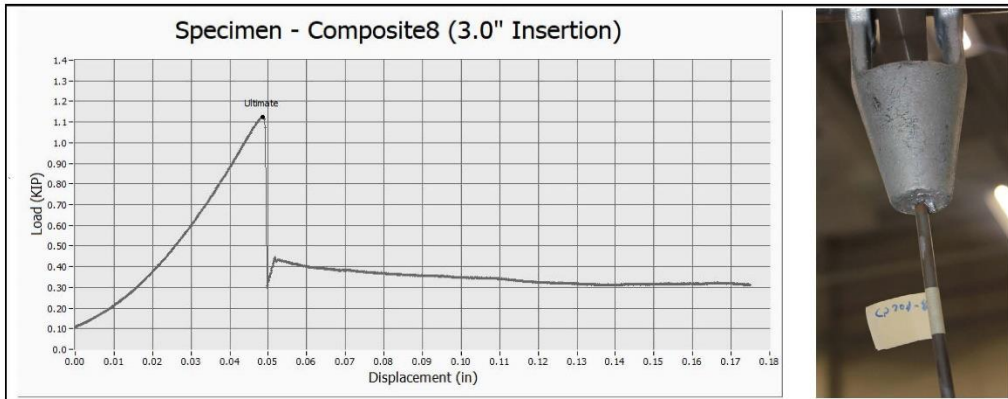
Version 4.3



EM22 Specimen ID	210110065
DHwr Specimen ID	Composite8
Operator	Eric King
Test Date	4/1/2021
Failure Location	Wire to Zinc Bond
Geometry	Circular
Initial Diameter (in)	0.246
Initial Cross Section Area (in ²)	0.048

Environment

	Stress (KSI)	Load (KIP)	Displacement (in)
Ultimate	25.65	1.12	0.05



Method File:

 Comments:



EM22 Specimen Test Results

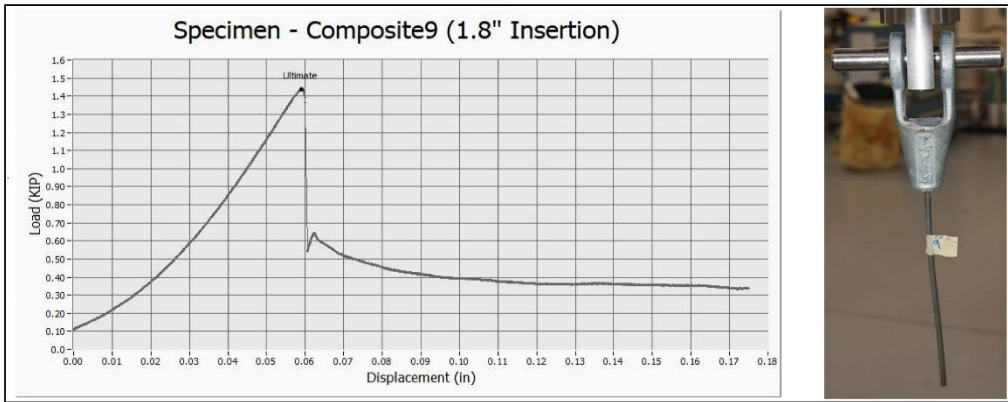


Version 6.1

EM22 Specimen ID	210110066
Other Specimen ID	Composite9
Operator	Eric King
Test Date	4/1/2021
Failure Location	Wire to Zinc Bond
Geometry	Circular
Initial Diameter (in)	0.247
Initial Cross Section Area (in ²)	0.038

Environment

	Stress (KSI)	Load (KIP)	Displacement (in)
Ultimate	30.04	1.44	0.06



Method File:

 Comments:



EM22 Specimen Test Results

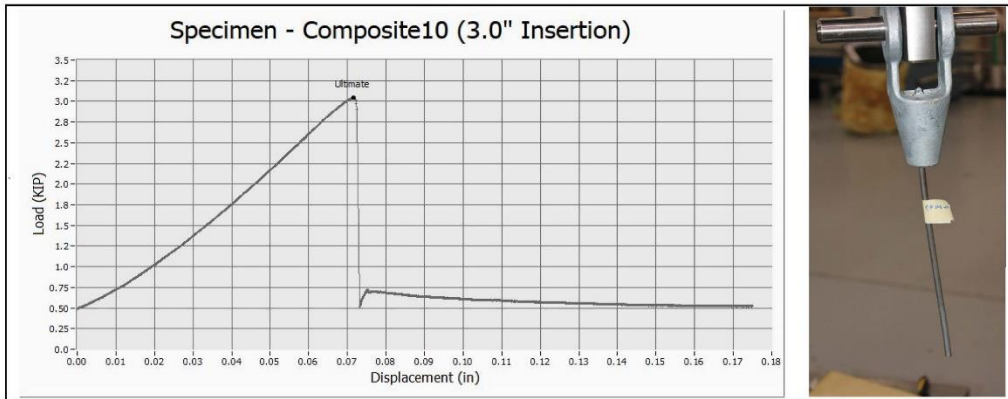
Version 4.3



EM22 Specimen ID	210110062
Other Specimen ID	Composite10
Operator	Eric King
Test Date	4/2/2021
Failure Location	Wire to Zinc Electrode
Geometry	Circular
Initial Diameter (in)	0.247
Initial Cross Section Area (in ²)	0.048

Environment:

	Stress (KSI)	Load (KIP)	Displacement (in)
Ultimate	63.44	3.04	0.07



Method File:

 Comments:



EM22

Zinc Socket / Wire Tensile Task Results

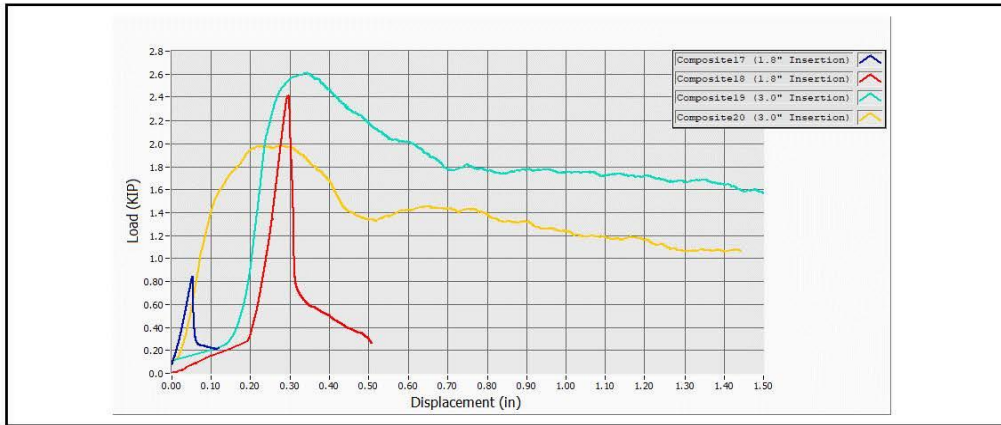


Version 4.3

MSFC Work Order	2021-0110
Work Order Task	8
Testing Organization	EM22

Average Data Acquisition Rate (Hz)	11
Control Mode	Stroke
Initial Test Rate (in/min)	0.05

Material	A586 Steel / Zinc
Nominal Temperature (°F)	70
Nominal Pressure (psig)	0
Test Frame	TS-5
Drawing Number	S-475
Pre-Load (lbf)	200



Results

EM22 Specimen ID	Other Specimen ID	Ultimate Stress (KSI)	Ultimate Load (KIP)	Comments
210110069	Composite17	17.04	0.84	A586 Wire Inserted to 1.75" Mark
210110070	Composite18	49.15	2.41	A586 Wire Inserted to 1.75" Mark
210110071	Composite19	53.23	2.61	A586 Wire Inserted through 3" Socket
210110072	Composite20	40.36	1.98	A586 Wire Inserted through 3" Socket



EM22 Smooth Tensile Specimen Test Results

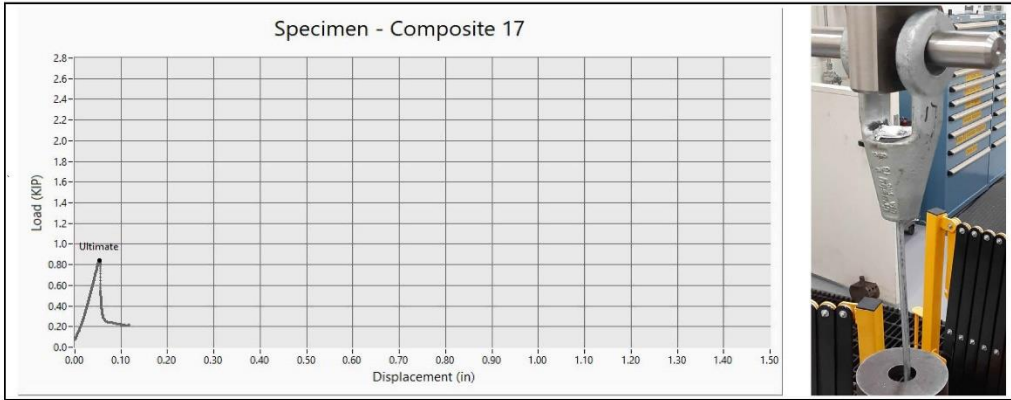
Version 4.3



EM22 Specimen ID	210110269
Other Specimen ID	Composite17
Operator	Charles Kay
Test Date	4/8/21
Failure Location	Wire to Zinc Bond
Geometry	Circular
Initial Diameter (in)	0.251
Cross Section Area (in ²)	0.049

Environment

	Stress (KSI)	Load (KIP)	Displacement (in)
Ultimate	17.04	0.84	0.05



Method File:

Comments:



EM22 Smooth Tensile Specimen Test Results

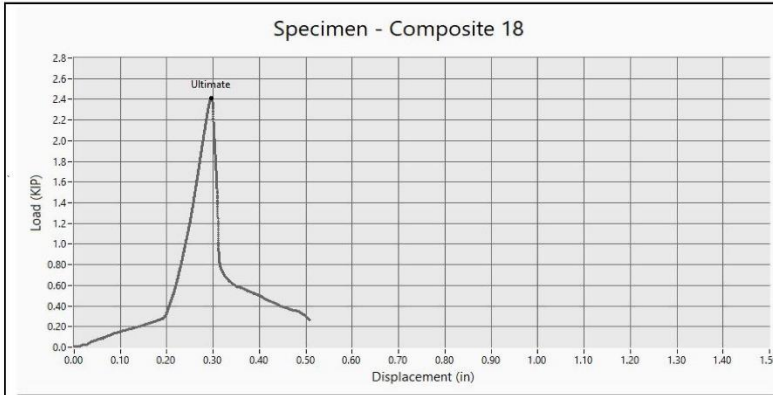


Version 4.3

EM22 Specimen ID	210110070
Other Specimen ID	Comacsi-c18
Operator	Charles Kay
Test Date	4/8/21
Failure Location	Wire to Zinc End
Geometry	Circular
Initial Diameter (in)	0.250
Cross Section Area (in ²)	0.049

Environment

	Stress (KSI)	Load (KIP)	Displacement (in)
Ultimate	65.15	2.61	0.30



Method File:

 Comments:



EM22 Smooth Tensile Specimen Test Results

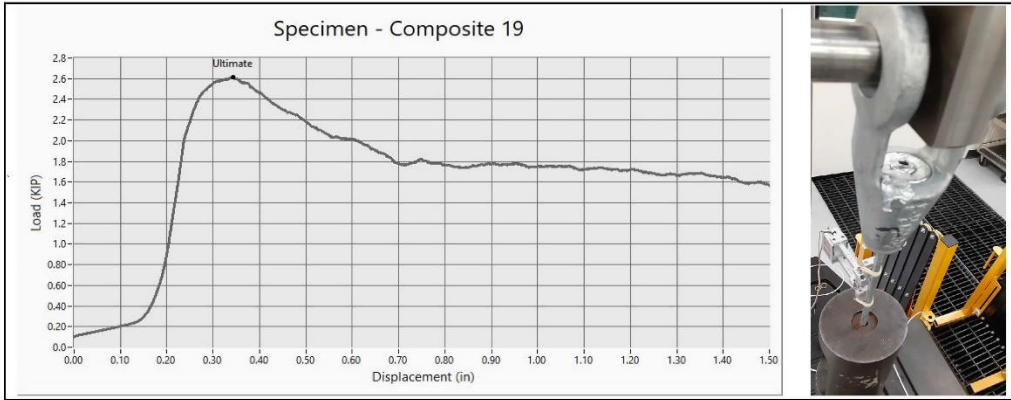


Version 4.3

EM22 Specimen ID	210110072
Other Specimen ID	Composile19
Operator	Eric King
Test Date	4/8/21
Failure Location	Wire to Zinc Bond
Geometry	Circular
Initial Diameter (in)	0.250
Cross Section Area (in ²)	0.049

Environment

	Stress (KSI)	Load (KIP)	Displacement (in)
Ultimate	53.23	2.61	0.34



Method File:

 Comments:



EM22 Smooth Tensile Specimen Test Results

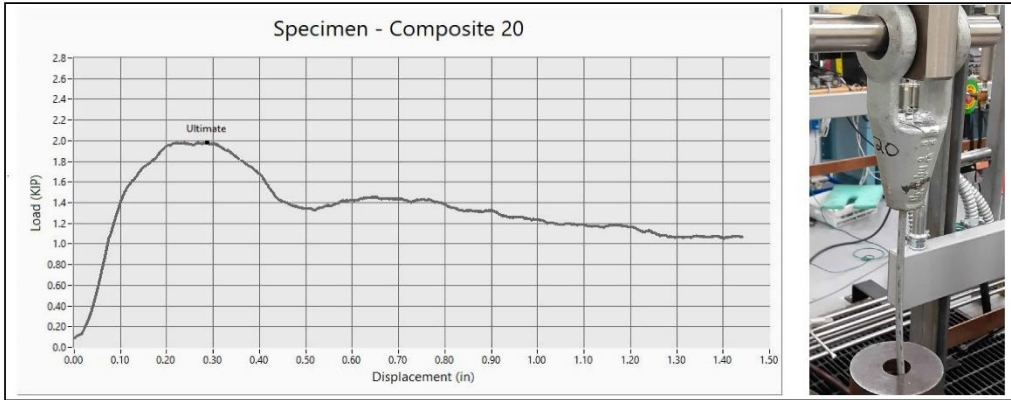
Version 6.1



EM22 Specimen ID	210110073
Other Specimen ID	Composite20
Operator	Annelle Gray
Test Date	4/9/21
Failure Location	Wire to Zmt. Bond
Geometry	Circular
Initial Diameter (in)	0.250
Cross Section Area (in ²)	0.049

Environment

	Stress (KSI)	Load (KIP)	Displacement (in)
Ultimate	40.36	1.98	0.29



Method File:

 Comments:

B.6 Arcicibo Failure Investigation Fracture Test, Work Order #2021-0110, Sequence 9



Arcicibo Failure Investigation Fracture Test Work Order # 2021-0110, Sequence 9



Eric King
Test Engineer
April 21, 2021

BACKGROUND

Information in this report is in support of the Arcicibo failure investigation. The Arcicibo Observatory main feature was a 1000 foot diameter radio telescope collecting dish. In December 2020, the final of a series of failures occurred that caused the collecting dish and support structures to collapse. The primary failed component being investigated is a spelter socket assembly that fastens a 3.25 inch diameter steel rope to the support structure. This particular test used zinc removed from ingot material that is comparative to that which was removed from the spelter socket assembly to get images of fracture surfaces.

APPROACH

This report describes one fracture pre-crack of a zinc middle tension specimen. The nominal dimensions of this specimen are 1.00 inch wide by 0.25 inch thick in the gage section with a 0.375 inch semicircular flaw in the center of the specimen. This specimen was fractured on Test Station 3 in building 4602 at Marshall Space Flight Center (MSFC). The environment for this testing was ambient laboratory air. The mechanical test frame consisted of a servo-hydraulic actuator and reaction frame. Load was measured with a 20,000 pound-force load cell. Load was applied to the specimen using the load cell for feedback to the control loop as a sine wave was applied in the following fashion:

Load (lbf)	Number of Cycles
185	20000
195	20000
210	14000
225	10
240	20000
260	10020
280	2000
300	23990
320	18153

RESULTS

Figures 1 through 6 of this report shows the fracture surfaces of the specimen. Figure 1 depicts the overall specimen and figure 6 depicts a closer image of the top surface. Figures 2 through 4 show different magnifications of the fractured surface. Several fractures formed in the specimen. However, none of these fractures appear to form at the flaw location. It is possible that heat generated from the machining (Electrical Discharge Machining) had an effect on the grain structure of the material. Furthermore, Figure 6 illustrates how several fractures occurred. Data for this procedure was uploaded into the MSFC EM Work Request System (EWRS) along with all pertinent calibration information.

Prepared By: ERIC KING <small>Digitally signed by ERIC KING Date: 2021.04.28 07:23:22 -05'00'</small>	Reviewed By: Annette Gray <small>Digitally signed by Annette Gray Date: 2021.04.28 09:14:18 -05'00'</small>
-------------------------------------------------------------------------------------------------------------------------	-------------------------------------------------------------------------------------------------------------------------------

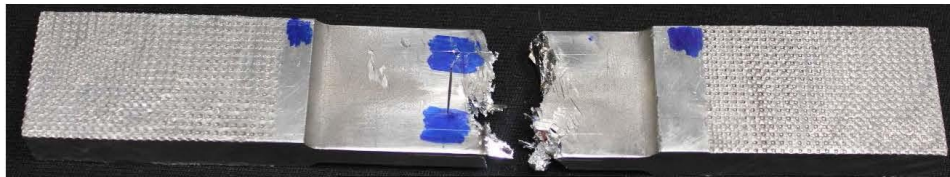


Figure 1: Image of Fractured Specimen



Figure 2: Digital Image of Fractured Specimen



Figure 3: Image of Fractured Specimen – Originally 12x

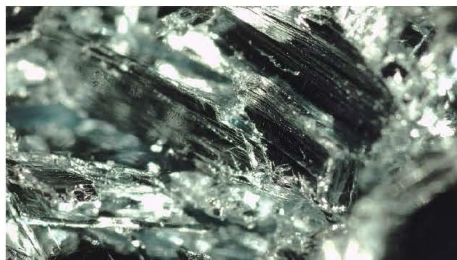


Figure 4: Image of Fractured Specimen – Originally 40x

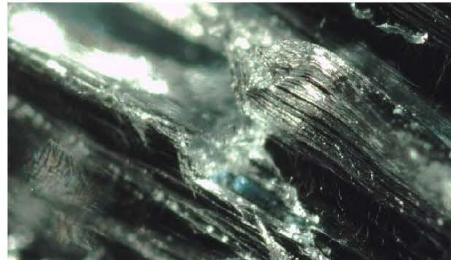


Figure 5: Image of Fractured Specimen – Originally 120x

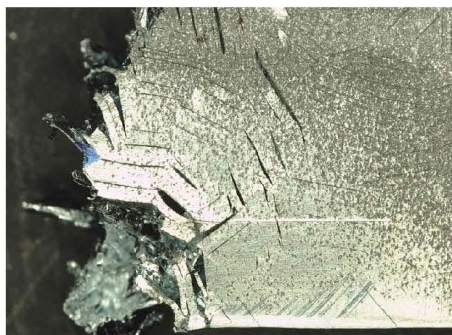


Figure 6: Top Image of Fractured Specimen

Appendix C. Structural Analysis of the Failed Arecibo Observatory Auxiliary Main Socket Joint

Contributors: Vinay Goyal and Pavel Babuska

Finite element analysis (FEA) of the Arecibo Observatory Auxiliary Main (M4N) Socket Joint design was leveraged to support the failure investigation of the M4N socket failure that proceeded and led to the eventual structural collapse of the entire facility. This section discusses the model construction, relevant inputs, general mechanics of the socket loading, sensitivity studies of varying material properties and dimensions, analysis of the as-built/as-failed socket condition, and assessment of potential contributors to the failure.

C.1 Description of the Model

A detailed three-dimensional (3D) model of the structural strand termination into the M4N socket was developed using Abaqus/CAE to investigate the individual wire, zinc, and steel socket mechanics and to support the failure investigation under observatory service loads. The detailed model served to complement an existing system analysis model used by Wiss, Janney, Elstner Associates, Inc. (WJE) to characterize loading in the structural strands, on the telescope receiver, and on the adjacent support hardware. Included in the detailed finite element model (FEM) were the following major components comprising the socket joint: the outer cast steel socket, the end of the structural strand including the broomed wires within the socket, and the cast zinc spelter that fills the socket volume and surrounds all the broomed wires. The purpose of this model was to develop a comprehensive understanding of the mechanics of failure of the joint and to understand the sensitivity of various parameters on the strength of the socket. Finally, the model was also used to evaluate specific metallurgical findings from the failure analysis and to support evaluation of failure scenarios.

C.1.1 Finite Element Mesh

Throughout the entire modeling effort, multiple models were constructed of varying fidelity and format to aid in the rapid trade study process. Wedge models (30-degree sections) with cyclic boundary conditions and full 360-degree models were created, each with varying levels of individual wire brooming. A separate model consisting of the as-built/as-failed wire brooming specific to M4N was also constructed to complement the generic wire brooming models. The reduced wedge models were used to enable dozens of sensitivity studies to understand the effects of various parameters including the degree of brooming, zinc material properties, and voids observed during metallurgic examinations. The findings from the wedge models were anchored to those observed in the full 360-degree models and the as-built configuration model.

Model construction involved several complicated steps unique to which model was being developed. Creating the as-built configuration model was the most complicated. First, visual video evidence from various structural strand and wire rope manufacturers was reviewed to understand the brooming process and develop an idealized computer-assisted design (CAD) model of the broomed wires. Proper brooming at the root of the strand is critical to distributing the stresses effectively throughout the whole section. The structural strand used in the Arecibo design is denoted as a 1×127 format, or 127 individual wires in concentric rings that consist of the following number of wires per radial row from the center outward: 1 (center), 6, 12, 18, 24, 30, and 36 (outer row). Each individual wire is 0.25 inch in diameter and forms the structural

strand that is 3.25 inches in total diameter. Multiple versions of an axisymmetric, “idealized” brooming configuration were created such that the wires in each radial row are equally spaced and travel the length of the socket uniformly. The different wedge model configurations varied in the level of brooming that each row of wires experienced. Having multiple levels of brooming helped examine the effects that brooming and workmanship play on the overall capability of the socket termination.

Because the manufacturing process of structural strand socket terminations involves manual brooming and technician involvement, it is easily understood that each individual socket termination is unique. The as-failed M4N socket was recovered and sectioned at multiple stations down its length, with all remaining wires marked and denoted with a unique identifier. From this forensic examination, the data could be combined to form a best-effort 3D mapping of each individual wire within the socket volume. The process for constructing the as-built model involved mapping each of these wires, porting them into SolidWorks via macro, generated sweep profiles around the splined pathways, and exporting for meshing.

The socket itself was easily constructed from the manufacturer drawings and was represented multiple ways. First it was modeled as its own elastic body, which showed that the socket’s elasticity played a minimal role in the overall mechanics of failure. Later, it was represented as a discrete rigid condition against which the zinc reacted.

Finally, the zinc casting was modeled as the negative volume between the bundle of broomed wires and the socket geometry. In each case of brooming and for the as-built configuration, the conical zinc volume was created in SolidWorks and the wire volumes were hollowed out via the Cavity feature to generate the final geometry, which was then imported to FEA software for meshing.

In all cases, the wires were straightforward to mesh, but the volume of zinc between them proved to be challenging due to the wire-to-wire proximities. All wedge models were able to be meshed with eight-noded linear brick elements (C3D8), while the as-built configuration had to use second-order tetrahedral elements (C3D10). The elements for the wires, zinc, and outer shell all passed element quality checks.

The interfaces between the wires and the zinc were modeled one of two ways depending on the desired analytical study. In select instances, the interfaces were considered rigidly connected (“tied” in Abaqus terminology) for convergence efficiency. Otherwise, the interfaces were modeled with a nearly-infinite stiffness contact condition (“contact pair” in Abaqus terminology) to enable extraction interface shear and pressure stresses. Contact modeling with friction was also implemented between the zinc and the socket casing to allow for zinc “seating” within the socket. Material nonlinearity was included for the steel wires and the zinc spelter to predict the post-yield material response. Across all the various model configurations, the number of total degrees of freedom ranged between 1 and 5 million. Model solution times ranged between 20 minutes and 7 hours when parallelized across 20 CPUs for a single load step. Examples of the idealized wire brooming, simplified socket model, and wedge model mesh density are shown in Figure C-1.

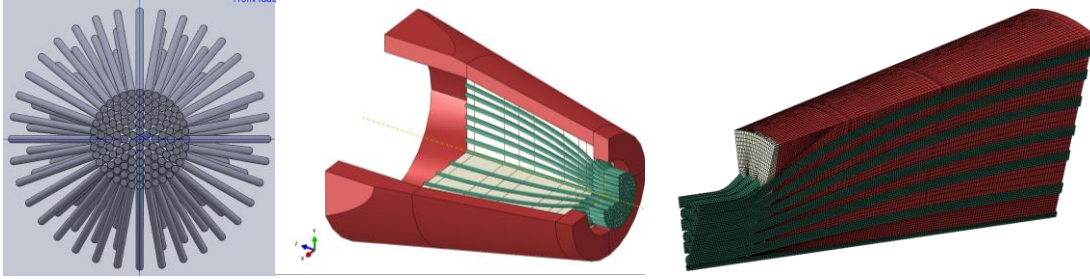


Figure C-1. Socket is Modeled as Simplified Version that does not Consider Clevis Pin and Holes

C.1.2 Material and Strength Properties

The baseline set of mechanical properties of the various constituents of the joint were as follows; however, some were altered further during the suite of trade studies performed:

- Auxiliary Main Strand Wires (A586-91 Steel Cable)
 - Elastic Modulus: 23 Msi to 29 Msi, Poisson's Ratio: 0.29
 - Yield Strength: 160 ksi (min spec), Ultimate Strength: >220 ksi (min spec)
- Cast Steel Socket (A148 Grade 90-60 Cast Steel)
 - Elastic Modulus: 27 Msi, Poisson's Ratio: 0.29
 - Yield Strength: ~70 ksi, Ultimate Strength: ~100 ksi
- Commercially Pure Zinc Casting
 - Elastic Modulus: 10 Msi to 14 Msi, Poisson's Ratio: 0.25
 - Yield Strength: 1 ksi to 8 ksi, Ultimate Strength: 5 ksi to 50 ksi

Dozens of analyses were performed using varying material properties for the zinc casting and strand wires. While a significant body of material testing was performed on the zinc and steel constituents, the only information leveraged for the purpose of analytical model development were the tensile and compressive strength properties to estimate stress-strain curve material models using the Ramberg-Osgood method.

True stress-strain curves were generated and incorporated into the models based on NASA testing of the steel wire and the zinc. Several different zinc material models were developed for use in sensitivity studies to determine socket termination capability based on the variability in material properties. These sensitivity studies were performed to mitigate concerns associated with uncertainty stemming from zinc material test data. Sensitivity studies were also performed to investigate variability in wire elastic modulus, but analysis results showed minimal sensitivity and are not reported in detail.

Commercially pure zinc is a unique structural material in structural socket terminations because its tensile capability is extremely low. However, its compressive capability is high. Grain sizes also vary significantly based on manufactured method and rates of cooling during casting (see Appendix A, Section 4.3.1). As such, it is difficult to construct a high-confidence material model that accurately reflects both tension and compression response or when attempting to model progressive damage. This acknowledgment was the impetus for considering the range of zinc material properties that will be discussed later in this report. An example true stress-strain curve for the range of zinc mechanical properties and for the wire mechanical properties is shown in Figure C-2.

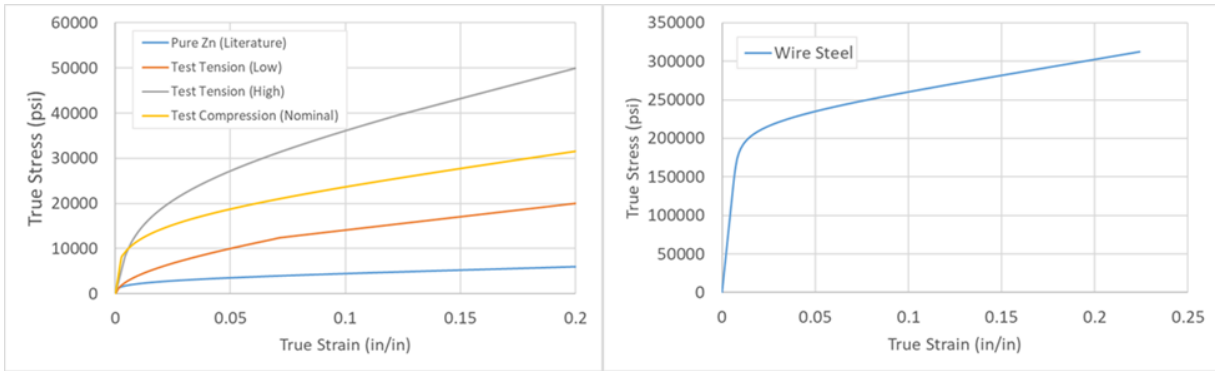


Figure C-2. True Stress-Strain Curves for the Range of Zinc Material Properties (left) and Baseline Steel Material Property (right)

C.1.3 Boundary Conditions

Due to the high-level of mesh refinement required to characterize the zinc and wire constituents, additional model simplifications were needed. An initial coarse FEM of the socket was developed to understand the effects of the clevis joint attached to the socket. This analysis demonstrated that the local stresses at the clevis hole did not influence stress levels in the zinc casting or on individual wires. Further, the socket deflections were predicted to be small (less than 0.010 inch compared with the conical socket dimension of >12 inches) and the net section stresses in the cast steel socket were near 15 ksi (Figure C-3), well below the ultimate material capability of 100 ksi. Stresses adjacent to the boundary condition were even lower than those near the zinc casting interface. FEA showed that the pin-clevis connection at the back of the open socket termination did not need to be included in the baseline FEMs, as its effects were found to be insignificant in the overall socket mechanics. The loads did not cause ovalization of the socket and was shown to behave axisymmetrically. Because of the local nature of the stresses within the zinc casting, there was no need to model the clevis joint in subsequent modeling efforts.

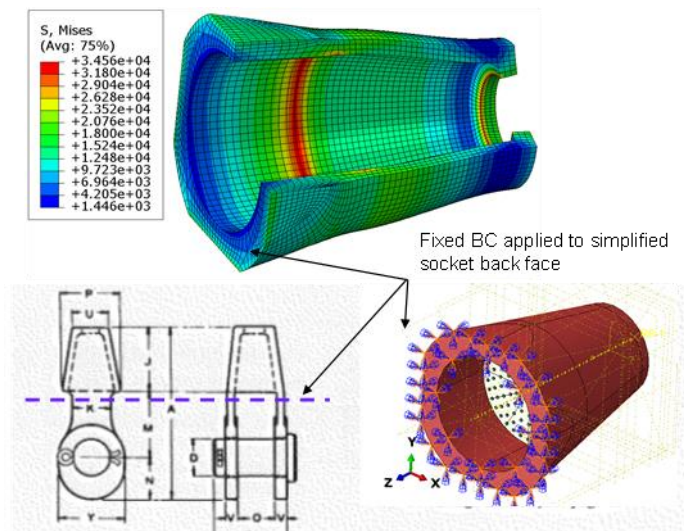


Figure C-3. Clevis Joint was not Modeled in Baseline FEMs as its Effects were Found to be Insignificant

C.1.4 Loads

The first load experienced by a newly manufactured socket is the socket proof test to 50% of the specified cable breaking strength. In the case of Aux M4N, this corresponds to a load of roughly 660 kips. The socket joint is loaded axially by reacting all the tension developed in the structural strand from suspending the Arecibo telescope receiver. Torsional forces from tension loading will arise but are balanced by alternating layers of strand wires, denoted as a “torsion-balanced” configuration. For the purpose of modeling simplicity, only axial loads were applied after determining that the minimal torsion and bending loads were negligible. While these asymmetric non-uniform effects are likely to be present, these were determined to be a small component of the total axial load acting on the joint.

As a modeling assumption, the load was applied to a single node reference point that was kinematically coupled to the wires. This assumption allows effective load transfer to each of the individual wires and is a realistic modeling representation, as the load is applied far field from the socket and at that point the entire strand is being loaded uniformly across the cross section.

Regarding operational loads, the observatory drawings specified three relevant loading cable conditions for the Aux Main cable (see Appendix D):

Loading Condition 1: Initial tension under dead loads at 90 degrees Fahrenheit (°F) and includes all loads from modified central feed structure, new Gregorian Dome, cables, loads due to raising the platform, loads due to tie downs, and loads from wave guide supporting system. *The final loads after initial erection is 602 kips.*

Loading Condition 2: Operational loads includes all loads in Condition 1 plus 50-mph wind and 90 °F: *615 kips.*

Loading Condition 3: Operational loads includes all loads in Condition 1 plus 100-mph wind and 90 °F: *622 kips.*

During “survival” conditions, the Gregorian Dome was stowed, and tie-down forces were relaxed so that the observatory receiver was free to displace as needed with the winds. WJE’s analysis predicted a maximum cable load of 720 kips [ref. 1], nearly 100 kips higher than the value prescribed in the drawing. Dead loads were a significant portion of the maximum cable load: (602 kips/720 kips) ~84%, resulting in a design factor of safety against the 1314-kip cable breaking strength of (1314 kips/720 kips) ~1.83. Finally, a proof factor of roughly 0.92 is achieved when considering proof test of 657 kips and a survival load of 720 kips.

Fluctuating cable loads and corresponding load spectra due to wind oscillations from hurricanes, earthquakes, temperature fluctuations, and telescope movements was not fully characterized. Due to limited data available to WJE, they did not characterize the many variations in loads that could occur and did not analyze the effects of various combinations of tie-down loads with static/dynamic wind loads. However, when examining the three loading conditions per the drawings, loads caused by winds are a small percentage of the total cable loads based on a comparison of load conditions 1, 2, and 3.

Due to the uncertainty in the maximum tensile load expected in Aux M4N, all FEA sensitivity studies were performed with a baseline cable load of 602 kips (load condition 1). Residual stresses from manufacturing, and thermal and vibration sources were not included in the model.

It should be noted from Figure C-4 that the survival condition load is only 7,000 lb above the expected dead load, making the dead load a uniquely high proportion of total load demand for these socket terminations. Representative in-service loads were extracted from instrumentation on the remaining M4S socket hardware, including strain gages on both the North arm (M4S_Aux_N-Strain), the South arm (M4S_Aux_S-Strain), a thermocouple (M4S_Aux-Thermal) installed on the underside of the M4S structural strand, and a wind reading from the platform on Tower T-12. For typical tropical conditions, Figures C-5 and C-6 demonstrate that the strain measurements were more sensitive to temperature than wind and were small in magnitude. The data imply that the structural system is sufficiently flexible such that the transient external loading results in a small load increase into the cable compared with the dead load, as shown in Figure C-4.

**CABLE TENSIONS –
STRENGTHENED CABLE SYSTEM**

CABLES MK	301
NO.	6
DIAMETER	3 1/4"
MINIMUM BREAKING STRENGTH (KIPS)	1314
TENSION PER CABLE	
(I) INITIAL TENSION UNDER ALL DEAD LOADS EXISTING *	—
INITIAL ERECTION	450
FINAL	602
(II) OPERATIONAL LOADS	615
(III) SURVIVAL CONDITION	622
DESCRIPTION	AUX. CABLES
	NEW

* FROM ORIGINAL CONTRACT DRAWINGS.
ACTUAL VALUES ARE SLIGHTLY LOWER.

Figure C-4. Operational Load is Roughly 600,000 lb (see Appendix D)

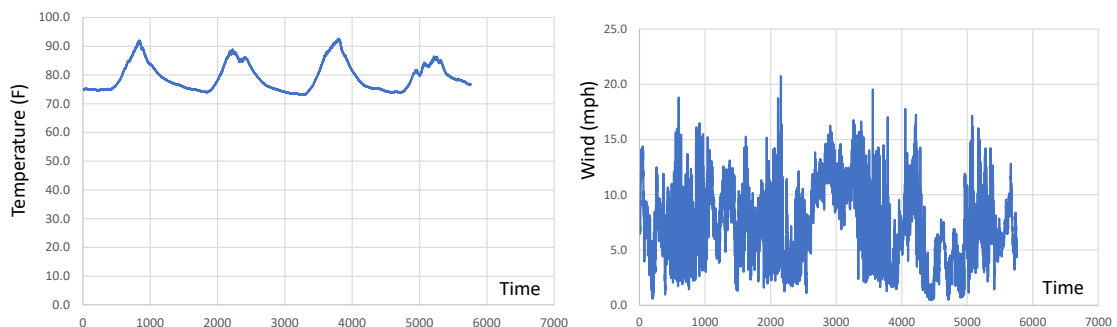


Figure C-5. Temperature (F) and Wind (mph) Trends between October 30 and November 2, 2020 (time scale in seconds)

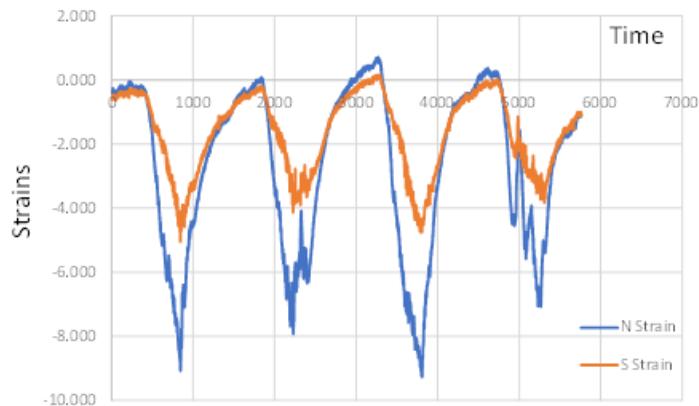


Figure C-6. Strain Measurements in Microstrain between October 30 and November 2, 2020 (timescale in seconds)

F-25. Observatory dead load resulted in sustained cable tensions within 20% of the maximum expected cable tension.

C.1.5 Socket Joint Physics

Cable tensions from observatory dead load, operational loads, and survival transients are transmitted to the socket termination through the 126 individually broomed wires that are held in place by the cast zinc spelter within the steel open socket conical volume. The zinc that fills the socket cavity is bonded to the wires, and this bond creates an efficient load transfer among the wires within the socket.

A special characteristic of the socket termination is that the combination of zinc plasticity and the conical volume forces a “squeezing” effect to occur around the broomed wire bundle in the narrow part of the socket. The high confining pressures experienced at the outlet of the socket keep the broomed wires from pulling out of the zinc and allow the failure to occur in the cable outside the socket, thus developing the cited 100% efficiency termination.

The load transfer mechanism is analogous to fiber-reinforced metal matrix composites, whereby the matrix material aids in transferring load to the fibers that handle the axial loading. Most of the load is carried by the wires within and just outside the socket (see Figure C-7).

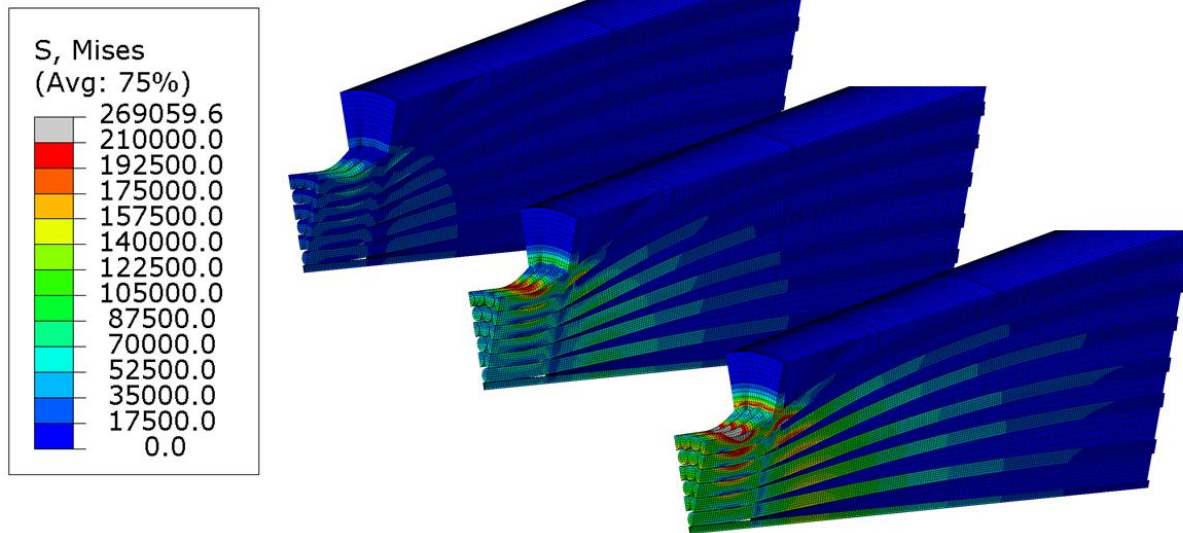


Figure C-7. As Loading in Cables Increases (left to right), the Zinc Distributes Load amongst Wires within Socket in Mechanism Analogous to Metal Matrix Reinforced Composites

Note: The magnitude of the contour stress plots is not particularly relevant for this demonstration.

It is worth noting that some sockets, specifically those manufactured in the field, use a thermoset poured resin rather than molten zinc to confine the broomed wires within the socket.

Functionally, the nearly incompressible resin achieves the same mechanical locking and squeezing of the wires as the zinc plasticity and conical socket shape. Reference 14 states:

“When a load is applied to the rope, the resin cone must move forward into the socket. This effect generates high wedging pressures in the resin, tightly gripping the embedded wires. This movement, and the resulting wedging process, is essential to the operation of the system...”

A properly manufactured socket termination should develop the full breaking strength of the structural strand or wire rope, meaning that the socket termination itself should not be the limited strength factor in the capability of the whole cable. This is observed during testing when the failure mode is breakage in the cable rather than individual wire pullout of the zinc or resin casting. The exact progressive failure is complicated, and it is not obvious which individual wire fails first or where along the length of the cable the first failures should occur. Once individual wires fail, the failure mode may or may not exchange to the cast zinc or resin or may remain somewhere within the strand.

Figure C-8 shows the distribution of plastic shear strain in the zinc for three configurations of model brooming. The effects of brooming on performance are discussed later in this appendix, but it is worth noting that the bands of shear strain in the middle and lower configurations show how brooming affects stress and strain level in the zinc. Better brooming traps the wires and redistributes stress out to the wires, while poor brooming puts more shear stress into the zinc, which can have deleterious effects on termination performance (discussed in more detail later).

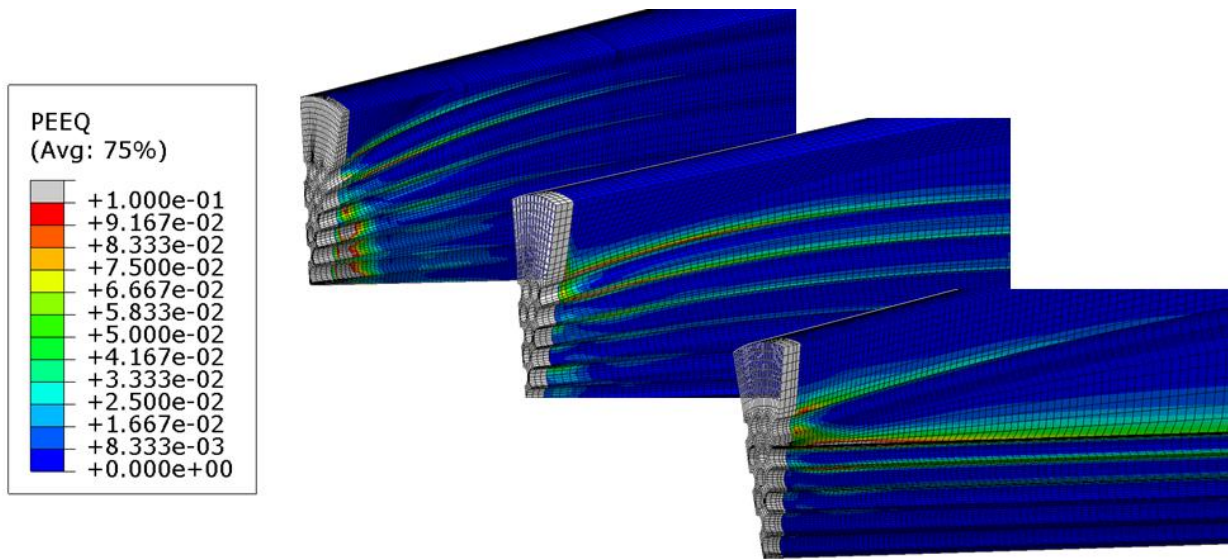


Figure C-8. Comparison of Representative Zinc Plastic Strain Fields for Three Different Wire Brooming Configurations, highlighting Bands of Significant Shear for Less-broomed Cable Ends

In reference 15, the cable fails at the far socket termination. In this failure example, it appears as though the cable core (i.e., the remaining unfractured wires) would have pulled out of the socket by zinc overload, like the Arecibo failure, had the test rig continued to move. In other tests, the structural strand has been shown to fail away from the socket, somewhere within the span of the strand length. However, it is not possible to predict which configurations would fail in the strand near the socket and which would fail in span.

C.1.6 Analysis-Test Correlation

The socket joint is designed to fail outside the socket joint in the load-bearing structural strand and not due to interfacial bond breakage at the zinc/wire interface. Per Figure C-4, the breaking strength of the strand is near 1,314 kips. While no other documentation exists, verbal information from the supplier also indicated a breaking strength of the joint in excess of 1,300 kips, consistent with Figure C-4.

The breaking strength of the strand is rated at 1,314 kips and is consistent with hand calculations based on cross-sectional area of each wire: $A_{wire} = \pi * 0.125^2 = 0.049 \text{ in}^2$. Based on the single-wire minimum strength specification of 220 ksi, the predicted load at failure is 1,360 kips ($= 126 \text{ wires} \times A_{wire} \times 220 \text{ ksi}$). This value is theoretical and assumes that all wires are loaded equally and does not account for variability in strength. Note that in this particular calculation the interfacial shear stress is not considered along the length of the embedded wires, which would be a different failure mode inconsistent with proper manufacturing and design.

The wedge FEM predicted the highest stresses in the outer wires, and the ultimate strain to failure of the whole cable cross section was not predicted until the failure load was above 1,200 kips. However, the Aux M4N socket joint failed at operational loads near 600 kips. So, one key question is why a socket with a rated breaking strength of over 1,300 kips failed near 600 kips. As stated previously, the rated breaking strength is determined in a test where the cable is loaded until total net section failure occurs. Total cable overload does not occur until most of the individual wires are yielding and collectively reaching their ultimate elongation limit. In all versions of the model, as-built and wedge models, analysis predictions showed that at 600 kips

the entire row of outer wires has begun to yield and plastically elongate, albeit not grossly. As intended, this causes a load redistribution to the inner rows of wires, which eventually yield next, and the process continues. All analyses show agreement that the breaking strength of the full strand would not occur at 600 kips of applied load for a pristine, newly constructed cable termination of this design.

Hand calculation and FEA of the socket joint show that the breaking failure load is near that specified in Figure C-4. Predicting explicit failure of the zinc is difficult due to the complicated stress states that occur in the zinc through the socket volume. Further, the commercially pure zinc test data obtained by constituent level testing does not lend well to a failure criterion in this type of socket. As such, sensitivity studies across the range of possible zinc material properties and failure criteria showed that predicting zinc failure is less crucial to predicting the strength of the overall socket joint because the zinc material variability plays little role on the overall stress development in the wires in a properly functioning socket.

Strain gage data were not available as a method for model anchoring, but other approaches were available from the forensic evidence. The FEAs were helpful in understanding the basic mechanisms of failure for such designs. A qualitative comparison to the failed socket shows that the FEM predicts the “stepped” pattern wire failures observed during forensic examination, as shown in Figure C-8. The highest stresses were not predicted to be planar from wire to wire; rather, the failure surface followed the surface of a rough spheroid, matching the stepped patterns seen from forensic examination. The outer wires were predicted to fail closer to the socket face wire outlet region, while the inner wires would fail slightly inboard to the socket, as identified in the forensic evidence (see Appendix A, Section 4.2.2). The stress field suggested that the wires failed adjacent to the greatest confining pressure within the zinc. The zinc plastic flow and the shape of the socket create a region of confining pressure in the shape of a half spheroid, which causes the highest wire stresses adjacent to the boundary of the highest confining pressure. In Figure C-9, the red output showing interface contact pressure (“CPRESS”) reflects the area of highest confining pressure at the zinc/wire interface, which would squeeze the individual wires, suggesting the fracture location would be ahead of this region (near the wire outlet of the socket). The graphic on the right-hand side of Figure C-9 is reproduced in greater detail in Figure C-10.

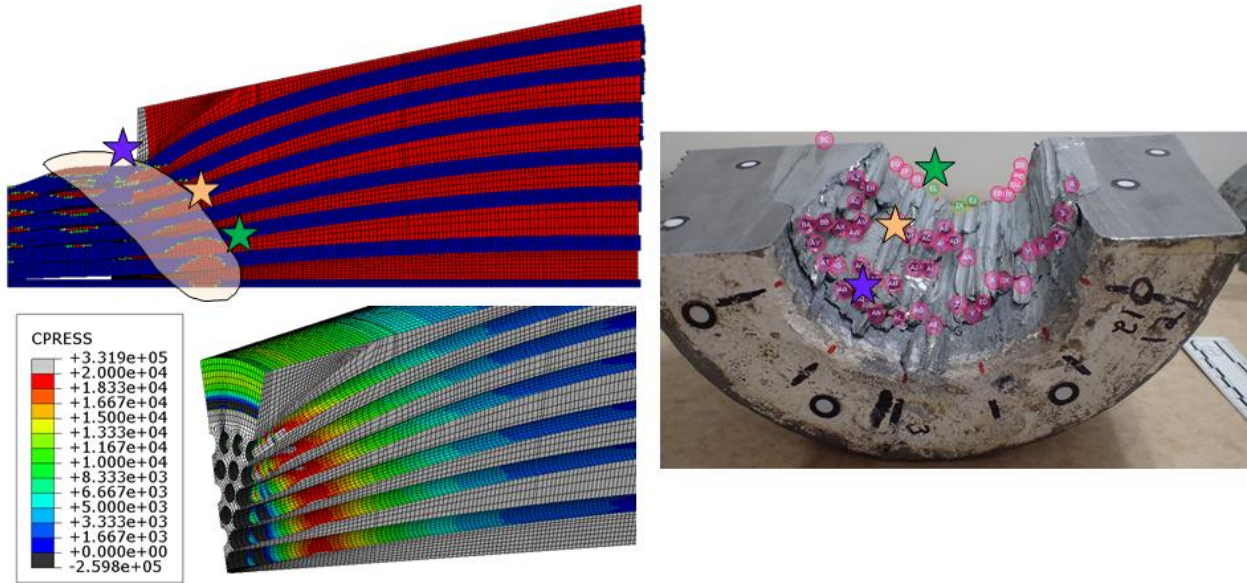


Figure C-9. Highest Stresses were not Predicted to be Planar; Failure Surface followed a Spheroid Shape, matching Stepped Patterns seen in Forensic Investigation
 Regions of colored stars show different "steps" of failure in socket. Note that yellow shading (top left) and red high stress zones (lower left) match shape of failure surfaces in right figure.

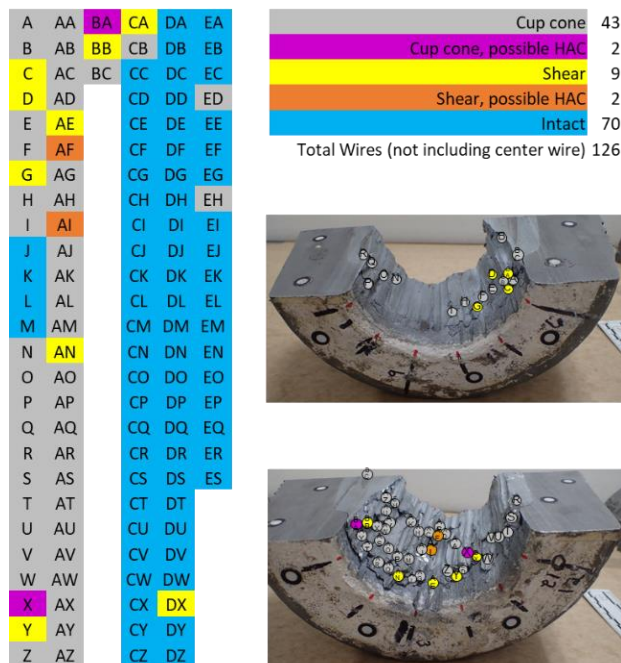


Figure C-10. Many Outer Wires Exhibited a Shear-type Failure (orange and yellow), while Inner wires exhibited Cup-cone Failure (gray and purple)

Model predictions were qualitatively consistent with the observed wire failure modes from the Aux M4N socket. Forensics identified that the majority of wires failed in cup-cone fracture, although a select number of outer wires failed in shear (see Figure C-10). Analysis shows that

the inner wires are under significant confining pressure, thus increasing elongation capability and resulting in a “ductile” cup-cone failure mode. The outermost wires have unbalanced confining pressure and are geometrically more broomed, which increases the likelihood of a shear failure mode.

F-27. Finite element modeling predictions were qualitatively in agreement with the NASA forensic analysis:

- Maximum wire stresses predicted followed the stepped pattern observed in the forensic analysis.
- Outer wires were predicted to fail in a shear failure.
- Inner wires were predicted to fail in a cup-cone failure mode due to the compression effects of the zinc on the wires.

C.1.7 Analysis of Confidence in Analytical Model

Confidence in the analytical model was qualitatively assessed using the model confidence matrix. This allows identification of sensitivity studies that should be conducted to mitigate potential concerns with an aspect of the model. Model confidence was assessed for the material model, boundary conditions, loads, and mesh refinement. A rating of ‘1’ indicates low confidence, ‘5’ indicates high confidence, and ‘3’ indicates moderate confidence. The model was evaluated relative to the material model for the various constituents of the socket joint, boundary conditions, loads, and mesh refinement, shown in Table C-1. The assessment indicates a modeling confidence of moderate or lower for the material properties of the zinc casting and the as-built model. These concerns were subsequently mitigated by conducting several sensitivity studies targeting the zinc material model and the as-built configuration. There was also a limited understanding of zinc failure mechanics within the socket.

Table C-1. Overall Confidence in Model, Assessed using Confidence Matrix along with Mitigation Options for Areas of Low Confidence

Aspect	Conf. Rating	Rationale	Mitigation
Material Model			
Cast Steel Socket	5	Cast steel elastic properties at low stress levels are well-understood	N/A
Zinc Casting	2	Literature of the zinc material exists but there was less confidence in the stress-strain data. Lack of clear failure mechanics and applicable damage models for zinc.	Perform sensitivity studies to understand socket behavior sensitivity to wide range zinc material properties.
Steel Wire	4	Literature data exists and it was supported by NASA testing. There was less confidence in the elongation to failure data.	Perform sensitivity studies to understand steel wire behavior to wire material properties.
Boundary Conditions	5	Wire stress and socket behavior were insensitive to boundary conditions.	N/A
Loads			
Load application	5	Wire load is determinate, and load was applied at a distance from the socket face.	N/A
Magnitude of load	4	The operational loads were applied but there was less clarity on how to include other loads from asymmetric loading and wind/temperature	Determine if further analysis is required pending conclusions.
Mesh Refinement	5	Mesh sensitivity studies and hand calculations suggested a converged mesh. All elements passed quality checks.	None
As-built Model	3	Drawings and forensic evidence were used to reconstruct an as-built model of the failed socket. The effort required making some engineering assumptions.	Perform sensitivity studies to understand the effects of wire stress to parameters affecting the as-built quality of the socket.

C.2 Strength Assessment

Due to uncertainty in the zinc material properties, sensitivity analyses were performed with a suite of zinc material models ranging from “soft” to “stiff” that envelop NASA independent test data of the zinc spelter and ingot indicated earlier in this report.

For an applied load of 600 kips, the range of zinc material models resulted in outer wire stress predictions ranging from 220 to 230 ksi, yielding in all cases. With a factor of safety of unity,

this corresponds to structural margins ranging from +15% to -4% considering a range of wire ultimate strengths of 220 to 250 ksi. Margins are considerably lower with the maximum cable load of 720 kips predicted by WJE's analysis.

For typical aerospace applications, structures with highly complicated stress distributions are analyzed and compared not only against the breaking strength of the joint but also for constituent stresses against their respective material strengths. Regardless of the zinc material model, the wires support the majority of the sustained load, and the outermost wires are stressed near the ultimate strength of the wire steel material, even at 600 kips of applied load, which is well below the rated breaking strength of the structural strand. The yielding of the outer wires results in load transfer to inner wires that can more readily accommodate the further increases in load before full cable failure. This can be understood by examining Figure C-11.

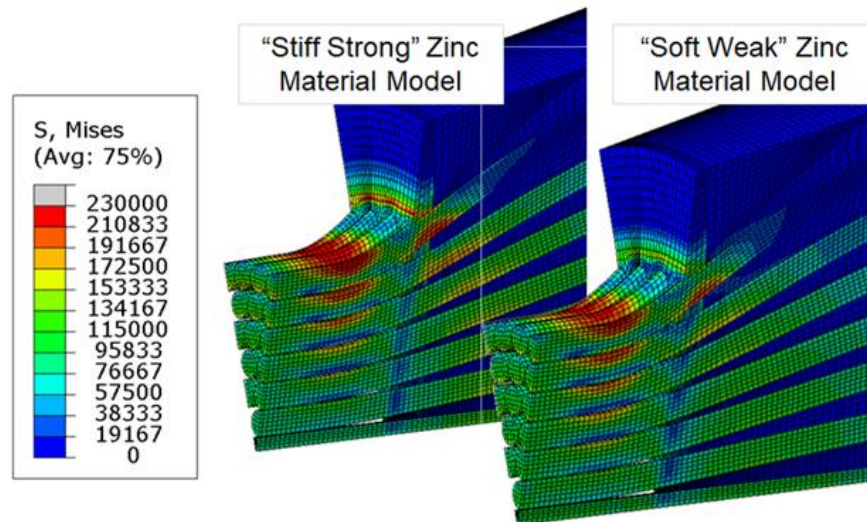


Figure C-11. Wire Stresses are Highest in Outer Wires; Wire Stress was Relatively High Compared with Material Capability, Regardless of Zinc Material Model

In a perfect world, the zinc materials would be well characterized and repeatable in manufacture, but the sensitivity studies have helped show that, regardless of zinc material model, the wires at the outlet of the socket take the majority of the sustained load, and the outer-most wires are stressed near the ultimate strength of the wire steel material. This is shown to occur even for the 600 kips of nominal observatory use tension, well below the rated breaking strength of the structural strand. The yielding of the outer wires results in load transfer to inner wires that can more readily accommodate the further increases in load before full cable failure.

F-28. For a large range of realistic zinc material properties, all models predict that outer wire stresses are near ultimate strength of individual wires, even at operational observatory loads, demonstrating low or even negative margins of safety for the Aux M4N socket.

C.3 Cumulative Damage Assessment

The topic of cumulative damage arises when considering structures with long lifetimes, structures subject to significant loading transients, or structures with minimal design margin. In the Aux M4N socket termination, the low structural margin and long time in service may limit the joint's ability to accommodate loading transients, creep, and other time-dependent factors ad infinitum. The topic of damage accumulation was explored in a basic assessment of creep and fatigue for the joint.

Socket Corrosion Discussion: Forensic analysis and associated microstructural studies found corrosion within the zinc casting, at the wire-zinc interfaces, and at the zinc-socket interface. FEA was leveraged to assess the potential role of each forensic finding in the failure progression.

Corrosion was found in the upper two-thirds region between the socket housing and the zinc casting outer diameter, while negligible corrosion was found in the lower third. An FEA sensitivity study examined the influence of corrosion between the zinc casting and the socket housing. The analyses varied the coefficient of friction from 0.3 to 0.8 and then as permanently affixed between the zinc casting and the socket housing and found minimal effects on the wire stresses. The findings are consistent with understood socket physics that pulling the wires also pulls the zinc against the socket housing. A high compression zone develops between the socket housing and the zinc during this process, and the presence of any corrosion has a low influence on wire stresses because the load transfer mechanism remains intact.

FEA was used to evaluate the corroded wire ends of eight wires that were cast protruding from the zinc outer diameter. Analysis showed that the wires were not stressed as highly in the wider region of the socket as they were in the narrower front region, and that the as-identified corroded interfaces should not have been detrimental to the load transfer mechanism. A separate analysis evaluated the voids and defects within the casting near the wider socket casting region and found that these likely had a negligible effect on the maximum predicted wire stress located adjacent to the wire outlet from the socket.

Corrosion throughout the zinc casting was also evaluated for potential degradation of zinc mechanical properties and potential influence on wire stresses. Results of this sensitivity study did not change the conclusion that individual outer wire stresses are near ultimate strength at operational observatory loads.

Finally, the analysis showed that the highest stresses were near the narrow diameter of the socket where corrosion was less pervasive. While corrosion was present in smaller quantities, the potential influence on wire stresses was significantly lower than the role of low structural margins at operational loads and the influence of long-term sustained loading.

Zinc Creep: The cast zinc is under a large amount of shear and compression stress in this design due to the wires shearing the zinc at the bonded interface and the overall compression that develops once the volume of zinc flows and becomes compressed by the narrow end of the socket. Literature of zinc spelter sockets suggests that the zinc is susceptible to creep behavior at a higher rate than steel wires. Shear stresses vary throughout the cast spelter volume, with the highest stressed regions being in the narrow half of the socket and sufficiently high in magnitude to expect the occurrence of creep. The significant stress and strain levels in the zinc are evident in the plastic strain field shown in Figures C-7 and C-8 in Section C.1.5. This is also confirmed

by WJE testing, in which samples were subjected to constant loading, resulting in creep behavior [ref. 1].

Steel Wire Surface Defects: Forensic analysis revealed wire surface defects on five fractured wires and that defects influenced the failure of two of the wires. From the structural assessment perspective, surface defects can cause local stress risers that decrease the strength capability of those respective wires. The negative structural margins predicted with a factor of safety of 1.0 at limit load further deteriorate when the stress riser due to the surface defect is considered.

Steel Wire Creep: Adjacent to the socket termination, the brooming of the wires and the geometric stress concentration results in the outer wires being stressed to a significant percentage of their strength capability. As such, there is limited structural margin remaining that can accommodate overloading events or reduction of capacity due to “time-dependent” failure mechanisms for infinite durations. Steel wire is known to exhibit creep response [refs. 16-18] under sustained loading and, as the stress increases relative to the strength of the wire, the creep strain rate also increases.

Strain loading was sufficiently high that it could not accommodate creep and cyclic loading. The creep mechanism is therefore a credible phenomenon, particularly on the heavily stressed outer wires of the socket joint. Increasing the strain level in the wire also results in decreasing elongation capability. *Due to a lack of reliable stress rupture failure criteria, no attempt was made to predict creep failure of the wire, but the assessment demonstrates qualitative relevance.*

Cyclic Loading of Socket Joint: An FEM was constructed to understand the zinc and wire mechanical behavior due to proof testing followed by fluctuating cable loads. A six-step analysis process was performed: (1) conduct socket proof test to 50% rated breaking strength (660 kips), (2) unload (<12 kips), (3) load to initial operational load (624 kips), (4) reduce to low operation load (500 kips), (5) increase to survival load (720 kips), and (6) return to original operational load (624 kips). In reference to Figure C-12, it was confirmed that cyclic loading beyond proof-test loading progressively increases strain in wires, progressively increases plastic flow in zinc, and exhibits structural hysteresis. During subsequent loading events at lower magnitudes, the response in outer wires remains linear.

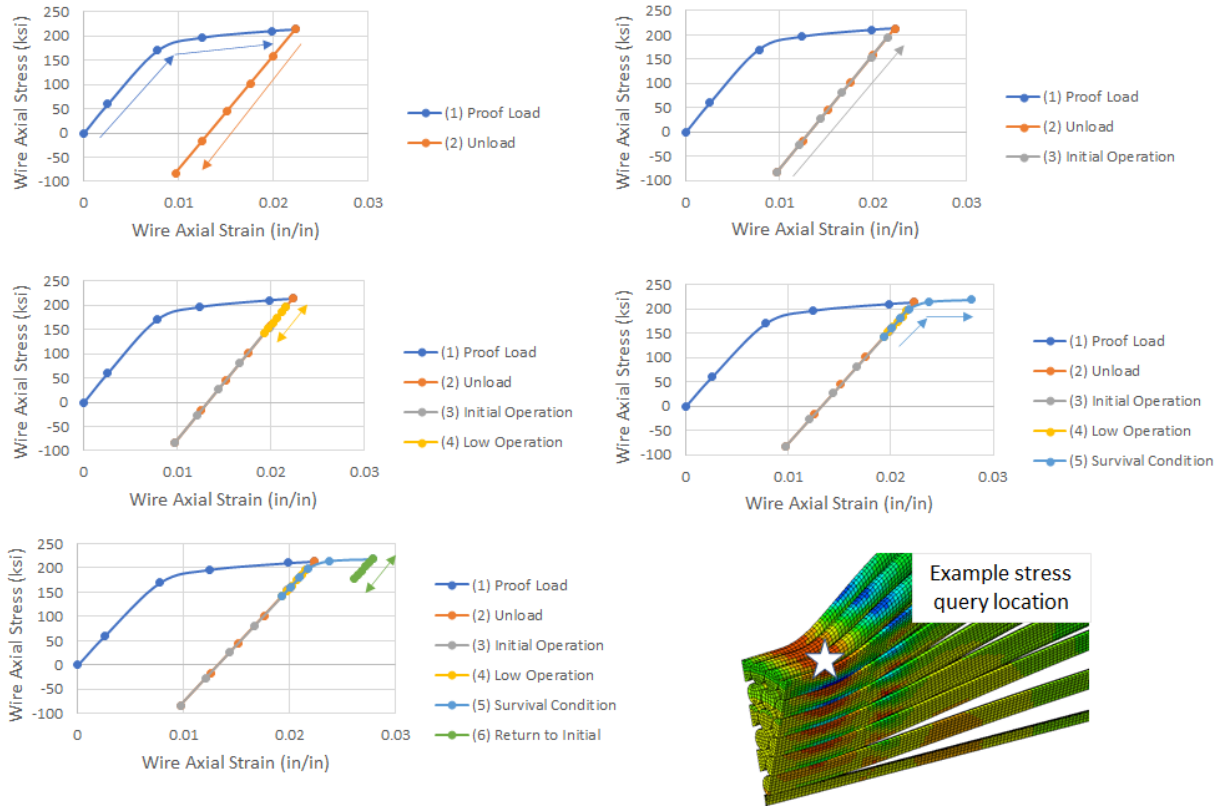


Figure C-12. Stress History and Hysteresis from Repeated Loading above Proof Load Level
Stresses Shown from Starred Location in Bottom Right Graphic.

Comparing field output plots of the yield state in each step confirms that the majority of the structure responds linearly for loading below previously achieved loads (from proof test, initial operations, or survival conditions). Figure C-13 shows the yielding portions of the socket in red for each of the six analysis steps. Subsequent elevated loading or loading reversal results in yielding of both the zinc and the wire steel, although the zinc repeatedly yields in compression during load removal while the wires do not yield.

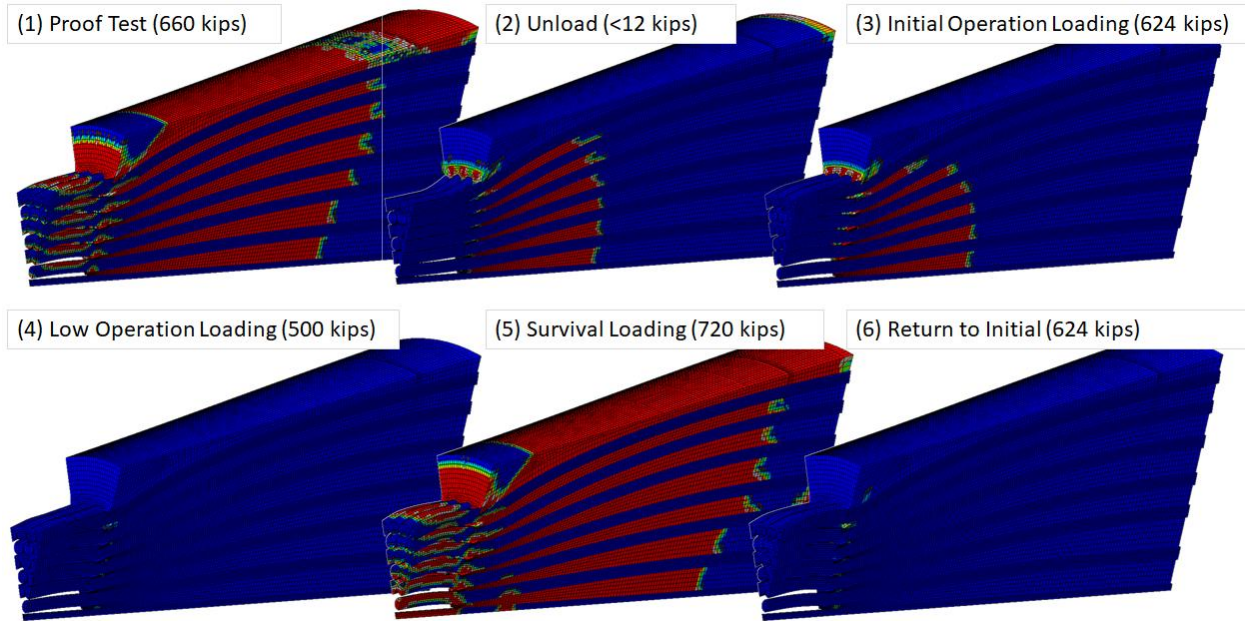


Figure C-13. Yield State (shown in red) for Zinc and Wires for each Analysis Step

Fatigue Life Characterization of Steel Wires: The observatory receiver suspension cables were subject to load fluctuations from temperature cycles, winds from tropical storms, routine daily winds, and earthquakes. *Due to lack of available information relative to the load spectra, it was not possible to predict damage accumulation with high degree of confidence.* Rather, a qualitative assessment was performed illustrating that the design will accumulate damage from cyclic loading, preventing the structure from possessing an infinite life.

The concept of a modified Goodman diagram can be employed to demonstrate the relationship between mean stress offset, cyclic stresses, and their combined effect on expected life. Qualitatively, the modified Goodman diagram gives information on whether the design space (mean and alternating stress combination) possesses effectively infinite life or whether some finite life failure is expected. The diagram is constructed by establishing axes for mean stress (horizontal) and alternating stress (vertical) and drawing one line between ultimate tensile strength and endurance limit strength and another line between yield strength on both axes. The conservative inner envelope of yield strength and endurance limit stress is the region where effectively infinite life would exist for combinations of mean and alternating stresses existing within that region. Outside this envelope, some finite lifetime is expected, dependent on the exact load history, material capability, susceptibility to environmental degradation, etc. The modified Goodman diagram for the highly loaded outer wires at the Aux M4N socket termination is indicated by the yellow oval in Figure C-14. The diagram indicates finite life due to cyclic loading conditions. The diagram was constructed for specification yield and ultimate strengths of the individual wires, but the concept can be extended to nominal strengths, design minimum strengths, or those specified by a customer.

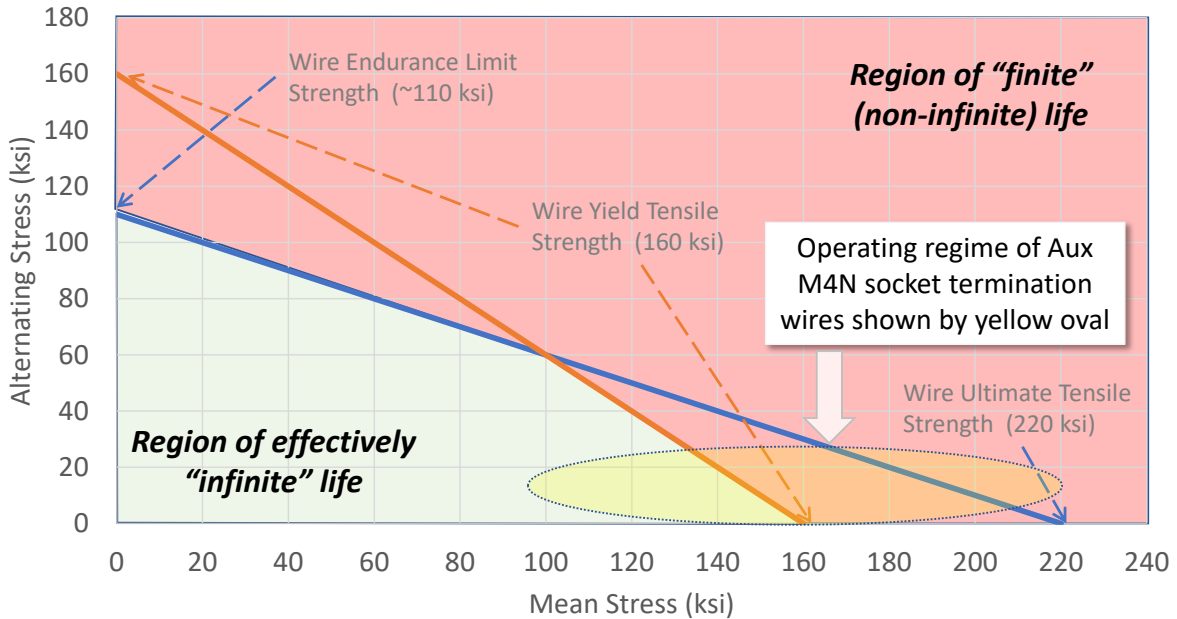


Figure C-14. Modified Goodman Diagram showing Separation of Finite and Infinite Life Regions with Annotations for Aux M4N Operational Space

The modified Goodman equation was used to qualitatively conclude that the number of cycles to failure can vary drastically depending on the assumptions made. The modified equation is as follows:

$$N = \left(\frac{\sigma_a}{\frac{(f \sigma_u)^2}{\sigma_e} \left(1 - \frac{\sigma_m}{\sigma_u} \right)} \right)^{1/b} ; \quad b = - \left(\frac{1}{3} \right) \log \left[\frac{f \sigma_u}{\sigma_e} \right]$$

where a mean stress correction is necessary due to sustained cable tension from observatory dead loads. Here, σ_a is the stress amplitude due to fluctuating loads, σ_u is the wire ultimate strength, σ_m is the mean stress in the wire, f is the fatigue strength adjustment factor (typically 0.9), b is the Basquin coefficient (approximately -0.1 for metals), and σ_e is the endurance limit. In examining the above equation, it can be seen that the ability to accommodate alternating stresses is reduced as the mean stress approaches the strength of the material.

The prediction for mean stress related to the sustained loading condition (e.g., dead loads) was estimated for the purpose of calculating a range of allowable cycles. However, because the load spectra defining the alternating cable load and the stress spectra were not fully characterized, a quantitative prediction with high confidence could not be performed. Since the sustained loads are roughly 80% to 90% of the total cable load, the remaining percentage of the load can be assigned to transient effects. Given the uncertainties in load spectra, the range of predicted cycles to failure showed anywhere from 100 to 1 million cycles, which is instructive because a finite life is predicted but the range is too big to draw conclusive statements on the amount of accumulated damage due to cyclic loading. Given the nature of the Arecibo Observatory operation, it is known that the Aux M4N successfully endured a significant number of cycles. Nonetheless, every cycle generally contributes to accumulation of damage.

In conclusion, a qualitative cumulative damage analysis considering cable load fluctuations shows that cumulative damage occurs during operation, but the total accumulation of damage is unknown due to uncharacterized load spectra.

Creep and Cyclic Loading: Generally, materials incur cumulative damage due to both sustained loading and cyclic loading, as structures are not likely operating in conditions where one of the contributors is totally absent. Per ASME Section III Division 5, accumulation of damage occurring due to sustained loading and cyclic loading can be linearly combined using Miner’s rule. This is illustrated by the interaction diagram in Figure C-15. Here, n and N_d are the number of cycles and the allowable number of cycles for the loading condition j ; t and T_d are the actual time at stress level k and the allowable time at that stress level. D is the allowable combined damage fraction. The point of this diagram is to illustrate that time-dependent degradation modes are not only due to sustained loading, but that cyclic loading can accelerate creep-related failure modes. Figure C-15 shows an example exchange rate between cyclic and time-dependent contributors to total accumulated damage.

In the Arecibo Observatory Aux M4N application, sustained loads are due to observatory dead loads, which makes up most of the total cable load envelope (in the range 80% to 90%). Comparing the alternating cable load with the mean cable load (sustained) demonstrates that the failure event was influenced by creep mechanisms. Considering creep to be a dominating factor is consistent with metallurgical observations that revealed no evidence of typical fatigue failures (e.g., beach marks and striations). However, contributions from cyclic loading cannot be entirely dismissed, as they can be masked by the occurrence of creep, and can accelerate creep-dominated failure modes and contribute to the total cumulative damage of the hardware.

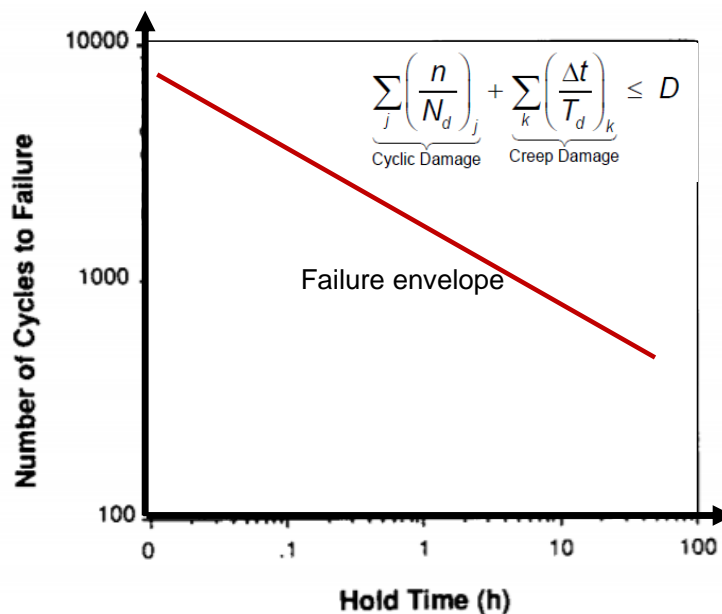


Figure C-15. Cumulative Damage Can Occur due to Combination of Cyclic Loading and Sustained Loading

F-29. The socket design had low wire structural margins and a large percentage of sustained loading, which made the design susceptible to a creep-dominated failure, likely accelerated by fluctuating cable loads.

C.4 Discussion on Transient Loading (e.g., Hurricane Maria, Earthquakes)

Structural elements cannot easily endure both near-ultimate static sustained load and large alternating loads for long periods of time. In the Aux M4N design, at operational observatory loads, the outer wires of the cable adjacent to the socket termination experience significant stresses and local yielding, and possess limited structural margin. While the transient loading of the Arecibo Observatory may be small compared with the sustained dead load, it is recognized that cyclic loading only accelerated the creep-dominated failure mechanism. Environments such as hurricanes, earthquakes, and temperature fluctuations can increase creep, per the ASME interaction curve, and reduce the life of the socket joint.

According to WJE [ref. 1], Arecibo collected wind data every 15 seconds to determine peak velocity. For Hurricane Maria, the peak recorded wind velocity was 110 mph, while the average wind speed over 15 minutes peaked at about 70 mph. It is worth reflecting on the original design that considered the “survival” condition to be 100 mph winds.

During normal daily operations, one body of data collected at 200 Hz did not show evidence of significant cable load oscillations due to wind or temperature transients. No data were provided for conditions during Hurricane Maria or for those reflective of tropical storms, hurricanes, or earthquakes. Therefore, no correlation between measured values and significant transient environments can be made. As such, the real structural response due to wind gusts or vortex shedding during transient environments are unknown and can only be qualitatively assessed as a general contributor to the accumulation of damage.

C.5 Effects of As-Built Wire “Brooming”

All results presented so far were based on a representation of the brooming condition that enables the development and use of a reasonable FEM. At the time of the analysis, the reconstruction of the as-built condition was not available. Subsequently, the team developed several representations of brooming where the wire distribution is axisymmetric around the cross section. The model version containing the largest degree of brooming is referred to as the “ideal brooming condition,” although it is recognized that such a brooming would not materialize in actual socket manufacturing. Nevertheless, analyses with various brooming conditions can provide insight into the sensitivity of brooming quality to the critical stress of the socket joint and help develop a more thorough understanding of socket termination mechanics.

The brooming operation ensures that the wires are as evenly distributed as possible within the socket so that the load distribution is efficient. Since the brooming operation is a manual operation, no two sockets are exactly alike. The exact brooming geometry and the quality of the wire-to-zinc bond are affected by the manual operations.

Forensic data were used to reconstruct the wire geometry within the socket. NASA KSC performed sectioning of the failed socket to estimate wire location at each of the exposed sections. The Aerospace Corporation subsequently used a digitizer to translate wire location information at each of the cuts into data points within the CAD software. By curve fitting through each dataset for each of the wires, it was possible to reconstruct a solid model of the wire geometry. This was also described in Section C.1.1.

This process was completed for 113 wires for which geometric data were readily available. Only partial data were available for the reconstruction of the remaining 14 wires. Figure C-16 illustrates various views of the wire geometry and shows the nonuniform wire distribution within

the socket. The figures also help the reader understand how the manual brooming operation results in a unique set of wire positions for each socket as it would be nearly impossible to repeat the same brooming twice.

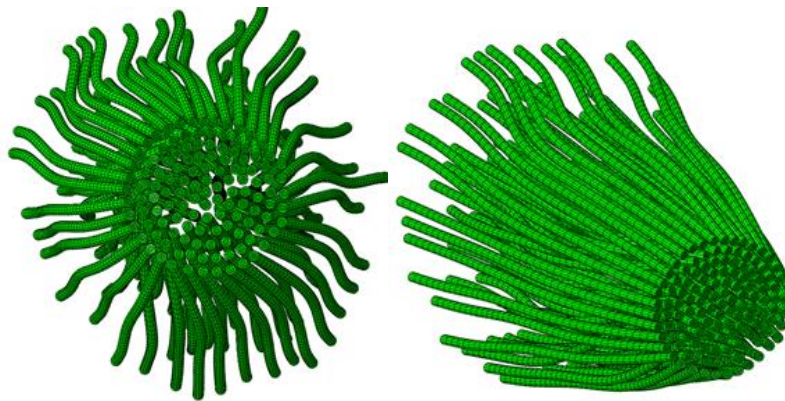


Figure C-16. Isometric Views of As-built Wire Brooming within Failed M4N Socket

Multiple models were developed that assumed various “qualities” of brooming in attempt to bound the problem. Specifically, three levels of broomed models were created: “ideal,” “medium,” and “poor.” The “medium” brooming resembled the “ideal” configuration in terms of relative distribution of wires, but the wires were broomed to a small final footprint. For the “poor” brooming, only the outermost row of wires was broomed; the inner rows were not broomed significantly.

Analysis results suggest that a more uniform distribution of wires within the zinc matrix leads to development of better confining pressure on the broomed wires, reduced excessive extrusion of the zinc, and a more predictable failure wire mode outside the socket termination. The more non-uniform the density distribution of wires over a cross section of the zinc matrix, the “worse” the brooming is considered. In Figure C-17, it is visually apparent that the as-built configuration falls somewhere between an “ideal” and a “poor” brooming, as expected. It should be noted that when making this qualitative assessment the brooming in the socket that failed could be similar to other socket “brooming,” while the “ideal” brooming configuration modeled may never be achieved in practice.

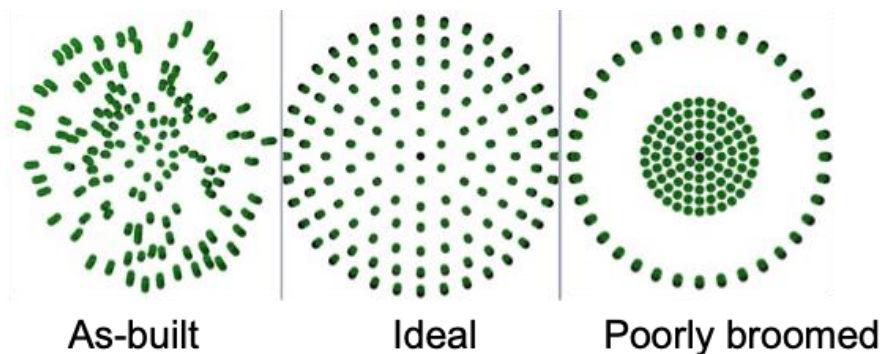


Figure C-17. As-built Wire Distribution compared with Ideal Brooming Configuration and Poorly Broomed Configuration

Analysis shows that, for marginal designs like the M4N socket, brooming quality becomes more important than designs with robust structural margin (see Figure C-18). A sensitivity analysis

was performed comparing the outer wire stresses for the three brooming configurations with decreasing levels of quality of brooming. The plastic strains and tensile stresses in the outer wires increased with decreasing quality of brooming. The proposed explanation for this phenomenon is that more brooming leads to better development of confining pressure in the narrow end of the socket that results in a more distributed load across the cable cross section. Better brooming prevents excessive zinc seating extrusion and time-dependent extrusion due to the distribution of wires through the zinc volume, resulting in a composite system that uses the entire embedded wire surface to resist flow. When there is a lesser degree of brooming, there is more zinc plastic flow, and the mechanical response exhibits a softening phenomenon (i.e., reduction of tangent modulus), which leads to a distribution of load into the outer wires as the wire and zinc continues to experience excessive seating extrusion. For poorly broomed configurations, a lower volume of high triaxial compression is predicted, which is directly correlated to the effects of confining pressure on the wires that keeps the wire-zinc bond intact; more brooming redistributes load into wires across the cross section.

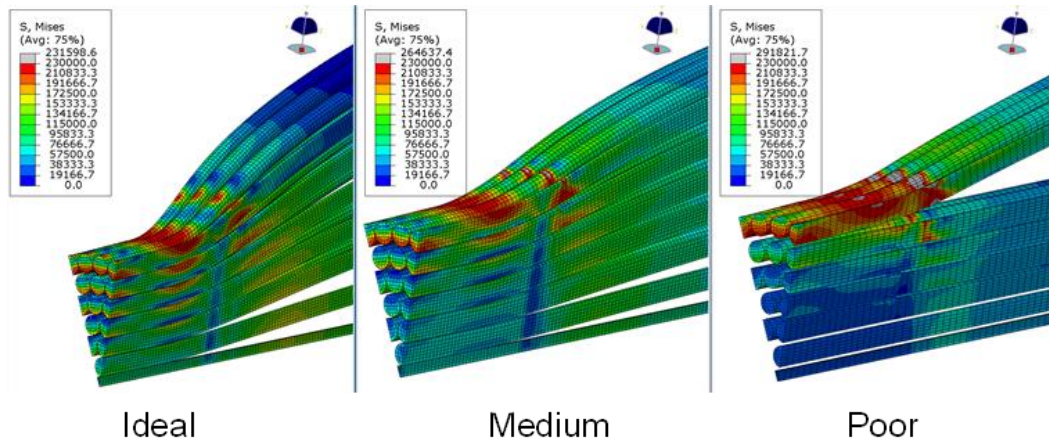


Figure C-18. Outer Wire Stresses Increase with Decreasing Levels of Quality Brooming

Qualitatively, the as-built brooming does not have wires distributed uniformly across every cross section of the socket like the ideal brooming configuration. The as-built brooming will develop higher stresses in the outer wires in comparison to the ideal brooming configuration.

This finding and discussion may seem arbitrary at first read; however, it should be recognized that brooming quality becomes increasingly important when the design is operating near its capability. Something like the level of brooming may be the explanation for why one socket fails but another one does not despite being installed at the same time and seeing the same loading profile. The workmanship sensitivity might not significantly affect capability when operating with significant margins of safety but can play a bigger role in marginal designs.

F-29. The socket design had low wire structural margins and a large percentage of sustained loading, which made the design susceptible to a creep-dominated failure, likely accelerated by fluctuating cable loads.

C.6 Effects of Defects within Zinc Slug

Forensic evidence indicated zinc voids from the manufacturing process (See Appendix A, Section 4.3). Corrosion products were also observed in the some of the zinc surfaces (see Appendix A, Section 4.4). An analytical study was pursued to examine whether zinc voids could have accelerated the failure of the outer wires. Three analytical models were developed, one with a void toward the socket face side, one with a void midway down the length of the socket, and one with a void toward the casting cap side of the socket. The voids were simulated by deleting elements representative of the zinc material. Analyses predicted negligible effects on the outer wire stresses due to the presence of these voids. All effects of the voids were limited to the local area adjacent to the voids within the socket volume and did not affect the overall stress distribution of the wires outside the socket. This is because the most highly stressed wires occur near the socket face and remain unaffected by the existence of voids a substantial distance away in the zinc. However, the analysis cannot rule out the effects of voids on time-dependent effects, local zinc damage, or damage to the wire/zinc interface that would have progressively contributed to an increase in plastic flow and affected wires elsewhere.

A separate model configuration was run where 20% of the zinc volume was removed from the casting-cap side of the socket to mimic the existence of the cavity tear that was observed just under the casting cap. The loss of zinc away from the wire outlet of the termination indicated no change in critical wire stress level and did not indicate a difference in termination capacity. Termination capacity is influenced significantly by the zinc in the narrow side of the conical volume but is largely unaffected by the zinc at the open end of the socket.

F-31. Analysis predicts that stresses in the zinc and wires are not affected by the zinc voids identified in the forensic examination of the Aux M4N socket.

C.7 Analysis Progression of Failure

An analytical exercise was undertaken to examine the load redistribution and stress concentration effects of progressively failing wires adjacent to the socket termination. The intent of the study was to quantify the stress increase of failure on adjacent wires, determine a failure pattern assuming select failed outer row wires, and qualitatively compare to forensic evidence. Figures C-19 and C-20 show the first configuration considering three failed wires at the 3 o'clock side of the cross section.

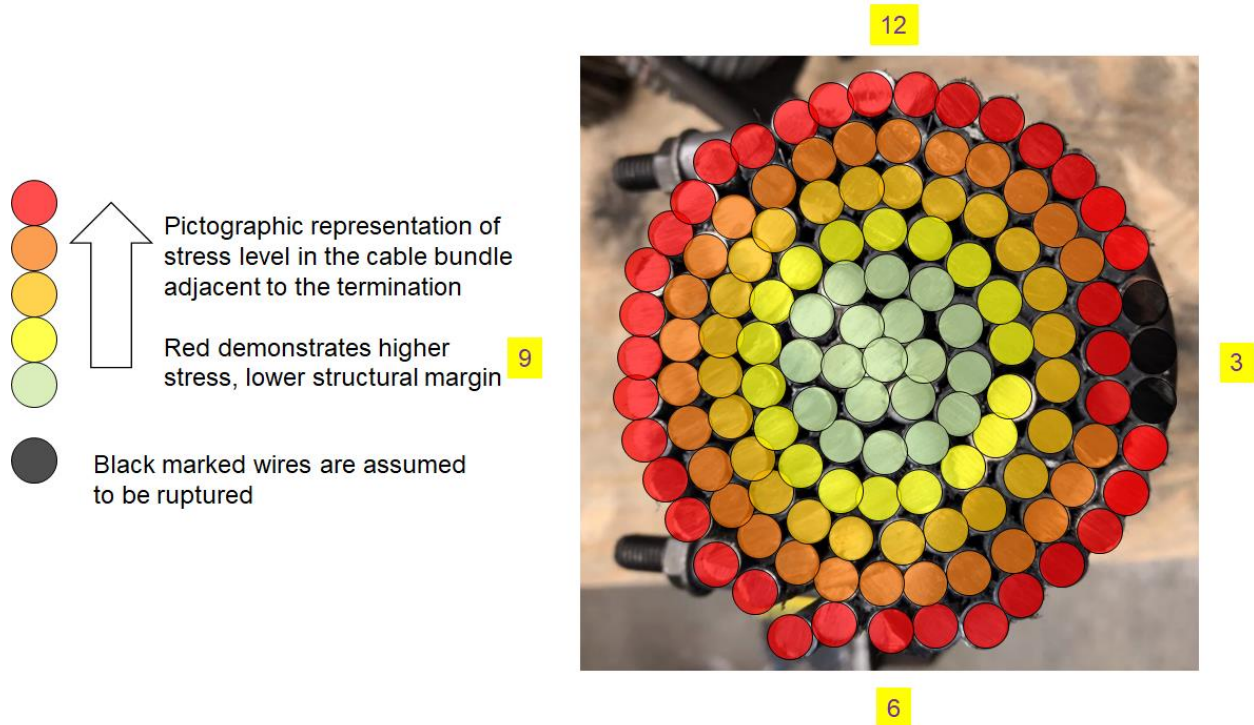


Figure C-19. Pictographic Representation of Wire Stress over Cross Section and Initially Failed Wires at 3 o'clock Side

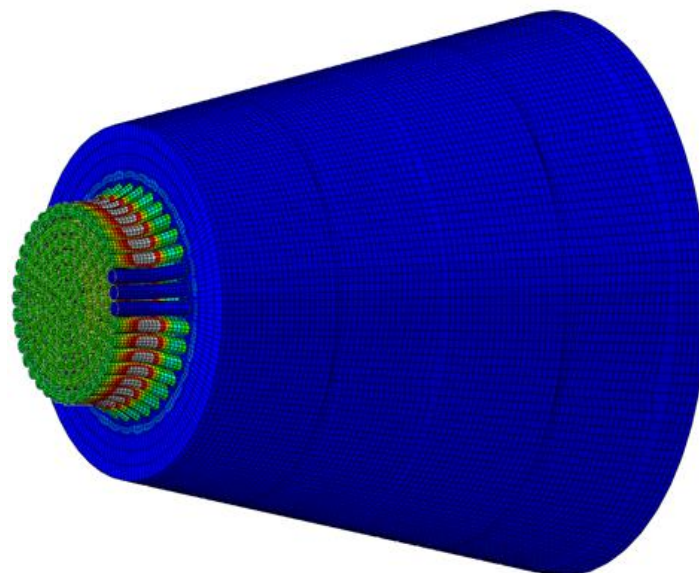


Figure C-20. FEM Visualization of Three Initially Failed Wires

Six FEAs were conducted, each with differing number of failed wires. Models containing 3, 9, 15, 21, 31, and 38 disconnected wires representing a post-fracture configuration were leveraged for the purpose of this study. Figure C-21 shows a representative change in stress distribution across the cross section, considering the increasing number of failed wires. For the first configuration of three failed wires, the adjacent wire stresses increase by roughly 5%. The stress

increase changes as the number of failed wires increases, creating more load transfer. In Figure C-21, the cross-sectional stress distribution is shown for a specific distance from the socket face, and there are complicated 3D effects that are not captured by this two-dimensional image.

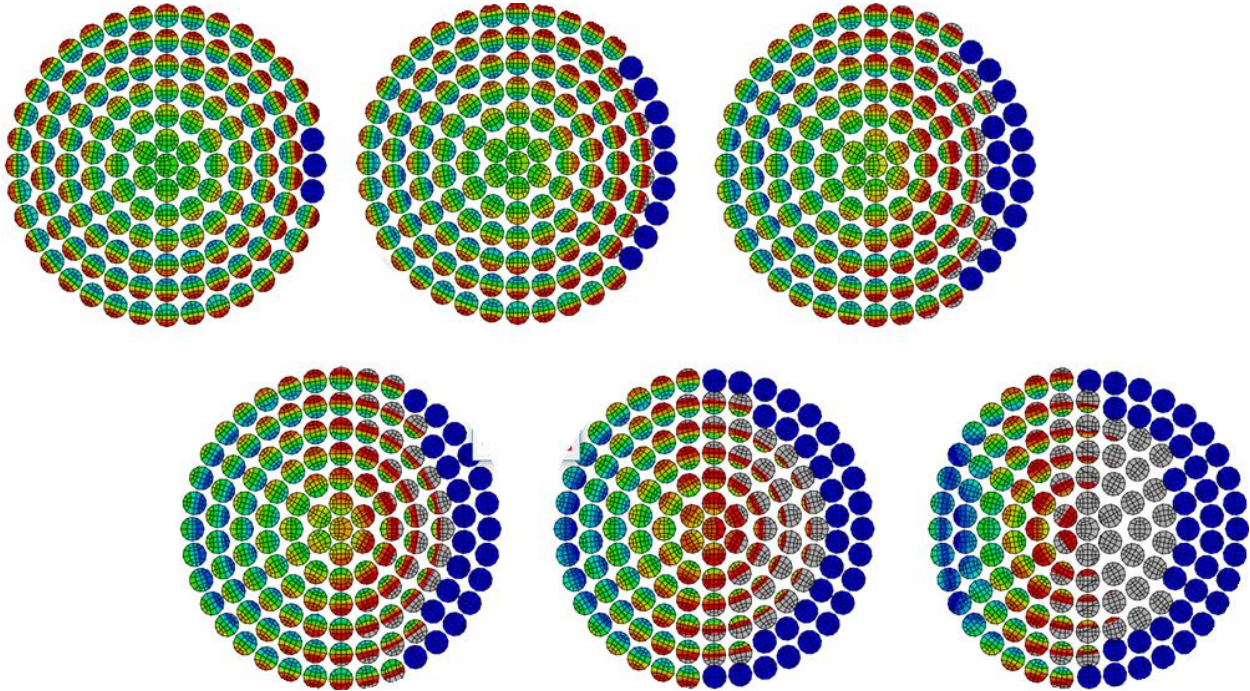


Figure C-21. Model Cross-sectional Stresses for Differing Numbers of Failed Wires showing Stress Redistribution Radially and Circumferentially

The forensics analysis identified which wires in the cross section remained intact and pulled out of the socket with the core of the cable versus those that fractured in the socket. There was a clear bias of the wire failures to one side of the socket, with a distribution of wire failures emanating radially and circumferentially from the 3 o'clock side of the socket. This can be seen in the composite image in Figure C-22. The red arrows show the theme of failure progression radially and circumferentially overlaid on the forensics cross-sectional naming and fracture type.

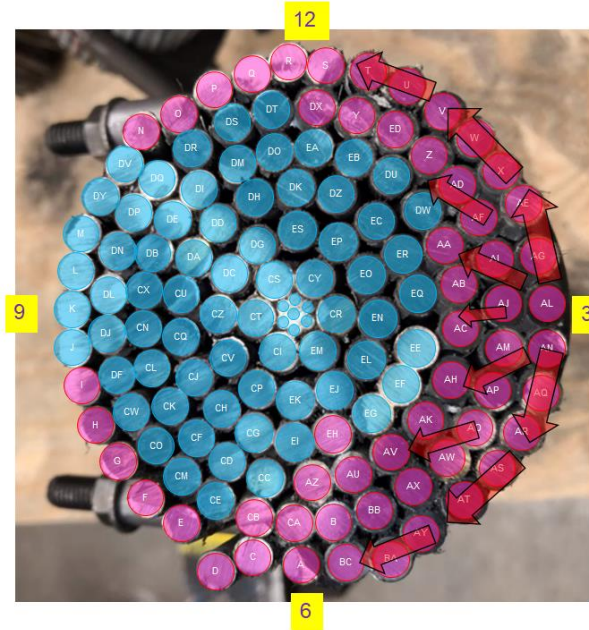


Figure C-22. Pictographic Representation of Failure Progression Overlaid on Forensics Failure Mode Coloring

Lastly, the strain distribution within the zinc is markedly different when considering only three failed wires versus 38 failed wires. The shape and magnitude of strain is compared in Figure C-23, which shows that peak plastic strains are more than 4 times those of the pristine design when considering 38 failed wires. Note that, qualitatively, the shape of the zinc strain field is roughly similar to the cross section of cable that pulled from the socket during the failure event.

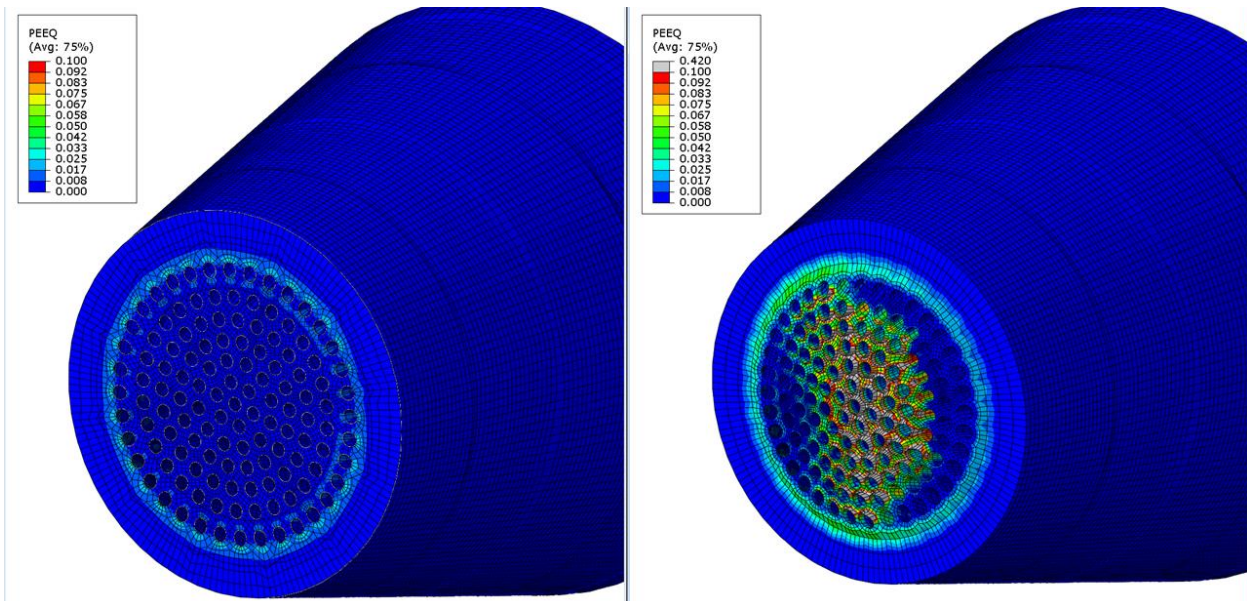


Figure C-23. Plastic Strain Field Comparison between Three (left) and 38 Failed Wires (right)

C.8 Summary and Root Cause Based on Analysis Predictions

A combination of the design factors of safety, local socket mechanics, and high dead load resulted in small or negative margins of safety for the critical outer wires adjacent to the failed socket termination. There was no structural margin to accommodate time-dependent mechanisms under sustained loading, additional loads from dynamic environments (e.g., thermal fluctuations, hurricanes, earthquakes), or degradation mechanisms such as corrosion. A hypothetical use case with a higher factor of safety (e.g., 4.0) predicts wire stresses below yield and reduced zinc yielding. In this case, the design is more accommodating of time-dependent degradation mechanisms and less sensitive to socket fabrication variability.

A key question in this study examines why this socket failed versus others at Arecibo or across the industry. While many designs exist in industry that could potentially use similar factors of safety, the Arecibo Observatory application required that most of the tension load in the cable was dead load due to constant suspension of the receiver. Fluctuating loads do occur from wind and temperature, but these are a relatively small relative to the magnitude of dead load. In contrast, other civil structural applications of structural strand socket terminations (e.g., bridges) are designed for conditions where there are live loads and dead loads and the dead load is a smaller percentage of the peak load condition. Therefore, in those applications, the strength margins are effectively larger for a longer period of the hardware life and provide comparably more margin to resist time-dependent failure mechanisms.

Despite the socket termination receiving a dedicated proof test, the intent of socket proof tests is not to screen for time-dependent degradation mechanisms such as creep, but rather to test gross manufacturing intactness by demonstrating an adequate bond between the wires and the zinc at the individual interfaces within the socket. Due to the low margins in this application, the design was less accommodating of time-dependent mechanisms (e.g., the creep-dominated failure mode) and the multitude of environments over 25 years that combined to erode already low margins until the point of failure.

Finally, analyses were leveraged to investigate the possible sequences for progression of failure based on progressively increasing the number of failed wires. Results show qualitative congruence with forensic examination of the failed wires in the socket termination cross section. Failures of outer row wires lead to stress increases in the adjacent radial and circumferential wires, which propagates around the cross section until final zinc overload.

C.9 Design Factors and Standards

C.9.1 Insufficient Design Factor of Safety

The design factors of safety and their role in the failure of socket joint are discussed in this section. The Aux M4N socket has a defined minimum rated breaking strength of the cable (1,314 kips) compared with the maximum survival cable load predicted by WJE's analysis of 720 kips [ref. 1]. This results in an effective design factor of safety of less than 1.83. Because insight into the exact factors of safety targeted in the original design and the original design analyses were unavailable, this section references the effective safety of 1.83, acknowledging that the actual safety factor targeted in the design may have been different. The following sections consider the Aux M4N socket in the context of design standards, live load to dead load ratio, factors of safety, analysis results, nonlinearity, and redundancy. It is postulated here that a 1.83 design factor of safety for the cable in question was insufficient to protect for time-

dependent creep-dominated failure modes and application in environments subject to hurricanes, earthquakes, and moisture.

C.9.2 Design Standards

The design upgrades involving the failed socket joint predated ASCE 19-96 [ref. 19], which was the requirements document governing the design of steel cables for buildings. Further, SEI/ASCE 7-02 [ref. 20] amends ASCE 19-96 steel cable design requirements. ASCE 19-96 was superseded by ASCE 19-10 [ref. 21]. While the inapplicability of ASCE 19-10 to the failed socket design is recognized, it is useful to discuss how current governing standards compare against this design. In the observatory application, the effective design factor was 1.83 or less, while current civil engineering design standards evaluate various combinations of loads (e.g., live loads, dead load) against a design factor of approximately 2.2.

According to reference 22, there is open debate concerning the structural redundancies of cable-stayed bridges (CSBs) and to what extent these structures are structurally sound under various extreme loading conditions. Table C-2, reproduced from reference 22, shows factors of safety for cables.

Table C-2. Design Factors of Safety from Various Industry Standards [ref. 22]

Standards	Design Factor of Safety for Stay cables of CSBs
Japan Road Association. Specifications for highway bridges: part II, steel bridges. Tokyo: Japan Road Association; 2017. Japanese.	2.5
EN 1993-1-11: Eurocode—3. Design of steel structures—Part 1–11: Design of structures with tension components. European standard. Brussels: European Committee for Standardization; 2006.	2.2
Post-Tensioning Institute. Recommendations for stay-cable design, testing and installation. 5th ed. Farmington Hills: Post-Tensioning Institute; 2007.	2.22
Service d'Etudes Techniques des Routes et Autoroutes. Cable stays—recommendations of French interministerial commission on prestressing. Bagneaux Cedex: Service d'Etudes Techniques des Routes et Autoroutes; 2001. French.	2.174
International Federation for Structural Concrete. Acceptance of stay cable systems using prestressing steels. Report. Lausanne: International Federation for Structural Concrete; 2005.	2.2

The selection of an appropriate design factor of safety for stayed cables is discussed in the literature, and it is argued that their selection depends on the ratio of live load to dead load stress, frequency of live load stress, fatigue, and corrosion, among other factors [ref. 22].

C.9.3 Qualification Methodology Discussion

Correspondence with subject matter experts indicated that the only testing performed at the time of Aux M4N design was a single pull test to failure that demonstrated a breaking strength in excess of the required rated breaking strength of the structural strand. Subsequently, builds were production units for Arecibo, receiving only socket proof tests and no additional qualification-type tests. No documentation of this qualification strength test was available for review.

While zinc spelter sockets are not specifically aerospace structures, it is insightful to examine the recommended design/build process of the socket as though it were aerospace hardware. Aerospace industry standards such as SMC-S-016 and NASA-STD-5001 recommend the following: (1) fatigue/fracture testing demonstrating that the design is robust to the minimum detectable flaw size to at least four times the service life; (2) thermal cyclic tests; (3) vibration tests, (4) creep tests, (5) static strength tests, and (6) acceptance tests (e.g., proof test). This comprehensive verification methodology is of high importance in aerospace applications because factors of safety are typically lower than in civil engineering applications.

Larger structural margins generally reduce the potential for fatigue and creep failure modes. In the Arecibo Observatory socket verification, the static strength qualification test did not explicitly consider other failure modes. Comparing the minimum breaking strength specified in the drawing (1,314 kips) and the WJE limit load calculation (720 kips), the effective test factor of safety was calculated as:

$$\text{Effective Qualification Strength Factor} = (1314 \text{ kips}) / (720 \text{ kips}) = 1.82$$

The acceptance test is performed at half the breaking strength, so the effective proof test factor is calculated as follows:

$$\text{Effective Proof Test Factor} = (657 \text{ kips}) / (720 \text{ kips}) = 0.91$$

In aerospace applications, the proof test factor is typically required to be >1.0 to demonstrate the hardware's capability of enduring greater than limit-load-level loading. In some instances, specifically fatigue and creep are critical, the chosen qualification and proof test factors are significantly greater than 1.0. For the Aux M4N socket in question, a proof test factor of 0.91 may demonstrate the no grossly unacceptable manufacturing conditions exist, but no credit can be taken for demonstrating margin to life or other deleterious failure modes.

Potential shortfalls of Aux M4N design/build verification include:

1. Proof test factor was <1.0.
2. Incomplete identification of failure modes associated with the Aux M4N socket. Potential failure scenarios include intra-material (e.g., adhesive failure between steel rope and zinc) or inter-material (e.g., crack propagation within the zinc itself). An analog to the design can be found with structural composites, particularly those that include face sheets bonded to a core material. In such cases, qualifying the design for life may entail dedicated subcomponent tests.
3. Socket joint fabrication is sensitive to workmanship. Testing just a single unit, as is often done for aerospace hardware, may not be appropriate. Instead, the sample size should be large enough to account for lot-to-lot variability considering material, human, and process elements. In the aerospace community, manufacturers often establish expected strength based on multiple specimens pulled from multiple builds. For such process-sensitive components, workmanship testing is critical. It may be the case that the socketing community possesses an additional body of data related to this topic, but nothing specific was made available to the authors of this investigation.

C.9.4 Redundancy

Per ASCE 19-10 Section 3.1.1, cable system structures should be configured to maximize structural redundancy, and failure or malfunction of any one local component should not result in

structural collapse. For example, in one structural application, the City of Chicago Department of Buildings required that structural engineers review the redundancy of a structure, and the city established criteria requiring the investigation of instantaneous cable failure and associated effects [ref. 23]. It is argued here that the concept of redundancy must be demonstrated for sufficient duration such that corrective actions can be implemented to prevent total collapse. Failure of a single element delaying Arecibo Observatory collapse by several weeks or months is not sufficiently redundant for corrective action to occur.

While reference 22 was not peer reviewed by NASA or The Aerospace Corporation, there are some conclusions worth noting relative to structural redundancies and factors of safety of CSBs. In reference 22, simplified FMEs of bridges were developed, and static analyses were conducted to study redundancy through a parametric study of the safety factor. The effects of overloading, cable loss, and corrosion on the structural redundancy of both bridges were investigated. The reference indicates that CSBs are sufficiently redundant at a safety factor of 2.5, and that a safety factor of 2.2 yields minimum structural redundancy for a CSB under normal loading conditions. However, it is noted that a CSB can lose its redundancy significantly at 2.2 in the case of an unexpected rupture/collapse of a stay cable.

Despite the Arecibo Observatory load ratios being proportionally different than CSB designs, the conclusions in reference 22 point to a potential deficiency in the observatory design due to lack of structural redundancy, especially considering the observatory's comparably low safety factor (~1.83) and exposure to extreme conditions (e.g., hurricanes, earthquakes). Failure of the main cable in the Arecibo Observatory application resulted in an eventual catastrophic collapse, indicating lack of structural redundancy.

C.9.5 Live Load to Dead Load (LL/DL) Ratio

In typical design, dead loads are much more certain and predictable than live loads. In the observatory application, the source for most of the cable load was from dead loads. Live loads from operation and thermal transients were a small percentage of the total cable load. Apart from live loads, extreme environments (e.g., winds and earthquake loads) contribute to the total cable load and had to be considered in the observatory's cable upgrade designs. The LL/DL ratio, its relationship to the factor of safety 1.83, and the role in the observatory failure event are further explored.

While the observatory was not designed per ASCE 19-10 [ref. 21], it is instructive to understand how the observatory design compares with this design standard. ASCE 19-10 indicates that temperature effects on cables, vibrations, deflections, and erection analysis must be evaluated for cable structures. The ASCE standard also states the minimum breaking strength of cables shall always be at least twice the maximum cable design loads, including the envelope of loading combinations of cable self-weight, structure dead load, cable pre-stress forces, and live-load and environmental-load combinations. Cables also should maintain a minimum tensile force under all loading conditions to minimize visible cable sag and the potential for induced cable vibrations. Table C-3 describes five of nine examples of various load combinations required in the evaluation.

Table C-3. Load Factors required in Evaluation of Load Combinations

Combination	Deadload	Live Load	Pretension	Wind	Earthquake	Erection	Rain
T ₁	1.0	0	1.0	0	0	0	0
T ₂	1.0	1.0	1.0	0	0	0	0
T ₃	1.0	0	1.0	0	0	0	1
T ₄	1.0	0.75	1.0				0.75
T ₅	1.0		1.0	0.6 (OR)	0.7 (OR)		

There are four other combinations in ASCE 19-10 not listed in Table 7.4.4-1. The largest load combination multiplied by 2.2 should not exceed the cable nominal breaking strength. Other reduction factors may be applicable that require consideration per ASCE 19-10, but these are not discussed here.

For the Arecibo Observatory, the cable final load is 602 kips for dead loads and potentially includes pre-tension. Under operational conditions (e.g., live load) the cable tension load is 615 kips. Survival cable load, which presumably includes loads from hurricanes and earthquakes, is 622 kips. Based on these loads, it is not possible to meet the ASCE 19-10 design factor of 2.2. With the WJE maximum predicted cable load of 720 kips, the gap is even wider against this standard.

Further, based on The Aerospace Corporation's FEM, the operational loads of the observatory cause the outer wire stress to approach the strength capacity of the wire at nearly half the rated cable breaking strength of 1,314 kips and remain high for the service life (+20 years). The zinc within the socket is also under sustained shear loads that continuously cause the outer wire stresses to increase. Per ASCE 19-10 [ref. 21], creep in cables can occur even after pre-stretching. High stress levels relative to the breaking strength will result in a creep rate that can increase the wire strains over time, thus limiting the ability to accommodate other environmental effects stemming from cyclic loading and corrosion.

This analysis postulates that the observatory design was susceptible to creep more so than a CSB design. This will be illustrated via an example that considers roughly the same cable design load as the observatory but appropportionates a greater live load percentage of the total cable load compared with that of the observatory. In many CSB designs, live load tends to be a sizeable portion of the (LL+DL), for example, in reference 22, an LL/DL ratio of 0.45 was used in the analysis of the bridge design, while an LL/DL of 0.67 was used in reference 24.

Adapting the dead load ratio for the sake of example, consider a hypothetical socket design application where the dead load and pretension cable load is 350 kips, live loads are 150 kips, and the survival loads due to wind are 170 kips. The only sustained loading is the dead load and pre-tension of the cable. Based on the socket joint FEM, this results in an outer wire stress level of 175 ksi, which is near the yield strength of the individual wires without significant yielding observed. Creep due to sustained loading at this level will result in a lower creep rate than in the Arecibo Observatory application and leave more capability in the wires to accommodate other time-dependent effects (e.g., creep). In this example, the design load combination per T₅ is still 620 kips, similar to the Arecibo Observatory application.

F-32. Socket joints in the Arecibo Observatory application were subjected to a relatively higher percentage of sustained cable load versus total load compared with a survey of bridge designs, increasing susceptibility to creep.

C.9.6 Cable Nonlinearity

Cables exhibit both geometric and material nonlinearities during operation. Cables are inelastically prestretched until individual wires settle into their final positions at a high percentage of their minimum breaking strength, which allows them to behave more predictably. Gossen [ref. 25], an expert in cable design, discusses the incongruity of how factors of safety are used in conjunction with the working stress design (WSD), where the stress, force, and deformation behaviors are assumed to be linear even though the behavior of the cable is nonlinear. Gossen reports that the factor of safety is intended to account for accidental overloads, material variability, and fabrication imperfections. *Note that the intended purpose of safety factors is inconsistent across industries.* The argument made by Gossen is that due to the nonlinear nature of the cable, the structural margins remaining against overload can vary significantly and remain indeterminate unless the structure is analyzed beyond nominal conditions. In most standards, the loads effects are superimposed with varying amplification factors, but this is not applicable for nonlinear cables.

To illustrate this point, an independent FEM of the socket joint was developed to understand the relationship between stress and the load applied for two zinc material models. The rated breaking strength of the cable is 1,314 kips, so at half the breaking strength a linear stress response of the wire is expected. However, due to the complexity in the geometry and the nonlinear behavior of the zinc and the wires, the outer wire stress approaches the ultimate strength at half the cable breaking strength and exhibits a nonlinear response at one-fourth of the breaking strength of the cable, as shown in Figure C-24. The model illustrates a nonlinear scaling of outer wire stress to load applied.

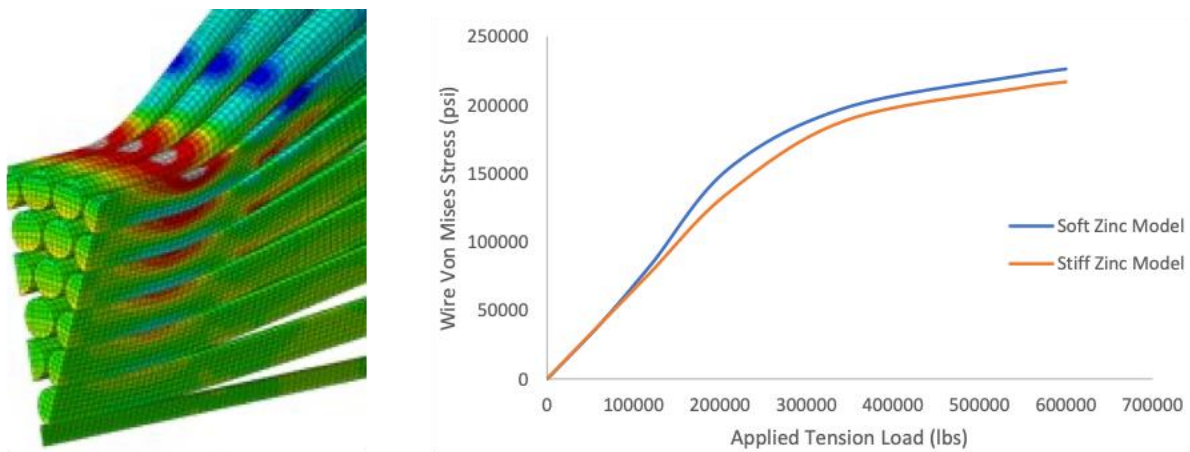


Figure C-24. Stress Response in Wire is Nonlinear with Increasing Applied Tension Load

The finite element results confirm the thesis by Gossen [ref. 25] that “the ultimate load approach may result in individual cables stressed beyond their accepted level under service loads, while still satisfying the ultimate load design requirements. It is apparent that the analysis and design of

these structures can be much more laborious than what is common in the design and analysis of conventional structures.”

C.9.7 Design Factors of Safety

ASCE 19-10 [ref. 21] requires a minimum design factor of safety of 2.2 for steel cables. WJE [ref. 1] conducted a survey of the factors of safety required by other standards and stated:

“AASHTO Movable Bridge Specifications provides for cable factors of safety of between 4 and 8 depending on the function of the cable, while the U.S. Department of the Interior Bureau of Reclamation suggested a factor of safety of 5 for hoisting ropes due to the expected application of frequent dynamic loads and possible abrasion during normal service applications.”

The Crosby Group design manual for socket designs indicates a factor of safety ranging between 3 and 5 depending on the specific application [refs. 26-28].

Returning to the FEM of the Aux M4N socket, one-fifth of the rated breaking strength of the cable is 262 kips, and the outer wire stress at this load is well below the yield strength of the wire. The nonlinearity in the stress response at this cable load is associated with the zinc behavior and unrelated to material plasticity. At one-third the rated cable breaking strength, the outer wire stress exhibits mild yielding. *This further supports the use of a higher factor of safety than the 1.83 used in this application.*

In typical design, dead loads are much more certain and predictable than live loads. In the observatory application, the source of most of the cable load was dead load. Live loads from operation and thermal transients were a small percentage of the total cable load. Apart from live loads, extreme environments such as winds and earthquake loads contribute to the total cable load and had to be considered in the observatory’s cable upgrade designs.

F-33. The Arecibo Observatory had an effective design factor of safety of ≤ 1.83 , which is significantly less than the minimum suggested by literature (i.e., >2.1) to ensure structural redundancy in the event of cable failure.

C.9.8 Summary

Wire stress does not scale linearly with increasing cable load, so applying standard factors of safety to cable designs results in uncertainty regarding whether the cable is structurally robust. The complexity in this evaluation is compounded by the known socket-to-socket fabrication variability.

Design standards and literature point to the importance of designing in structural redundancy when employing stayed-cable socket designs. It is recognized, however, that the level of redundancy to which the Arecibo Observatory was intentionally designed is unknown, and it is possible that the observatory was never meant to be redundantly designed in the first place. Nevertheless, a study on bridges found a factor of safety of 2.5 can yield sufficient redundancy in CSBs. The observatory application used a value of 1.83 against maximum cable load, but as soon as one socket failure occurred, other cables eventually failed. The collapse of the structure indicates the lack of structural redundancy and is consistent with the use of a lower factor of safety.

The 1.83 factor of safety in the observatory application is below cable factor of safety recommendations in the AASHTO Movable Bridge Specifications [ref. 29], the Crosby Group design manual [ref. 26], and various ASME standards. If the recommended higher factors were used in the observatory cable designs, then the outer wire stress would have been below the yield strength of the material and would have been more likely to accommodate creep, fatigue, and corrosion failure mechanisms.

Finally, the dead loads in the Arecibo application were a significant percentage of the total cable load compared with CSBs, where live loads can be a larger percentage of the total cable load. For the same cable load, the observatory application had higher sustained load over 25 years compared with a bridge design, resulting in higher creep rates and leaving no structural margin for cyclic loading from hurricanes and earthquakes. Further, the observatory application had lower structural margins to ASCE 19-10 [ref. 21] compared with a generic bridge design.

Appendix D. Arecibo Reference Drawings, 1992

NATIONAL ASTRONOMY AND IONOSPHERE CENTER CORNELL UNIVERSITY ARECIBO RADIO OBSERVATORY GREGORIAN UPGRADING

CONTRACT NO. 92.146

LIST OF DRAWINGS

CONTRACT DRAWING NO.	S-1A	TITLE SHEET	CONTRACT DRAWING NO.	S-26	AZIMUTH TROLLEY LINK TRUSS
CONTRACT DRAWING NO.	S-1	GENERAL I	CONTRACT DRAWING NO.	S-27	AZIMUTH FEED TRACK
CONTRACT DRAWING NO.	S-2	GENERAL II	CONTRACT DRAWING NO.	S-28	FEED ARM MISCELLANEOUS I
CONTRACT DRAWING NO.	S-3	ANCHORAGES I	CONTRACT DRAWING NO.	S-29	FEED ARM MISCELLANEOUS II
CONTRACT DRAWING NO.	S-4	ANCHORAGES II	CONTRACT DRAWING NO.	S-30	GREGORIAN TROLLEY I
CONTRACT DRAWING NO.	S-5	ANCHORAGE REINFORCING	CONTRACT DRAWING NO.	S-31	GREGORIAN TROLLEY II
CONTRACT DRAWING NO.	S-6	ANCHORAGE METALWORK	CONTRACT DRAWING NO.	S-32	GREGORIAN TROLLEY III
CONTRACT DRAWING NO.	S-7	TOWER SADDLE I	CONTRACT DRAWING NO.	S-33	GREGORIAN ENCLOSURE
CONTRACT DRAWING NO.	S-8	TOWER SADDLE II	CONTRACT DRAWING NO.	S-34	GREGORIAN SUPPORT SYSTEM I
CONTRACT DRAWING NO.	S-9	FEED PLATFORM I	CONTRACT DRAWING NO.	S-35	GREGORIAN SUPPORT SYSTEM II
CONTRACT DRAWING NO.	S-10	FEED PLATFORM II	CONTRACT DRAWING NO.	S-36	GREGORIAN SUPPORT SYSTEM III
CONTRACT DRAWING NO.	S-11	FEED PLATFORM III	CONTRACT DRAWING NO.	S-37	GREGORIAN SUPPORT SYSTEM IV
CONTRACT DRAWING NO.	S-12	FEED PLATFORM IV	CONTRACT DRAWING NO.	S-37A	GREGORIAN SUPPORT SYSTEM V
CONTRACT DRAWING NO.	S-12A	FEED PLATFORM V	CONTRACT DRAWING NO.	S-38	GREGORIAN SUPPORT SYSTEM VI
CONTRACT DRAWING NO.	S-13	CABLE DETAILS	CONTRACT DRAWING NO.	S-39	FEED MODULE I
CONTRACT DRAWING NO.	S-13A	TENSIONING CABLE SYSTEM	CONTRACT DRAWING NO.	S-40	FEED MODULE II
CONTRACT DRAWING NO.	S-14	FEED ARM REINFORCING I	CONTRACT DRAWING NO.	S-41	FEED MODULE FRAMING I
CONTRACT DRAWING NO.	S-15	FEED ARM REINFORCING II	CONTRACT DRAWING NO.	S-42	FEED MODULE FRAMING II
CONTRACT DRAWING NO.	S-16	FEED ARM REINFORCING III	CONTRACT DRAWING NO.	S-43	FEED MODULE FRAMING III
CONTRACT DRAWING NO.	S-17	FEED ARM REINFORCING IV	CONTRACT DRAWING NO.	S-44	AZIMUTH TROLLEY I
CONTRACT DRAWING NO.	S-18	FEED ARM REINFORCING V	CONTRACT DRAWING NO.	S-45	AZIMUTH TROLLEY II
CONTRACT DRAWING NO.	S-19	FEED ARM REINFORCING VI	CONTRACT DRAWING NO.	S-46	AZIMUTH TROLLEY III
CONTRACT DRAWING NO.	S-20	FEED ARM OUTRIGGERS I	CONTRACT DRAWING NO.	S-47	TOWER COLLARS STEEL PLATFORMS AND LADDERS
CONTRACT DRAWING NO.	S-21	FEED ARM OUTRIGGERS II			
CONTRACT DRAWING NO.	S-22	FEED ARM OUTRIGGERS III			
CONTRACT DRAWING NO.	S-23	FEED ARM OUTRIGGERS IV			
CONTRACT DRAWING NO.	S-24	ELEVATION RAIL AND RACK GEAR I			
CONTRACT DRAWING NO.	S-25	ELEVATION RAIL AND RACK GEAR II			

NATIONAL ASTRONOMY AND IONOSPHERE CENTER
CORNELL UNIVERSITY
ARECIBO RADIO OBSERVATORY
GREGORIAN UPGRADING

TITLE SHEET

AW AMMANN & WHITNEY, CONSULTING ENGINEERS
NEW YORK, NEW YORK

DRAWN BY:	APPROVED:	DATE:
DESIGNED BY:		SCALE: NONE
CHECKED BY:		DWG. NO. S-1A

FILE #ARTITL

CABLE TENSIONS - STRENGTHENED CABLE SYSTEM									
CABLES MK	101	102	103	104	301	302	303	304	305
NO.	12	5	5	5	6	2	2	2	6
DIAMETER	3"	3 1/4"	3 1/4"	3 1/4"	3 1/4"	3 5/8"	3 5/8"	3 5/8"	1 1/2"
MINIMUM BREAKING STRENGTH (KIPS)	1044	1212	1212	1212	1314	1614	1614	1614	290
TENSION PER CABLE									
(I) INITIAL TENSION UNDER ALL DEAD LOADS									
EXISTING*	527	593	541	566	—	—	—	—	—
INITIAL ERECTION	307	381	351	354	450	544	495	544	2.5
FINAL	480	543	503	514	602	728	662	727	24
(II) OPERATIONAL LOADS	493	561	519	530	615	746	678	743	59
(III) SURVIVAL CONDITION	496	577	532	540	622	769	698	760	2.5
DESCRIPTION	MAIN CABLES		MAIN BACKSTAY CABLES		AUX. CABLES	AUX. BACKSTAY CABLES			TIE DOWNS
	EXISTING					NEW			

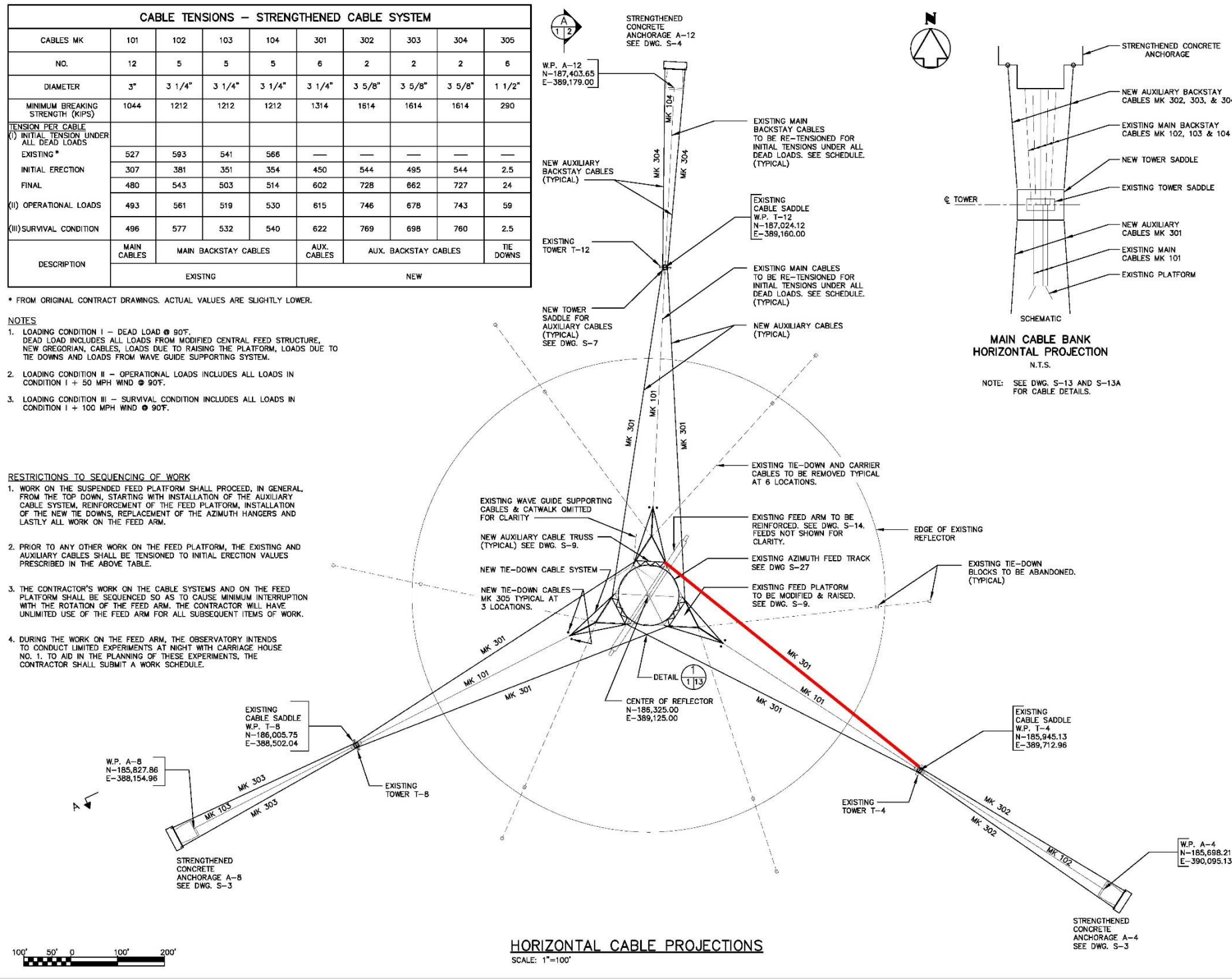
* FROM ORIGINAL CONTRACT DRAWINGS. ACTUAL VALUES ARE SLIGHTLY LOWER.

NOTES

- LOADING CONDITION I - DEAD LOAD @ 90°. DEAD LOAD INCLUDES ALL LOADS FROM MODIFIED CENTRAL FEED STRUCTURE, NEW GREGORIAN CABLES, LOADS DUE TO RAISING THE PLATFORM, LOADS DUE TO TIE DOWNS AND LOADS FROM WAVE GUIDE SUPPORTING SYSTEM.
- LOADING CONDITION II - OPERATIONAL LOADS INCLUDES ALL LOADS IN CONDITION I + 50 MPH WIND @ 90°.
- LOADING CONDITION III - SURVIVAL CONDITION INCLUDES ALL LOADS IN CONDITION I + 100 MPH WIND @ 90°.

RESTRICTIONS TO SEQUENCING OF WORK

- WORK ON THE SUSPENDED FEED PLATFORM SHALL PROCEED, IN GENERAL, FROM THE TOP DOWN, STARTING WITH INSTALLATION OF THE AUXILIARY CABLE SYSTEM, REINFORCEMENT OF THE FEED PLATFORM, INSTALLATION OF THE NEW TIE DOWNS, REPLACEMENT OF THE AZIMUTH HANGERS AND LASTLY ALL WORK ON THE FEED ARM.
- PRIOR TO ANY OTHER WORK ON THE FEED PLATFORM, THE EXISTING AND AUXILIARY CABLES SHALL BE TENSIONED TO INITIAL ERECTION VALUES PRESCRIBED IN THE ABOVE TABLE.
- THE CONTRACTOR'S WORK ON THE CABLE SYSTEMS AND ON THE FEED PLATFORM SHALL BE SEQUENCED SO AS TO CAUSE MINIMUM INTERRUPTION WITH THE ROTATION OF THE FEED ARM. THE CONTRACTOR WILL HAVE UNLIMITED USE OF THE FEED ARM FOR ALL SUBSEQUENT ITEMS OF WORK.
- DURING THE WORK ON THE FEED ARM, THE OBSERVATORY INTENDS TO CONDUCT LIMITED EXPERIMENTS AT NIGHT WITH CARRIAGE HOUSE NO. 1. TO AID IN THE PLANNING OF THESE EXPERIMENTS, THE CONTRACTOR SHALL SUBMIT A WORK SCHEDULE.



GENERAL NOTES

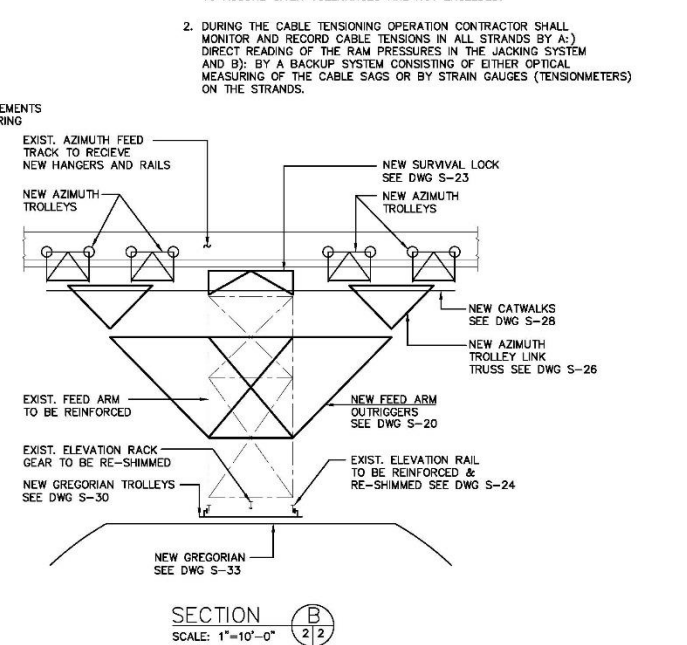
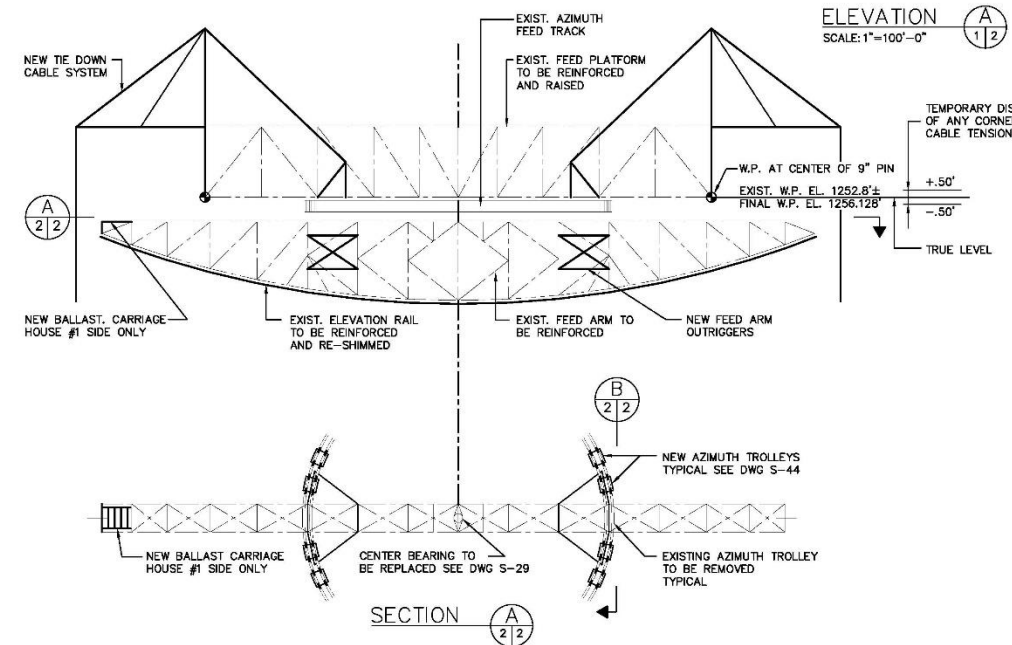
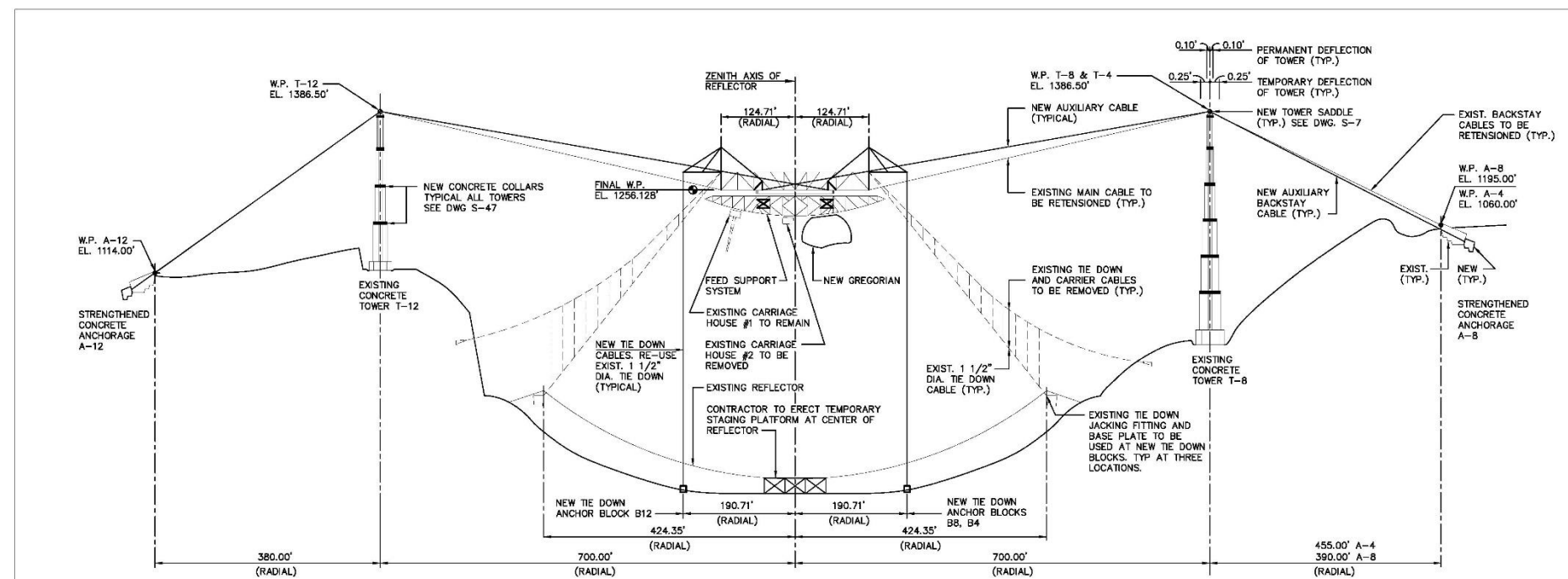
- (UNLESS OTHERWISE SHOWN OR NOTED)
- ELEVATIONS ARE IN FEET AND BASED ON THE USGS DATUM FOR PUERTO RICO, FOR WHICH MEAN SEA LEVEL IS 0.00 FT.
 - WORK POINT COORDINATES OF THE EXISTING STRUCTURE ARE IN FEET AND BASED ON THE PUERTO RICO DATUM, LAMBERT PROJECTION, PUERTO RICO ZONE.
 - STRUCTURAL STEEL SHAPES AND PLATES SHALL CONFORM TO ASTM STANDARD A572 GRADE 50.
 - SQUARE AND RECTANGULAR STRUCTURAL TUBING SHALL CONFORM TO ASTM STANDARD A500 GRADE B.
 - STRUCTURAL STEEL PIPE SHALL CONFORM TO ASTM STANDARD A501.
 - STEEL CASTINGS SHALL CONFORM TO ASTM STANDARD A148 GRADE 90-80.
 - THREADED RODS SHALL CONFORM TO ASTM STANDARD A576 GRADE 1045. NORMALIZE TO MIN. YIELD OF 50 KSI AND MIN. U.T. 90 KSI. MAGNIFLUX TO ASTM E138 (CIRCULAR AND LONGITUDINAL MAGNETIZATION REQUIRED.)
 - ALL BOLTED CONNECTIONS SHALL BE MADE OF HIGH STRENGTH STEEL BOLTS, FRICTION TYPE, TIGHTENED BY THE TURN-OF-THE-NUT METHOD. BOLTS, NUTS, AND WASHERS SHALL CONFORM TO ASTM STANDARD A325.
 - ALL HIGH STRENGTH STEEL BOLTS TO BE 7/8 INCH DIAMETER EXCEPT AS NOTED.
 - STRUCTURAL STRAND SHALL CONFORM TO ASTM STANDARD A586 PREMIUM GRADE WITH CLASS A GALVANIZED COATING ON ALL WIRES.
 - PIN HOLES SHALL BE REAMED WITH PLATES FULLY ASSEMBLED.
 - WELDING SHALL CONFORM TO AMERICAN WELDING SOCIETY STANDARD D.11. (BRIDGE SPECIFICATIONS SHALL GOVERN.)
 - ALL FULL PENETRATION WELDS SHALL BE TESTED ULTRASONICALLY.
 - ALL CABLE END FITTINGS, END BLOCKS, RODS, PINS AND ACCESSORIES SHALL BE GALVANIZED IN ACCORDANCE WITH ASTM A123 OR A153, AS APPLICABLE.
 - ALL PINS SHALL BE FORGED STEEL CONFORMING TO ASTM A521 CLASS AG. SEE TYPICAL DETAIL ON DRAWING S-13.
 - FOR ALL PAINTING SYSTEMS REFER TO SPECIFICATIONS.
 - FIELD WELDS SHALL BE MADE WITH E7018 LOW HYDROGEN ELECTRODES.
 - ALL CONCRETE SHALL BE NORMAL WEIGHT STONE CONCRETE WITH A MINIMUM COMPRESSIVE STRENGTH OF 3000 PSI AFTER 28 DAYS.
 - CONCRETE REINFORCEMENT SHALL BE GRADE 60 DEFORMED BARS CONFORMING TO ASTM STANDARD A615.
 - REINFORCING SHALL BE DETAILED ACCORDING TO THE MANUAL OF STANDARDS FOR DETAILING CONCRETE REINFORCEMENT AC - 315.
 - CABLE END FITTINGS SHALL BE PROOF LOADED TO 50% OF THE SPECIFIED BREAKING STRENGTH.
 - THE CONTRACTOR SHALL SUBMIT FOR APPROVAL BY THE ENGINEER, WORKING DRAWINGS SHOWING ERECTION SEQUENCES AND PROCEDURES, STRUCTURAL ELEMENTS, CONNECTIONS, AND ALL RELATED DETAILS.
 - SHOP DRAWINGS OF THE EXISTING STRUCTURE WILL BE MADE AVAILABLE. THE CONTRACTOR IS EXPECTED TO WORK THESE SHOP DRAWINGS IN CONJUNCTION WITH THE CONTRACT DOCUMENTS. IT WILL BE THE CONTRACTOR'S RESPONSIBILITY TO VERIFY ALL EXISTING CONDITIONS IN THE FIELD BEFORE PROCEEDING WITH FABRICATION.
 - ALUMINUM PLATES AND SHAPES SHALL BE 6061-T6.
 - FASTENERS FOR ALUMINUM SHAPES AND PLATES SHALL CONFORM TO ASTM A193 CLASS 2, GR. B8T OR GR. B8M.
 - WELDING FOR ALUMINUM SHALL BE IN ACCORDANCE WITH THE ALUMINUM STRUCTURAL WELDING CODE ANSI/AWS D1.2-90.

NATIONAL ASTRONOMY AND IONOSPHERE CENTER
 CORNELL UNIVERSITY
 ARECIBO RADIO OBSERVATORY
 GREGORIAN UPGRADING

GENERAL I

AW AMMANN & WHITNEY, CONSULTING ENGINEERS
 NEW YORK, NEW YORK

DRAWN BY:	APPROVED	DATE:
DESIGNED BY:		SCALE: 1"=100'
CHECKED BY:		DWG. NO. S-1



FEED SUPPORT SYSTEM

- NOTES:**
- CONTRACTOR SHALL MONITOR TOWER DEFLECTIONS DURING CONSTRUCTION TO ASSURE GIVEN TOLERANCES ARE NOT EXCEEDED.
 - DURING THE CABLE TENSIONING OPERATION CONTRACTOR SHALL MONITOR AND RECORD CABLE TENSIONS IN ALL STRANDS BY A: DIRECT READING OF THE RAM PRESSURES IN THE JACKING SYSTEM AND B: BY A BACKUP SYSTEM CONSISTING OF EITHER OPTICAL MEASURING OF THE CABLE SAGS OR BY STRAIN GAUGES (TENSIONMETERS) ON THE STRANDS.

FEED SUPPORT SYSTEM BALANCING REQUIREMENTS AND USE LIMITATIONS

- WITH EQUAL TIE DOWN TENSIONS AT EACH APEX, THE PLATFORM SHALL BE LEVEL WITH THE GREGORIAN AT 10 DEGREES APPROXIMATELY AND CARRIAGE HOUSE 1 AT 13 DEGREES APPROXIMATELY.
- FEED ARM COUNTERWEIGHT GROSS WEIGHT SHALL NOT EXCEED 54 KIPS. FINAL COUNTERWEIGHT LOAD WILL DEPEND UPON THE FINAL WEIGHT OF THE GREGORIAN AND THE WEIGHT AND POSITION OF THE FAN COIL UNITS, PUMPS AND ARTICULATED ARM ON THE FEED ARM.
- CARRIAGE HOUSE 1 MAY BE LOADED TO A GROSS WEIGHT OF 40 KIPS MAXIMUM. THE GROSS WEIGHT OF THE GREGORIAN SHALL NOT EXCEED 180 KIPS.
- EXCEPT AS OTHERWISE PERMITTED BY NOTES 5 AND 6 BELOW, THE GREGORIAN AND CARRIAGE HOUSE 1 SHALL BE OPERATED IN SLAVE POSITIONS. THIS REQUIREMENT IS MANDATORY FOR STRUCTURAL SAFETY WHEN THE GREGORIAN IS BETWEEN ITS STOW POSITION (7.3 DEGREES) AND 20 DEGREES.
- WHEN THE GREGORIAN IS STOWED, CARRIAGE HOUSE 1 MAY BE OPERATED OVER ITS NORMAL RANGE BETWEEN MINUS 2 DEGREES (SLIGHTLY ON THE GREGORIAN SIDE) AND 20 DEGREES.
- WHEN CARRIAGE HOUSE 1 IS STOWED, MOVEMENT OF THE GREGORIAN SHALL BE RESTRICTED BETWEEN THE ZENITH AND ITS STOW POSITION.
- DURING ACTIVE CONTROL WITH THE TIE DOWN CABLES, THE MAXIMUM TENSION IN ANY TIE DOWN SHALL NOT EXCEED 59 KIPS, BROKEN DOWN AS FOLLOWS PER CABLE:
 PRESTRESS AT 90 DEGREES F - 24 KIPS
 ACTIVE PULL DOWN DUE TO 30 DEGREE TEMP DROP - 16 KIPS
 ACTIVE PULL DOWN DUE TO UNBALANCED MOMENT - 19 KIPS
- THE AGGREGATE TENSION IN ALL SIX TIE DOWNS SHALL NOT EXCEED 240 KIPS.
- UNDER STOW CONDITIONS, THE TENSION IN EACH TIE DOWN CABLE SHALL BE REDUCED TO 2.5 KIPS.

FEED SUPPORT SYSTEM WEIGHT INCREASE TABLE		(KIPS)
1.0 FEED PLATFORM		
1.1	MAINTRUSS REINFORCEMENT, AUXILIARY CABLE TRUSSES AND CONNECTIONS	70.0
1.2	NEW TIE DOWN CABLE SYSTEM	48.0
1.3	NEW TIE DOWN CABLE PRESTRESS: OPERATIONAL SURVIVAL	144.0
	OPERATIONAL SURVIVAL	15.0
		267.0
2.0 AZIMUTH FEED TRACK		
2.1	ADDITIONAL AZIMUTH TROLLEYS INCL. DRIVES	53.0
2.2	NEW HANGERS (NET INCREASE)	3.3
2.3	LINK TRUSSES	22.0
		78.3
3.0 FEED ARM		
3.1	REINFORCEMENT	62.0
3.2	OUTRIGGERS	48.0
3.3	ELEVATION RAIL AND RACK GEAR SHIM BLOCKS (NET INCREASE)	5.0
3.4	ELEVATION RAIL GUIDE ANGLES	4.0
3.5	BALLAST PLATFORM AND BALLAST	54.0
3.6	TRANSMITTER EQUIPMENT INCL. HEAT EXCHANGERS PUMPS, ARTICULATED ARM, PIPING, CONDUIT, WATER, ETC. (NET INCREASE)	15.0
3.7	CATWALKS AND PLATFORMS (NET INCREASE)	.5
3.8	CARRIAGE HOUSE NO. 2 REMOVED	-33.0
		155.5
4.0 EXISTING TIEDOWN CABLES REMOVED		-50.0
5.0 GREGORIAN		
5.1	ALUMINUM DOME INCL. BOTT. CAP AND ROOF	42.0
5.2	SECONDARY REFLECTOR INCL. BACKUP TRUSSES	25.0
5.3	TERTIARY REFLECTOR	2.0
5.4	GREGORIAN TROLLEYS	11.0
5.5	ELEVATION DRIVE SYSTEM INCL. HYDRAULICS, TRANSVERSE BEAMS, COLLAR TRUSS, DRAG LINK BEAMS, GUIDE ROLLERS	18.0
5.6	SUPERSTRUCTURE INCL. LONGITUDINAL TRUSSES, TRANSVERSE BEAMS, COLLAR TRUSS, DRAG LINK BEAMS, GUIDE ROLLERS	37.0
5.7	FEED MODULE INCL. FRAMING, WALLS, ROTATING FEED FLOOR, KLYSTRON FLOOR, SERVICE PLATFORM STAIRS AND CATWALKS	12.0
5.8	FEEDS	6.0
5.9	TRANSMITTER EQUIPMENT INCL. KLYSTRONS, ELECTRONICS, SWITCH GEAR, CONSOLES, PIPING AND WATER	15.0
5.10	VENTS, FANS, AIRCONDITIONERS	2.0
		170.0
TOTAL INCREASE OPERATIONAL		615.8
TOTAL INCREASE SURVIVAL		496.8

NOTE: CONTRACTOR SHALL PROVIDE OWNER WITH A FINALIZED FEED SUPPORT SYSTEM WEIGHT INVENTORY TO INCLUDE ALL ITEMS ADDED AND ALL ITEMS REMOVED FROM FEED SUPPORT SYSTEM.

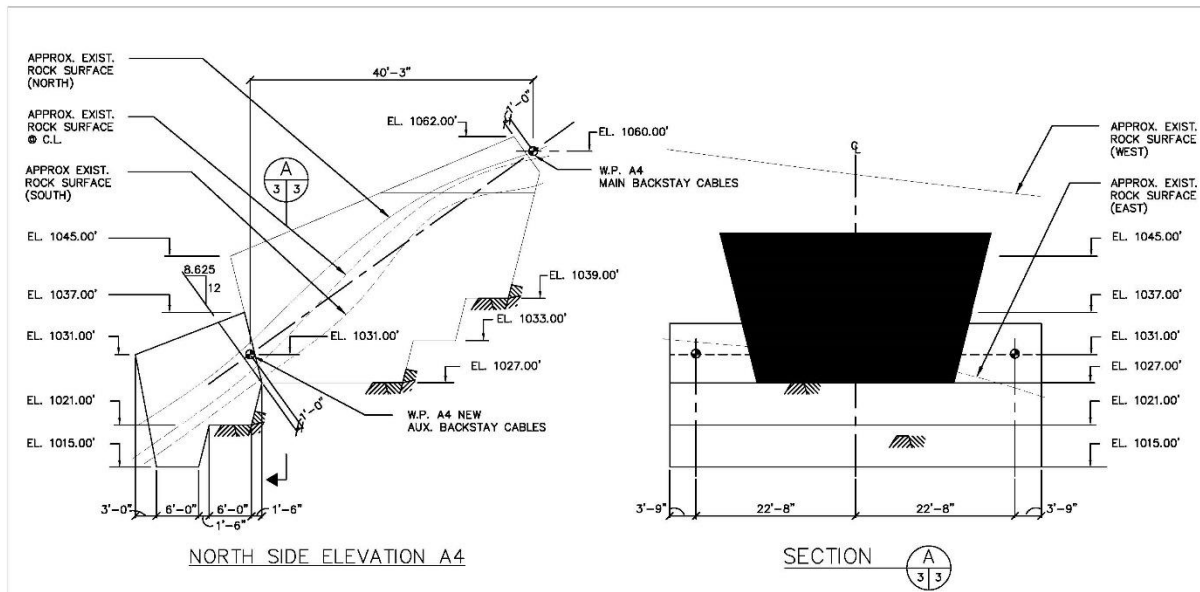
NATIONAL ASTRONOMY AND IONOSPHERE CENTER
 CORNELL UNIVERSITY
 ARECIBO RADIO OBSERVATORY
 GREGORIAN UPGRADING

GENERAL II

AW AMMANN & WHITNEY, CONSULTING ENGINEERS
 NEW YORK, NEW YORK

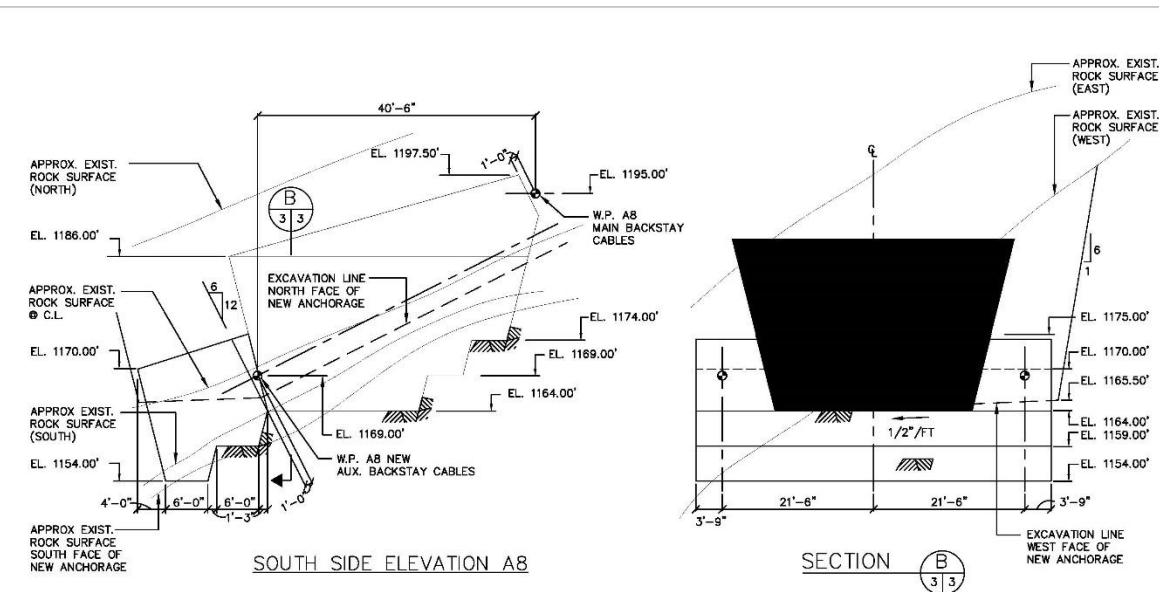
DRAWN BY:	APPROVED	DATE:
DESIGNED BY:		SCALE: AS NOTED
CHECKED BY:		DWG. NO. S-2





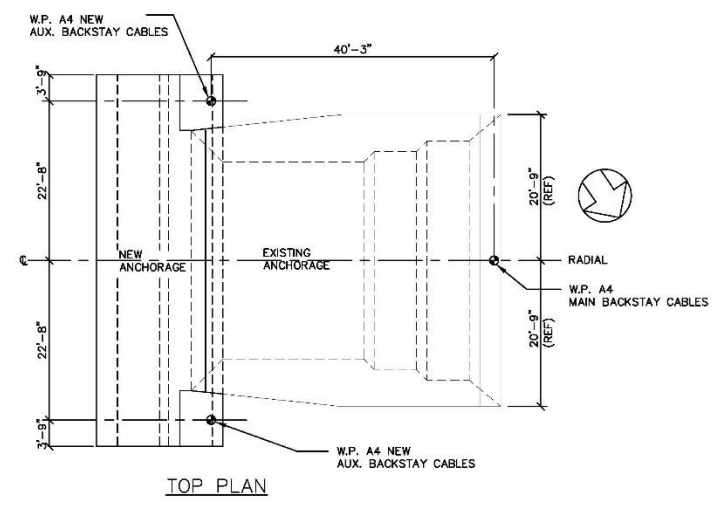
NORTH SIDE ELEVATION A4

SECTION A-A
3/3



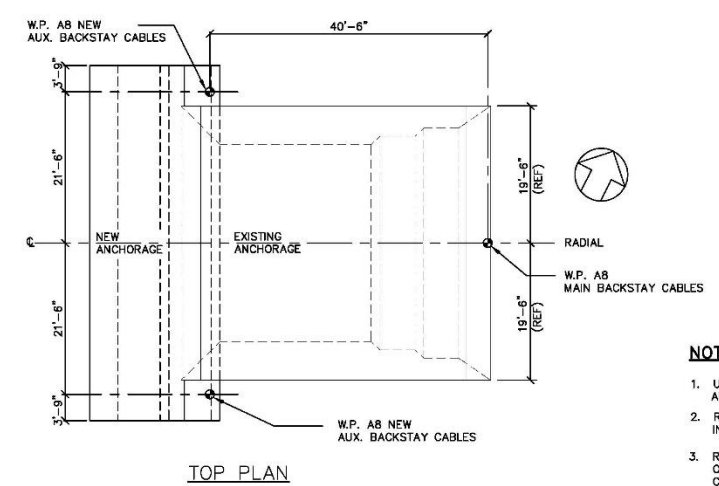
SOUTH SIDE ELEVATION A8

SECTION B-B
3/3



TOP PLAN

STRENGTHENED ANCHORAGE A4
SCALE: 1"=10'-0"



TOP PLAN

STRENGTHENED ANCHORAGE A8
SCALE: 1"=10'-0"

- NOTES**
- UNLESS INDICATED OTHERWISE, ROCK SURFACES SHOWN ARE AT THE FACES OF THE EXISTING ANCHORAGES.
 - ROUGHEN BACK SURFACE OF EXISTING ANCHORAGE AT INTERFACE OF NEW ANCHORAGE.
 - ROCK SHALL BE EXCAVATED TO A MINIMUM CLEARANCE OF 3'-0" ALONG THE LINE OF THE AUXILIARY BACKSTAY CABLES.
 - FOR ANCHORAGE REINFORCING SEE DWG S-5.
 - FOR ANCHORAGE METALWORK SEE DWG S-6.

NATIONAL ASTRONOMY AND IONOSPHERE CENTER
CORNELL UNIVERSITY
ARECIBO RADIO OBSERVATORY
GREGORIAN UPGRADING

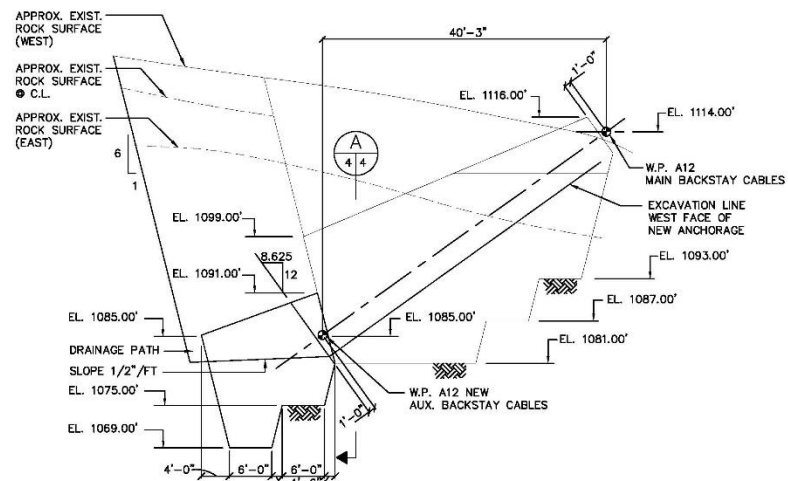
ANCHORAGES I

AW AMMANN & WHITNEY, CONSULTING ENGINEERS
NEW YORK, NEW YORK

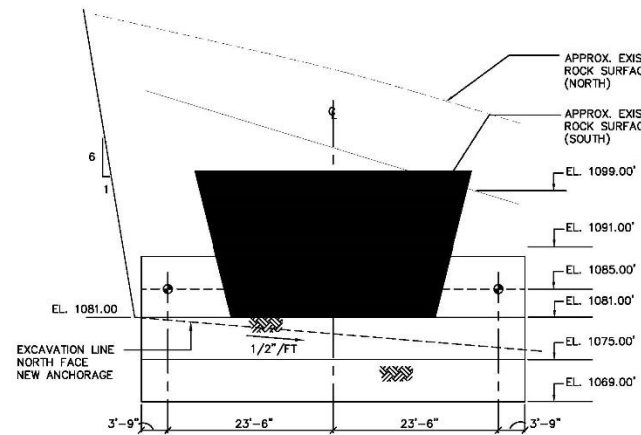
DRAWN BY:	APPROVED	DATE:
DESIGNED BY:		SCALE: 1"=10'-0"
CHECKED BY:		DWG. NO. S-3



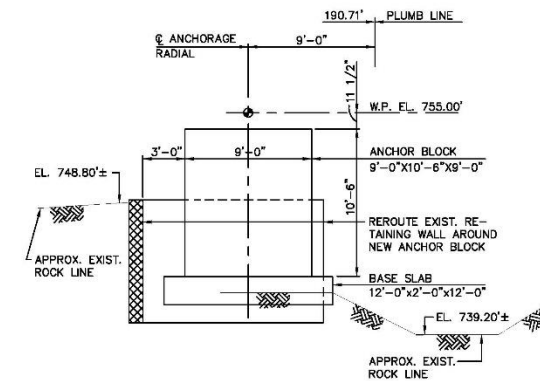
FILE #ARC3



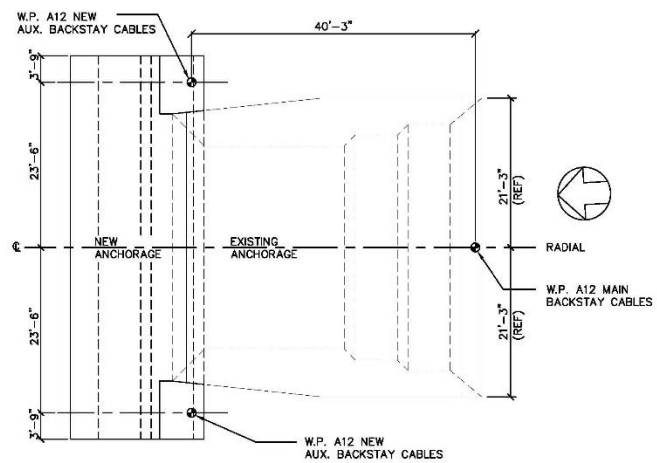
WEST SIDE ELEVATION A12



SECTION A

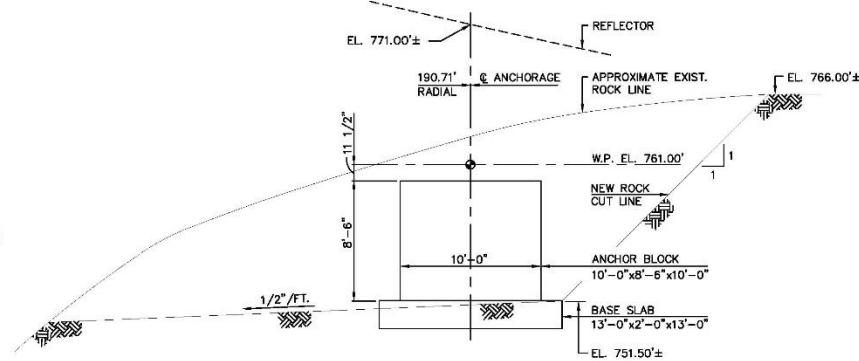


TIE DOWN ANCHORAGE B-4
SCALE: 1"=5'-0"

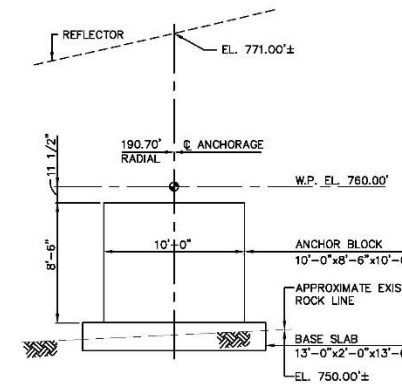


TOP PLAN

STRENGTHENED ANCHORAGE A12
SCALE: 1"=10'-0"



TIE DOWN ANCHORAGE B-8
SCALE: 1"=5'-0"



TIE DOWN ANCHORAGE B-12
SCALE: 1"=5'-0"

NATIONAL ASTRONOMY AND IONOSPHERE CENTER
CORNELL UNIVERSITY
ARECIBO RADIO OBSERVATORY
GREGORIAN UPGRADING

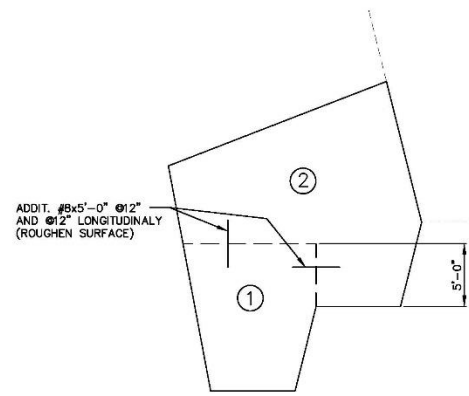
ANCHORAGES II

AMMANN & WHITNEY, CONSULTING ENGINEERS
NEW YORK, NEW YORK

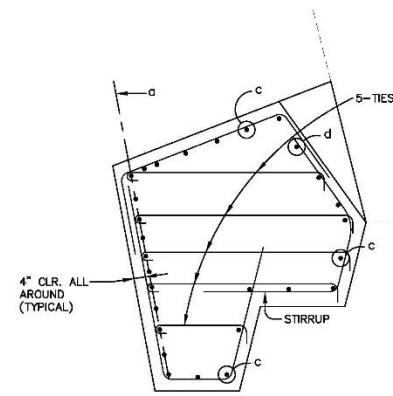
DRAWN BY:	APPROVED	DATE:
DESIGNED BY:		SCALE: AS NOTED
CHECKED BY:		DWG. NO. S-4



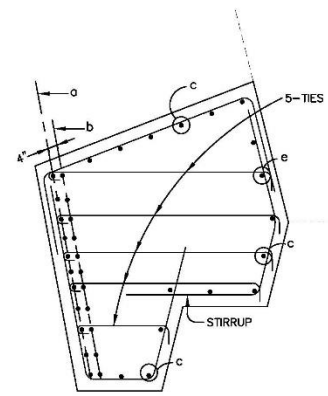
FILE #ARC16



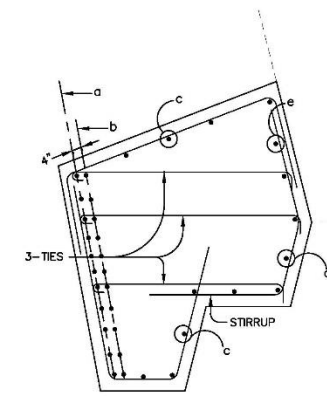
POUR SEQUENCE
(SUGGESTED)



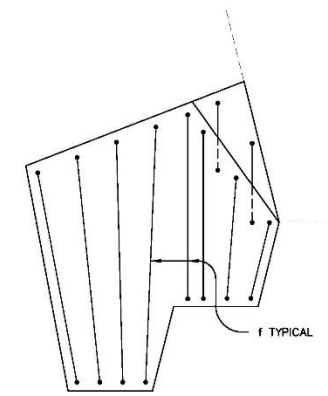
SECTION A
NTS



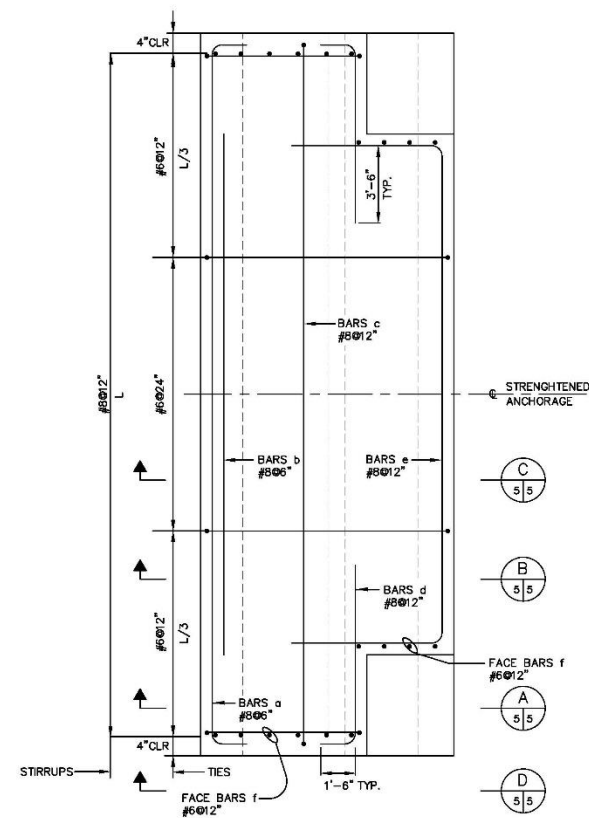
SECTION B
NTS



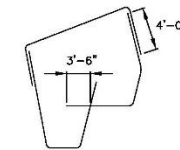
SECTION C
NTS



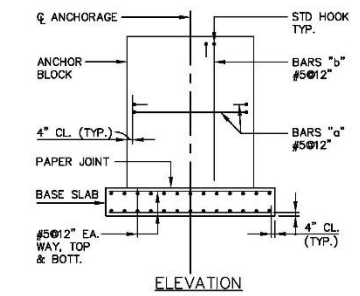
SECTION D
NTS



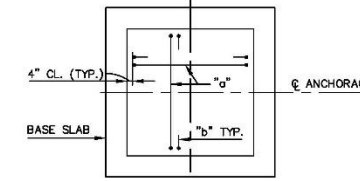
STRENGTHENED CONCRETE ANCHORAGE
REINFORCING PLAN
NTS



TYPICAL STIRRUP
N.T.S.



ELEVATION



PLAN

TIE DOWN ANCHORAGES
N.T.S.

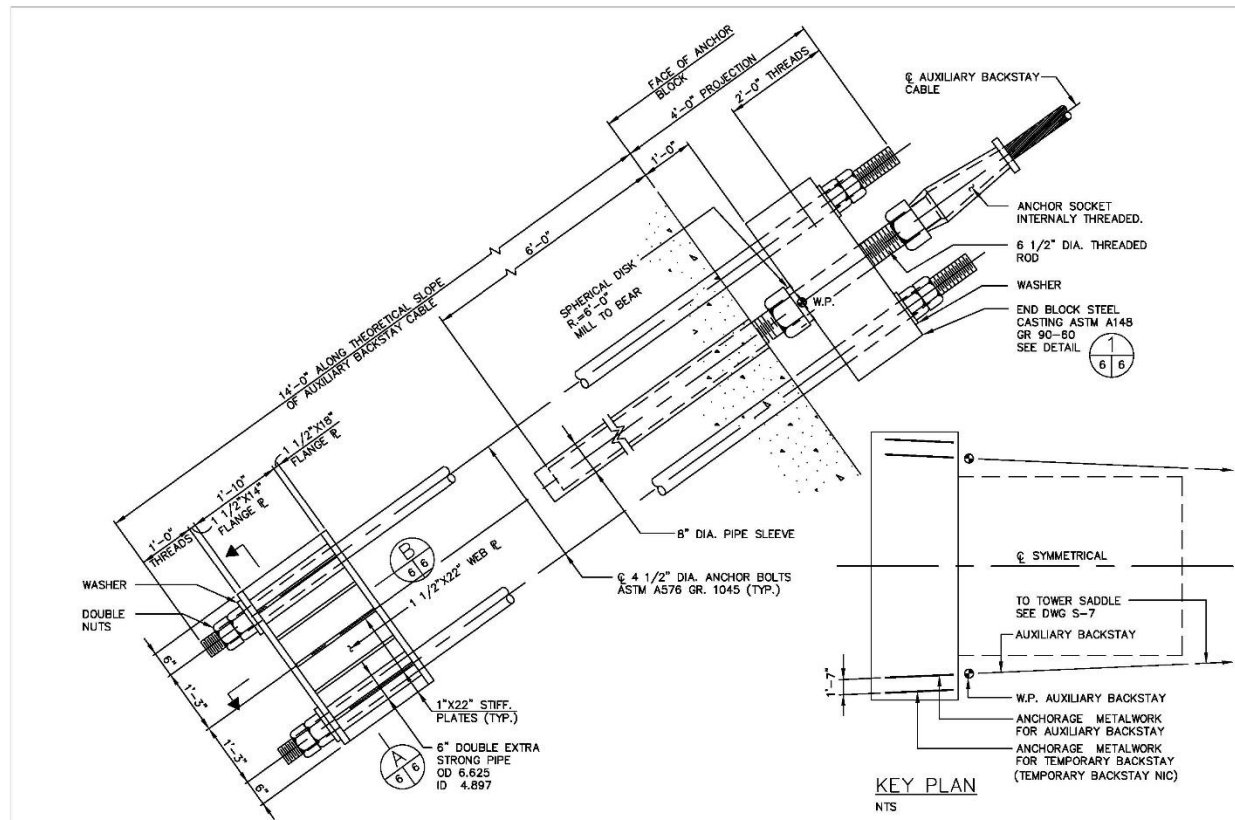
NATIONAL ASTRONOMY AND IONOSPHERE CENTER
CORNELL UNIVERSITY
ARECIBO RADIO OBSERVATORY
GREGORIAN UPGRADING

ANCHORAGE REINFORCING

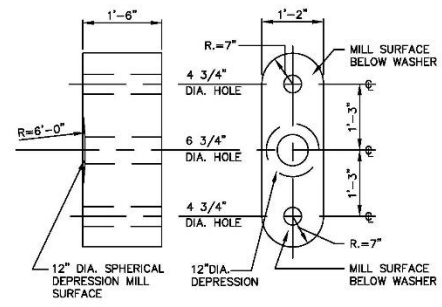
AMMANN & WHITNEY, CONSULTING ENGINEERS
NEW YORK, NEW YORK

DRAWN BY:	APPROVED	DATE:
DESIGNED BY:		SCALE: AS NOTED
CHECKED BY:		DWG. NO. S-5

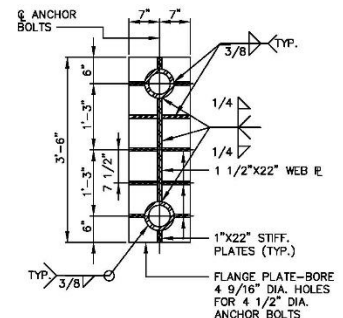
FILE #ARC4



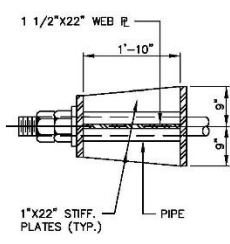
STRENGTHENED ANCHORAGES - A4, A8 & A12
 (12 ASSEMBLIES REQUIRED)
 SCALE: 3/4"=1'-0"



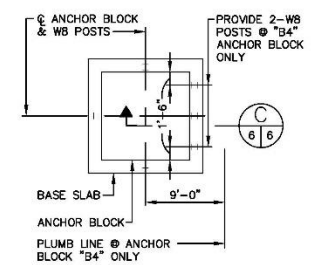
END BLOCK
 DETAIL SCALE: 3/4"=1'-0"



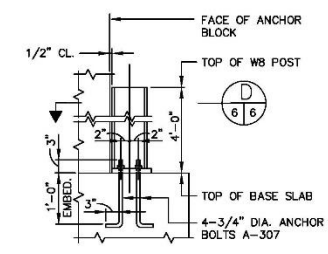
SECTION A
 SCALE: 3/4"=1'-0"



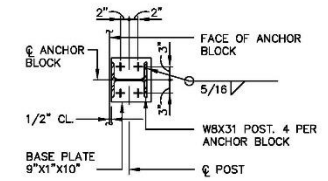
SECTION B
 SCALE: 3/4"=1'-0"



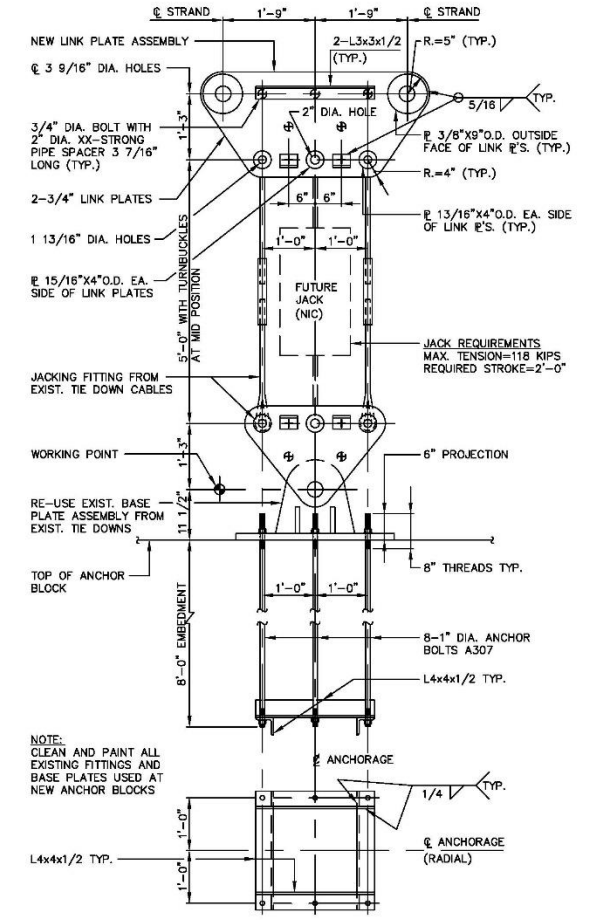
TYPICAL ANCHOR BLOCK TIE DOWN POSTS LOCATION PLAN
 SCALE: 1/8"=1'-0"



SECTION C
 SCALE: 3/4"=1'-0"



SECTION D
 SCALE: 3/4"=1'-0"



TIE DOWN ANCHORAGES B4, B8 & B12
 SCALE: 3/4"=1'-0"

NOTES:
 1. AUXILIARY BACKSTAY ANCHOR BOLTS SHALL BE POSITIONED IN ANCHORAGE BY MEANS OF AN EMBEDDED STEEL FRAME TO INSURE THEY ARE LOCATED ALONG THE SLOPE OF AUXILIARY BACKSTAYS.

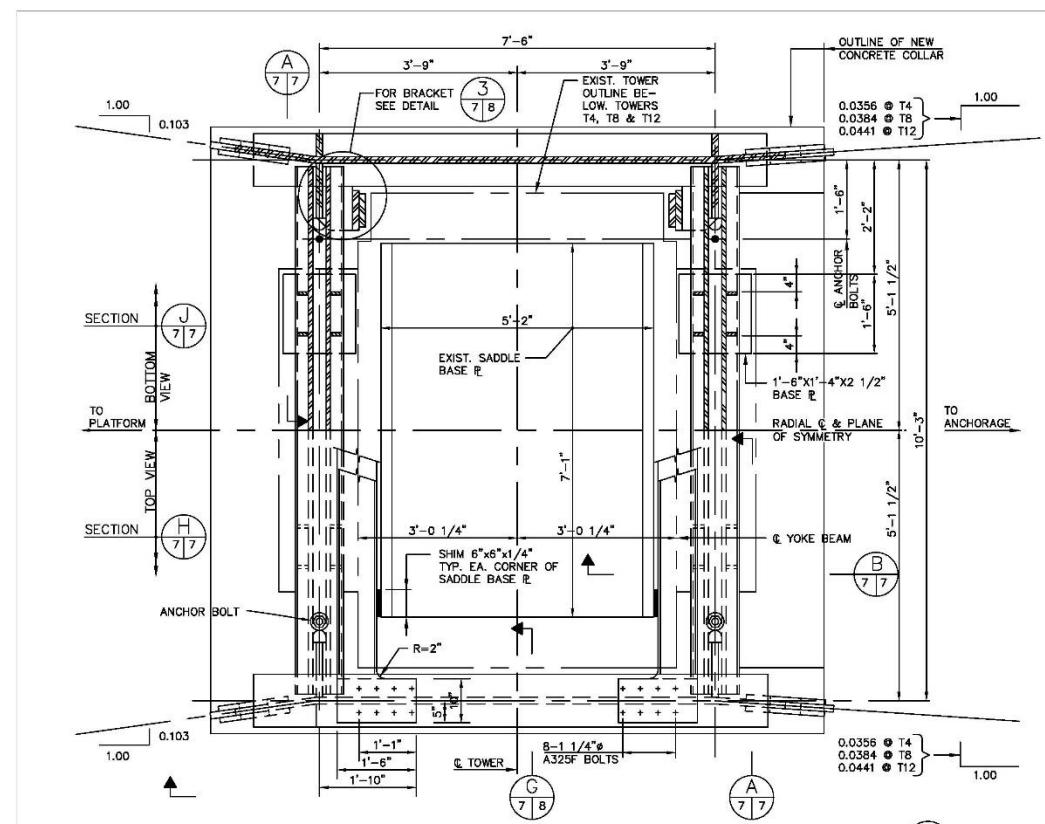
NATIONAL ASTRONOMY AND IONOSPHERE CENTER
 CORNELL UNIVERSITY
 ARECIBO RADIO OBSERVATORY
 GREGORIAN UPGRADING

ANCHORAGE METALWORK

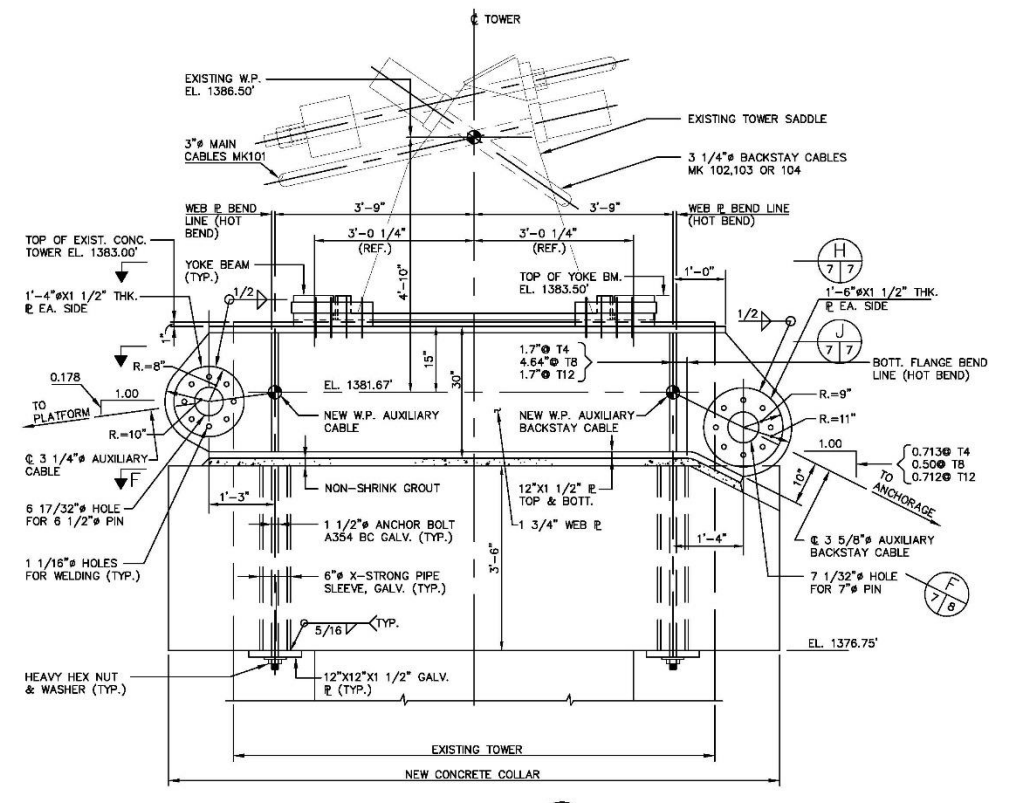
AMMANN & WHITNEY, CONSULTING ENGINEERS
 NEW YORK, NEW YORK

DRAWN BY:	APPROVED	DATE:
DESIGNED BY:		SCALE: AS NOTED
CHECKED BY:		DWG. NO. S-6

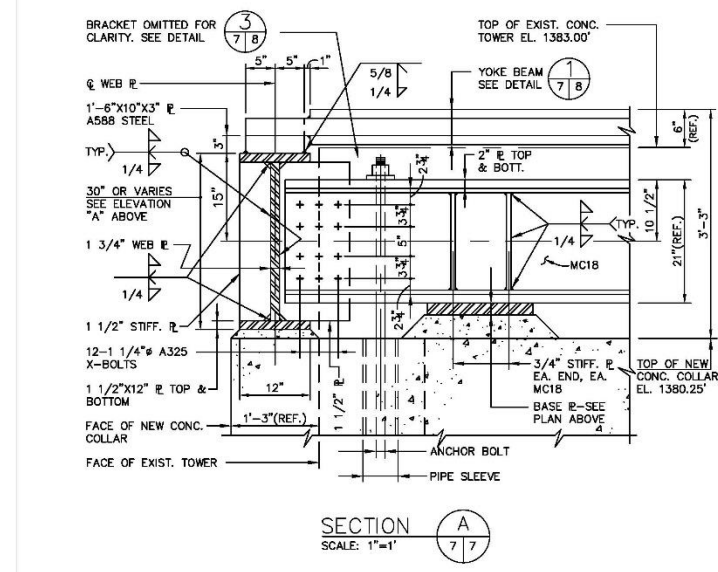
FILE #ARC5



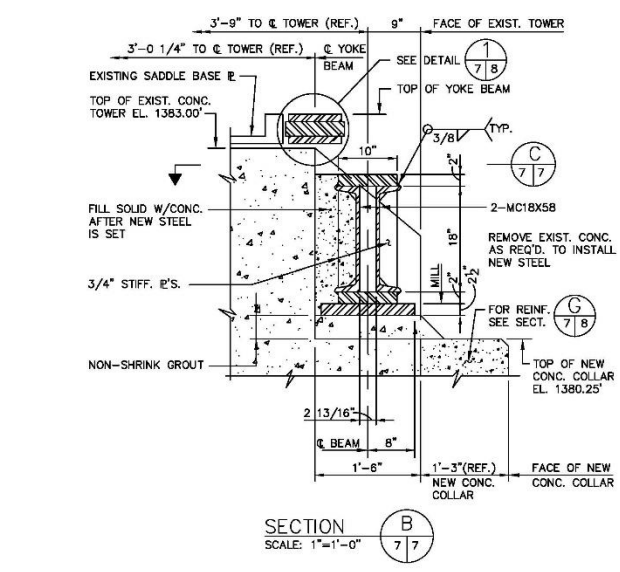
TOWER SADDLE PLAN
SCALE: 3/4"=1'



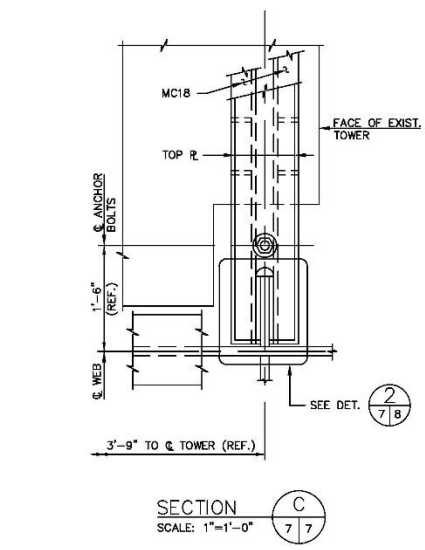
ELEVATION A
SCALE: 3/4"=1'-0"



SECTION A
SCALE: 1"=1'



SECTION B
SCALE: 1"=1'-0"



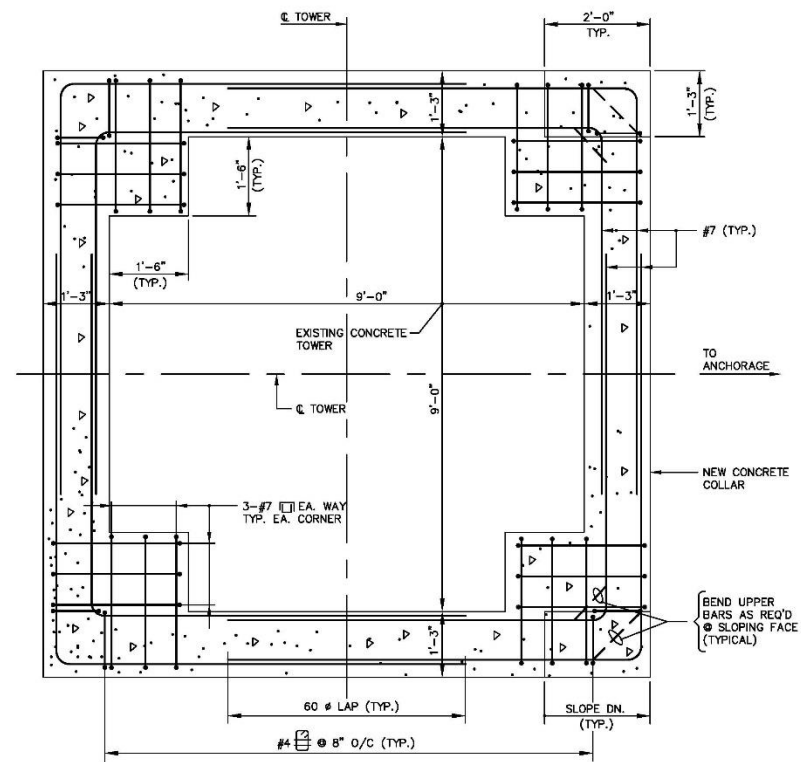
SECTION C
SCALE: 1"=1'-0"

- NOTES:
- 1) MINIMUM CONCRETE COMPRESSIVE STRENGTH f_c SHALL BE 4000 PSI AT 28 DAYS FOR ALL CONCRETE COLLARS.
 - 2) CAMFER ALL EXPOSED CONCRETE EDGES 1"x1".

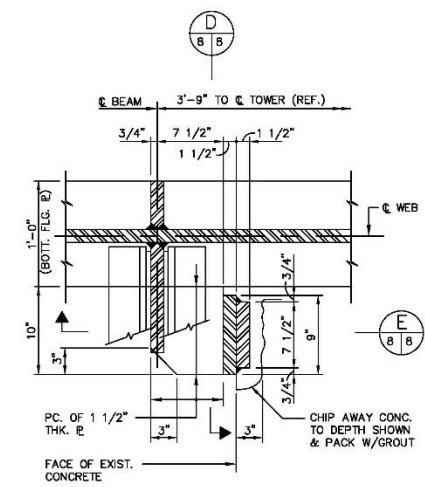
NATIONAL ASTRONOMY AND IONOSPHERE CENTER
CORNELL UNIVERSITY
ARECIBO RADIO OBSERVATORY
GREGORIAN UPGRADING
TOWER SADDLE I

AW AMMANN & WHITNEY, CONSULTING ENGINEERS NEW YORK, NEW YORK	
DRAWN BY:	APPROVED:
DESIGNED BY:	DATE:
CHECKED BY:	SCALE: AS NOTED DWG. NO. S-7

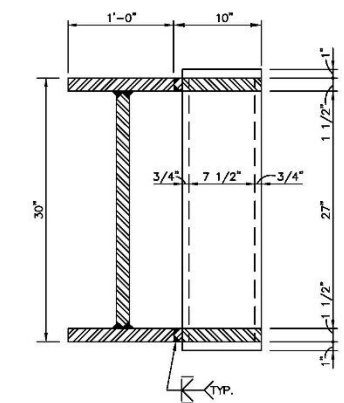
FILE #ARC6



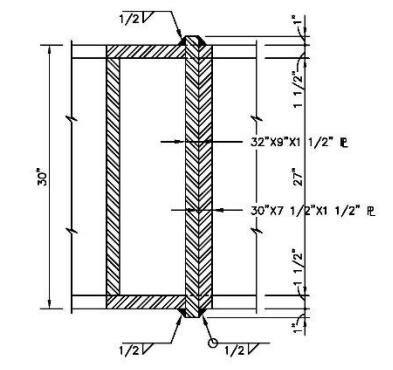
SECTION F
SCALE: 3/4"=1'-0" 7/8



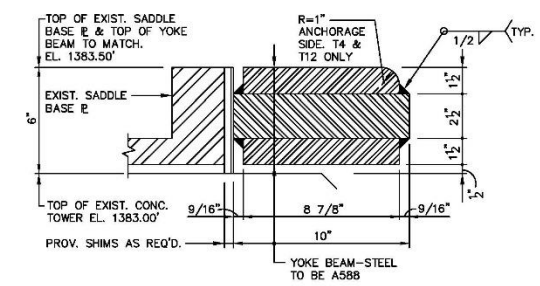
DETAIL 3
SCALE: 1 1/2"=1'-0" 7/8



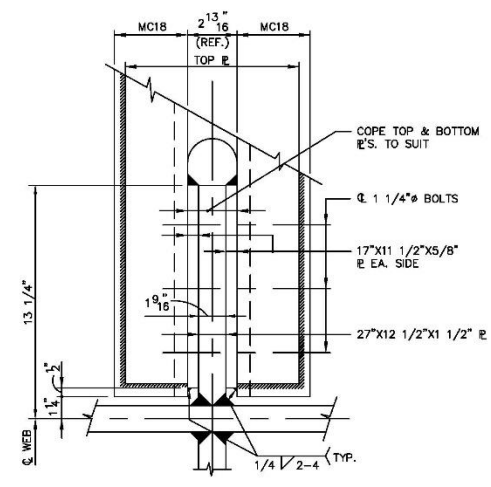
SECTION D
SCALE: 1 1/2"=1'-0" 7/8



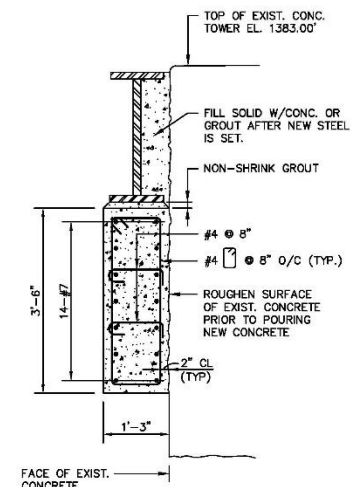
SECTION E
SCALE: 1 1/2"=1'-0" 7/8



DETAIL 1
SCALE: 3"=1'-0" 7/8



DETAIL 2
SCALE: 3"=1'-0" 7/8

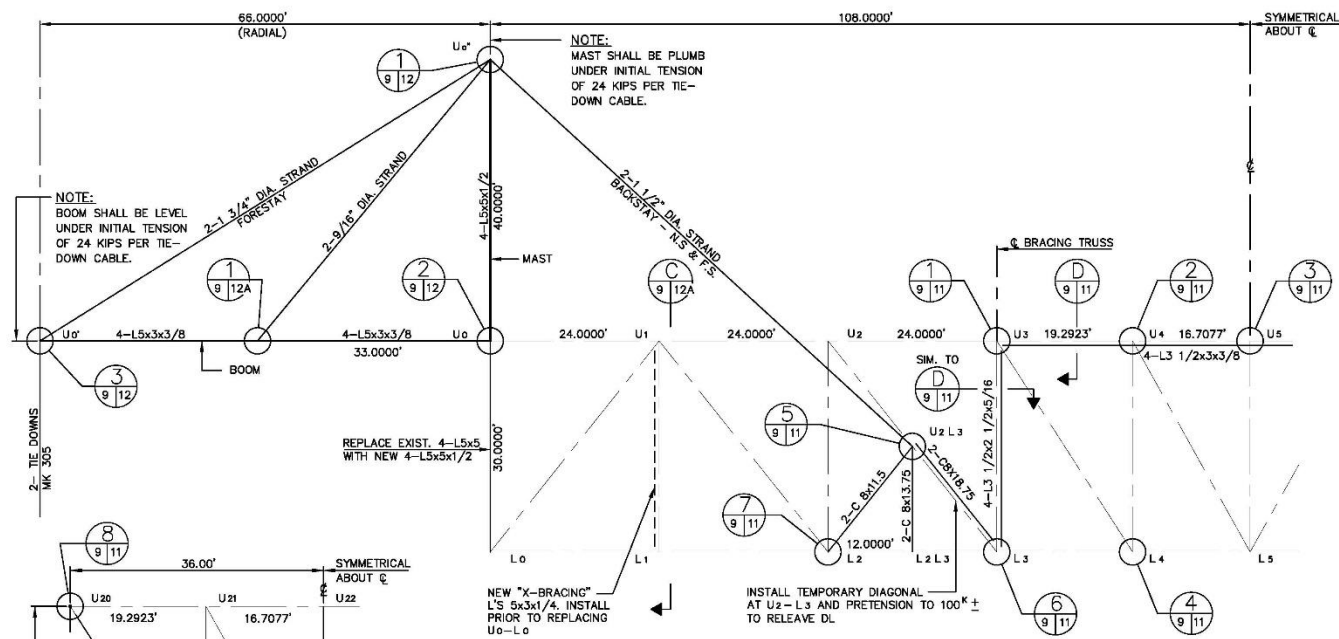


SECTION G
SCALE: 3/4"=1'-0" 7/8

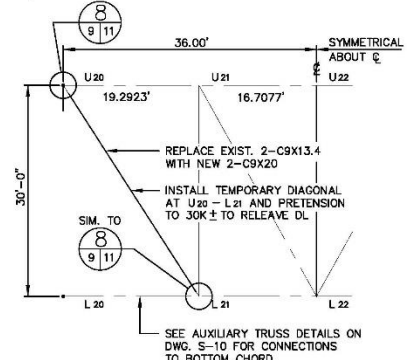
NATIONAL ASTRONOMY AND IONOSPHERE CENTER
CORNELL UNIVERSITY
ARECIBO RADIO OBSERVATORY
GREGORIAN UPGRADING
TOWER SADDLE II

AMMANN & WHITNEY, CONSULTING ENGINEERS
NEW YORK, NEW YORK
DRAWN BY: APPROVED DATE: SCALE: AS NOTED
DESIGNED BY: DWG. NO. S-8
CHECKED BY:

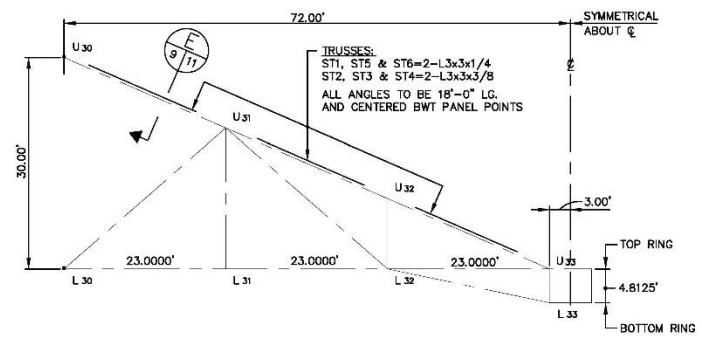
FILE #ARC25



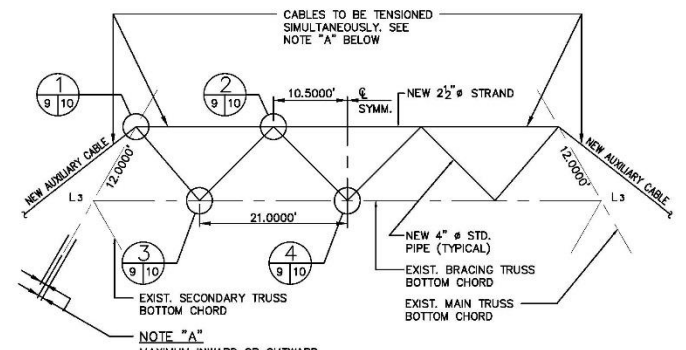
MAIN TRUSS
SCALE: 1"=10'-0"



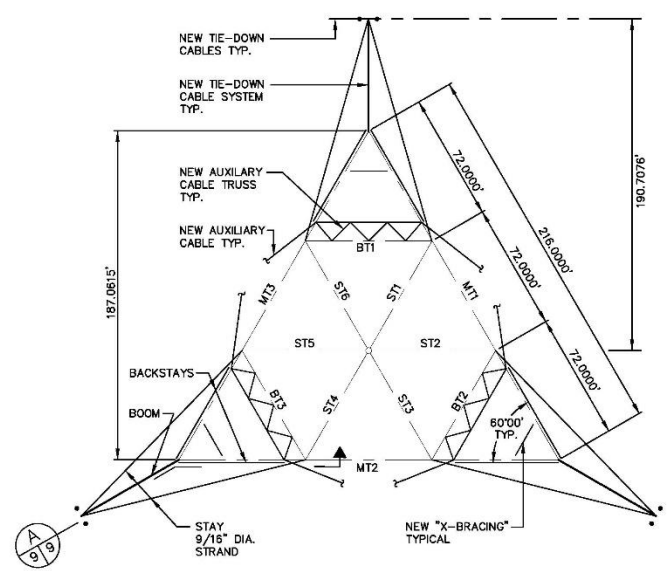
BRACING TRUSS
SCALE: 1"=10'-0"



SECONDARY BRACING TRUSS
SCALE: 1"=10'-0"



NEW AUXILIARY CABLE TRUSS
SCALE: 1"=10'-0"



FEED PLATFORM PLAN
SCALE: 1"=40'-0"

LEGEND
MT - EXISTING MAIN TRUSS
BT - EXISTING BRACING TRUSS
ST - EXISTING SECONDARY BRACING TRUSS

REINFORCED FEED PLATFORM FORCE TABLE		
MEMBER	OPERATIONAL	SURVIVAL
U0 - U0	-185	-82
U0 - U1	-104	-35
U1 - U2	-395	-401
U2 - U3	-592	-611
U3 - U4	-776	-735
U4 - U5	-775	-722
L0 - L1	+1301	+1274
L1 - L2	+1301	+1274
L2 - L3	+1430	+1469
L3 - L4	+1699	+1645
L4 - L5	+1510	+1568
U0 - L0	-312	-105
U1 - L1	-302	-96
U2 - L2	-282	-287
U2L3 - L23	-104	-105
U3 - L3	+65 / -307	-282
U4 - L4	-106 / +151	-173
U5 - L5	0	0
U1 - L0	-232	+323
U1 - L2	+285	+302
U2 - U2L3	+316	+332
U2L3 - L3	+410	+381
U3 - L3	+312 / -23	+297 / -36
U4 - L5	+115 / -102	+138 / -125
U20 - U21	-151	-172
U21 - U22	-154	-165
L30 - L21	+41 / -59	+98 / -49
L31 - L22	-17 / -56	+105 / -45
U21 - L21	+36 / -23	+53 / -66
U22 - L22	0	0
U20 - L21	+304	+271
U21 - L22	+41 / -25	+74 / -84
U30 - U31	+23 / -61	+30 / -43
U31 - U32	+25 / -61	+22 / -34
U32 - U33	+25 / -61	+22 / -34
L30 - L31	+74	+100
L31 - L32	+74	+100
L32 - L33	+59 / -12	+70 / -14
U31 - L31	0	0
U32 - L32	0	0
U33 - L33	-27	-26
L30 - U31	+21 / -12	+20 / -11
U31 - L32	+21 / -12	+20 / -11
L32 - L33	+42	+42

NOTES: 1) ALL FORCES IN KIPS. TENSION DENOTED +, COMPRESSION DENOTED -.

- NOTES**
- DURING REINFORCING OPERATIONS THE FEED ARM SHALL BE PARKED IN A POSITION PARALLEL TO THE TRUSS BEING REINFORCED.
 - REPLACEMENT MEMBERS SHALL BE IDENTICAL TO EXISTING MEMBERS EXCEPT AS SHOWN.
 - ALL BOLTS IN FEED PLATFORM CONNECTIONS ARE 1" DIAMETER UNLESS SHOWN OTHERWISE.
 - APPROXIMATELY 500 BOLTS IN FEED PLATFORM ARE TO BE REPLACED. LOCATION OF BOLTS TO BE PROVIDED BY OWNER.

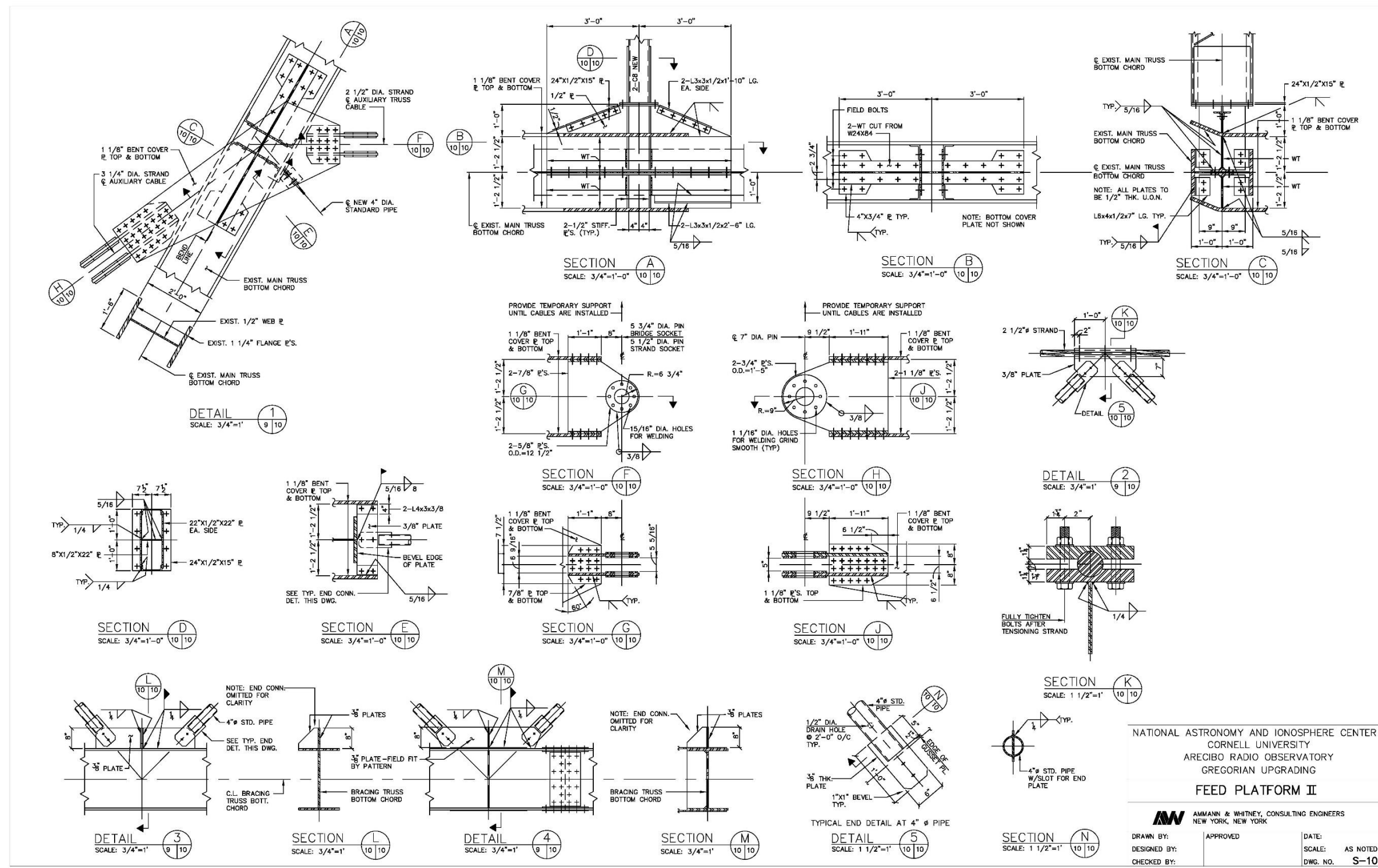
NATIONAL ASTRONOMY AND IONOSPHERE CENTER
CORNELL UNIVERSITY
ARECIBO RADIO OBSERVATORY
GREGORIAN UPGRADING

FEED PLATFORM I

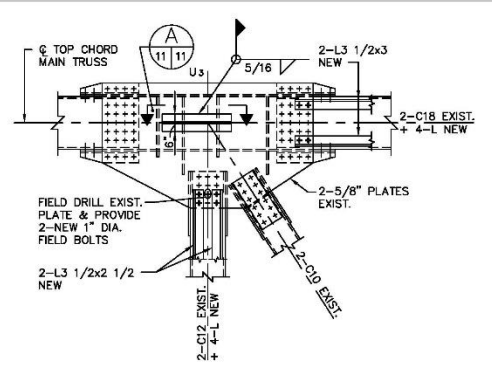
AMMANN & WHITNEY, CONSULTING ENGINEERS
NEW YORK, NEW YORK

DRAWN BY: [] APPROVED: [] DATE: []
DESIGNED BY: [] SCALE: AS NOTED
CHECKED BY: [] DWG. NO. S-9

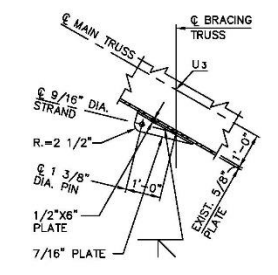
FILE #ARC7



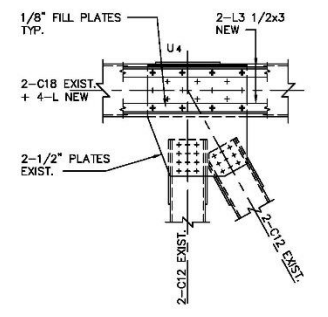
FILE #ARC8



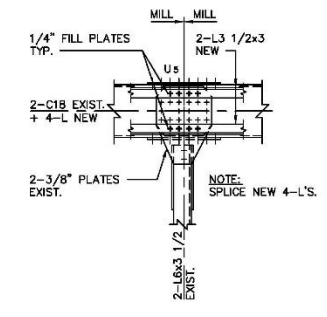
DETAIL 1
SCALE: 1/2"=1'-0" 9 11



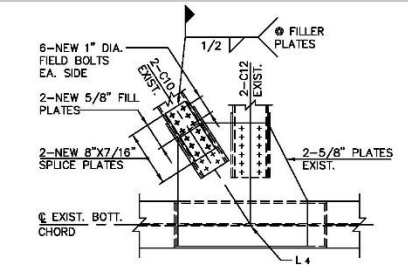
SECTION A
SCALE: 1/2"=1'-0" 11 11



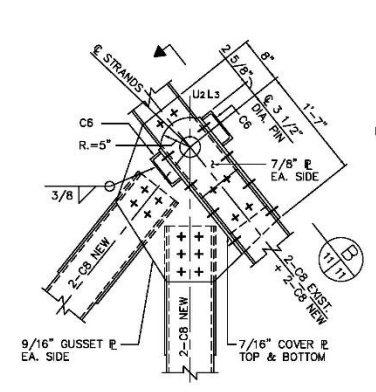
DETAIL 2
SCALE: 1/2"=1'-0" 9 11



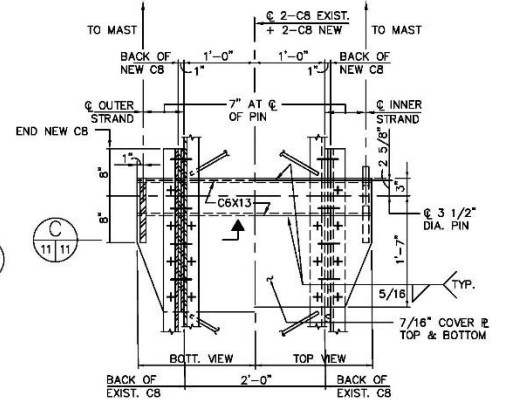
DETAIL 3
SCALE: 1/2"=1'-0" 9 11



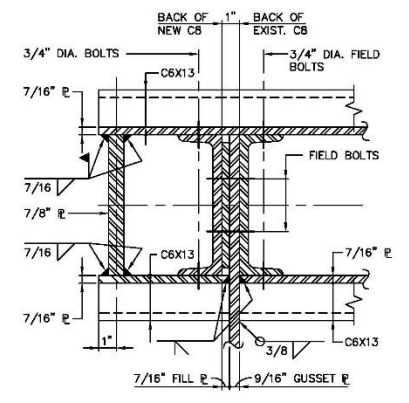
DETAIL 4
SCALE: 1/2"=1'-0" 9 11



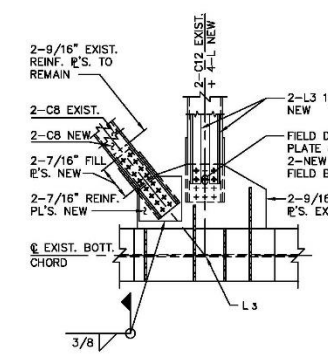
DETAIL 5
SCALE: 1"=1'-0" 9 11



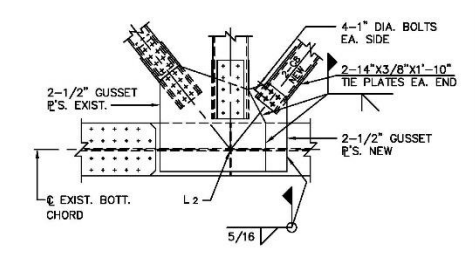
SECTION B
SCALE: 1"=1'-0" 11 11



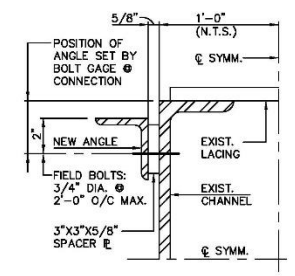
SECTION C
SCALE: 3/8"=1'-0" 11 11



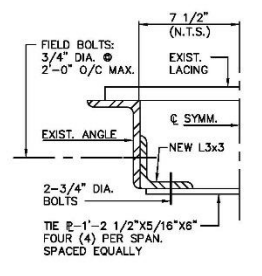
DETAIL 6
SCALE: 1/2"=1'-0" 9 11



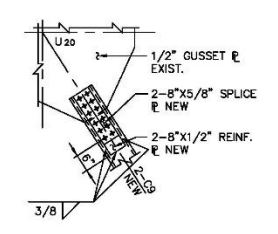
DETAIL 7
SCALE: 1/2"=1'-0" 9 11



SECTION D
SCALE: 3/8"=1'-0" 9 11



SECTION E
SCALE: 3/8"=1'-0" 9 11



DETAIL 8
SCALE: 1/2"=1'-0" 9 11

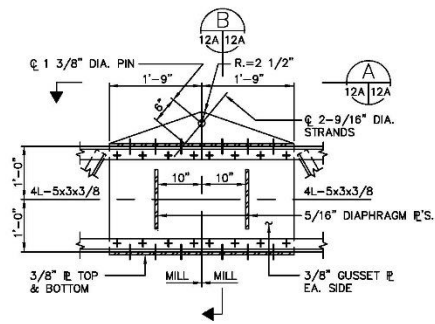
NATIONAL ASTRONOMY AND IONOSPHERE CENTER
CORNELL UNIVERSITY
ARECIBO RADIO OBSERVATORY
GREGORIAN UPGRADING

FEED PLATFORM III

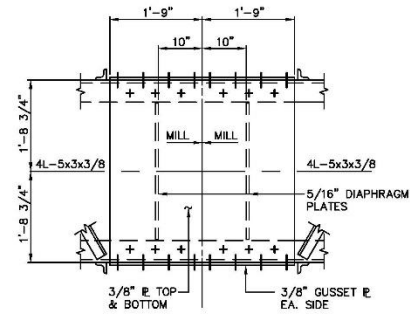
AMMANN & WHITNEY, CONSULTING ENGINEERS
NEW YORK, NEW YORK

DRAWN BY:	APPROVED	DATE:
DESIGNED BY:		SCALE: AS NOTED
CHECKED BY:		DWG. NO. S-11

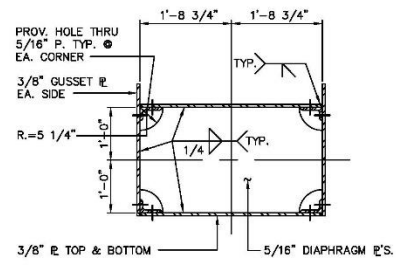
FILE #ARC15



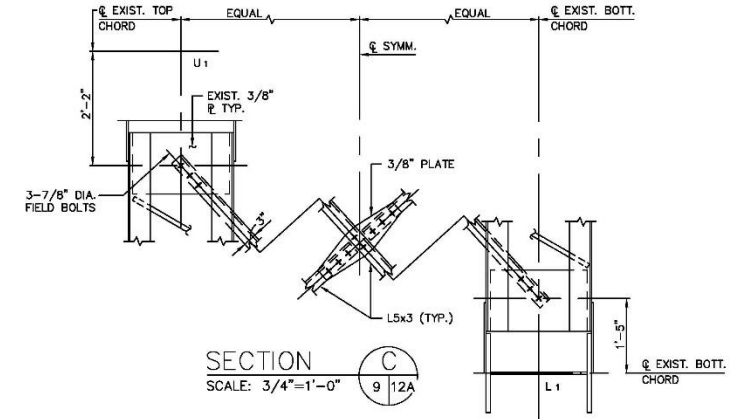
DETAIL 1
SCALE: 3/4"=1'-0"
9 12A



SECTION A
SCALE: 3/4"=1'-0"
12A 12A



SECTION B
SCALE: 3/4"=1'-0"
12A 12A



SECTION C
SCALE: 3/4"=1'-0"
9 12A

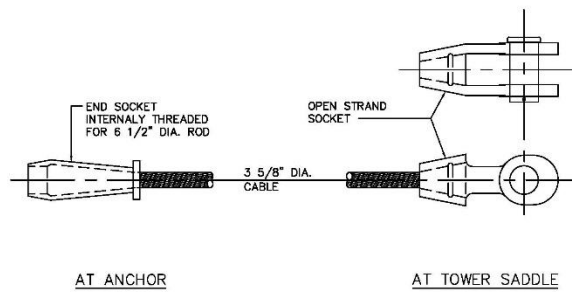
FILE #ARC12A

NATIONAL ASTRONOMY AND IONOSPHERE CENTER
CORNELL UNIVERSITY
ARECIBO RADIO OBSERVATORY
GREGORIAN UPGRADING

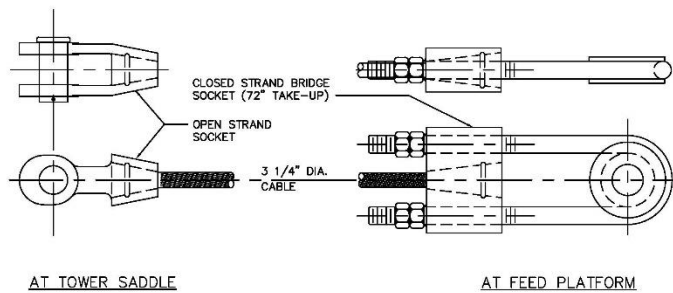
FEED PLATFORM V

AMMANN & WHITNEY, CONSULTING ENGINEERS
NEW YORK, NEW YORK

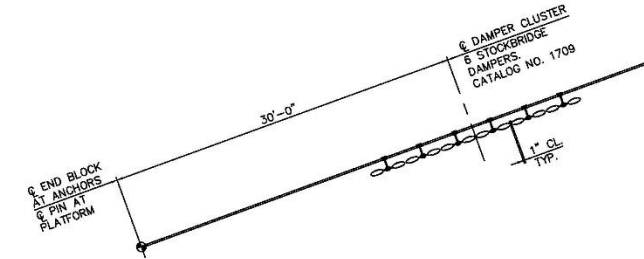
DRAWN BY:	APPROVED	DATE:
DESIGNED BY:		SCALE: AS NOTED
CHECKED BY:		DWG. NO. S-12A



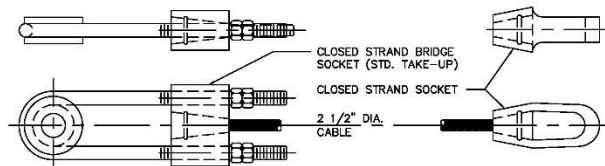
AUXILIARY BACKSTAY CABLES: MK302, MK303 & MK304
N.T.S.



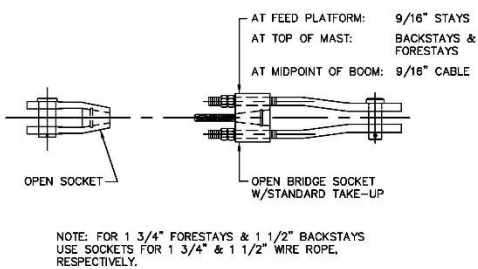
AUXILIARY CABLES: MK 301
N.T.S.



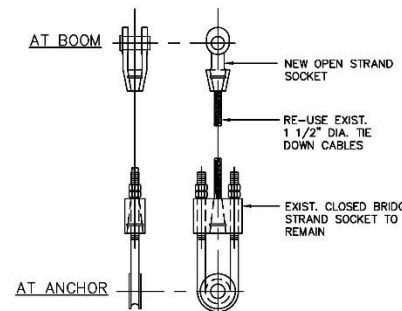
CABLE DAMPERS: CABLES MK 301, MK 302, MK 303 & MK 304
N.T.S.



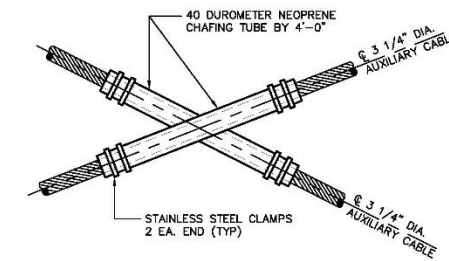
AUXILIARY TRUSS CABLES
N.T.S.



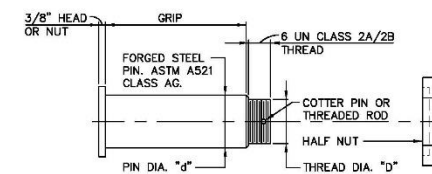
TIE DOWN CABLE SYSTEM
N.T.S.



TIE DOWN CABLES: MK 305
N.T.S.



AUXILIARY CABLE INTERSECTION POINT
N.T.S.



TYPICAL PIN DETAIL
N.T.S.

- NOTES:
- PIN DETAILS SHALL CONFORM TO AMERICAN INSTITUTE OF STEEL CONSTRUCTION DETAILS FOR RECESSED PIN NUTS AND COTTER PINS.
 - FOR PIN DIA. "d" GREATER THAN 3 3/4", NUTS SHALL BE USED AT BOTH ENDS OF PIN.

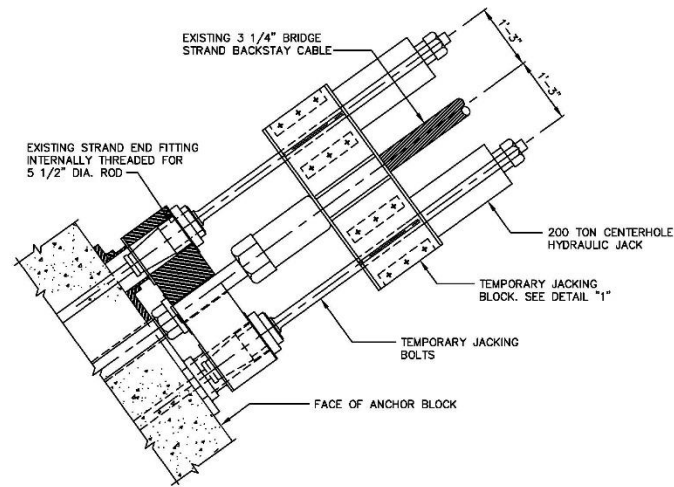
NATIONAL ASTRONOMY AND IONOSPHERE CENTER
CORNELL UNIVERSITY
ARECIBO RADIO OBSERVATORY
GREGORIAN UPGRADING

CABLE DETAILS

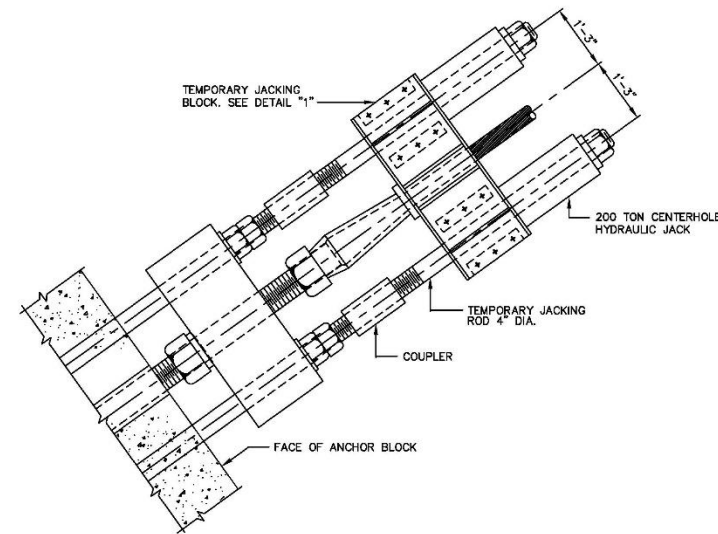
AW AMMANN & WHITNEY, CONSULTING ENGINEERS
NEW YORK, NEW YORK

DRAWN BY: R.C.	APPROVED:	DATE:
DESIGNED BY: J.G.		SCALE: AS NOTED
CHECKED BY: J.V.		DWG. NO. S-13

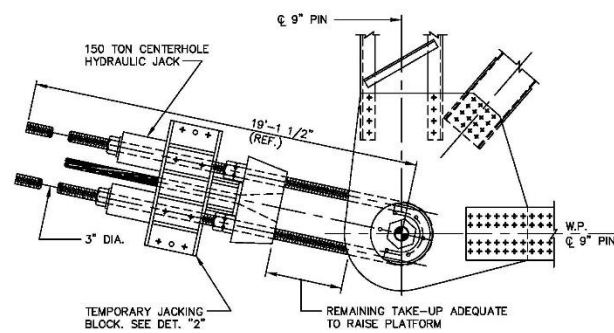
FILE #ARC21



TENSIONING BACKSTAYS – MK 102, MK 103 & MK 104
SCALE: 3/4"=1'-0"

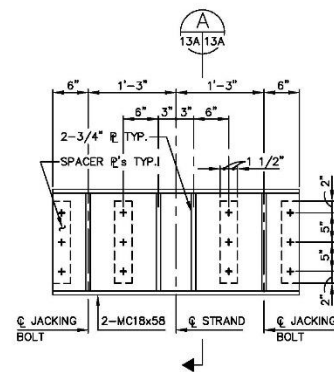


TENSIONING AUXILIARY BACKSTAYS – MK 302, MK 303 & MK 304
SCALE: 3/4"=1'-0"

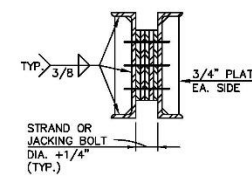


TENSIONING MAIN CABLES – MK101
SCALE: 3/4"=1'-0"

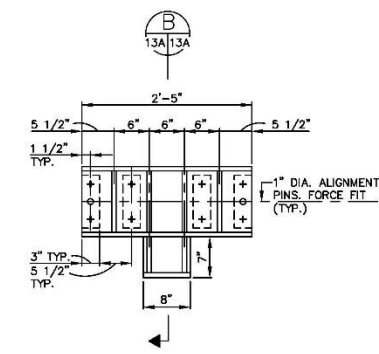
NOTE:
TENSIONING NEW AUXILIARY CABLES MK 301 SIMILAR.



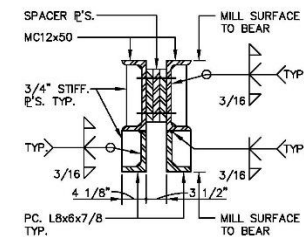
TYPICAL BACKSTAY TEMPORARY JACKING BLOCK DETAIL
SCALE: 1"=1'-0"



SECTION A
SCALE: 1"=1'-0"



TYPICAL MAIN CABLE TEMPORARY JACKING BLOCK DETAIL
SCALE: 1"=1'-0"



SECTION B
SCALE: 1"=1'-0"

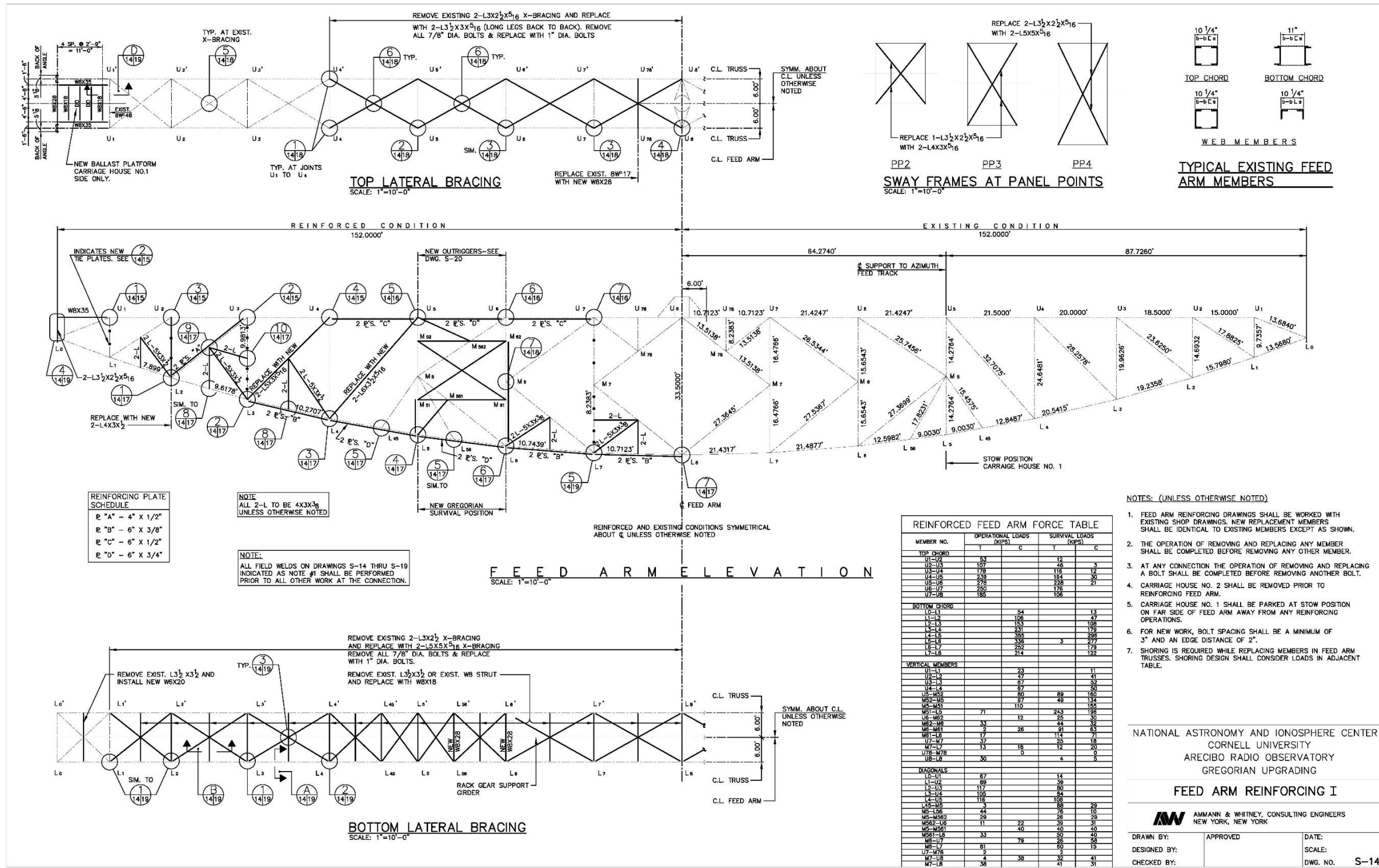
NATIONAL ASTRONOMY AND IONOSPHERE CENTER
CORNELL UNIVERSITY
ARECIBO RADIO OBSERVATORY
GREGORIAN UPGRADING

TENSIONING OF CABLE SYSTEM

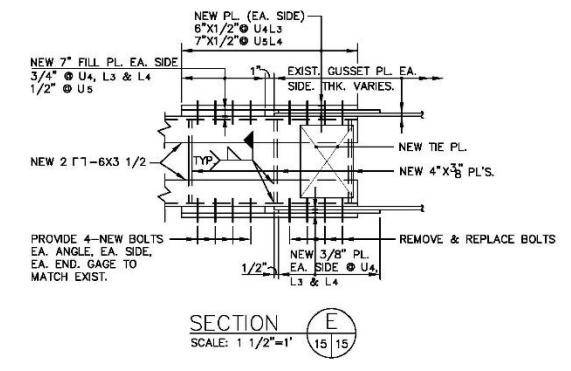
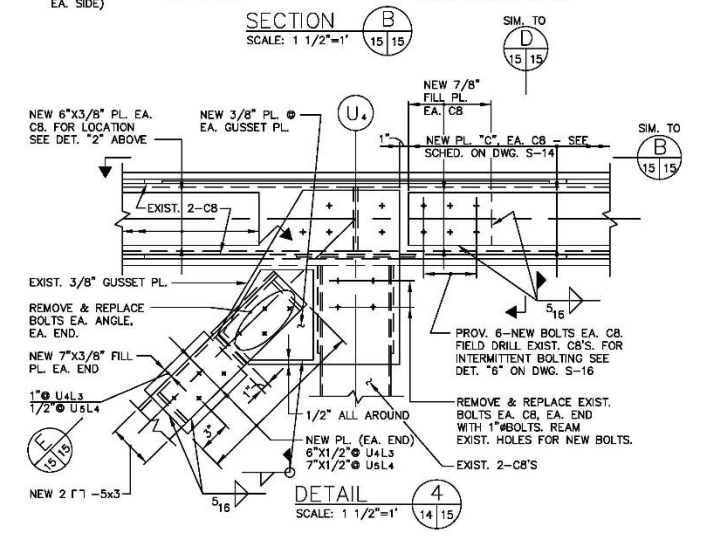
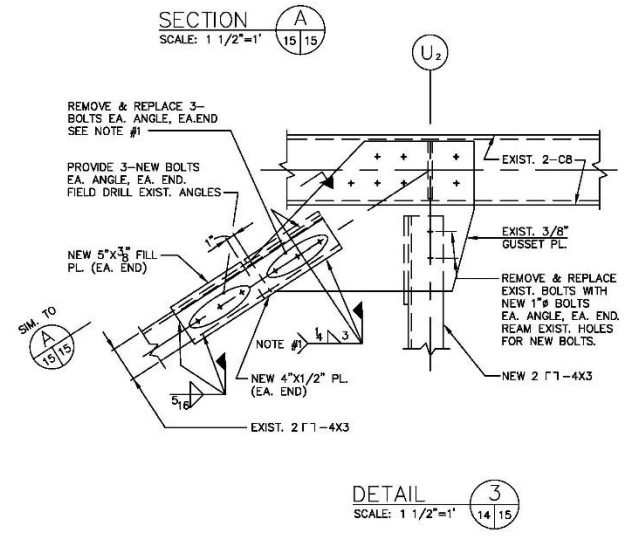
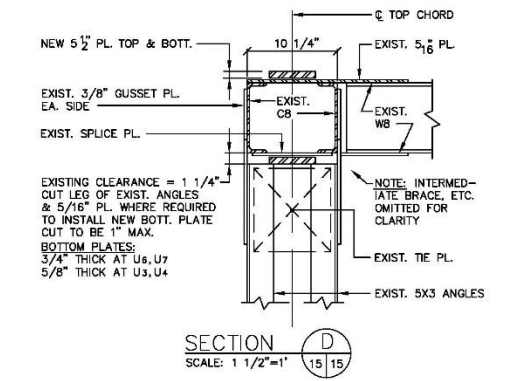
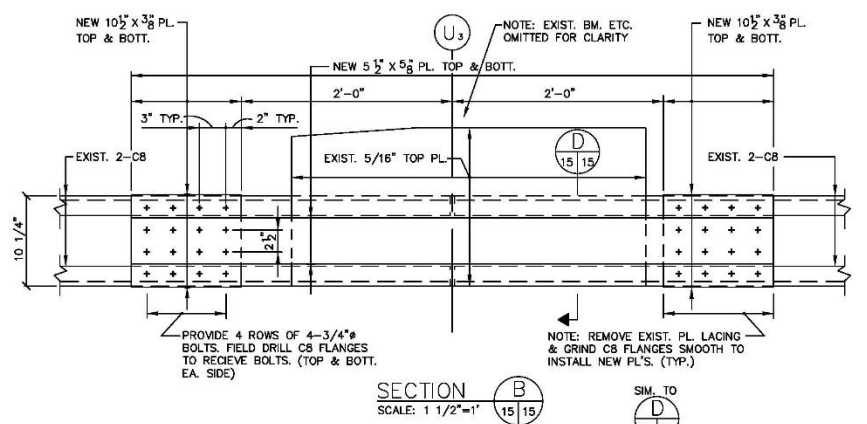
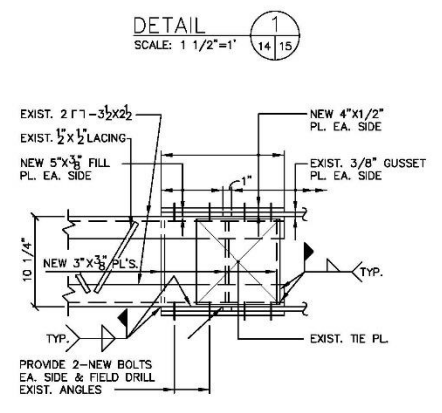
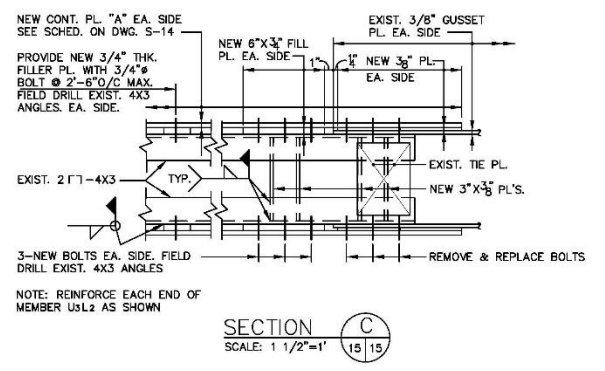
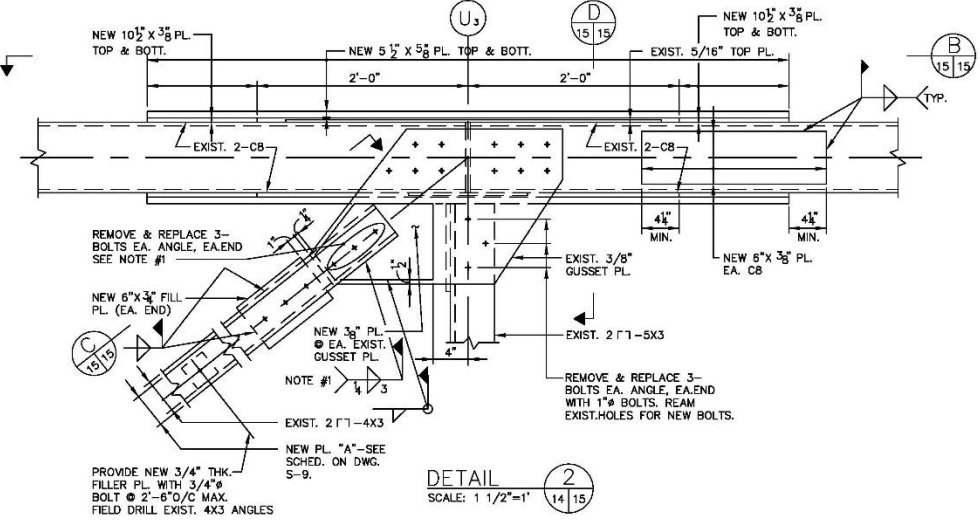
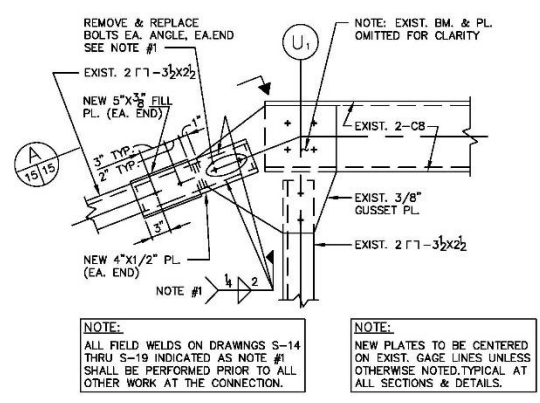
AW AMMANN & WHITNEY, CONSULTING ENGINEERS
NEW YORK, NEW YORK

DRAWN BY:	APPROVED	DATE:
DESIGNED BY:		SCALE: AS NOTED
CHECKED BY:		DWG. NO. S-13A

FILE #ARC34



FILE #ARC9

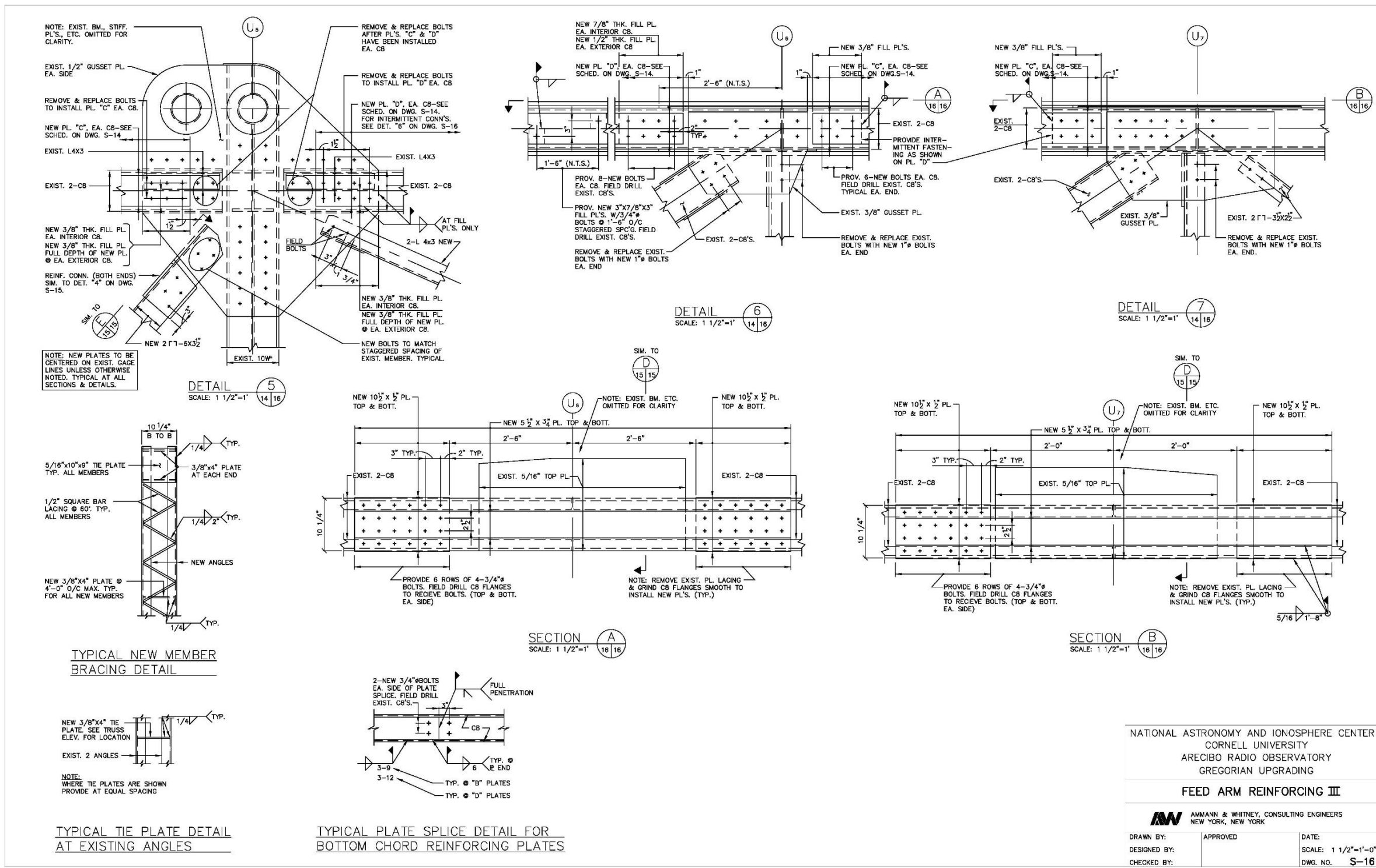


NATIONAL ASTRONOMY AND IONOSPHERE CENTER
CORNELL UNIVERSITY
ARECIBO RADIO OBSERVATORY
GREGORIAN UPGRADING
FEED ARM REINFORCING II

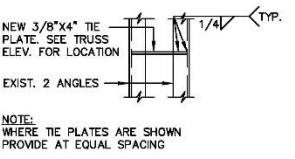
AW AMMANN & WHITNEY, CONSULTING ENGINEERS
NEW YORK, NEW YORK

DRAWN BY:	APPROVED	DATE:
DESIGNED BY:		SCALE: AS NOTED
CHECKED BY:		DWG. NO. S-15

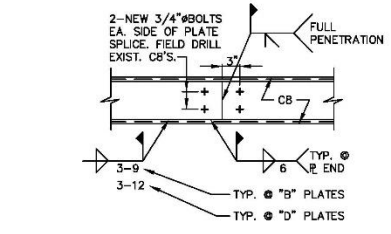
FILE #ARC12



TYPICAL NEW MEMBER BRACING DETAIL



TYPICAL TIE PLATE DETAIL AT EXISTING ANGLES



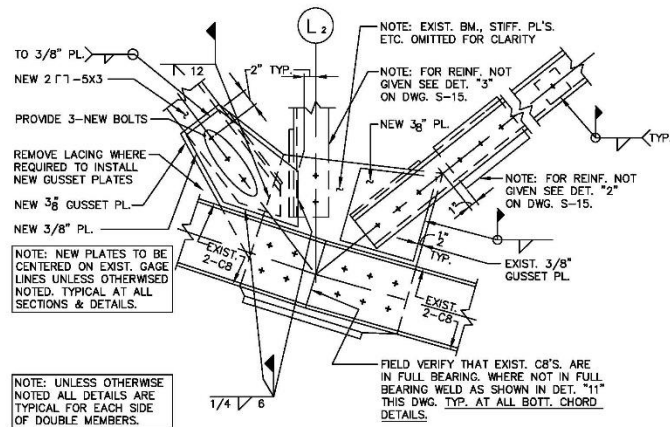
TYPICAL PLATE SPLICE DETAIL FOR BOTTOM CHORD REINFORCING PLATES

NATIONAL ASTRONOMY AND IONOSPHERE CENTER
 CORNELL UNIVERSITY
 ARECIBO RADIO OBSERVATORY
 GREGORIAN UPGRADING

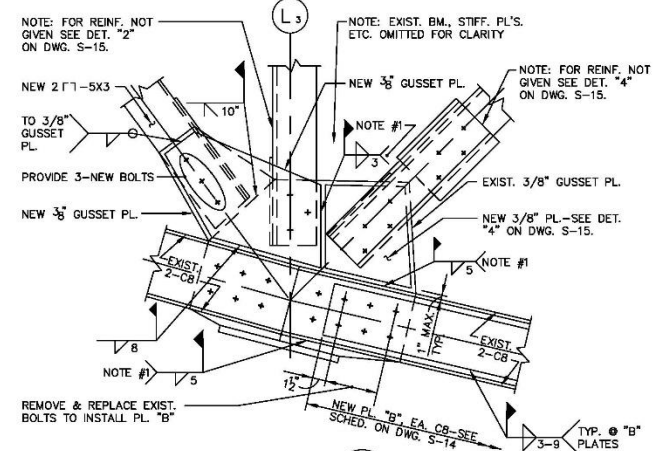
FEED ARM REINFORCING III

AMMANN & WHITNEY, CONSULTING ENGINEERS
 NEW YORK, NEW YORK

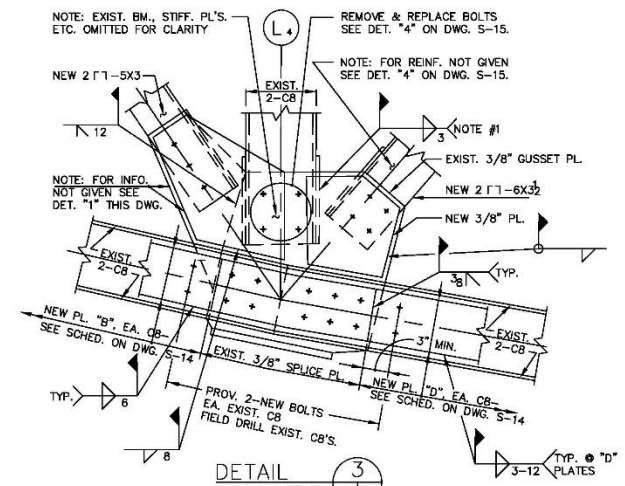
DESIGNED BY:	APPROVED	DATE:
CHECKED BY:		SCALE: 1 1/2"=1'-0"
		DWG. NO. S-16



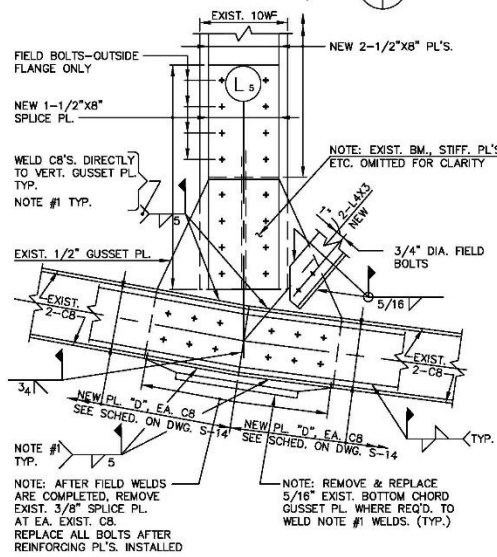
DETAIL 1
SCALE: 1 1/2"=1'
14 | 17



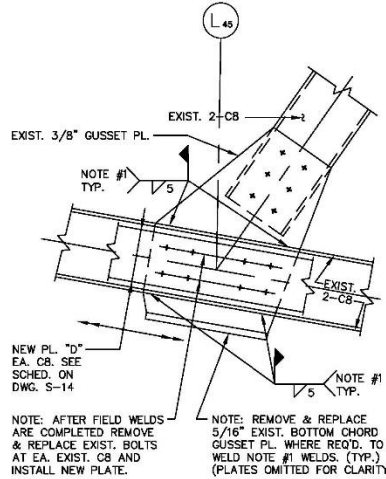
DETAIL 2
SCALE: 1 1/2"=1'
14 | 17



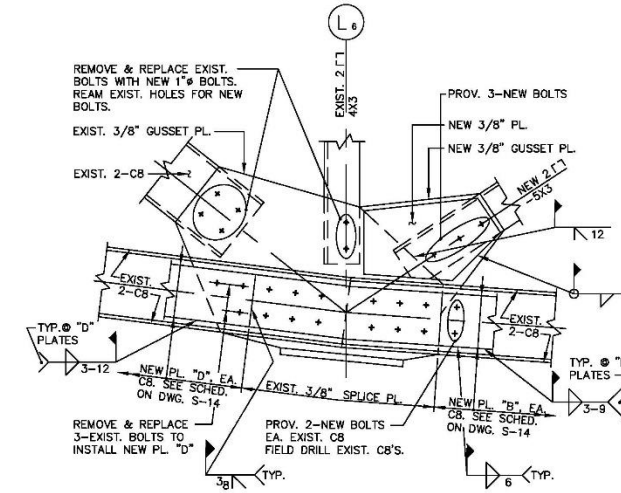
DETAIL 3
SCALE: 1 1/2"=1'
14 | 17



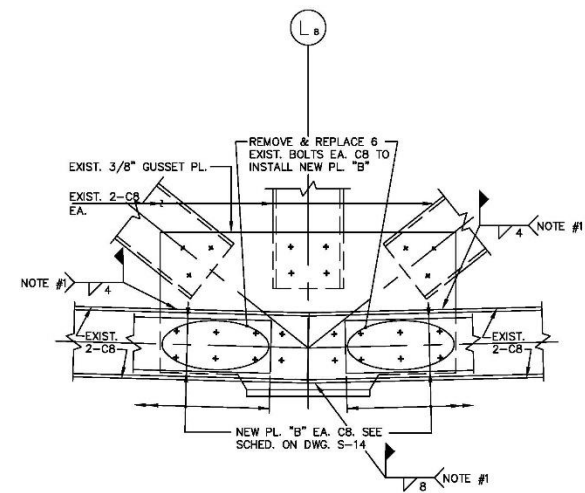
DETAIL 4
SCALE: 1 1/2"=1'
14 | 17



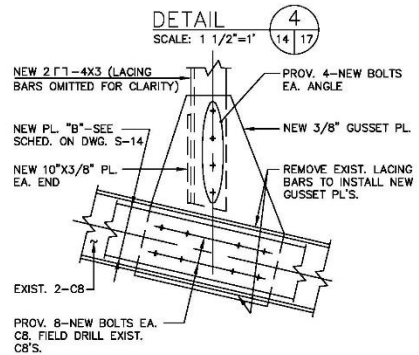
DETAIL 5
SCALE: 1 1/2"=1'
14 | 17



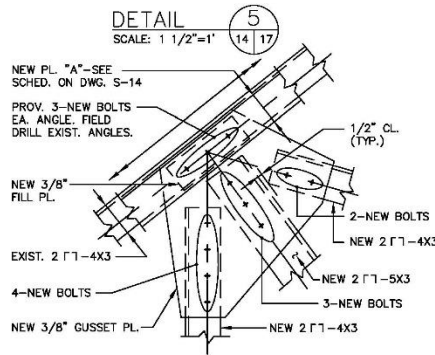
DETAIL 6
SCALE: 1 1/2"=1'
14 | 17



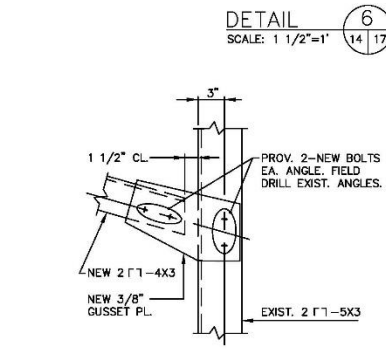
DETAIL 7
SCALE: 1 1/2"=1'
14 | 17



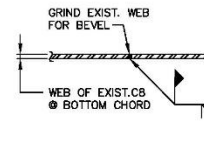
DETAIL 8
SCALE: 1 1/2"=1'
14 | 17



DETAIL 9
SCALE: 1 1/2"=1'
14 | 17



DETAIL 10
SCALE: 1 1/2"=1'
14 | 17



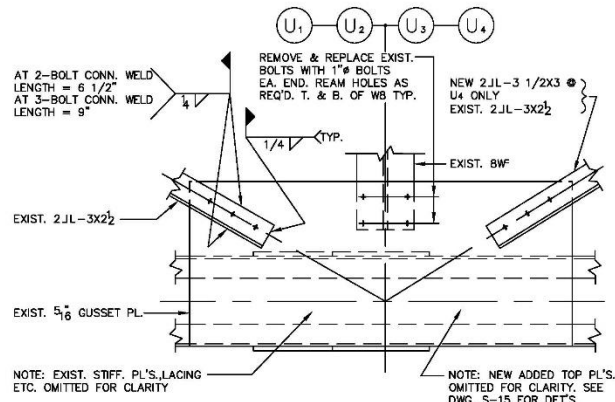
DETAIL 11
SCALE: 3"=1'
17 | 17

NATIONAL ASTRONOMY AND IONOSPHERE CENTER
CORNELL UNIVERSITY
ARECIBO RADIO OBSERVATORY
GREGORIAN UPGRADING
FEED ARM REINFORCING IV

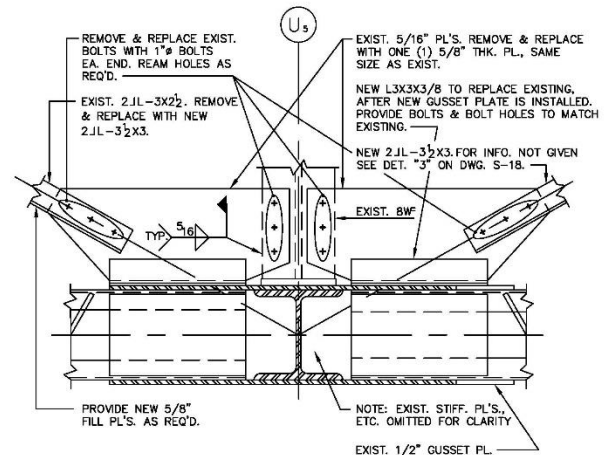
AMMANN & WHITNEY CONSULTING ENGINEERS
NEW YORK, NEW YORK

DRAWN BY:	APPROVED	DATE:
DESIGNED BY:		SCALE:
CHECKED BY:		DWG. NO. S-17

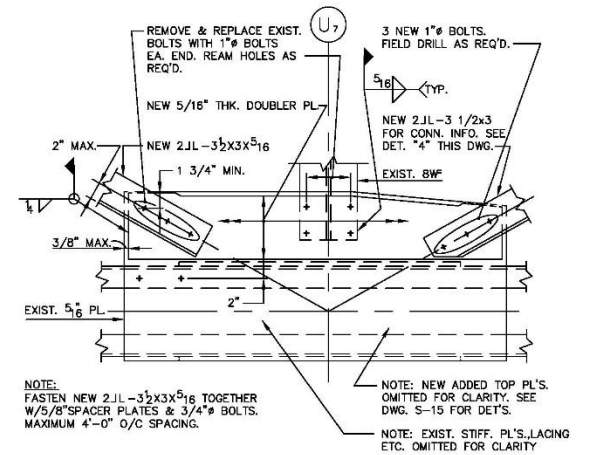
FILE #ARC14



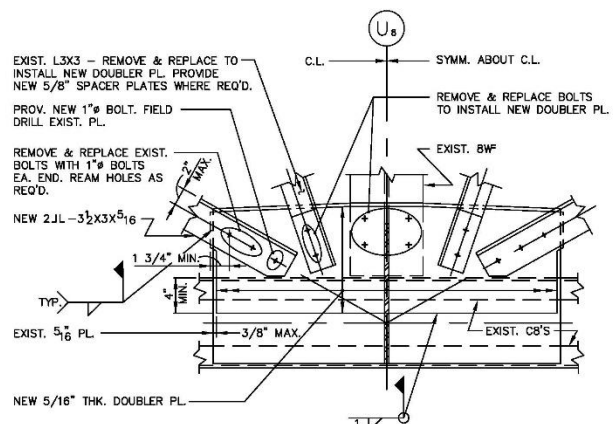
DETAIL 1
SCALE: 1 1/2"=1'
(TYPICAL EA. TRUSS)



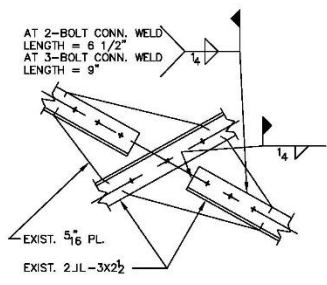
DETAIL 2
SCALE: 1 1/2"=1'
(TYPICAL EA. TRUSS)



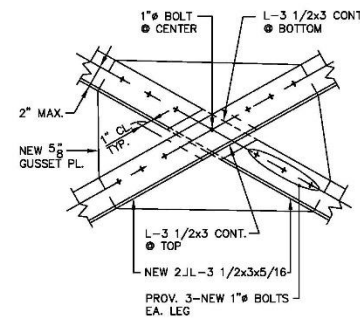
DETAIL 3
SCALE: 1 1/2"=1'
(TYPICAL EA. TRUSS)



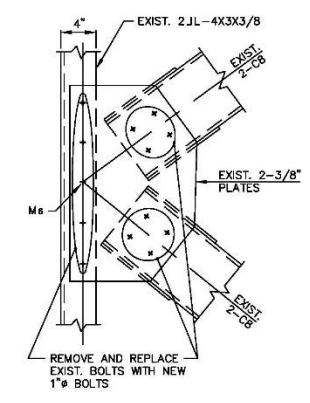
DETAIL 4
SCALE: 1 1/2"=1'
(TYPICAL EA. TRUSS)



DETAIL 5
SCALE: 1 1/2"=1'
(TYPICAL EA. TRUSS)



DETAIL 6
SCALE: 1 1/2"=1'
(TYPICAL EA. TRUSS)



DETAIL 7
SCALE: 1 1/2"=1'
(TYPICAL EA. TRUSS)

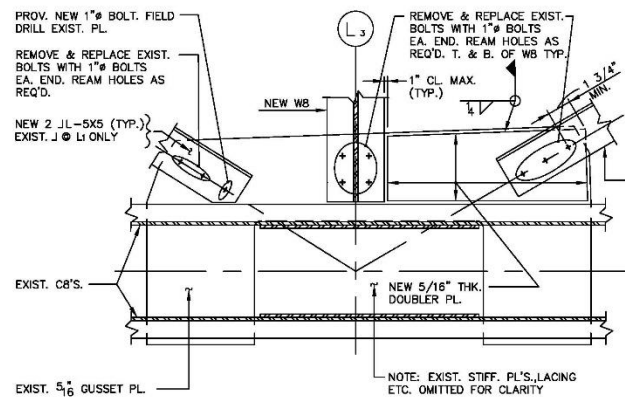
NATIONAL ASTRONOMY AND IONOSPHERE CENTER
CORNELL UNIVERSITY
ARECIBO RADIO OBSERVATORY
GREGORIAN UPGRADING

FEED ARM REINFORCING VI

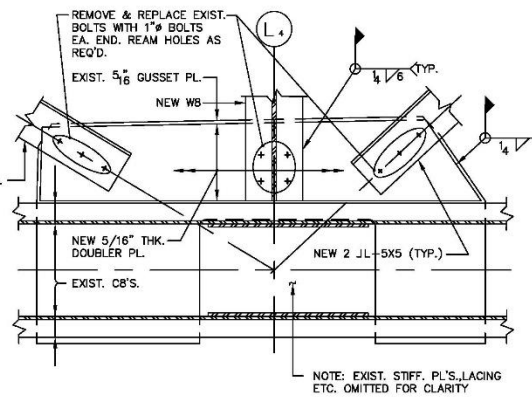
AMMANN & WHITNEY CONSULTING ENGINEERS
NEW YORK, NEW YORK

DRAWN BY:	APPROVED	DATE:
DESIGNED BY:		SCALE:
CHECKED BY:		DWG. NO. S-18

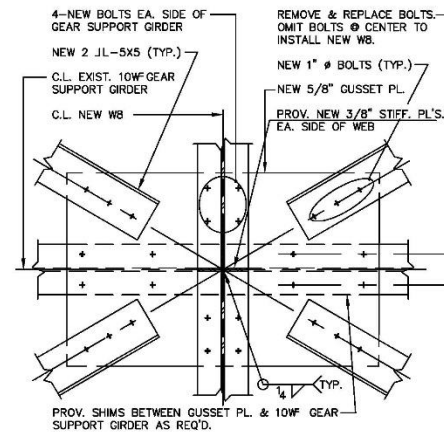
FILE #ARC26



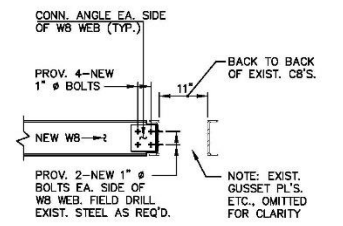
DETAIL 1
SCALE: 1 1/2"=1'
14 | 19
(TYPICAL EA. TRUSS)



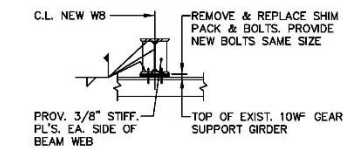
DETAIL 2
SCALE: 1 1/2"=1'
14 | 19
(TYPICAL EA. TRUSS)



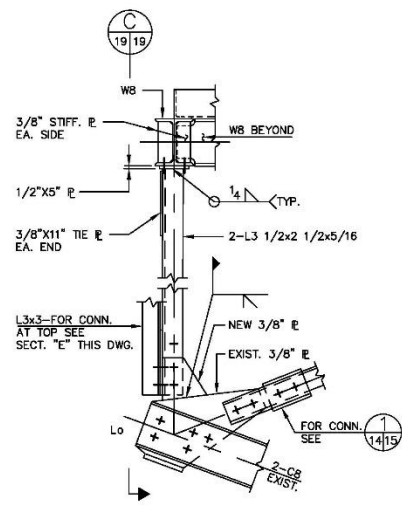
DETAIL 3
SCALE: 1 1/2"=1'
14 | 19



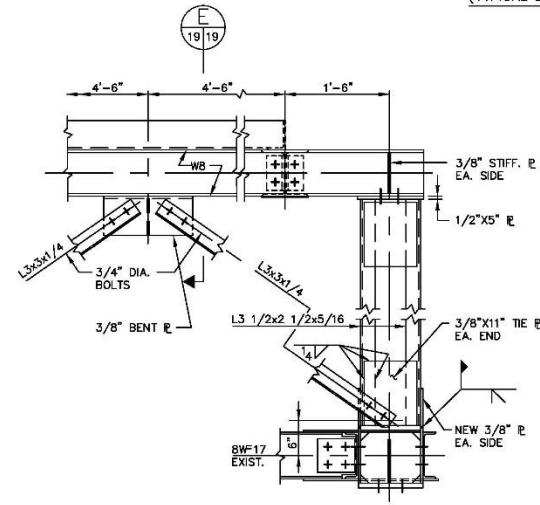
SECTION A
SCALE: 3/4"=1'
14 | 19



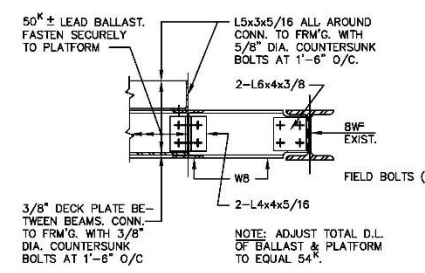
SECTION B
SCALE: 3/4"=1'
14 | 19



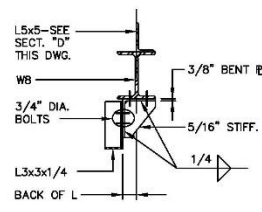
DETAIL 4
SCALE: 1"=1'-0"
14 | 19



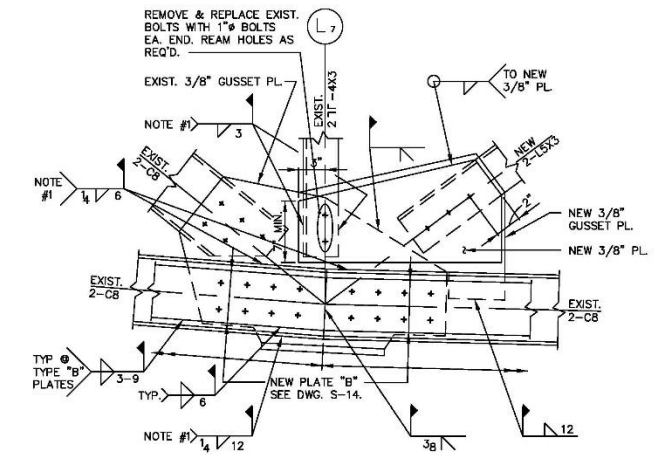
SECTION C
SCALE: 1"=1'-0"
19 | 19



SECTION D
SCALE: 1"=1'-0"
14 | 19



SECTION E
SCALE: 1"=1'-0"
19 | 19



DETAIL 5
SCALE: 1 1/2"=1'-0"
14 | 19

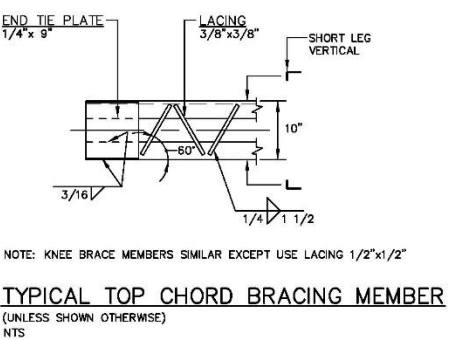
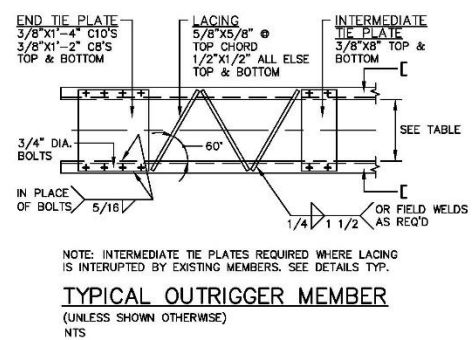
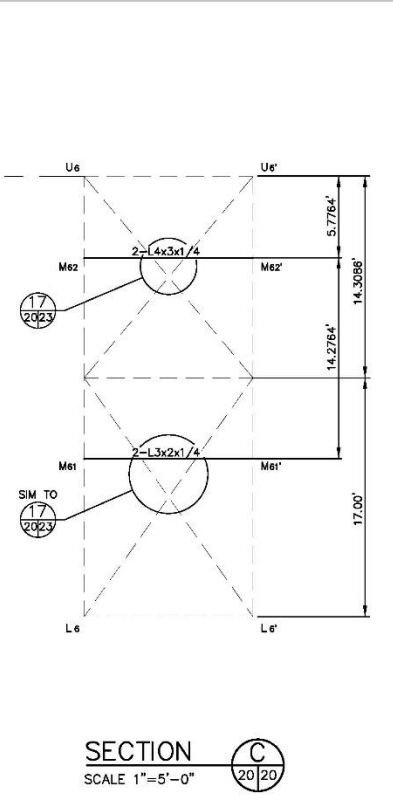
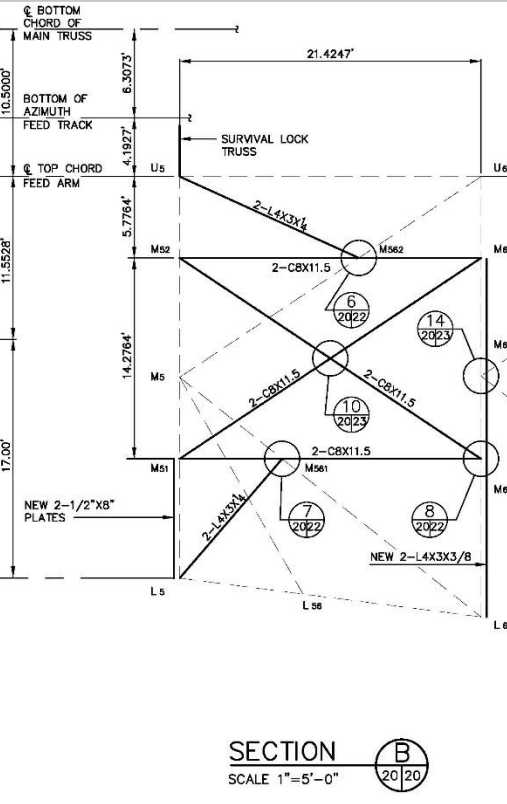
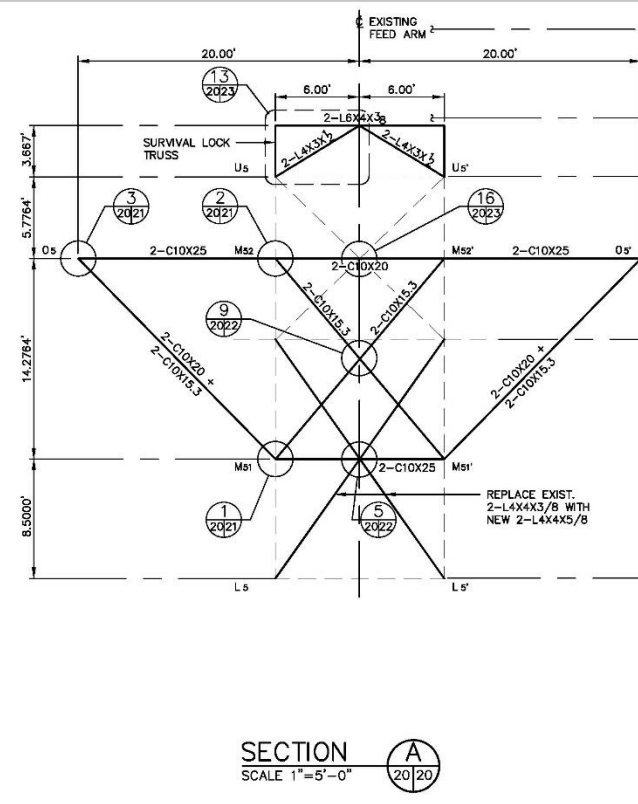
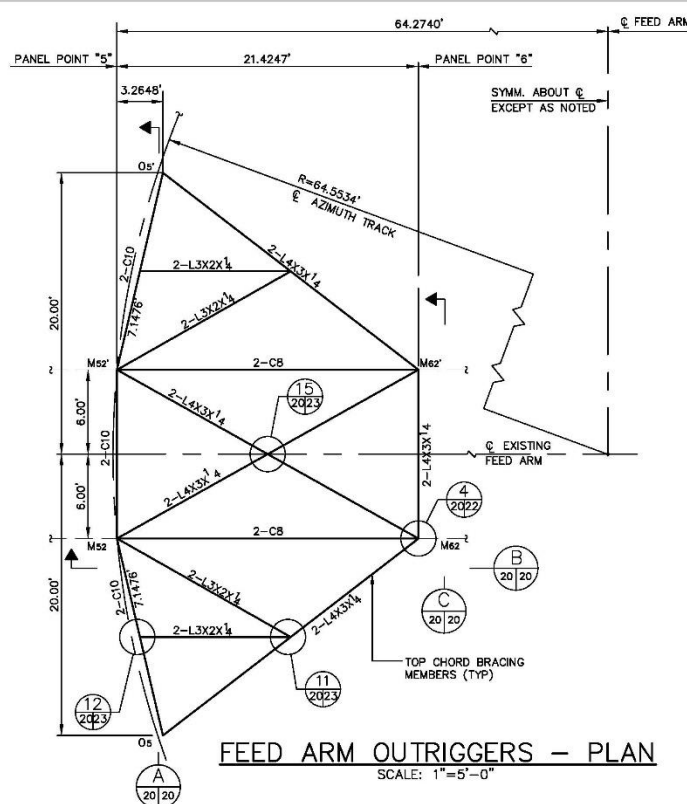
NATIONAL ASTRONOMY AND IONOSPHERE CENTER
CORNELL UNIVERSITY
ARECIBO RADIO OBSERVATORY
GREGORIAN UPGRADING

FEED ARM REINFORCING VI

AMMANN & WHITNEY, CONSULTING ENGINEERS
NEW YORK, NEW YORK

DRAWN BY:	APPROVED	DATE:
DESIGNED BY:		SCALE:
CHECKED BY:		DWG. NO. S-19

FILE #ARC27



FEED ARM OUTRIGGER FORCE TABLE						
MAKE-UP	MEMBER	OPERATIONAL LOAD (KIPS)		SURVIVAL LOAD (KIPS)		
		T	C	T	C	
2-C 13 1/4"	OUTRIGGERS TOP CHORD					
	Os - Ms2		199		291	
	M52 - M52'		190		248	
4-C 13 1/4"	OUTRIGGERS BOTTOM CHORD					
	Os - Ms1	296		413		
2-C 13 1/4"	X-BRACES	M51 - Ms1'	212		285	
		M52 - Ms1'		17	45	85
		M51 - Ms2'		17	45	85
2-C 12"	FACE MEMBERS HORIZ.	M52 - Ms22	16	9	34	10
		M522 - Ms2	60		60	
		M51 - Ms21	15		15	31
		M521 - Ms1		44		50
2-C 12"	FACE MEMBERS X-BRACES	M51 - Ms2	53	65	60	73
		M51 - Ms2			60	
2-L 10 1/4"	FACE MEMBERS KNEE BRACES	Us - Ms22	46		38	4
		Ls - Ms21		35	37	5

NOTES:
1. ALL BOLTS IN FEED ARM OUTRIGGERS ARE 7/8" DIA. UNLESS OTHERWISE NOTED.

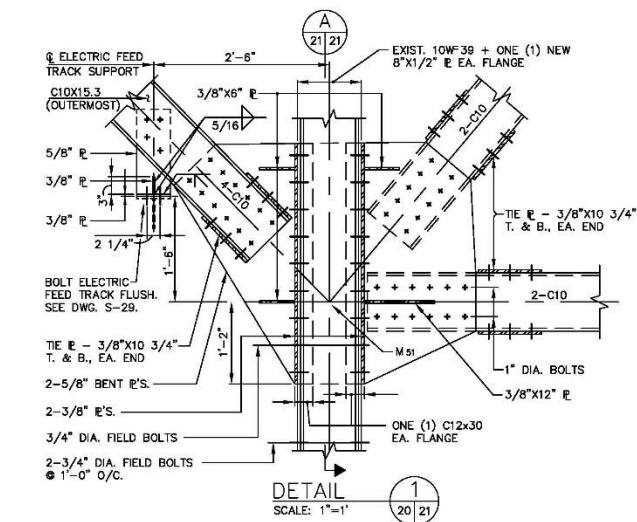
NATIONAL ASTRONOMY AND IONOSPHERE CENTER
CORNELL UNIVERSITY
ARECIBO RADIO OBSERVATORY
GREGORIAN UPGRADING

FEED ARM OUTRIGGERS I

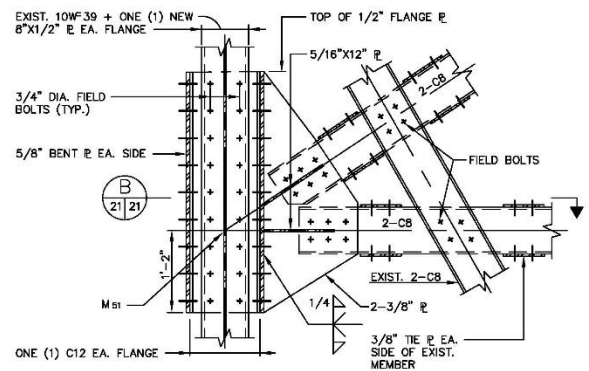
AW AMMANN & WHITNEY, CONSULTING ENGINEERS
NEW YORK, NEW YORK

DRAWN BY: APPROVED: DATE:
DESIGNED BY: SCALE: AS NOTED
CHECKED BY: DWG. NO. S-20

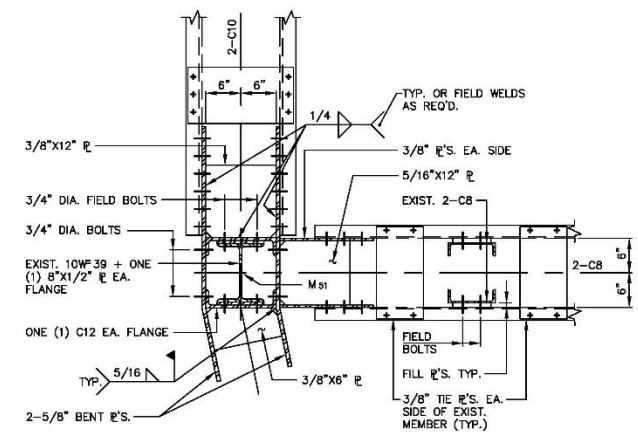
FILE #ARC10



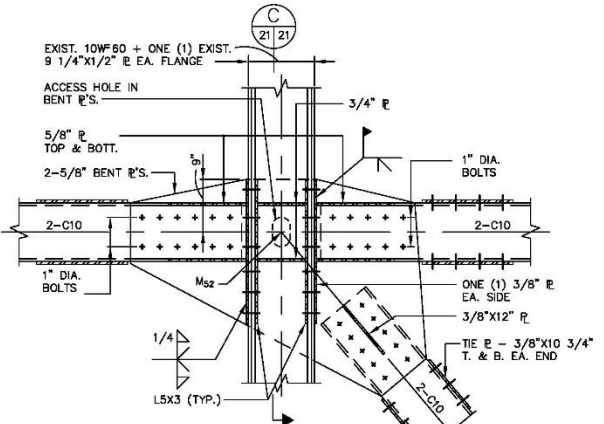
DETAIL 1
SCALE: 1"=1"



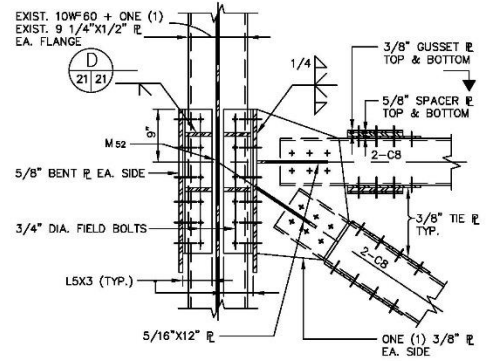
SECTION A
SCALE: 1"=1"



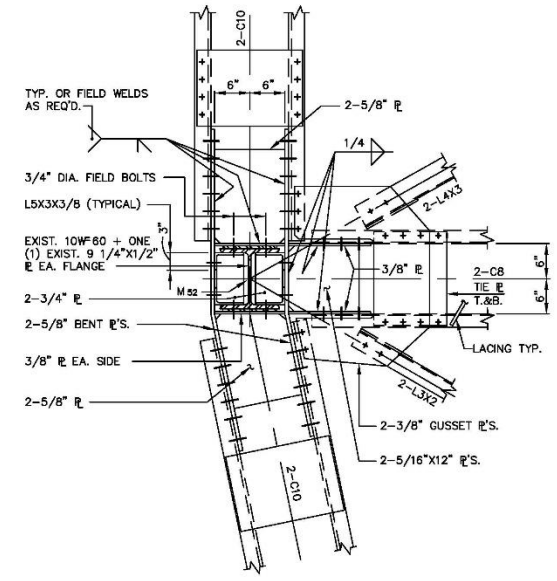
SECTION B
SCALE: 1"=1"



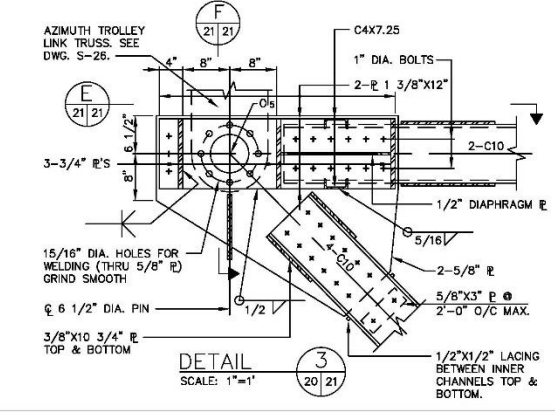
DETAIL 2
SCALE: 1"=1"



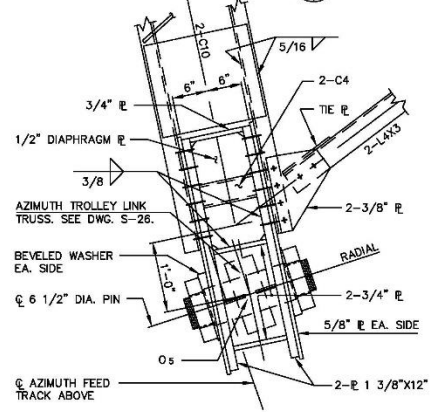
SECTION C
SCALE: 1"=1"



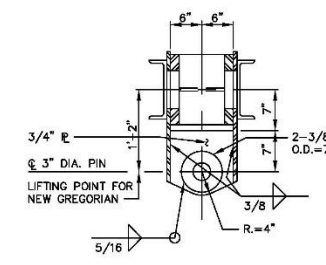
SECTION D
SCALE: 1"=1"



DETAIL 3
SCALE: 1"=1"



SECTION E
SCALE: 1"=1"

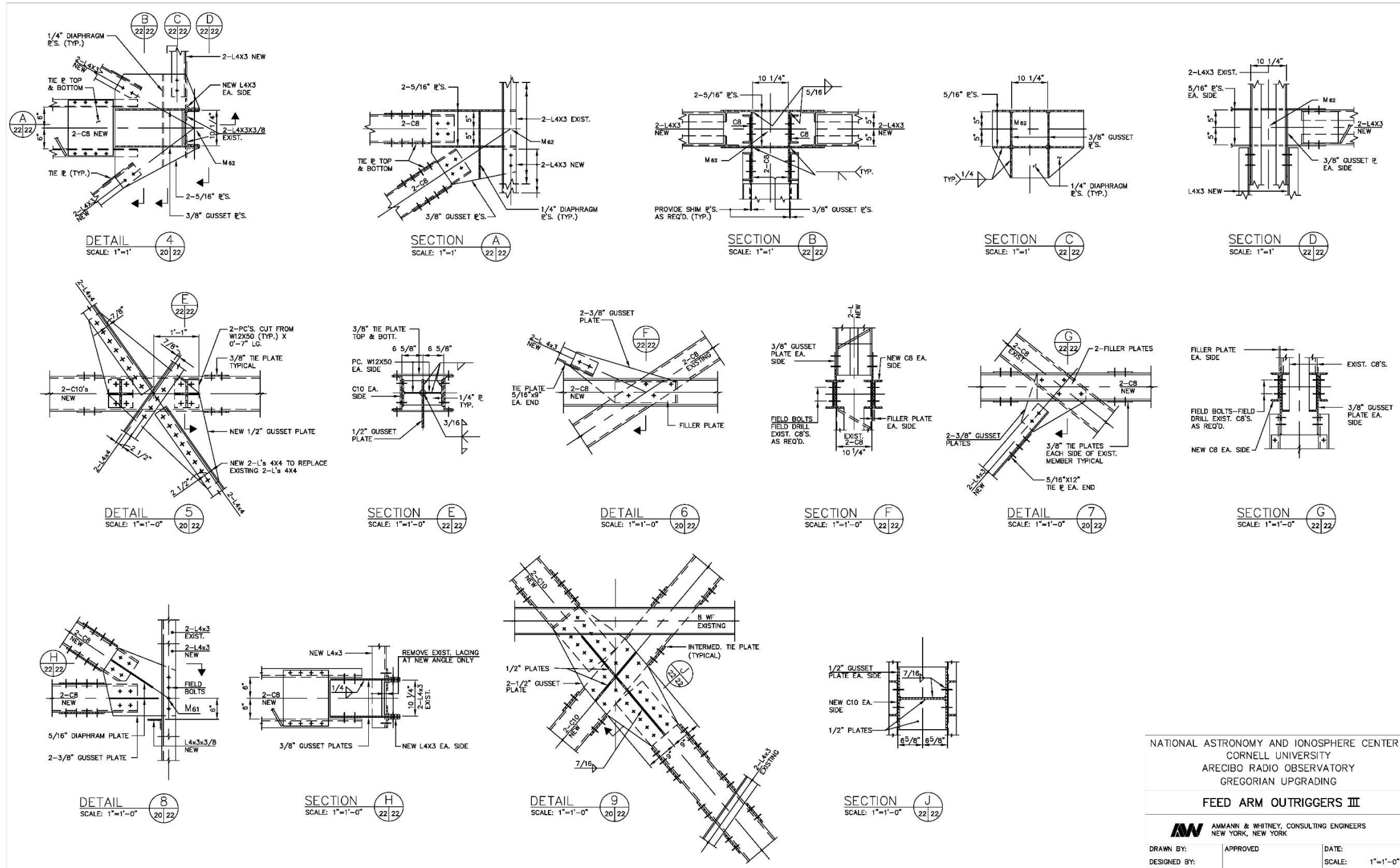


SECTION F
SCALE: 1"=1"

NATIONAL ASTRONOMY AND IONOSPHERE CENTER
CORNELL UNIVERSITY
ARECIBO RADIO OBSERVATORY
GREGORIAN UPGRADING
FEED ARM OUTRIGGERS II

AMMANN & WHITNEY, CONSULTING ENGINEERS NEW YORK, NEW YORK	DRAWN BY:	APPROVED	DATE:
	DESIGNED BY:		SCALE: 1"=1'-0"
	CHECKED BY:		DWG. NO. S-21

FILE #ARC11



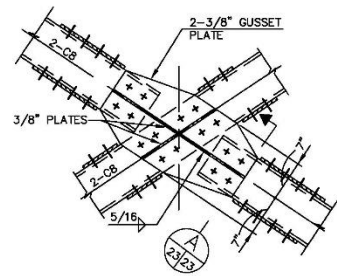
NATIONAL ASTRONOMY AND IONOSPHERE CENTER
 CORNELL UNIVERSITY
 ARECIBO RADIO OBSERVATORY
 GREGORIAN UPGRADING

FEED ARM OUTRIGGERS III

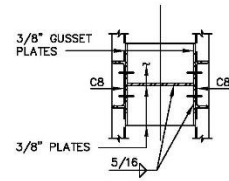
AW AMMANN & WHITNEY, CONSULTING ENGINEERS
 NEW YORK, NEW YORK

DRAWN BY:	APPROVED	DATE:
DESIGNED BY:		SCALE: 1"=1'-0"
CHECKED BY:		DWG. NO. S-22

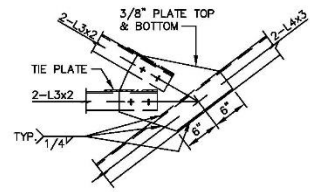
FILE #ARC30



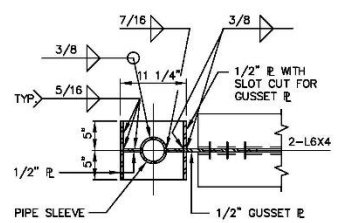
DETAIL 10
SCALE: 1"=1'-0"
20/23



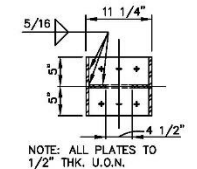
SECTION A
SCALE: 1"=1'-0"
23/23



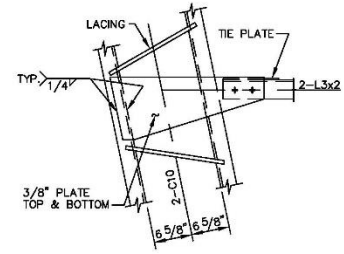
DETAIL 11
SCALE: 1"=1'-0"
20/23



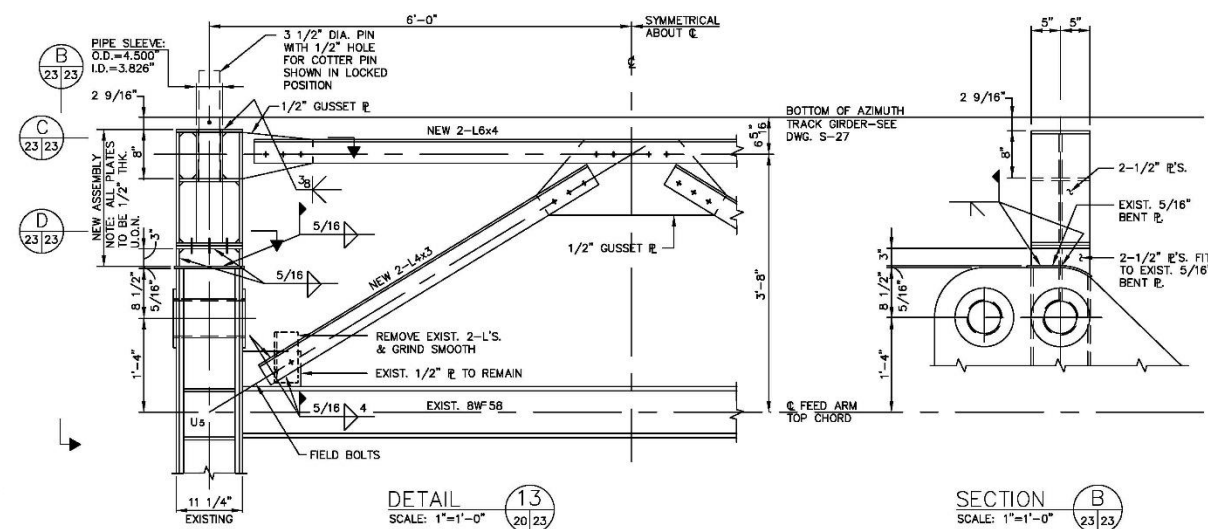
SECTION C
SCALE: 1"=1'-0"
23/23



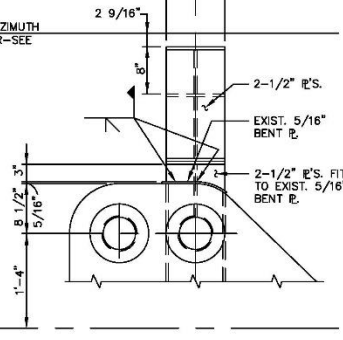
SECTION D
SCALE: 1"=1'-0"
23/23



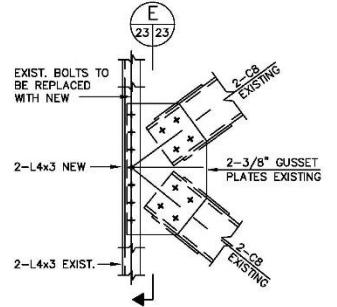
DETAIL 12
SCALE: 1"=1'-0"
20/23



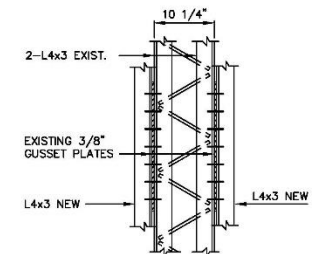
DETAIL 13
SCALE: 1"=1'-0"
20/23



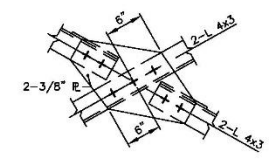
SECTION B
SCALE: 1"=1'-0"
23/23



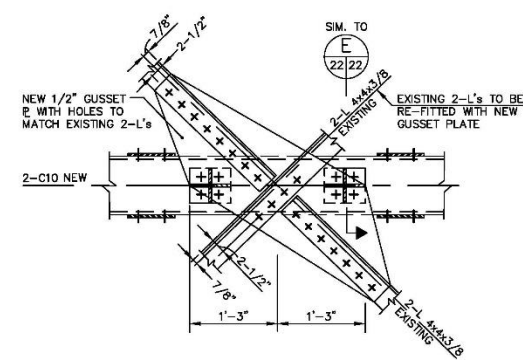
DETAIL 14
SCALE: 1"=1'-0"
20/23



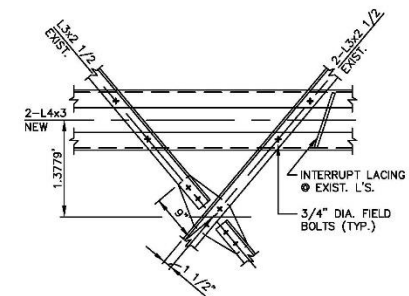
SECTION E
SCALE: 1"=1'-0"
23/23



DETAIL 15
SCALE: 1"=1'-0"
20/23



DETAIL 16
SCALE: 1"=1'-0"
20/23



DETAIL 17
SCALE: 1"=1'-0"
20/23

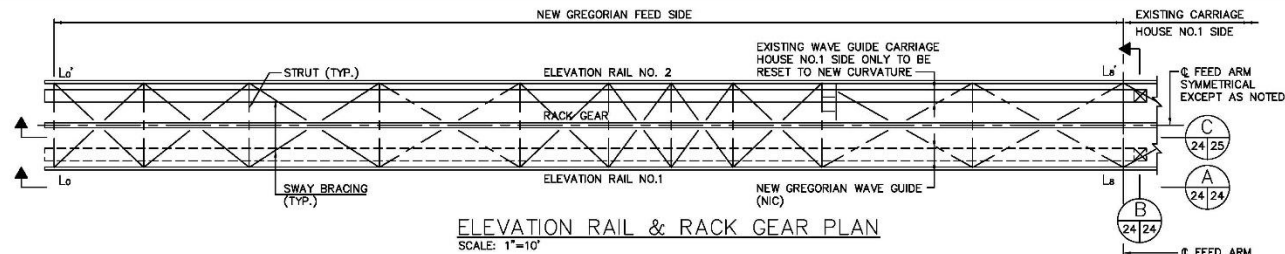
NATIONAL ASTRONOMY AND IONOSPHERE CENTER
CORNELL UNIVERSITY
ARECIBO RADIO OBSERVATORY
GREGORIAN UPGRADING

FEED ARM OUTRIGGERS IV

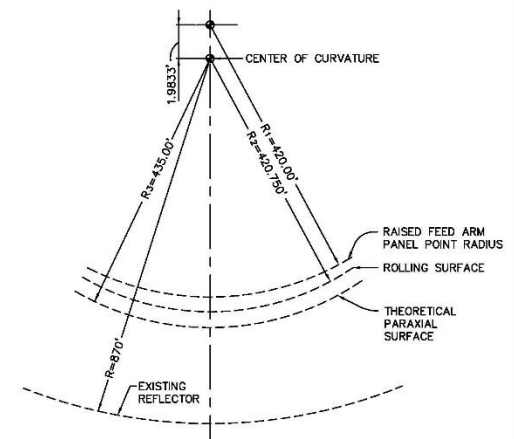
AMMANN & WHITNEY, CONSULTING ENGINEERS
NEW YORK, NEW YORK

DRAWN BY:	APPROVED	DATE:
DESIGNED BY:		SCALE: 1"=1'-0"
CHECKED BY:		DWG. NO. S-23

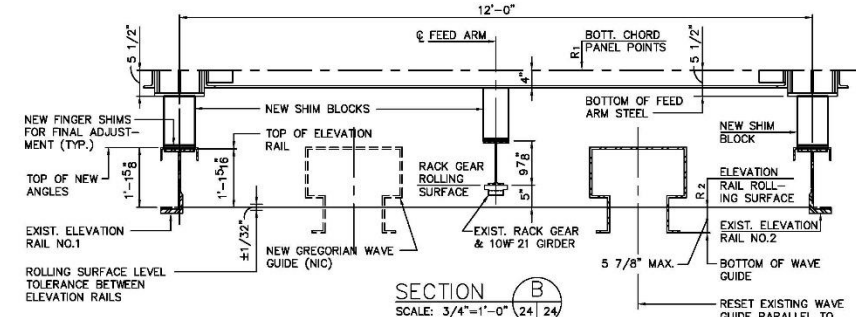
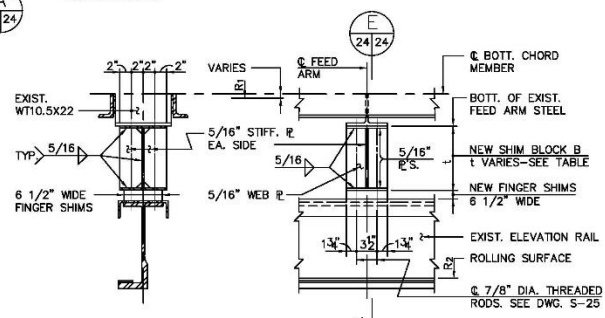
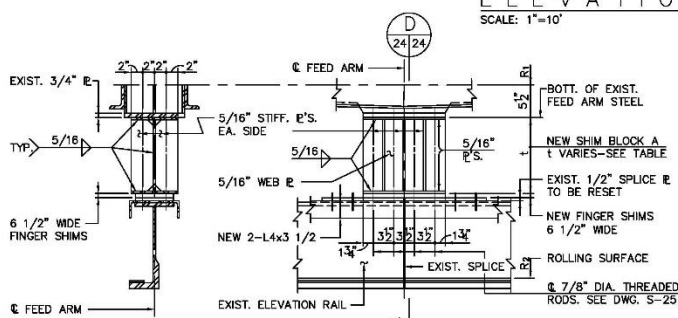
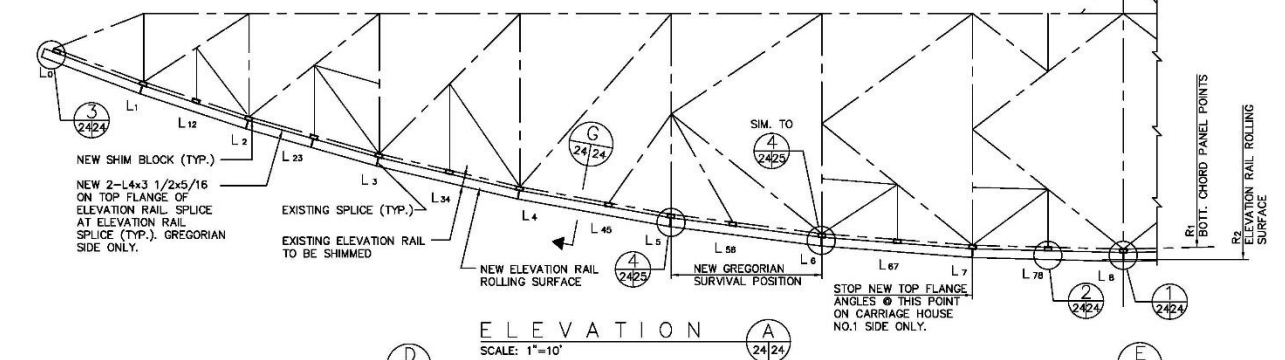
FILE #ARC28



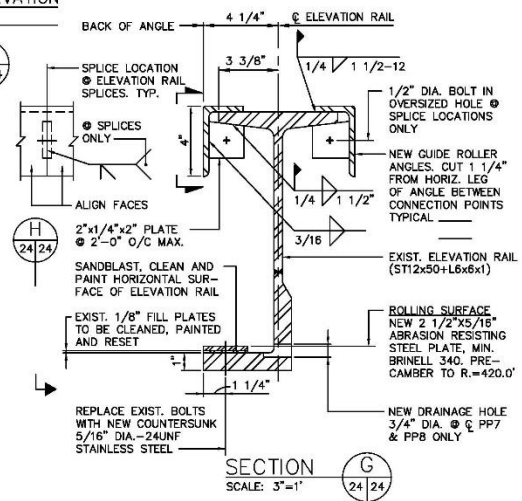
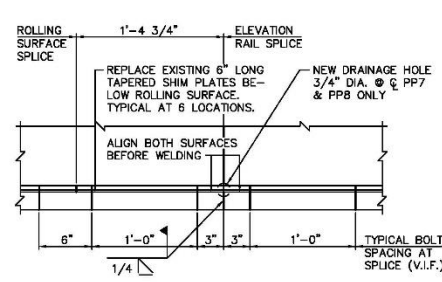
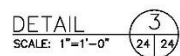
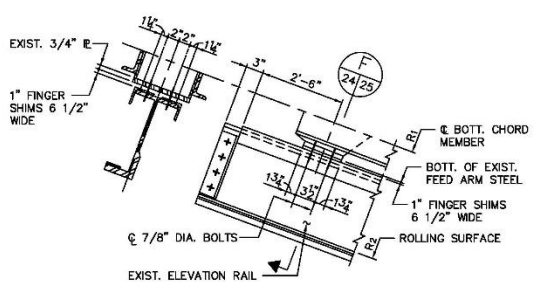
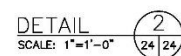
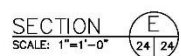
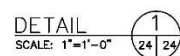
ELEVATION RAIL SHIM BLOCKS			
FEED ARM PANEL POINT	SHIM BLOCK THICKNESS 1" (Inches)	BLOCK TYPE	
L0	NOTE #1	B	B
L1	3.5	A	A
L12	4.0	B	B
L2	5.5	A	A
L23	6.5	B	B
L3	8.0	A	A
L34	9.0	B	B
L4	10	A	A
L45	11	A	A
L5	12	SEE DET.	A
L56	12	A	A
L6	12.5	SEE DET.	A
L67	12.5	B	B
L7	13	A	A
L78	13	B	B
L8	14	A	A
REGORIAN FEED SIDE		REGORIAN FEED SIDE	REGORIAN FEED SIDE
CARRIAGE HOUSE NO. 1 SIDE		CARRIAGE HOUSE NO. 1 SIDE	CARRIAGE HOUSE NO. 1 SIDE



NOTES:
 1. WHERE FINGER SHIMS ONLY ARE REQUIRED BLOCK TYPE REPRESENTS HOLE LAYOUT FOR FINGER SHIMS.



NOTES:
 1. FINGER SHIMS SHALL BE STAINLESS STEEL.
 2. THE THICKNESS OF FINGER SHIMS SHALL BE DETERMINED BY LOADING EACH PANEL POINT WITH APPROPRIATE FEED SYSTEM, TO FORM THE REQUIRED ROLLING SURFACE. HOWEVER, THE THICKNESS SHALL NOT EXCEED 1". IF NECESSARY INCREASE BLOCK SIZE.
 3. THE ROLLING SURFACE R2 SHALL MEET A TOLERANCE OF ±.01" WITH THE UPHILL ROLLERS, OF EITHER FEED SYSTEM, CENTERED ON EACH SHIM PACK.
 4. ALL THREADED RODS SHALL CONFORM TO ASTM A354 GR. BC.
 5. NEW ELEVATION RAIL CURVATURE MAY CAUSE EXISTING HOLES IN TOP FLANGE OF RAIL TO MISALIGN WITH HOLES IN BOTTOM OF FEED ARM. HOLES IN TOP FLANGE OF RAIL SHOULD BE REAMED IF REQUIRED.
 6. CONTRACTOR SHALL SUBMIT HIS PROCEDURE FOR SETTING THE ELEVATION RAIL CURVATURE AND MEETING THE LEVEL TOLERANCE BETWEEN RAILS.



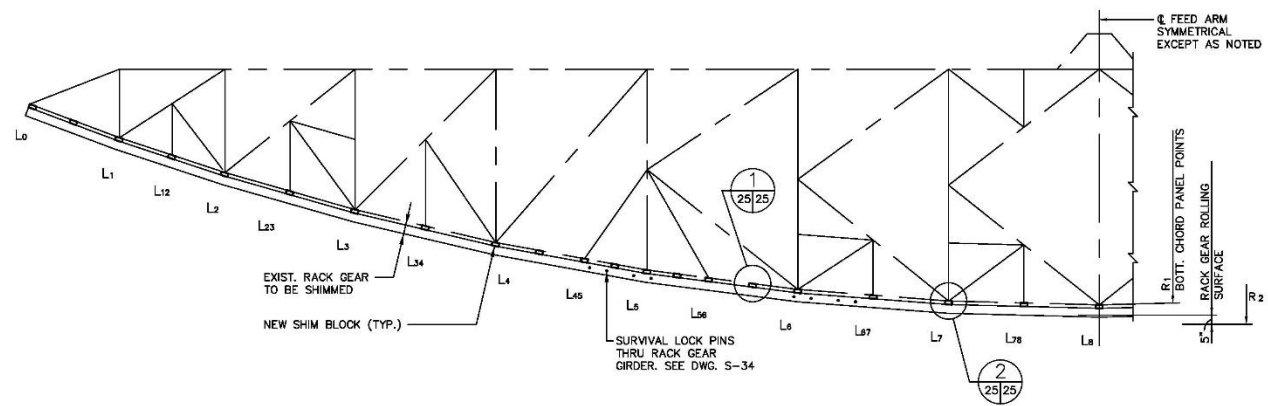
NATIONAL ASTRONOMY AND IONOSPHERE CENTER
 CORNELL UNIVERSITY
 ARECIBO RADIO OBSERVATORY
 GREGORIAN UPGRADING

ELEVATION RAIL & RACK GEAR I

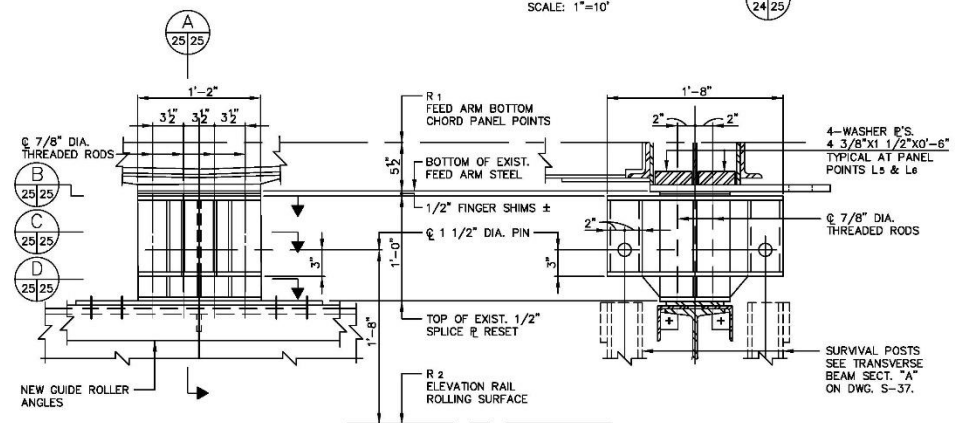
AMMANN & WHITNEY, CONSULTING ENGINEERS
 NEW YORK, NEW YORK

DRAWN BY: APPROVED DATE:
 DESIGNED BY: SCALE: AS NOTED
 CHECKED BY: DWG. NO. S-24

FILE #ARC24

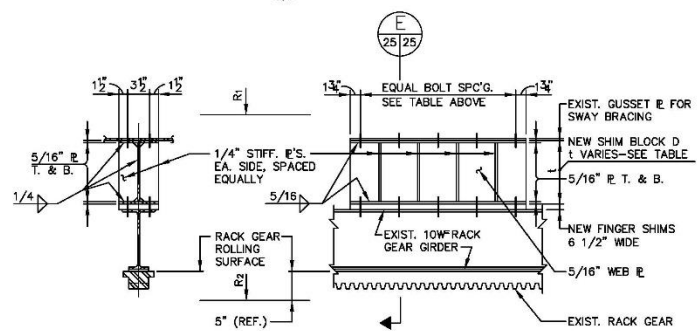


SECTION C
SCALE: 1"=10"
24/25



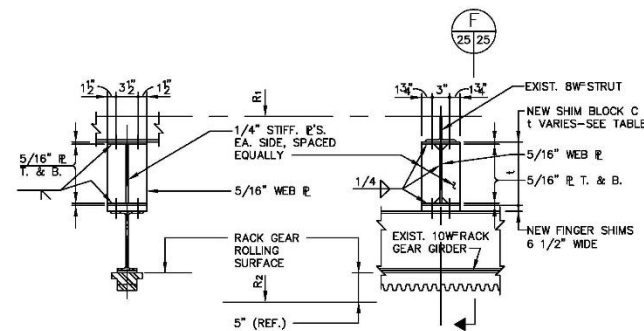
DETAIL 4
SCALE: 1 1/2"=1'-0"
24/25

SECTION A
SCALE: 1 1/2"=1'-0"
24/25



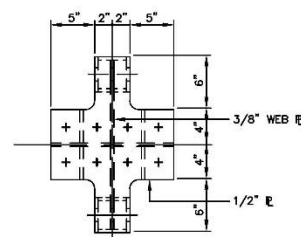
SECTION E
SCALE: 1 1/2"=1'-0"
24/25

TYPICAL DETAIL OF RACK GEAR SEGMENT AT SWAY BRACING INTERSECTION
SCALE: 1"=1'-0"
25/25

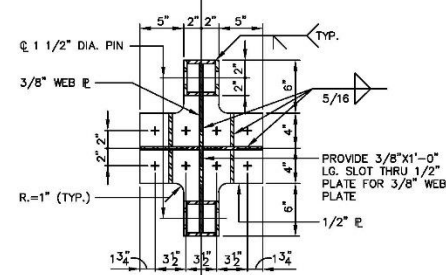


SECTION F
SCALE: 1 1/2"=1'-0"
25/25

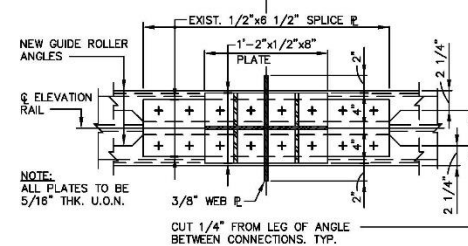
TYPICAL DETAIL OF RACK GEAR SEGMENT AT STRUT INTERSECTION
SCALE: 1"=1'-0"
25/25



SECTION B
SCALE: 1 1/2"=1'-0"
25/25



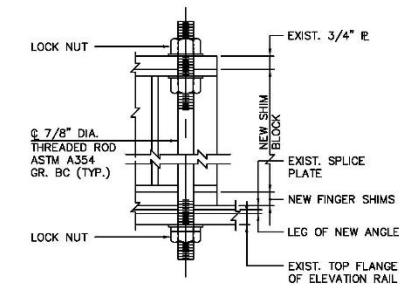
SECTION C
SCALE: 1 1/2"=1'-0"
25/25



SECTION D
SCALE: 1 1/2"=1'-0"
25/25

RACK GEAR SHIM BLOCKS				
FEED ARM PANEL POINT	BLOCK C @ STRUT "t" (inches)	BLOCK D @ SWAY BRACING "t" (inches)	BOLT SPACING	
L0	4.25	6.00	4 5/8	
L1	3.75	7.75	5 1/4	
L12	4.25	8.25	4.00	8.00
L2	5.75	10.25	6 1/4	
L23	6.75	10.25	6.25	10.25
L3	8.25	10.25	7 7/8	
L34	9.25	10.25	8.75	10.25
L4	10.25	12.25	10.75	12.25
L45	11.25	12.25	11.75	12.25
L5	12.25	12.25	12.25	12.25
L56	12.25	12.25	12.50	12.50
L6	12.75	12.75	5 1/2	
L67	12.75	12.75	12.75	12.75
L7	13.25	13.25	8	
L78	13.25	13.25	13.75	13.75
L8	14.25	14.25	6 5/8	

- NOTES:
- WHERE FINGER SHIMS ONLY ARE REQUIRED BLOCK TYPE REPRESENTS HOLE LAYOUT
 - SEE ORIGINAL SHOP DRAWINGS FOR BOLT SPACING.



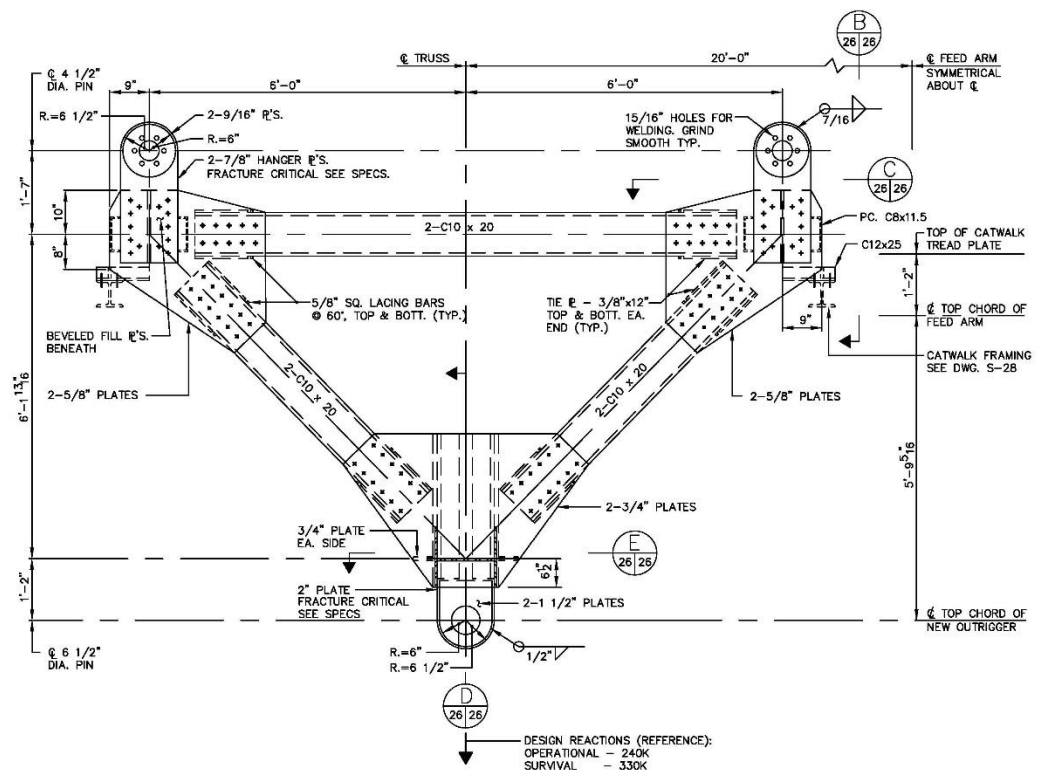
TYPICAL THREADED ROD DETAIL
SCALE: 3"=1'-0"

NATIONAL ASTRONOMY AND IONOSPHERE CENTER
CORNELL UNIVERSITY
ARECIBO RADIO OBSERVATORY
GREGORIAN UPGRADING

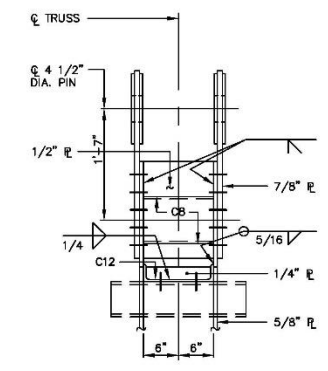
ELEVATION RAIL & RACK GEAR II

AMMANN & WHITNEY, CONSULTING ENGINEERS
NEW YORK, NEW YORK

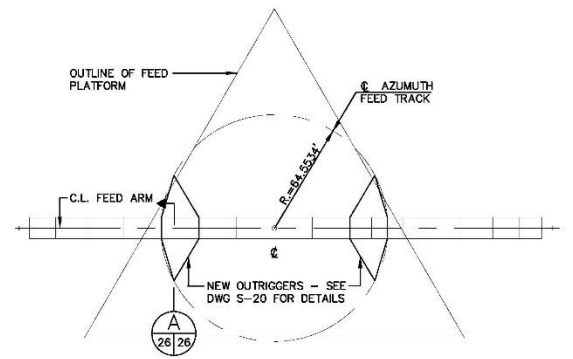
DRAWN BY: APPROVED: DATE:
DESIGNED BY: SCALE: AS NOTED
CHECKED BY: DWG. NO. S-25



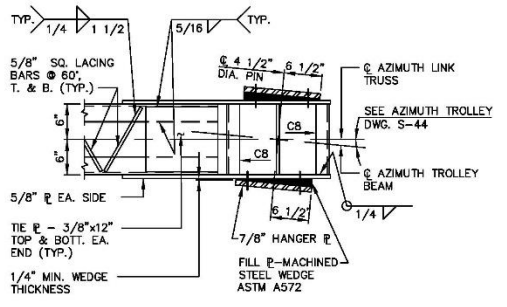
SECTION A
SCALE: 3/4\"=1\"



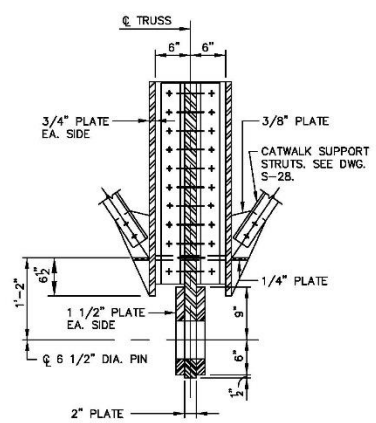
SECTION B
SCALE: 1\"=1\"-0\"



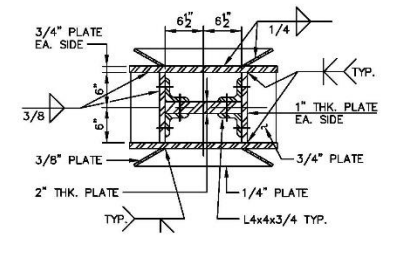
KEY PLAN
SCALE: 1\"=40\"



SECTION C
SCALE: 1\"=1\"-0\"



SECTION D
SCALE: 1\"=1\"-0\"



SECTION E
SCALE: 1\"=1\"-0\"

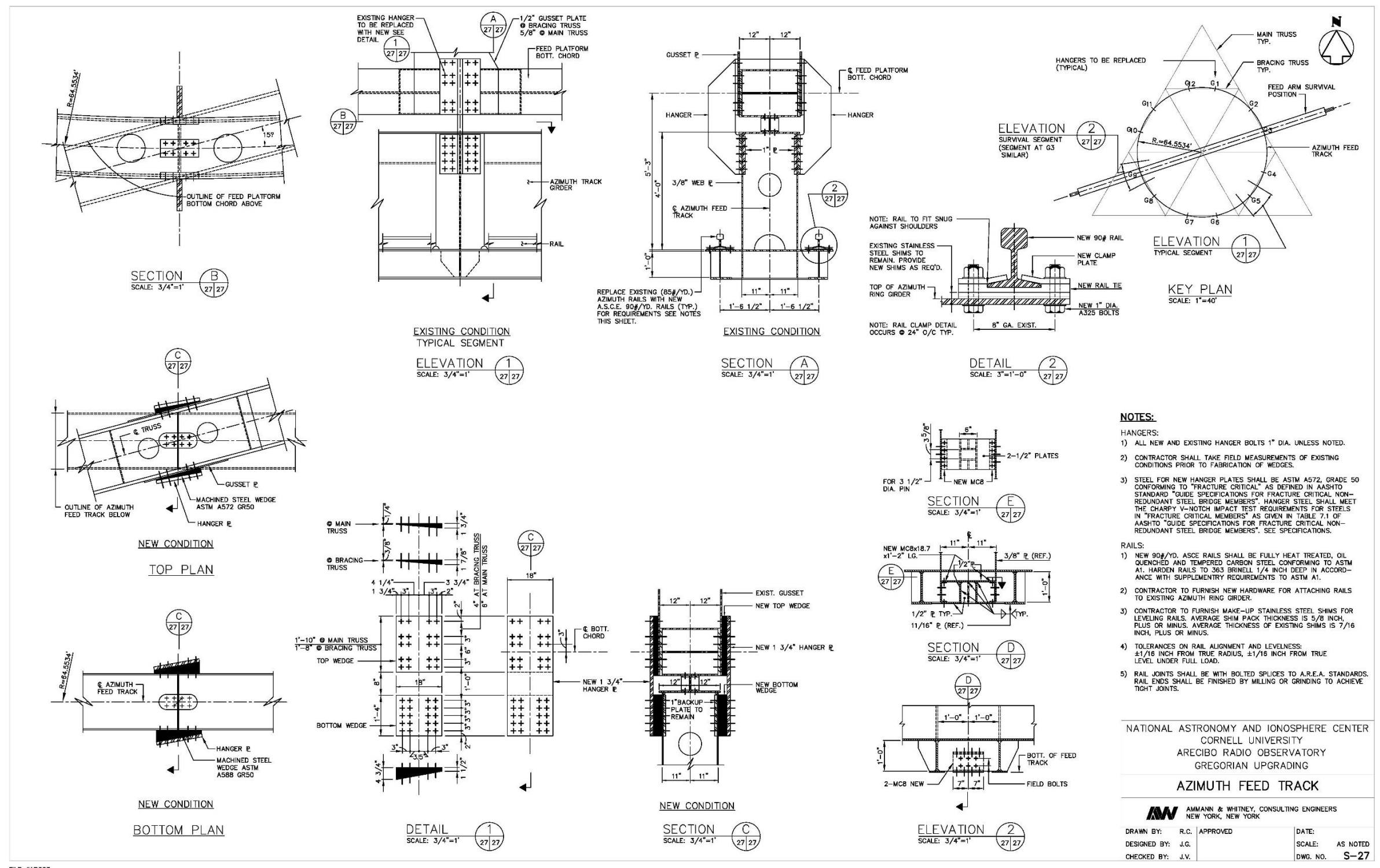
NATIONAL ASTRONOMY AND IONOSPHERE CENTER
CORNELL UNIVERSITY
ARECIBO RADIO OBSERVATORY
GREGORIAN UPGRADING

AZIMUTH TROLLEY LINK TRUSS

AMMANN & WHITNEY, CONSULTING ENGINEERS
NEW YORK, NEW YORK

DRAWN BY:	R.C.	APPROVED	DATE:
DESIGNED BY:	J.G.		SCALE: AS NOTED
CHECKED BY:	J.V.		DWG. NO. S-26

FILE #ARC20



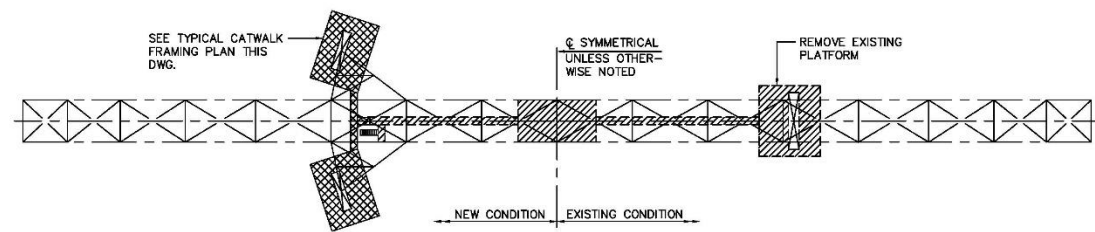
- NOTES:**
- HANGERS:**
- 1) ALL NEW AND EXISTING HANGER BOLTS 1" DIA. UNLESS NOTED.
 - 2) CONTRACTOR SHALL TAKE FIELD MEASUREMENTS OF EXISTING CONDITIONS PRIOR TO FABRICATION OF WEDGES.
 - 3) STEEL FOR NEW HANGER PLATES SHALL BE ASTM A572, GRADE 50 CONFORMING TO "FRACTURE CRITICAL" AS DEFINED IN AASHTO STANDARD "GUIDE SPECIFICATIONS FOR FRACTURE CRITICAL NON-REUNDANT STEEL BRIDGE MEMBERS". HANGER STEEL SHALL MEET THE CHARPY V-NOTCH IMPACT TEST REQUIREMENTS FOR STEELS IN "FRACTURE CRITICAL MEMBERS" AS GIVEN IN TABLE 7.1 OF AASHTO "GUIDE SPECIFICATIONS FOR FRACTURE CRITICAL NON-REUNDANT STEEL BRIDGE MEMBERS". SEE SPECIFICATIONS.
- RAILS:**
- 1) NEW 90#/YD. ASCE RAILS SHALL BE FULLY HEAT TREATED, OIL QUENCHED AND TEMPERED CARBON STEEL CONFORMING TO ASTM A1. HARDEN RAILS TO 363 BRINELL 1/4 INCH DEEP IN ACCORDANCE WITH SUPPLEMENTARY REQUIREMENTS TO ASTM A1.
 - 2) CONTRACTOR TO FURNISH NEW HARDWARE FOR ATTACHING RAILS TO EXISTING AZMUTH RING GIRDER.
 - 3) CONTRACTOR TO FURNISH MAKE-UP STAINLESS STEEL SHIMS FOR LEVELING RAILS. AVERAGE SHIM PACK THICKNESS IS 5/8 INCH, PLUS OR MINUS. AVERAGE THICKNESS OF EXISTING SHIMS IS 7/16 INCH, PLUS OR MINUS.
 - 4) TOLERANCES ON RAIL ALIGNMENT AND LEVELNESS: ±1/16 INCH FROM TRUE RADIUS, ±1/16 INCH FROM TRUE LEVEL UNDER FULL LOAD.
 - 5) RAIL JOINTS SHALL BE WITH BOLTED SPLICES TO A.R.E.A. STANDARDS. RAIL ENDS SHALL BE FINISHED BY MILLING OR GRINDING TO ACHIEVE TIGHT JOINTS.

NATIONAL ASTRONOMY AND IONOSPHERE CENTER
 CORNELL UNIVERSITY
 ARECIBO RADIO OBSERVATORY
 GREGORIAN UPGRADING
AZIMUTH FEED TRACK

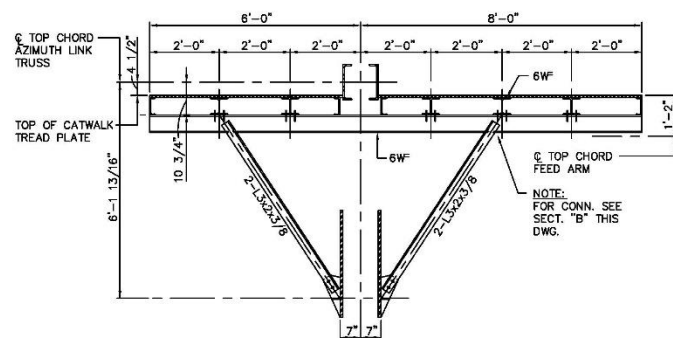
AW AMMANN & WHITNEY, CONSULTING ENGINEERS
 NEW YORK, NEW YORK

DRAWN BY: R.C.	APPROVED:	DATE:
DESIGNED BY: J.G.		SCALE: AS NOTED
CHECKED BY: J.V.		DWG. NO. S-27

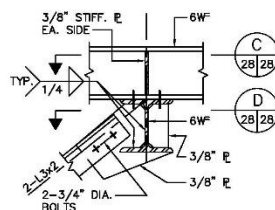
FILE #ARC23



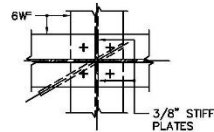
CATWALK PLAN - TOP CHORD OF FEED ARM
SCALE: 1"=20'-0"



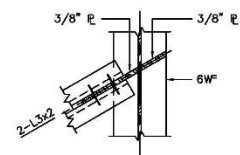
SECTION A
SCALE: 1/2"=1'-0" 28/28



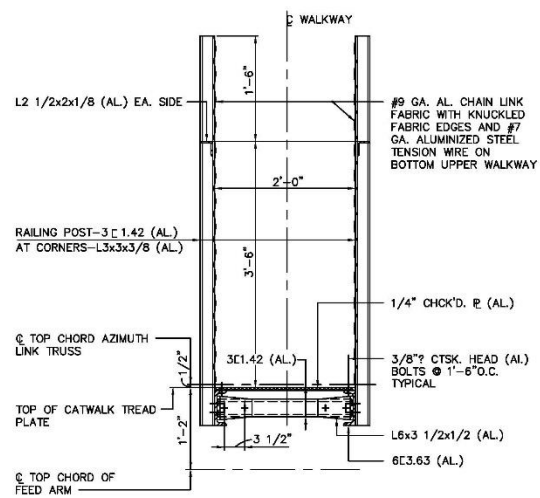
SECTION B
SCALE: 1 1/2"=1'-0" 28/28



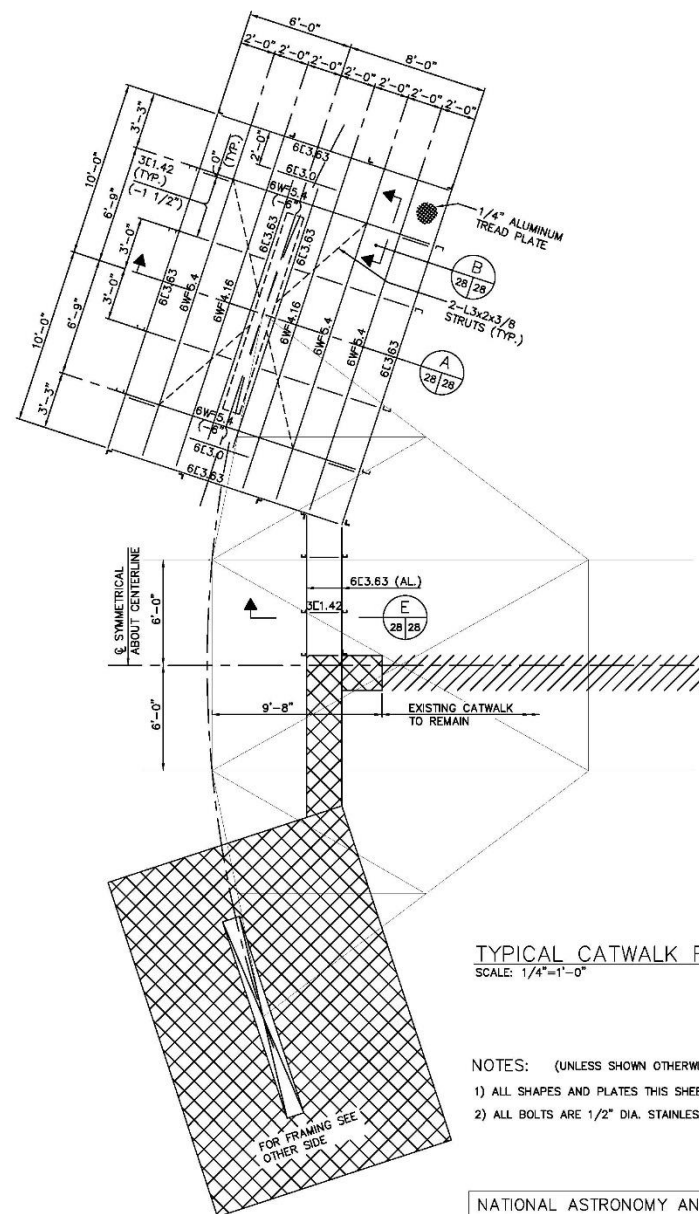
SECTION C
SCALE: 1 1/2"=1'-0" 28/28



SECTION D
SCALE: 1 1/2"=1'-0" 28/28



SECTION E
SCALE: 1"=1'-0" 28/28



NOTES: (UNLESS SHOWN OTHERWISE)
1) ALL SHAPES AND PLATES THIS SHEET ARE 6061-T6 ALUMINUM.
2) ALL BOLTS ARE 1/2" DIA. STAINLESS STEEL.

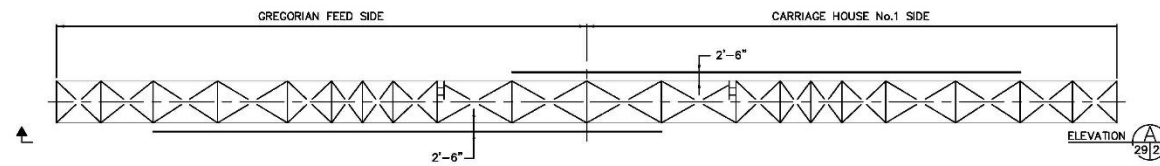
NATIONAL ASTRONOMY AND IONOSPHERE CENTER
CORNELL UNIVERSITY
ARECIBO RADIO OBSERVATORY
GREGORIAN UPGRADING

FEED ARM MISCELLANEOUS I

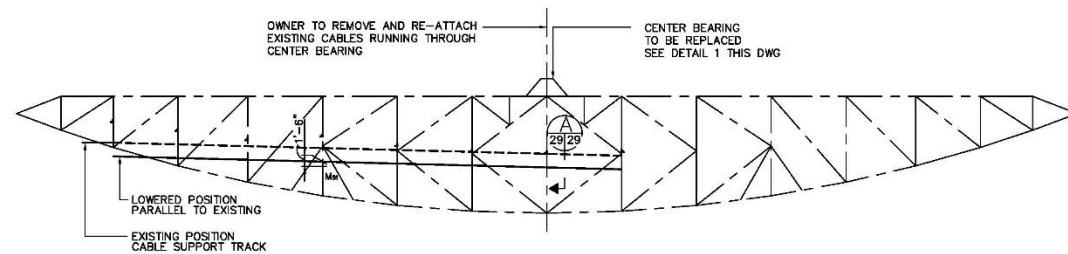
AMMANN & WHITNEY, CONSULTING ENGINEERS
NEW YORK, NEW YORK

DRAWN BY:	APPROVED	DATE:
DESIGNED BY:		SCALE: AS NOTED
CHECKED BY:		DWG. NO. S-28

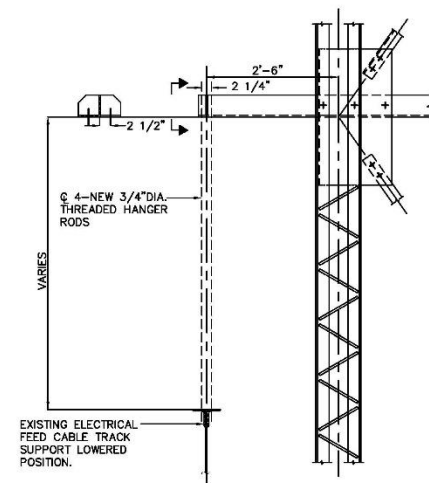
FILE #ARC35



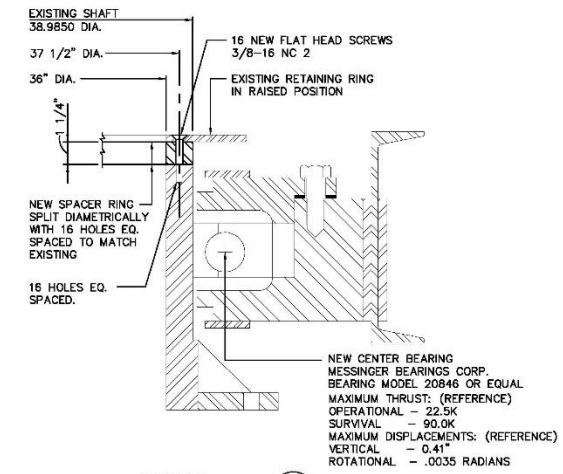
ELECTRIC FEED TRACK - PLAN
SCALE: 1"=20'-0"



ELEVATION A
SCALE: 1"=20'



SECTION A
SCALE: 3/4"=1'-0"



DETAIL 1
SCALE: 3"=1'-0"

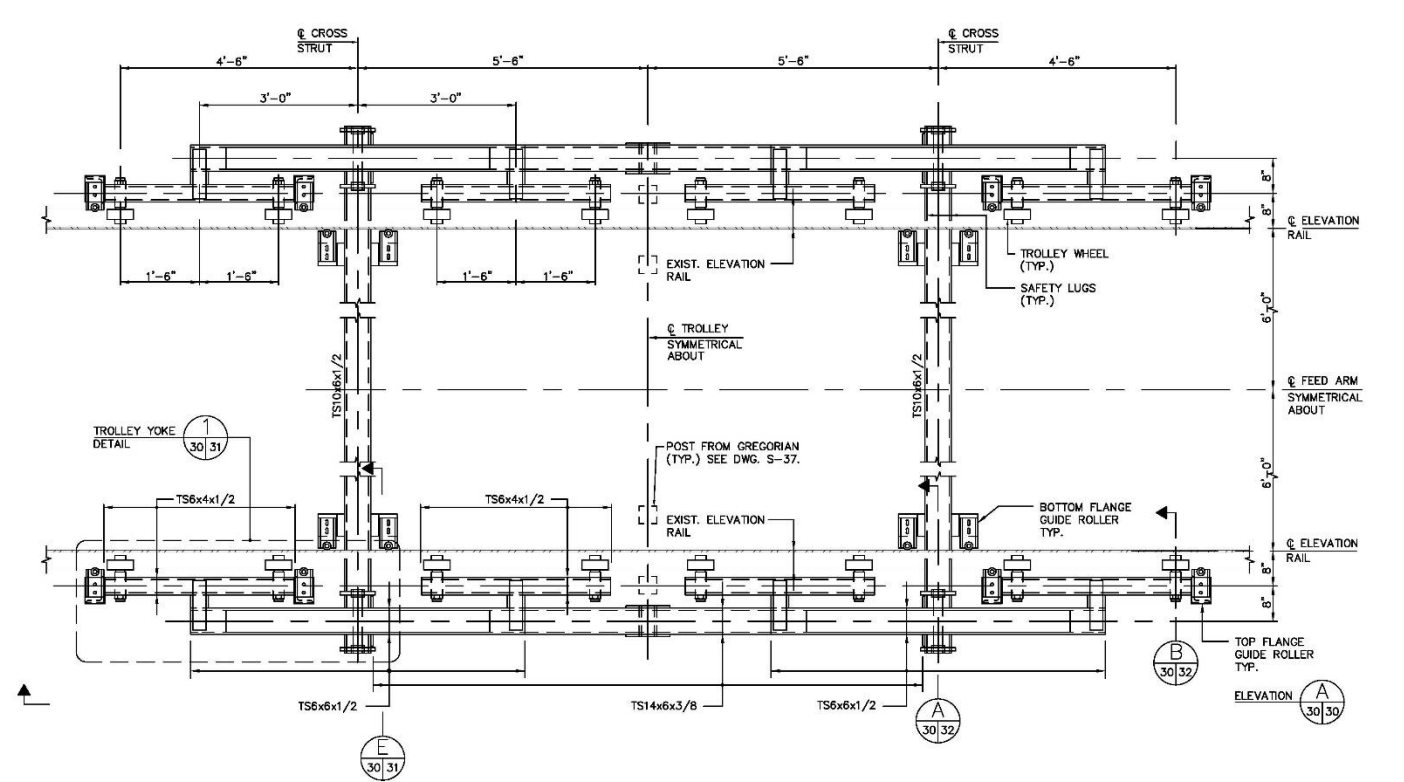
NATIONAL ASTRONOMY AND IONOSPHERE CENTER
CORNELL UNIVERSITY
ARECIBO RADIO OBSERVATORY
GREGORIAN UPGRADING

FEED ARM MISCELLANEOUS II

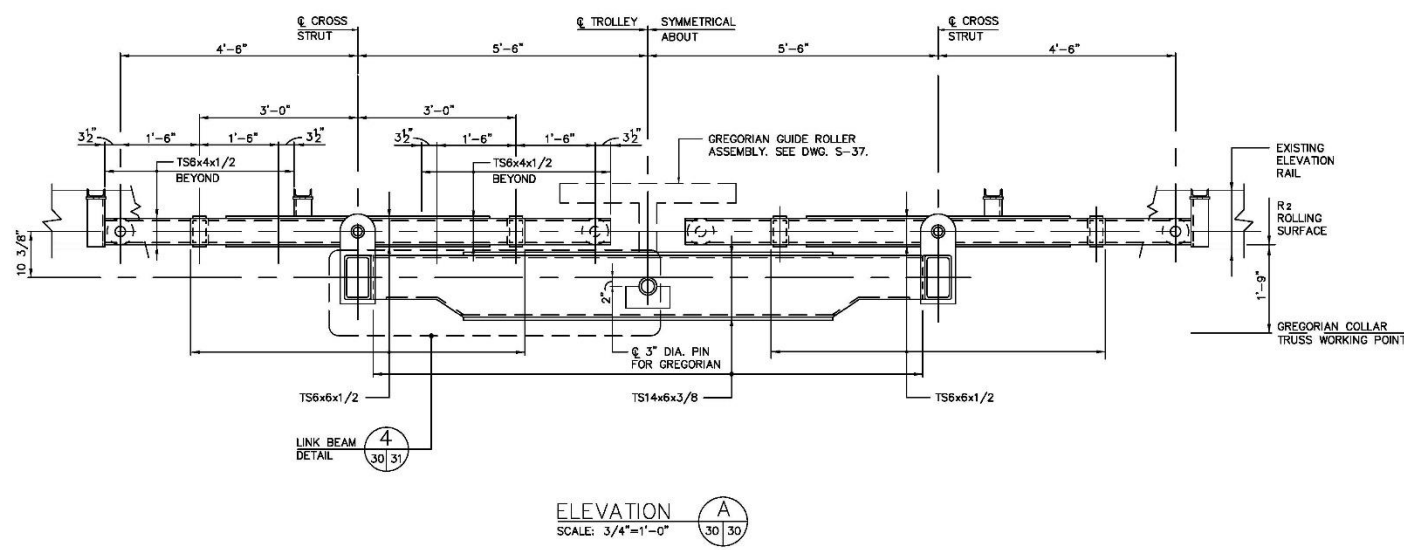
AW AMMANN & WHITNEY, CONSULTING ENGINEERS
NEW YORK, NEW YORK

DRAWN BY:	APPROVED	DATE:
DESIGNED BY:		SCALE: AS NOTED
CHECKED BY:		DWG. NO. S-29

FILE #ARC32



GREGORIAN TROLLEY PLAN
SCALE: 3/4"=1'-0" (2 REQUIRED)



ELEVATION A
SCALE: 3/4"=1'-0"

NOTES:

1. ROUND TUBING SHALL CONFORM TO ASTM A519 GRADE 1026.
2. ALL SHAFTS SHALL CONFORM TO ASTM A108 GRADE 1144.
3. TROLLEY WHEELS SHALL CONFORM TO ASTM A108 GRADE 1045 HARDEN RIMS TO 360 BRINELL, 1/8" DEEP.
4. ALL HARDWARE SHALL BE SILICON COATED WITH LOCKING DEVICES ON ALL BOLTS.
5. PLATES CONFORM TO ASTM A242 GRADE 50.

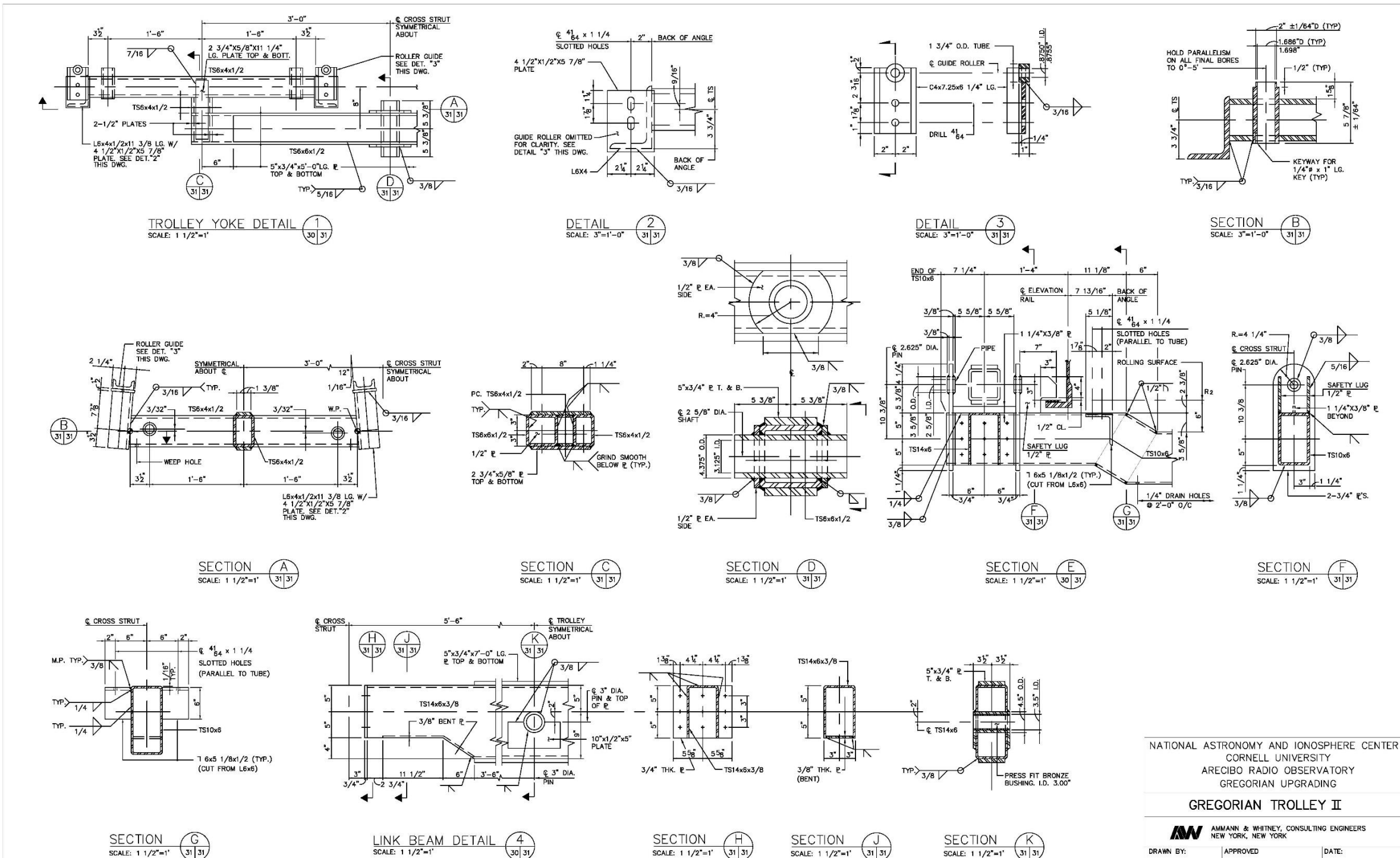
NATIONAL ASTRONOMY AND IONOSPHERE CENTER
CORNELL UNIVERSITY
ARECIBO RADIO OBSERVATORY
GREGORIAN UPGRADING

GREGORIAN TROLLEY I

AW AMMANN & WHITNEY, CONSULTING ENGINEERS
NEW YORK, NEW YORK

DRAWN BY:	APPROVED	DATE:
DESIGNED BY:		SCALE: 3/4"=1'-0"
CHECKED BY:		DWG. NO. S-30

FILE #ARC18



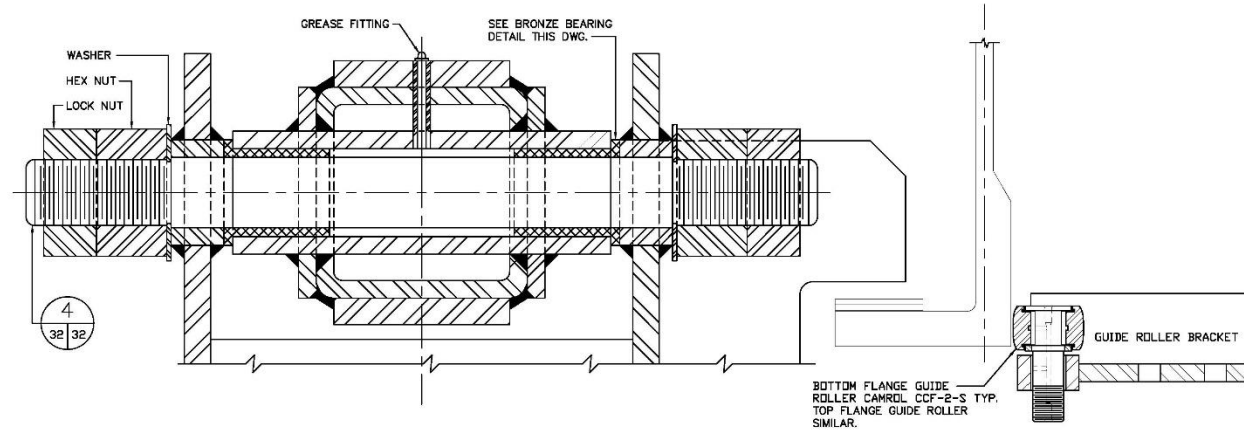
NATIONAL ASTRONOMY AND IONOSPHERE CENTER
 CORNELL UNIVERSITY
 ARECIBO RADIO OBSERVATORY
 GREGORIAN UPGRADING

GREGORIAN TROLLEY II

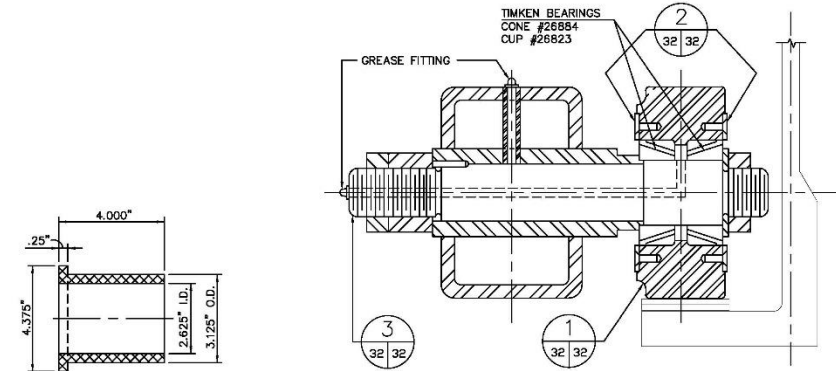
AW AMMANN & WHITNEY, CONSULTING ENGINEERS
 NEW YORK, NEW YORK

DRAWN BY:	APPROVED	DATE:
DESIGNED BY:		SCALE: AS NOTED
CHECKED BY:		DWG. NO. S-31

FILE #ARC19

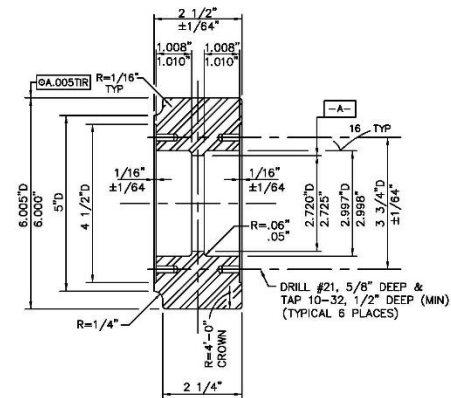


SECTION A
SCALE: 6"=1"

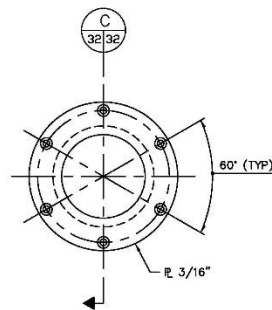


FLANGED OIL-IMPREGNATED
BRONZE BEARING
SCALE: 6"=1"-0"

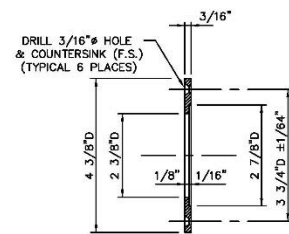
SECTION B
SCALE: 6"=1"-0"



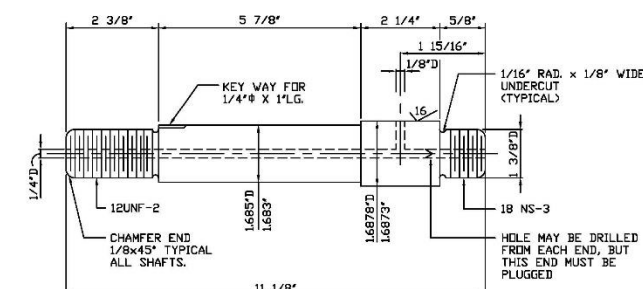
DETAIL 1
SCALE: 6"=1"-0"



DETAIL 2
SCALE: 3"=1"-0"

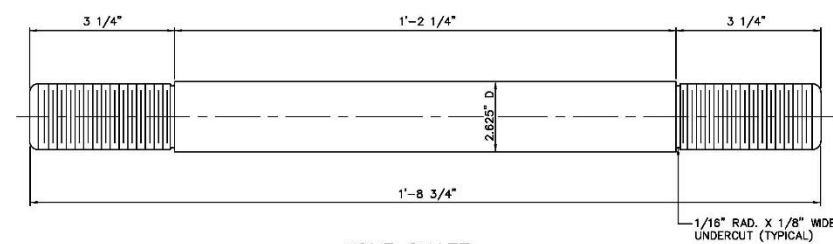


SECTION C
SCALE: 6"=1"-0"



WHEEL SHAFT

DETAIL 3
SCALE: 6"=1"-0"



YOKE SHAFT
DETAIL 4
SCALE: 6"=1"-0"

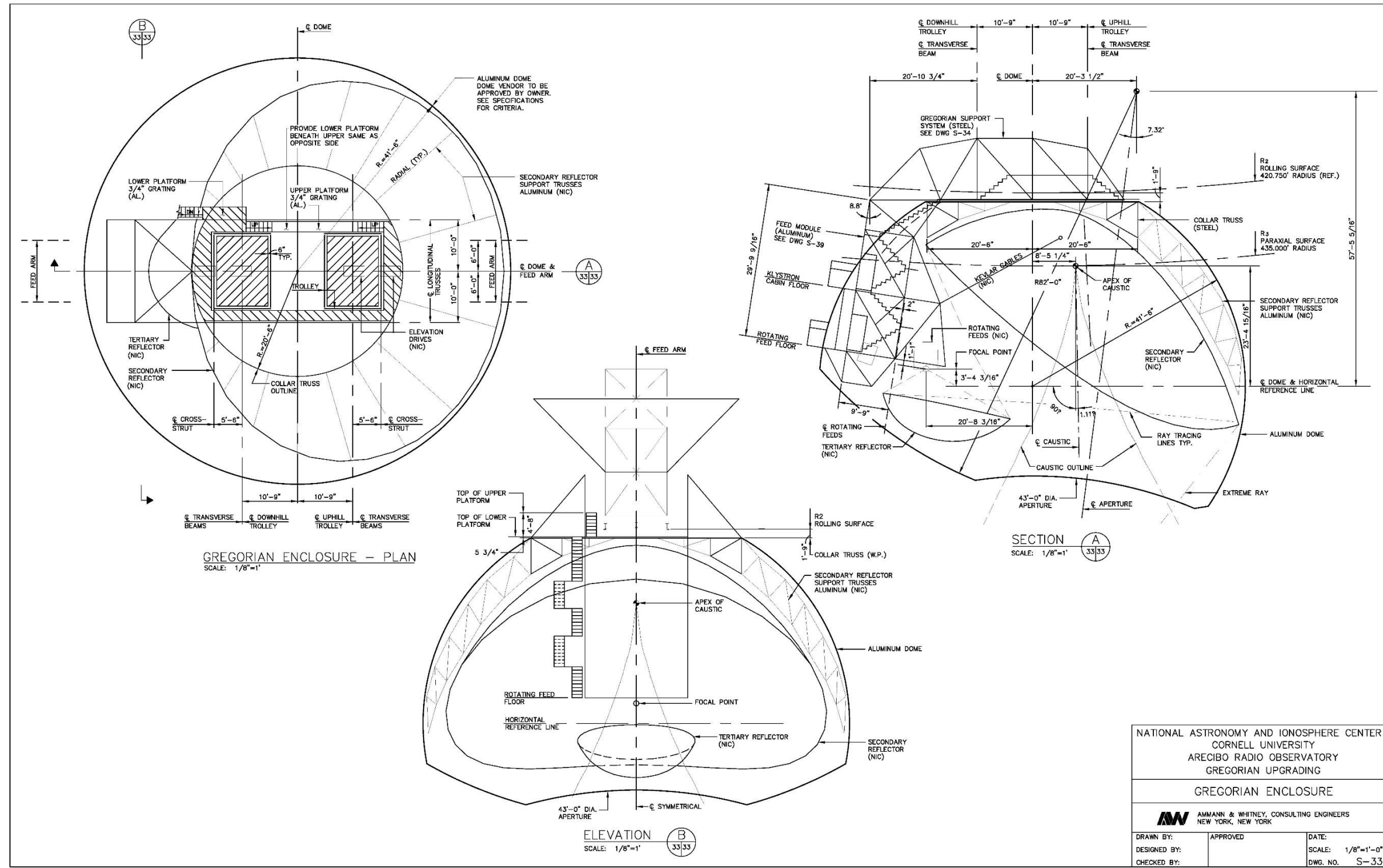
NATIONAL ASTRONOMY AND IONOSPHERE CENTER
CORNELL UNIVERSITY
ARECIBO RADIO OBSERVATORY
GREGORIAN UPGRADING

GREGORIAN TROLLEY III


AMMANN & WHITNEY, CONSULTING ENGINEERS
NEW YORK, NEW YORK

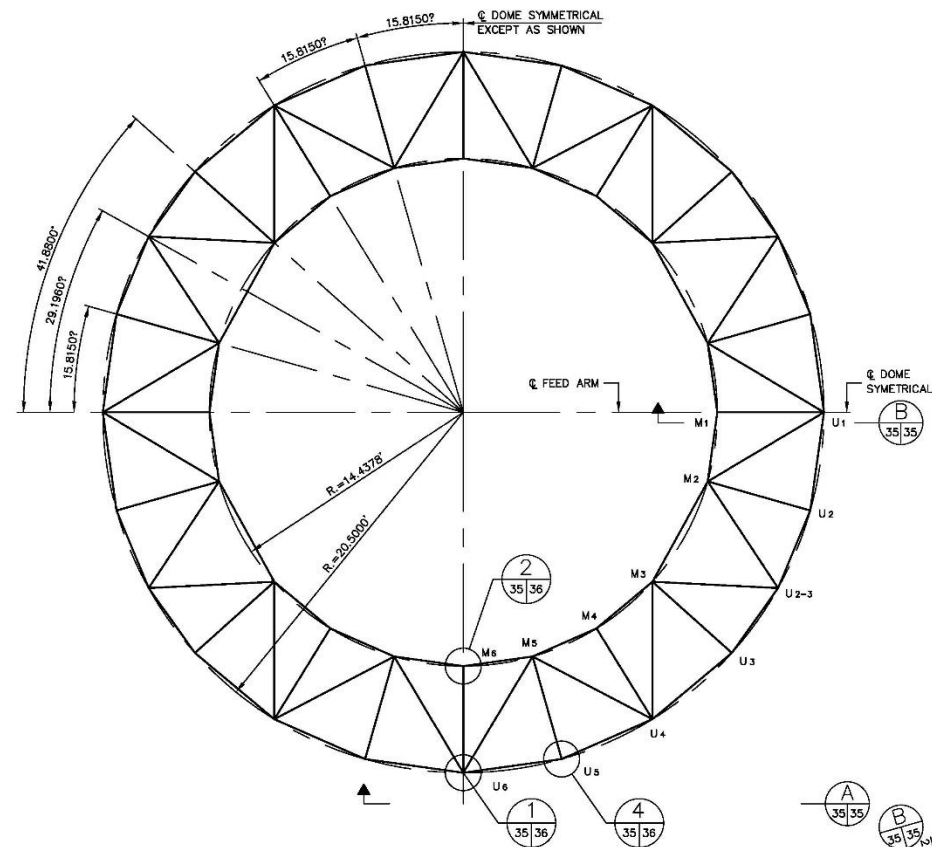
DRAWN BY:	APPROVED	DATE:
DESIGNED BY:		SCALE: 6"=1"-0"
CHECKED BY:		DWG. NO. S-32

FILE #ARC22



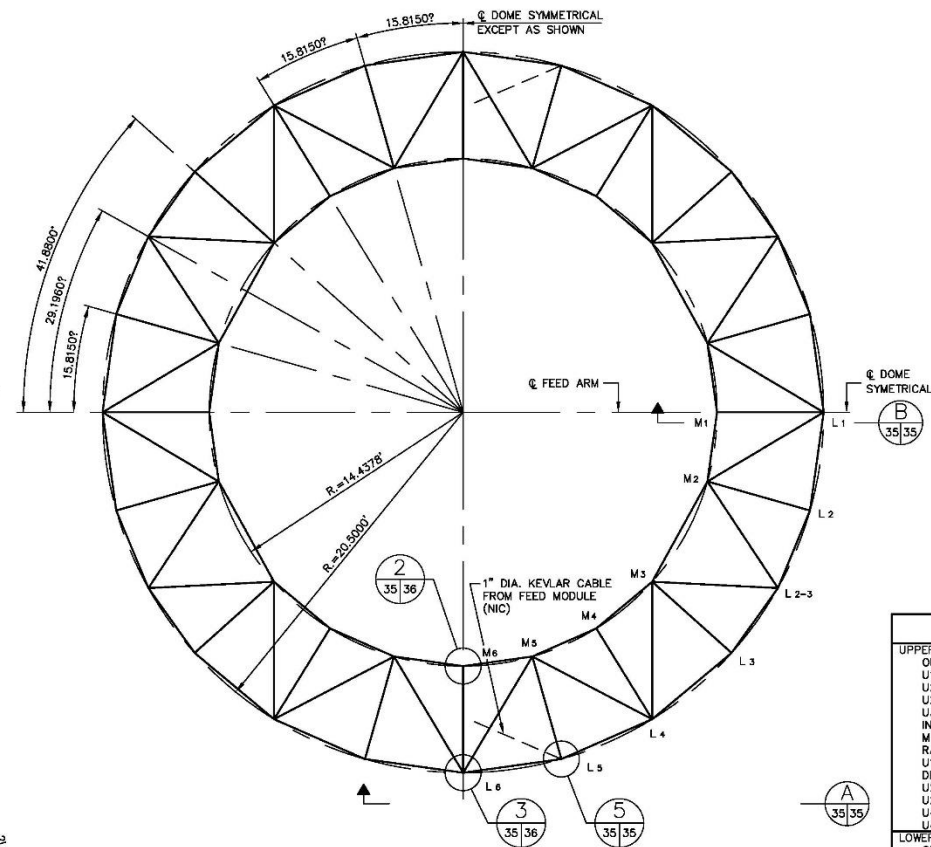
FILE #GRG1

NATIONAL ASTRONOMY AND IONOSPHERE CENTER CORNELL UNIVERSITY ARECIBO RADIO OBSERVATORY GREGORIAN UPGRADING		
GREGORIAN ENCLOSURE		
 AMMANN & WHITNEY, CONSULTING ENGINEERS NEW YORK, NEW YORK		
DRAWN BY:	APPROVED	DATE:
DESIGNED BY:		SCALE: 1/8"=1'-0"
CHECKED BY:		DWG. NO. S-33



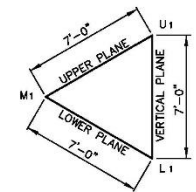
NOTE:
ALL MEMBERS TO BE 2-L2 1/2x2x3/16 UNLESS OTHERWISE NOTED

COLLAR TRUSS - UPPER PLANE
SCALE: 1/4"=1'-0"



NOTE:
ALL MEMBERS TO BE 2-L2 1/2x2x3/16 UNLESS OTHERWISE NOTED

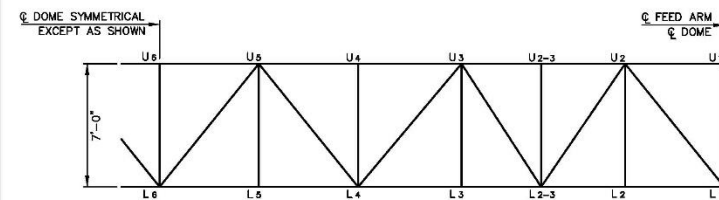
COLLAR TRUSS - LOWER PLANE
SCALE: 1/4"=1'-0"



SECTION B
SCALE: 1/4"=1'-0"

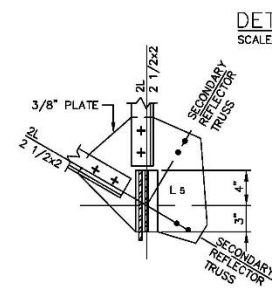
COLLAR TRUSS MEMBERS	
UPPER PLANE	
OUTER CHORD	
U1 - U2	2L- 2 1/2 X 2 X 5/16
U2 - U3	2L- 2 1/2 X 2 X 5/16
U3 - U4	2L- 2 1/2 X 2 X 5/16
U4 - U5	2L- 2 1/2 X 2 X 5/16
U5 - U6	2L- 2 1/2 X 2 X 5/16
INNER CHORD	
M1 - M2	2L- 2 1/2 X 2 X 5/16
RADIALS	
U1 - M2	2L- 2 1/2 X 2 X 5/16
DIAGONALS	
U2-3 - M2	2L- 2 1/2 X 2 X 5/16
U2-3 - M3	2L- 3 1/2 X 2 1/2 X 1/4
U4 - M3	2L- 3 1/2 X 2 1/2 X 1/4
U4 - M5	2L- 2 1/2 X 2 X 5/16
LOWER PLANE	
OUTER CHORD	
L1 - L2	2L- 2 1/2 X 2 X 5/16
L2 - L3	2L- 2 1/2 X 2 X 5/16
L3 - L4	2L- 2 1/2 X 2 X 5/16
L4 - L5	2L- 2 1/2 X 2 X 5/16
L5 - L6	2L- 2 1/2 X 2 X 5/16
RADIALS	
L1 - M2	2L- 2 1/2 X 2 X 5/16
DIAGONALS	
L2-3 - M2	2L- 2 1/2 X 2 X 5/16
L2-3 - M3	2L- 3 1/2 X 2 1/2 X 1/4
L4 - M3	2L- 3 1/2 X 2 1/2 X 1/4
L4 - M5	2L- 2 1/2 X 2 X 5/16
VERTICAL PLANE	
VERTICALS	
U1 - L1	2L- 3 1/2 X 2 1/2 X 1/4
U2-3 - L2-3	2 1/2" SOLID ROUND
DIAGONALS	
L1 - U2	2L- 2 1/2 X 2 X 5/16
U2 - L2-3	2L- 3 1/2 X 2 1/2 X 1/4
L2-3 - U3	2L- 2 1/2 X 2 X 5/16
U3 - L4	2L- 3 1/2 X 2 1/2 X 1/4
L4 - U5	2L- 2 1/2 X 2 X 5/16
U5 - L6	2L- 2 1/2 X 2 X 5/16

NOTES
1) ALL BOLTS IN COLLAR TRUSS ARE 3/4" DIAMETER UNLESS OTHERWISE SHOWN.

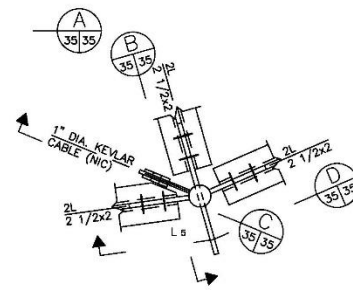


NOTE:
ALL MEMBERS TO BE 2-L2 1/2x2x3/16 UNLESS OTHERWISE NOTED

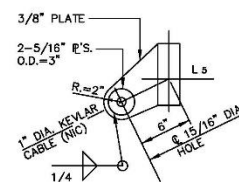
DEVELOPED ELEVATION
SCALE: 1/4"=1'-0"



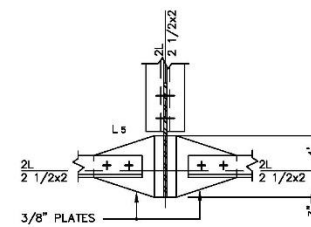
SECTION B
SCALE: 1 1/2"=1"



DETAIL 5
SCALE: 1 1/2"=1'-0"



SECTION C
SCALE: 1 1/2"=1"



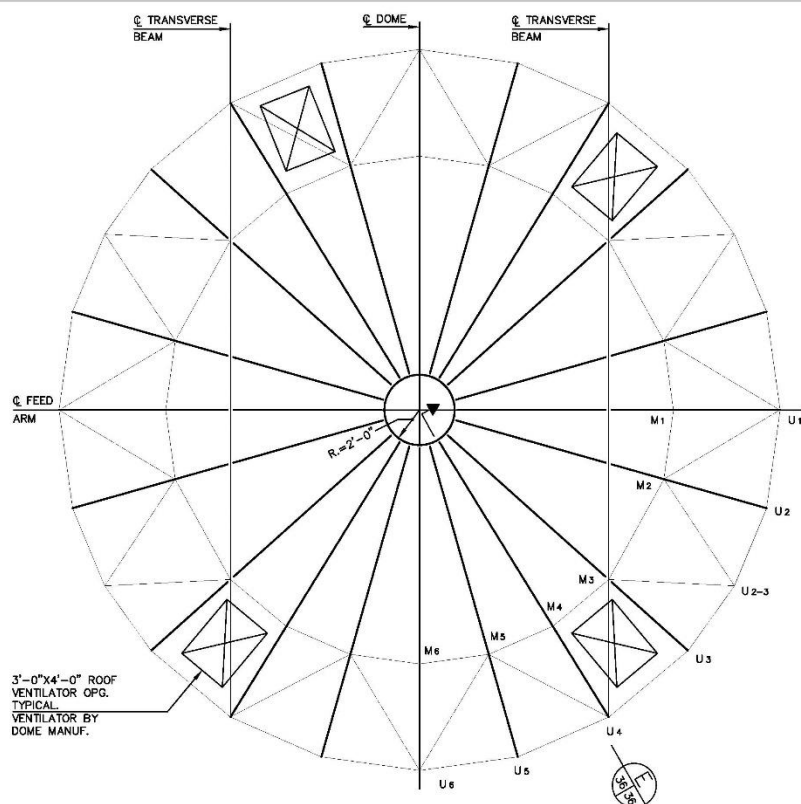
SECTION D
SCALE: 1 1/2"=1"

NATIONAL ASTRONOMY AND IONOSPHERE CENTER
CORNELL UNIVERSITY
ARECIBO RADIO OBSERVATORY
GREGORIAN UPGRADING

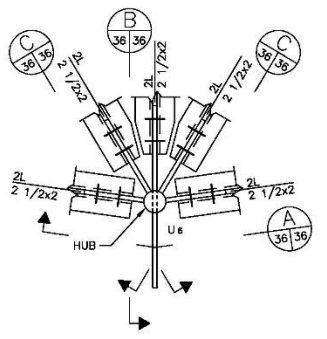
GREGORIAN SUPPORT SYSTEM II

AMMANN & WHITNEY, CONSULTING ENGINEERS
NEW YORK, NEW YORK

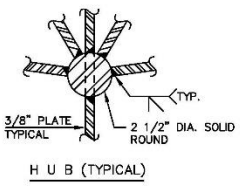
DRAWN BY: APPROVED DATE:
DESIGNED BY: SCALE: 1/4"=1'-0"
CHECKED BY: DWG. NO. S-35



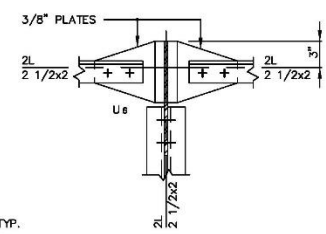
COLLAR TRUSS - ROOF FRAMING PLAN
SCALE: 1/4"=1'



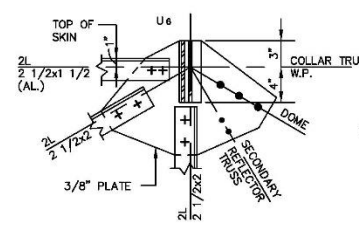
DETAIL 1
SCALE: 1 1/2"=1'-0" 36/36



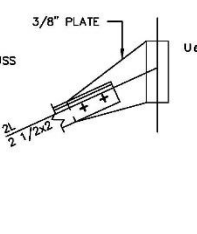
HUB (TYPICAL)



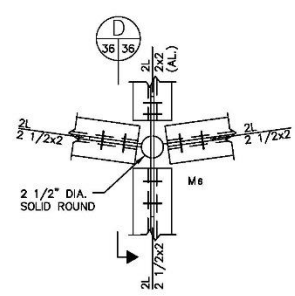
SECTION A
SCALE: 1 1/2"=1' 36/36



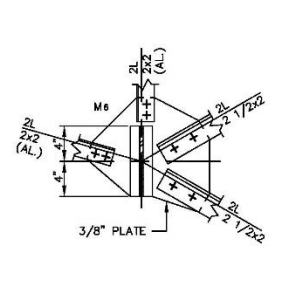
SECTION B
SCALE: 1 1/2"=1' 36/36



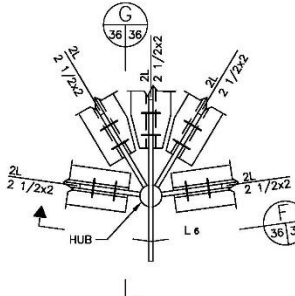
SECTION C
SCALE: 1 1/2"=1' 36/36



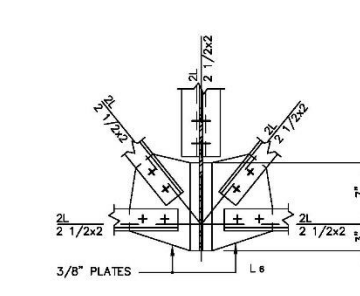
DETAIL 2
SCALE: 1 1/2"=1'-0" 35/36



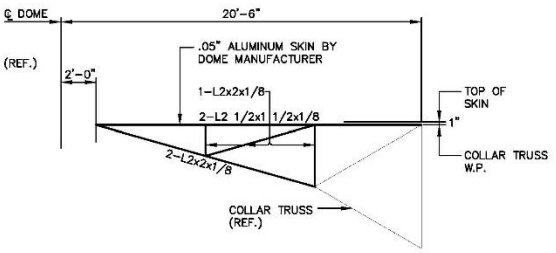
SECTION D
SCALE: 1 1/2"=1'-0" 36/36



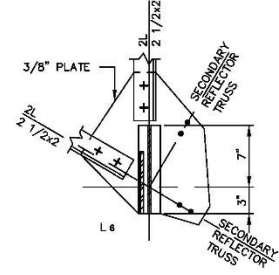
DETAIL 3
SCALE: 1 1/2"=1'-0" 35/36



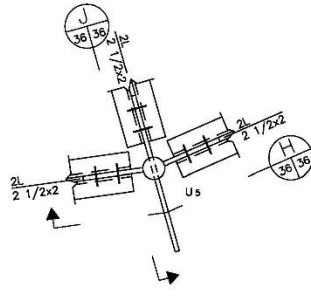
SECTION F
SCALE: 1 1/2"=1'-0" 36/36



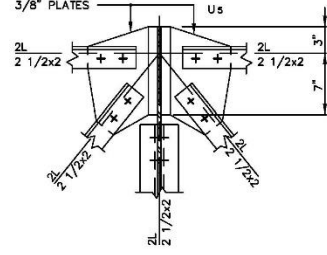
HUB TRUSS (E)
SCALE: 1/4"=1'-0" 36/36



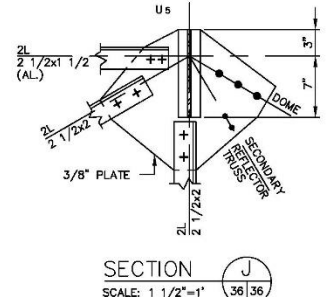
SECTION G
SCALE: 1 1/2"=1'-0" 36/36



DETAIL 4
SCALE: 1 1/2"=1'-0" 35/36



SECTION H
SCALE: 1 1/2"=1'-0" 36/36



SECTION J
SCALE: 1 1/2"=1' 36/36

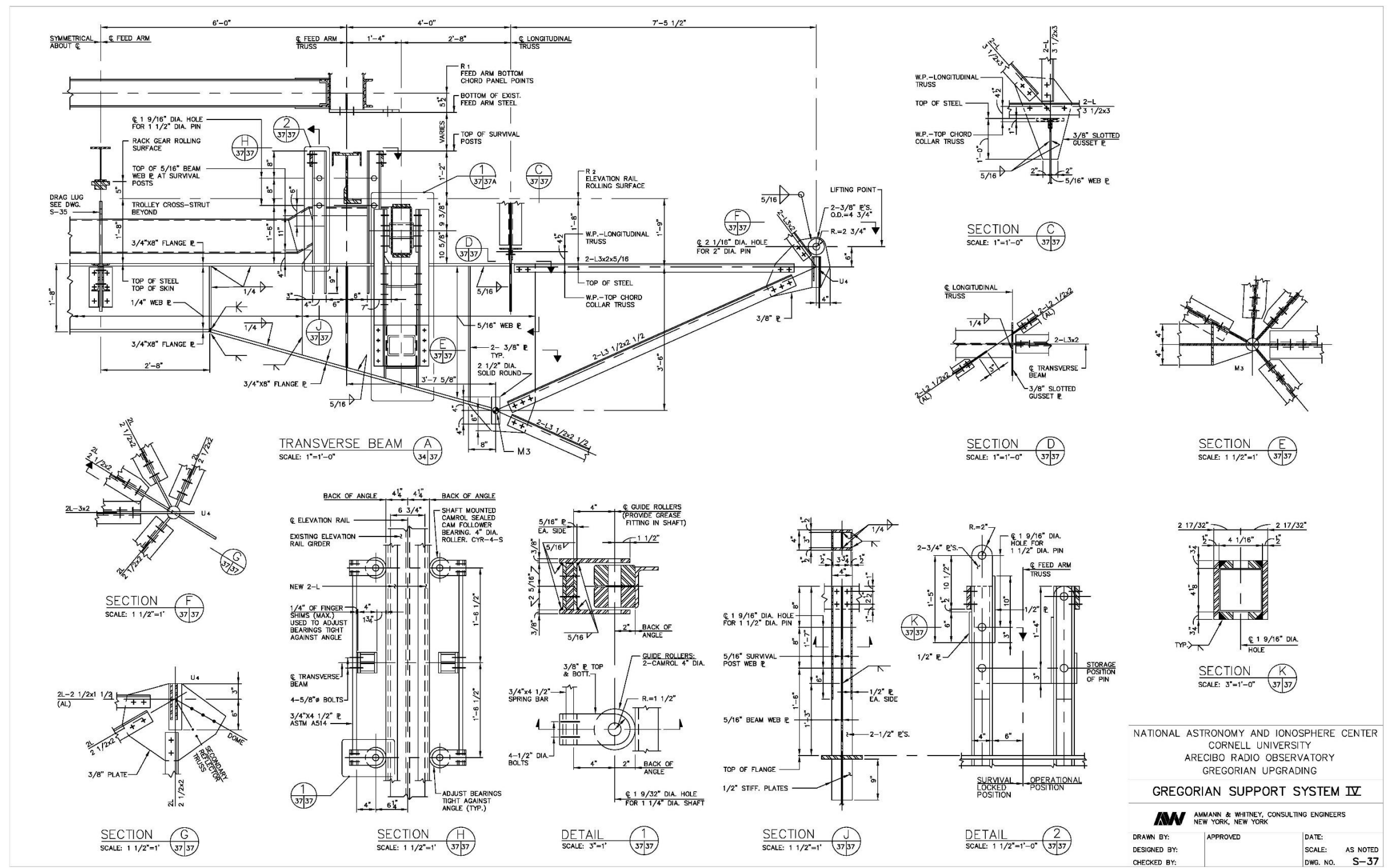
NATIONAL ASTRONOMY AND IONOSPHERE CENTER
CORNELL UNIVERSITY
ARECIBO RADIO OBSERVATORY
GREGORIAN UPGRADING

GREGORIAN SUPPORT SYSTEM III

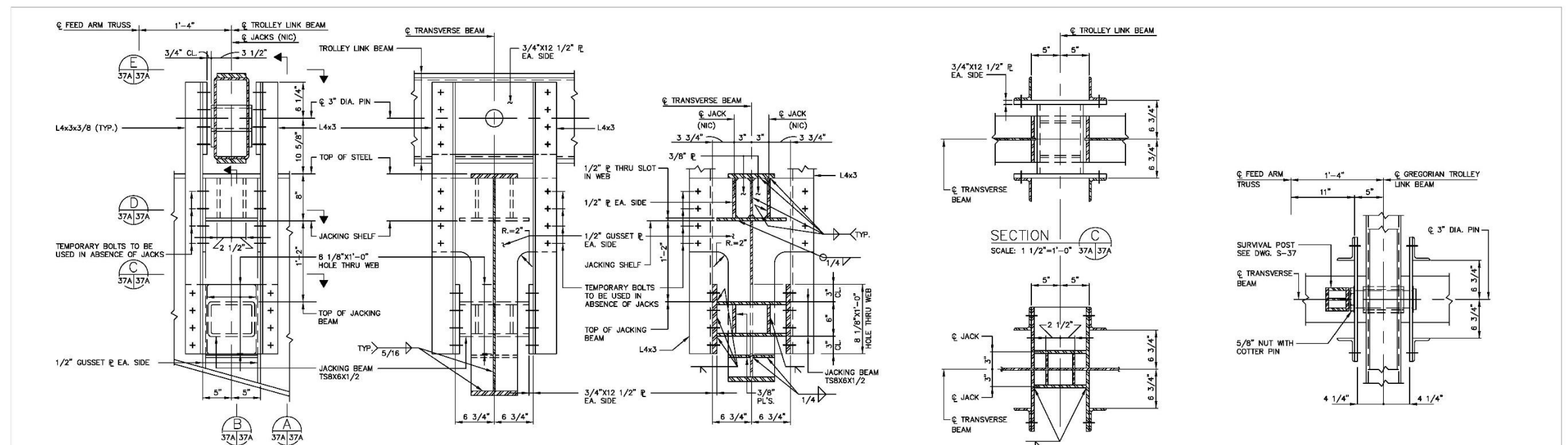
AMMANN & WHITNEY, CONSULTING ENGINEERS
NEW YORK, NEW YORK

DRAWN BY:	APPROVED	DATE:
DESIGNED BY:		SCALE: AS NOTED
CHECKED BY:		DWG. NO. S-36

FILE #ARC40



FILE #ARC38



DETAIL 1
SCALE: 1 1/2"=1'-0" 37A 37A

SECTION A
SCALE: 1 1/2"=1'-0" 37A 37A

SECTION B
SCALE: 1 1/2"=1'-0" 37A 37A

SECTION D
SCALE: 1 1/2"=1'-0" 37A 37A

SECTION E
SCALE: 1 1/2"=1'-0" 37A 37A

NOTES:
1) JACK REQUIREMENTS: 35TON CAPACITY (EACH), 6" STROKE
TOTAL FOR UPWARD OR DOWNWARD MOVEMENT OF 3".

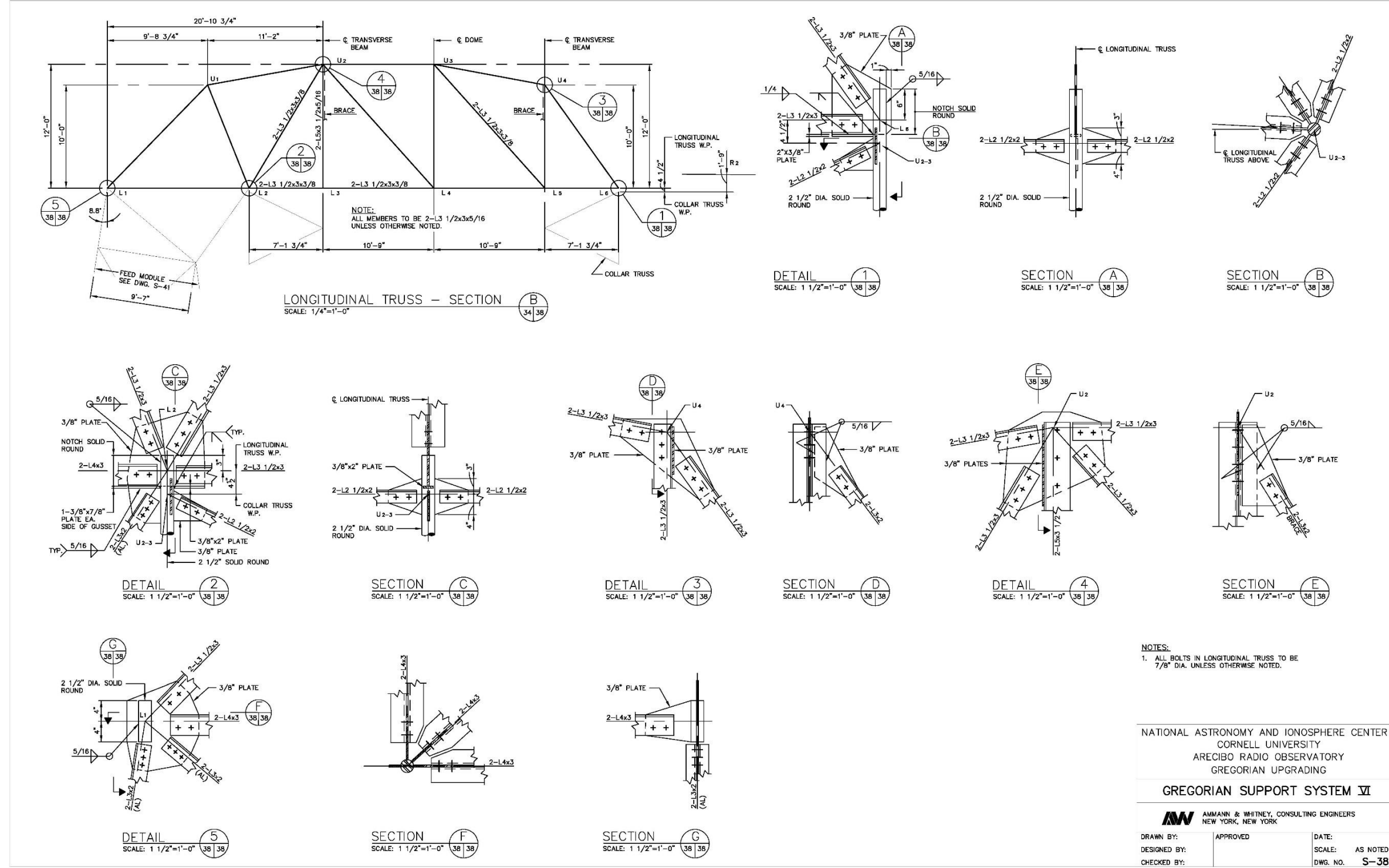
NATIONAL ASTRONOMY AND IONOSPHERE CENTER
CORNELL UNIVERSITY
ARECIBO RADIO OBSERVATORY
GREGORIAN UPGRADING

GREGORIAN SUPPORT SYSTEM IV

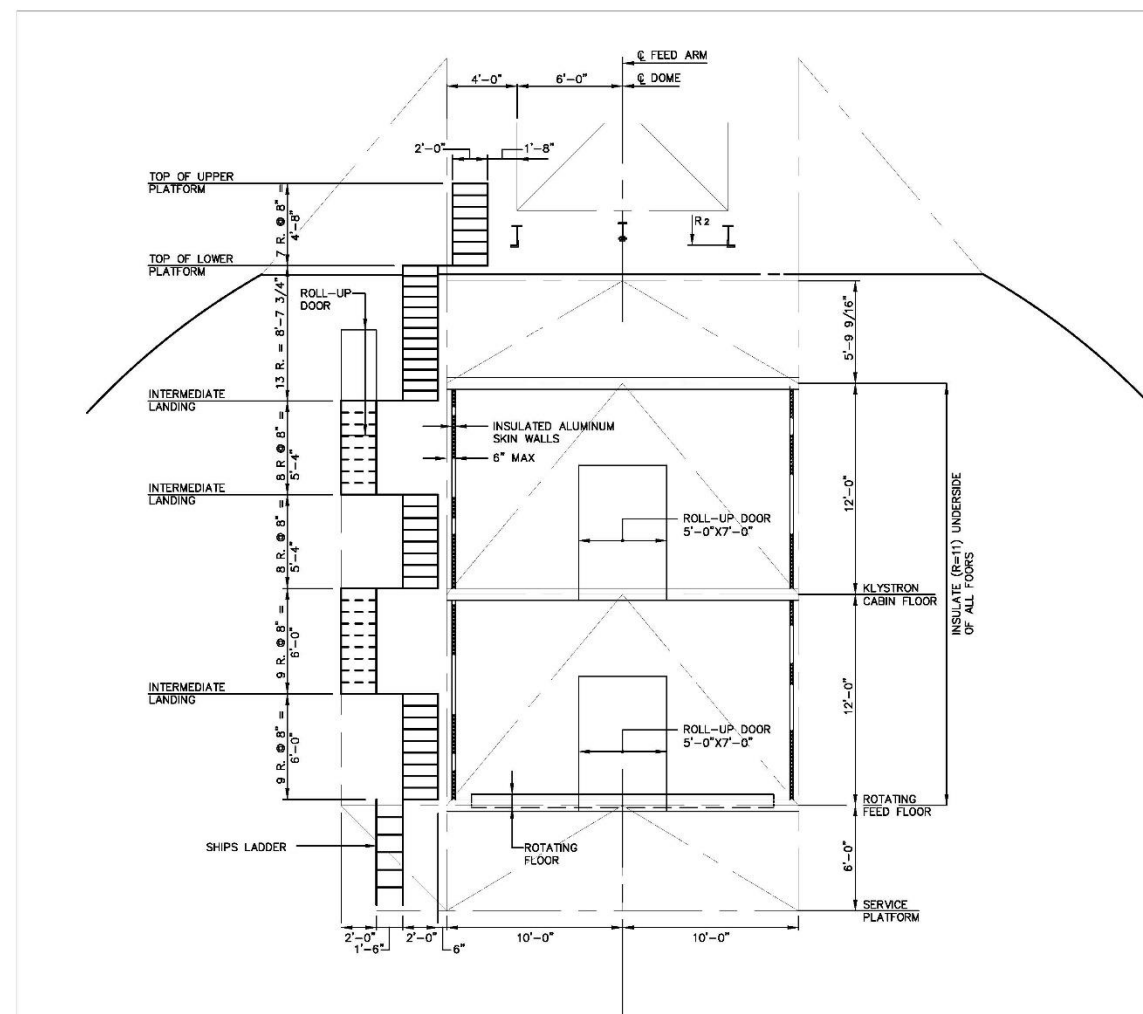
AMMANN & WHITNEY, CONSULTING ENGINEERS
NEW YORK, NEW YORK

DRAWN BY:	APPROVED	DATE:
DESIGNED BY:		SCALE: AS NOTED
CHECKED BY:		DWG. NO. S-37A

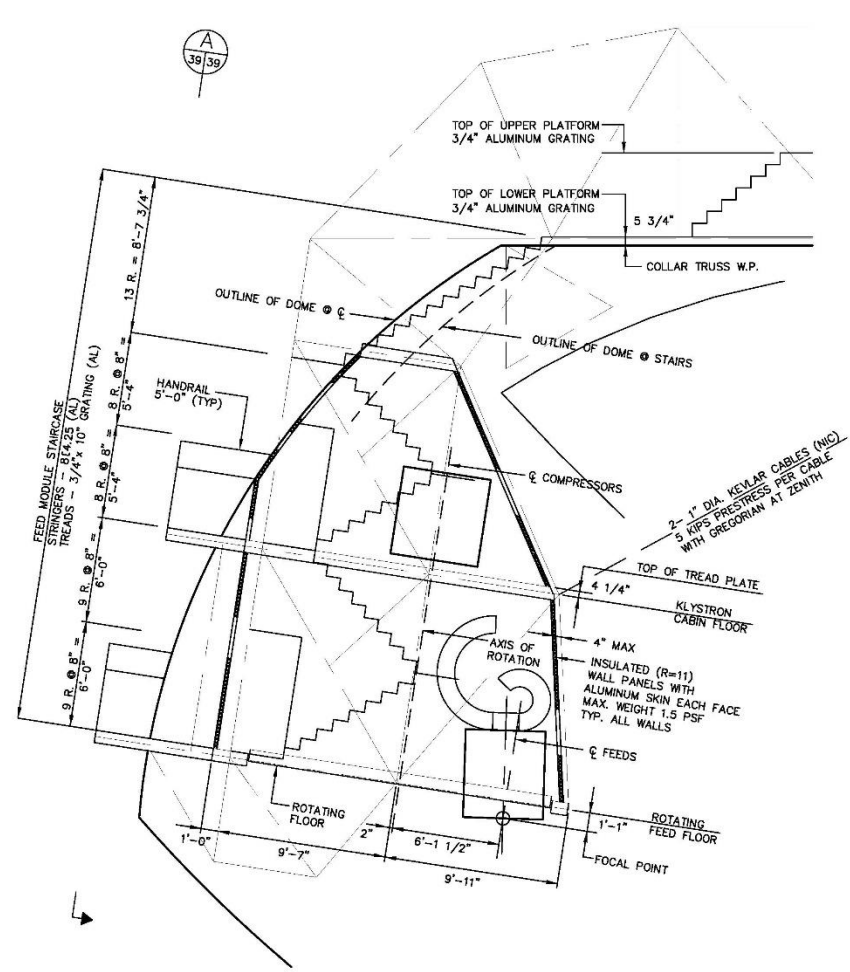
FILE #ARC37A



FILE #ARC37



ELEVATION A
SCALE: 1/4"=1'-0" 39/39



FEED MODULE - SIDE ELEVATION
SCALE: 1/4"=1'-0"

- NOTES:
- 1) PROVIDE 5'-0" ALUMINUM CHAIN LINK FABRIC GUIDE RAILING AT ALL STAIR STRINGERS, LANDINGS, AND PLATFORMS.
 - 2) ALL DOORS INTO DOME SHALL BE WATERTIGHT AND HAND OPERABLE IN 30 MPH WINDS.

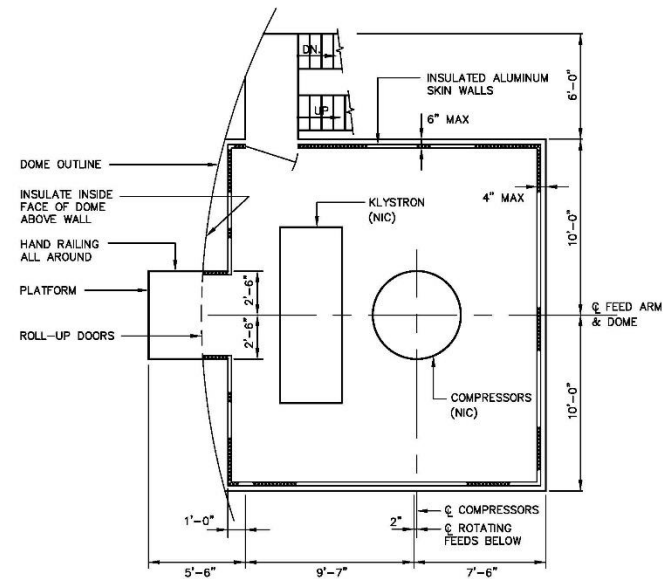
NATIONAL ASTRONOMY AND IONOSPHERE CENTER
CORNELL UNIVERSITY
ARECIBO RADIO OBSERVATORY
GREGORIAN UPGRADING

FEED MODULE I

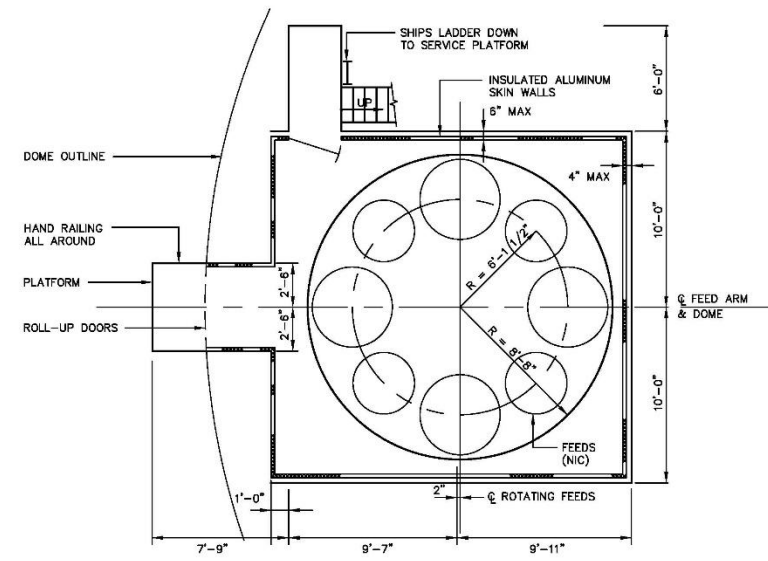
AMMANN & WHITNEY, CONSULTING ENGINEERS
NEW YORK, NEW YORK

DRAWN BY:	APPROVED	DATE:
DESIGNED BY:		SCALE: AS NOTED
CHECKED BY:		DWG. NO. S-39

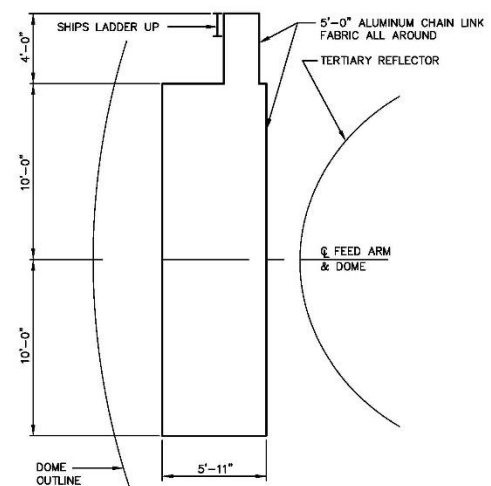
FILE #ARC51



PLAN — KLYSTRON CABIN FLOOR
SCALE: 1/4"=1'-0"



PLAN — ROTATING FEED FLOOR
SCALE: 1/4"=1'-0"



PLAN — SERVICE PLATFORM
SCALE: 1/4"=1'-0"

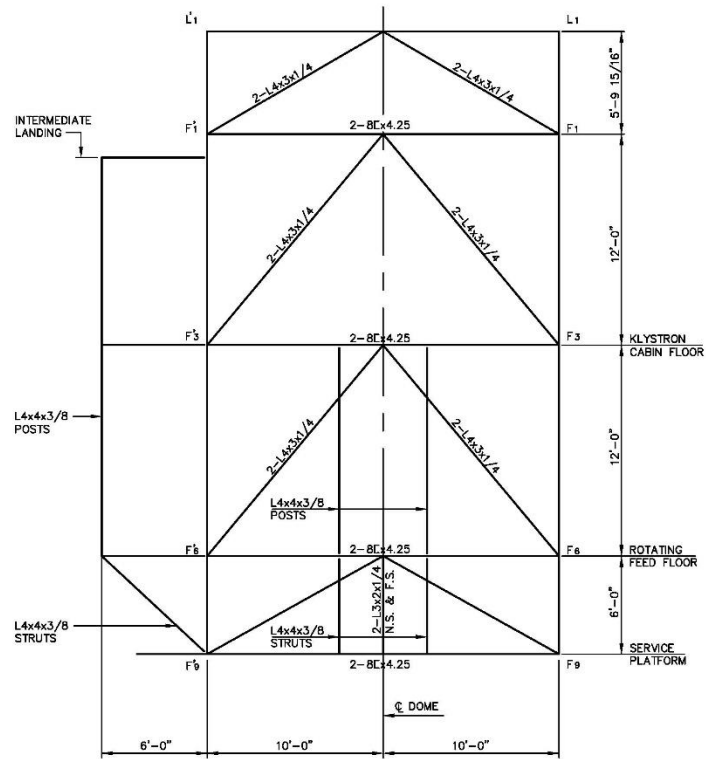
NATIONAL ASTRONOMY AND IONOSPHERE CENTER
CORNELL UNIVERSITY
ARECIBO RADIO OBSERVATORY
GREGORIAN UPGRADING

FEED MODULE II

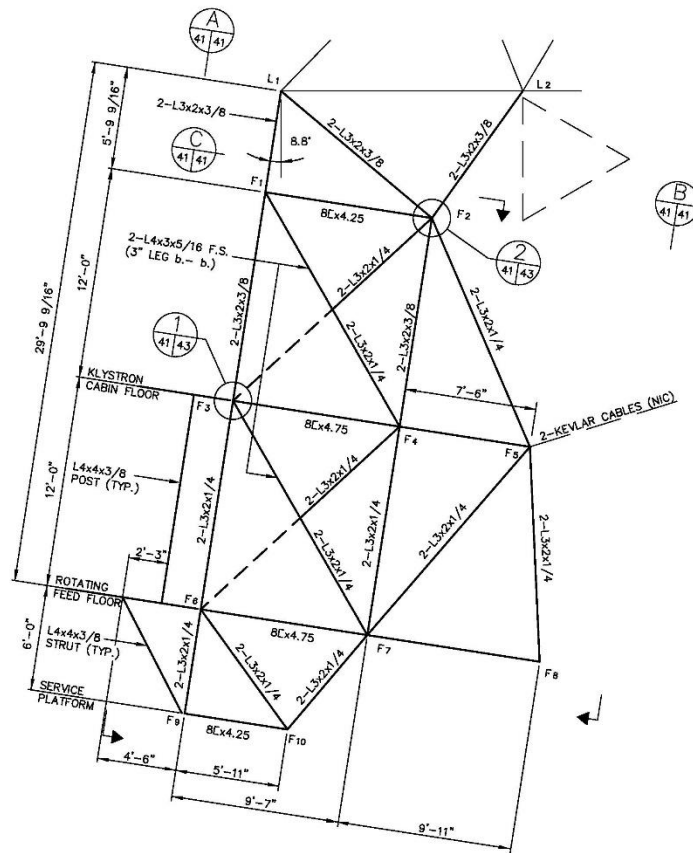
AW AMMANN & WHITNEY, CONSULTING ENGINEERS
NEW YORK, NEW YORK

DRAWN BY:	APPROVED	DATE:
DESIGNED BY:		SCALE: AS NOTED
CHECKED BY:		DWG. NO. S-40

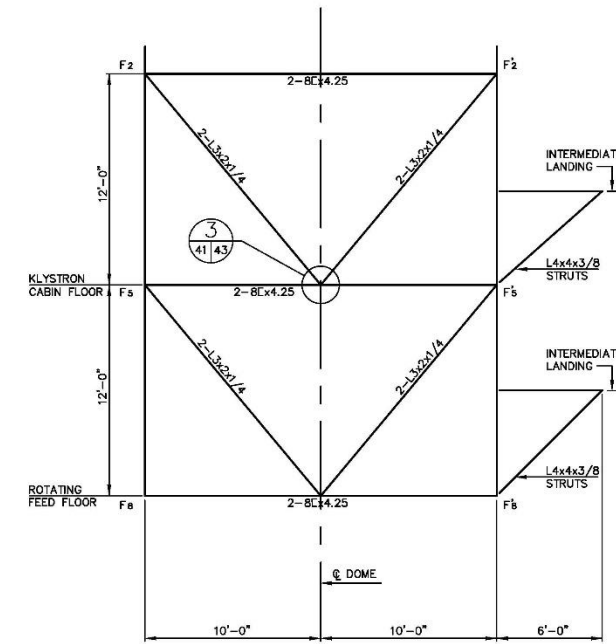
FILE #ARC41



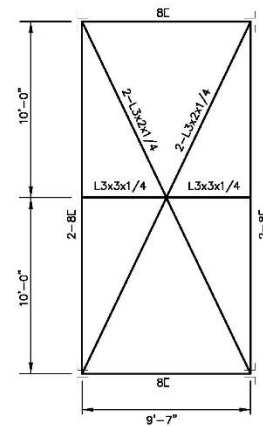
ELEVATION A
SCALE: 1/4"=1'-0" 41 41



FEED MODULE - SIDE ELEVATION
SCALE: 1/4"=1'-0"



ELEVATION B
SCALE: 1/4"=1'-0" 41 41



SECTION C
SCALE: 1/4"=1'-0" 41 41

- NOTES:
1. ALL BOLTS TO BE 1/2" DIA. STAINLESS STEEL. MINIMUM OF TWO (2) BOLTS PER CONNECTION.
 2. ALL GUSSET PLATES TO BE 3/8" THICK ALUMINUM.
 3. ALL SHAPES 6061-T6 ALUMINUM.

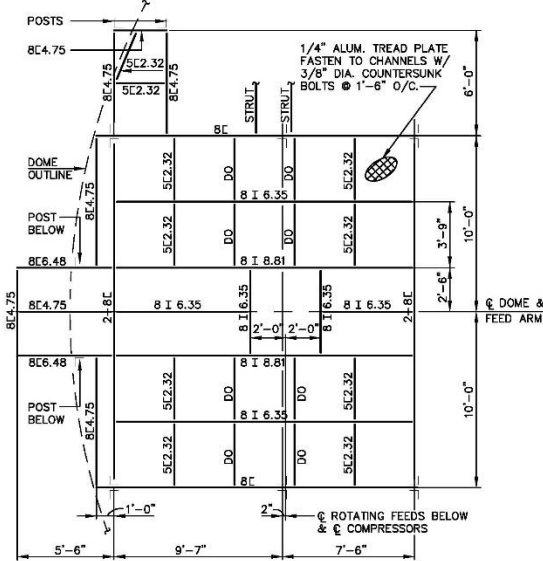
NATIONAL ASTRONOMY AND IONOSPHERE CENTER
CORNELL UNIVERSITY
ARECIBO RADIO OBSERVATORY
GREGORIAN UPGRADING

FEED MODULE FRAMING I

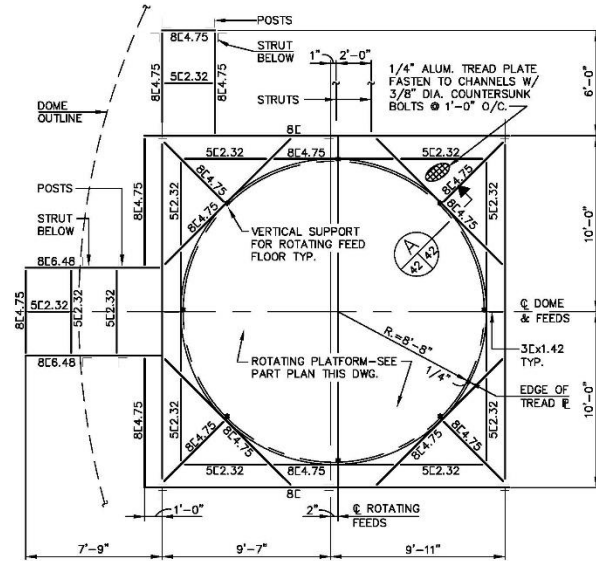
AMMANN & WHITNEY, CONSULTING ENGINEERS
NEW YORK, NEW YORK

DRAWN BY:	APPROVED	DATE:
DESIGNED BY:		SCALE: AS NOTED
CHECKED BY:		DWG. NO. S-41

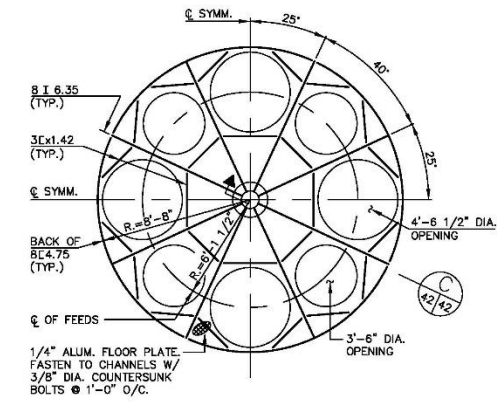
FILE #ARC42



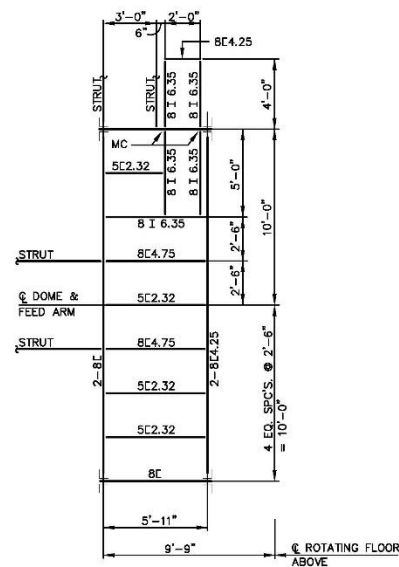
KLYSTRON CABIN FLOOR FRAMING PLAN
SCALE: 1/4"=1'-0"



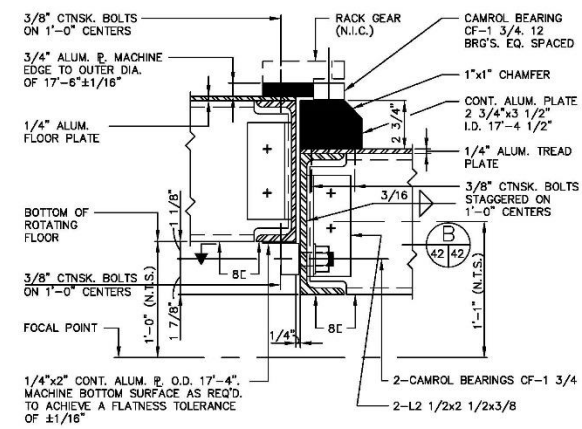
ROTATING FEED FLOOR FRAMING PLAN
SCALE: 1/4"=1'-0"



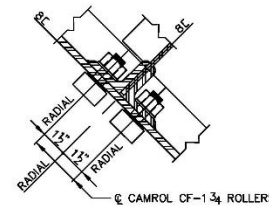
ROTATING FEED PLATFORM FRAMING PLAN
SCALE: 1/4"=1'-0"



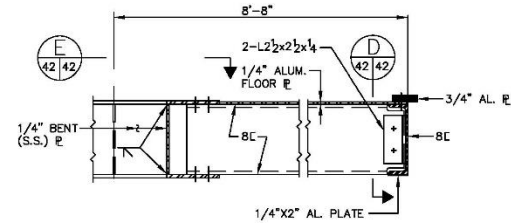
SERVICE PLATFORM FRAMING PLAN
SCALE: 1/4"=1'-0"



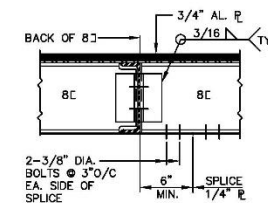
SECTION A
SCALE: 3"=1'-0" 42/42



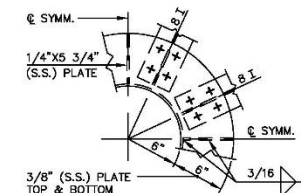
SECTION B
SCALE: 3"=1'-0" 42/42



SECTION C
SCALE: 1 1/2"=1'-0" 42/42



SECTION D
SCALE: 1 1/2"=1'-0" 42/42



SECTION E
SCALE: 1 1/2"=1'-0" 42/42

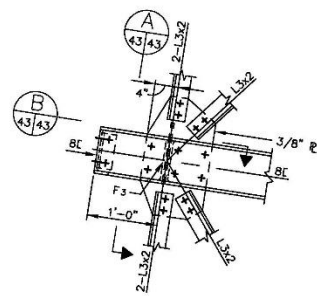
NATIONAL ASTRONOMY AND IONOSPHERE CENTER
CORNELL UNIVERSITY
ARECIBO RADIO OBSERVATORY
GREGORIAN UPGRADING

FEED MODULE FRAMING II

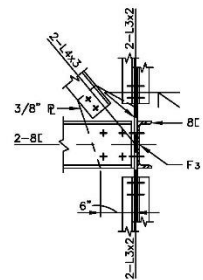
AW AMMANN & WHITNEY, CONSULTING ENGINEERS
NEW YORK, NEW YORK

DRAWN BY:	APPROVED	DATE:
DESIGNED BY:		SCALE: AS NOTED
CHECKED BY:		DWG. NO. S-42

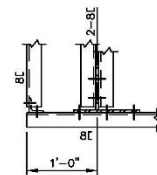
FILE #ARC43



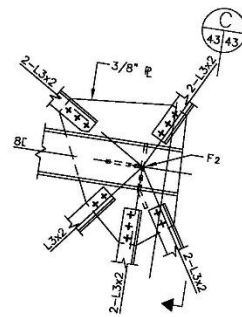
DETAIL 1
SCALE: 1"=1'-0" 41 | 43



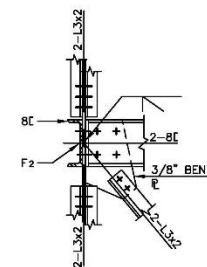
SECTION A
SCALE: 1"=1'-0" 43 | 43



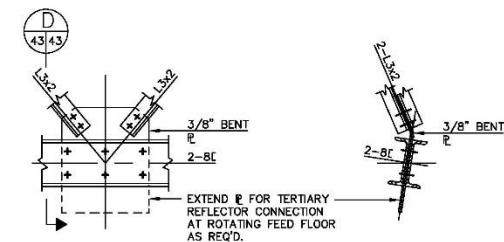
SECTION B
SCALE: 1"=1'-0" 43 | 43



DETAIL 2
SCALE: 1"=1'-0" 41 | 43



SECTION C
SCALE: 1"=1'-0" 43 | 43



DETAIL 3
SCALE: 1"=1'-0" 41 | 43

SECTION D
SCALE: 1"=1'-0" 43 | 43

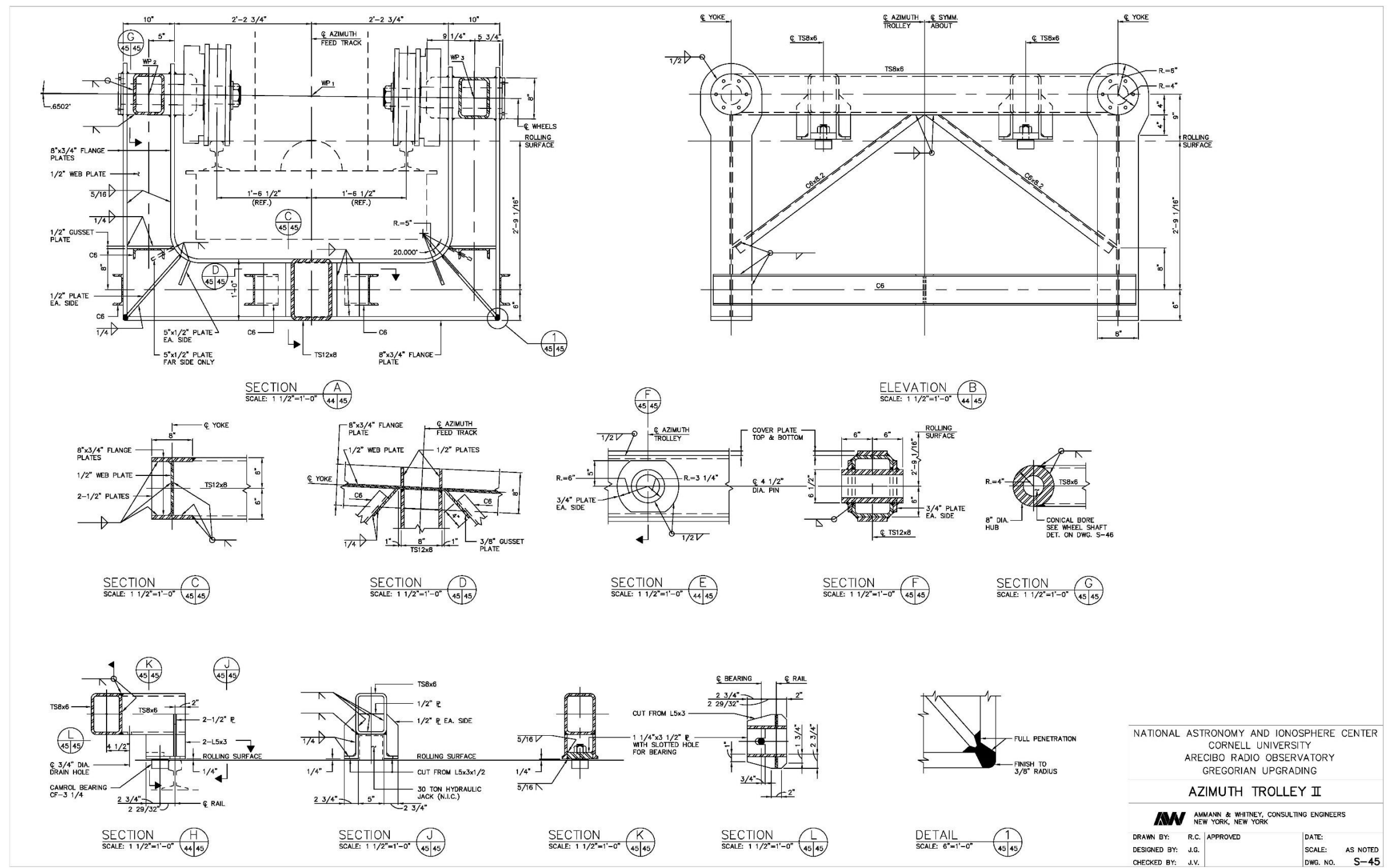
NATIONAL ASTRONOMY AND IONOSPHERE CENTER
CORNELL UNIVERSITY
ARECIBO RADIO OBSERVATORY
GREGORIAN UPGRADING

FEED MODULE FRAMING III

AW AMMANN & WHITNEY, CONSULTING ENGINEERS
NEW YORK, NEW YORK

DRAWN BY:	APPROVED	DATE:
DESIGNED BY:		SCALE: AS NOTED
CHECKED BY:		DWG. NO. S-43

FILE #ARC52



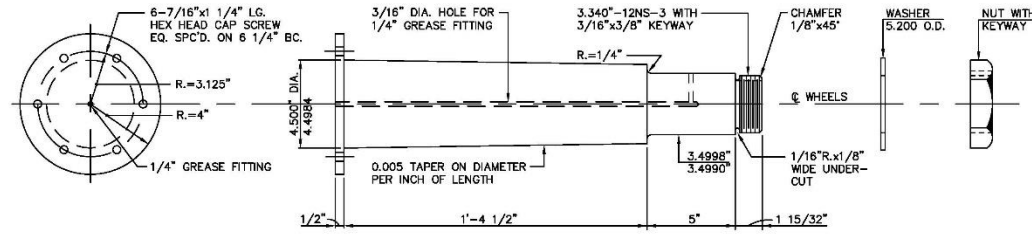
NATIONAL ASTRONOMY AND IONOSPHERE CENTER
 CORNELL UNIVERSITY
 ARECIBO RADIO OBSERVATORY
 GREGORIAN UPGRADING

AZIMUTH TROLLEY II

AW AMMANN & WHITNEY, CONSULTING ENGINEERS
 NEW YORK, NEW YORK

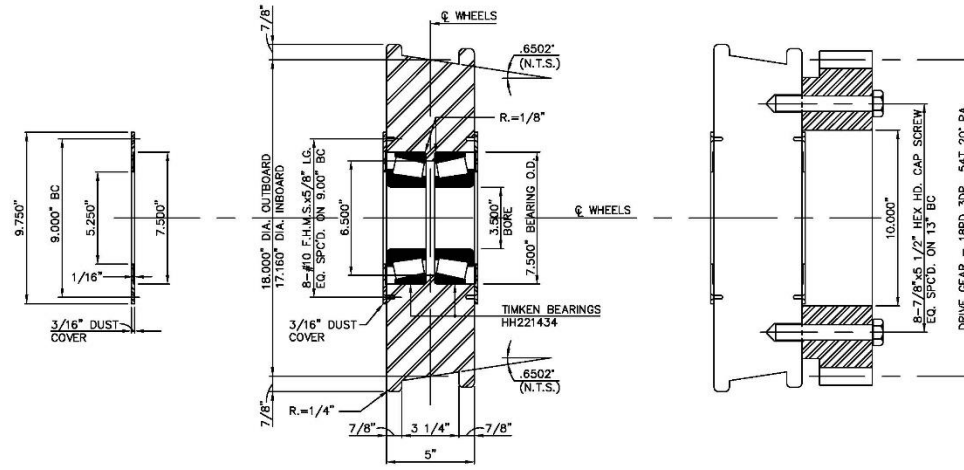
DRAWN BY:	R.C. APPROVED	DATE:
DESIGNED BY:	J.G.	SCALE:
CHECKED BY:	J.V.	DWG. NO. S-45

FILE #ARCS4



TYPICAL WHEEL SHAFT

SCALE: 3"=1'-0"
 NOTE: WHEEL SHAFTS SHALL BE ASTM A108 GR 11L44.



TYPICAL WHEEL

SCALE: 3"=1'-0"
 NOTE: WHEELS SHALL BE ASTM A108 GR. 1045 HARDENED RIMS TO 360 BRINELL 1/8" DEEP.

TYPICAL DRIVE GEAR

SCALE: 3"=1'-0"
 NOTES:
 1) INBOARD DRIVE WHEEL SHOWN, OUTBOARD DRIVE WHEEL SIMILAR.
 2) GEAR MATERIAL TO BE SAE 2512.

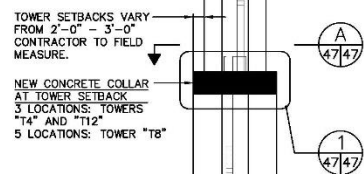
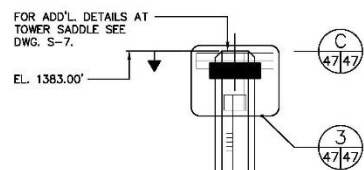
FILE #ARC55

NATIONAL ASTRONOMY AND IONOSPHERE CENTER
 CORNELL UNIVERSITY
 ARECIBO RADIO OBSERVATORY
 GREGORIAN UPGRADING

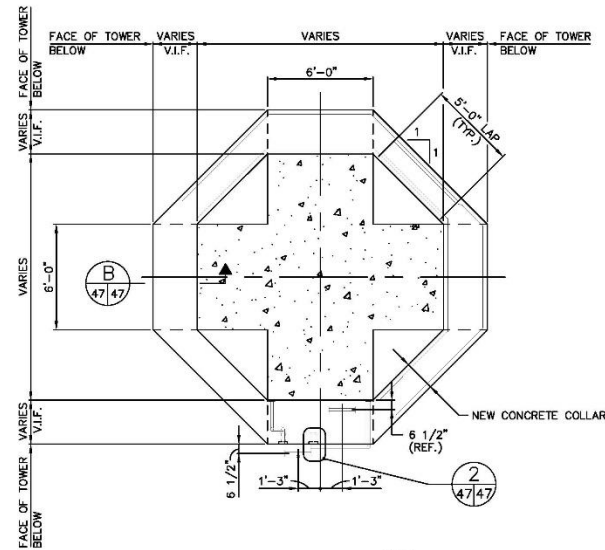
AZIMUTH TROLLEY III

AW AMMANN & WHITNEY, CONSULTING ENGINEERS
 NEW YORK, NEW YORK

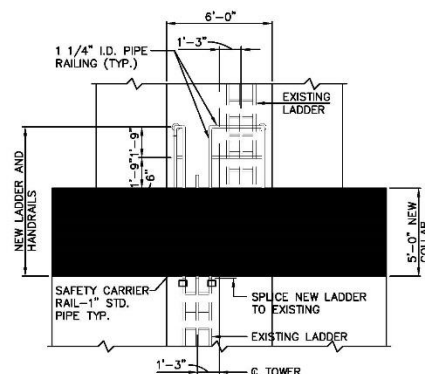
DRAWN BY: R.C.	APPROVED:	DATE:
DESIGNED BY: J.G.		SCALE: AS NOTED
CHECKED BY: J.V.		DWG. NO. S-46



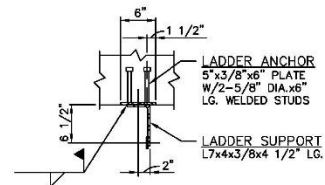
TYPICAL EXISTING TOWER ELEVATION
SCALE: 1/16"=1'-0"



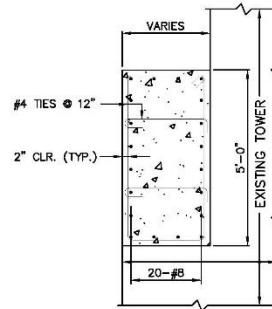
SECTION A
SCALE: 1/4"=1'-0"
47/47



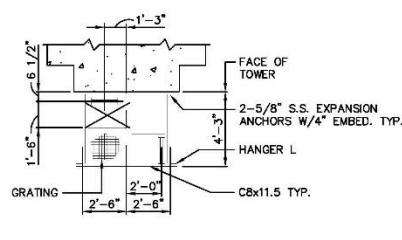
DETAIL 1
SCALE: 1/4"=1'-0"
47/47



DETAIL 2
SCALE: 1/4"=1'-0"
47/47

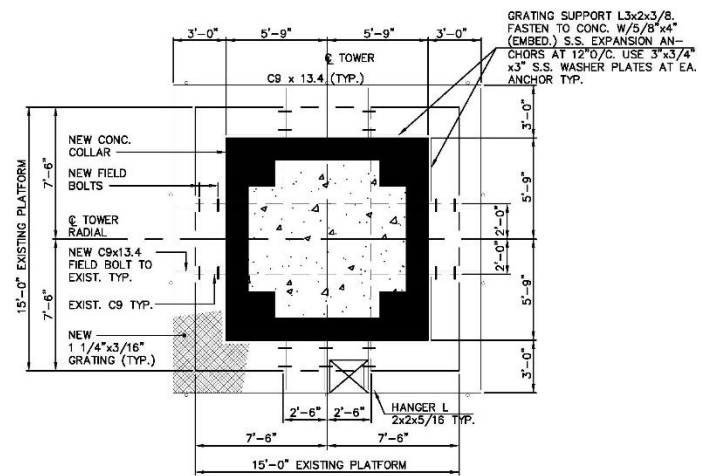


SECTION B
SCALE: 1/4"=1'-0"
47/47

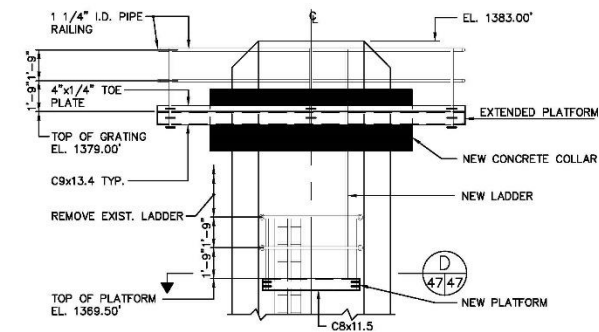


PLATFORM AT EL. 1369.50'

SECTION D
SCALE: 1/4"=1'-0"
47/47



SECTION C
SCALE: 1/4"=1'-0"
47/47



DETAIL 3
SCALE: 1/4"=1'-0"
47/47

- NOTES:
1) MINIMUM CONCRETE COMPRESSIVE STRENGTH f_c SHALL BE 4000 P.S.I. AT 28 DAYS.
2) CHAMFER ALL EXPOSED CONCRETE EDGES 1"x1".

NATIONAL ASTRONOMY AND IONOSPHERE CENTER
CORNELL UNIVERSITY
ARECIBO RADIO OBSERVATORY
GREGORIAN UPGRADING

TOWER COLLARS, STEEL PLATFORMS & LADDERS

AMMANN & WHITNEY, CONSULTING ENGINEERS
NEW YORK, NEW YORK

DRAWN BY: R.C. APPROVED
DESIGNED BY: J.G.
CHECKED BY: J.V.

DATE:
SCALE: AS NOTED
DWG. NO. S-47

REPORT DOCUMENTATION PAGE

*Form Approved
OMB No. 0704-0188*

The public reporting burden for this collection of information is estimated to average 1 hour per response, including the time for reviewing instructions, searching existing data sources, gathering and maintaining the data needed, and completing and reviewing the collection of information. Send comments regarding this burden estimate or any other aspect of this collection of information, including suggestions for reducing the burden, to Department of Defense, Washington Headquarters Services, Directorate for Information Operations and Reports (0704-0188), 1215 Jefferson Davis Highway, Suite 1204, Arlington, VA 22202-4302. Respondents should be aware that notwithstanding any other provision of law, no person shall be subject to any penalty for failing to comply with a collection of information if it does not display a currently valid OMB control number.
PLEASE DO NOT RETURN YOUR FORM TO THE ABOVE ADDRESS.

1. REPORT DATE (DD-MM-YYYY) 06/24/2021	2. REPORT TYPE Technical Memorandum	3. DATES COVERED (From - To)
--------------------------------------------------	-----------------------------------------------	-------------------------------------

4. TITLE AND SUBTITLE Arecibo Observatory Auxiliary M4N Socket Termination Failure Investigation	5a. CONTRACT NUMBER
	5b. GRANT NUMBER
	5c. PROGRAM ELEMENT NUMBER

6. AUTHOR(S) Harrigan, Gregory; Valinia, Azita; Trepal, Nathan; Babuska, Pavel; Goyal, Vinay	5d. PROJECT NUMBER
	5e. TASK NUMBER
	5f. WORK UNIT NUMBER 869021.01.23.01.01

7. PERFORMING ORGANIZATION NAME(S) AND ADDRESS(ES) NASA Langley Research Center Hampton, VA 23681-2199	8. PERFORMING ORGANIZATION REPORT NUMBER
---------------------------------------------------------------------------------------------------------------------	-------------------------------------------------

9. SPONSORING/MONITORING AGENCY NAME(S) AND ADDRESS(ES) National Aeronautics and Space Administration Washington, DC 20546-0001	10. SPONSOR/MONITOR'S ACRONYM(S) NASA
	11. SPONSOR/MONITOR'S REPORT NUMBER(S) NASA/TM-20210017934

12. DISTRIBUTION/AVAILABILITY STATEMENT
Unclassified - Unlimited
Subject Category Electronics and Electrical Engineering
Availability: NASA STI Program (757) 864-9658

13. SUPPLEMENTARY NOTES

14. ABSTRACT
The NASA Engineering and Safety Center (NESC) was requested to support the Arecibo Observatory failure investigation in determining the root cause of the Auxiliary M4N cable failure. The NESC and Kennedy Space Center led an integrated NASA investigation with support from Marshall Space Flight Center and The Aerospace Corporation that included forensic investigation of failed hardware, finite element modeling, materials characterization, and root cause analysis. This document contains the outcome of the NESC Assessment.

15. SUBJECT TERMS
NASA Engineering and Safety Center; Arecibo Observatory; Auxiliary M4N Cable Failure

16. SECURITY CLASSIFICATION OF:			17. LIMITATION OF ABSTRACT	18. NUMBER OF PAGES	19a. NAME OF RESPONSIBLE PERSON
a. REPORT	b. ABSTRACT	c. THIS PAGE			STI Help Desk (email: help@sti.nasa.gov)
U	U	U	UU	640	19b. TELEPHONE NUMBER (Include area code) (443) 757-5802